Fluid Flow and Deformation Partitioning during blueschist exhumation, Syros, Greece

Clare E. Bond

This thesis is submitted for the degree of
Doctor of Philosophy
University of Edinburgh
1999

I declare that this thesis is my own work,
except where otherwise stated

Clare E. Bond

Abstract

Deformation, metamorphism and fluid infiltration are important processes in crustal evolution. This thesis is concerned with how these processes interact to remodel the crust after orogenesis. Localisation of strain, fluid infiltration and metamorphic reactions all play a part in controlling the rheological properties of rocks deep in the crust and these factors will therefore influence the process of exhumation, and control the structural and metamorphic development of an exhuming terrain. It has been shown that these processes do not act independently. Complex patterns of inter-linked deformation and hydration of metamorphic assemblages are often superimposed, such that orogenic fabrics and mineral assemblages are partially overprinted by exhumation fabrics and assemblages. Thus, a chronology of deformation, metamorphism and infiltration can be determined and by identifying the depths and temperatures at which events occurred, the exhumation process can be unravelled.

The island of Syros in the Attic Cycladic blueschist belt of Greece was chosen for study as it is characterised by a high pressure blueschist facies assemblage (T = 450 ^{o}C and P >14 kbars) which has been variably overprinted within the greenschist facies stability field. The partial overprinting has resulted in the preservation of high pressure fabrics. This preservation combined with local down-pressure superimposition of deformation fabrics and recrystallisation allows a chronology of events to be determined making Syros an ideal locality for the study of structural and metamorphic evolution during exhumation. Syros consists of interleaved schist and marble units, with local metabasite horizons. The units are layered and generally dip shallowly to the NE. The partial overprinting of metamorphic assemblages has been used to link down-pressure fabric development, fluid infiltration and metamorphism, whilst the interleaving of lithologies has allowed an assessment to be made of the lithological controls on fluid channelling.

Direct observations of fluid channelling cannot always be made. Evidence for fluid infiltration is often overprinted during recrystallisation and fabric development. This study has therefore combined field observations with petrographic, geochemical and stable isotope studies to document fluid pathways. By combining field and analytical techniques I have demonstrated that fluid pathways are spatially associated with the partitioning of deformation, and in reactive lithologies with retrogressive metamorphism. In northern Syros the greenschist overprint is localised and spatially associated with brittle fracture-controlled fluid infiltration. Locally, blueschist assemblages are cut by greenschist facies veins, which are surrounded by greenschist retrogressive haloes. I have shown by geochemical analysis that retrogression in vein haloes is the result of fluid infiltration from the vein into the host rock. In haloes containing albite porphyroblasts, hydration is accompanied by Na-influx. These localised areas of retrogression have been used to link fracture controlled fluid infiltration and metasomatic exchange to greenschist recrystallisation. In comparison the south of the island documents a more pervasive greenschist facies overprint. Fabrics associated with greenschist recrystallisation in the south of Syros are locally found to be both ductile and brittle, as well as static (inherited) from the blueschist event.

Fluid infiltration into marble bands is documented isotopically by the formation of stable isotope fronts at marble contacts. I have modelled the isotope fronts using chromatographic theory to show that fluid infiltration of marble bands associated with front formation was not by pervasive flow. The spatial arrangement of hydrated silicates in impure marble horizons and the heterogeneities in $\delta^{18}O$ composition in the front imply that fluid infiltration was localised. Macro- and micro-scale stable isotope and geochemical studies of calcite from the marble bands document localised fluid infiltration in zones of fracture and cataclasis. In marble bands that have been affected by ductile deformation, or that have subsequently recrystallised, the patterns of isotopic heterogeneity are less well defined. This is interpreted to be the result of homogenisation of calcite isotopic compositions during recrystallisation.

Deformation fabrics accommodating pure shear, layer-parallel extension are identified in all lithologies. In schist units the fabrics are defined by blueschist and locally in southern Syros by retrogressive greenschist mineral assemblages. It is inferred that this horizontal layer extension was the main mechanism for exhumation of the metamorphic terrain, from peak metamorphism through to greenschist facies. Extensional greenschist veins and faults accommodate extension in the same direction, documenting a continuum of E-W to NE-SW directed extension into the brittle regime. The localisation of extensional strain within the terrain during decompression appears to have controlled fluid pathways, by transiently increasing the permeability of all lithologies. This has led to the resulting spatial distribution of retrogressive metamorphism on Syros.

Acknowledgements

I would like to thank my supervisors John Dixon, Marian Holness and Patience Cowie for their help and advice during the work for and completion of this thesis. I would also like to thank Colin Graham who 'took me on' in the last six months and read my isotope chapters. I have also benefited from discussion with Rob Butler, Stephanie Lewis and Alasdair Skelton.

Field work would not have been the same without the many people who spent time on Syros with me; my three supervisors; JED, Marian and Patience and a range of field assistants, contemporaries and assorted extras; Steph Lewis, Jamie Conolly, Nicky White, Rachel Robson, Leigh Edwards and Rob Butler.

I have used a range of facilities in the Edinburgh Department and would like to thank the following people for their help and advice. Dodie James for help with XRF; Mike Hall for thin section preparation; Pete Hill, Simon Burgess and Paula McDade for help with electron probe analyses and John Craven and Paula McDade for introducing me to the SEM. John Craven must also be thanked for his help and advice on using the ion microprobe; for getting up very early so that it was ready for when I came in and for being on the other end of the telephone if it all went wrong. He must also be thanked for a years worth of Friday beers.

My bulk stable isotope analyses were completed at SURRC and I would like to thank Tony Fallick for use of the lab and Terry, Julie, Andy, Elspeth, Kirsten and Chris for help and advice in the lab. East Kilbride was made pleasanter with company on the drive and company there thanks, Lynne, Kathryn and Susannah. I thank Alasdair Skelton for use of his computer program which I used to model the bulk stable isotope data and for answering my queries by email.

Life in the department has been made great by many people. In particular thanks to my era of the Mouse house possie who stayed from start to finish Steph, Paula and Amanda. I will remember the hysteria of Syros Steph; indulging in one of your chocolate creations Amanda, a continual supply of recipes for life I hope; and beer, beer, beer +.... n' a wee one Paula. Thanks to Zoe for introducing me to the US and sharing the flat for a while. Thanks to all those other mouse house and

department people who have shared social times with me, it is impossible to name you all. Paula gets a special thanks for proof reading vast chunks of my thesis, proof reading thanks also go to Fiona and Rob. Rob also helped by drafting figures for a TSG poster, which have subsequently been used in this thesis.

Outside the department Fiona has provided me with a home for the majority of the time I have been in Edinburgh and has been a great person to live with. She is also thanked for dragging me round mountain marathons and persuading me to take part in the odd Sunday run or orienteering event. Thanks to the department (Simon, Ruth and Alasdair) of geology at Paisley Uni for employing me and making me feel wanted and welcome.

My parents have supported me both financially and emotionally through all my time at university and I owe them a little more of my time and lots more, thanks for your support. Rob has never failed to remind me why I enjoy geology. He has always managed to re-enthuse me, even at my lowest, and has made me see the bigger picture. He has shared many great times, and others, and has always been somewhere during my PhD, thanks Rob.

This PhD was supported by NERC, GT4/95/89/E.

Abbreviations

ACM	Attic Cycladic Massif	CL	cathodoluminescence
PPL	Plane polarised light	XPL	Cross polarised light
HP	high pressure	LT	low temperature
LOI	Loss on Ignition	T	temperature
P	pressure	‰	per mil
$\delta^{18}O$	ratio of oxygen 18/16 relative to SMOW (Standard Mean Ocean Water)	$\delta^{13}C$	ratio of carbon 13/12 relative to PDB (Pee-Dee Belemnite)

Mineral abbreviations
NB The term glaucophane is used for all sodium-rich amphiboles, unless otherwise stated.

ab	albite	epd	epidote
gl	glaucophane	cc	calcite
qz	quartz	zois	zoisite
gnt	garnet	Na-px	sodic-pyroxene
pa	paragonite	chl	chlorite
cam	calcic amphibole	act	actinolite
rieb	riebeckite	mt	magnetite
hem	hematite	ox	oxide
law	lawsonite	jd	jadeite
ank	ankerite	dol	dolomite
di	diopside	an	anorthite
pmp	pumpellyite	czo	clinozoisite
ky	kyanite		

Chapter 1 Introduction

Blueschists are rocks containing a high pressure-low temperature mineral assemblage and are now found on the Earth's surface. For metastable blueschist assemblages to be preserved there must be a mechanism for returning material subducted to depths of 45 km or greater back to the surface. There are two significant problems with this. Firstly, the scale of the unroofing involved is difficult to explain in terms of a mechanism which will remove 45 km and more of overlying rock. The second problem is that of kinetics. The results of most thermal modelling studies suggest that the high pressure-low temperature conditions of blueschist formation do not represent points on a stable continental crustal geotherm. Blueschists would therefore be expected to convert to amphibolite or greenschist facies assemblages if they are not exhumed faster than they thermally re-equilibrate. Radiogenic self-heating will enhance this self-destructive tendency of blueschist assemblages. Given this inherent metastability and the length of the exhumation path, the exhumation rate is critical to blueschist preservation. Two other factors will also be important in promoting or inhibiting recrystallisation during unroofing, namely the availability of fluid and the deformation experienced by the rocks. This study is largely concerned with these last two factors and how they have interacted.

During prograde metamorphism the evolving mineral assemblage is usually progressively dehydrated. For the prograde metamorphic reactions to be reversed during retrograde metamorphism high pressure mineral assemblages must, in general, be re-hydrated. Hydration of high pressure mineral assemblages to allow retrograde recrystallisation has occurred on Syros. Therefore, the availability of fluid is crucial for recrystallisation to lower pressure assemblages. The pervasiveness of fluid infiltration during exhumation will determine the extent to which regionally metamorphosed high pressure terrains are overprinted by lower pressure assemblages.

The pathway of an infiltrating fluid is controlled by the permeability distribution in the rock sequence. The permeability of a metamorphic rock is largely

determined by its mineralogy and anisotropy. As different lithologies have different permeabilities and fabrics, fluid pathways will in general be controlled by the stratigraphy and structure. Deformation can also decrease or increase rock permeability. In a deforming rock sequence fluid pathways are controlled not only by lithological variations but also by deformation. Deformation will also kinetically enhance recrystallisation to new assemblages which is in turn dependent on fluid availability. Thus, deformation, fluid infiltration and recrystallisation are intrinsically linked.

To assess the relative contributions of lithology, deformation and fluid infiltration in controlling retrogressive metamorphism, the Greek island of Syros, part of a blueschist terrain, was used as a case study. The Attic Cycladic massif, the metamorphic belt in which Syros crops out, was chosen for study as it is a relatively young blueschist terrain which is undergoing present day extension. The metamorphic belt is well documented both in terms of metamorphism and present day extensional tectonics.

On Syros, previous studies have documented aspects of the structure, metamorphic and fluid infiltration history of the rock sequence. These earlier studies have highlighted gaps in the knowledge and understanding of the subsequent exhumation of the terrain and the relationships between fluid infiltration, recrystallisation and deformation of lithologies on the unroofing path.

The previous studies established that the island has a well exposed layered metasedimentary sequence, providing lithological and therefore permeability contrasts within the rock succession. The high pressure fabric development has been documented and the pattern of brittle faulting mapped. Crucially it was shown that retrogression of high pressure assemblages was partial and patchily developed. This partial retrogression of high pressure assemblages is important as it allows comparisons to be made between retrogressed and non-retrogressed areas. This potentially allows a spatial correlation to be made between fabric development and retrogression. Observation of a spatial link between deformation and recrystallisation of assemblages would enable inferences to be made between the interplay of fluid infiltration, deformation and recrystallisation of metamorphic assemblages.

This study has used an integrated approach to document the interaction of deformation, fluid infiltration and recrystallisation of the Syros rock sequence during exhumation. In doing so, a decompressional P-T-fluid-deformation path has been charted. The decompression path and associated processes have been used to infer a mechanism for exhumation of the blueschists.

Chapter 2 Geological setting, review of previous work, and aims of thesis

2.1 Regional Geology

The Aegean island of Syros lies within the high pressure metamorphic belt of the Attic Cycladic Massif (ACM). The ACM is an alpine orogenic belt which extends from Greece through the Aegean to Turkey (figure 2.1). The ACM is described in detail by Durr et al. (1978), Robertson and Dixon (1984) and references therein. High pressure eclogite-epidote blueschist facies assemblages are preserved on several islands within the Aegean section of the ACM, including Syros (figure 2.2). This high pressure metamorphism is dated by K-Ar, Rb-Sr and Ar-Ar cooling ages of micas at 45-50 Ma (Altherr et al., 1979; Wijbans et al., 1990; Okrusch and Bröcker, 1990). Mineral assemblages define pressures for the blueschists of 15 kbar and temperatures of 450-500 °C (Okrusch and Bröcker, 1990; Kornprobst et al., 1979).

Subsequent to blueschist metamorphism there was a retrogressive episode marked by rehydrated greenschist assemblages. These completely and partially overprint the high pressure assemblages. Retrogression to chlorite- and albite-bearing assemblages is interpreted to have developed at 7-4 kbars, 400-500 °C (Schliestedt and Matthews, 1987; Bröcker, 1990) but without significant deformation. The retrogression has been dated using K-Ar and Rb-Sr dating of mica in retrogressed rocks. The dates obtained define a spread from 25-21 Ma for Sifnos and Tinos (Schliestedt et al., 1987 and Okrusch and Bröcker, 1990). South of Syros and notably documented on Naxos, the retrogressive metamorphism is affected by thermal doming associated with intrusion of Miocene granitoids. Dating of samples from Naxos, Paros, Mykonos and Ikaria show a spread in cooling ages from 21-10 Ma. These are interpreted as representing a prolonged cooling history (Schliestedt et al., 1987).

Fluid infiltration associated with the retrogression has been documented in several studies (e.g. Matthews and Schliestedt, 1984; Schliestedt and Matthews, 1987;

Figure 2.1
Location map of the Attic Cycladic Massif (ACM), after Gautier et al. (1993) and Jolivet et al. (1998)

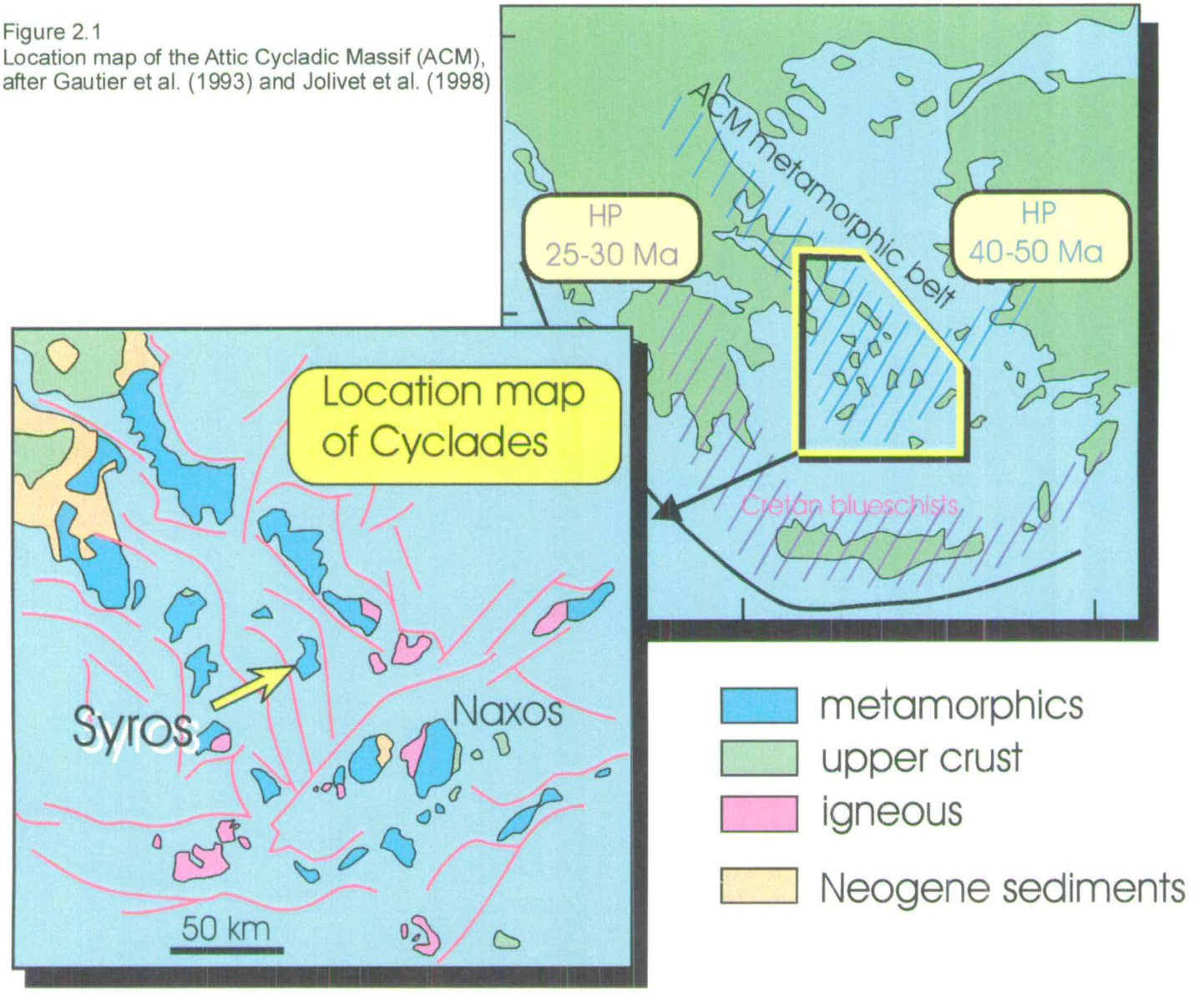

Figure 2.2
Geological map of Syros, after Ridley (1982a). Key localities annotated

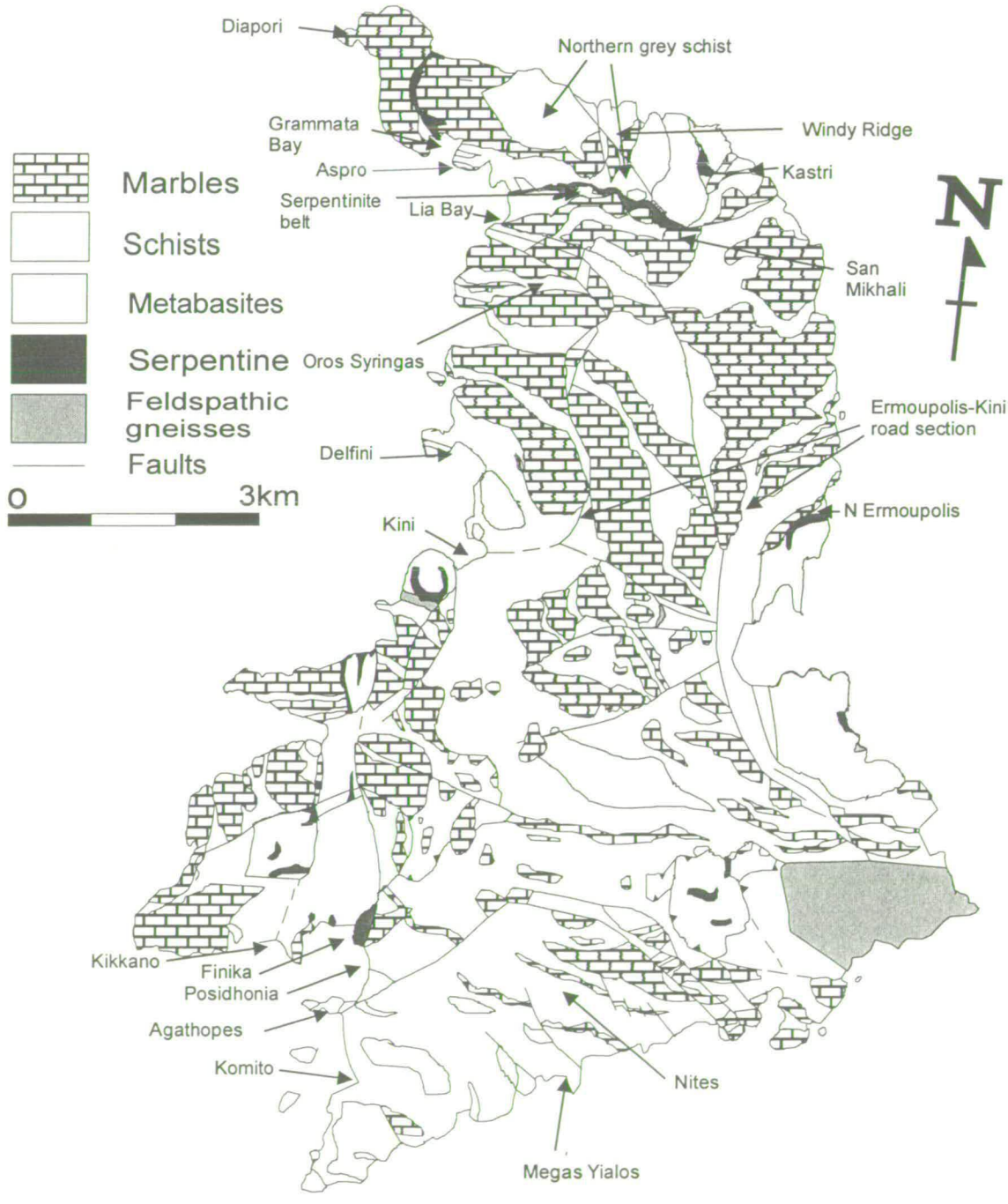

Ganor et al., 1989; Bröcker, 1990; Baker and Matthews, 1995; Ganor et al., 1996). These studies have concentrated on the islands of Sifnos, Tinos and Naxos. The studies relate fluid infiltration to the transformation from blueschist to greenschist assemblages. Studies on Tinos and Naxos suggest that infiltrating fluid was channelled in discrete horizons rather than pervasive (Bröcker, 1990; and Baker and Matthews, 1995). This is consistent with the interpretation that small quantities of fluid were involved in the retrogressive metamorphism on the island of Sifnos (Schliestedt and Matthews, 1987; and Ganor et al., 1989).

2.2 Geology of Syros

As described in the regional geology section (2.1) Syros was apparently metamorphosed in an Eocene subduction-related high-pressure, low temperature (HP-LT) metamorphic event. Constraints on peak metamorphism from mineral equilibria for Syros, are reported by Dixon (1969), as 14-19 kbar and 470 ± 30 °C, depths of 45-50 km in the subduction zone. Two areas on Syros are not affected by this Eocene metamorphism, the Azolimnos gneisses and the chloritic schist of Vari (Ridley, 1982a). These units crop out in the south east of Syros and are not part of the general rock succession. Ridley (1982a) suggests they may have been down faulted from higher structural levels in the metamorphic pile. These two units will not be discussed again as they are not relevant to the present study.

Syros consists of a layered metasedimentary sequence. Repeated bands of marble and schist with local metabasic layers dip generally northwards at approximately 30°. Marble is one of the most abundant lithologies on Syros. Marble units, up to 300 m thick, are dominantly calcitic but often contain dolomite, quartz and phyllosilicates. Where dolomite is present it tends to form fine grained layers parallel to lithological contacts. In the field this gives the marble a striped appearance, caused by a combination of colour contrast and differential weathering. This relationship is particularly notable on the Nites hillside, where close-isoclinal folds are clearly identified by folding of interbanded dolomite and calcite. Syros marble is generally cream in colour, but can

also be grey. The crystallographic form of the calcite varies but can often be seen to form elongate crystals sub-perpendicular to lithological layering. These are interpreted to have formed during the transition from aragonite to calcite, with calcite taking up the aragonite crystallographic structure (Barr, 1989 (on Syros) and Van der Maar, 1981). Brecciated marble is found in fault zones and boudin necks.

Impure marble bands, marble containing silicates and or phyllosilicates, are widespread particularly in the north of the island. Siliceous minerals present include quartz, mica (phengite and paragonite), epidote, garnet, sodic-pyroxene, glaucophane and chlorite. The chlorite is often secondary in nature. Marbles with a preserved clastic texture were identified on the Nites hillside, at Delfini on the west coast and at Diapori in the north. Clasts are mainly calcite or quartz, but at Delfini and Diapori metabasic clasts were also noted.

In southern Syros the schist units are variable in composition and consist of pelitic schists, quartzites and quartzose schists. The greenschist overprint is well developed in the majority of these southern schist units. Recrystallisation in general appears to be static, with growth of albite porphyroblasts over fabrics outlined by mica, chlorite, actinolite, quartz, calcite, opaques, rutile and sphene. Further north there are more quartz-rich schists and some quartzites. In the centre of the island the schists are generally pelitic in nature and variably retrogressed. The blueschists contain glaucophane, calcite, quartz, epidote, mica ± lawsonite (pseudomorphed by mica and clinozoisite), opaques, rutile or sphene. Greenschists are often simply the retrogressed equivalent of the blueschist and are generally green in colour. The greenschists are dominated by albite and chlorite but also contain variable amounts of calcite, quartz, actinolite, mica, opaques, rutile and sphene. North of Kini, mica, chlorite, graphite, glaucophane schists are common, termed grey schists by Dixon (1969). The grey schists north of the serpentinite belt are described in detail by Bloor (1998). They are distinguished from other blueschists by the metallic lustre of the graphite.

Metabasite layers are rarely continuous and form large pods or lenses from cm to km in size. These massive metabasic bodies often preserve high-pressure metamorphic assemblages even when the surrounding schist is retrogressed to a greenschist assemblage. In the south of the island, notably on the Nites hillside the main meta-

igneous lithology is a massive glaucophane-epidote rock. The rock has a retrogressed, chlorite-epidote-equivalent which often contains calcite and mica. The edges of the metabasic lenses are often foliated whilst the centre of the bodies are undeformed (Barr, 1989). Over much of the island, small metabasic lenses are generally intercalated with schist units. Other notable areas of meta-igneous material are the coastal areas north of Kini and North Ermoupolis. The meta-igneous material at these localities is spatially associated with serpentinite. The rocks at Kini are banded metabasites containing variable amounts of sodic-pyroxene, garnet, glaucophane, epidote and mica. At Ermoupolis similar rocks have a strong foliation and often contain isoclinal folds.

In the north of the island the metamorphic sequence is cut by a band of ultramafic material. All ultramafic lithologies are mapped as serpentinite; these include serpentine and chlorite, talc, actinolite derivatives. Within the serpentinite lie blocks of metabasic and some sedimentary material. The included blocks are variable in character and size, ranging from centimetres to tens of metres, and have developed metasomatic rinds where they are in contact with the serpentinite (Dixon and Ridley, 1987). On the eastern side of the serpentinite belt an igneous breccia lies structurally above the serpentinite and there is a zone of serpentinite melange below. These units are described in detail by Dixon (1969) and Dixon and Ridley (1987). Other areas of serpentinite melange are seen at isolated localities on the periphery of the island, South Kini, Ermoupolis and Finika (figure 2.2).

Fluid infiltration during metamorphism and its affect on the mineral assemblage has been studied in the northern lawsonite-bearing outcrop (Barr, 1989 and Bloor, 1998) and more widely from non lawsonite-bearing blueschist and greenschist units (Barr, 1989). These two studies follow on from the earlier thesis work on the petrography and structure of northern Syros by Dixon (1969) and Ridley (1982a). Ridley also documented the structure and metamorphism of the whole island, producing a 1:10,000 geological map. This map was one of two geological maps available when starting this thesis in 1995. The other map was a Greek geological survey map at 1:50,000 scale. The map of Ridley (1982a) proved the most useful, and detailed mapping of areas during the present study were put into a regional context using the Ridley map. The lithologies mapped in the present study are the same as those mapped by Ridley (1982a), apart from

the addition of sub-sections which were used to highlight structures and mineralogical variations important to the present study. The correlation between the descriptions used by Ridley (1982a) and this study are shown in table 2.1. Geological maps of the north of the island and serpentinite belt produced by Dixon during his thesis study (Dixon, 1969) were used in the present study during field work. Sections of the maps were redrafted on a smaller scale for presentation in this thesis and this source is acknowledged in the relevant figure captions.

The areas re-mapped on a smaller scale during the present study are marked on a simplified version of the Ridley (1982a) map, figure 2.3. The consistency of lithological and structural descriptions used for the small scale maps depends on the size and detail of the area mapped. The main inconsistencies are outlined here. Brecciated marble is only marked where it forms a large coherent body, notably on well exposed fault surfaces. Brecciated marble is not marked on the Oros Syringas map or Nites maps, as the brecciation zones are not extensive. In the Diapori area three types of marble are mapped: marble, brecciated marble and marble rudite. Impure marble, marble containing bands of silicate impurities, on all other maps are not distinguished from pure marble. In areas of completely retrogressed or unretrogressed assemblages the schist was mapped as greenschist and blueschist respectively. However, in many areas the high pressure assemblage is only partially overprinted. Local variability in retrogression is also common, even within a single layer. In these areas schists were mapped as variably retrogressed schist.

Table 2.1 Mapped lithologies, a comparison from Ridley (1982a) and this study.

Ridley, (1982a) lithologies	Correlation to this study
Metacarbonates	
Calcite or dolomite marbles	Calcite or dolomite marbles
	Brecciated marble
Impure, micaceous or quartzose marbles	Ruditic marble
Metaclastites and metapelites	
Mica quartz schists with variable calcite, glaucophane etc.	Blueschist or grey schist (those containing graphite)
Chlorite, albite schists showing relics of a blueschist assemblage	Greenschist
Quartzites and quartzose schists	N/A
Metaigneous rocks	
Quartz, glaucophanities, often banded	Quartz-rich rock
Schistose glaucophanities with variable phengite, epidote, pyroxene etc.	Metaigneous
Massive glaucophane-epidotites, often calcic and retrograde equivalents	Glaucophane-epidote rock Chlorite-epidote rock
Gneissic glaucophane ecologities, transitional to glaucophane-zoisite metagabbro	N/A
Metaconglomerates of igneous derivation	N/A
Ultramafics and associated rock types	
Serpentinite or chlorite, talc, actinolite derivative	Serpentinite
Metasomatised schists and impure marbles	N/A or mapped as marble
Included blocks within the serpentinite	Metasomatised included blocks
Greenschist facies schists and gneisses of Vari	
Quartzo-feldspathic gneisses of Azolimnos	N/A
Amphibolitic gneisses of Azolimnos	N/A
Chloritic schists of Vari	N/A

N/A = not part of this study.

Figure 2.3
Geological map of Syros, after Ridley (1982a). Locations of small-scale maps are annotated. Small-scale map locations are listed from north to south: A-Diapori, B-Windy Ridge area, C-Oros Syringas, D-Delfini, E-Nites.

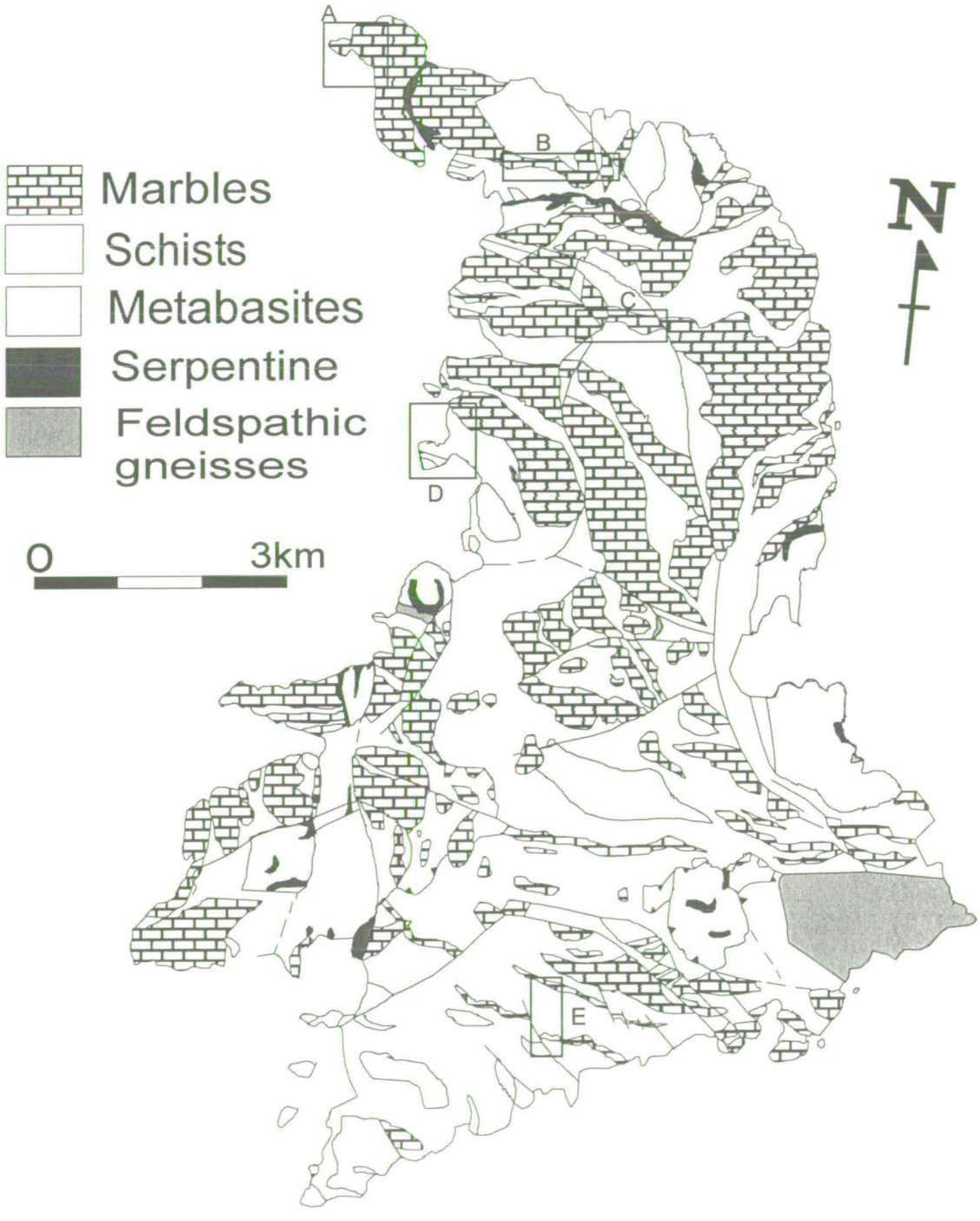

2.3 Review of previous work on Syros

Dixon (1969)

The study of Dixon (1969) was based in northern Syros from the Oros Syringas hillside to the north coast. He presents two maps, one of the north of the island and a detailed map of the serpentinite belt. The zone he termed the 'northern gneiss-serpentinite belt' is referred to in the present work as the serpentinite belt.

Dixon describes the geology of Syros, noting the interlayered northward dipping schist and marble units and contrasts the well-preserved high pressure assemblages in the north with the overprinted greenschist assemblages in the south. Patchy retrogression in the north is interpreted as static whilst in the south, deformation is assumed to have continued to low grade greenschist assemblages (Dixon, 1969).

Despite the general comments above, Dixon's (1969) study, is concerned chiefly with a structural and petrographic description and interpretation of the serpentinite belt. He also carried out a detailed petrographic and structural study of the northern lithologies, documenting a layer parallel cleavage in schist units and describing local evidence for folding, both upright and reclined. On the Oros Syringas hillside he describes pinch and swell structures and boudinage of massive glaucophane-epidote layers, with low pressure zones filled with quartz and epidote. Dixon (1969) also documents brittle faulting and the formation of marble breccia where adjacent marbles are faulted. However, he concentrates in greatest structural detail on the nature of the contact between the serpentinite belt in the north and the surrounding rocks.

Within the serpentinite belt he describes layer parallel boudinage in a range of lithologies. The lithologies include well foliated gneiss and isoclinally folded schist and marble units which are attenuated and horizontally boudinaged. Within the serpentinite belt he observes mineral lineations of glaucophane and mica, with local boudinage of glaucophane crystals. Dixon (1969) documented recrystallisation of high pressure assemblages in folds and boudins in lithologies abutting the serpentinite. He describes localised deformation in the serpentinite and in the edges of contact lithologies. His interpretation of the documented structures and recrystallising mineral assemblage

requires the serpentinite belt to be part of a coherent stratigraphy during the deformation. He interprets the deformation in the serpentinite and surrounding lithologies as occurring within the high pressure stability field for Syros.

Ridley (1982)

A structural interpretation of the island was presented by Ridley (1982a). This interpretation has been published in a series of papers: (Ridley, 1982b; Ridley and Dixon, 1984; Ridley, 1984a; 1984b; and 1986).

Ridley (1982b; 1984a; and 1986) concentrate on the relationship between the arcuate lineation trend and the south easterly directed ductile thrusting during subduction. Ridley and Dixon (1984) focus on reactions within blocks of metabasite in ultramafic melange. They discuss the role of chemical equilibration and reaction progression in relation to localised deformation of the blocks. Ridley (1984b) describes the post-metamorphic listric normal faulting. An overall narrative may be summarised-starting with subduction-related fabrics, through to listric faulting associated with regional extension.

Ridley (1982b) describes the dominant foliation as penetrative, including tight-isoclinal folds on a macro-microscale. The folds are documented as having a constant sense of asymmetry, verging south or south east. Fold axial planes parallel to the regional dominant foliation are interpreted to have formed during horizontal, thrust sense shear (Ridley, 1982b and 1984a). Fold hinges plunge gently east to north east except in localised zones where the trend is south-easterly (Ridley, 1982a).

As well as planar fabrics Ridley (1982a) also recognised two lineations: an intersection lineation and a mineral lineation of aligned glaucophane and quartz crystals. The intersection lineation is parallel to fold hinge lines. The mineral lineation locally transects the intersection lineation and fold hinges. However, over much of the island the intersection lineation and mineral lineations are parallel (figure 2.4). The arcuate trend of the intersection lineation and fold hinges, particularly those north of the serpentinite belt, Ridley (1982a) interpreted to have developed during a single progressive deformation event. This single deformation event, comprising of interacting

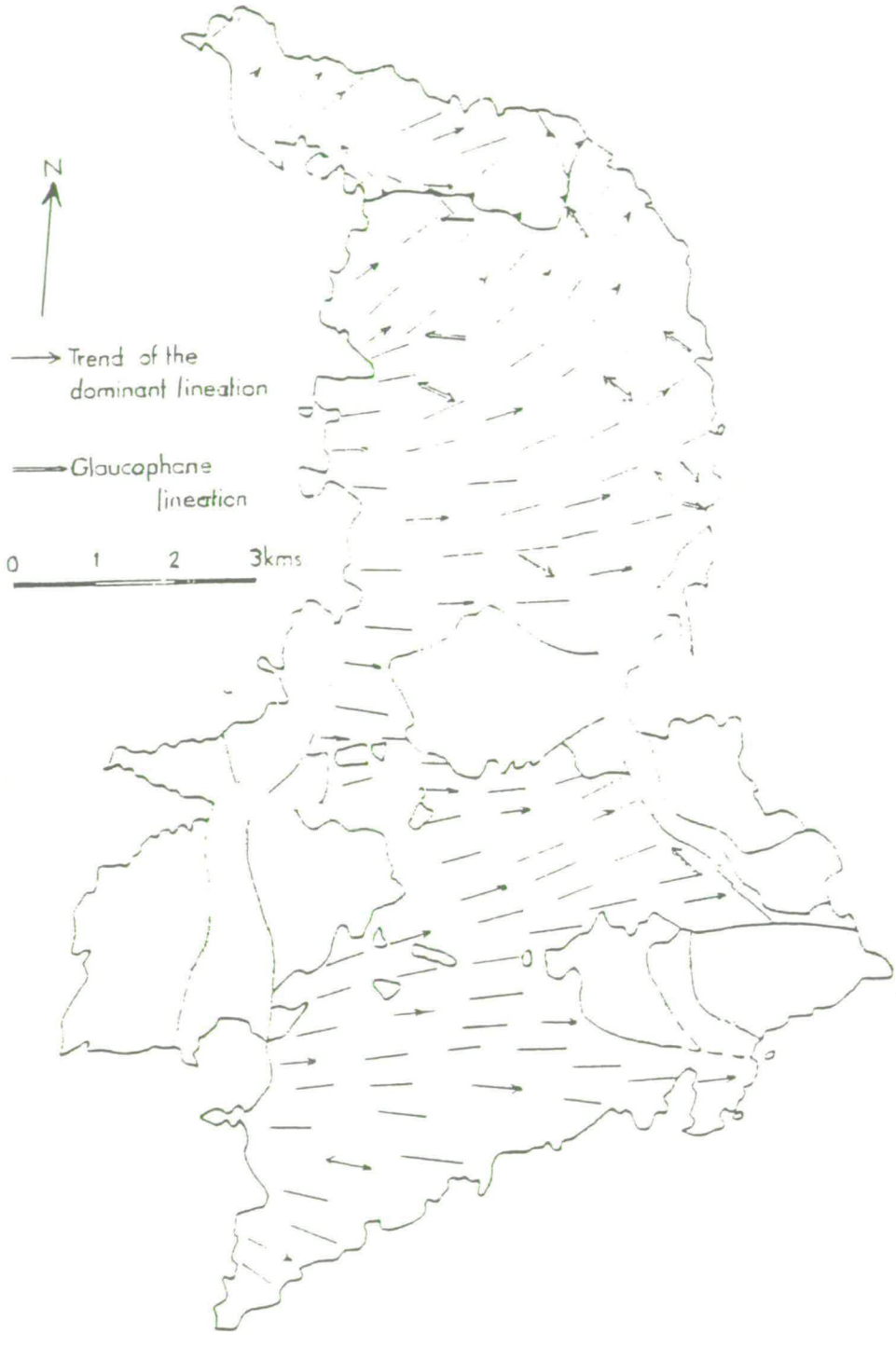

Figure 2.4

Map of dominant lineations on Syros, from Ridley (1982a)

simple, pure and wrench shear, developed during south easterly directed lobate thrusting (Ridley 1982b). The variation in lineation and fold hinge orientation north of the serpentinite belt have been interpreted as forming during wrench shear between thrust lobes (Ridley 1982a and 1982b) (figure 2.5). Ridley interprets the serpentinite belt as a structural discontinuity during the thrusting, with no correlation between lineation development above or below the serpentinite. Figure 2.4 includes glaucophane mineral lineation data, which transects the dominant linear fabric, an intersection lineation. Ridley (1984a) describes the transecting lineation as glaucophane outlining fold limbs, with glaucophane only aligned parallel to fold hinge lines in the hinges of folds. Slight scatter in the trend of the glaucophane data is ascribed to reorientation during close-open folding in a north easterly trend. This folding post dates the earlier fabric but has little affect on the pattern of the main lineation trend (Ridley, 1982b). Ridley (1982a and 1982b) also noted boudinage of glaucophane crystals parallel to the dominant lineation on the south coast and interpreted the lineation as having a true stretching component. Ridley (1982a and b) suggests that the stretching was coeval with south easterly directed thrusting. Ridley (1982a) also documents local boudinage in the Delfini area (Ridley, 1982a, figure 6.20a). He interprets the boudinage as forming during folding and attenuation of fold limbs during metamorphism.

Using microstructure and mineral assemblages, Ridley (1984a) suggests that the cessation of deformation and metamorphic recrystallisation were approximately synchronous. He therefore, interprets all fabrics as having formed during subduction of the complex, prior to exhumation. Ridley (1982a) describes the overprint of albite and chlorite as static and post tectonic, recognising only two localised examples of syn-greenschist deformation. These are zones of recumbent folding and localised formation of an axial planar spaced cleavage east of Posidhonia and at Finika. The kinematics of the deformation structures imply the same shear sense as the original fabric development (Ridley, 1982a).

Post-metamorphic normal faulting cuts through the syn-metamorphic stratigraphy. The faults are listric and trend northeast-southwest (Ridley, 1984b). The down throw side of major listric faults is always away from the spine of the island,

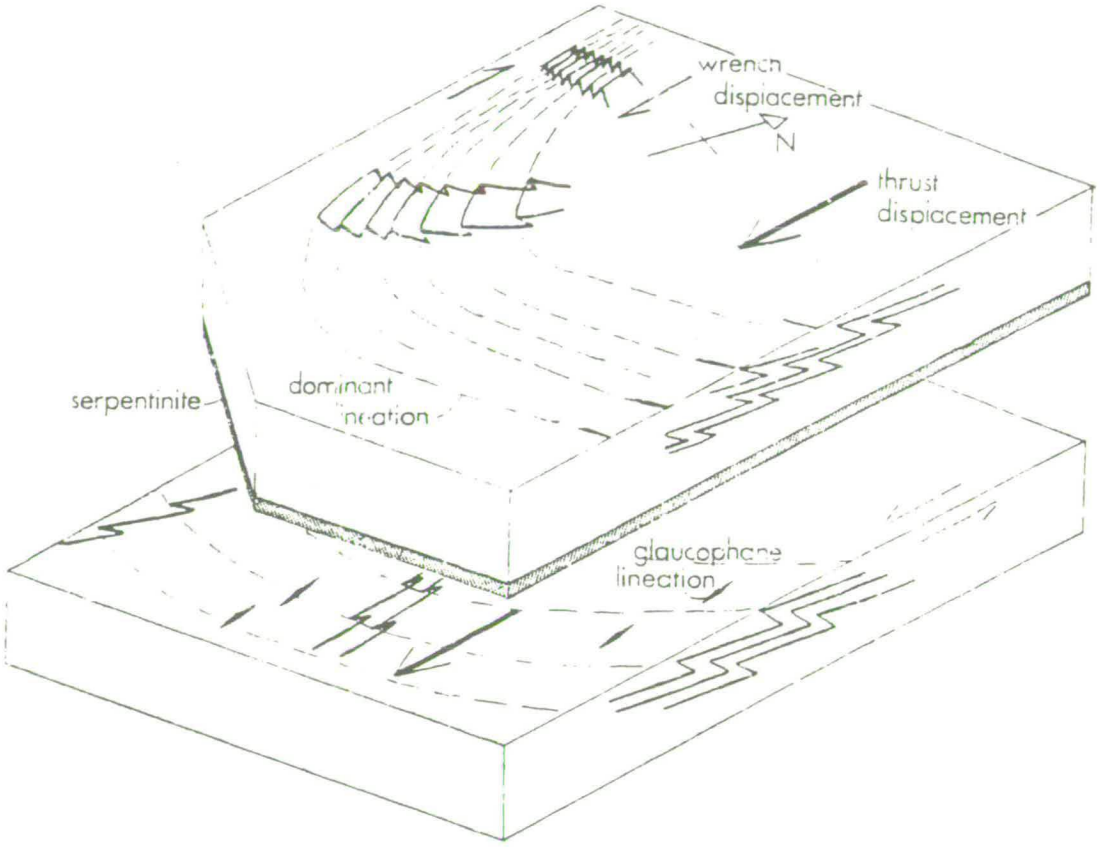

Figure 2.5

Block diagram of lineation and fold development above and below the serpentinite belt on Syros, from Ridley (1982a).

developing a horst block structure. Antithetic faults are developed only when the major fault is oriented northwest-southeast. Ridley (1984b) suggests that the extensional tectonics may also contain a minor component of strike-slip faulting oriented northeast-southwest, which may account for the described fault pattern. However, the faults were interpreted as being entirely distinct from the syn-metamorphic ductile deformation.

Barr (1989)

The study of Barr (1989) concentrated on fluid infiltration during metamorphism and its affect on mineral stability. By construction of T-X(CO_2) sections of blueschist assemblages and comparison with blueschist petrography she determined the composition of fluid in equilibrium with the blueschist assemblage. Her conclusions were backed up by stable isotope and fluid inclusion studies.

The T-X(CO_2) grids that Barr produced suggested that a water rich fluid was present during blueschist facies metamorphism. This conclusion is supported by the presence of lawsonite and sphene in the blueschist assemblage of Syros. Sphene and lawsonite are stable only under H_2O-buffered conditions (Nitsch, 1972 and 1974; Schuiling and Vink, 1967 and Hunt and Kerrick, 1977). She also documented heterogeneities in fluid composition between layers, from mineral equilibria and stable isotopes, leading to the conclusion that layers acted as closed internally-buffered systems with little input from externally derived fluid (Barr, 1989). Her fluid inclusion work, presented in Barr (1990) documented a H_2O-rich saline fluid trapped in fluid inclusions.

A H_2O-rich fluid supports the presence of lawsonite. However, lawsonite formation apparently requires external buffering by a H_2O-rich fluid, since the production of lawsonite by reactions involves the breakdown of calcite, the most reasonable Ca source, producing CO_2 (Barr, 1989). In a closed system the reaction will buffer itself and a limited amount of lawsonite will be produced. Barr (1989) suggested that fluid infiltration must have been channelled to produce the documented local equilibria, while the bulk-rock maintains a high percentage of lawsonite. This conclusion and the paradox of large volumes of lawsonite in an apparently internally-buffered system was the target of another thesis study (Bloor, 1998), discussed below.

Barr (1989) also studied fluid infiltration during the blueschist to greenschist transition. She documented the petrography of greenschist assemblages and compared stable isotope compositions from blueschist and greenschist lithologies. Barr (1989) suggests that the blueschist-greenschist transformation occurred as a result of an influx of fluid during regional heating. She documents retrogression of glaucophane to albite, chlorite, calcite and actinolite, a mineral assemblage stable under greenschist facies conditions, 5-8 kbar and 400-500 °C. She interpreted the composition of the infiltrating fluid as H_2O-rich, due to the continued stability of sphene (Barr, 1989).

The stable isotope studies of Barr show localised depletion of $\delta^{18}O$ in marble-band boundary layers adjacent to greenschist. Such depletion was not documented in boundary layers adjacent to blueschists in the north of Syros. She interpreted the asymmetry of the depletion as the result of upward directed fluid infiltration through the sedimentary pile. From the isotope data, the volume of infiltrating fluid during the transformation is thought to have been small (Barr, 1989). Extensive depletion in $\delta^{18}O$ was documented at only one locality. This locality was interpreted by Barr (1989) as being an area of localised fluid infiltration during the blueschist to greenschist transformation. Greenschist veins with alteration haloes of albite and chlorite also document localised fluid infiltration and retrogression of assemblages (Barr, 1989).

Bloor (1998)

Bloor studied the spatial distribution of lawsonite within the greyschist units (graphitic schist) north of the serpentinite belt. He found that lawsonite was concentrated around quartz veins; implying channelled infiltration of a H_2O-rich fluid in veins. By linking vein formation with deformation fabric in the greyschist he constrained the relative timing of fluid infiltration. Bloor describes the fracture flow as occurring syn-deformation parallel to the dominant regional foliation. He describes the fluid infiltration as occurring during a change in deformation from a dominantly flattening fabric to folding (Bloor, 1998). Lawsonite was precipitated in response to metasomatic reactions between the veins and wall rock.

As part of this process he assigned the fabrics described by Ridley (1982a) relative S and D numbers. He documented an S1 horizontal foliation transposed from

original sedimentary layering (a composite fabric equivalent to Ridley's dominant foliation). Bloor described the S1 as being reworked by thrusting and folded (D2) with a locally formed axial planar cleavage (S2). Finally Bloor (1998) also recognised a locally developed extensional crenulation cleavage (S3). Bloor also described the local occurrence of layer boudinage. He interprets the boudins as forming during (S1) flattening.

Summary of previous work

Petrographic assemblages are well described, the northern lithologies by Dixon (1969), lawsonite-bearing graphitic schists by Bloor (1998) and various high and low pressure assemblages across the island by Barr (1989). Only high pressure assemblages have been linked to deformation by fabric formation (Dixon, 1969; Ridley, 1982 and Bloor, 1998).

High pressure fabric formation was documented in the north of the island by Dixon (1969), Ridley (1982a) and Bloor (1998). However, this previous work on the structure of Syros has been dominated by interpretation in relation to subduction (Ridley, 1982a). Dixon (1969) and Ridley (1982a and 1984b) also describe normal faulting, interpreted to be unrelated to the documented ductile deformation (Ridley, 1984b). There is therefore, a gap in the structural history of Syros between high-pressure fabric formation related to subduction, and high level brittle extensional faulting.

Fluid compositions have been well constrained for fluid infiltration associated with lawsonite precipitation (Bloor, 1998) and for blueschist high pressure metamorphism in general (Barr, 1989). Barr also described the petrography of greenschist assemblages, concluding that retrogression was controlled both by fluid infiltration and regional heating. She suggested that the fluid associated with retrogression was H_2O-rich, from the presence of sphene. Preliminary work on isotopic alteration of marble bands was also completed by Barr, documenting isotopic alteration of marble bands adjacent to greenschist assemblages.

2.4 Aims of the present study

The work in this thesis uses the earlier studies as a basis for determining the mechanisms for exhumation of the terrain and associated fluid infiltration, recrystallisation and deformation. The structural gap between high-pressure fabric formation and high-level brittle faulting is one of the main targets of this study. Ridley's interpretation of the structure of the island is dominated by fabric formation during orogenesis. In this thesis the balance is redressed and the fabrics and structures are considered in terms of exhumation of the terrain. The partial greenschist retrogression documented by the earlier studies implies that recrystallisation was localised whilst the terrain was in the greenschist facies stability field. Key localities were chosen to document and interpret structures and deformation fabrics associated with greenschist recrystallisation, the aim being to link the kinematics of greenschist deformation fabrics down-pressure to high-level brittle faulting and also to higher grade eclogite-epidote-blueschist fabrics. Such a kinematic link would allow the fabrics to be interpreted as documenting down-pressure recrystallisation during deformation associated with exhumation of the terrain.

Linked to greenschist recrystallisation is fluid infiltration associated with re-hydration of peak assemblages. Fluid infiltration associated with the blueschist-greenschist transformation was documented by Barr (1989). In her section on further work Barr (1989 pages 327-328) suggested further study in two areas; 1) Further isotope work to assess the degree of isotopic homogeneity between layers and 2) data on the occurrence and distribution of veins at different grades. Barr used stable isotope data to assess the pervasiveness of fluid flow within and between lithologies. In this study stable isotopes have been used to continue this idea. Isotope data have been collected to qualitatively determine the degree of fluid infiltration into marble bands, mainly from adjacent schist. This study aimed to show that isotopic heterogeneities in calcite marble $\delta^{18}O$ were related to fluid infiltration rather than depletion associated with silicate phases present in the marble. This being the case, to determine whether fluid infiltration of marble bands was associated with retrograde fluid infiltration during the blueschist-

greenschist transition. A microscale isotope study was also undertaken to assess the affect of marble band deformation on fluid infiltration and isotope exchange.

Documentation of vein mineralogies and their structural settings allows a history of fracture associated fluid infiltration to be established. The fracture history can be correlated with the metamorphic and structural evolution of the terrain, to build a picture of fluid infiltration during metamorphism and exhumation. The fluid infiltration studies of this thesis also compliment the work of Bloor (1998) on infiltration during peak metamorphism and early fabric formation. Greenschist retrogression haloes around veins identified in the present study were used to associate rehydration and metasomatic exchange with fluid infiltration. The outcome of the study was compared with the work of Bloor on metasomatic exchange between wall rock and quartz-lawsonite-bearing veins, during peak metamorphic conditions on Syros.

In summary, the thesis contains four main data chapters: a structural interpretation of fabrics associated with exhumation; a fracture controlled fluid infiltration chapter, which documents vein mineral assemblages, recrystallisation of mineral assemblages in vein wall rock and the effects of metasomatic exchange on the bulk chemistry and mineral assemblage of vein wall rock. These are followed by two chapters based on stable isotope analysis of marble bands. The first of these chapters consists of bulk stable isotope data from marble and schist bands. The data are used to qualitatively assess the degree of fluid infiltration and isotopic homogenisation between schist and marble units. The degree of fluid infiltration allows an assessment to be made of the extent to which lithological variations controlled fluid pathways through the terrain. The subsequent chapter looks at the mechanisms for fluid infiltration of marble bands on a macro and microscale concentrating on permeability formation associated with deformation. The results of the main data chapters are synthesised in chapter 7, which is followed by conclusions and suggestions for further work.

Chapter 3 Structure and deformation

Chapter 3 Structure and deformation

3.1 Introduction

The previous chapter (chapter 2) summarised the work of early structural studies on Syros. These previous studies (Ridley, 1982a and Bloor, 1998) have interpreted ductile deformation features as syn-orogenic, related to prograde thickening of the metamorphic sequence. However, the Aegean is presently an extensional regime dominated by brittle faulting (Taymaz et al., 1991 and Jackson, 1994). Ridley (1982a and 1984b) documented listric normal faults on the island of Syros. He interpreted the faults as being related to present day extension, with no relation to ductile structures. Thus there appears to be a 'structural gap' on Syros between ductile structures interpreted to have formed during orogenesis at depths of approximately 45 km and brittle deformation in the upper crust.

In the modern Aegean sea subduction is occurring south of Crete. Roll back of the subducting slab has progressively resulted in movement of the thrust front south with subsequent post-orogenic extension in the back basin (Jolivet et al., 1998). Modern seismicity studies are interpreted to show north-south directed extension (Hatzfeld et al., 1990). Field studies in the southern Cyclades, back up this seismic interpretation of north-south directed extension (e.g. Lister et al., 1984; Gautier et al., 1993; Jolivet et al., 1994 and 1996). Kinematics from the field studies are based on ductile extensional structures, which are interpreted as documenting asymmetrical extensional shear. However, the direction of shear is variously reported Lister et al., (1984) report top to the south directed asymmetrical shear for Naxos, whilst Urai (1990), Buick (1991) and Gautier et al., (1993) interpret the structures as indicating top to the north simple shear.

The field studies documenting, north-south, non-coaxial ductile extension were based on the islands of Naxos and Paros, south of the disputed southern Cyclades detachment zone (Gautier et al., 1993). North of this disputed tectonic

break, where Syros is located, the pattern of normal faults is different from those in the south (figure 3.1). The normal faults trend NW-SE to N-S and on Syros are described as horst block structures (Ridley 1984b). Limited studies in the northern Cyclades suggest rotation of the stretching direction to a NE-SW trend in the northern Cyclades (Jolivet et al. 1998) (figure 3.1).

This chapter documents evidence for down-pressure ductile-brittle extension on Syros. Documentation of the kinematics of fabrics and structures have been used to describe coaxial extension related to the exhumation of this part of the Cyclades. If ductile extensional structures associated with exhumation were present on Syros, one would expect to see deformation fabrics defined by minerals representative of the decompression path for exhumation. Greenschist extensional fabrics would overprint earlier blueschist fabrics. High-pressure extensional fabrics may, therefore, be hard to distinguish from earlier polyphase deformation associated with orogenesis. Grütter (1993), who describes extensional fabrics associated with decompression from Ios, suggests that descriptions of well-preserved subduction related fabrics by Avigad (1990) and Ridley (1982a) for northern Sifnos and northern Syros respectively may have been misinterpreted.

It is obviously crucial to establish textures both structurally and metamorphically so that they can be tied to the relevant part of the PT path. Up to 6 kbars of decompressional extension may have been accommodated within the blueschist stability field for Syros (figure 3.2). Therefore, identifying decompressional extensional structures in high pressure assemblages, from subduction related fabrics, may provide the key to the kinematics of exhumation of the terrain. For Syros this has been achieved by linking the kinematics of blueschist deformation to greenschist fabrics, down-pressure and ultimately to brittle deformation. From the down-pressure links a picture has been pieced together of the kinematics and associated decompressional PT path for exhumation.

Figure 3.1

Map of Aegean cyclades with Miocene stretching and shear directions annotated.

After, Jolivet et al. (1998) and Gautier et al. (1993).

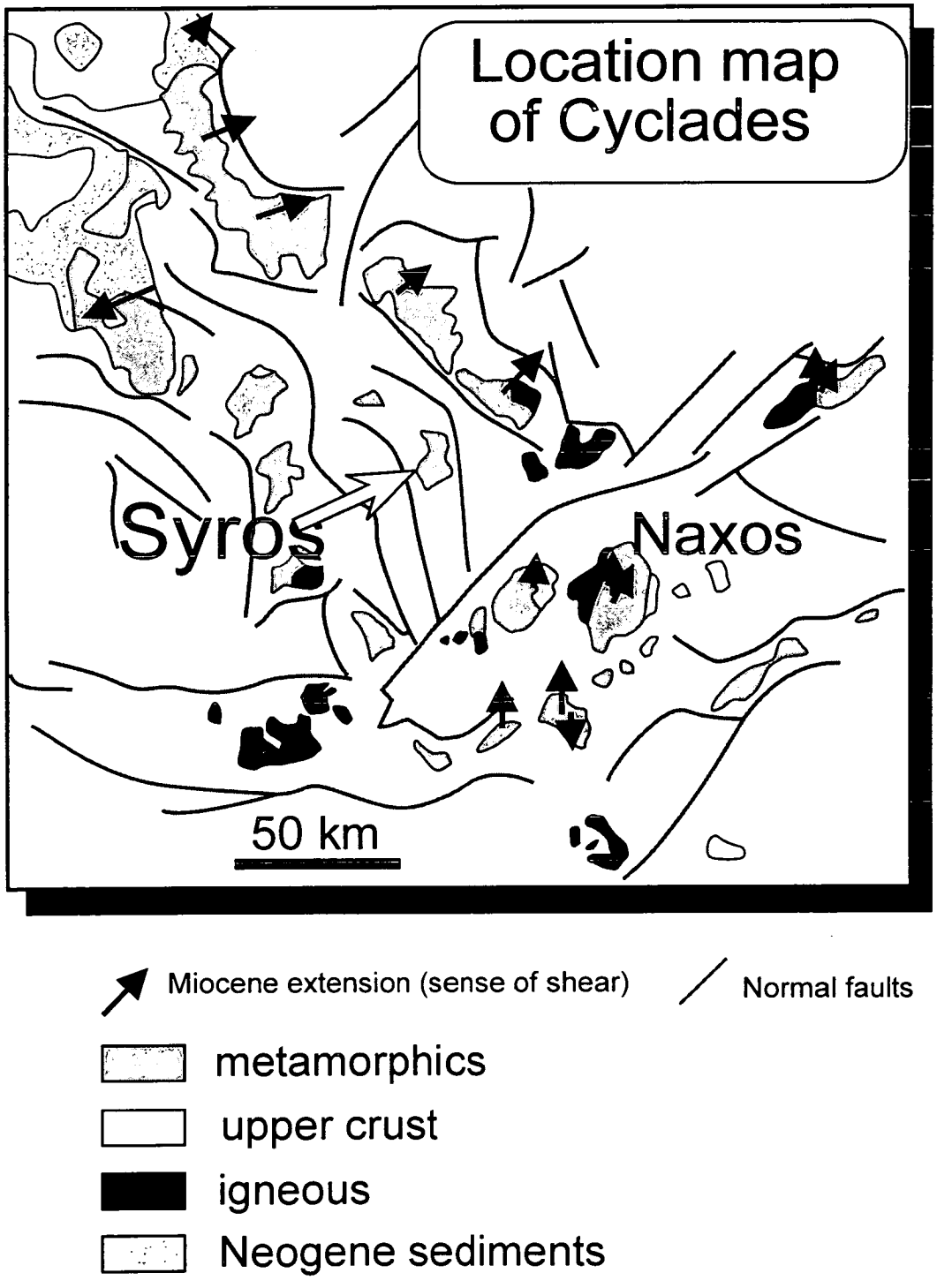

Figure 3.2

PT plot showing the primary crystallisation field for Syros blueschist (Barr, 1990). The estimated PT for crystallisation of Syros blueschist is 14 Kbars, 450 °C (Dixon, 1969). Using one of the PT plots of Evans (1990), for a realistic Syros bulk composition, the amount of decompression within the blueschist facies stability field required to reach pressures associated with greenschist crystallisation is > 6kbars.

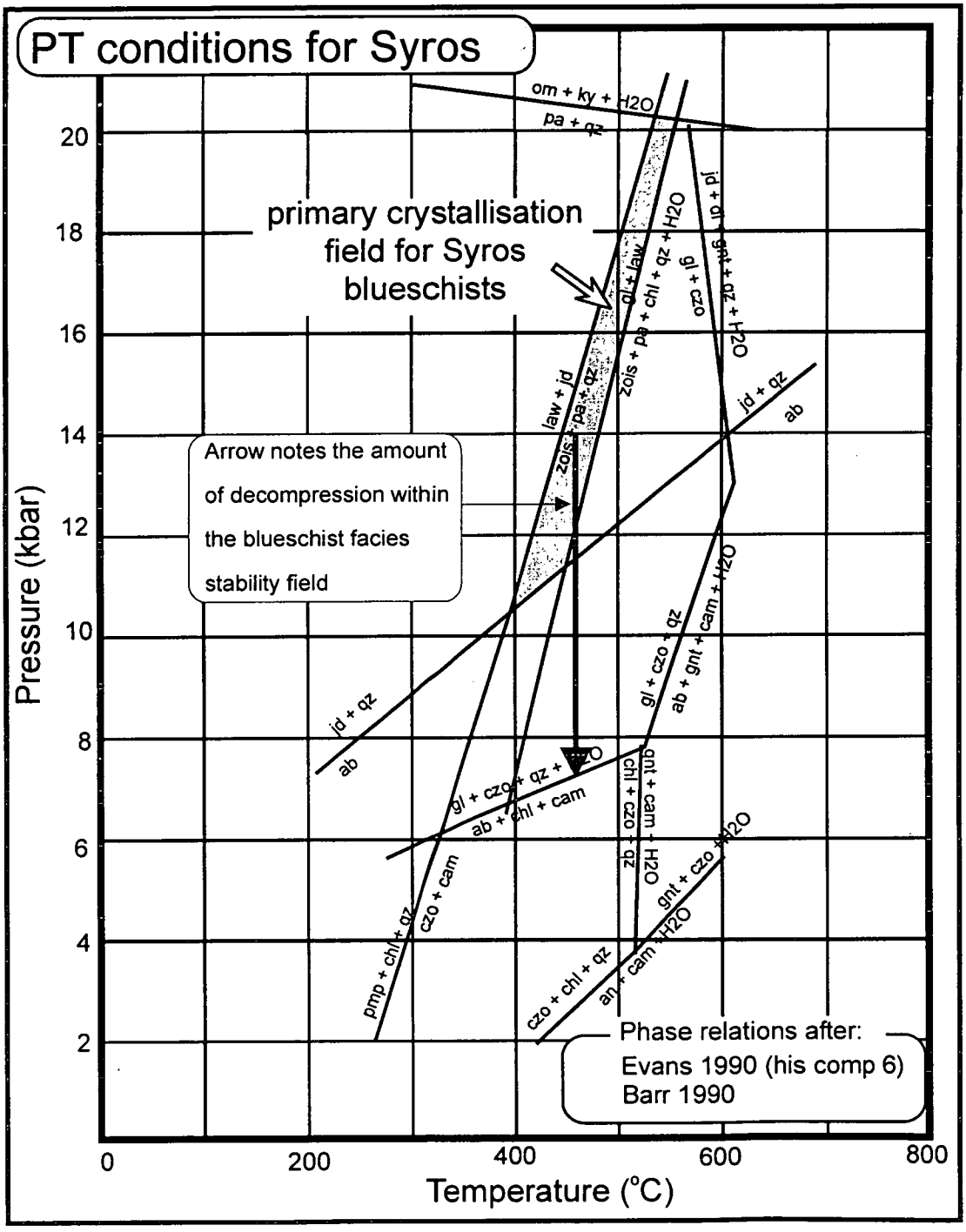

3.2 Aims

The aim of the chapter is to describe the structural geology of Syros, and in doing so to evaluate the roles of compression and extension and their potential relation to exhumation of the terrain. Within that aim the key objectives are: to establish evidence for greenschist deformation and its kinematics; to kinematically link the greenschist and blueschist fabrics; to link ductile structures to brittle deformation. Thus, charting a down pressure blueschist-greenschist-sub-greenschist, kinematic story. Building on the work of Ridley (1982a) and observations of high pressure boudinage by Dixon (1969) key localities were chosen to document the significance of linear fabrics and the kinematics of shear criteria to fabric development.

3.3 Locality observations and interpretations

Syros is characterised by a series of sedimentary packages, consisting of interlayered marble and schist units with some interleaved metabasic material (figure 3.3). The overall structure is simple, the units are tilted to the NE by approximately 30°. A detailed examination of the structure reveals large scale folding and boudinage of the sedimentary pile. The folding and boudinage are scale invariant and intrafolial folds and micro-boudinage are also identified. Documentation of these structures and their role in accommodating extension are presented from the localities marked on figure 3.3. The localities were chosen for a combination of good exposure and because they contained deformation fabrics identifiable in the field.

In terms of preservation of metamorphic assemblages greenschist overprinting is more pervasive in the south of the island, while almost pristine blueschist assemblages are preserved in the north (Dixon, 1969; Ridley, 1982a; Barr, 1989 and this study). Ridley (1982a) and Barr (1989) describe the retrogressive overprint in the south of the island as static. In this study many areas of the south

Figure 3.3
Geological map of Syros, after Ridley (1982a). Key localities annotated

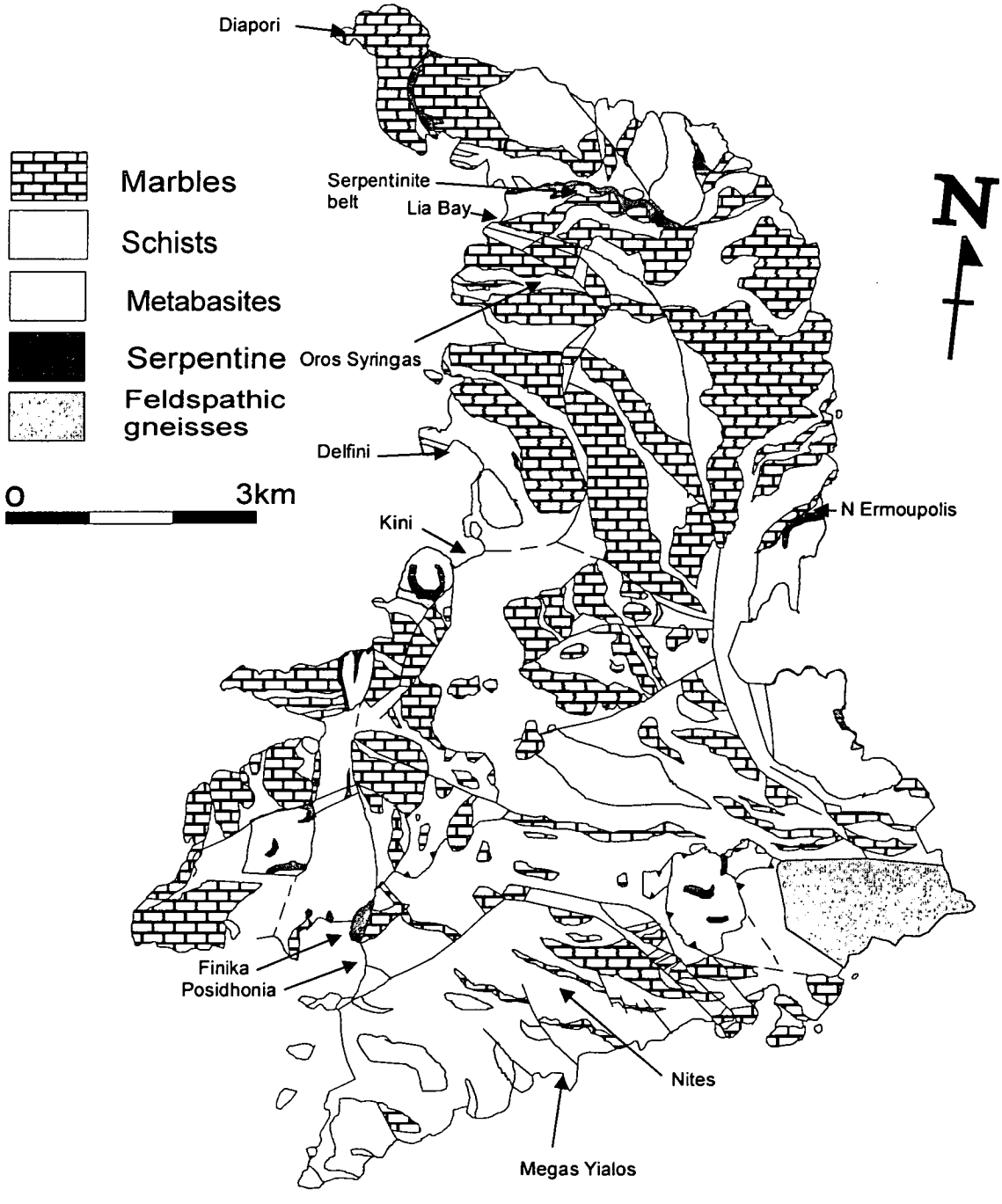

were also documented as showing static growth of albite porphyroblasts, which generally overprint deformation fabrics. However, key localities from the south of the island were found with evidence for ductile deformation associated with the greenschist overprint. These southern localities are presented first documenting the evidence for greenschist ductile deformation.

Southern Localities

Megas Yialos

At Megas Yialos on the south coast of Syros the schist appears to be completely overprinted by chlorite- and albite-bearing assemblages. The outcrops on the Megas Yialos peninsula are strongly foliated and contain albite- and chlorite-bearing veins and segregations in shear zones. Mineral lineations on foliation surfaces are defined by chlorite and trend E-W (figure 3.4). Conglomeratic horizons containing quartz and carbonate clasts also crop out on the eastern side of the peninsula. The clasts are flattened and extended to form an L-S tectonite, the x-axis direction of the flattened pebbles was found to be coincident with mineral lineations in the same section (figure 3.5). The mineral lineation trend is parallel to the finite extension direction and can therefore be used as a proxy for the elongation direction.

Near the end of the Megas Yialos peninsula glaucophane is preserved in the schist. The foliation surfaces measured are slightly tilted due to subsidence of the peninsula into the sea. However, glaucophane mineral lineations are approximately parallel to the chlorite mineral lineations and pebble x-axis measurements from the peninsula (figures 3.4 and 3.5). The parallelism of chlorite and glaucophane mineral lineations to deformed pebble x-axes, suggests that both glaucophane and chlorite mineral lineations define the finite extension direction.

On the eastern side of the Megas Yialos peninsula shear zones are defined by a mineral fabric of chlorite and albite. Chlorite- and albite-bearing segregations are also wrapped by this ductile greenschist fabric, showing that the greenschist minerals are not simply inheriting the early HP fabric. A small-scale map of a rock platform

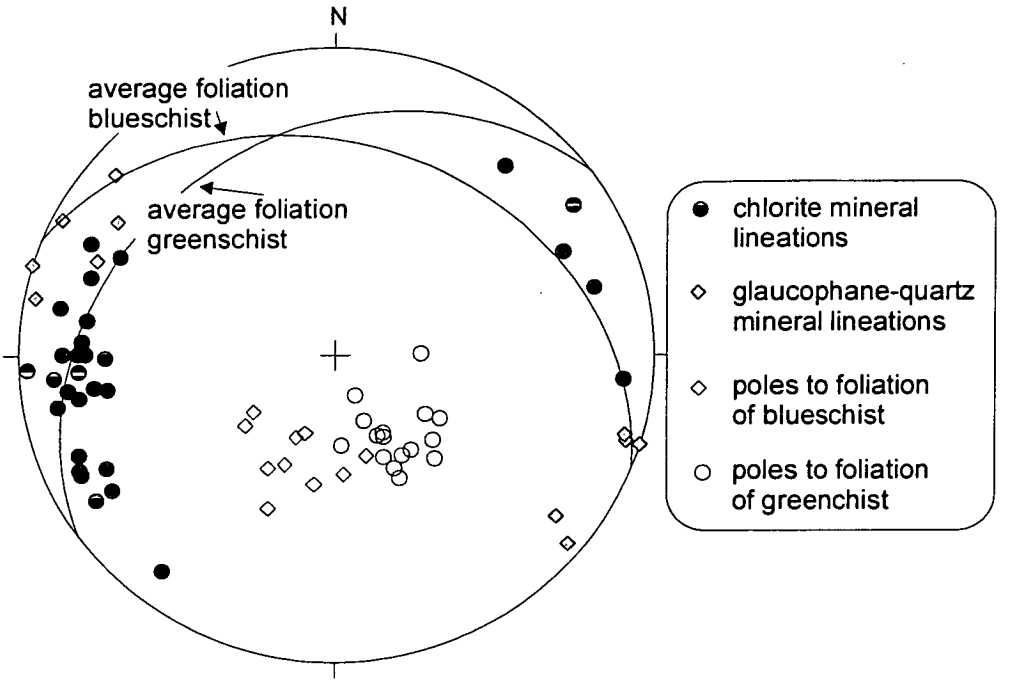

Figure 3.4
Mineral lineations defined by blueschist and greenschist minerals, Megas Yialos. The mineral lineations are from two different areas of the peninsula. The area conatining glaucophane lineations is tilted due to subsidence of the peninsula into the sea.

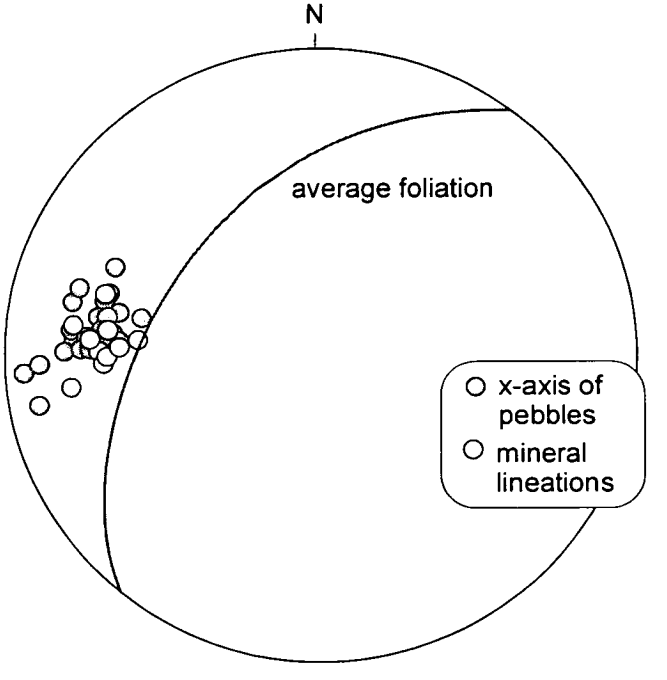

Figure 3.5
Mineral lineations defined by greenschist minerals and deformed pebble x-axis directions in the conglomeratic and adjacent schist horizons, Megas Yialos.

adjacent to the sea shows these greenschist ductile fabrics bending into and cross-cut by brittle fault zones (figure 3.6). Detailed areas are shown in figure 3.7. The semi-brittle faults imply a continuum of deformation from ductile greenschist fabrics through to brittle faulting.

Summary of Megas Yialos

At this first locality, the Megas Yialos peninsula, the outcrops document a range of deformation fabrics formed at different times in the history of the rock. Firstly, chlorite mineral lineations were shown to be parallel to the finite elongation direction of deformed pebbles, this suggests that chlorite mineral lineations formed as a result of extensional deformation and can be used as a proxy for the extension direction. The finite extension direction outlined by both chlorite mineral lineations and the pebble x-axis direction is oriented E-W. This extension direction was in turn shown to be parallel to glaucophane mineral lineations cropping out on the peninsula, suggesting a link between greenschist and blueschist linear fabrics. Finally, extensional brittle faults have been shown locally to be semi-ductile by the bending of greenschist fabrics into fault zones, this is inferred to represent a continuum of deformation from the ductile-brittle regime. The brittle faults described by Ridley (1984b) have the same extension direction as that defined by the mineral lineations and pebble x-axis orientations on the Megas Yialos peninsula.

Deformation fabrics from other localities from southern Syros are presented in the next sections. The rocks from Finika southwards have generally been overprinted by chlorite- and albite-bearing assemblages, which have previously been documented as static (Ridley, 1984a). Local areas within the south document further evidence for greenschist ductile deformation. Data collected at the localities builds a picture of the kinematics of ductile extensional deformation within the greenschist facies stability field.

Figure 3.6
Sketch map of greenschist shear zones bending into and being cross-cut by brittle faults,
Megas Yialos

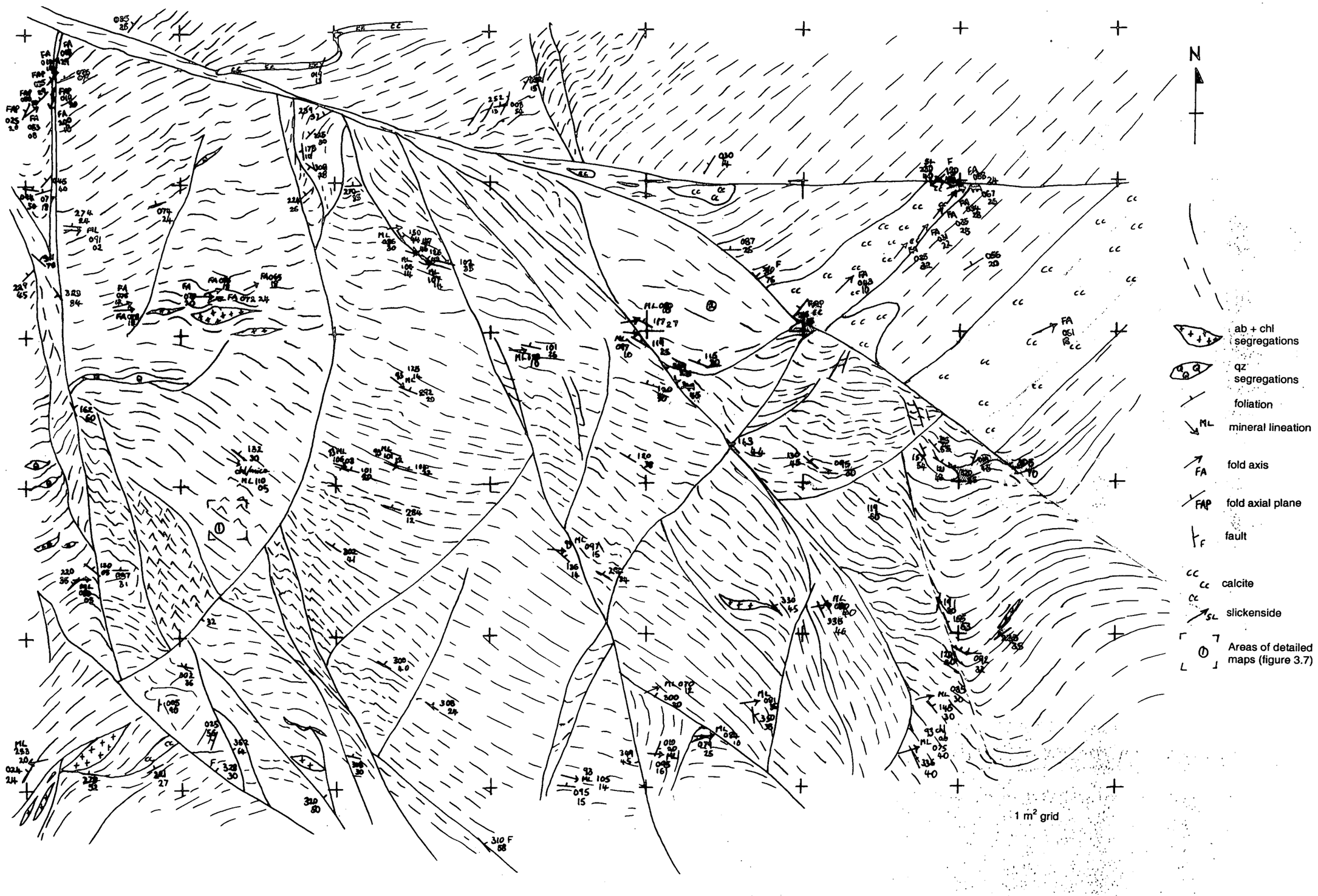

Figure 3.7
Detailed sketches of areas in figure 3.6. Foliation defined by greenschist minerals, which bend into the brittle fault zone. Key as for figure 3.6.

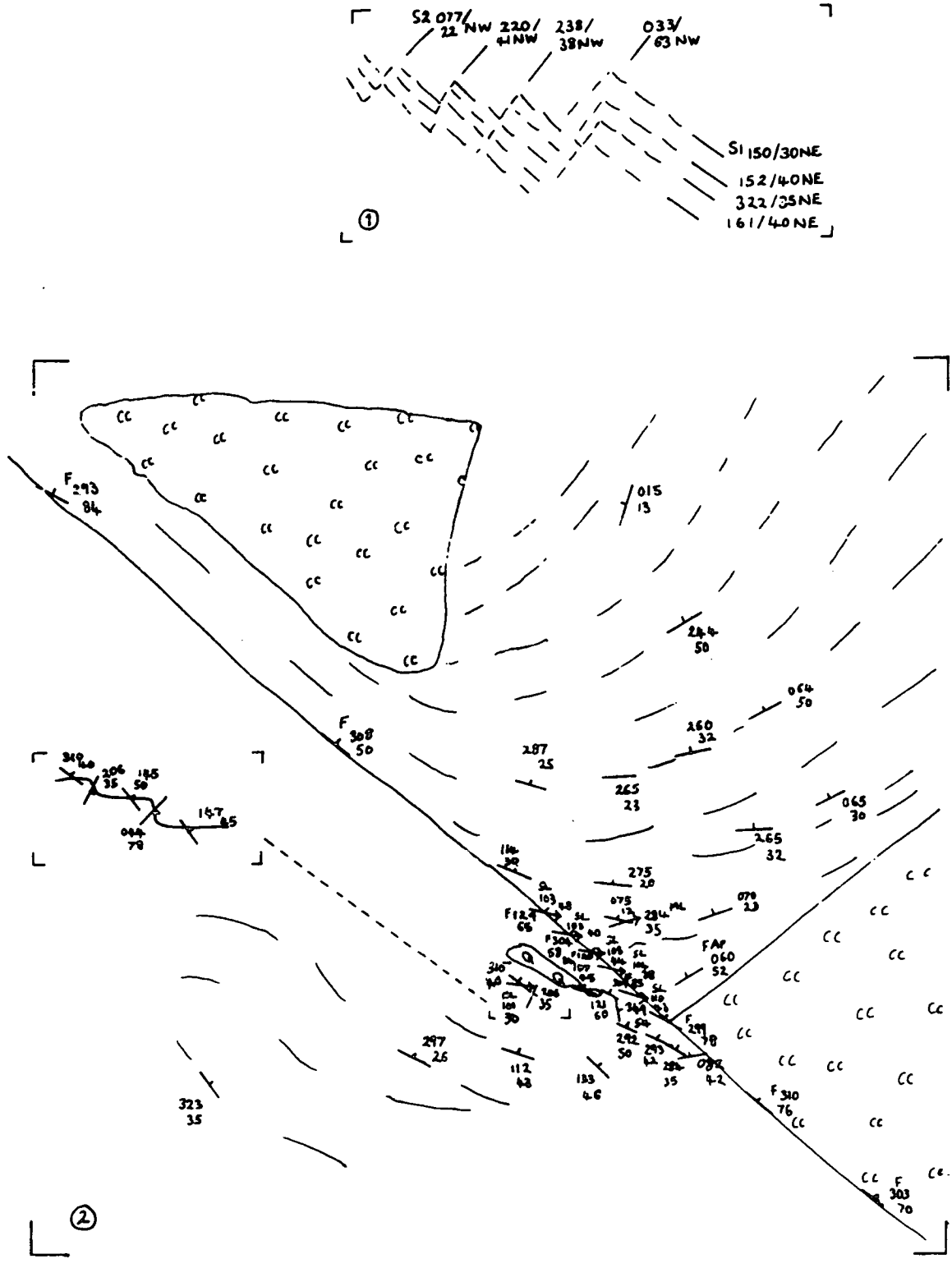

Nites

The hillside north of Megas Yialos is part of the Nites massif. The rocks that crop out on the hillside are variably overprinted with retrogressive chlorite- and albite-bearing assemblages. Figure 3.8 is a map of a section of the southern side of the massif. The map shows boudinage of marble and metabasite layers with an E-W oriented extension direction. This extension direction is parallel to that defined by mineral lineations and pebble x-axes at Megas Yialos on the southern coast. All units are boudinaged on a map to outcrop scale. Marble horizons and layers which are rich in epidote porphyroblasts tend to form the boudin bodies and are inferred to have been more competent than surrounding layers.

Veins containing varying mineral assemblages including, epidote, quartz, albite, chlorite and calcite infill boudin necks, documenting fracture of necks and fluid infiltration within the greenschist facies stability field. The veins and shape of boudin necks are similar to those documented by Platt and Visser (1980) and are consistent with layer parallel extension.

A single boudinaged layer was targeted for detailed study. Vein orientations in boudin necks and boudin neck axes are consistent with NW-SE to E-W directed extension of the layer (figure 3.9). Greenschist vein orientations from across the Nites hillside are also consistent with this extension direction (figure 3.10), except at a single locality where veins trend E-W. The change in length of the boudinage layer was measured to estimate boudinage by elongation (e) of the layer, where e is:

$$e = l_1 - l_o / l_o$$

l_1 = present layer length

l_o = original layer length prior to boudinage

Elongation (e) of the layer by boudinage is 0.06 (6 %). A more realistic estimation of elongation would be achieved if ductile elongation was taken into account. For example the maximum thickness of the layer over the 20.85 m length

Figure 3.8
Map of Nites hillside

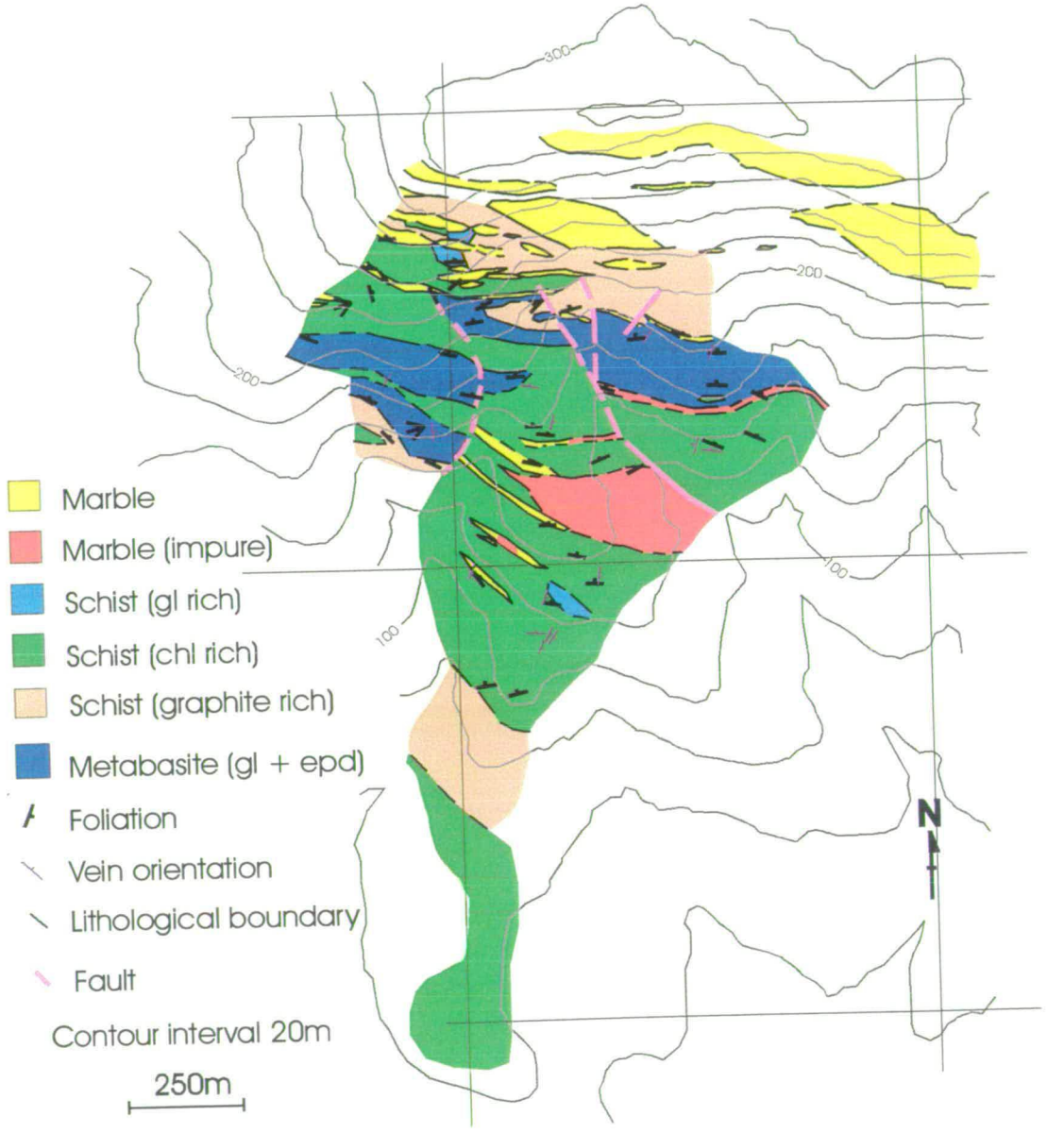

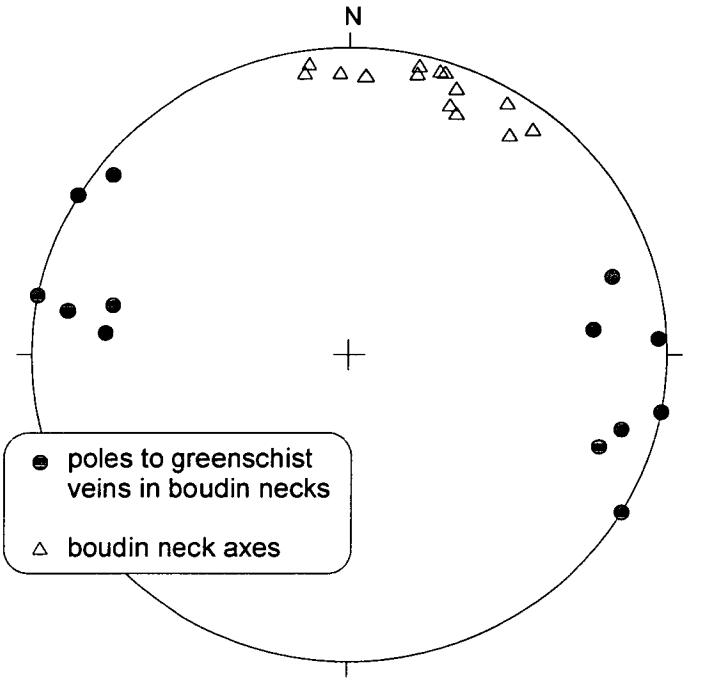

Figure 3.9
Stereonet of vein orientations and boudin axes from a single boudinaged layer, Nites

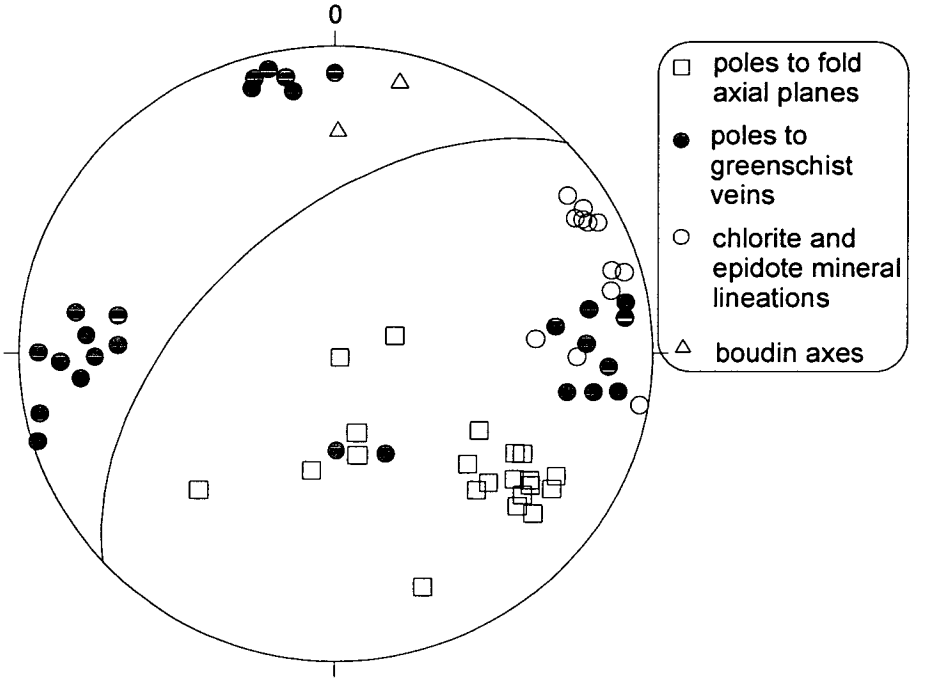

Figure 3.10
Equal area stereonet of planar and linear features from the Nites hillside. The average foliation is marked as a great circle and is the average of foliation measurements from across the hillside.

used in the study was 15 cm. A further 35 measurements of layer thickness were made along the layer; the average thickness of the layer calculated from these 35 measurements was 7.4 cm, indicating a thinning of 49%. This 49% thinning is thought to be closer to the actual value than the 6% elongation estimated by boudinage. The percentage of the thinning that occurred within the greenschist facies stability field is unknown, but potentially only the 6 % extension achieved by boudinage occurred within the greenchist field. Fabrics in the boudinaged schist are now defined by greenschist minerals, although these minerals may simply be inheriting an earlier HP fabric. The presence of metabasic, lens shaped, bodies of glaucophane and epidote on the hillside suggests that at least some of the boudinage occurred within the blueschist facies stability field. This is supported by the observations of Barr (1989) who noted the development of foliations in the margins of the glaucophane-epidote metabasite bodies.

Summary of Nites

The outcrops on the Nites hillside document layer parallel extension of all units at a range of scales, from map to outcrop. The extension direction is E-W to NW-SE, documenting local variability in the extension direction. The extension direction is however approximately parallel to the extension direction marked by mineral lineations and pebble x-axes at Megas Yialos. Albite- and chlorite-bearing vein fills in boudin necks suggest boudinage occurred within the greenschist facies stability field. Extensional greenschist veins that are not structurally associated with the boudinage also document E-W directed extension. A high percentage of the ductile thinning is thought to have occurred within the blueschist facies stability field.

Finika-Posidhonia

The geology of central Finika is dominated by an ultramafic melange. The melange crops out below the house on the peninsula which separates the two bays of Finika. Deformation within the ultramafic melange is complex. This is partly due to

localisation of deformation onto serpentinite. The edge of the serpentinite belt to the south between Finika and Posidhonia was targeted for study.

An albite-, chlorite-bearing mylonite crops out on a short, approximately 20 m long, coastal section at the southern contact of the serpentinite. The mylonite is distinctively striped green and white on foliation surfaces (photograph 3.1). The rock is both folded and flattened to form an L-S tectonite (photograph 3.2). The rock is flattened parallel to the foliation and the extension direction, defined by mineral lineations and rodded fold hinge lines, trending NE-SW (figure 3.11). Thin section observations reveal a fine grained banded rock (photograph 3.3 and 3.4). The bands are 1-2 mm wide and contain albite and chlorite, and, chlorite, calcite and epidote. With detailed examination extensional fabrics are observed defined by chlorite shear fabrics around albite crystals (figure 3.5). The extensional shears are symmetrical about the albite crystals, documenting pure shear. Albite-chlorite extensional veins form perpendicular to the extension direction (figure 3.12 and photograph 3.6), with chlorite and albite growing in from the wall rock (photographs 3.7 and 3.8).

Summary of Finika-Posidhonia

The locality documents intense localised, NE-SW oriented, extensional deformation and layer parallel flattening within the greenschist facies stability field across the full 20 m of outcrop. The deformation is coaxial, pure shear, layer parallel extension. This area of localised deformation documents accommodation of extensional strain within the greenschist facies stability field. Some of the strain was accommodated by fracture and vein formation as well as ductile thinning.

Kini

The short accessible coastal section just north of Kini was chosen for detailed work. The section was chosen because the metabasic blocks, which crop out at Kini, show partial preservation of high pressure assemblages and greenschist ductile deformation. It was thought that the locality might preserve evidence for a kinematic link between partially retrogressed high pressure assemblages and the greenschist

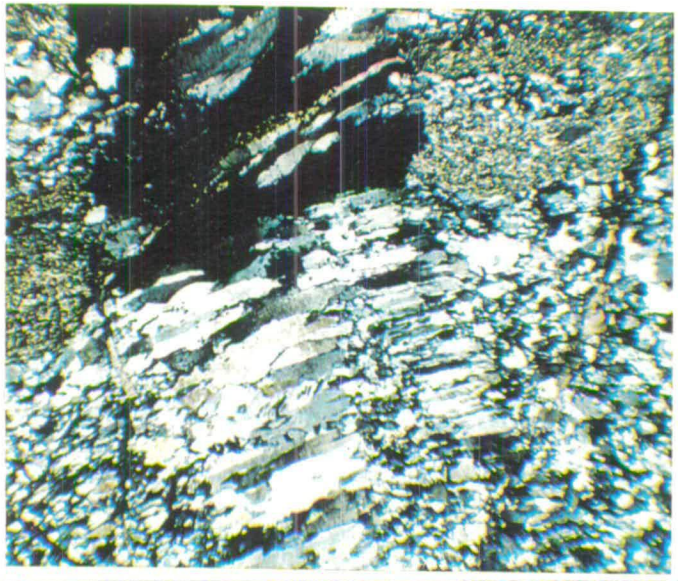

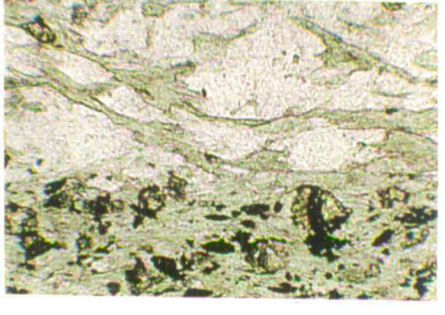

Finika

Photograph 3.7

Cross polars view of thin section S'96/25, shown in photograph 3.8. Finika-Posidhonia.

Field of view approximately 8 mm

Photograph 3.6

Field photograph of extensional chlorite and albite veins, Finika-Posidhonia.

Field of view approximately 5 cm

Photograph 3.1

Stripey appearance and flattening fabric of the mylonite in the field, Finika-Posidhonia. Photograph taken looking approximately north.

Field of view approximately 12 cm

Photograph 3.8

Thin section photograph of S'96/25, Finika-Posidhonia. An extensional albite and chlorite vein. Note that the vein mineralogy is controlled by the wall rock, with minerals growing into the vein from the wall rock.

Field of view approximately 8 mm

Photograph 3.3

Cross polars view of sample S'96/27, showing the banding within the mylonite at Finika-Posidhonia.

Field of view approximately 2 mm

Photograph 3.4

Banding in the mylonite sample S'96/27, at Finika-Posidhonia. Bands contain epidote and chlorite (darker layers) or albite and chlorite +/- calcite.

Field of view approximately 2 mm

Photograph 3.2

Folding with an axial planar flattening fabric. Photograph taken looking approximately northeast.

Field of view approximately 40 cm

Photograph 3.5

Detail of chlorite shear zones around albite, sample S'96/27, Finka-Posidhonia.

Field of view approximately 1 mm

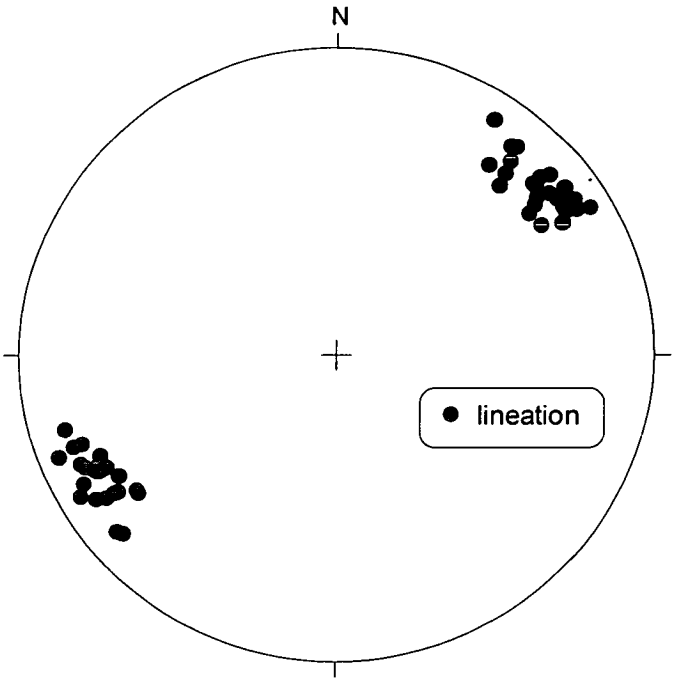

Figure 3.11
Lineation defined by albite chlorite L-S tectonite, Finika-Posidhonia

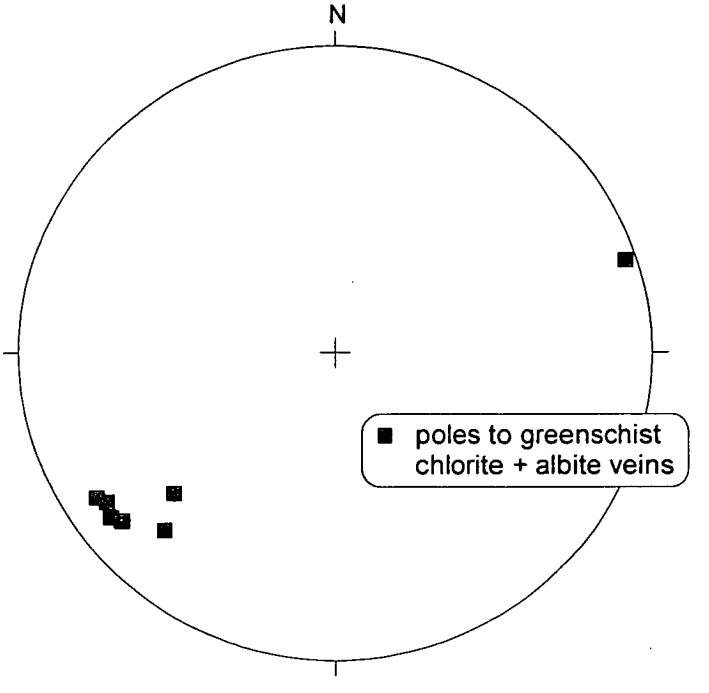

Figure 3.12
Poles to extensional albite-chlorite veins, Finika-Posidhonia

deformation documented at the southern localities. The majority of the section forms a small cliff which is sketched and annotated (figure 3.13). The sketched section is described from right to left (SE-NW).

The first 10 m of the section are dominated by a sub-layer parallel extensional shear zone (197/17 NE) which forms the contact between an upper pale grey, quartz-epidote porphyroblast rock and a lower green, chlorite-epidote porphyroblast rock (photograph 3.9). The contact between the two lithologies is lined with serpentinite and blocks of the lower green rock are found within the serpentinite.

In thin section the pale grey rock is dominated by quartz and epidote, but contains glaucophane, mica, chlorite and an opaque phase (photograph 3.10). An early fabric is outlined by opaque minerals which are included in the epidote porhyroblasts; glaucophane crystals are also included in epidote porphyroblasts. The early fabric is planar and outlines small intrafolial folds. The main fabric in the rock is outlined by mica, glaucophane, and opaque crystals and is generally oblique to the internal fabric of the epidotes. Small undulations in the foliation around epidote porphyroblast suggests minor rotation of the epidotes. Small fractures in the epidote and glaucophane are perpendicular to the foliation and are generally infilled with calcite or chlorite. Both epidote and glaucophane are partially retrogressed to chlorite. Epidotes are also cut by 'major' fractures and adjacent crystals are pulled apart parallel to foliation, accommodating foliation parallel extension. These fractures are infilled with quartz, mica and chlorite.

The thin section (photograph 3.10), from the quartz-epidote porphyroblast rock, is oriented and the extension direction is approximately E-W. The majority of the strain was probably accommodated by the serpentinite, which lines the contact between the two rocks. However, the upper, quartz-epidote rock clearly preserves brittle extensional structures which have accommodated strain post epidote-porphyroblast growth, within the greenschist facies stability field.

The green rock below has an assemblage of chlorite, epidote, calcite, mica, and quartz. The rock is folded on a macro-scale (photograph 3.9) and fold hinge lines are oriented E-W. Epidote porphyroblasts appear to be randomly oriented in sections

Figure 3.13
Field sketch of Kini section, distances in metres.

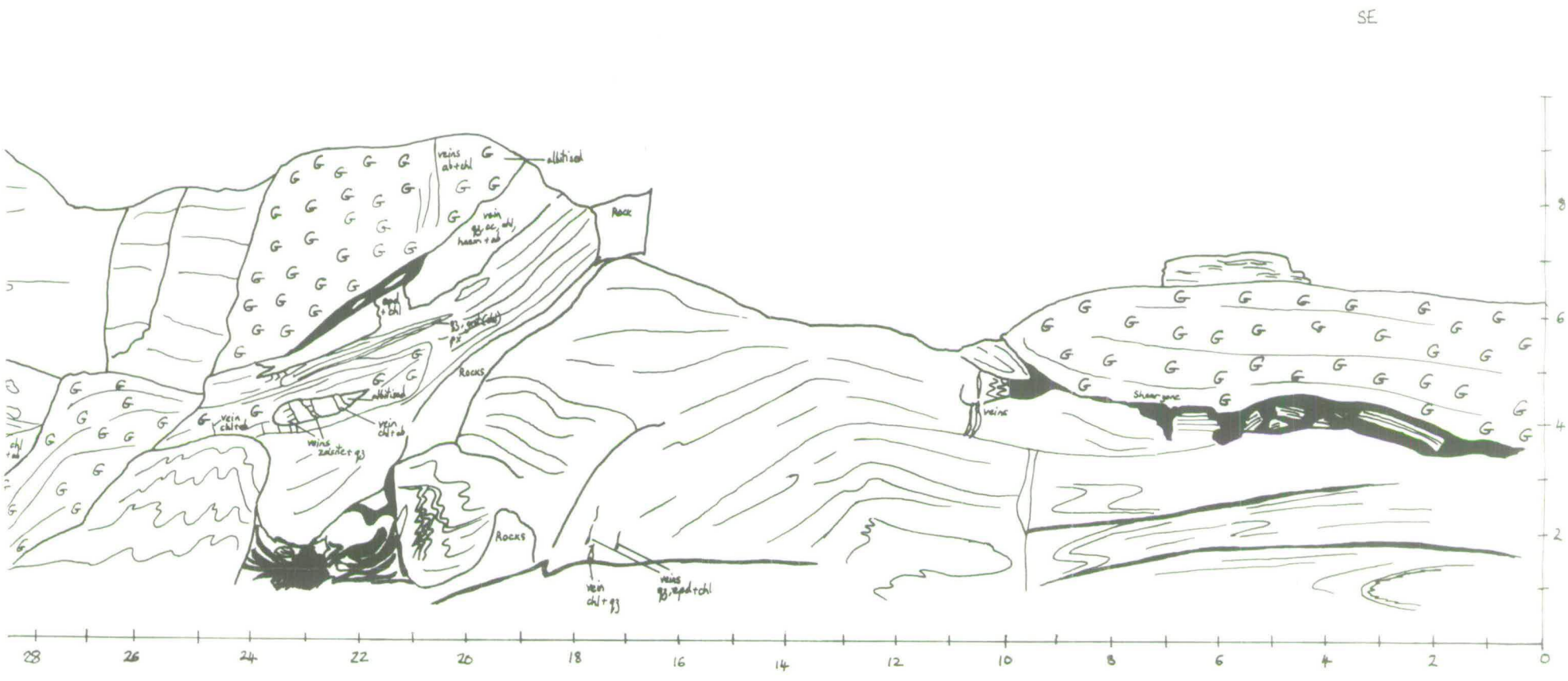

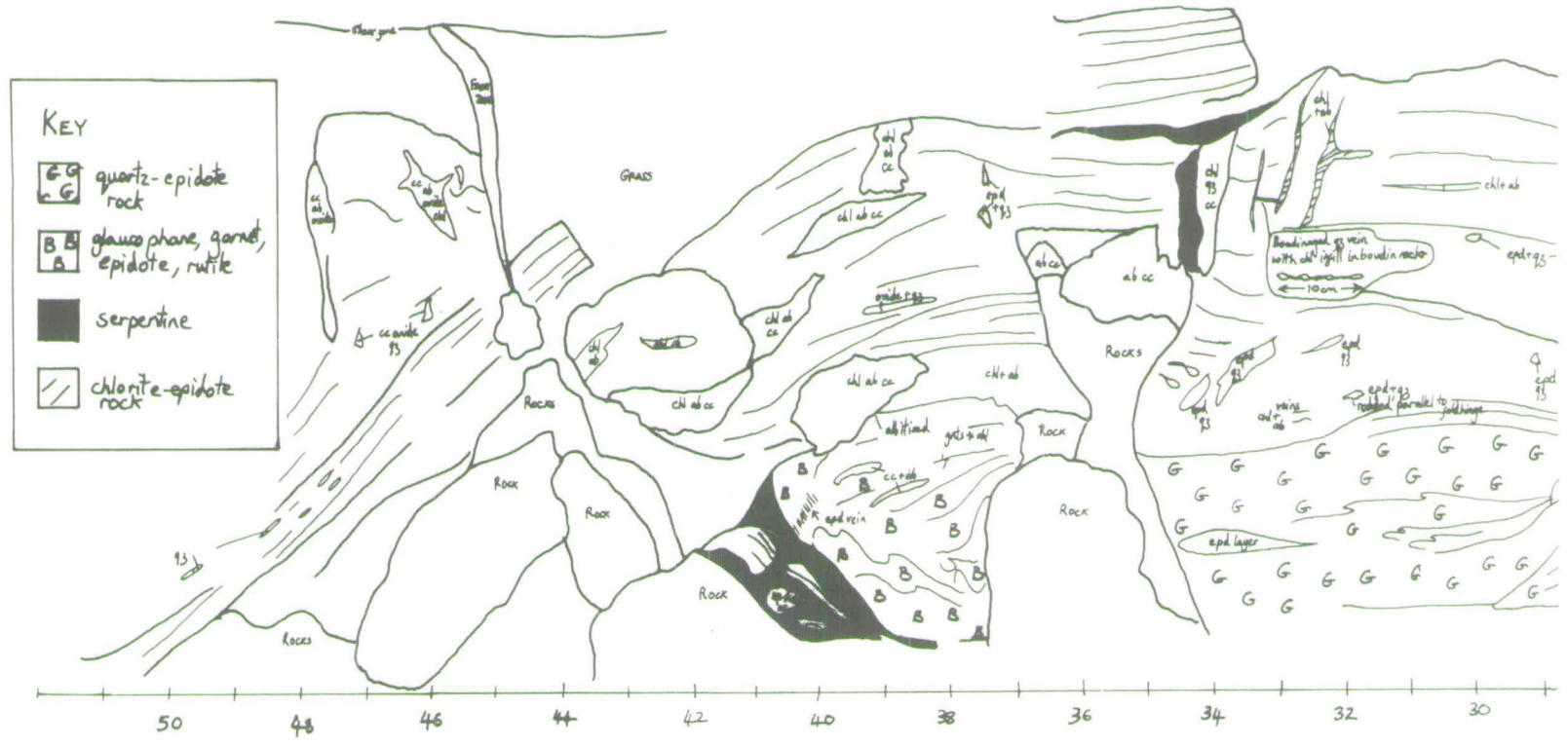

perpendicular to the fold axial plane but on foliation surfaces are seen to form a mineral lineation that parallels fold hinge lines (figure 3.14 and 3.15). The timing of the folding and lineation development is inferred to have formed within the blueschist facies field, as glaucophane crystals are included in the epidote. The rock also contains extensional shears infilled with a calcite precipitate, which accommodate coaxial layer parallel extension. Epidote crystals are zoned (photograph 3.11) and have Fe^{3+} depleted rims. The epidotes are partially statically pseudomorphed by chlorite, calcite, paragonite and quartz (photographs 3.11 and 3.12), probably by the reaction:

$$3\ Gl + 6\ Epd + 8\ H_2O + 12\ CO_2 \rightarrow 1\ Chl + 12\ Cc + 19\ Qz + 6\ Pa$$

The reaction requires infiltration of a H_2O and CO_2 bearing fluid and may be related to the formation of the calcite extensional shears.

From 15 m the section becomes complex and the grey quartz-epidote porphyroblast rock cuts down through the section. The contact is marked by a quartz, calcite, chlorite, albite, oxide vein; surrounded by an albite halo. The base of the section is blocky and entrained in serpentinite; thin metasomatic alteration haloes are noted to have formed along the contact of blocks with the ultramafic. Epidote and quartz segregations are present in the chlorite-epidote porphyroblast rock above, epidote crystals in segregations are fibrous and aligned E-W. Extensional chlorite albite veins and chlorite, albite, calcite segregations are also present. At the base of the section, at a distance of 38 m, the block in contact with the ultramafic has partially retained its blueschist mineral assemblage and contains epidote, glaucophane, garnet and rutile. It is retrogressed to an albite and chlorite-bearing assemblage adjacent to a chlorite, albite, calcite segregation. The block also contains an extensional epidote vein.

Epidote-bearing assemblages show alignment of epidote-porphyroblasts and epidote crystal fibres in veins in an E-W oriented direction. This is parallel to the documented brittle extension of epidote porphyroblasts, within the greenschist

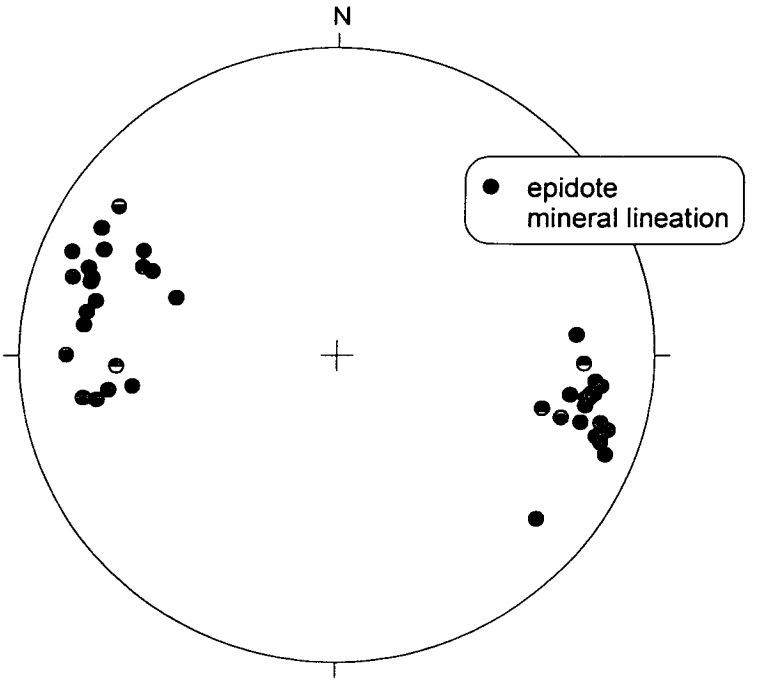

Figure 3.14
Equal area stereonet of epidote mineral lineations, Kini

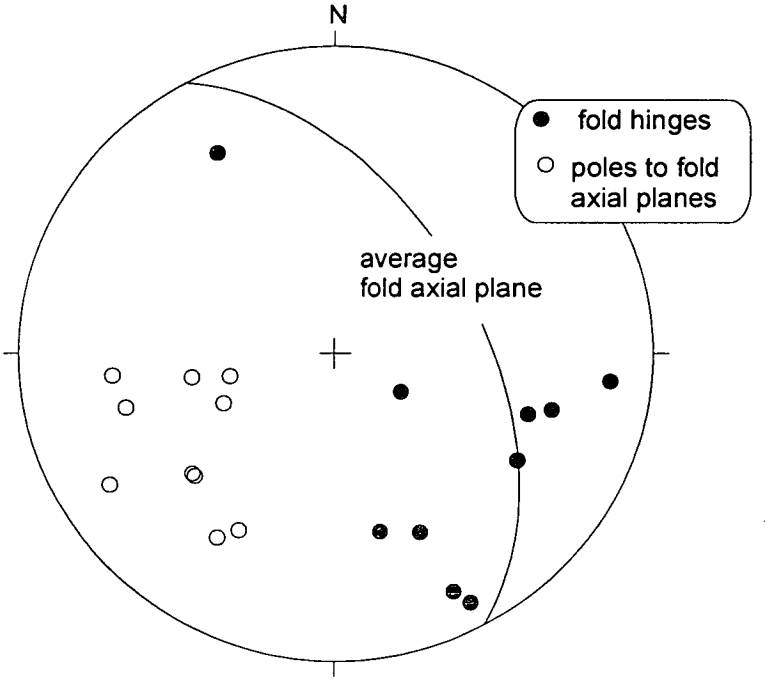

Figure 3.15
Equal area stereonet of fold axial planes and hinge lines, Kini

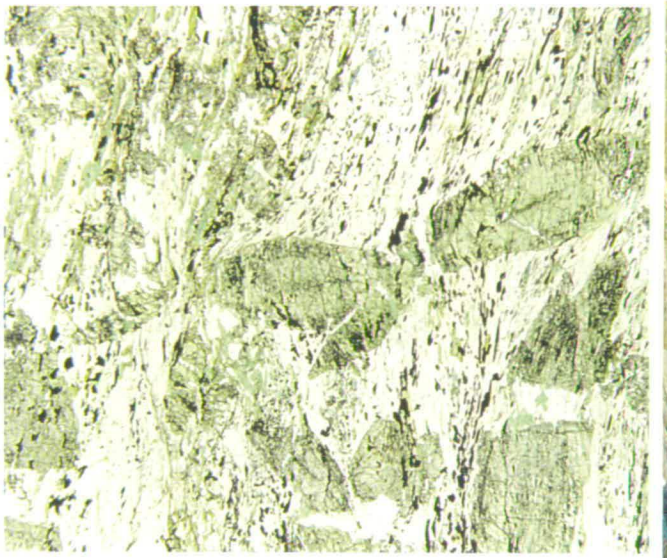

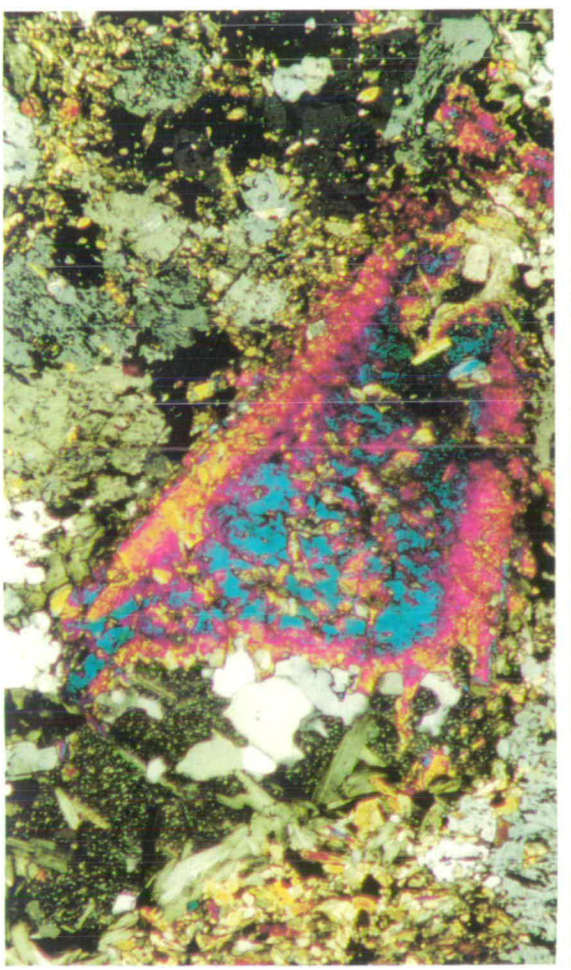

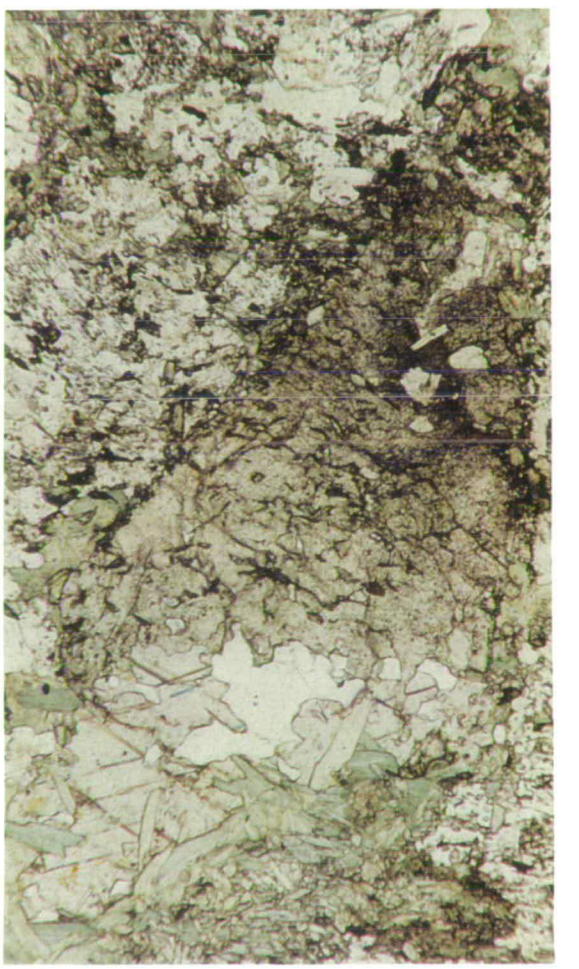

Photograph 3.9

Photograph of extensional shear zone contact between quartz-epidote, grey rock (top) and chlorite-epidote, green rock (bottom), Kini. Note folds in the lower left hand corner. Photograph taken facing NE.

Field of view approximately 10m

Photograph 3.10

Thin section photograph of sample S'96/162 from the quartz-epidote rock at the contact. Epidote porphyroblasts are fractured perpendicular to the fabric. Fractures are infilled with quartz and chlorite (e.g. upper right)

Field of view approximately 8 mm

Photograph 3.12

Photograph of epidote in green chlorite-epidote rock below the shear zone in photograph 3.9. The epidote is being pseudomorphed by chlorite, calcite and quartz. Sample S'95/8, Kini.

Field of view approximately 4 mm

Photograph 3.11

Cross polars view of sample S'95/8, photograph 3.12. Note the zoning in the epidote crystal.

Field of view approximately 4 mm

stability field, at the SE end of the section. The parallelism of epidote and greenschist fabrics implies a kinematic link between E-W directed extension during epidote growth and later greenschist facies deformation.

At the SE end of the section blocks preserve higher pressure assemblages including a banded sodic pyroxene, glaucophane, epidote rock and glaucophane epidote porphyroblast rock. These are thought to be the precursors, prior to down-pressure recrystallisation and hydration, to the chlorite-epidote porphyroblast rock found in the sketched section. At the very south eastern end, near the harbour wall, the outcrop forms an angled platform which was sketched and annotated to document vein assemblages and orientations (figure 3.16) Veins mainly of greenschist grade, containing albite and chlorite, trend N-S to NE-SW.

Summary of the Kini coastal section

The Kini section documents a kinematic link between high pressure, epidote-bearing, fabrics and greenschist deformation. There is evidence for extensional strain during epidote growth as extensional fibres of epidote are observed in veins and epidote porphyroblasts are aligned E-W. Fold hinge lines in the chlorite-epidote porphyroblast rock are aligned E-W parallel to the epidote porphyroblasts. The epidote porhyroblasts include glaucophane crystals and the folding and epidote mineral lineation is inferred to have formed within the epidote-blueschist facies stability field. This epidote mineral lineation is parallel to chlorite and albite mineral lineations documented in the fully retrogressed and deformed greenschists of the south. The fold hinge lines aligned parallel to the mineral lineation may be related to layer parallel extension by flattening. Flattened folds at Finika had rodded fold hinge lines parallel to the extension direction defined by a mylonitic greenschist fabric.

Epidote was also seen in extensional veins at Kini. Fibres of epidote trending E-W are seen growing into veins and segregations. These epidote veins are parallel to chlorite- and albite-bearing veins, which open perpendicular to sub-perpendicular to the extension direction. Alignment of epidote mineral lineations and extensional epidote veins parallel to chlorite and albite mineral lineations and veins suggest that

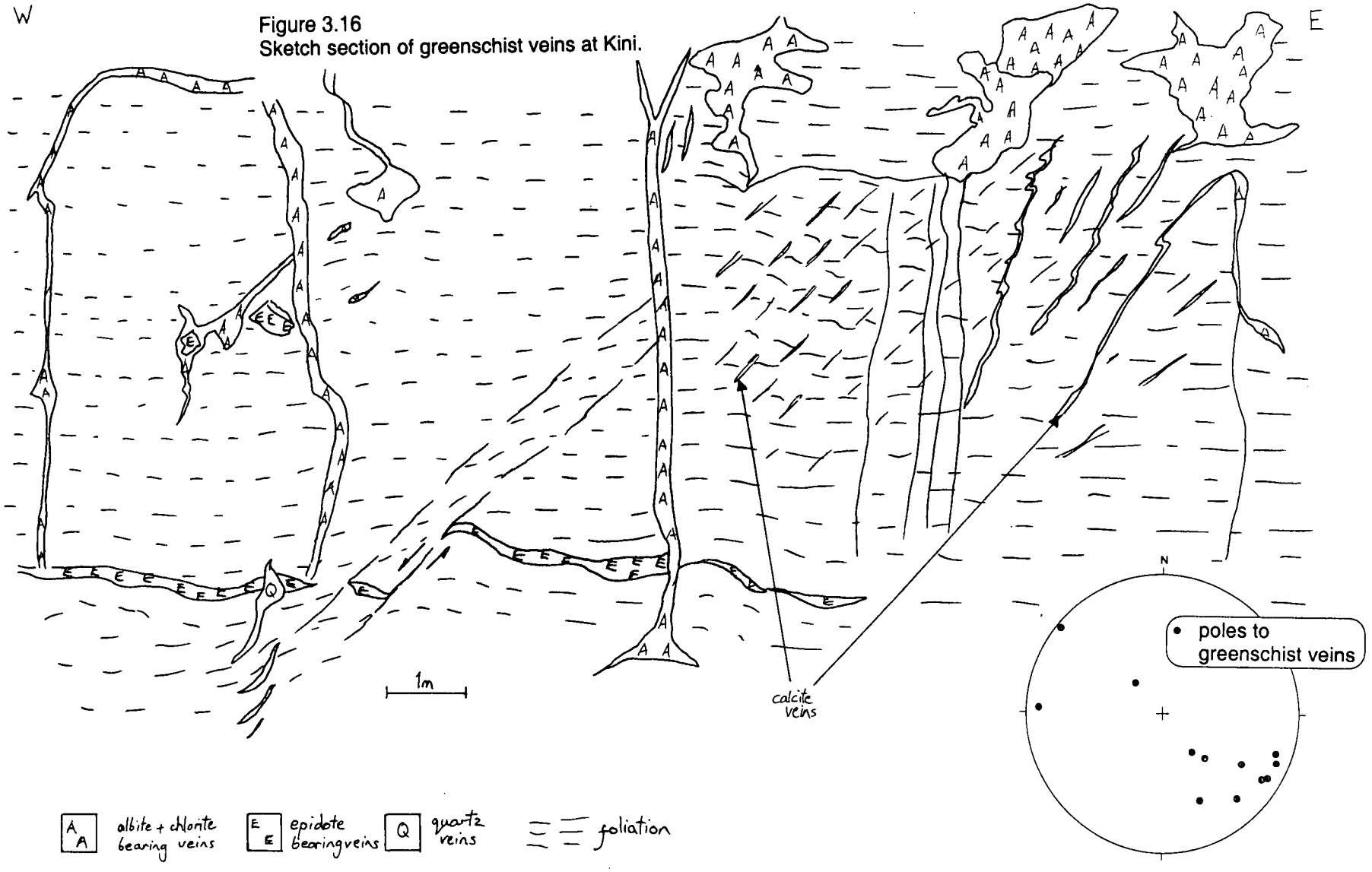

Figure 3.16
Sketch section of greenschist veins at Kini.

the kinematics of extension were the same during epidote growth and greenschist facies overprinting.

Evidence for layer parallel extension is documented by brittle fracture of epidote porphyroblasts along the quartz-epidote and chlorite-epidote lithological contact. Deformation is probably concentrated in the serpentinite which lines the contact. The extension occurred within the greenschist facies stability field, post epidote growth and fractures of porphyroblastic epidotes are filled with quartz, chlorite and mica. Later retrogression of epidote appears to be static, but may be related to the infiltration of fluid associated with the formation of coaxial extensional shear zones and precipitation of calcite.

Summary of the Southern Localities

Ridley (1982a) and Barr (1989) both describe greenschist retrogression in southern Syros as a static process. This study has documented localised zones of greenschist fabric development in the south of the island. These greenschist structures are interpreted as being related to extension and exhumation during greenschist recrystallisation. Between these zones of localised deformation the greenschist overprint appears static, and in the majority of the south it is clear that there has been no penetrative deformation since albite porphyroblast growth. The ductile greenschist deformation was shown at Megas Yialos to bend into zones of brittle faulting, documenting a continuum of deformation from ductile-brittle deformation. The E-W to NE-SW extension direction inferred from extensional greenschist veins, mineral lineations and boudinage is parallel to that documented by Ridley (1984b) for island scale brittle faults. At Kini there is evidence that this localised E-W to NE-SW directed extensional deformation is kinematically linked to HP fabrics. The HP fabrics are defined by epidote minerals, which include a glaucophane fabric and are parallel to greenschist fabrics. Further evidence for a kinematic link to HP fabrics is presented for localities in central and northern Syros.

Central-northern localities

As documented by earlier workers (Ridley, 1982a and Barr, 1989) greenschist retrogression in southern Syros is almost pervasive. This recrystallisation to greenschist mineral assemblages generally precludes documentation of extensional structures related to early decompression within the blueschist facies stability field and of documenting a kinematic link between greenschist and blueschist deformation. The following locality descriptions are from the central-northern area of Syros (below the serpentinite belt) where retrogression of high pressure assemblages is patchy. These localities therefore contain ideal mineral assemblages to identifiy kinematic links between greenschist and blueschist deformation.

Delfini

The Delfini area was chosen for its diversity in structure, lithology and metamorphic assemblage. It seemed the obvious locality at which to try and kinematically link high pressure fabrics with retrogressed equivalents. Ridley (1982a) identified high pressure boudinage in the area, and described it as an area of deformation which was structurally distinct from other areas in which he had documented structure (mainly northern localities). He interpreted the Delfini peninsula and the coast line from Kini to Delfini as representing a large fold pair in the metabasite. He documented high pressure boudinage in the metabasite interpreting it as attenuation of fold limbs. Ridley suggested that the boudinage was synchronous with early fabric formation and inferred shear parallel extension and shortening. Contrary to this study he also noted the lack of a linear fabric in this area.

North of Delfini bay the coast line forms a prominent peninsula. This peninsula and the coast line to the north were mapped up to the marble band which caps the hill over looking the bay and forms a prominent cliff line (figure 3.17). The sequence consists of a layered succession of marble, schist, quartzites, conglomerates and metabasites. The coastline is almost continuous exposure and provides an opportunity to document strain localisation in the sequence and the structural and

Figure 3.17
Map of Delfini area, with locations of logs marked.

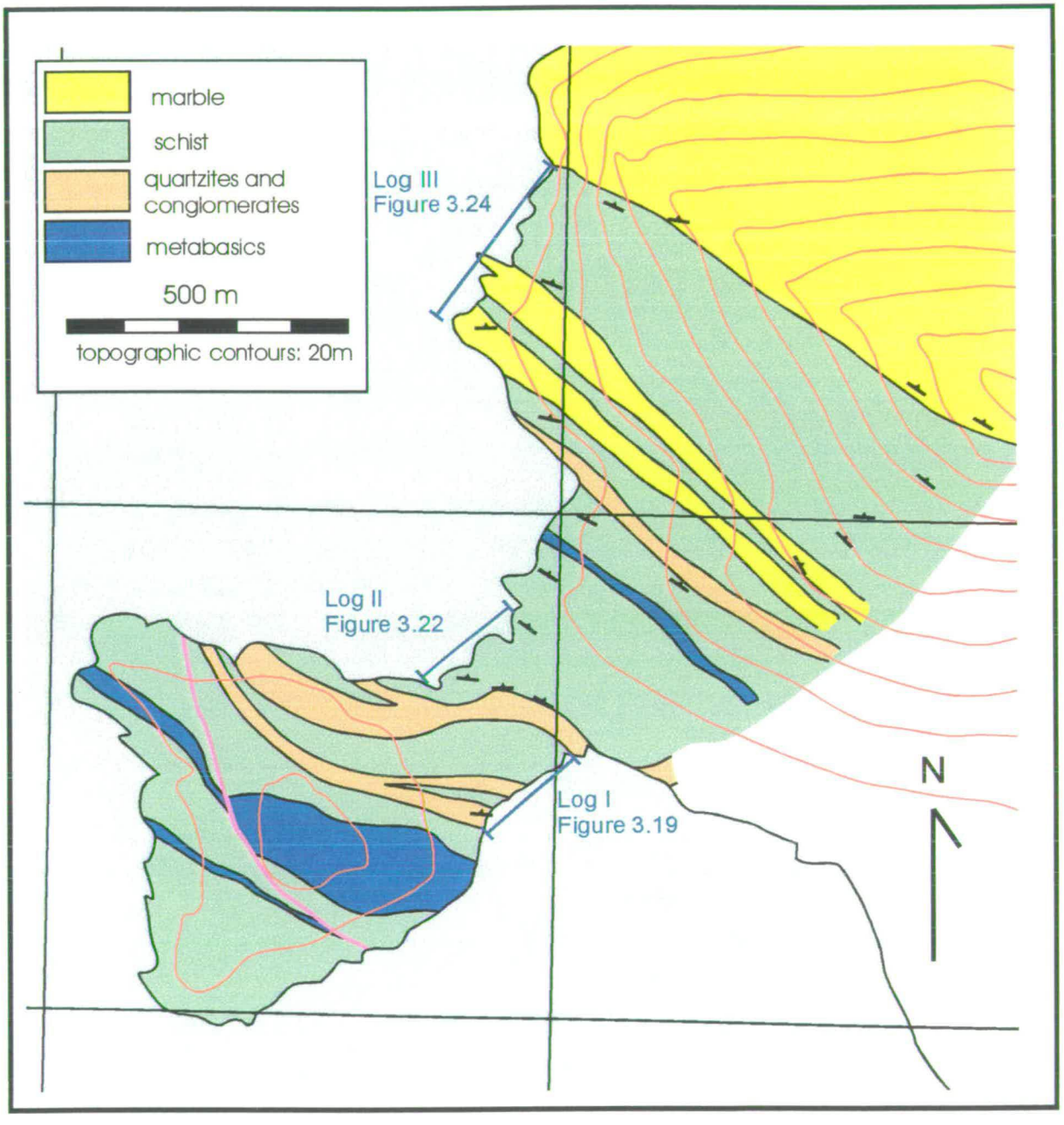

kinematic continuity between lithologies and rocks of different metamorphic grades. To document this, sections of the coast line were logged and structural data were collected. The key to the logged lithologies is shown in figure 3.18.

The area logged on the SE side of the peninsula (log I, figure 3.19) was chosen because it contains a range of metamorphic assemblages from epidote-blueschist to fully retrogressed greenschist. It also contains a deformed conglomeratic horizon, so the direction of the mineral lineation can be compared with the finite extension direction defined by deformed pebble x-axes. The orientation of the pebble x-axes can also be compared with those measured in the conglomeratic horizon on the south coast at Megas Yialos.

All lithologies are interleaved, with no evidence for fault contacts between the lithologies. In the logged section macro-scale coaxial layer parallel extension in epidote-blueschist layers was documented. Figure 3.20 A, is a field sketch of the extensional fabric. Extension was accommodated by symmetrical shear zones of glaucophane and quartz boudinaging epidote layers, the boudinage extending an earlier layer-parallel foliation. Macro-scale boudinage is common in the section (photograph 3.13). The same epidote-blueschist horizons are also symmetrically boudinaged on a metre scale, with fractured boudin necks infilled with greenschist grade albite and chlorite veins (figure 3.20 B). Early segregations of epidote are also fractured and cross-cut by albite, chlorite veins (figure 3.20 C). The early macro-scale blueschist grade boudinage is being overprinted by metre scale boudinage within the greenschist facies stability field, evidence for a kinematic link between greenschist extensional structures and higher grade deformation.

Mineral lineations of glaucophane and epidote in the epidote-blueschist trend E-W. This is parallel to mineral lineations outlined by chlorite and albite assemblages in southern Syros. This parallelism of mineral lineations is further evidence to suggest a kinematic link between blueschist and greenschist mineral fabrics.

Sketch map 3.21 shows a section of the logged sequence in which a quartzite layer is pinched out by boudinage (photograph 3.14). The pinched-out area contains numerous albite, chlorite and ankerite segregations and the area around the quartzite

Figure 3.18
Key for Delfini logs

Marble

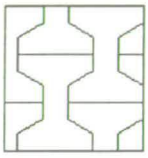

Carbonate rich metabasite

Schist, variably retrogressed

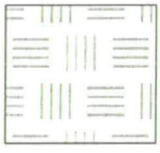

Brecciated marble

Calcite clasts in calcite matrix

Quartzite

Quartz mica schist +/- garnet

Metabasite clasts in calcite matrix

Figure 3.19
Log (l) on map, figure 3.17. Letters refer to field sketches in figure 3.20.
See figure 3.18 for lithology key, distances in m.

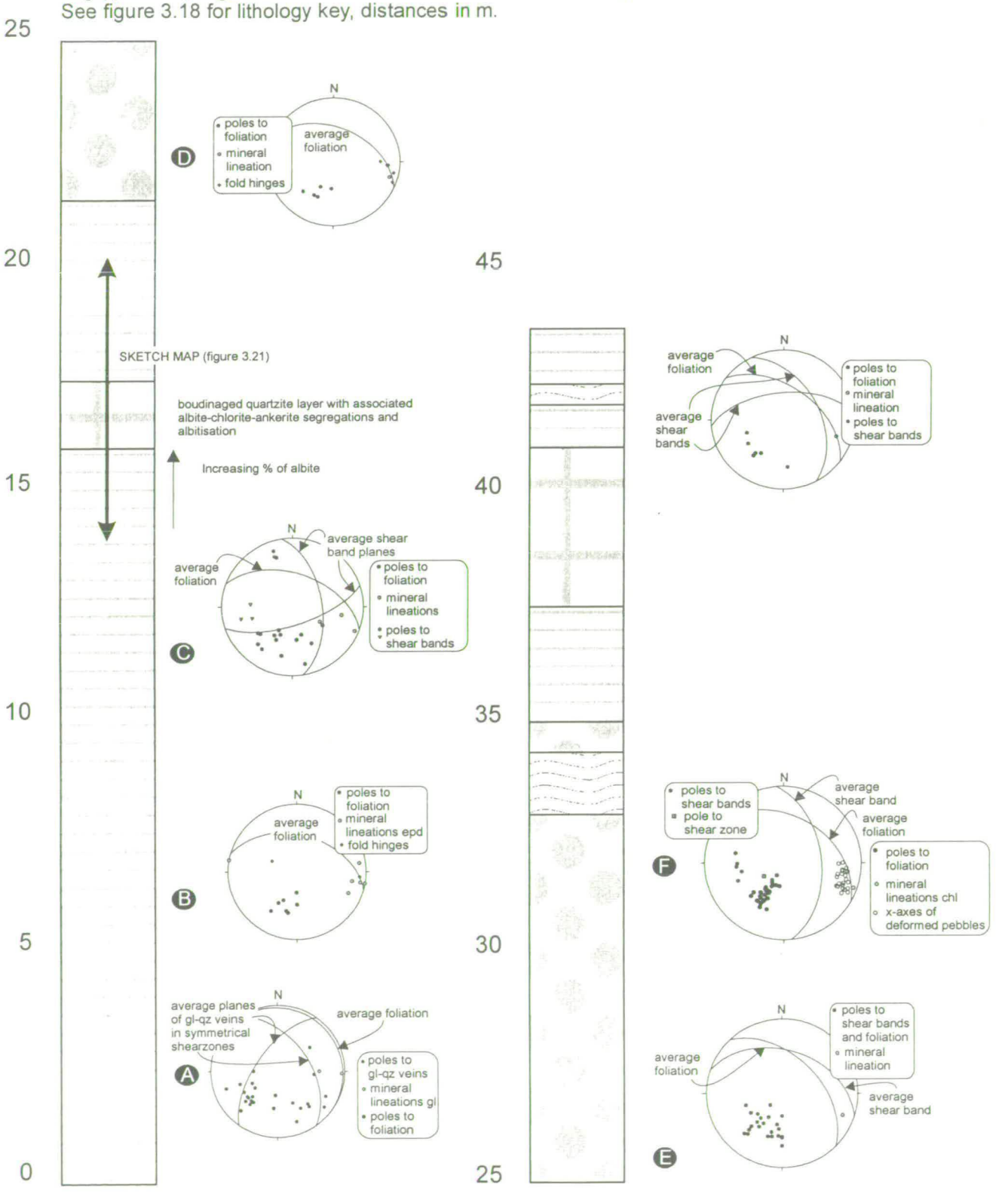

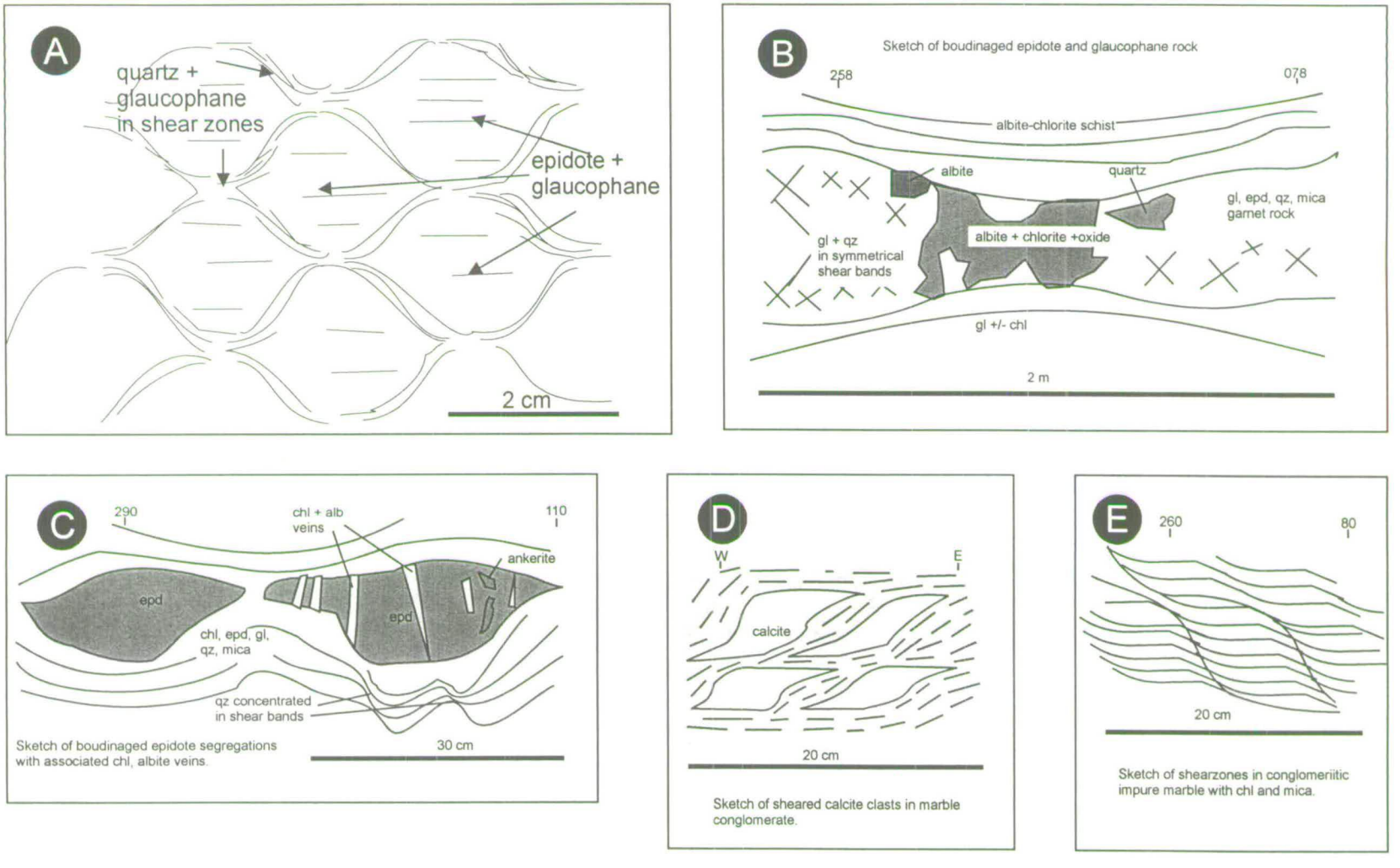

Figure 3.20
Field sketches linking to log I, figure 3.19.

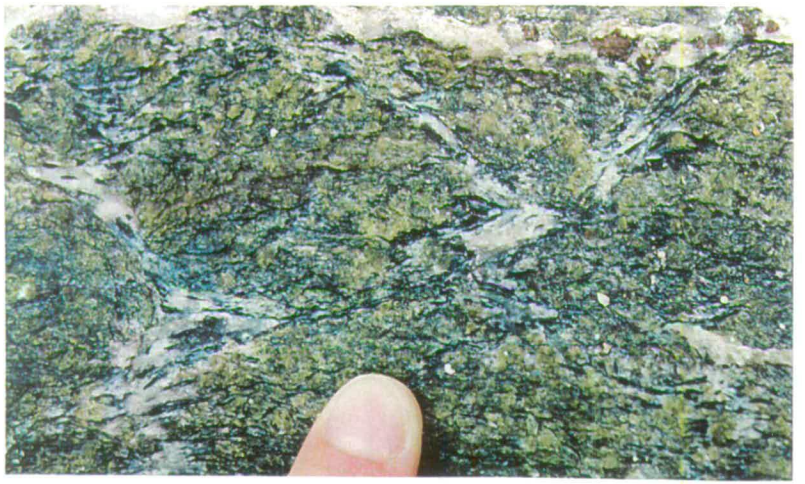

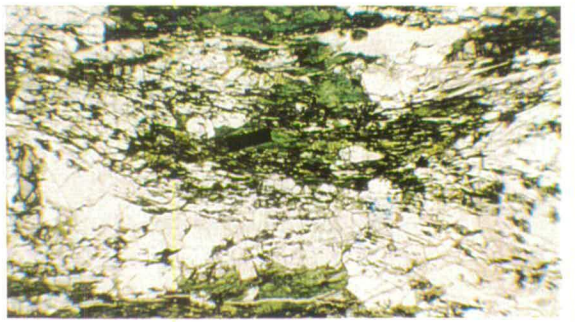

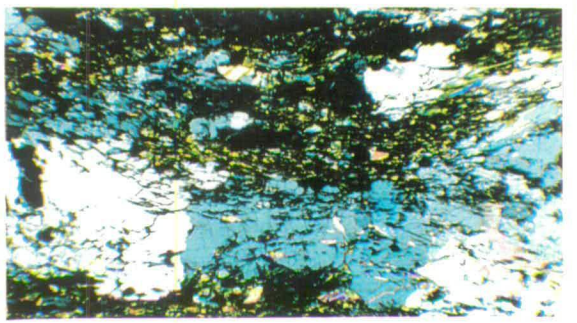

Delfini 1

Photograph 3.13

Symmetrical boudinage of glaucophane and epidote layer, with quartz and glaucophane growing in macro-shears, Delfini. Photograph taken looking north.

Field of view approximately 10 cm

Photograph 3.14

Boudinaged quartzite layer, Delfini. Photograph taken looking northeast.

Field of view approximately 5 m

Photograph 3.15

Albite mineral lineation, adjacent to quartz, albite, chlorite vein.

Field of view approximately 20 cm

Photograph 3.17

Thin section of albite-chlorite, with minor mica, epidote and oxide, in a shear zone, Delfini. Sample S'97/98.

Field of view approximately 4 mm

Photograph 3.16

Flattened albites in shear zone, Delfini

Field of view approximately 20 cm

Photograph 3.18

Cross polars view of photograph 3.17 Sample S'97/98, Delfini.

Field of view approximately 4 mm

Figure 3.21
Sketch map of boudinaged quartzite layer and associated fabrics and segregaions, stereonets show average foliations and mineral lineations.

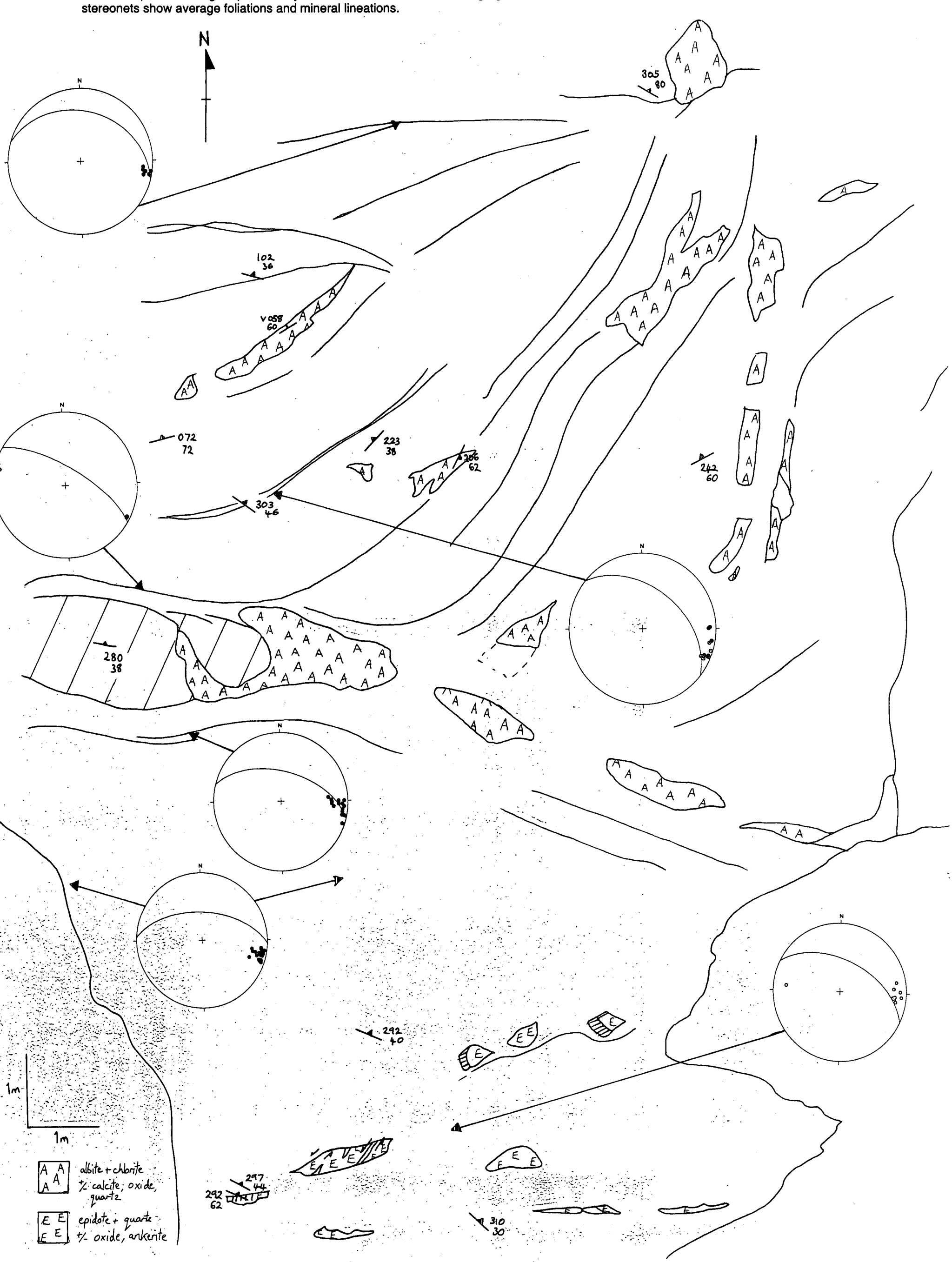

is retrogressed to greenschist assemblages which define a strong foliation, this foliation wraps the greenschist segregations. On foliation surfaces there is an E-W oriented mineral lineation. Adjacent epidote-blueschists and fully retrogressed chlorite-albite schist have parallel mineral lineations oriented E-W on foliation surfaces.

The conglomeratic horizon, 25-35 m, contains mainly calcite clasts which are flattened and sheared, top to the east (figures 3.20 D and E). Albite and chlorite mineral lineations (photograph 3.15) and x-axes of deformed pebbles trend E-W. As at Megas Yialos, mineral lineations are parallel to the finite stretching direction defined by the deformed pebble x-axes. Mineral lineations of both blueschist and greenschist grade can therefore be used as a proxy to the extension direction. As well as mineral lineations being parallel to the x-axis direction they are also oriented E-W as documented at localities in the south in retrogressed greenschist assemblages. Within the conglomeratic horizon the extension shows localised simple shear top to the east.

Albite porphyroblasts are predominant in a 2m wide zone of localised deformation at 42 m (photograph 3.16). Thin section photographs 3.17, and 3.18, show albite, chlorite, calcite and mica in the shear zone. The albite is flattened and surrounded by chlorite and mica. Micro-scale structures in the greenschist suggest predominantly pure shear flattening, like those documented on a macro-scale in the epidote-blueschists, in the first 15 m of the log. However, albite porphyroblasts in pressure shadows to segregations and haloes to veins in other parts of the section overgrow fabrics outlined by greenschist minerals. The presence of blueschist fabrics, greenschist fabrics and overprinting by albite porphyroblasts demonstrates the importance of partitioning of deformation in localised zones at all stages.

In summary the log shows a kinematic link between greenschist and epidote-blueschist extensional fabrics, within a 40 m section. The blueschist and greenschist lithologies show symmetrical layer parallel extension, along an E-W oriented axis. This is the same extension direction as that documented in greenschist lithologies at localities in southern Syros. Extensional boudinage was documented from micro- and

macro-scales to boudinage of a whole quartzite band. Minor greenschist overprinting of extensional epidote-blueschist fabrics was identified. To check that the observed kinematic links between deformation at the different metamorphic grades were not isolated examples two further logs were made on the NW side of the peninsula.

Log II (figure 3.22) documents E-W striking foliations and E-W trending mineral lineations parallel to those observed on the SE side of the peninsula. Fold hinges in a folded carbonate layer are oriented NE-SW to E-W approximately parallel to the mineral lineation. Fold hinge lines parallel to the mineral lineation were also observed at Finika and Kini. Extensional greenschist veins are associated with boudinage and trend N-S accommodating E-W oriented extension. Small scale shear zones (figure 3.23 B, C and G) document localised, top to the east, asymmetry. A zone of top to the east asymmetry was also identified in the conglomeratic horizon in log I from the SE side of the peninsula.

The structures and kinematics of the deformation are very similar to those already identified, dominated by layer parallel symmetrical boudinage, except in localised zones of top to the east shear. Extensional greenschist veins are associated with the boudinage and mineral lineations and fold hinge lines lie parallel to the E-W extension axis. The lithologies and mineral assemblages preserved in the log are however different from those on the SE side of the peninsula. Boudinage of competent layers preserving high pressure assemblages including sodic-pyroxene and garnet are common (figure 3.23 F and photograph 3.19 and 3.20). Early folds which are foliation parallel are outlined by sodic-pyroxene, glaucophane, garnet and epidote, and have been extended and sheared during layer flattening (photograph 3.21 and field sketch 3.23 E).

Progressive deformation during decompression is documented within a single shear zone. Boudinaged sodic-pyroxene and garnet layers are preserved adjacent to a glaucophane garnet rock which is sheared asymmetrically top to the east. The glaucophane layer is also boudinaged, the fracture is infilled with an extensional chlorite- and albite-bearing vein (figure 3.23 G). The log documents layer parallel extension of lithologies deformed at different metamorphic grades. The coaxiality of

Figure 3.22
Log (II) on map, figure 3.17. Letters refer to field sketches in figure 3.23.
See figure 3.18 for lithology key, distance in m.

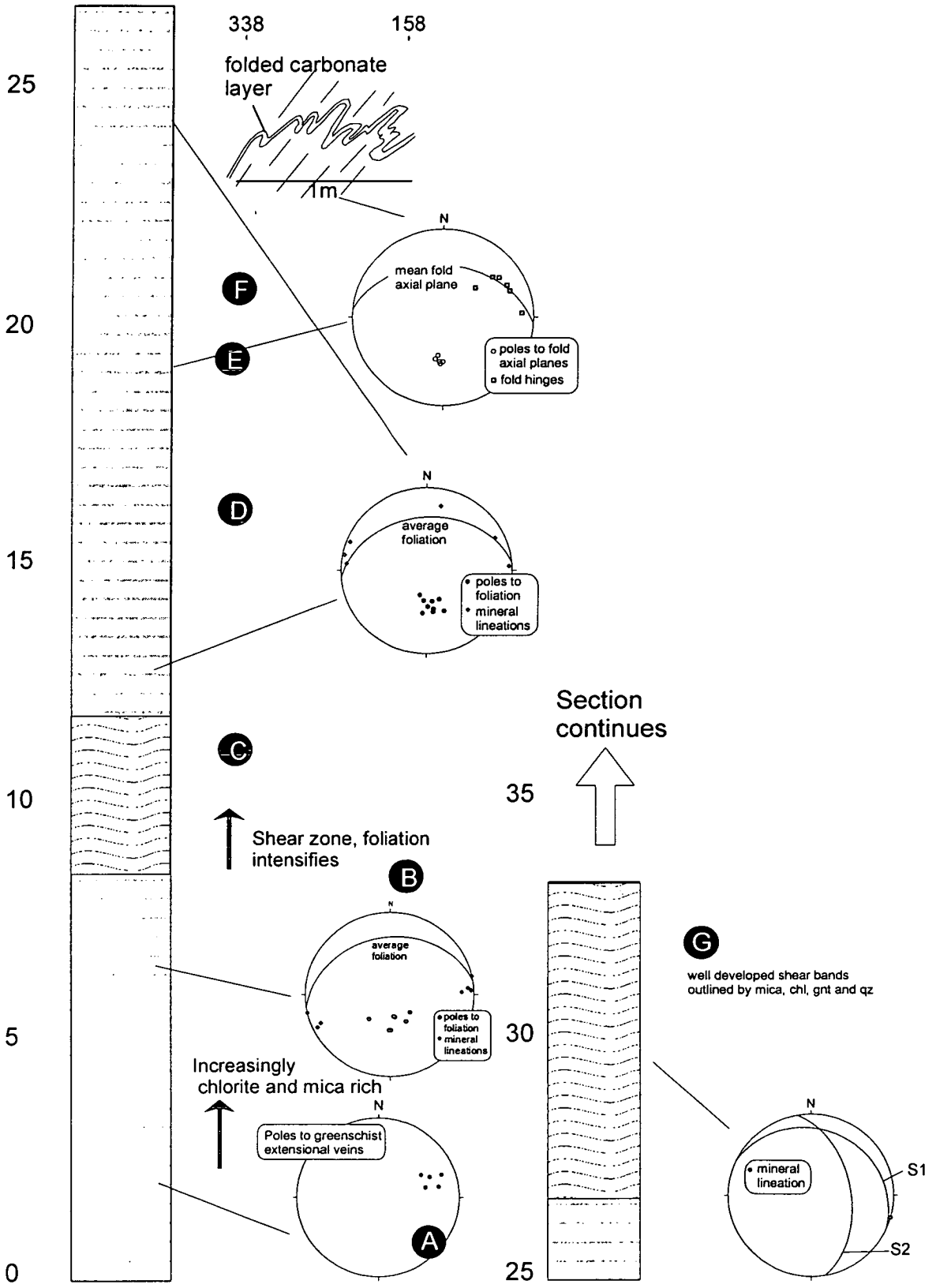

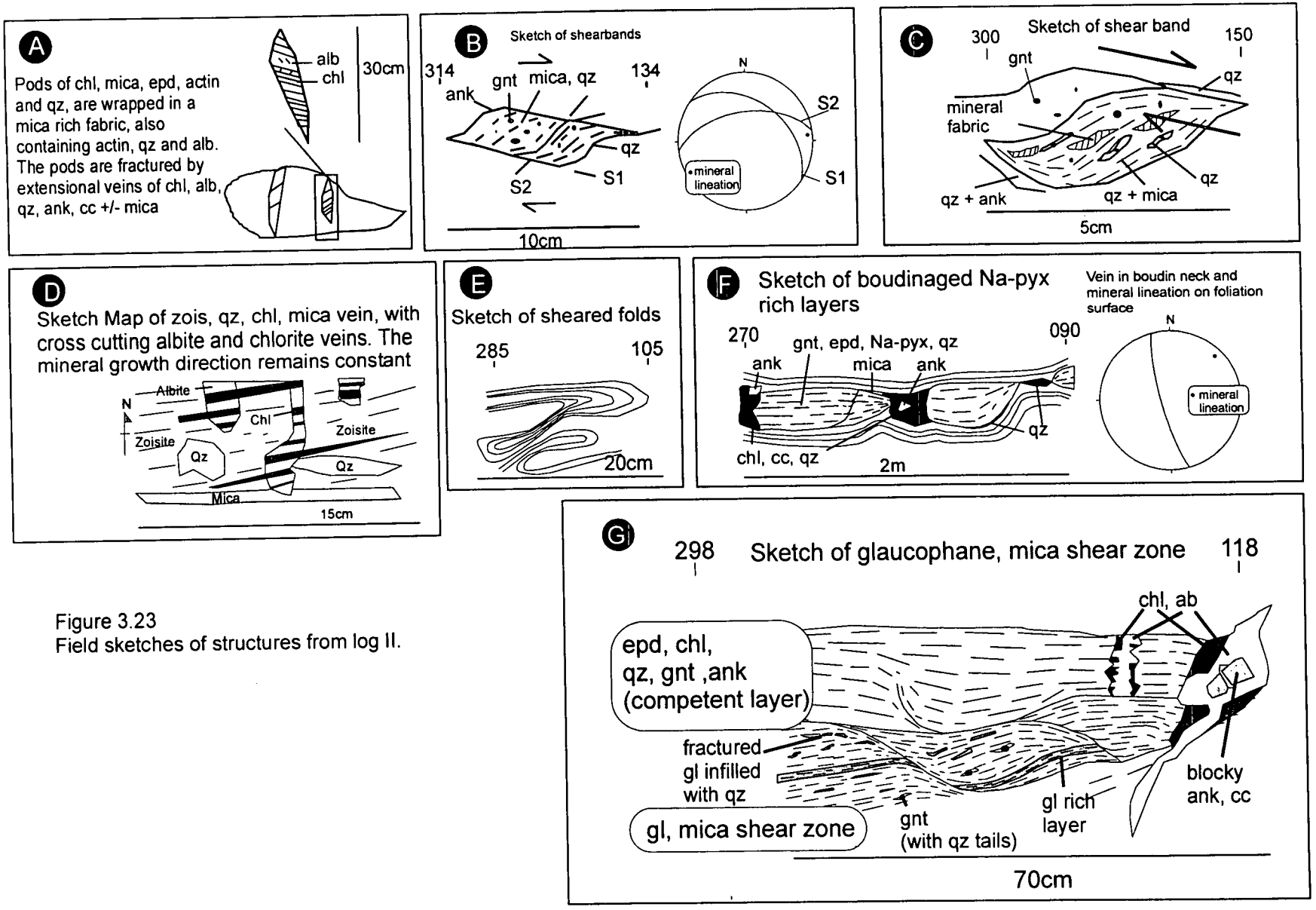

Figure 3.23
Field sketches of structures from log II.

the extension at all grades suggests that extension was accommodated by localised zones of pure shear separated by asymmetrical shear zones, for strain compatibility, through out decompression.

In comparison log III (figure 3.24) from further north on the coast is dominated by calcic assemblages, many of which have a clastic sedimentary protolith. The first 24 m consist of interlayered calcite and dolomite marble. The dolomite layers within calcite are boudinaged on a range of scales from metres-centimetres (photograph 3.22 and figure 3.25, D). In this area (10-20 m) the direction of localised asymmetrical shear zones is reversed (top to the west). Small scale brittle fractures in dolomite layers link into ductile shear zones in an impure micaceous rich horizon. A link between brittle and ductile extension was also observed at Megas Yialos.

Figure 3.25, F and photograph 3.27 show deformed metabasic clasts in a carbonate matrix which are sheared top to the east. Evidence for coaxial NW-SE to E-W directed extension is also documented by layer parallel boudinage (figure 3.25, A) and flattening of carbonate clasts within the rudites. Well defined shear bands in albite-chlorite schist (35-40 m) and poles to mineral lineations outlined by albite and chlorite are consistent with E-W oriented extension documenting extension within the greenschist facies stability field as seen elsewhere.

Summary of Delfini

Within the Delfini sequence I have documented evidence of layer-parallel extension, extending the layer parallel foliation and folding. Boudinaged high pressure, sodic-pyroxene-, garnet-, glaucophane- and epidote-bearing assemblages, through to greenschist mineralogies and evidence for brittle faulting linking into ductile extensional fabrics, are documented. The area is dominated by symmetrical boudinage on a range of scales with some areas of localised asymmetric shearing. The strain accommodates coaxial E-W directed layer parallel extension of all units. A map of the area (figure 3.26) has mineral lineations and pebble x-axes annotated from the different areas targeted for study. Note that the lineation trends in the upper

Figure 3.24
Log (III) on map, figure 3.17. Letters refer to field sketches in figure 3.23.
See figure 3.18 for lithology key, distances in m.

CONT ON NEXT PAGE

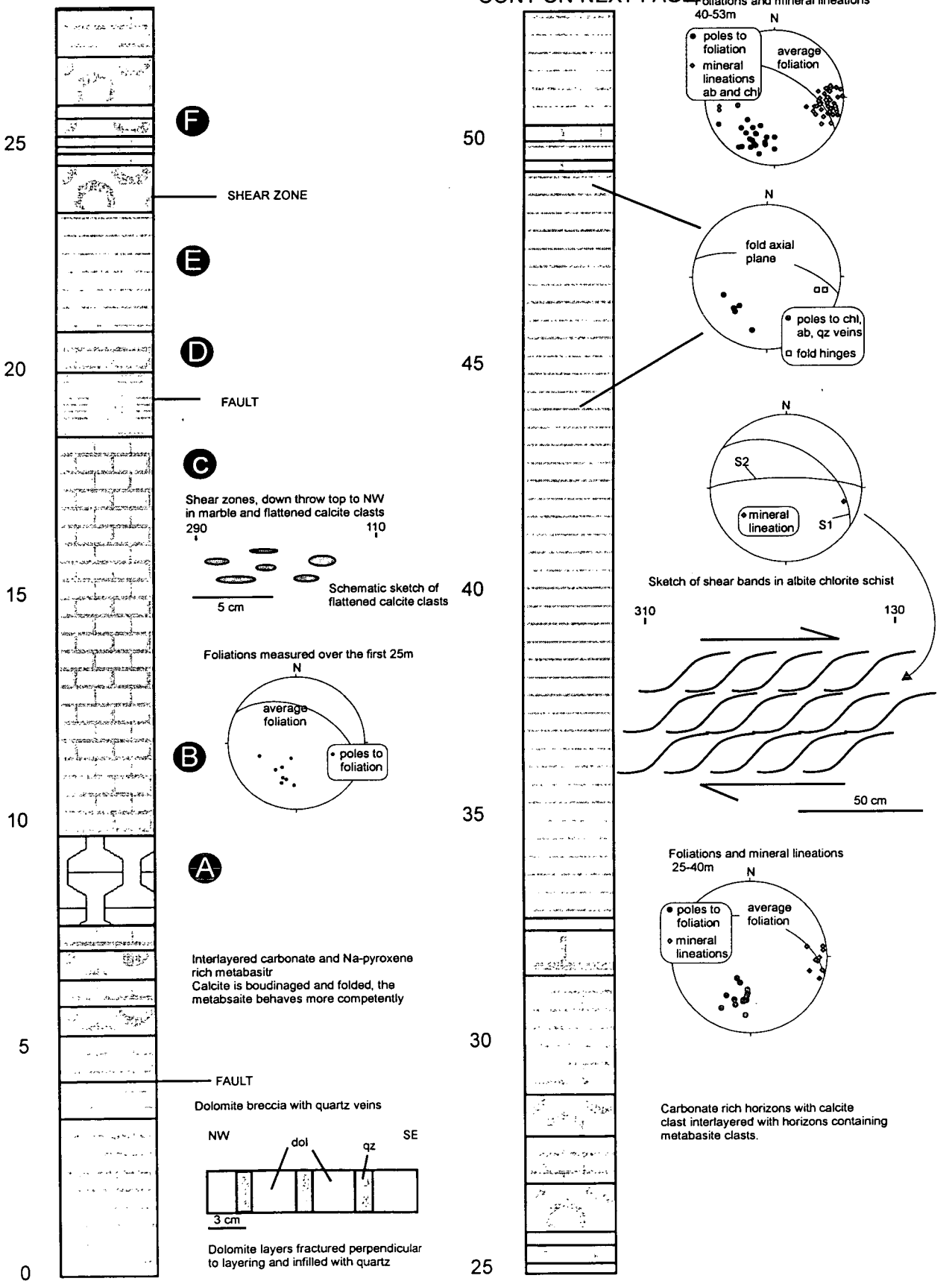

Marble continues

70

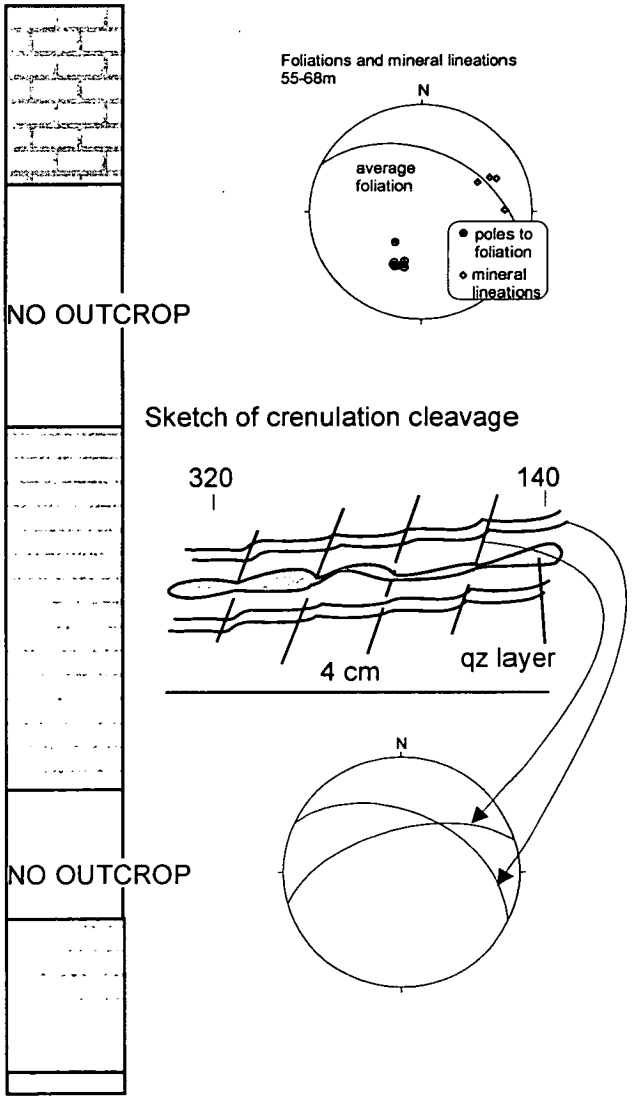

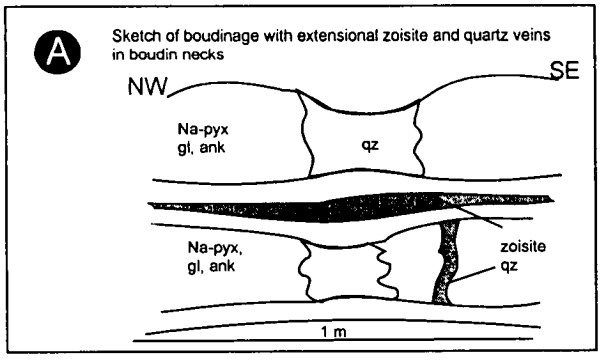

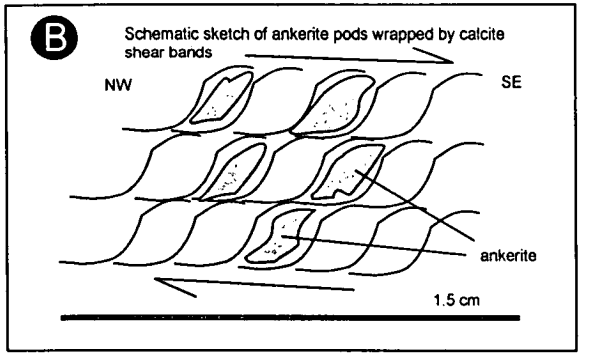

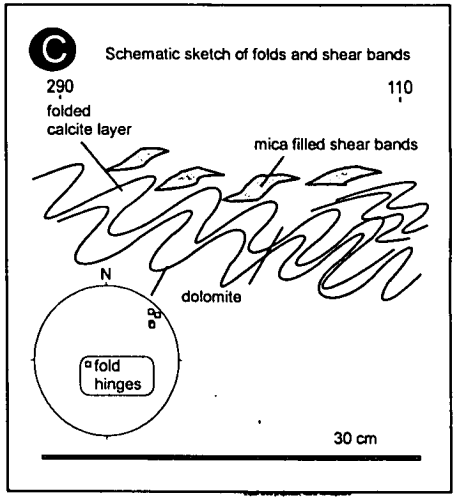

Figure 3.25
Field sketches from localities marked on log III, figure 3.24.

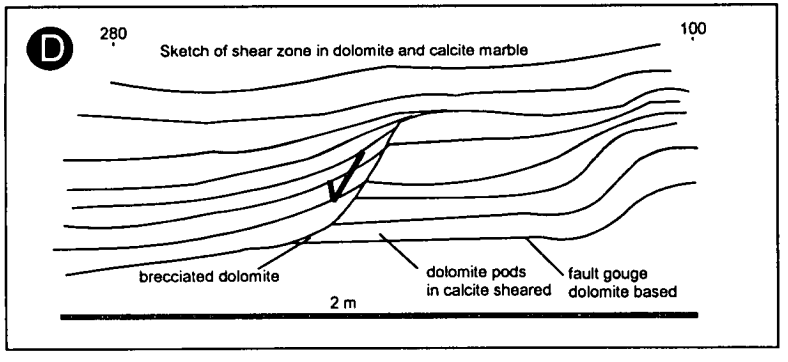

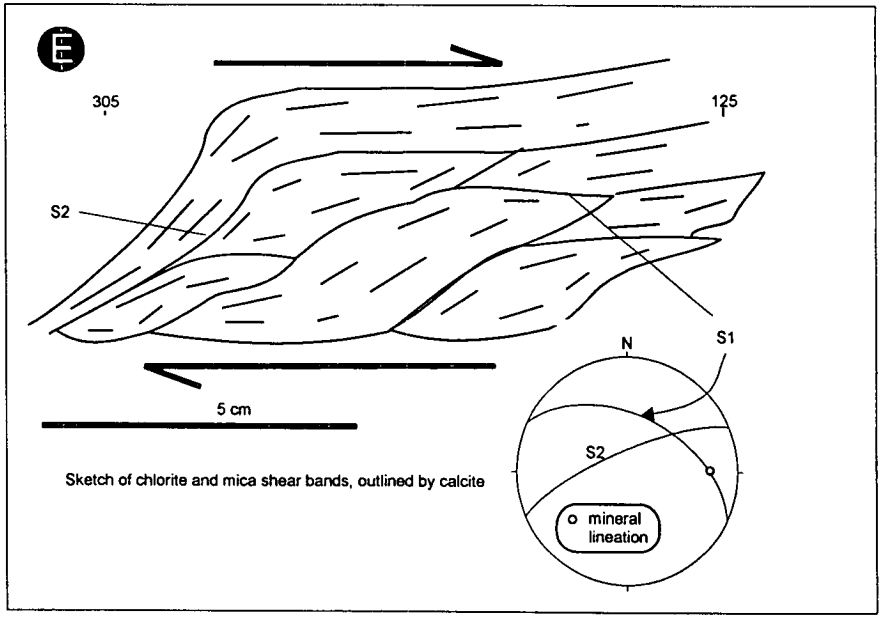

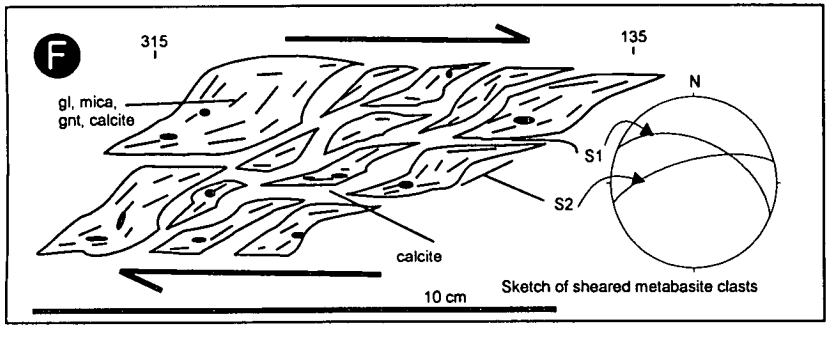

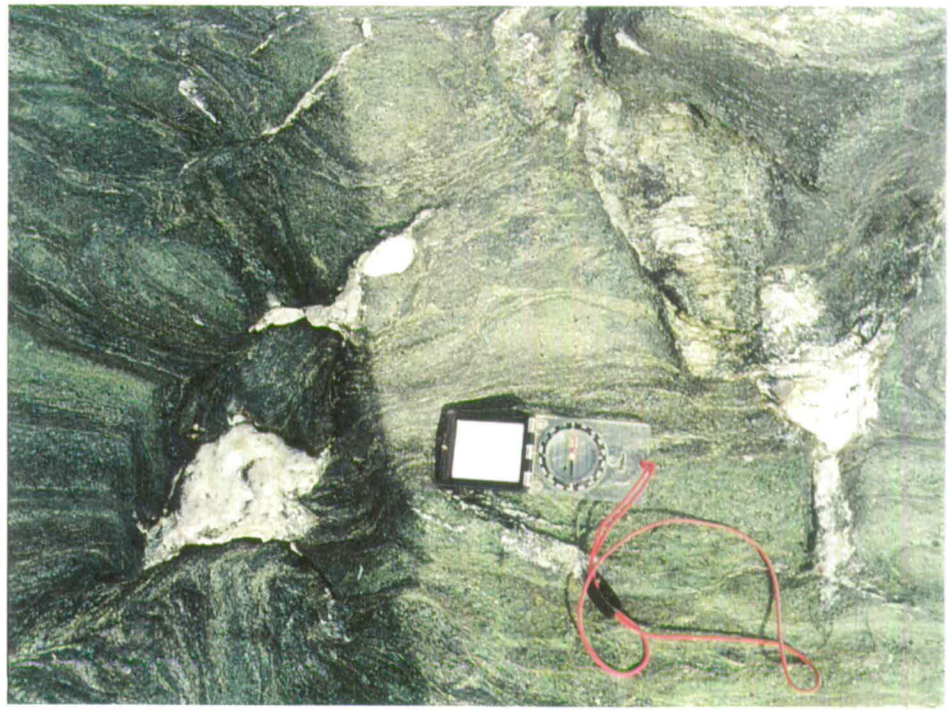

Photograph 3.19

Layer parallel boudinage of metabasite, with epidote and quartz vein formation in boudin necks, Delfini. Photograph taken looking north.

Field of view approximately 2.5 m

Photograph 3.21

Folds outlined by glaucophane, garnet and epidote show intense shearing of limbs, rootless folds are found cut by extensional shears showing both top to the east and top to the west vergence. Photograph taken facing north.

Field of view approximately 80 cm

Photograph 3.23

Sheared top to east metabasic clasts (glaucophane, mica and garnet) in calcite matrix. Photograph taken facing north.
Field of view approximately 60 cm

Photograph 3.20

Boudinage of sodic-pyroxene, garnet, chlorite, epidote and quartz layers with quartz, epidote veins in boudin necks. Photograph taken looking north to northeast.

Field of view approximately 1 m

Photograph 3.22

Assymetrical boudinage of dolomite layer, top to west, above the lens cap. Below the lens cap, local symmetrical boudinage.

Field of view approximately 30 cm

Figure 3.26
Map of Delfini with stereonets of mineral lineations and pebble x-axes annotated.

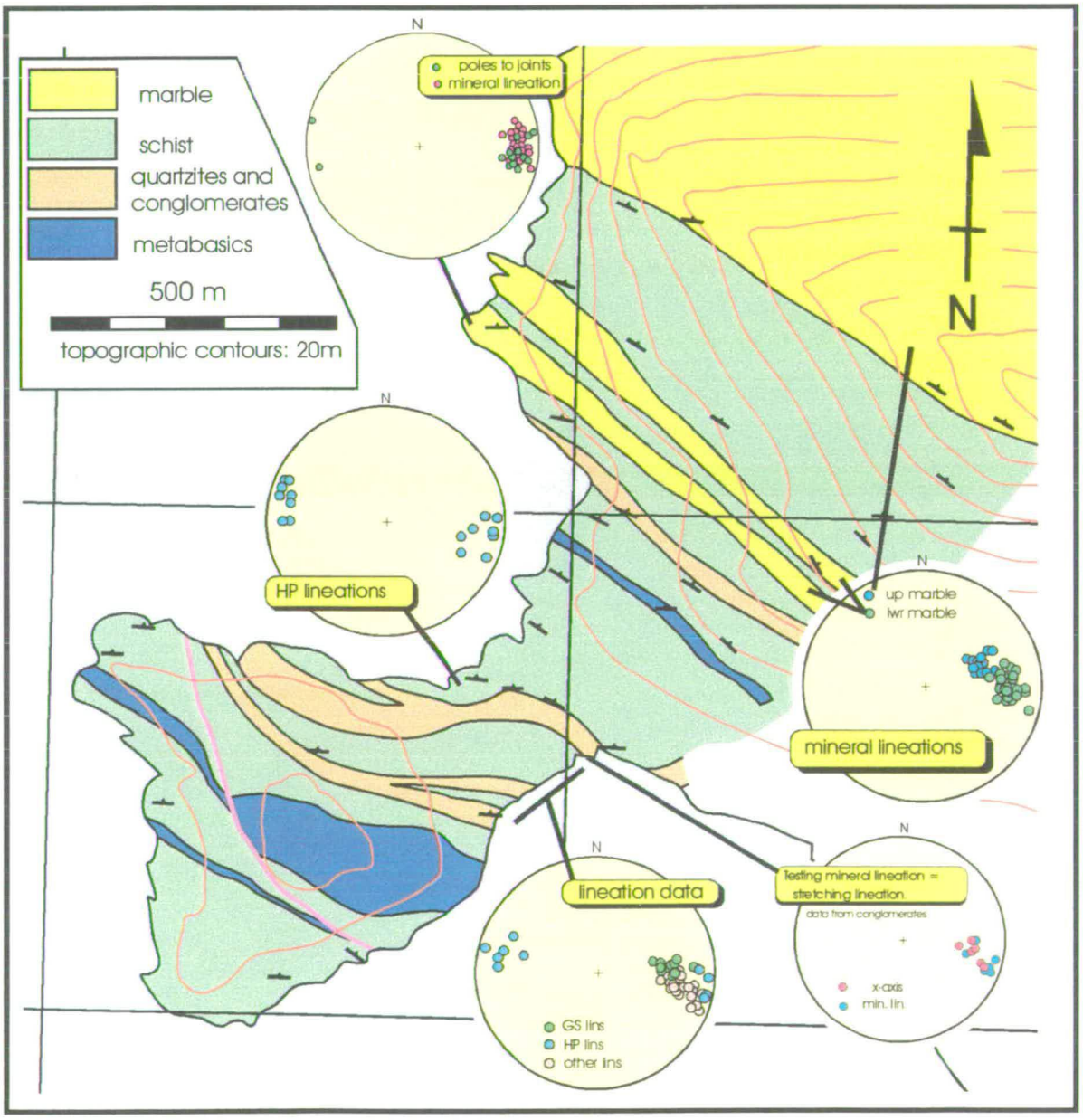

marble are oriented NE-SW rather than E-W, which suggests that the marble contact may have acted as a detachment during the extension.

Localisation of deformation appears to have been controlled by relative competence contrasts between layers during the progressive deformation. Fluid infiltration and the formation of veins were localised in boudin necks. Some areas are pervasively retrogressed to a greenschist assemblages, but the preservation of higher pressure assemblages implies that localised fluid infiltration, controlled by deformation partitioning, regulated retrogression of assemblages.

Crucially the partial recrystallisation, preserving mineral assemblages of different metamorphic grades, allows the kinematics of extensional deformation during decompression to be constrained. As symmetrical boudinage, indicative of coaxial deformation, is recorded in layers of different metamorphic grades (with only local evidence for asymmetry) then pure shear thinning is interpreted to have been dominant during decompression. If decompression occurred by pure shear, the strain axes for increments of strain during exhumation must be parallel. The finite stretching direction, inferred from deformed pebble x-axes, defines this extension direction during the decompression.

North Ermoupolis

The outcrops of North Ermoupolis are also located within the central area of Syros. Both high pressure and low pressure mineral assemblages are preserved in metabasic blocks in a serpentinite melange. Small scale detailed structural work was completed on the blocks of metabasite. The blocks are now loose so collection of oriented structural data was not applicable. The study therefore concentrates on qualitative descriptions of block mineralogy, fabric and veining.

The blocks are mineralogically banded on a cm scale and well foliated. Bands contain varying proportions of sodic-pyroxene, glaucophane, zoisite/epidote, garnet, quartz, mica and secondary chlorite and albite. Figure 3.27, a log across part of a block gives an example of the mineralogical banding in the blocks, the location of the log is annotated on photograph 3.24. Veins and segregations form in small scale

Figure 3.27
Log across centre of metabasite block in photograph 3.24, North Ermoupolis. Distances in cm, sketches in boxes relate to the log.

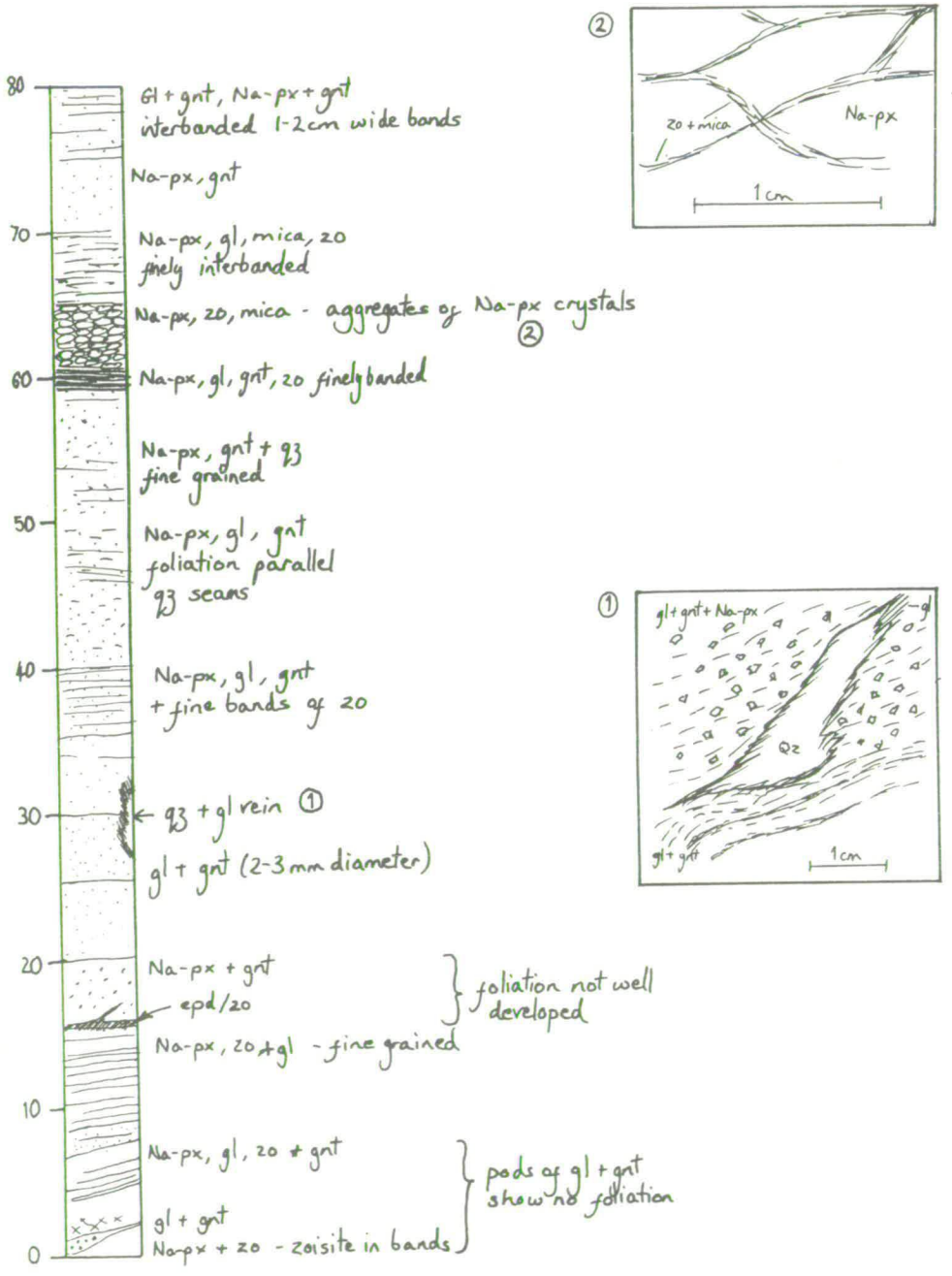

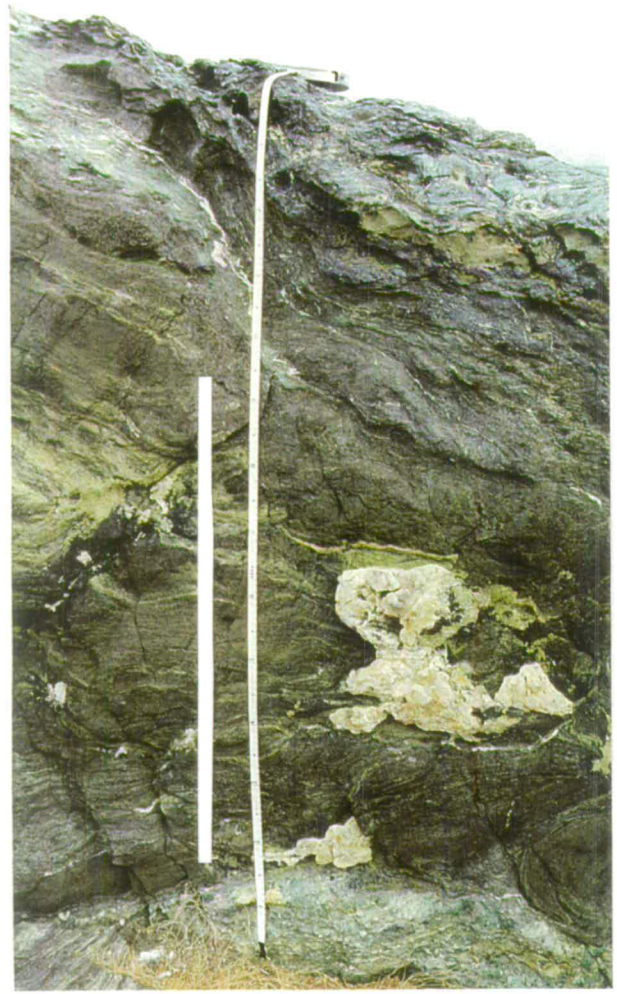

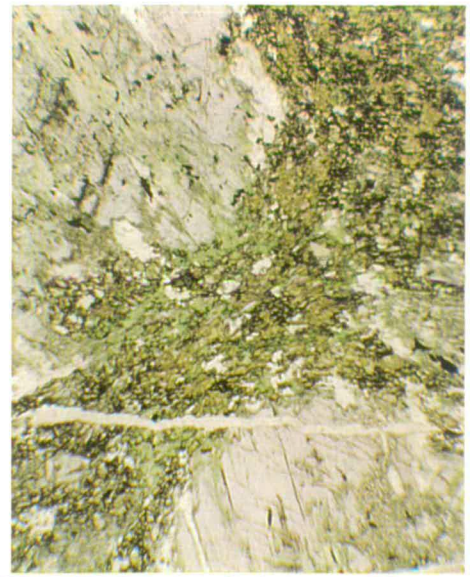

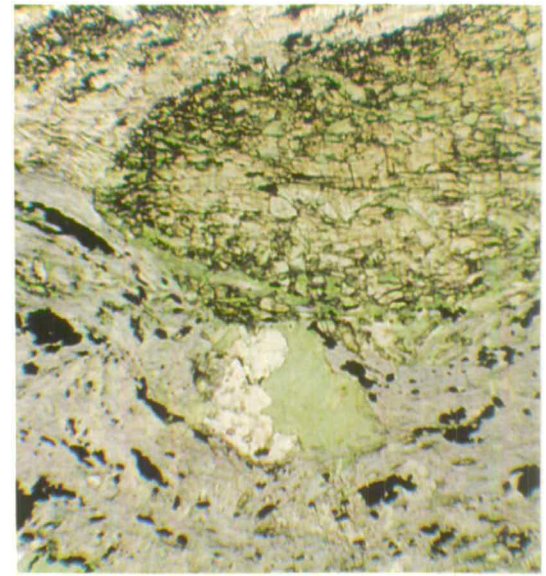

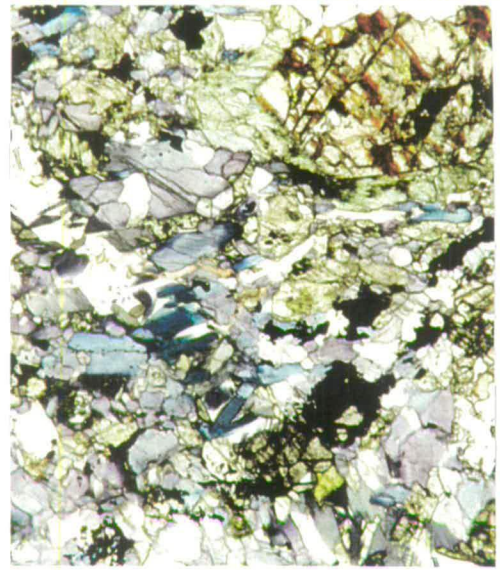

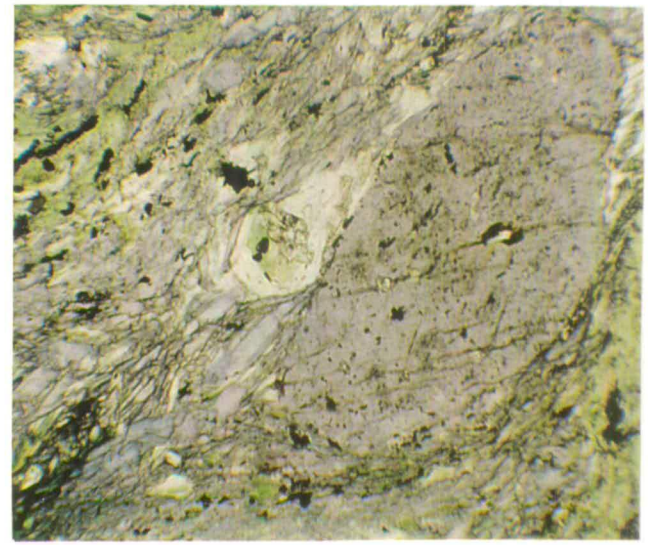

North Ermoupolis

Photograph 3.24

Photograph of block studied at North Ermoupolis. White bar is the line of the log in figure 3.27.

Tape measure is 1.4 m long.

Photograph 3.26

Large glaucophane crystals (bottom right and upper left) are rimmed and partially replaced by green amphibole. The amphiboles are separated bya chlorite, epidote green amphibole, calcite shear zone. Sample S'95/116A from metabasite block, North Ermoupolis.

Field of view 4 mm.

Photograph 3.27

Composite clast of epidote, chlorite, albite and mica (upper right), surrounded by a glaucophane and rutile shear zone. Area of albite and chlorite lower centre is thought to be a pseudomorph after garnet.
Sample S'95/3 from metabasite block, North Ermoupolis.

Field of view 8 mm.

Photograph 3.25

Vein of quartz, dark blue glaucophane and sphene, from a metabasite block at North Ermoupolis. The surrounding glaucophane has dark blue rims suggesting growth in response to fluid infiltration. Green pyroxene and garnet upper right are unaltered.
Sample S'96/42.

Field of view 4 mm.

Photograph 3.28

Large glaucophane crystal, surrounded by metastable glaucophane shear zone. In the centre a patch of chlorite and albite appears to have pseudomorphed garnet. Lower left glaucophanes in the shear zone show the formation of a dark blue glaucophane rim and in the corner are rimmed with blue-green amphibole and show reaction to chlorite.
Sample S'96/40 from metabasite block, North Ermoupolis.

Field of view 8 mm.

shear zones, these include segregations of; quartz, glaucophane, albite, mica, epidote and chlorite; glaucophane, epidote, sphene, albite and mica; quartz, glaucophane and oxide; and quartz segregations.

Planar greenschist veins containing calcite, albite, chlorite and pyrite cut across the fabric in the blocks and are surrounded by haloes of patchy retrogression. Glaucophane in some haloes appears to be stable, whilst garnets retrogress to chlorite or albite or both. In thin section glaucophanes have dark blue rims and veins of dark blue glaucophane, quartz, and sphene, suggests grain boundary infiltration of fluid forming dark blue rims on glaucophanes (photograph 3.25). The slide also contains the deep green pyroxene, aegirine-augite. The breakdown of high pressure jadeite to aegirine-augite was documented by Dixon (1969) and Barr (1989) and was associated with growth of riebeckitic, dark blue, rims on glaucophane. Dixon (1969) showed that the aegirine-augite had a low jadeite composition and inferred that recrystallisation must have taken place at pressures lower than 6 kbar.

Areas away from veins also document retrogression of high pressure assemblages; this retrogression is associated with deformation. The planar fabric outlined by the high pressure mineral assemblage has been folded and retrogressed to chlorite- and albite-bearing assemblages. High pressure assemblages are interfolded with lower pressure chlorite and albite bearing layers which define an axial planar cleavage. The zone of retrogression and deformation is complex and contains rotated blocks and pods of material surrounded by shear zones (figure 3.28). The area is cut by a chlorite, calcite and quartz shear zone, which may be a sheared vein. The blocks and pods around which shear zones have developed are of two different types; one containing glaucophane and the other containing chlorite, calcite, albite and epidote. The surrounding shear zones are dominated by calcite and chlorite (figure 3.28, A), but glaucophane, green-amphibole, mica and albite are also documented. Photographs 3.26, 3.27 and 3.28 are thin section photographs of the shear zones, which have developed during transformation from blueschist to greenschist assemblages.

Figure 3.28
Sketch of part of a metabasite block, North Ermoupolis. Close up sketch shows glaucophane pods in a chlorite, epidote, albite and calcite shear zone.

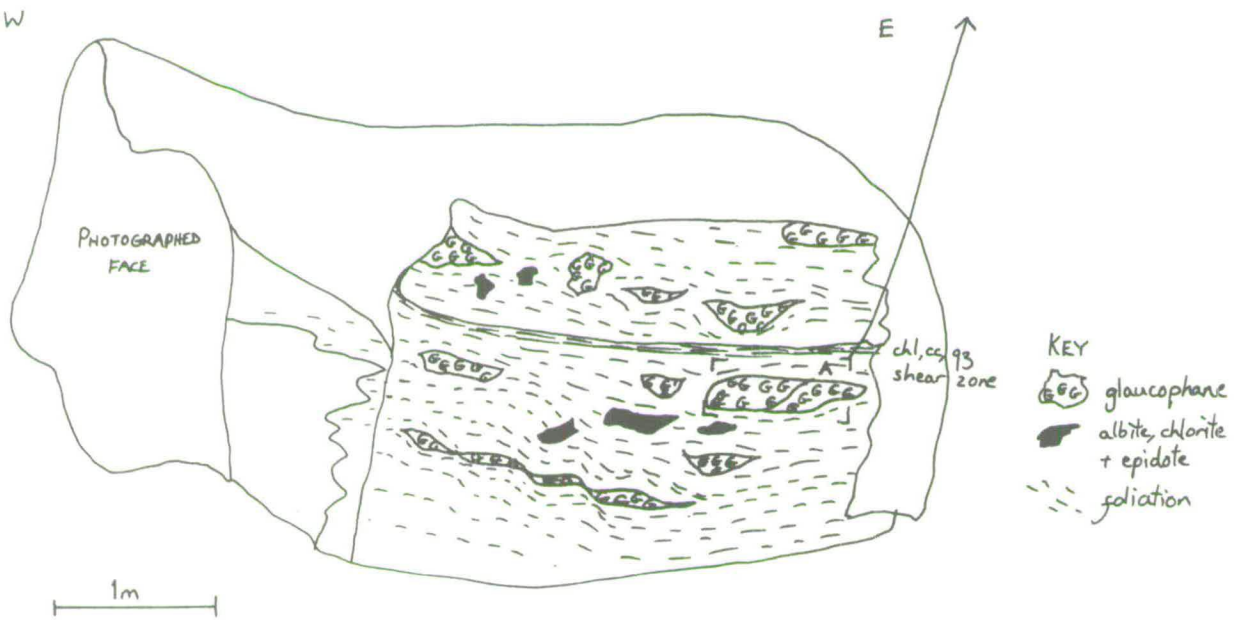

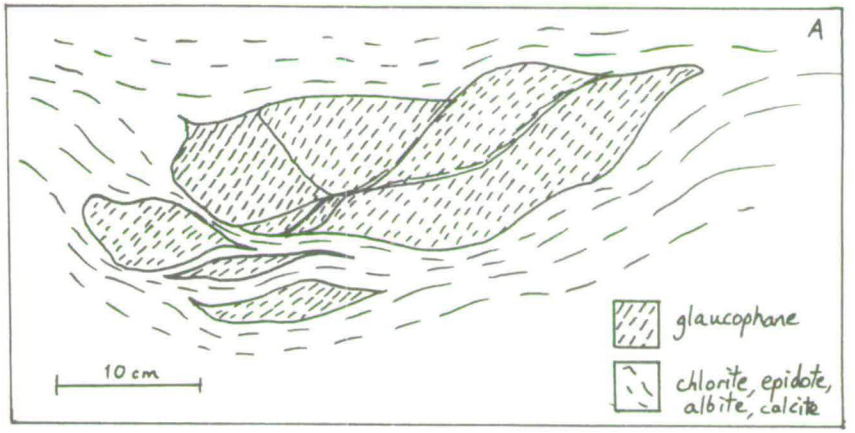

Large glaucophane crystals are rimmed and partially retrogressed to blue-green amphibole (photograph 3.26). Rutile appears to be spatially associated with glaucophane (photograph 3.27), and is rimmed by sphene in areas of retrogression. Garnets are replaced by albite and chlorite, whilst glaucophane is stable (photographs, 3.27 and 3.28). Glaucophane forms shear zones around epidote, chlorite and albite clasts (photograph 3.27) and chlorite-bearing assemblages form shear zones around glaucophane. Glaucophane was stable during the deformation. Evidence for fluid infiltration, probably post deformation, in the shear zones is seen in photograph 3.28, where glaucophane is rimmed by dark blue glaucophane and is partially replaced by chlorite. If fluid infiltration was originally localised, then some areas may have retrogressed to albite and chlorite, whilst adjacent glaucophane remained stable. Subsequent deformation partitioned on a cm-scale, post fluid infiltration, could have resulted in the observed textures. Localised deformation could have resulted in retrogressed pods of material surrounded by glaucophane shear zones, as well as glaucophane surrounded by albite- and chlorite-bearing shear zones.

Summary of North Ermoupolis

The locality documents the interplay of deformation and fluid infiltration with preservation of high pressure mineral assemblages. Fabrics in the blocks document folding of an early high pressure foliation, which bend into shear zones accommodating strain during the blueschist-greenschist transition. The locality provides further evidence for kinematic links between high pressure and low pressure deformation fabrics, and the importance of both localised fluid infiltration and partitioned deformation on mineralogical and structural development.

Oros Syringas

This locality was largely selected for stable isotope work, but structures noted during the isotope work are presented here. The Oros Syringas hillside, in northern Syros, consists of a series of marble and schist layers which are cut by normal faults (figure 3.29). The hillside was mapped and logged to asess the extent of retrogression

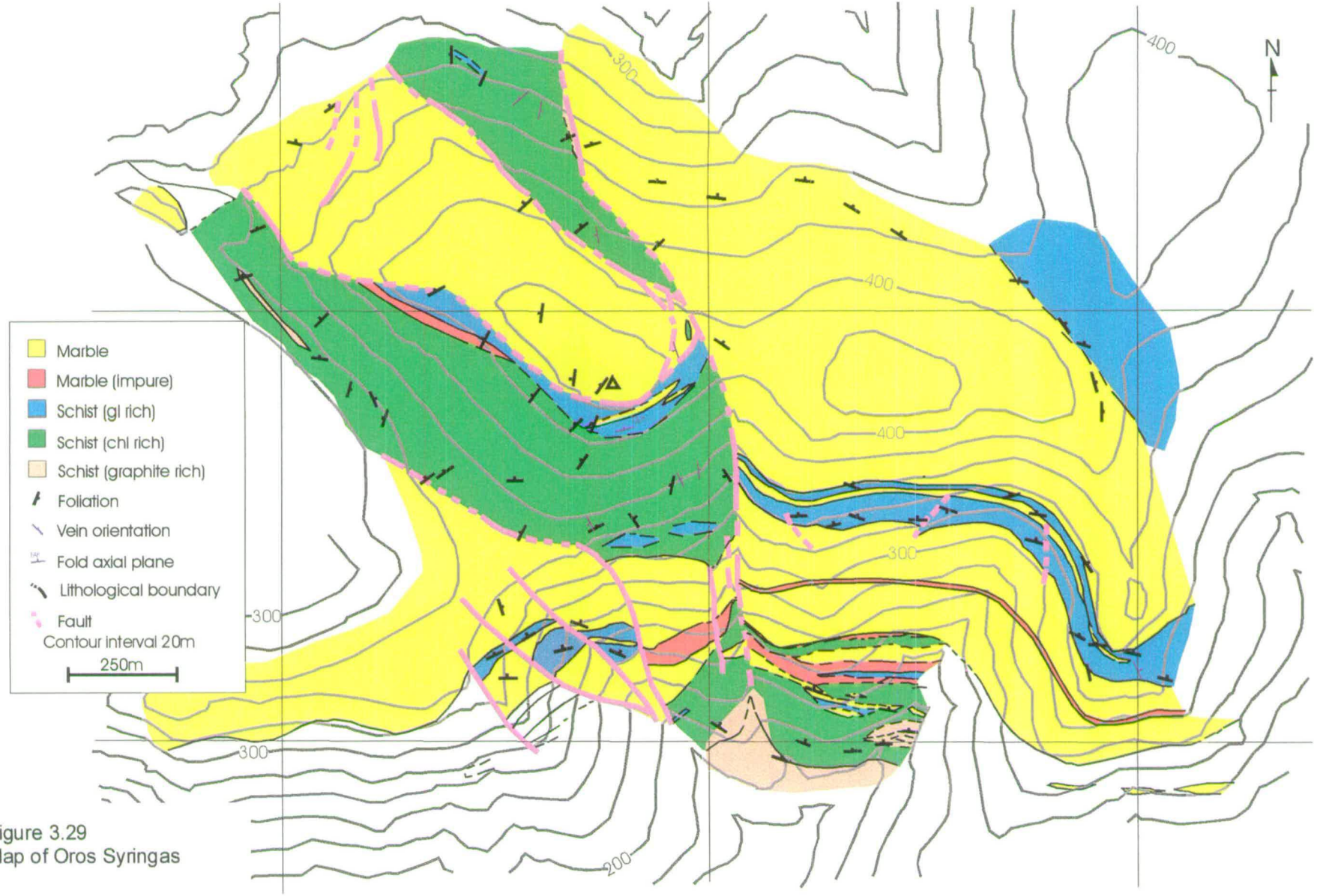

Figure 3.29
Map of Oros Syringas

and its relationship to structures. The schist is variably retrogressed to a greenschist assemblage of chlorite, albite, calcite, quartz and mica, which is found at the base of the hillside; the schist becomes increasingly glaucophane-rich upwards through the succession. However, in the schist beneath the uppermost marble there are numerous greenschist veins and the schist is clearly retrogressed. Foliations, fold axial planes and greenschist vein orientations are shown in figure 3.30. Garnets are pseudomorphed by chlorite and form elongate 'clots' of chlorite, but remnants of garnet are seen in thin section. Orientation measurements of x-axes of chlorite pseudomorphs after garnet were made on foliation surfaces to find the elongation direction. Stereonets of data from four foliation surfaces are shown in figure 3.31. The x-axis direction trends NE-SW and is parallel to the mineral lineation defined by chlorite, figure 3.31, A. The timing of chlorite pseudomorphing of the garnet with respect to the deformation is unconstrained by thin section textures.

Mapping of normal faults across the hillside suggests that they were late in comparison to retrogression of the schist units (figure 3.29). The faults off-set retrogressed layers. The faults were described by Ridley (1984b) and are consistent with E-W directed extension. Fault patterns suggest that Syros is a horst block with extensional faults down throwing away from the back bone of the island (Ridley, 1984b).

Summary of Oros Syringas

Extension is inferred, from deformation fabrics, to be oriented along an E-W to NE-SW axis, which is parallel to that reported for southern Syros. The kinematics of the extension are the same from the southern coast of Syros to Oros Syringas, just south of the serpentinite belt (figure 3.3). This suggests that the meta-sedimentary sequence was part of a coherent stratigraphy during deformation. The extensional faulting on the Oros Syringas hillside appears to have formed post-retrogression. Brittle faulting cannot be seen linking into zones of ductile deformation, unlike those seen at Delfini and Megas Yialos.

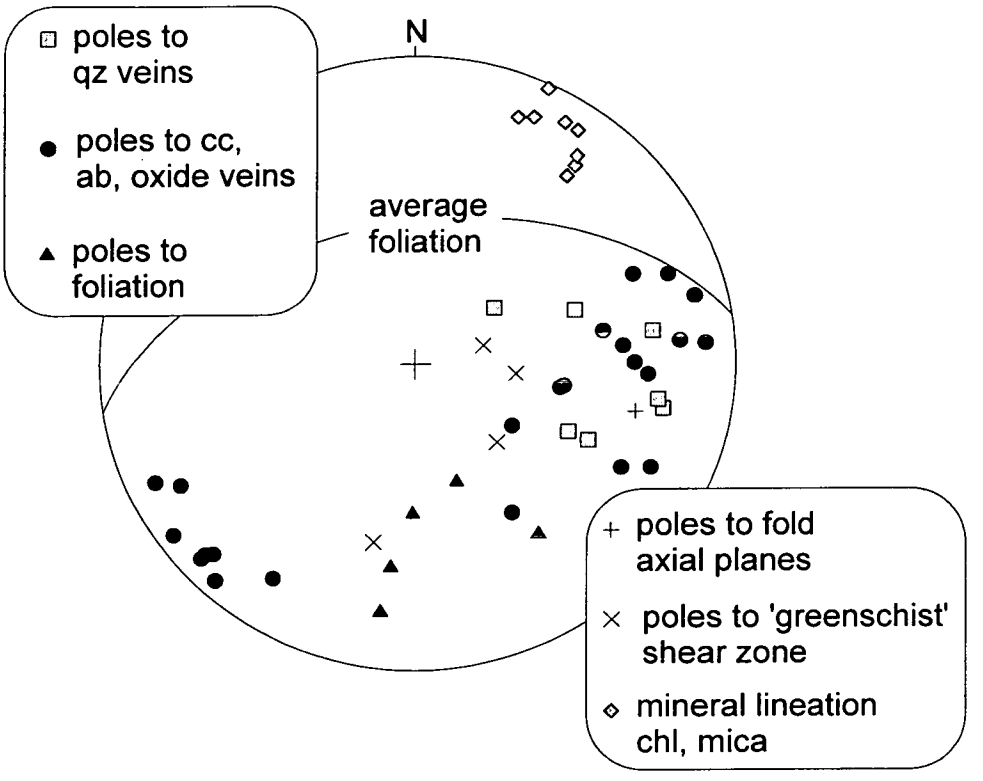

Figure 3.30
Fabric data collected on the Oros Syringas hillside. The foliation is averaged from measurements across the whole hillside.

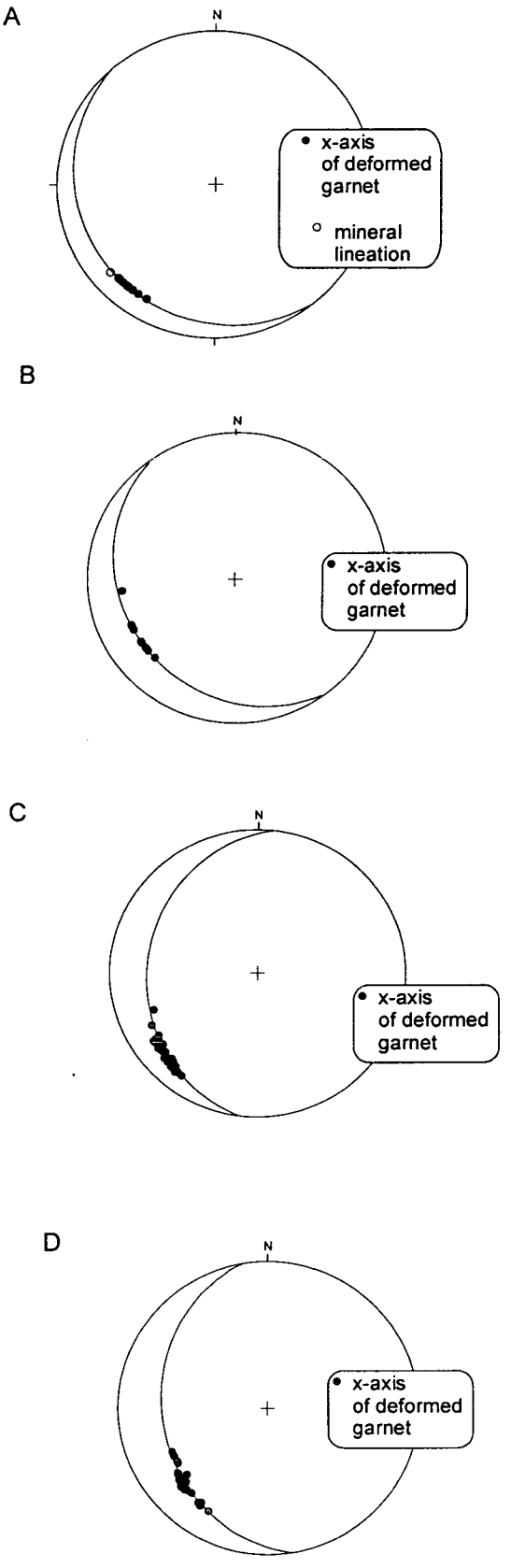

Figure 3.31
Equal area stereonets of x-axis directions from deformed garnet pseudomorphs on foliation surfaces.

Summary of central-northern localities

The central-northern localities, notably Delfini, were crucial for kinematically linking greenschist and blueschist fabrics. The preservation of a range of metamorphic assemblages and structures, from high pressure-low pressure, at Delfini allowed the kinematics of extensional deformation to be linked down-pressure. Coaxial layer parallel extension was documented on a range of scales defined by both high pressure and low pressure mineral assemblages. There was also evidence for brittle structures linking into zones of ductile deformation. From the structures a coaxial extension axis oriented E-W was inferred. This extension axis is oriented parallel to that documented in the deformed greenschist assemblages in southern Syros.

Evidence for deformation during the blueschist-greenschist transition was observed in shear zones at North Ermoupolis. The fabrics kinematically link blueschist and greenschist deformation. Assemblages just south of the northern serpentinite belt on the Oros Syringas hillside were interpreted to document E-W oriented extensional fabrics. This is parallel to the extension direction inferred from observations of deformation fabrics from central and southern Syros. The extension, in the lithological units between the south coast and Oros Syringas has a constant orientation and is inferred to be kinematically linked.

Northern Localities

Ridley (1982a) described the northern serpentinite belt as forming a structural discontinuity between the very northern part and southern Syros. It was in the area north of the serpentinite belt that Ridley described, in detail, structures and fabrics related to thrusting. This next section, based on observations from the north of the island and the serpentinite belt, will determine whether deformation fabrics in the high pressure assemblages can be re-interpreted in terms of extensional tectonics.

The first locality described is from the northern most point of the island, Diapori, where large folds are documented within marble bands (Ridley, 1982a).

Diapori

The large scale folds which crop out at the northern most peninsula of Syros, Diapori are best seen from the sea, particularly from the ferry as you arrive from or depart to Piraeus on the Greek mainland. The folds which are clearly seen in the marble (photographs 3.29 and 3.30) were mapped (figure 3.32) in the peninsula area. There is a distinctive succession of three mappable units, marble containing thin layers of dolomite, but mainly of grey and cream calcite, a ruditic lithology containing deformed clasts of quartz and calcite and metabasite. The matrix of the rudite contains calcite, quartz, mica and glaucophane which is partially retrogressed to chlorite and albite. A thin layer (4.6 m thick) of retrogressed albite-chlorite schist crops out above the rudite and is too thin to map. The thin schist layer is variably retrogressed at its southern end and layers of glaucophane-rich material (1-2 cm wide) are preserved adjacent to retrogressed schist. Above this is a quartz, graphite, chlorite schist containing thin marble and quartz layers.

Early foliations in the marble are folded. In order to determine fold hinge trends, π-girdles were plotted (figure 3.33). These can be compared with intersection lineations on foliation surfaces and hinge lines of small scale folds in the marble. The fold hinges and intersection lineations in the marble are oriented NE-SW. Minor fold hinge lines and intersection lineation orientations fall symmetrically around the hinge lines of the map scale folds.

The thin albite-chlorite schist layer is folded on a macro-scale folds (figure 3.34), with fold amplitudes and wavelengths of several metres. At its northern end, where the schist is retrogressed, containing chlorite, albite, epidote and green amphibole, fold axial planes are approximately parallel to the regional foliation (figure 3.35). At its southern end the schist is more variably retrogressed and folding is sub-horizontal to upright (figure 3.36). Glaucophane rich layers preserved adjacent to albite-chlorite layers retain their distinction where folded (photograph 3.31). The

Figure 3.32
Map of Diapori. Boxed area A is the marble fold in photograph 3.30
Boxed area B is the fold in photograph 3.29. Areas 1, 2 and 3 relate to figures 3.34, 3.35, and 3.36 respectively.

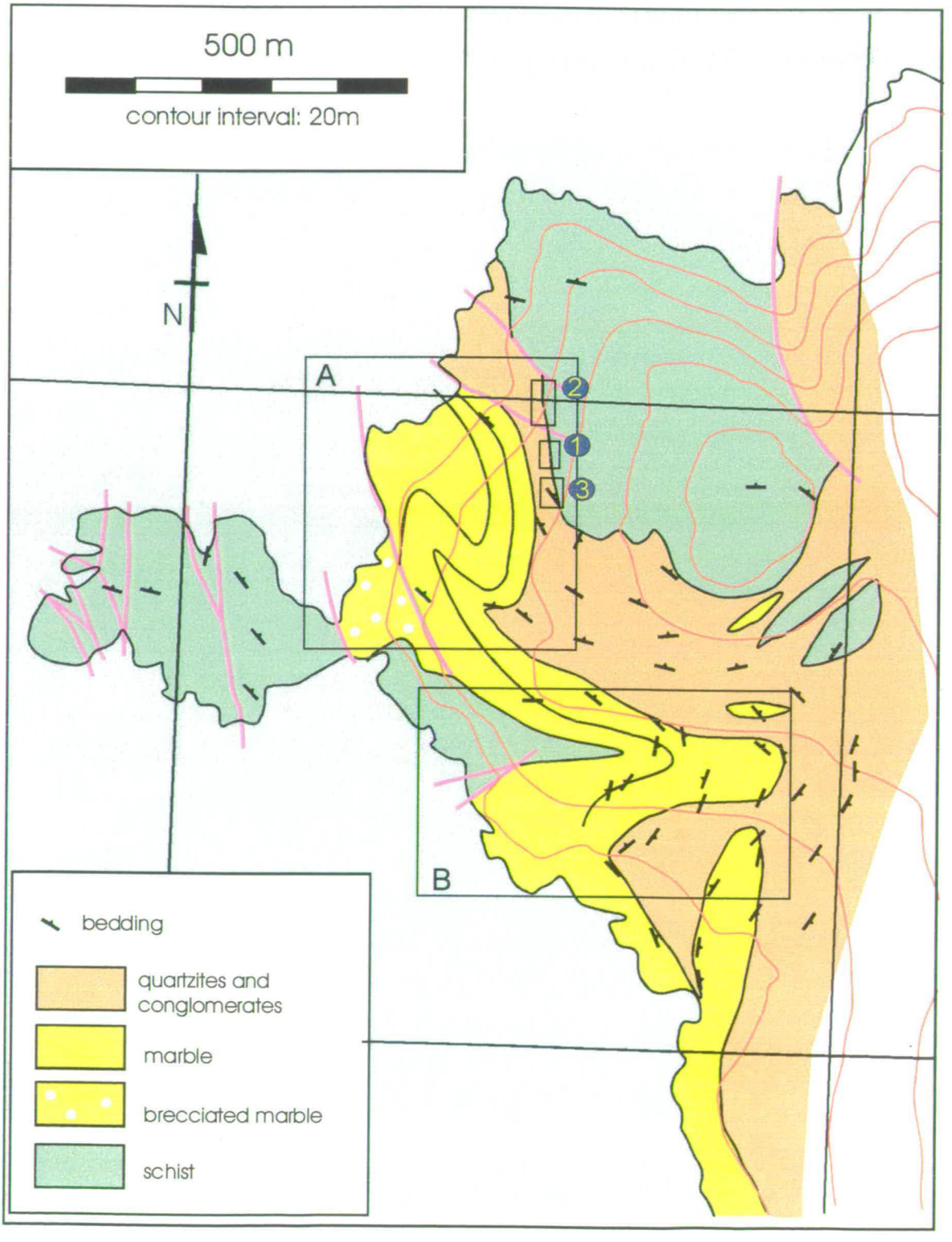

Figure 3.33
Foliations around major folds in marble. Macro-scale intersection lineations and fold hinges.

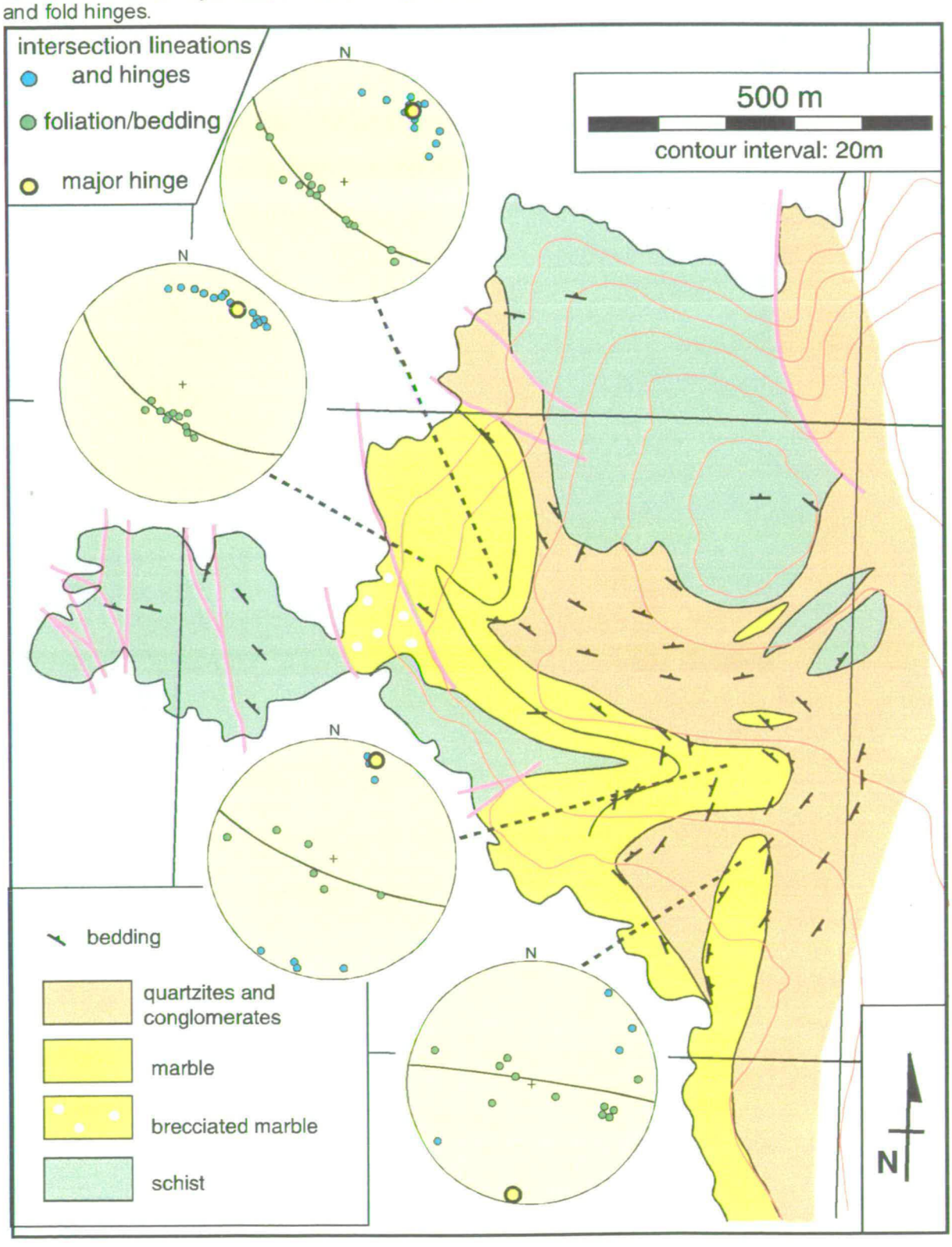

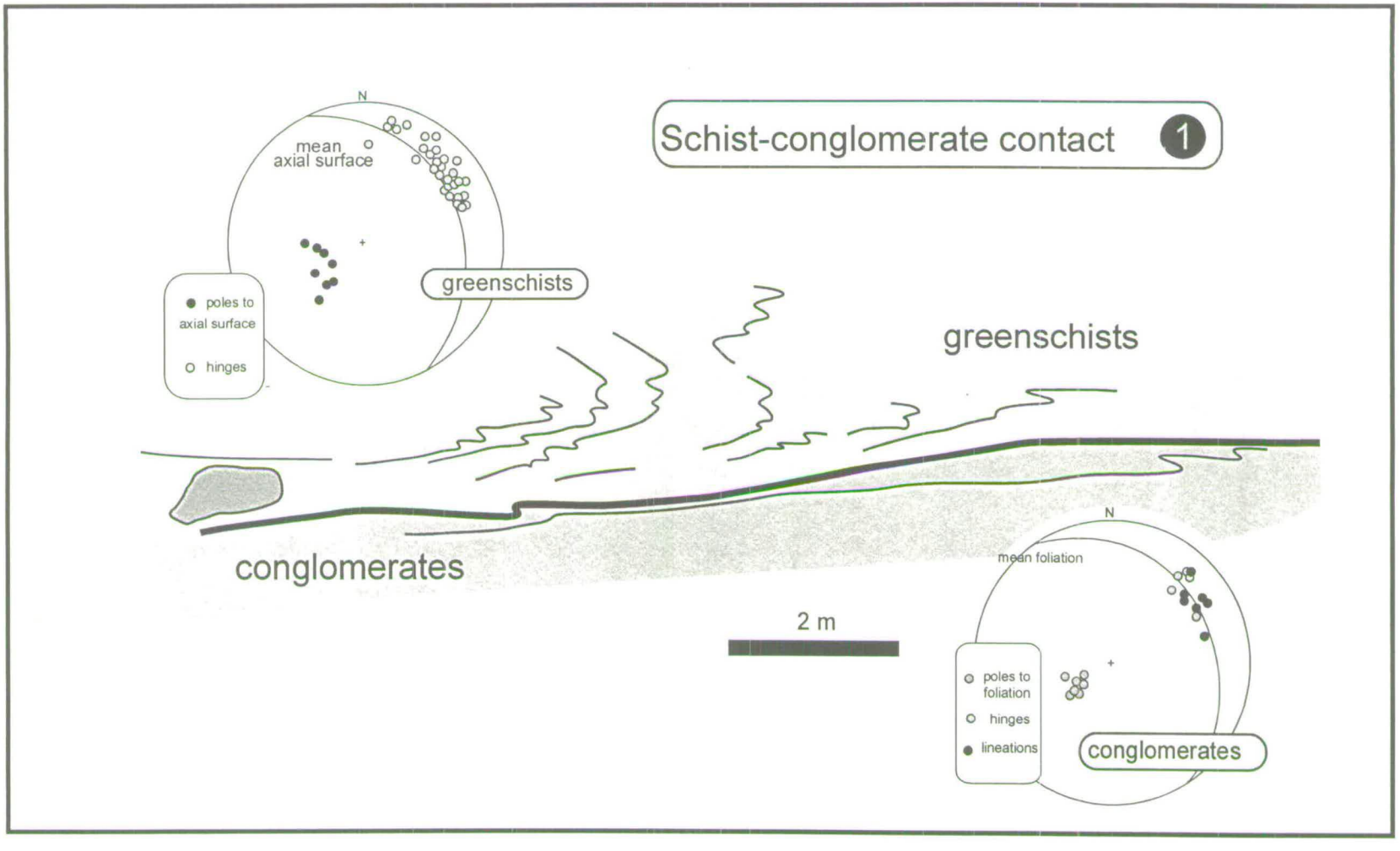

Figure 3.34
Sketch of folds in schist and folded contact of rudite with the schist. Stereonets show poles to axial surfaces and fold hinge lines in the schist and hinge lines and lineation in the rudite conglomerate.

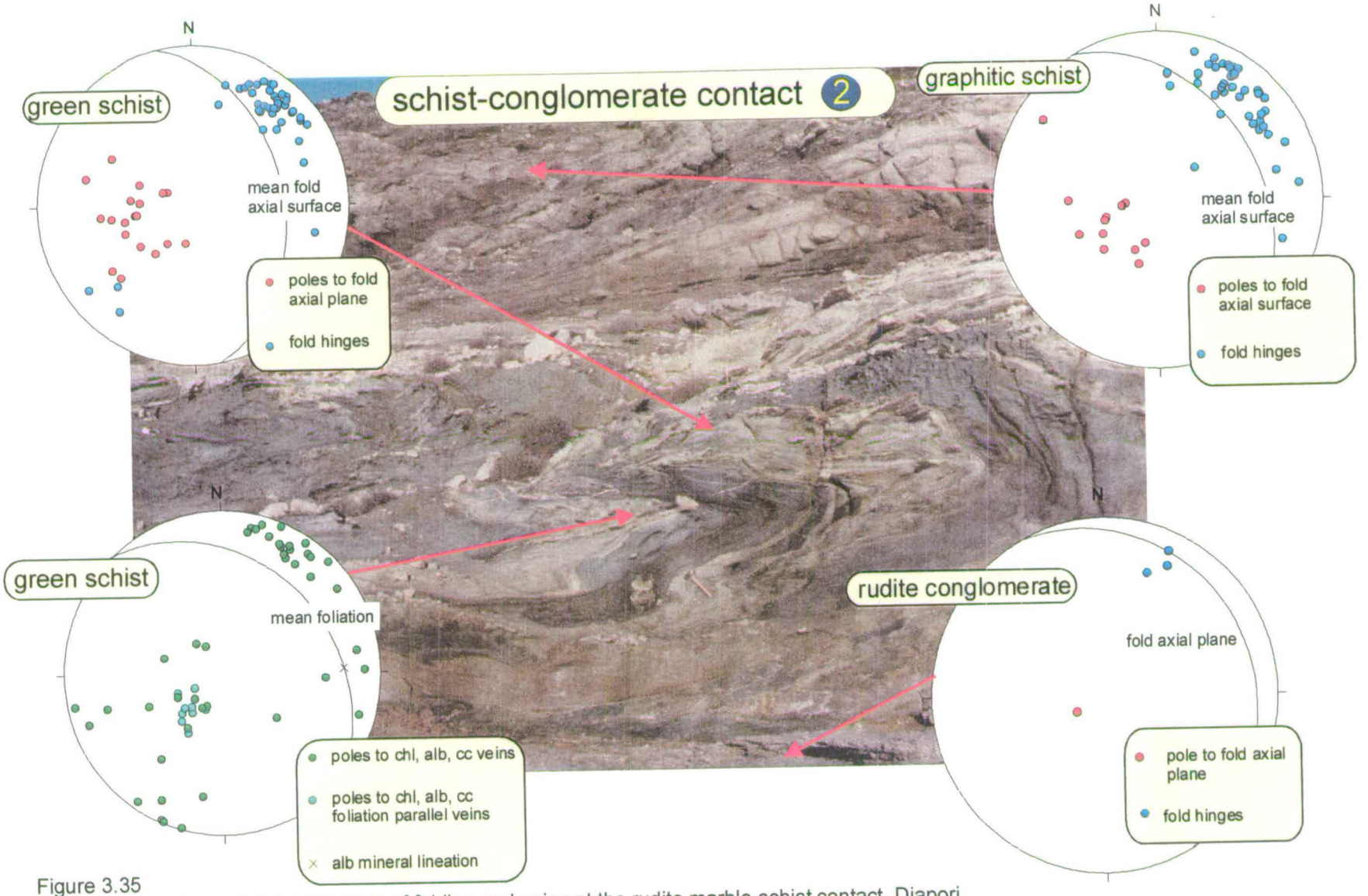

Figure 3.35
Photograph and annotated stereonets of folding and veins at the rudite marble-schist contact, Diapori. Hammer for scale, lower centre.

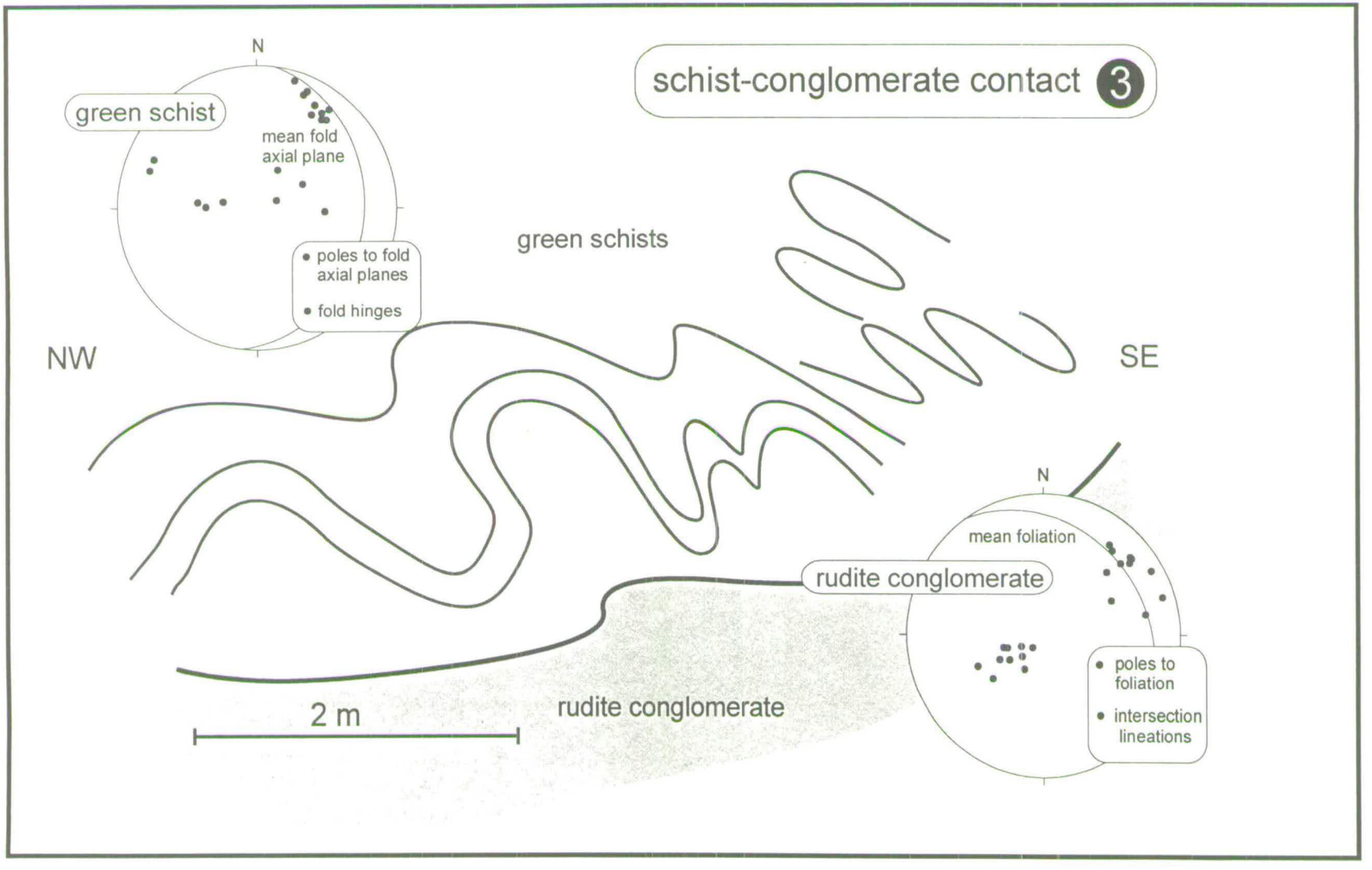

Figure 3.36 Folds hinges and fold axial planes in the schist. Foliations and intersection lineations in the ruditic conglomerate.

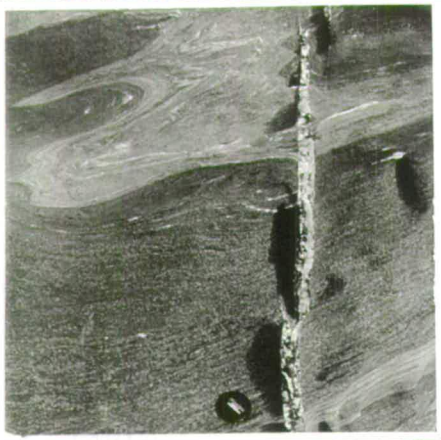

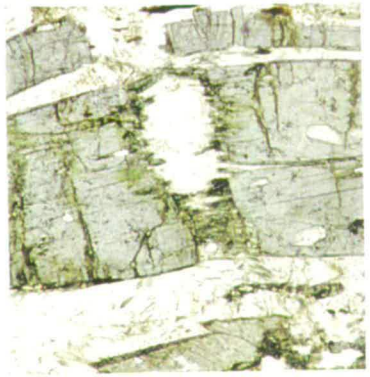

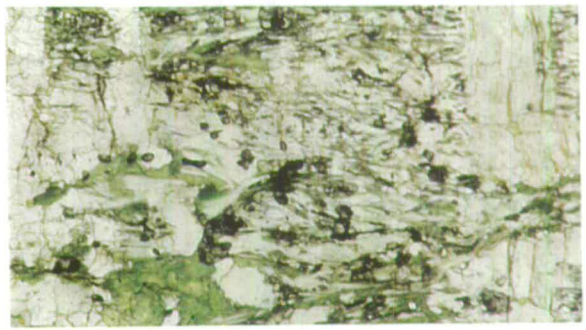

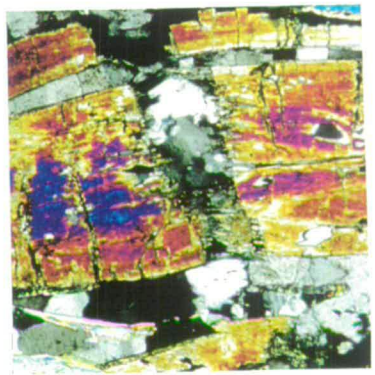

Diapori

Photograph 3.29

Large fold in marble at Diapori. See figure 3.32 for locality and scale.

Photograph 3.30

Fold pair in marble at Diapori, photograph taken from the peninsula. See figure 3.32 for locality and scale.

Photograph 3.33

Extensional chlorite, albite, oxide vein in the greenschist above the marble at Diapori. The vein cross-cuts foliation and folding.
Field of view approximately 1 m.

Photograph 3.32

Folding and crenulation of graphite, quartz, chlorite, mica schist at Diapori. Sample S'96/9B.

Field of view approximately 4 mm.

Photograph 3.31

Inter-layered glaucophane and albite chlorite within the schist unit Diapori. The base of the photograph shows folded glaucophane layers, which are increasingly retrogressed upwards (in the photograph) to form a chlorite, mica, albite porphyroblast layer, sample S'96/6E.

Field of view approximately 4 mm.

Photograph 3.36

Microboudinage of glaucophane crystal showing growth of blue-green amphibole into the boudin neck, from the rudite marble, Diapori. Sample S'96/10B.

Field of view approximately 3 mm.

Photograph 3.37

Cross polars photograph of the microboudinaged glaucophane crystal in photograph 3.3.d.
Sample S'96/10B.

Field of view approximately 3 mm.

Photograph 3.34

Albite, chlorite, calcite, epidote, mica, green amphibole schist cut by extensional albite veins, Diapori. Note the albite micro vein on the right cuts through the green amphibole included in the albite.
Sample S'96/145.
Field of view approximately 4 mm.

Photograph 3.35

Gl crystal in the rudite marble, Diapori. With a pale core and dark rim and a thin outer rim of blue-green amph, which also grows into the fracture
Sample S'96/6D.
Field of view approximately 3 mm.

Photograph 3.38

Pseudomorphing of glaucophane by chlorite, in the rudite marble, Diapori. Note replacement of the inner pale blue core prior to the darker rim. Sample S'96/5A.
Field of view approximately 10 mm.

textures imply that glaucophane was stable during the folding and that recrystallisation to greenschist is associated with minor zones of localised deformation and fluid infiltration, described below. The quartz-graphite schist is also folded but on a micro-scale. The folds outline a strong crenulation fabric in the schist (photograph 3.32).

Lineations and fold hinge line orientations from both the rudite and the thin schist layer are plotted in figures 3.34, 3.35, 3.36 and 3.37. The fold hinge lines and lineations show a constant orientation in all lithologies trending NE-SW. This is parallel to the map and small scale fold hinges in the marble unit.

Extensional albite and chlorite veins are common in the thin layer of retrogressed schist, they are either foliation-parallel or cross-cut layering and folds (photograph 3.33). Locally the veins are surrounded by metasomatic alteration haloes containing albite porphyroblasts, which generally over grow the rock fabric. Albite micro-veins accommodate extension within the schist post growth of green amphibole (photograph 3.34). Greenschist veins, unless foliation parallel, have extensional vein fibres. The veins trend N-S to NW-SE, accommodating NE-SW to E-W directed extension (figure 3.35). At the southern end of the horizon where the schist is variably retrogressed, micro-fabrics document extension. Glaucophane crystals, zoned with pale blue cores and dark blue rims, are micro-boudinaged. Fracture of the glaucophane crystals is perpendicular to their long axes, which are generally aligned E-W on foliation surfaces. The glaucophane is partially altered to chlorite along the fractures. Similar microboudinage fabrics observed in the ruditic marble are described below.

Large glaucophane crystals are observed on foliation surfaces in the ruditic marble. The glaucophane crystals are aligned parallel to fold hinge lines and intersection lineations. In thin section the glaucophane crystals are zoned with pale blue cores and dark blue rims, locally a fine outer rim of blue-green amphibole is also observed (photograph 3.35). The glaucophane is micro-boudinaged (photographs 3.35, 3.36 and 3.37); the fractures cut the glaucophane perpendicular to their long axes. The glaucophane shows growth of blue-green amphibole into fractures, but

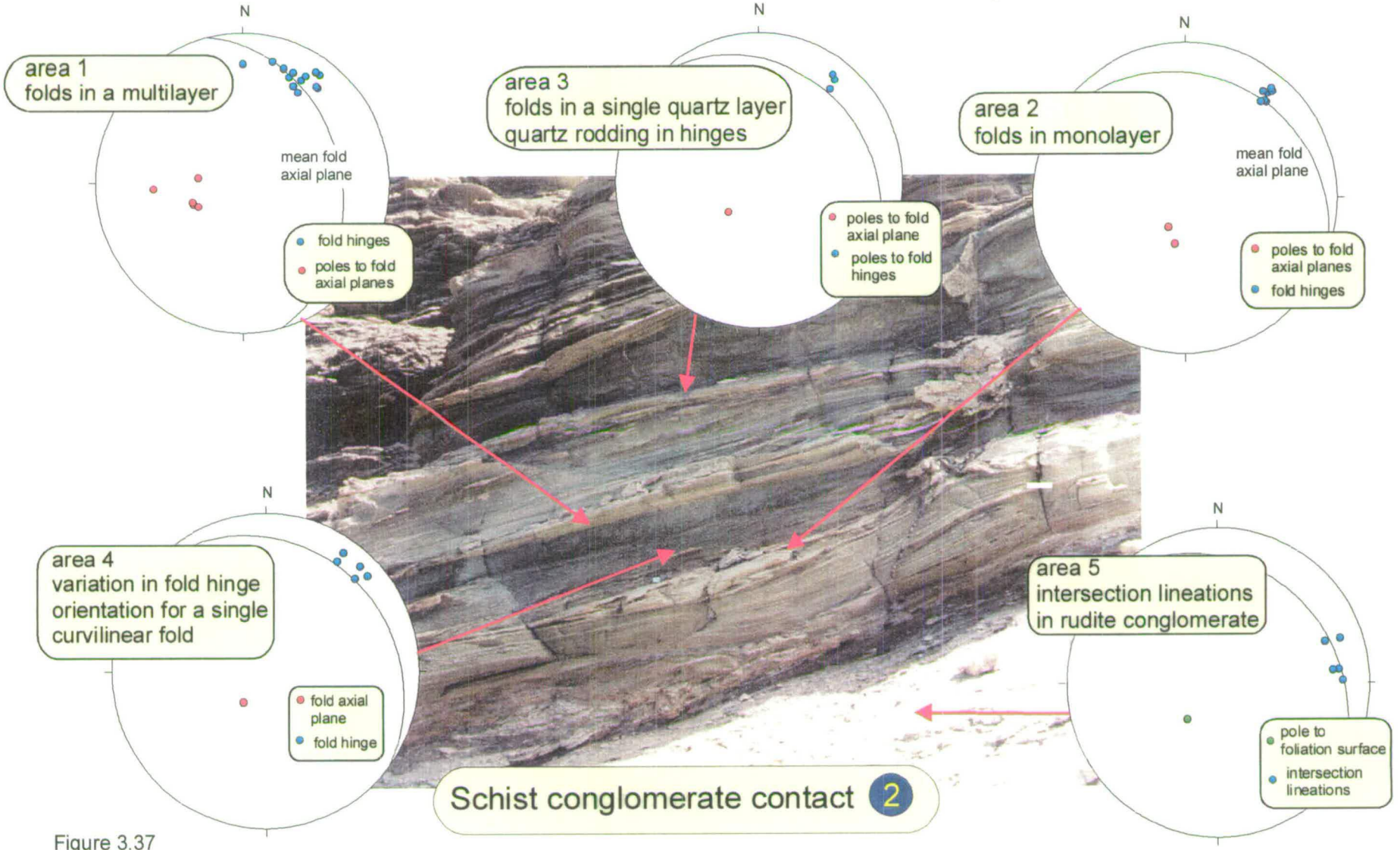

Figure 3.37
Photograph with annotated stereonets for folds and lineations at the rudite-schist contact. Photograph approximately 5 m wide.

rarely show an inner growth of dark blue glaucophane into fracture zones (photograph 3.35). The glaucophane is in places pseudomorphed by chlorite, with reaction nucleation along fractures (photograph 3.38).

To describe the textures in terms of decompression we must look to the work of Maruyama et al. (1986) and Liou et al. (1987) who describe the following sliding reaction as defining the boundary between the blueschist and greenschist facies stability fields:

$$\text{Gl-Rieb}_{SS} + \text{Epd}_{SS} + \text{Qz} + \text{H}_2\text{O} \rightarrow \text{Act}_{SS} + \text{Ab} + \text{Chl}_{SS} + \text{Mt/Hem}$$

Decompression through the blueschist-greenschist transition produces an increasingly riebeckitic amphibole which is eventually replaced by actinolite. This amphibole solid solution transition associated with decompression and extension has also been documented for Ios blueschists (Grütter, 1993). He suggested the following continuous reactions to explain the reaction and replacement textures of glaucophane-actinolite and chlorite. The reactions explain well the textures observed in the glaucophanes, although the final reaction has hardly progressed in this example from Syros.

$$\text{Gl}_{\text{(pale blue)}} + \text{Pa} + \text{Qz} + \text{H}_2\text{O} \rightarrow \text{Gl}_{\text{(dark blue)}} + \text{Ab} + \text{Chl}$$

$$\text{Gl}_{\text{(dark blue)}} + \text{Pa} + \text{Qz} + \text{H}_2\text{O} \rightarrow \text{Ab} + \text{Chl} + \text{Mt}$$

$$\text{Gl}_{\text{(pale-dark blue)}} + \text{Epd} + \text{Qz} + \text{H}_2\text{O} \rightarrow \text{Cam} + \text{Ab} + \text{Chl} + \text{Mt}$$

Summary of Diapori

An extension axis oriented NE-SW to E-W is inferred from the structures and fabrics cropping out at Diapori. These structures include extensional greenschist, albite, chlorite veins and micro-boudinage of glaucophane crystals. Brittle failure of glaucophane crystals, with associated growth of blue-green amphibole in fractures, suggests that extensional strain oriented E-W was accommodated by the rocks during the blueschist-greenschist transition. Evidence for vein forming fractures post green

amphibole growth implies that E-W oriented extension continued well into the greenschist facies stability field, albeit accommodating minor extension.

The parallelism of fold hinges, from map-metre scale, oriented NE-SW to E-W are also consistent with an E-W oriented extension direction associated with folding. The origin and form of the folds is unknown and may have been related to prograde metamorphism or inherited faulting. Ridley (1982a) and Bloor (1998) suggest that the folds formed during ductile shearing associated with thrusting. However, the present orientation of fold axial planes parallel to the regional flattening fabric and hinge lines parallel to the extension direction is consistent with the net-layer extension documented during down pressure recrystallisation (figure 3.38).

Serpentinite belt

The high pressure assemblages of the north are separated from southern Syros by a belt of serpentinite material, described in detail by Dixon (1969) (figure 3.39). The serpentinite belt is characterised by a swathe of serpentinite material, within which lie metabasic blocks centimetres to several tens of metres in size. The northern side of this zone is marked by boudinaged and folded layers which have in places become entrained into the serpentinite. The western part of the belt (figure 3.39) was chosen as the study area. The area was chosen for its almost continuous exposure and because the area had already been mapped and the structures and mineral assemblages documented by Dixon (1969).

Structurally the serpentinite belt is characterised by boudinage, with associated veins and folds. Here the area is described in terms of its structure and petrography from Kambos to the western coast, along its northern and southern margins. Data were collected from four main localities: i) Kambos goat cave area; ii) the central area; iii) the northside of Lia Bay, and iv) the southside of Lia Bay. The data are presented for each locality in turn.

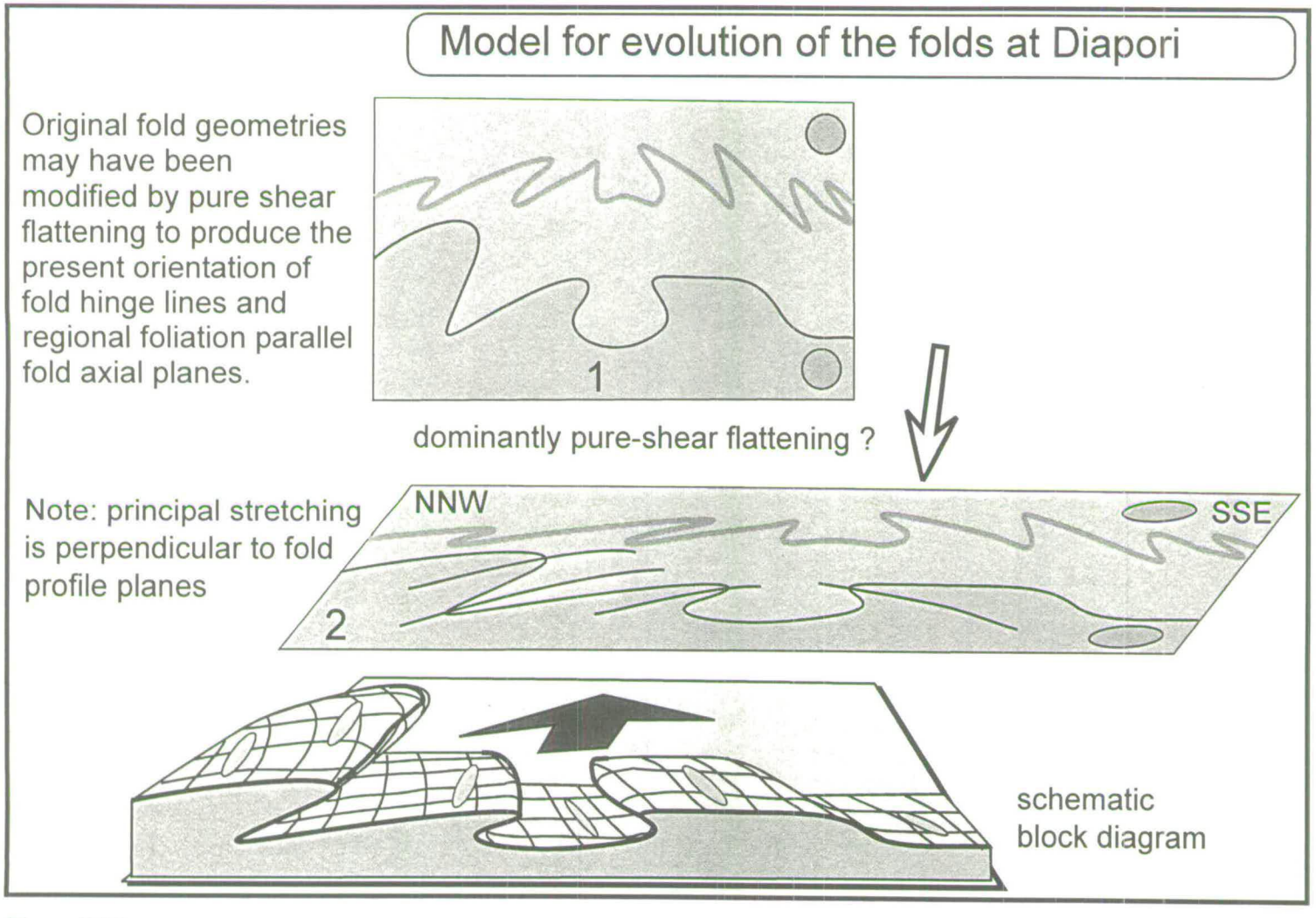

Figure 3.38
Block diagram for fold model evolution, Diapori. Early folds or inherited geometries can be flattened to produce folds with fold axial planes parallel to the regional foliation and parallel mineral lineations and fold axes.

Figure 3.39
Map of western serpentine belt from Kambos-Lia Bay, after Dixon (1969) and this study. The localities studied are marked and letters A and B refer to data in figures 3.43/3.44 and 3.45 respectively.

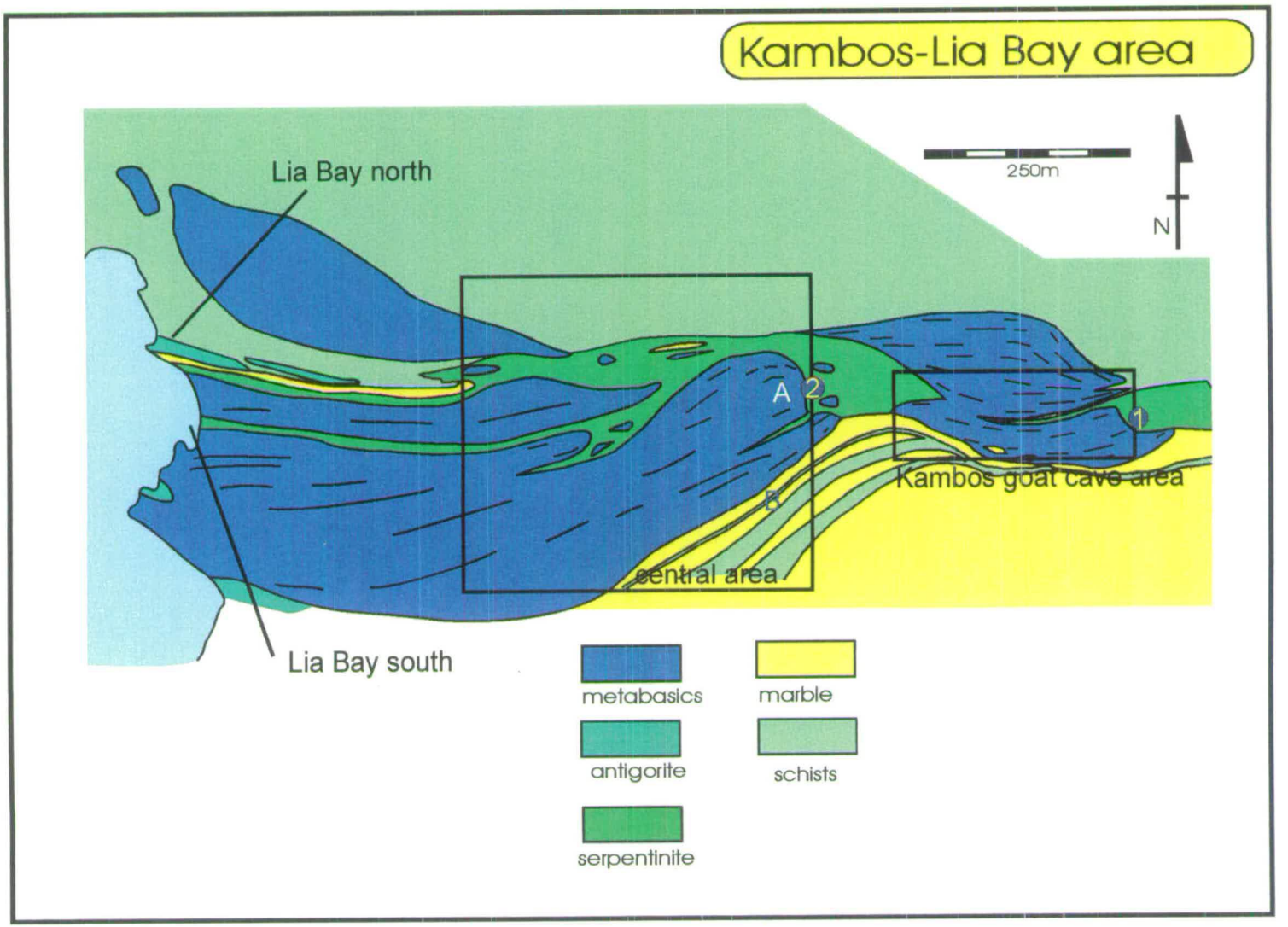

i) Kambos goat cave area

The path from Kambos-Lia Bay crosses a zone of boudinaged marble and pelite units. Greenschist veins which accommodate layer extension contain varying amounts of chlorite, albite, quartz, calcite and oxide. The veins have associated metasomatic alteration haloes. Photograph 3.39 shows alteration in the halo of one of the veins; note that glaucophane is zoned with a pale core and a blue-green amphibole rim, and that some glaucophane has retrogressed to chlorite. In the gneiss, minerals precipitate in boudin necks (photograph 3.40). The extensional veins of greenschist grade are inferred to accommodate NE-SW directed extension (figure 3.40)

Foliations in marble boudins were used to plot π-girdles to determine boudin axes, or where possible boudin axes were measured directly (figure 3.41). The boudin axes trend NW-SE to N-S, accommodating layer parallel extension along an E-W oriented axis by boudinage. This is parallel to the extension direction documented by greenschist fracture. Late normal faults cross cut the schist and marble layers, with N-S to NE-SW oriented fault planes which have oblique slickensides.

ii) Central area

Data were collected in the central area from both the gneiss and lower marble. The contact of the gneiss with the serpentinite forms a small gully (locality A, figure 3.39). The edge of the gneiss and the serpentinite is cross-cut by albite-chlorite veins. The area around the veins is chloritised and shows development of albite porphyroblasts. Garnets in the gneiss have been pseudomorphed by chlorite and are rimmed with albite. A sketch of the veins and a stereonet of their orientations is shown in figure 3.42. The veins are sub-vertical and accommodate E-W to NW-SE layer parallel extension.

The foliation in the gneiss at locality A curves into the contact with the serpentinite and a π-girdle has been drawn through poles to the foliation to find a hinge line (figure 3.43). The hinge line trends NW-SE implying NE-SW directed

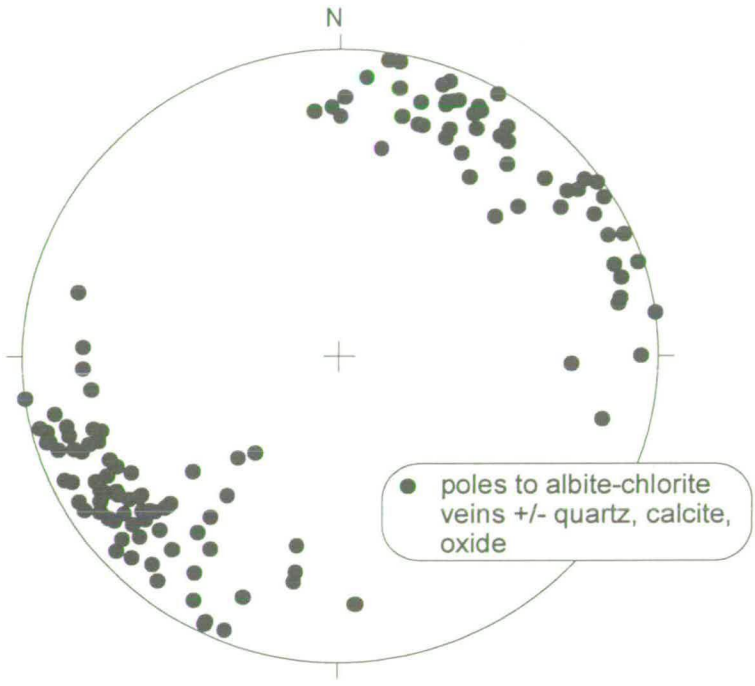

Figure 3.40
Poles to greenschist veins, northern Serpentine belt, Kambos goat cave area

Figure 3.41
Field sketch of Kambos goat cave area annotated with stereonets.

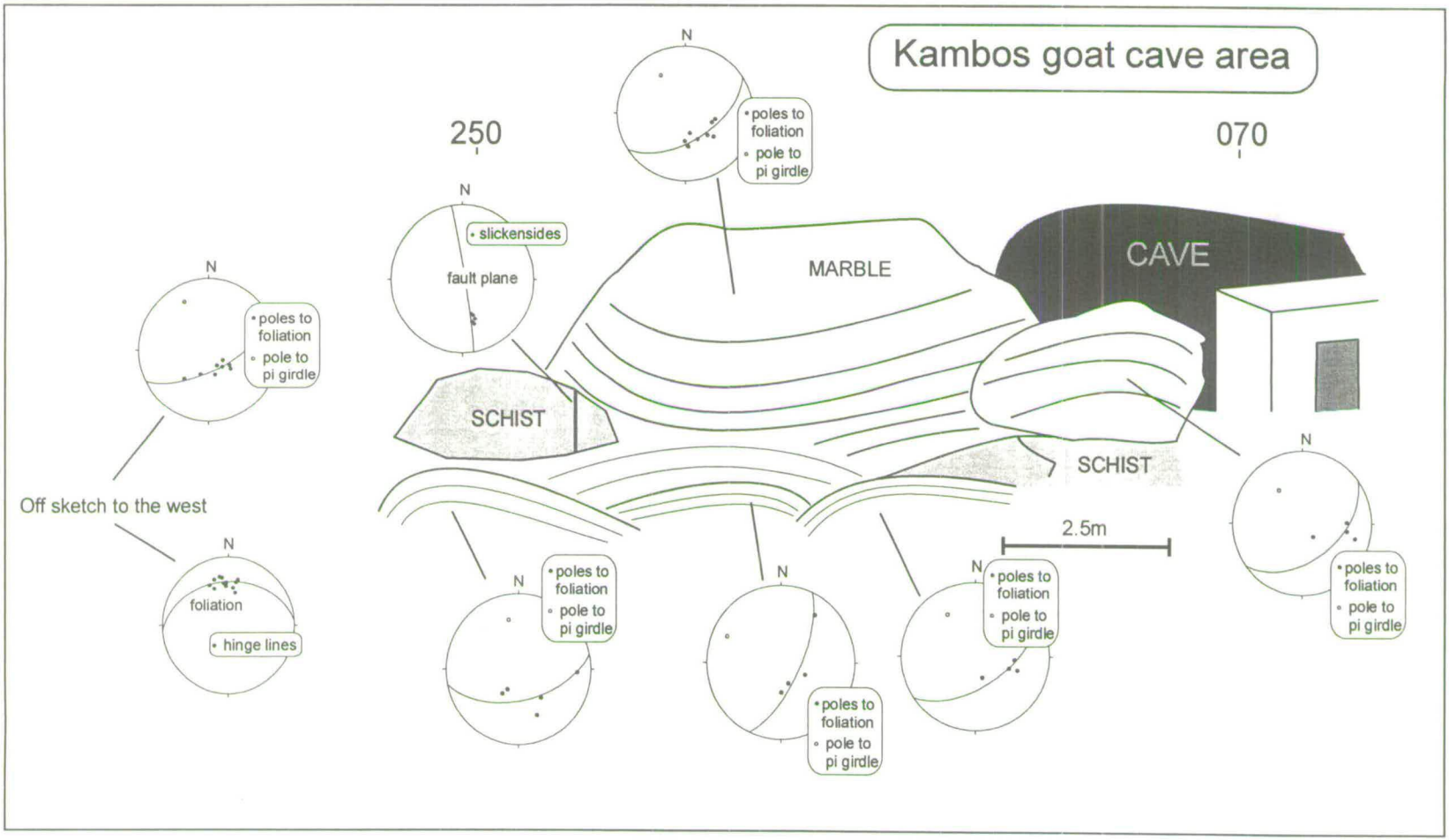

Photograph 3.40

Albite + minor chlorite and oxide in boudinaged gneiss, Kambos goat cave, serpentine belt. Photograph taken looking north.

Field of view approximately 60 cm.

Photograph 3.42

Folds at contact of impure marble and serpentine, serpentine belt. Photograph taken looking east.

Field of view approximately 1 m.

Photograph 3.41

Gully contact of impure marble and serpentine in the northern serpentine belt. Photograph taken looking east. Folds on the right are shown in photograph 3.42

Field of view approximately 15 m.

Photograph 3.39

Thin section photograph of halo to chlorite and albite vein at Kambos in the serpentine belt. Glaucophane is rimmed by blue-green amphibole and partially replaced by chlorite. Sample S'95/103.

Field of view approximately 2 mm.

Photograph 3.43

Boudinaged sodic-pyroxene, epidote, ankerite layer on face perpendicular to photograph 3.42, looking north.

Field of view approximately 1 m.

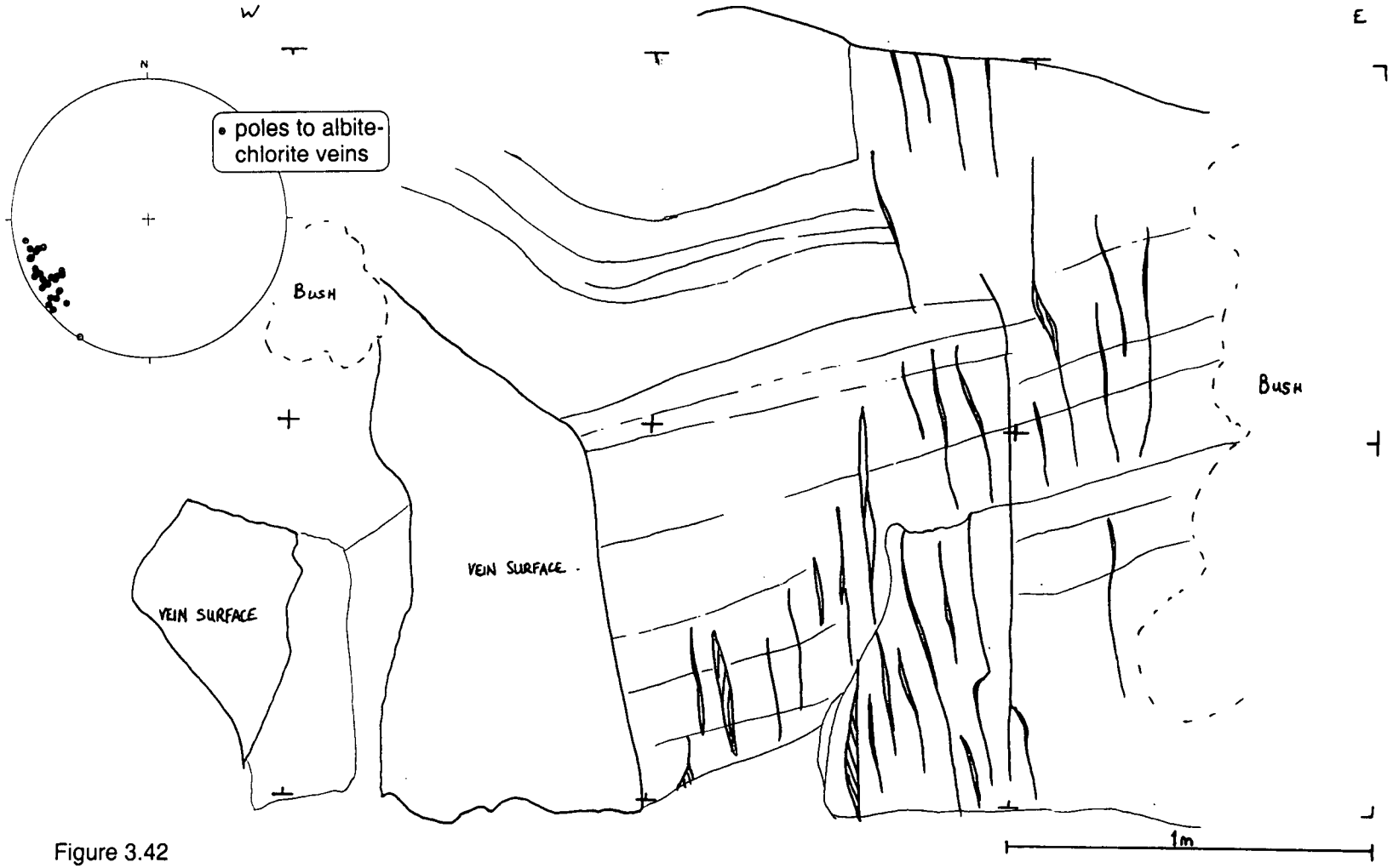

Figure 3.42
Field sketch of greenschist veins and equal area stereonet, Serpentinite belt.

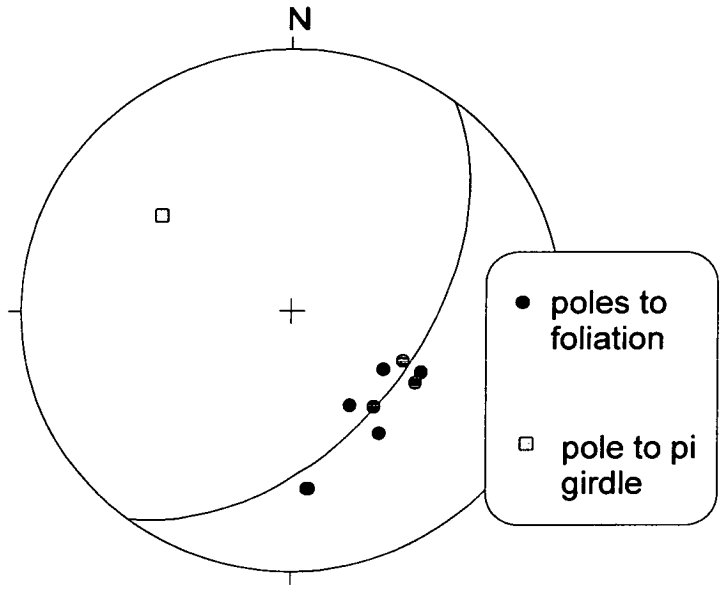

Figure 3.43
Foliation orientation around large boudin in the serpentinite belt, marked A on figure 3.39.

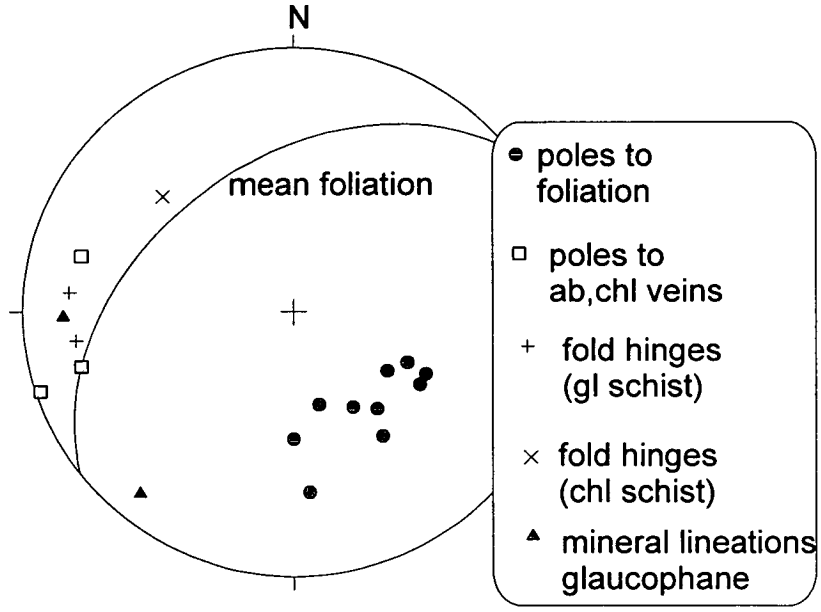

Figure 3.44
Foliations, mineral lineations veins and hinge lines from gneiss in the central area of the serpentinite belt.

layer parallel extension. In the gneiss to the west the foliation dips NW and fold hinges and mineral lineations trend NE-SW to E-W (figure 3.44). The mineral lineations and hinge lines are defined by glaucophane and glaucophane-bearing schists, respectively. Extensional chlorite-albite veins away from the contact with the serpentinite trend N-S and show E-W directed extensional fabrics (figure 3.44). The glaucophane mineral lineation is parallel to the extension direction inferred from greenschist veins.

Foliations in the lower marble mirror the foliations in the gneiss striking NE-SW. Minor hinge lines forming intersection lineations on marble surfaces are oriented N-S (figure 3.45). The hinge lines are not parallel to hinge lines or mineral lineations in lithologies entrained in the serpentinite.

The data collected in the central area was from the southern margin of the serpentinite belt and the observations are generally consistent with those from Kambos goat cave; mainly NE-SW to E-W directed extension and boudinage, with flattening fabrics and mineral lineations parallel to the extension direction. The deformation has continued into the greenschist facies accommodated by extensional chlorite and albite veins. In the lower marble (locality B) intersection lineations are oriented N-S and do not show flattening or reorientation; this is in contrast to the gneiss where fold hinges in glaucophane schist are parallel to extensional fabrics in greenschist veins and the stretching direction of layer parallel boudinage.

iii) The northside of Lia Bay

The northern contact of the serpentinite with an impure marble horizon, was studied to assess the concentration and style of deformation at the contact. The contact forms a gully at the coast; the northern wall of the gully is impure marble and is both isoclinally folded and boudinaged (photographs 3.41, 3.42 and 3.43). The folding and boudinage were described by Dixon (1969), who pointed out that the boudinaged, pyroxene-bearing, calc-silicates in a carbonate matrix owed their competence to metasomatic reactions at high pressure and low temperature (i.e. they had to have a period of growth at an ultramafic contact prior to disruption). He also

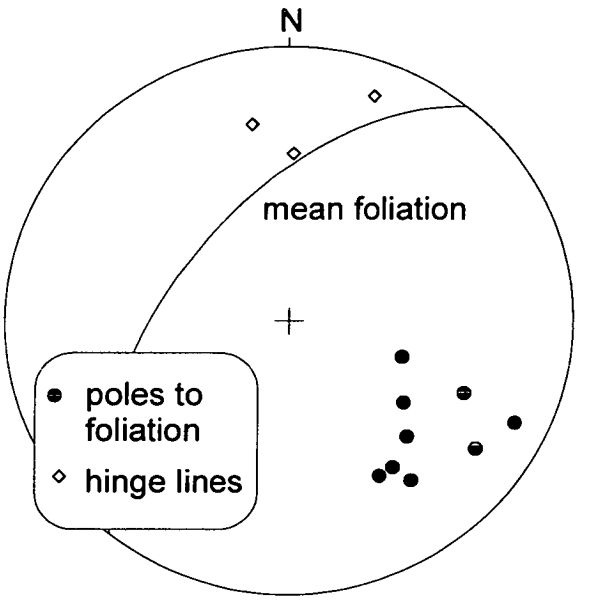

Figure 3.45
Poles to marble foliation and hinge lines of folds in the lower marble from the serpentine belt. The marble is marked B in figure 3.39.

interpreted garnet zoning in terms of a period of reversed metasomatic activity post-disruption, but still at high pressure. The contact with the serpentinite is at the base of this northern wall. Folds and boudins are identified in the marble by bands of schistose material, which preserve the high pressure minerals described by Dixon (1969). Pyroxene, glaucophane, mica, epidote, ankerite and chlorite can all clearly be identified in the field within the schistose marble.

The schistose layers are boudinaged with discrete fractures cutting the layers (photograph 3.43). Poles to the fractures define the extension direction which are approximately parallel to the strike of the foliation (NE-SW). Fold axial planes of intrafolial folds are parallel to the regional foliation and hinge line trends of folds near the contact trend E-W (figure 3.46). Mineral lineations defined by glaucophane and chlorite are parallel to the fold hinges (figure 3.47). Crenulations, associated with folding are axial planar and their intersection lineations trend E-W. The parallelism of mineral lineations and fold hinge lines with the direction of extension inferred from layer parallel boudinage, and fold axial planes parallel to the regional foliation is indicative of high strain and fold flattening. Flattening of folds was also documented in a greenschist mylonite in the south at Finika and has been suggested for fold structures at Diapori in the north of the island. Deformation in the marble next to the contact with the serpentinite is dominated by flattening and layer parallel extension, manifest by boudinage and veining.

Northwards into the marble away from the contact with the lower serpentinite, fold hinge lines and lineations trend in a N-S direction. The hinge lines and lineations change systematically in orientation as the contact is approached, bending E-W (figure 3.48). This change in the hinge line and lineation orientation implies that there is a deformation gradient southwards towards the contact with the serpentinite, N-S trending linear features have been bent into an E-W trend as the contact is approached. Within the high strain zone the fold hinge lines have been bent into parallelism with the stretching direction, inferred from high pressure boudinage of the layers adjacent to the serpentinite. Mineral lineations show the same change in orientation as the contact is approached (figure 3.48). (A similar deformation

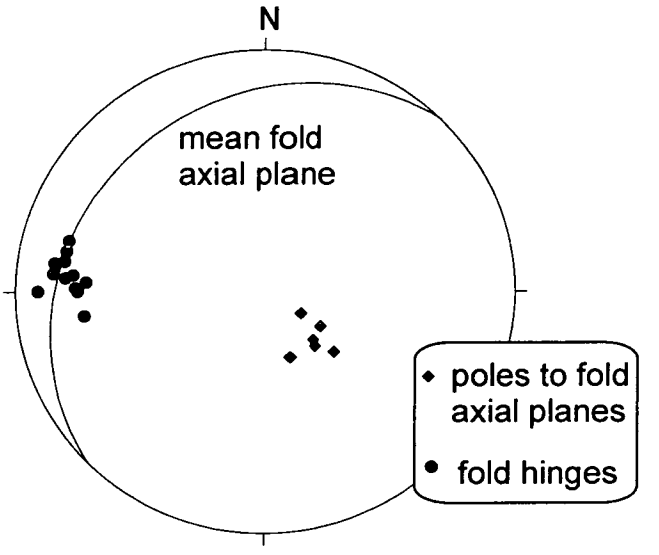

Figure 3.46
Fold and fold axial plane data from the impure marble above the contact with the serpentinite, Lia Bay north.

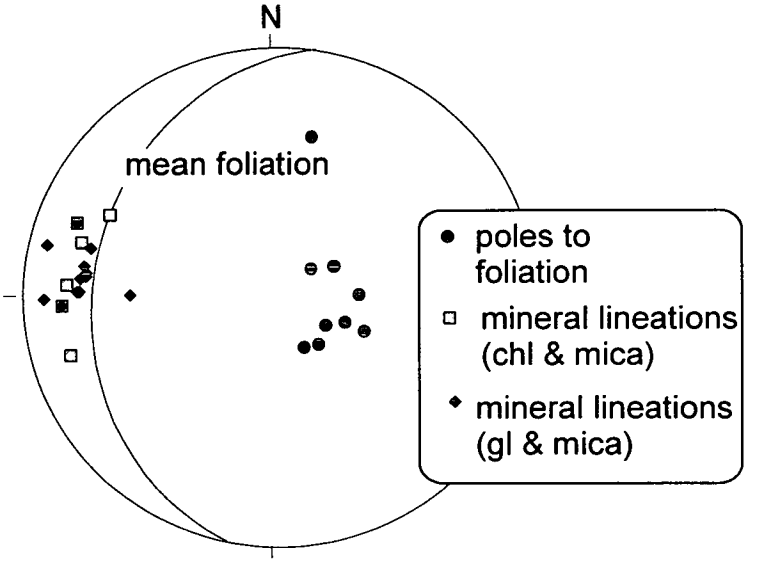

Figure 3.47
Mineral lineation data from the impure marble above the contact with the Serpentinite, Lia Bay north.

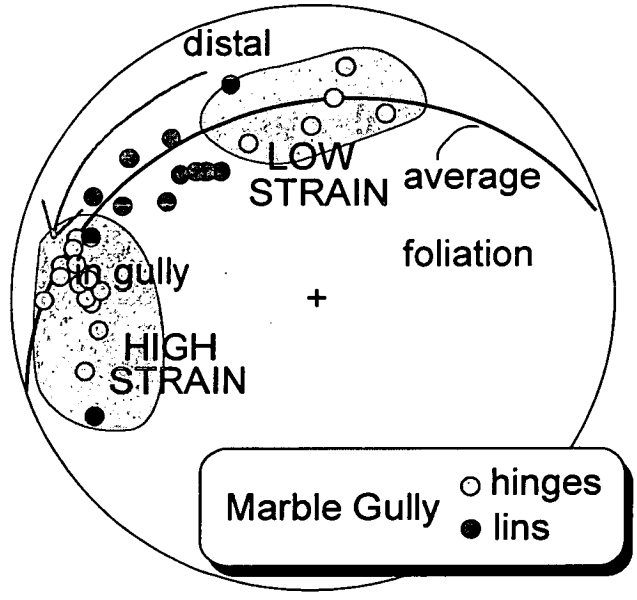

Figure 3.48
Variation in lineation and fold hinge trend in impure marble. The distance from the contact with the serpentinite in the gully is annotated qualitatively.

gradient, but reversed in sense, is though to be present south of the serpentinite belt. Lineations on marble foliation surfaces south of the belt (figure 3.45) are oriented N-S, whilst those in the gneiss entrained in the serpentinite are oriented E-W. Lack of outcrop between the two localities on this southern side meant that an equivalent progressive reorientation of linear fabrics could not be documented.)

Extensional glaucophane and quartz veins are observed in schistose layers near the northern contact. The glaucophane forms fibrous selvages around the veins that grow into the centre of the vein (figure 3.49). Small shear zones are also seen in these schist horizons. The shear zones continue into the serpentinite below (figure 3.50). Shear zones show local, top to the east, asymmetry. Evidence for intensification of deformation close to the contact is corroborated by localised asymmetrical shear zones in schist layers next to the contact which 'tap' down into the serpentinite, implying that the serpentinite acted as a decollement or high strain zone during coaxial deformation.

In the northern Lia Bay area the majority of the deformation appears to have occurred within the blueschist facies stability field. Glaucophane was stable during the formation of mineral lineations and veining. The pyroxene in boudinaged layers appears to be unaltered in the field and there are no greenschist extensional veins in this area. Dixon (1969) attributed garnet zoning to reversed meatsomatic activity post-disruption. The serpentinite also accommodated this E-W extensional strain. The orientation of the extension axis (E-W) is parallel to that south of the serpentinite belt. This parallelism suggests that the serpentinite belt was part of a continuous stratigraphy during decompression.

iv) The southside of Lia Bay

Greenschist (chlorite + albite +/- other minerals) vein orientations were measured in the glaucophane schist that crops out on the southern margin of Lia Bay. The veins form three distinct mutually cross-cutting arrays identified in the field. Vein orientations from all three arrays were measured (figure 3.51). The trends in

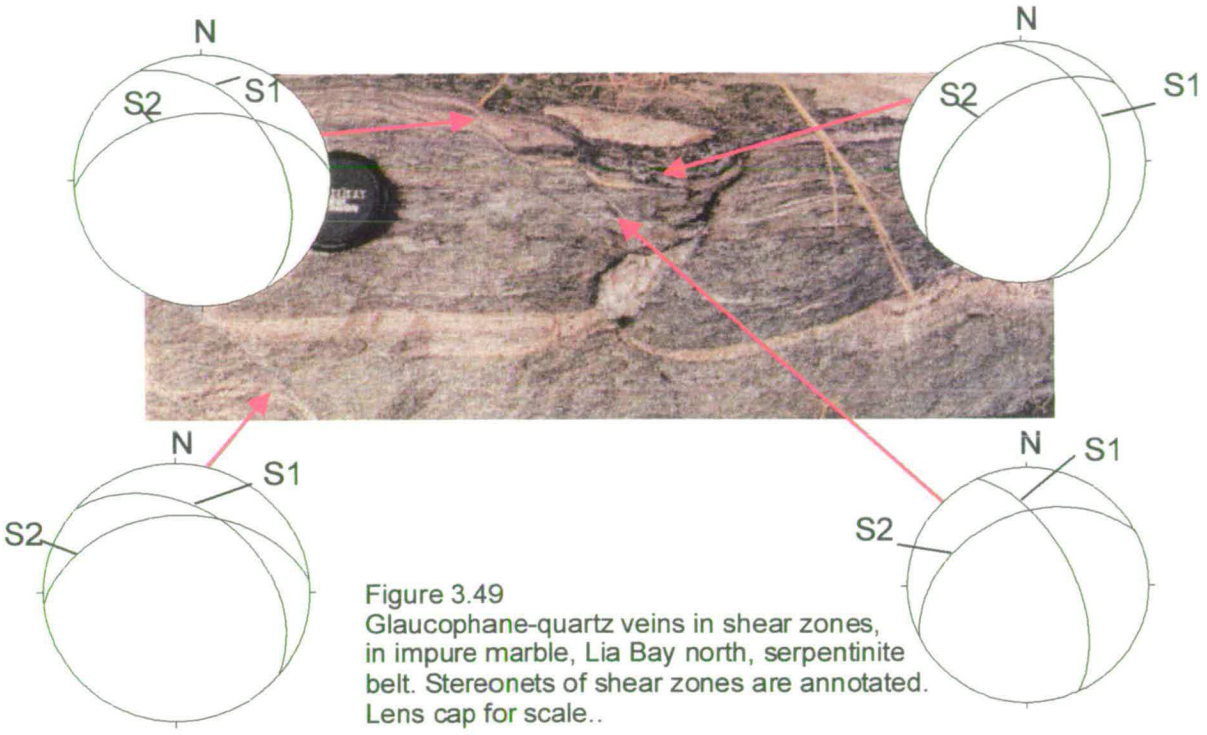

Figure 3.49
Glaucophane-quartz veins in shear zones, in impure marble, Lia Bay north, serpentinite belt. Stereonets of shear zones are annotated. Lens cap for scale..

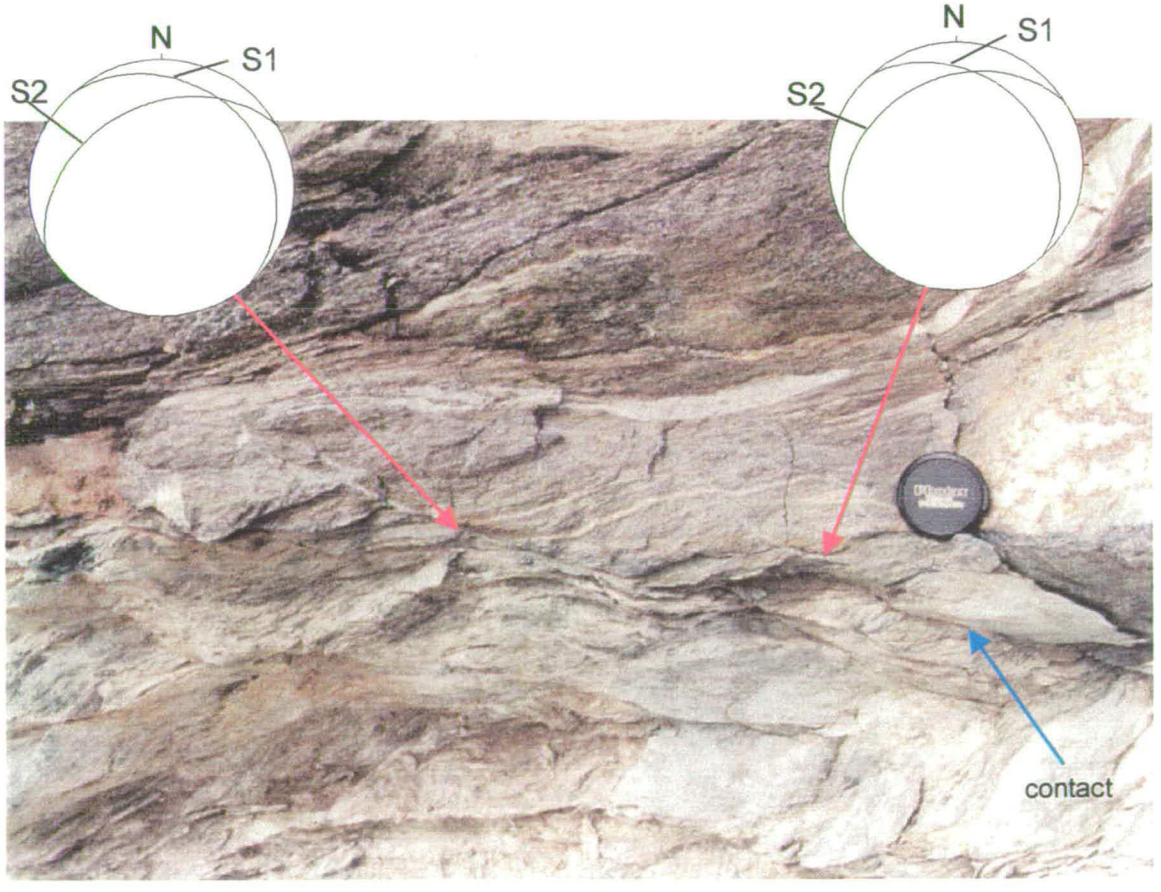

Figure 3.50
Photograph of contact between impure marble and serpentinite, Lia Bay, serpentinite belt. Extensional shear bands, annotated with stereonets, link down into the serpentine. Lens cap for scale.

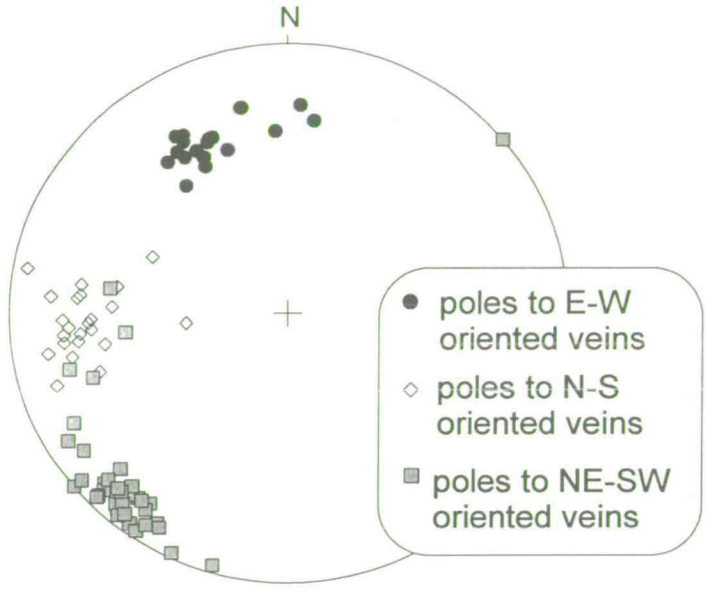

Figure 3.51
Stereonet of vein orientations from Lia Bay south, serpentinite belt.

vein orientation are more complex than those documented elsewhere in the serpentinite belt. The reason for the complexity in vein orientation is unknown.

Summary of the serpentinite belt

The serpentinite belt is dominated by NE-SW to E-W directed foliation parallel extension and layer flattening. Weak asymmetry (top to the east) is seen locally in an area adjacent to the serpentinite, which is interpreted as acting as a detachment during deformation, separating two areas of predominantly coaxial deformation. The majority of the deformation has occurred within the blueschist facies stability field. However, deformation associated with greenschist grade sub-vertical veining has the same extension direction.

On both the northern and southern margins of the serpentinite, ductile fabrics (folds and mineral lineations outlined by glaucophane) trend E-W. Further north and south, away from the serpentinite, fold hinges and lineations trend N-S. Rotation or recrystallisation of early fabrics has occurred in the proximity of the serpentinite to accommodate E-W extension. The extension has continued into the greenschist field during the formation of greenschist grade veins which are spatially associated with boudinage. Greenschist grade veins at the southern side of Lia Bay have a more complex geometry than elsewhere in the area, consisting of three mutually cross-cutting arrays. The reason for the complexity at this locality, as compared to elsewhere, is unknown. Zones of concentrated greenschist veining were identified at the contacts of the gneiss with serpentinite (localities 1 and 2, figure 3.39). These are inferred to have been caused by localised fracture within the greenschist facies stability field along lithological contacts. The principal structure of the area is high pressure boudinage along an E-W oriented axis. The boudinage is accommodating pure shear flattening, net-layer extension. The extension has continued weakly into the greenschist facies stability field and is fracture rather than ductile deformation controlled.

Summary of northern localities

The area north of and including the serpentinite belt is dominated by high pressure deformation fabrics. Early fabrics identified, which formed prior to extension, are a flat lying foliation which has been folded. However, geometrical observations of the fabrics suggest that these early fabrics have been subsequently modified by extensional tectonics. Fold axial planes parallel to the regional foliation and fold hinge lines and mineral lineations oriented E-W, can be explained by modification of folds by pure shear flattening, within the blueschist facies stability field.

In the serpentinite belt reorientation of linear fabrics into an E-W trend documents further evidence for modification of early fabrics. The constant orientation of the extension axis above and below the serpentinite belt suggests the island was part of a continuous stratigraphy during extensional deformation. This is supported by the evidence of strain localistation into the serpentinite from adjacent units.

3.4 Discussion

The structural data documented in this chapter suggests that coaxial layer parallel extension accommodated strain within both the brittle and ductile regimes. Evidence for horizontal net-layer extension was documented by fold flattening and boudinage of lithologies containing high pressure assemblages in the north of the island. The extension axis of the boudinage is oriented E-W to NE-SW. Observations of greenschist ductile extensional structures were made in southern Syros. The stretching direction defined by greenschist fabrics is parallel to that inferred from areas of high pressure boudinage. Kinematic links between the high pressure boudinage and low pressure greenschist deformation were demonstrated at Delfini, an area of partial retrogression, where both high pressure and low pressure mineral assemblages and structures are preserved.

In the north of the island extensional deformation associated with greenschist facies metamorphism is dominated by fracture and extensional veining. In southern Syros both greenschist facies ductile deformation and veining is observed. At Delfini and at Megas Yialos on the southern coast ductile greenschist fabrics were observed bending into brittle faults, documenting a kinematic link between brittle and ductile structures.

The structural data collected during this study can be compared with and linked to that of earlier structural work on Syros. By combining the work of this study with earlier studies a chronology of deformation events for Syros has been established. A collation of structural data and interpretations from Syros is shown in table 3.1. The table is based on data from Dixon (1969), Ridley (1982), Barr (1989) and Bloor (1998), as well as this study.

This study has expanded the previously documented deformation history by identifying areas of localised greenschist facies ductile deformation in zones up to 20 m wide, between the areas of static albite porphyroblast growth documented by Ridley (1982a) and Barr (1989). Observations of brittle faults cutting the metamorphic sequence (Ridley, 1984b) remain undisputed. However, observations of brittle faults linking into zones of ductile shearing at Megas Yialos and Delfini suggest a continuum of deformation from ductile to brittle extension.

In terms of high pressure deformation, extensional fabrics and boudinage were described in the northern serpentinite belt by Dixon (1969). Dixon noted that these fabrics had to have occurred at high pressures. Subsequent workers also recognised local evidence for extensional fabrics. Ridley (1982a) documented boudinage between Kini and Delfini. He interpreted these structures as part of a compressional folding fabric, with boudinage accommodating attenuation of fold limbs. Bloor (1998) noted boudinage and extensional shear zones in the northern grey schists. Bloor described these as the final phase of deformation within the grey schists.

There is evidence for earlier fabrics, described by Ridley (1982a) and Bloor (1998); which they interpret to have formed during compression and peak

Table 3.1 Summary of structural interpretations for Syros, from Dixon (1969), Ridley (1982), Barr (1989), Bloor (1998) and this study.

Fabric formation	*Summary of fabric development*	*Interpretations*
Sedimentary layering.	Identified in localised areas in northern Syros by Bloor (1998).	*Bloor (1998)* First planar fabric S_0.
Foliation	The major planar fabric on Syros, identified by all workers	*Dixon (1969)* major fabric associated with peak metamorphism. *Ridley (1982)* major fabric forming event (dominant foliation) formed during thrust sense shear under peak metamorphic conditions. *Barr (1989)* major planar fabric. *Bloor (1998)* S_1, main fabric forming event during peak metamorphism. A dominantly flattening fabric. *This study:* the main regional foliation formed during peak metamorphism showing evidence for modification during later extensional deformation.
Folding and lineation development	Tight to isoclinal folds, generally with axial planes parallel to the main foliation. Mainly E-W trending linear fabric.	*Dixon (1969)* identified folds, cleavage development in folds and linear fabric. *Ridley (1982)* folding intrinsically associated with the formation of the dominant foliation, forming during horizontal thrust sense shear. He identified an intersection and a mineral lineation, and interpreted these as forming at the same time as the dominant foliation and folding, during thrusting. He attributed the obliquity of the two lineations to wrench shear, within the thrust system. Ridley also identified boudinage of aligned glaucophane crystals, he interpreted the boudinage as forming as a result of a stretching component within the thrust system. *Barr (1989)* identified folding and a linear fabric. *Bloor (1998)* S_1 reworked by thrusting and folding to form an S_2 axial planar fabric to folds. *This study:* folds and linear fabric formed at high pressure, modification of folds and linear fabric during down-pressure extensional deformation.
Axial planar cleavage	Secondary foliation associated with folding.	*Dixon (1969)* identified axial planar cleavage *Ridley (1982)* recognised the development of an axial planar cleavage and interpreted it as being part of the peak metamorphic horizontal thrust sense shearing episode and the formation of the dominant foliation. *Bloor (1998)* Reworking of S_1 a dominantly flattening fabric by shearing thrusting and folding to generate a secondary S_2 fabric, axial planar to folds. *This study:* recognition of axial planar cleavage in greyschist lithologies.

Boudinage	Extensional boudinage of regional foliation.	*Dixon (1969)* identified boudinage as a high pressure event extending the main foliation. *Ridley (1982)* boudinage of glaucophane crystals interpreted as a stretching component within the peak metamorphic thrusting event. Boudinage of lithologies at Kini and Delfini interpreted as attenuation of fold limbs within the thrust system. *Bloor (1998)* boudinage of the S1 foliation during its formation by flattening. *This study:* boudinage identified across the island as accommodating dominantly coaxial extensional deformation during decompression from peak metamorphic assemblages to greenschist facies.
Extensional crenulation	Crenulation of the regional foliation.	*Bloor (1998)* formation of a third fabric S_3 by extension of the main foliation S_1. *This study:* extensional crenulation cleavage, associated with boudinage and down-pressure recrystallisation.
Brittle faulting	Brittle normal faults	Dixon (1969) identification of large scale brittle faults. Ridley (1982) discussed geometry of brittle faults and associated them with NE-SW to E-W directed extension in the Aegean area. This study: identified normal faults juxtaposing rocks of different metamorphic facies, but also identified ductile deformation linking into brittle faults. I interpreted the faulting as being the final part of exhumation of the terrain.

metamorphism. In this study I have shown that the orientation of these earlier fabrics have in certain localities been modified during the extensional deformation. In the northern areas these fabrics include an early foliation which is folded. Fold hinge lines are thought to have been oriented parallel to the extension axis and fold axial planes flattened to lie parallel to the regional foliation during NE-SW to E-W directed extension. Reorientation of linear fabrics are also documented in a deformation gradient north of the serpentinite belt. As the serpentinite belt is approached fold axes and mineral lineations bend into alignment with the extension direction. This apparent rotation or recrystallisation of early lineations could account for the variations in lineations documented by Ridley (1982a and b) north of the serpentinite belt and the local obliquity of glaucophane lineations.

The presence of deformation gradients suggests that the strain was not accommodated homogeneously through the pile. Zones of high strain were identified, at the contact of the northern serpentinite, defined by high pressure fabrics and local asymmetry, and also at the contact with the serpentinite at Finika-Posidhonia defined by greenschist fabrics. It is inferred from these observation that the serpentinite within the metamorphic succession localised strain during the extension. The constant orientation in the extension axis, E-W to NE-SW, implies that the present succession was continuous during the extensional deformation.

The recognition of ductile extensional fabrics, within the blueschist facies stability field, during the transition to greenschist and locally within the greenschist facies stability field allows the structures to be interpreted in terms of extensional deformation during down-pressure recrystallisation and exhumation.

The average elongation direction defined by mineral lineations and pebble x-axes orientations (figure 3.52) is E-W, consistent with stretching directions documented on other Aegean islands in the western Cyclades (figure 3.1). However, coaxial ductile deformation is not reported in these other studies. This may be an artefact of the lack of studies in this part of the Aegean as compared to the southern Cycladean islands of Naxos and Paros (e.g. Gautier et al., 1993; Buick, 1991; Lister et al., 1984). Normal fault patterns of present day extensional structures (figure 3.1)

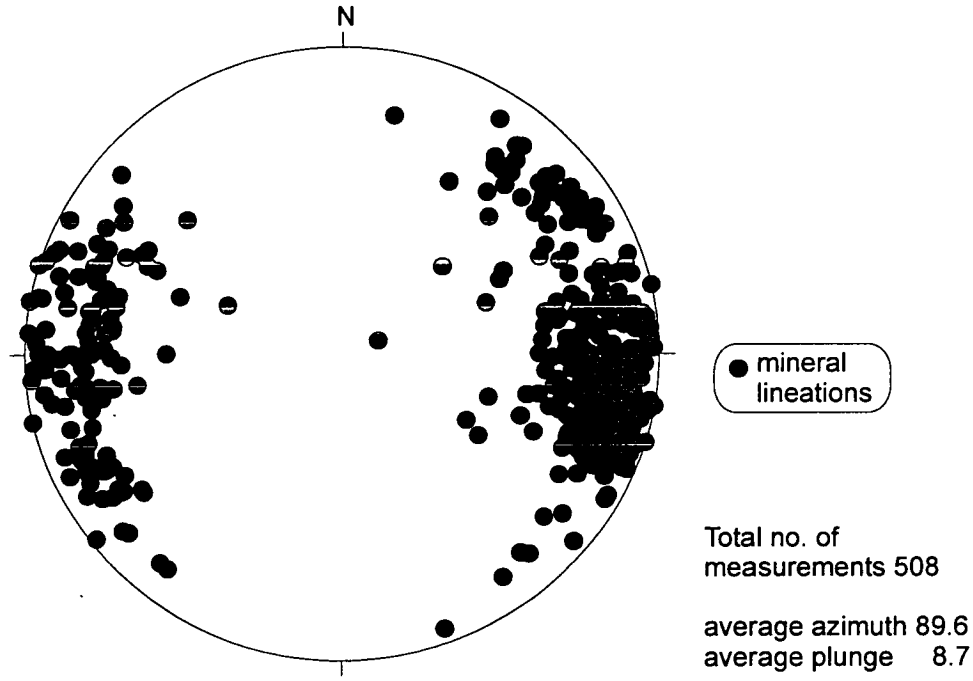

Figure 3.52
Stereonet of mineral lineation data from across Syros

show simple symmetrical faulting and horst block formation in the western Cyclades as compared to the southern islands where asymmetrical deformation is documented. Coaxial ductile deformation may have been occurring in the western Cyclades whilst deformation in the southern Cyclades was predominantly non-coaxial.

Evidence for ductile thinning within the greenschist facies is limited to localised areas south of the serpentinite belt, although minor extension is accommodated by greenschist veining across the whole island. Evidence for incremental strain is preserved, by a variety of mineral assemblages, documenting coaxial extension within the epidote-blueschist field, during the transition to greenschist and locally within the greenschist. The structures and mineral assemblages indicate that pure shear was dominant during decompression, accommodated by continuous coaxial extension.

Thinning of the unit by the coaxial layer parallel extension documented could account for the decompression of 5-6 kbars within the ductile regime (figure 3.2), through the blueschist field, assuming a homogeneous stretching of 2.3 to 3. Although strain is not homogeneous across the terrain, locally layers have been demonstrated to accommodate an elongation of 4.9. This 49% thinning of layers suggests that the decompression estimated from mineral assemblages could easily be accommodated by the extensional ductile deformation documented. A high percentage of the decompression occurred within the blueschist facies stability field, so recognition of early orogenic fabrics from those associated with exhumation is crucial (figure 3.2). Recognition of high pressure decompressional fabrics has been achieved by kinematically linking greenschist ductile extension with higher grade fabrics, structurally charting the decompression path for Syros.

3.5 Summary

I have documented a range of ductile and brittle structures inferred to be related to extensional tectonics. In summary the study has shown evidence for:

- layer parallel horizontal extension,
- extension along an E-W to NE-SW oriented axis,
- extension within the high pressure blueschist facies stability field,
- extension within the low pressure greenschist facies stability field,
- extension accommodated by brittle faulting linking into zones of greenschist ductile deformation.

The observations have been used to infer a history of syn-exhumation extension, accommodated by pure shear.

Chapter 4 Fluid infiltration-physical and chemical evidence for fluid infiltration of schist and metabasite units

4.1 Introduction

This chapter is primarily concerned with evidence for fluid infiltration of schist and metabasite units on Syros. Previous fluid infiltration work on Syros, has included studies of the chemical and isotopic heterogeneity of units (Barr, 1989 and Bloor, 1998). Barr (1989), as summarised in chapter 2, estimated the composition of fluid present during blueschist facies metamorphism. She also looked at fluid infiltration during the blueschist-greenschist transition and inferred that the transition required the influx of both heat and fluid. The work of Bloor (1998) was concerned with the formation of quartz-lawsonite veins during high pressure metamorphism of the Syros rock sequence. His studies related channelled fluid infiltration to lawsonite precipitation and linked vein formation by deformation fabrics to a relative timing in the structural history of the terrain. This chapter builds on the work of these two earlier studies concentrating on the relationship between fluid infiltration, deformation and retrograde greenschist recrystallisation.

Evidence for fluid infiltration can be divided into three categories; direct evidence, physical evidence and chemical evidence (Knipe and McCaig, 1994). This chapter documents physical and chemical evidence for fluid infiltration of the schists and metabasite on Syros. Physical evidence of fluid infiltration is in the form of veins; chemical evidence is derived from a study of vein chemistry and isotope compositions, the bulk chemistry of vein wall rocks and a study of fluid-driven reactions. I have used similar principles to those adopted by Bloor (1998) to link fluid infiltration during decompression, to deformation and recrystallisation. The chapter is based on work at localities introduced in the previous chapter: Megas Yialos, Nites, Finika, Kini, Delfini, North Ermoupolis, Oros Syringas, the Serpentinite Belt and Diapori; the locations are annotated on figure 4.1.

Field observations have been used to infer a control on fluid pathways through the terrain, linking deformation during decompression to fluid infiltration. The field observations have been combined with petrological studies of transitional blueschist-greenschist metamorphic assemblages, associated with an influx of fluid, so documenting a link between the three processes of deformation, fluid infiltration and

Figure 4.1
Geological map of Syros, after Ridley (1982). Key localities annotated

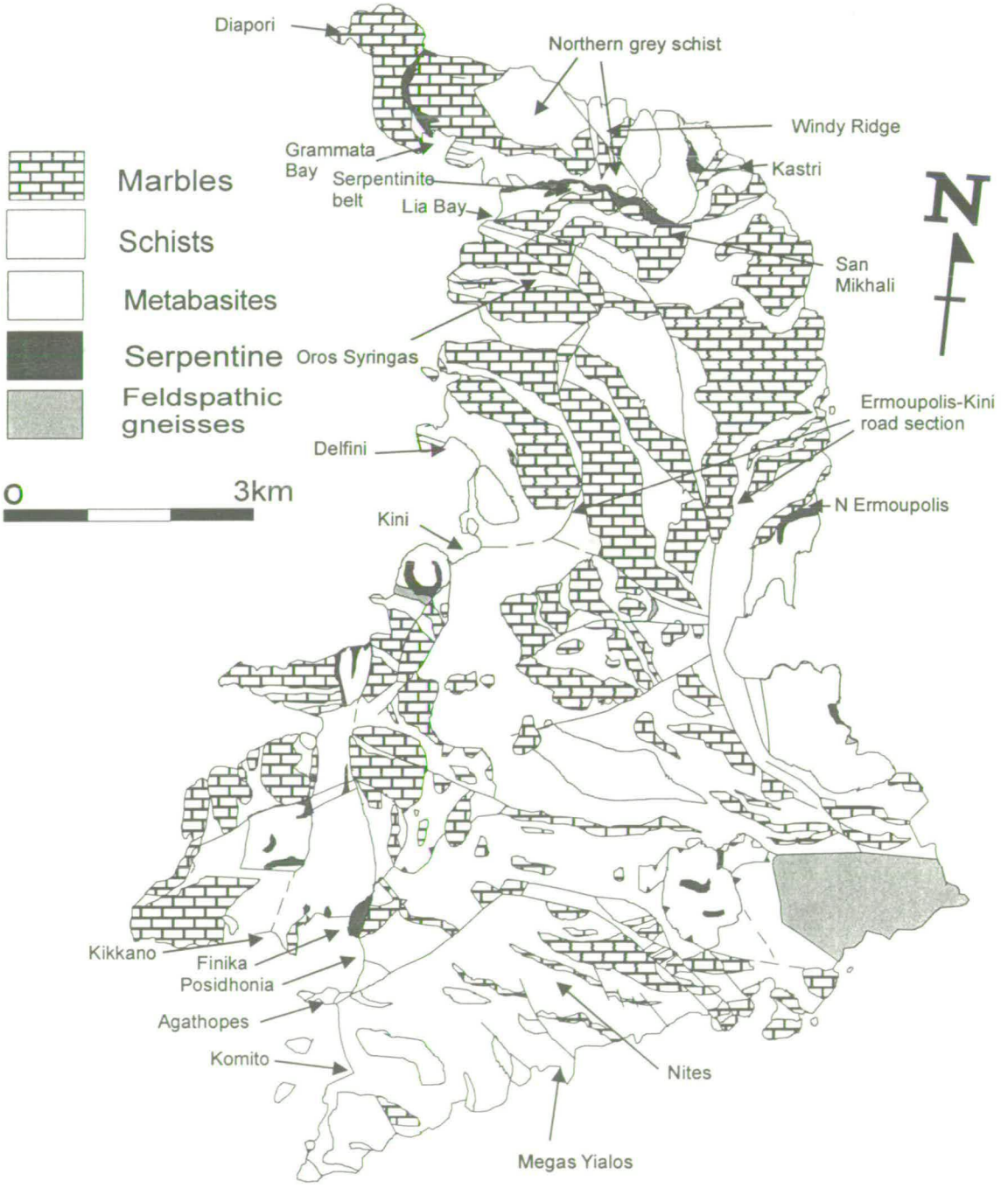

recrystallisation. The association of deformation, fluid infiltration and recrystallisation has been used to chart a down-pressure fluid infiltration history by relating evidence for fluid infiltration to the structural and metamorphic evolution of the terrain. The localities chosen are the same as those described in the structural study so that the deformation fabrics already documented can now be related to fluid flow and recrystallisation during decompression. The main aims of the chapter are outlined below and are followed by a short review of previous fluid infiltration studies and associated deformation and metamorphic recrystallisation.

4.2 Aims

The chapter aims to describe the fluid infiltration history of Syros, concentrating on the controls on fluid infiltration and associated down-pressure recrystallisation of metamorphic assemblages. The observations have been used to address the following questions.

- Is there evidence for fluid infiltration?
- Do the observations suggest channelled or pervasive fluid infiltration or both?
- What are the controlling factors on the type and style of fluid infiltration?
- How has fluid infiltration affected recrystallisation of mineral assemblages?

4.3 Controls on fluid infiltration, deformation and recrystallisation

The pathways along which fluids infiltrating metamorphic terrains are channelled can affect the chemical and mineralogical evolution of a terrain (e.g. Ague, 1997 and Bloor 1998) and the partitioning of deformation within it (e.g. Rutter and

Brodie, 1995). The degree to which fluid infiltration is channelled is therefore critical to the overall evolution of the terrain. Fluid pathways are controlled by variations in permeability, which are determined by lithological variations and deformation. The role of lithological variations in controlling fluid infiltration is addressed in detail by a stable isotope study, chapter 5. However, within a single lithology, such as a schist unit, fluid infiltration will be controlled by subtle differences in permeability influenced by minor variations in composition, anisotropy and deformation.

Evidence for deformation-controlled fluid infiltration is often present in the form of veins, directly related to fracture networks that have opened to accommodate extensional strain. However, observations of deformation mechanisms occurring at a micro-structural scale, particularly in a heterogeneous lithology, are difficult to identify, despite the fact that microstructures are fundamental to the understanding of deformation evolution and related fluid flow. These microstructural deformation mechanisms will control micro- macro- and meso-scale fluid pathways. Knipe and McCaig (1994) describe two ways by which deformation can influence fluid infiltration; 1) strain-related changes (increases and decreases) in the host rock porosity, creating changes in pore pressure gradients and the pattern of fluid pressure gradients; 2) permeability enhancement or restriction by the deformation (e.g. enhanced by the opening of fractures or grain boundary voids & restricted by pressure solution compaction and cementation). They note that the influences do not act independently of each other and often have feedback effects, one influencing the other.

Differing deformation mechanisms are dominant at different levels in the crust and in varying physical and chemical conditions. Close to the surface where the crust is cool fracture, cataclastic flow and particulate flows are important deformation mechanisms (Groshong, 1988). Diffusive mass transfer can occur at all crustal levels and is generally associated with a loss of porosity and permeability (Knipe & McCaig, 1994). In the middle to lower crust dislocation creep, grain boundary migration and dynamic recrystallisation are dominant and can cause transient increases in rock permeability (Knipe & McCaig, 1994). It is likely that deformation at all levels in the crust will transiently increase rock permeability in localised zones associated with deformation partitioning. The partitioning or pervasiveness of deformation will

therefore play a part in controlling fluid pathways through the rock sequence. In general brittle deformation will result in more channelled fluid infiltration than ductile deformation. In fact, dynamic recrystallisation of minerals as a result of ductile deformation will act to homogenise the chemical heterogenenities that can result from fluid infiltration (McCaig and Knipe, 1990).

The deformation controls on permeability creation, enhancement and restriction, described above, will play a role in controlling fluid pathways in metamorphic terrains. Therefore, the partitioning of deformation within a terrain will in part control the pervasiveness of fluid infiltration. The extent to which fluid infiltration of a terrain is channelled will regulate the chemical and, potentially, the mineralogical evolution of the rock. The scale on which fluid is channelled is therefore critical to the evolution of the terrain. Hence it is important to define the scale of the study when describing whether fluid infiltration was channelled or pervasive (e.g. Oliver, 1996). For a large scale study the definition of pervasive fluid infiltration may not be the same as that in a microscale study. Bulk sampling may give homogeneous results indicative of pervasive fluid infiltration, whereas grain scale sampling may give heterogeneous results documenting channelled fluid infiltration. Pervasive fluid infiltration in this study is defined as homogeneous grain edge flow. The scale of sampling will be detailed for individual studies to give an indication of the extent of pervasive versus channelled fluid infiltration.

The pervasiveness of fluid infiltration on a grain-scale will control the extent of recrystallisation in reactive lithologies during the blueschist-greenschist transition. Preservation of blueschist facies rocks is rare due to their limited HP-LT stability field. They are thought to form in a subduction zones (Peacock, 1990), where cold subducted slab is quickly transported to depth, so taking subducted rocks to high pressures before thermal re-equilibration can heat them to the temperatures normally associated with that depth in the Earth. During prograde metamorphism, most reactions to higher grade assemblages are devolatilisation reactions involving the release of bonded volatiles from the mineral structure producing an increasingly anhydrous mineral assemblage. On Syros for the same reactions to be reversed during retrogressive metamorphism, the rock must be rehydrated by an infiltrating fluid. Recently the effects of fluid infiltration

on the preservation of HP-LT blueschist assemblages has been much debated (e.g. Barrientos and Selverstone, 1993), and it is clear that in many localities fluid infiltration plays a major role in controlling retrogression to greenschist facies assemblages.

4.4 Veins

The presence of veins on Syros provides physical evidence for channelled fluid infiltration. Veins and vein mineralogies have previously been documented for Syros by Ridley (1982a), Barr (1989) and Bloor (1998). Ridley (1982a) noted veins of matrix minerals in metabasic units at Kini. Barr (1989) concentrated on greenschist facies veins in schist units. She described carbonate-bearing veins which in some instances had associated greenschist haloes. The veins also contained albite, chlorite and quartz, as well as the carbonate, and Barr (1989) described the growth of albite crystals inwards from the wall rock. Barr (1989) also carried out an oxygen isotope study on minerals from these greenschist facies veins. She documented isotopic $\delta^{18}O$ reversals between calcite and quartz in the veins and differences in $\delta^{18}O$ composition between minerals in the vein and the host rock. Barr (1989) attributed the reversal in $\delta^{18}O$ composition between minerals in veins as the result of several infiltration events. The lack of isotopic homogeneity between minerals in the vein and the host rock was taken to reflect minimal interaction between fluid channelled in the vein and wall rock (Barr, 1989).

Bloor (1998) worked extensively on quartz veins associated with lawsonite porphyroblast formation in grey schist units in the north of Syros. He looked at isotopic, major and trace element metasomatic alteration of vein wall rock, to try to determine the metasomatic affect of fluid infiltration associated with veining in the grey schist units. He invoked Ca metasomatism in quartz-vein wall-rock as an explanation of the observed spatial distribution of lawsonite growth in selvages around veins and he measured the increase in Ca towards the vein. He also documented the structural setting of the veins and determined that they were emplaced during 'peak'

metamorphism at the point when folds were beginning to develop in the S1 schistosity (Bloor, 1998).

Vein observations

In this study observations of vein mineralogy, structural setting, cross-cutting relationships, host rock lithology and metamorphic grade have been documented at localities across the island. The observations were combined with those of the afore mentioned authors, to characterise the mineralogical variation of veins and their associated structural settings on Syros. The observations are presented, grouped by geographical location, in the tables 4.1-4.10.

For each vein or segregation the mineralogy of the vein and host rock has been noted, together with the structural setting of the vein, including fabrics within the vein (where appropriate) and the deformation fabrics in the surrounding rock. The veins have been placed into one of four categories, depending on their mineralogy and relative timing of filling, determined from deformation fabrics associated with emplacement. The four categories are: 1) lawsonite-blueschist veins associated with peak metamorphism and precipitation of lawsonite, as described by Bloor (1998); these veins document pre- and post fill folding; 2) blueschist veins associated with high pressure fabrics and mineral assemblages, not associated with folding; 3) greenschist veins containing both albite and chlorite and 4) unclassified (?) veins with mineral assemblages that are not indicative of metamorphic grade. Where cross-cutting structures and mineralogy allow, the veins at a single locality are placed in a relative order of emplacement. Thus, a picture has been built of fluid infiltration by veining during decompression for Syros.

Key observations from the localities are described below. Localities from southern Syros are presented first. They mainly document veining associated with greenschist facies metamorphism.

Southern Localities

Megas Yialos

The veins and segregations at Megas Yialos contain minerals that are indicative of formation during greenschist facies metamorphism. The host schist in some areas contains glaucophane crystals, but is mainly retrogressed to chlorite- and albite-bearing assemblages. The presence of glaucophane crystals suggests that fluid infiltration associated with veining did not result in pervasive retrogression of the schist.

Early veins of quartz are folded; their axial planes are parallel to the regional foliation and they have attenuated fold limbs. These features maybe explained by net layer-parallel extension post vein precipitation. These quartz veins are cross-cut by quartz-, calcite-, chlorite-veins, which are in turn cut by quartz-, albite-, oxide-veins. These later veins are not deformed or folded and they cross-cut the layering, suggesting emplacement after the folding and extensive layer-parallel extension.

In areas of pervasive retrogression, extensional deformation is associated with emplacement of greenschist facies veins. Albite- and chlorite-bearing veins show extensional vein fabrics with growth of mineral fibres into the centre of the vein. Albite- and chlorite-segregations are wrapped by a foliation defined by greenschist mineral assemblages (figure 4.3). In chapter 3, the foliations wrapping greenschist segregations were documented as also forming shear zones, which bent into brittle faults.

Large quartz segregations at the end of the Megas Yialos peninsula are oriented parallel to the regional foliation. The quartz segregations are wrapped by the foliation, as though forming discrete boudins (figure 4.2). The quartz appears to have precipitated prior to horizontal layer parallel extension of the quartz-calcite schist.

Summary of Megas Yialos

Observations of veins at this locality document an early set of quartz veins which are both boudinaged and folded. The deformation associated with the boudinage and folding is consistent with net layer-parallel extension. Later veins cross-cut the early quartz veins. In areas where the schist is fully retrogressed to a greenschist

Table 4.4a Vein observations from Megas Yialos

Geographical location	Type of deposit	Mineralogy	Host rock	Structural setting	Metamorphic grade and relative timings of emplacement denoted by numbers	Observation
Megas Yialos	v	qz, ab, chl	epd, chl, qz, ank, cc		greenschist	CEB
Megas Yialos	v	epd, qz, chl	"	layer parallel discontinuous	?	CEB
Megas Yialos	v	ank, chl, qz	"		?	CEB
Megas Yialos	v	qz	"	layer parallel	?	CEB
Megas Yialos	v	ab, chl, qz	epd, chl, qz, ank, cc	extensional	greenschist	CEB
Megas Yialos	v	ank, qz, chl + ab pressure shadow	"		greenschist	CEB
Megas Yialos	s	qz, chl	"	approximately layer parallel	?	CEB
Megas Yialos	v	qz, ab, chl	epd, chl, qz, ank, cc +/- gl	folding around vein	greenschist	CEB
Megas Yialos	v	ab	qz, chl, cc	shear zone	? greenschist	CEB
Megas Yialos	s	qz,chl, ab	"	sheared and boudinaged	greenschist	CEB
Megas Yialos	v	qz, ab, oxide	qz, gl, mica, chl		? 3	CEB
Megas Yialos	v	qz, cc, chl	"	cross-cuts qz, ab, oxide vein	? 2	CEB
Megas Yialos	v	qz +/- chl	"	veins are folded and cut by other veins qz +/- chl & qz, cc, chl	? 1	CEB
Megas Yialos	s	ab, chl + ab pressure shadow	ab, chl, qz, cc		greenschist	CEB
Megas Yialos[1]*	v	qz, cc, chl, oxide	qz cc schist	large pegmatitic veins foliation wrapped	?	CEB
Megas Yialos	v	qz, cc, chl, ank, ab	qz cc schist		greenschist	CEB
Megas Yialos[2]*	v	qz,chl, ab	ab, chl schist	foliation wrapped segregation	greenschist	CEB
Megas Yialos	v	qz, epd, chl	ab, chl schist	layer parallel segregation	?	CEB

v vein, s segregation, mineral abbreviations (see front of thesis), [1,2,3] * refer to associated field sketch or photo, CEB (this study), PB (Bloor, 1998), HB (Barr, 1989), JR (Ridley, 1982)

assemblage, veins bearing albite and chlorite often have extensional fabrics. Albite- and chlorite-bearing segregations in retrogressed schist are wrapped by a greenschist foliation, which bends into shear zones and brittle faults. In areas of pervasive greenschist retrogression there is evidence for locally more pervasive deformation within the greenschist facies stability field, as greenschist mineral fabrics wrap segregations containing albite and chlorite.

Nites

The Nites hillside was described in chapter 3 as showing boudinage on a range of scales from tens of metres to metres. Precipitation of minerals associated with this boudinage has occurred in boudin necks. The precipitated minerals are mainly of greenschist grade, although epidote and quartz veins are also seen and are described below. Figure 4.4, is a photograph and field sketch of minerals which have precipitated in the neck of a boudinaged chlorite-, epidote-, quartz- and calcite-layer. The minerals have a vuggy infill and their geometry is consistent with formation during horizontal layer-parallel extension of an originally foliated body, as described by Platt and Visser (1980).

Extensional fabrics are also present within greenschist veins on the hillside (figure 4.6). The veins are subvertical and cross-cut layering accommodating E-W oriented extension. Boudinaged layers of metabasic epidote- and chlorite-rock, preserve evidence of multiple fracturing and mineralisation events, within a single boudin neck. Epidote fibres precipitated in the boudin neck are cross-cut by quartz and quartz-, albite-, chlorite- and oxide-veins (figure 4.8).

There is some evidence for earlier veining on the Nites hillside. A greenschist vein is seen to cross-cut a layer-parallel calcite-, quartz-, epidote-vein (figure 4.7). A horizontal quartz-calcite vein shows strong folding of the fabric around it (figure 4.5). The folding of an early foliation in this area is localised. Its exact relationship to the vein is unknown.

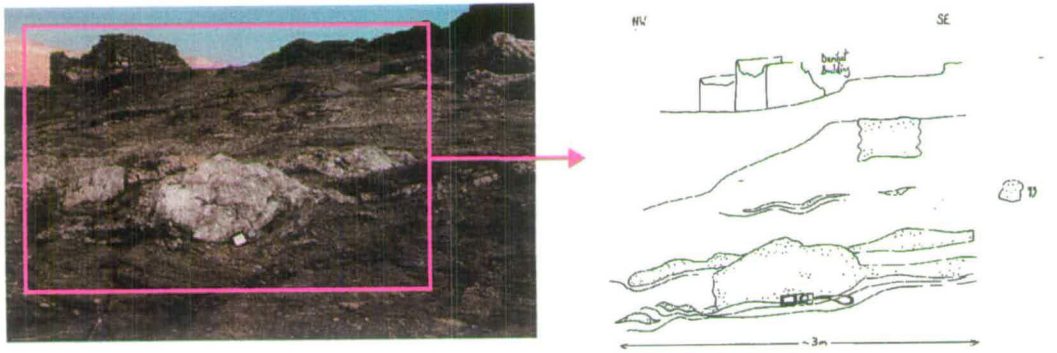

Figure 4.2 Field sketch and photograph of foliation wrapped quartz segregations, Megas Yialos

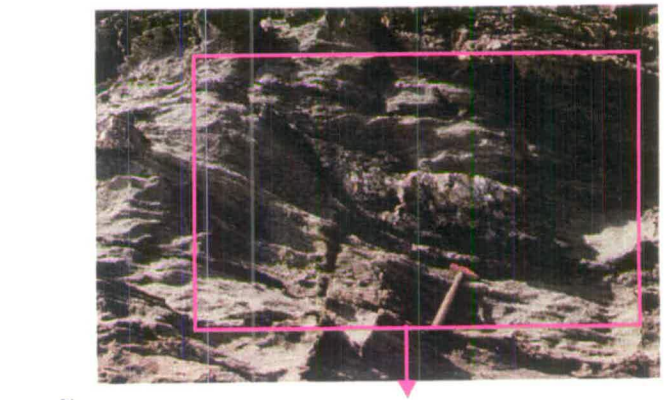

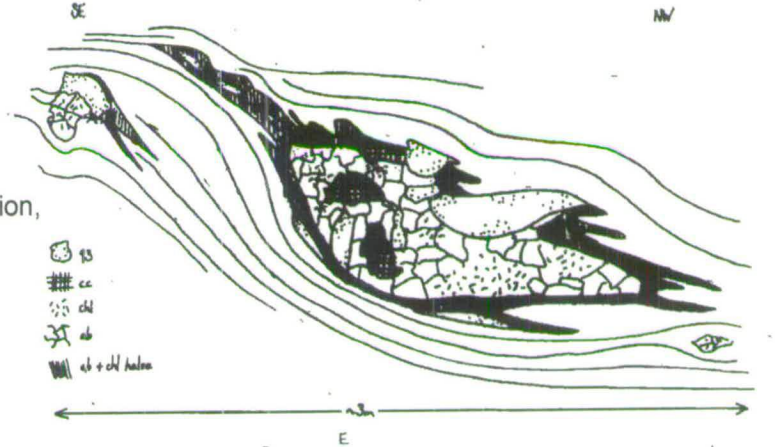

Figure 4.3 Field sketch and photograph of foliation wrapped greenschist segregation, Megas Yialos

Figure 4.4 Greenschist veins in boudin necks, Nites

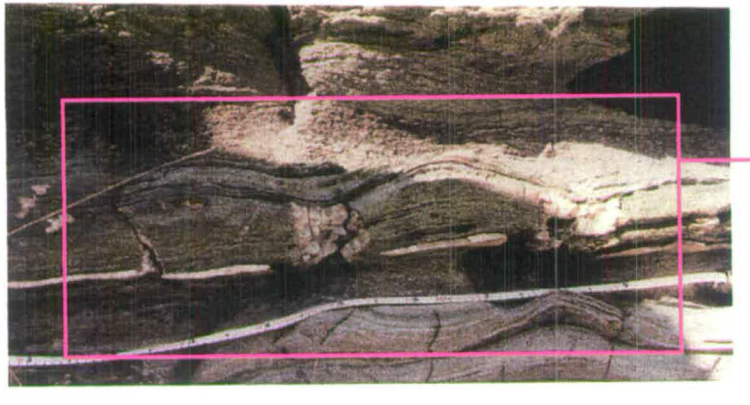

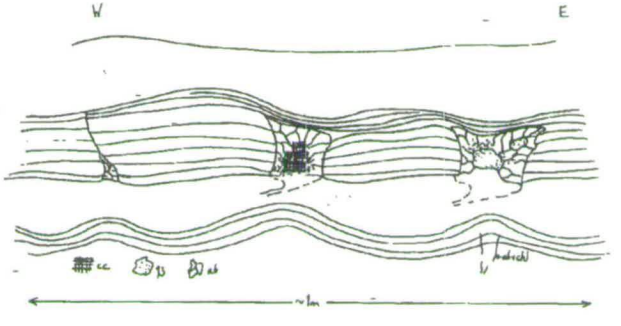

Table 4.4b Vein observations from Nites

Geographical location	Type of deposit	Mineralogy	Host rock	Structural setting	Metamorphic grade and relative timings of emplacement denoted by numbers	Observation
Nites[3]*	v	ab, cc, qz, chl	chl, epd, qz, cc	veins in boudin necks	greenschist	CEB
Nites[6]*	v	ab, cc, qz, chl, epd, oxide	ab, chl, epd, qz, cc	mutually cross cutting veins, extensional fabrics	greenschist	CEB
Nites[5]*	v	cc, ab, chl + chl, ab halo	chl, ab, epd	extensional vein	greenschist	CEB
Nites	v	qz	cc marble		?	CEB
Nites	v	chl, ab, cc	ab, chl schist	feeder veins to vuggy ab, chl, cc on foliation surfaces	greenschist	CEB
Nites	v	chl, ab	chl, ab, epd	extensional fibers in vein	greenschist	CEB
Nites[4]*	v	qz, cc	chl, ab schist	folded fabric around vein	?	CEB
Nites	v	epd, qz, chl	epd, chl , qz, cc	vein in neck of boudinaged epidote layer	?	CEB
Nites	v	ab +chl halo	gl, epd metabasite		greenschist	CEB
Nites[7]*	v	qz, oxide, chl, epd, cc, ab	epd, chl metabsaite	vein in boudin neck, with multiple mineralisation events	greenschist	CEB
Nites	v	epd, qz, oxide	ab, chl schist	Layer parallel segregation	?	CEB
Nites	v	chl, ab + epd	epd, gl	boudin infill with extensional epidote at vein edges and a vein core of chl + ab	greenschist	CEB

v vein, s segregation, mineral abbreviations (see front of thesis), [1,2,3] * refer to associated field sketch or photo, CEB (this study), PB (Bloor, 1998), HB (Barr, 1989), JR (Ridley, 1982)

Summary of the Nites hillside

Veining associated with retrogression on the Nites hillside is clearly controlled by layer-parallel extension within the greenschist facies stability field; minerals have precipitated in necks of boudins accommodating E-W oriented extension. Further extension is accommodated by albite- and chlorite-bearing veins which cross-cut the foliation and contain mineral fibres perpendicular to the vein walls. Recorded evidence for earlier veining is minimal; two quartz-bearing layer-parallel veins were noted. Their association with fabric formation is unclear.

Localities on the south west coast of Syros

Vein observations from localities on the south-west coast of Syros: Kikkano, Finika, Posidhonia, Agathopes and Komito are summarised in table 4.3. These veins and their structural associations are similar to those already documented at Megas Yialos and Nites. Two examples of veins from this area are shown in figures 4.9 and 4.10. The albite-chlorite vein in figure 4.9 at Agathopes, has precipitated in an extensional shear zone. The pegmatitic vein in figure 4.10 has an epidote rim, with a calcite-, chlorite- and albite-core, and lies oblique to layering.

Other veins in the area generally contain greenschist mineral assemblages, and many of the veins have extensional fibrous fabrics. At Kikkano greenschist veins are seen in glaucophane-bearing blueschist and show a distinct alteration halo of chlorite. Albite haloes are also observed around veins cutting retrogressed greenschist.

Summary of Southern Localities, including Megas Yialos and Nites

The southern localities provide evidence of veining associated with the greenschist extensional deformation documented in chapter 3. Veins bearing chlorite and albite precipitate in boudin necks and these locally cut earlier quartz- and epidote-veins in the boudin necks. Greenschist veins with extensional fibrous, mineral fabrics are seen where boudinage is not as dominant. Albite- and chlorite-bearing segregations are also observed wrapped by greenschist foliations and shear zones.

Evidence for pre-greenschist quartz veining was documented at Megas Yialos,

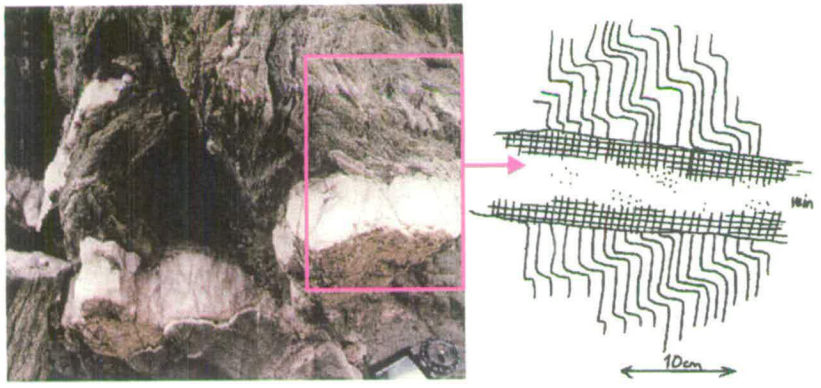

Figure 4.5 Quartz-calcite vein, Nites

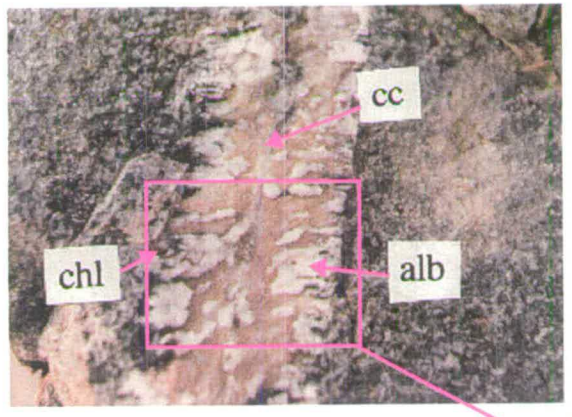

Figure 4.6 Extensional greenschist vein, Nites

Figure 4.7 Mutually cross-cutting veins, Nites

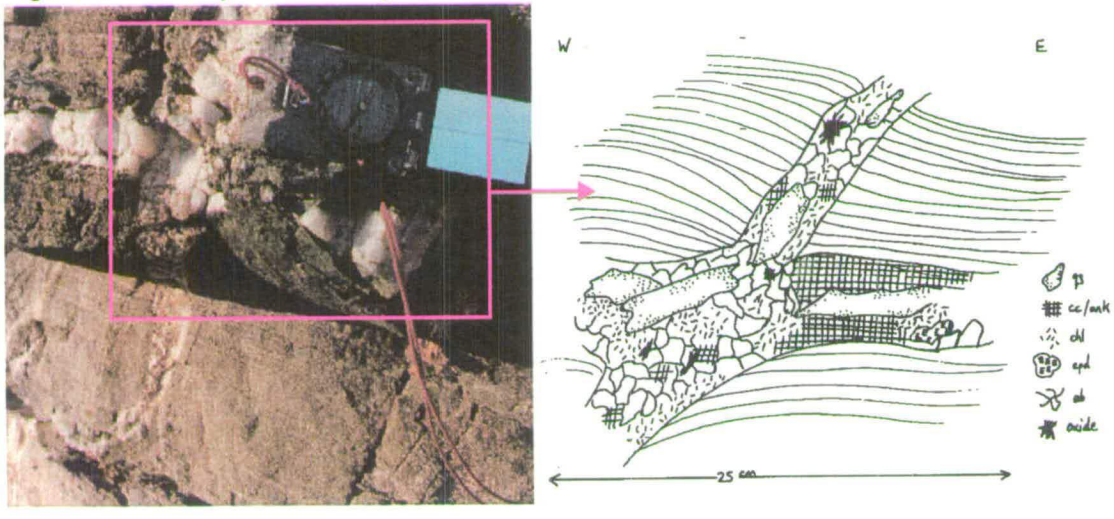

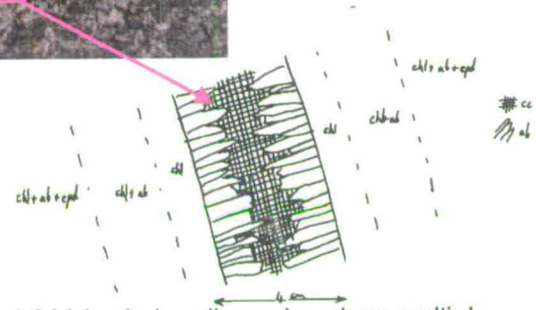

Figure 4.8 Veins in boudin necks, show multiple fracture and mineralisation events, Nites

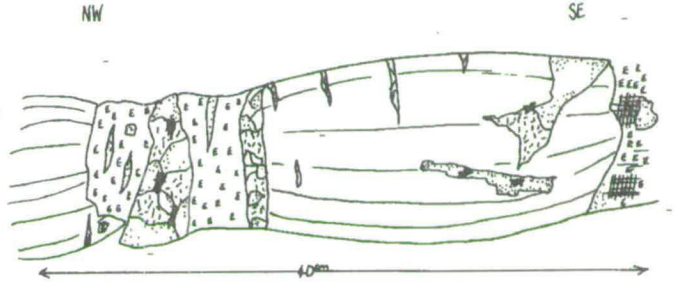

Table 4.4c Vein observations from the south west coast, Syros

Geographical location	Type of deposit	Mineralogy	Host rock	Structural setting	Metamorphic grade and relative timings of emplacement denoted by numbers	Observation
Kikkano	v	ab, chl +/- chl halo	blueschist	fingering of halo around vein, en-echelon micro veins	greenschist	CEB
Finika	v	cc, ab, oxide, chl	chl, ab schist	segregations	greenschist	CEB
Finika	v	cc, ab +/- oxide	chl, ab schist		?	CEB
Finika	v	ab, chl	chl, ab schist		greenschist	CEB
Finika	v	zoisite, cc, mica +/-chl	chl, ab schist	foliation wrapped boudinaged segregations	?	CEB
Finika	v	ab, chl, cc, qz	chl, ab, mica, zoisite schist with lawsonite pseudomorphs	pegmatitic segregations cross cut the foliation in the schist	greenschist	CEB
Finika	v	qz, cc, ab, chl + oxide	chl, ab, mica, zoisite schist with lawsonite pseudomorphs	pegmatitic segregations cut by late faults	greenschist	CEB
Finika	v	chl, ab	chl, ab schist	foliation wrapped ab, chl segregations	greenschist	CEB
Finika	v	cc +/- oxide	chl, ab schist		?	CEB
Finika	v	zoisite	chl, ab schist	segregation	?	CEB
Poshidonia	v	chl, ab + ab pressure shadow	ab, chl l'tectonite (meta-gabbro, protolith?)	l' tectonite, extensional fibrous veins	greenschist	CEB
Agkothorpes	v	qz + cc	greenschist			HB
Agkothorpes	v	cc +ab, chl halo	greenschist		greenschist	HB
Agkothorpes[9]*	v	epd (rim), cc, ab, chl	greenschist-albitised	large pegamatitic vein	greenschist	CEB
Agkothorpes	v	cc, ab	ab, chl greenschist	veins	?	CEB
Agkothorpes[8]*	v	ab, chl	alb, chl, epd greenschist	veins is sheared across a shearzone	greenschist	CEB
Agkothorpes-Komito	v	ab, chl	ab, chl, epd	boudinaged pegamtitic veins	greenschist	CEB
Agkothorpes-	v	chl, ab, epd	chl, ab, epd		greenschist 1	CEB

Komito Agkothorpes-Komito	v	Fe stained	ab, chl, epd	cross-cuts greenschist veins	greenschist 2	CEB
Komito	v	cc + chl haloe	metabasite		greenschist	HB

v vein, s segregation, mineral abbreviations (see front of thesis), [1, 2, 3] * refer to associated field sketch or photo, CEB (this study), PB (Bloor, 1998), HB (Barr, 1989), JR (Ridley, 1982)

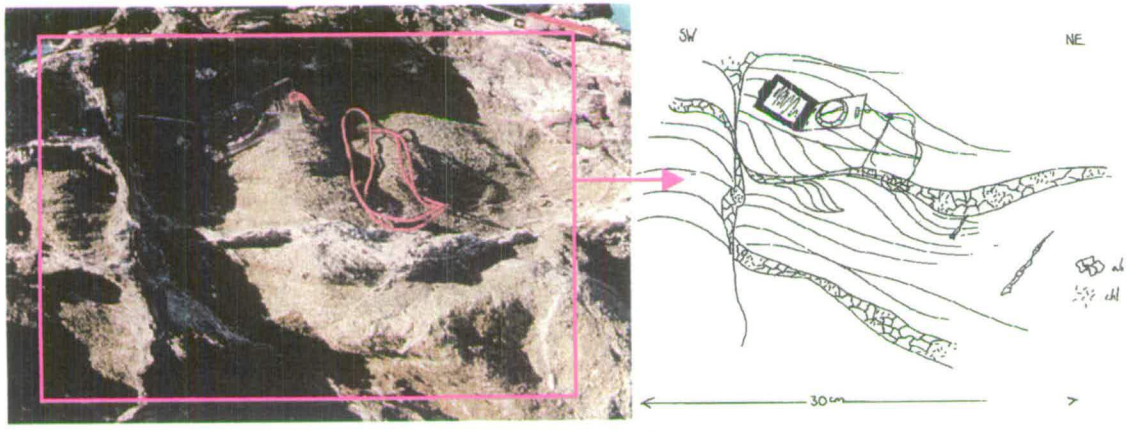

Figure 4.9 Albite-chlorite vein sheared and boudinaged, Agathopes

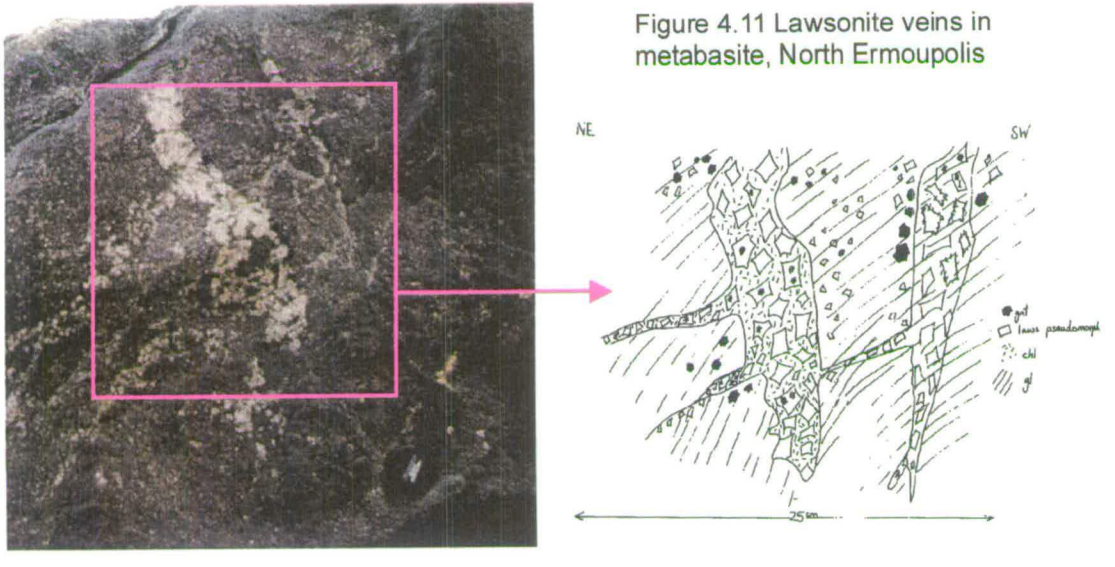

Figure 4.11 Lawsonite veins in metabasite, North Ermoupolis

Figure 4.10 Large calcite dominated pegmatite vein, Agathopes

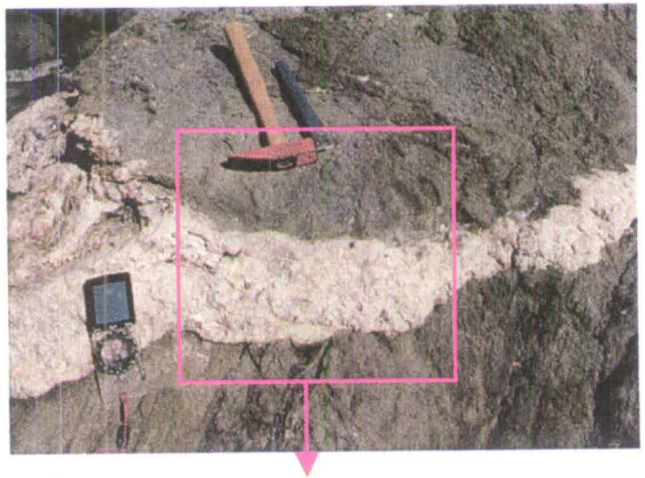

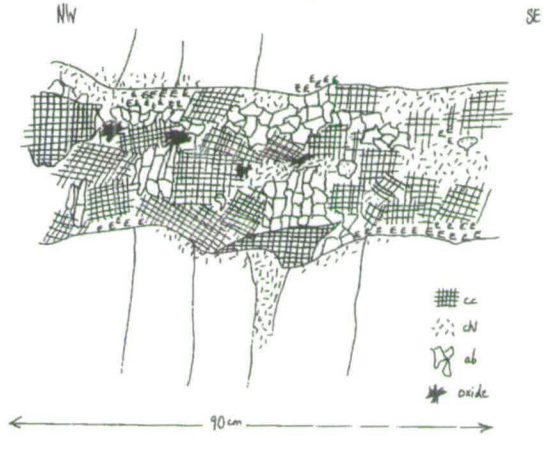

where early quartz veins had been deformed by layer-parallel extensional deformation. Apart from these localised examples, no evidence for early veining was found during the study in southern Syros, though it is fair to say that none were actively sought, as I was concerned with documenting greenschist deformation and associated fabrics and fluid infiltration in the south of the island. Evidence from the north of the island suggests that if veins largely pre-date the S2 of Bloor (1998), i.e. are early peak blueschist, and as S2 deformation is intense, it is very difficult to recognise disrupted quartz segregations as ever having been vein-like and connected.

Central-northern areas

The central areas document a wider range in vein mineral assemblage than elsewhere. This range in mineral assemblage is thought to be related to the metabasite host rock in which many of the veins have precipitated. Veins in metabasite in the central area were observed at North Ermoupolis, the Ermoupolis-Kini road section and Kini. Ridley (1982a) documented a range of vein mineralogies at Kini. Ridleys observations are tabulated, along side those from this study, in table 4.6. Veins were also observed in schist and metabasite at Delfini, and in schist at Oros Syringas.

North Ermoupolis

The full range of vein mineralogy observed in metabasite is present at North Ermoupolis. The associated metamorphic grade of the veins ranges from lawsonite-blueschist, associatd with folding, though blueschist to albite- and chlorite-bearing veins. A chronological distinction between lawsonite-blueschist and blueschist veins at this locality is however unfounded as the lawsonite veins are not folded and it is impossible to determine whether they formed prior to other blueschist veins. The lawsonite-bearing veins are anastomosing; they do not record a distinct fracture event in the host rock and they consist of a zone of lawsonite growth (figure 4.11). The lawsonites are now pseudomorphed by clinozoisite and mica. Other blueschist veins include quartz-glaucophane veins which precipitate in small shear zones. The centre of the vein is quartz and fibres of glaucophane grow into the vein from the wall rock.

Table 4.4d Vein observations from North Ermoupolis

Geographical location	Type of deposit	Mineralogy	Host rock	Structural setting	Metamorphic grade and relative timings of emplacement denoted by numbers	Observation
N Ermoupolis	v	cc	cc-marble	shear zones	?	CEB
N Ermoupolis	v	chl + ab	metabasite	extensional veins with fibers	greenschist	CEB
N Ermoupolis	v	epd + sphene	px, gl, qz. gnt, epidote etc.. meyabasite		?	CEB
N Ermoupolis[10]*	v	laws, gnt + laws/chl haloe	px, gl, qz. gnt, epidote etc.. metabasite	lawsonite associated vein	lawsonite blueschist	CEB
N Ermoupolis	v	epd	px, gl, qz. gnt, epidote etc.. metabasite		?	CEB
N Ermoupolis	v	qz, gl	px, gl, qz. gnt, epidote etc.. metabasite	segregations and veins in extensional shearzones, gl with extensional fabric	blueschist	CEB
N Ermoupolis	s	qz, gl, ab, epd, chl	px, gl, qz. gnt, epidote etc.. metabasite		?	CEB
N Ermoupolis	v	qz, gl, epd	px, gl, qz. gnt, epidote etc.. metabasite	qz and epd form extensional fibers	blueschist	CEB
N Ermoupolis	v	ab, chl, cc +/- oxide	px, gl, qz. gnt, epidote etc.. metabasite	Some veins have haloes of chlorite and/or albite, veins cross-cut foliation	greenschist	CEB
N Ermoupolis	v	cc	px, gl, qz. gnt, epidote etc.. metabasite	cc veins often associated with shearzones	?	CEB
N Ermoupolis	v	ab, gl, sphene	px, gl, qz. gnt, epidote etc.. metabasite	vein in sherazone	blueschist	CEB
N Ermoupolis	v	cc + chl, ab, qz haloe	metabasite		greenschist	HB

v vein, s segregation, mineral abbreviations (see front of thesis), [1, 2, 3] * refer to associated field sketch or photo, CEB (this study), PB (Bloor, 1998), HB (Barr, 1989), JR (Ridley, 1982)

Other glaucophane-bearing veins contain epidote, sphene and albite.

Chlorite- and albite-bearing greenschist veins with fibrous infills are also observed in the metabasic blocks. The veins often have associated metasomatic alteration haloes of chlorite and/or albite. Calcite precipitation in shear zones is also common but the timing of precipitation in relation to other veins is unknown.

North Ermoupolis Summary

The range of veins documented at North Ermoupolis attests to vein controlled fluid infiltration from peak lawsonite and blueschist metamorphism through to greenschist facies. The lawsonite veins did not form by obvious fracture of the host rock, but delineate zones of fluid infiltration and associated lawsonite precipitation. Glaucophane-bearing veins are often associated with small scale shear zones and show fibrous growth of glaucophane into the vein. Greenschist veins generally show extensional vein fabrics by growth of mineral fibres; these veins have caused retrogressive metasomatism of the surrounding host rock. Structurally the blueschist and greenschist veins appear to be associated with layer-parallel extension, but as the metabasite is a block in a melange and exposure of the ultramafic is poor, no sensible regional tectonic conclusions can be drawn from vein orientations.

Ermoupolis-Kini road section and Kini

Veins in metabasite on the Ermoupolis-Kini road section are similar in appearance to those in the metabasite blocks of North Ermoupolis. Blueschist and greenschist veins are seen, cross-cutting foliation, but with no particular structural association. In contrast, on the section of the road leading down to Kini, veins in a quartz-rich schist are spatially associated with shear zones. The vein material including quartz-, albite-, calcite- and chlorite is precipitated in shear zones (figure 4.12). Garnets in layers adjacent to the shear zones are retrogressed to chlorite.

At Kini a wide range of vein mineral assemblages are observed. Many of the veins contain high pressure mineral assemblages and crop out in loose blocks. In the metabasic blocks blueschist veins document evidence of channelled fluid infiltration. Within a single block (figure 4.13) early carbonate veins with thin glaucophane haloes

Table 4.4e Vein observations from the Ermoupolis-Kini road section

Geographical location	Type of deposit	Mineralogy	Host rock	Structural setting	Metamorphic grade and relative timings of emplacement denoted by numbers	Observation
Ermoupolis-Kini rd section	v	epd + sphene	metabasite and ultramafic melange		?	CEB
Ermoupolis-Kini rd section	v	ab, epd, chl	metabasite and ultramafic melange		greenschist	CEB
Ermoupolis-Kini rd section	v	qz, gl, epd	metabasite and ultramafic melange		epidote-blueschist	CEB
Ermoupolis-Kini rd section	v	ab, chl +chl halo	metabasite and ultramafic melange		greenschist	CEB
Ermoupolis-Kini rd section	v	cc	qz rich schist	cc vein in shearzone	?	CEB
Ermoupolis-Kini rd section[11]*	v	qz, chl, ab + broken wall rock + chl halo	qz rich schist	vein formed in shearzone, garnet-rich horizons have been altered to chl around the vein	greenschist	CEB
Ermoupolis-Kini rd section	s	qz, ab	qz rich schist	segregations in shearzone	?	CEB
Ermoupolis-Kini rd section	s	cc, qz	qz rich schist	segregations in shearzone	?	CEB

v vein, s segregation, mineral abbreviations (see front of thesis), [1,2,3] * refer to associated field sketch or photo, CEB (this study), PB (Bloor, 1998), HB (Barr, 1989), JR (Ridley, 1982)

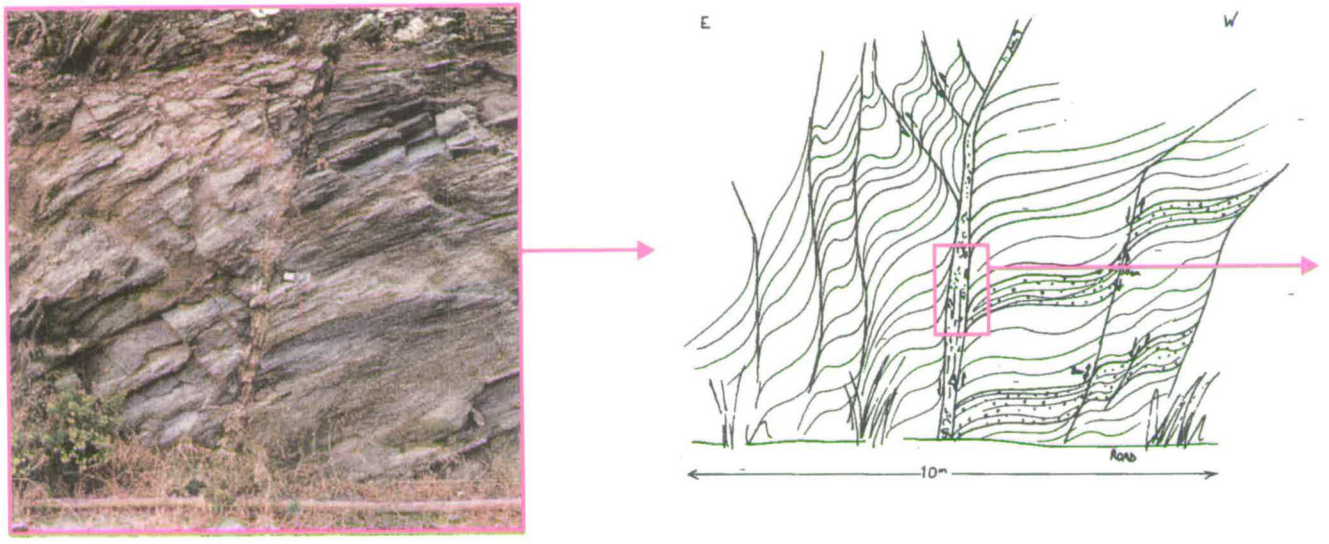

Figure 4.12 Vein in shear zone, Ermoupolis-Kini road section

Figure 4.13 Calcite macro-veins with glaucophane haloes, cross-cut by calcite, pyroxene, epidote, quartz veins in a loose block, Kini

Figure 4.14 Calcite macro-veins in shear zones, Kini

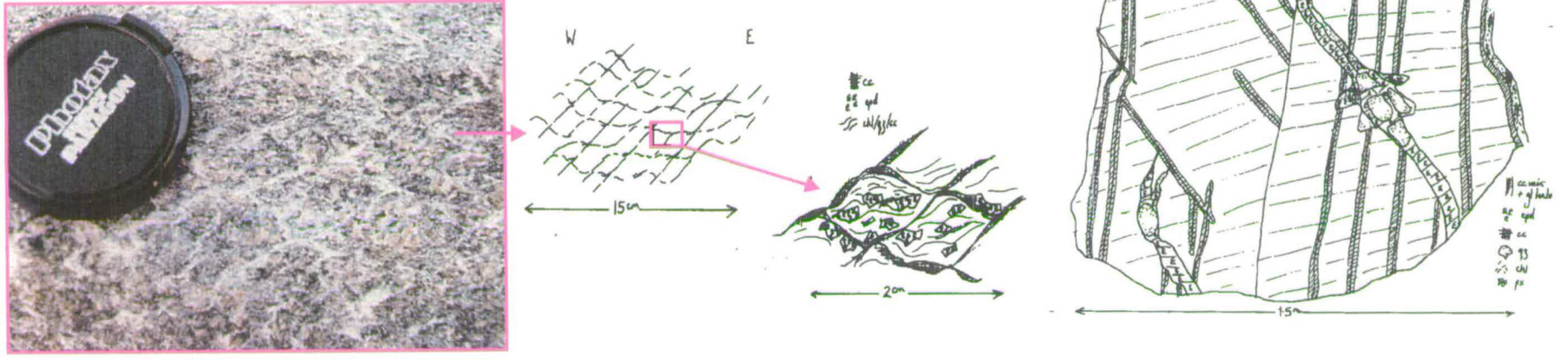

Table 4.4f Vein observations from Kini

Geographical location	Type of deposit	Mineralogy	Host rock	Structural setting	Metamorphic grade and relative timings of emplacement denoted by numbers	Observation
Kini	v	epd, gl, ank, qz	px, gl, gnt, qz metabasite	epd shows extensional fibers	blueschist	CEB
Kini[12]*	v	cc	epd, chl, qz, cc	veins in extensional shearzones	?	CEB
Kini	v	ab, chl, cc	epd, chl, gnt, mica, ab, cc, qz	mutually cross-cutting greenschist veins	greenschist 1a	CEB
Kini	v	cc	epd, chl, gnt, mica, ab, cc, qz	cross-cuts ab, chl, cc vein	greenschist or later 2a	CEB
Kini	s	qz, epd, chl, cc, oxide, ab	epd, chl, gnt, mica, ab, cc, qz	large segregation with qz core	greenschist	CEB
Kini	s/v	epd, qz, sphene, chl, cc in ab, chl vein	epd, chl, gnt, mica, ab, cc, qz	segregation surrounded by vein	greenschist	CEB
Kini	s	cc, ab, chl, oxide	epd, chl, gnt, mica, ab, cc, qz	segregation	greenschist	CEB
Kini	v	chl, ab, qz, cc	epd, chl, gnt, mica, ab, cc, qz		greenschist	CEB
Kini	v	epd, sphene, qz	epd, chl, gnt, mica, ab, cc, qz	foliation parallel	?	CEB
Kini	v	ab, chl	epd, chl, gnt, mica, ab, cc, qz	vein in shear zone	greenschist	CEB
Kini[13]*	v	cc + gl haloe	px, epd, cc, ank	micro veins	blueschist 1b	CEB
Kini[13]*	v	cc, px, epd, qz	px, epd, cc, ank	vein cross-cuts veins with gl haloes	blueschist 2b	CEB
Kini	v	cc, chl, qz,epd + gl haloe	px, epd, cc, ank		blueschist	CEB
Kini	v	qz	px, epd, gnt, gl	mutually cross cutting qz veins in small shearzones	?	CEB
Kini	v	cc, qz	metabasite		?	JR HB
Kini	v	epd, qz	metabasite		?	JR

v vein, s segregation, mineral abbreviations (see front of thesis), [1, 2, 3] * refer to associated field sketch or photo, CEB (this study), PB (Bloor, 1998), HB (Barr, 1989), JR (Ridley, 1982)

are cross-cut by a calcite-, sodic-pyroxene-, epidote-, quartz-vein. The blocks document evidence of multiple veining episodes within the blueschist facies stability field, with a wide variety of vein mineral assemblages.

Greenschist and epidote-bearing veins have precipitated in the coastal outcrop. The greenschist and epidote-bearing veins are generally perpendicular to sub-perpendicular to the foliation and often have vein mineral fibres oriented perpendicular to the vein walls. Calcite has precipitated in symmetrical shear zones, which criss-cross a chlorite-, epidote-, quartz- and calcite-lithology (figure 4.14). The calcite precipitation is related to coaxial layer-parallel extensional deformation of the unit. Elsewhere in the section thin calcite veins cross-cut albite- and chlorite-bearing veins.

Ermoupolis-Kini road section and Kini summary

A range of vein mineral assemblages in metabasic lithologies, document evidence for blueschist veining. Multiple periods of veining are identified by cross-cutting relationships and vein generations of distinct mineralogy. Later greenschist veins are generally vertical to sub-vertical, perpendicular to layering. The greenschist, albite- and chlorite-bearing, veins and epidote-bearing veins often have internal fabrics indicative of mineral growth parallel to an E-W oriented extension direction.

Delfini

The structures at Delfini were described in detail in chapter 3, because they imply a kinematic link between blueschist, greenschist and brittle extensional structures. The locality therefore, also provides an opportunity to link veining to the extensional structures documented for different metamorphic grades in the sequence. The structures at Delfini were dominated by layer-parallel extensional boudinage oriented E-W (see, chapter 3). The veins observed in the sequence are in the majority of examples spatially associated with extensional deformation precipitating in necks of boudins, or in extensional shear zones (figure 4.17).

Minerals precipitating in boudin necks in many cases show evidence for multiple fracturing events. Examples of re-fracturing include a glaucophane-quartz vein in a boudin neck which is cut by an extensional quartz-epidote vein, and early layer

Table 4.4g Vein observations from Delfini

Geographical location	Type of deposit	Mineralogy	Host rock	Structural setting	Metamorphic grade and relative timings of emplacement denoted by numbers	Observation
Delfini	v	gl, qz	gl, cc, ab, ank	boudin neck, extensional vein	blueschist 1a	CEB
Delfini	v	qz, epd	gl, cc, ab, ank	boudin neck, extensional vein cross-cuts gl, qz extensional veins	? 2a	CEB
Delfini	v	zois +/- qz	chl, mica, epd, +/- act (px in pods)	extensional	?	CEB
Delfini	v	qz, mica	"	assoc with px pod	?	CEB
Delfini	v	cc, chl, ab + ab pressure shadow	"	extensional	greenschist	CEB
Delfini	v	ank, qz, ab	qz, chl, mica, epd +/- act		?	CEB
Delfini	v	epd, qz, chl, mica, ab	epd, chl schist	layer parallel sheared vein	epd- greenschist	CEB
Delfini[15]*	s	epd, qz, ank, chl	"	layer parallel sheared	? 1b	CEB
Delfini[15]*	v	ab, chl	"	extensional vein, cross cuts epd, qz layer	greenschist 2b	CEB
Delfini	v	cc	"	layer parallel, folded	?	CEB
Delfini	v	qz	"	layer parallel, boudinaged	? 1c	CEB
Delfini	v	chl, ab +/- epd, mica	"	infills neck of boudinaged layer parallel qz vein	greenschist 2c	CEB
Defini	v	chl, cc, qz, ank +/- mica	gnt, epd, px, qz	infill in boudin neck of boudinaged layer	?	CEB
Delfini	s	epd, zois, qz, chl	"	infill in boudinaged layer	?	CEB
Defini	v	qz, epd, chl, ab, mica	qz, cc, chl, ab , epd +/- gnt	anastamosing shearzones or layer parallel segregations	greenschist	CEB
Delfini	v	chl, ab	epd,chl, qz, gnt, ank, gl	boudinaged layer	greenschist	CEB
Delfini[16]*	v	chl, ab, ank, cc, mica	"	boudinaged layer	greenschist	CEB
Delfini	v	qz	dolomite marble	neck of boudinaged layer	?	CEB
Delfini	v	cc, qz	px, gl, gnt, qz	boudin necks of boudinaged layer	?	CEB
Delfini	v	zois, qz	px, gl, ank	infill in boudin necks	?	CEB
Delfini	v	cc	dolomite marble	anstamosing veins	?	CEB
Delfini	v	epd, cc, chl, qz	px, gl	boudin necks	?	CEB

Delfini	v	qz, mica	"	boudin necks	?	CEB
Delfini	v	qz	epd rich layer	boudin necks	?	CEB
Delfini	v	qz, gl	epd, gl, ank, mica, qz, actin	shearzones	blueschist 1d	CEB
Delfini	v	chl, ab, qz	epd, zois, chl	boudin neck	greenschist	CEB
Delfini	v	ab, chl, oxide	epd, gl, qz	boudin necks	greenschist 2d	CEB
Delfini	v	qz	chl, ab, epd	shearzones	?	CEB
Delfini	v	qz, chl	epd, qz, chl or gl	shearzones	?	CEB
Delfini	v	epd, qz	epd, qz, chl	extensional vein	?	CEB
Delfini	v	ab, chl, ank + ab pressure shadow	quartzite	boudin neck	greenschist	CEB
Delfini	v	qz	quartzite	boudinaged quartzite	?	CEB
Delfini	v	ab	impure quartzite		?	CEB
Delfini	v	qz, ank, ab, chl	qz, chl, ab, cc, mica		greenschist	
Delfini[14]*	s	cc, ab, chl	ab, chl schist	segregation with albite pressure shadow	greenschist	CEB
Delfini	s	epd, qz, ank, sphene	gl, epd, qz, mica	foliation wrapped boudinaged segregation	blueschist 1e	CEB
Delfini	v	gl, qz	gl, epd, qz, mica	cut through boudinaged epd, qz, ank, sphene segregation and are sheared	blueschist 2e	CEB

v vein, s segregation, mineral abbreviations (see front of thesis), [1, 2, 3] * refer to associated field sketch or photo, CEB (this study), PB (Bloor, 1998), HB (Barr, 1989), JR (Ridley, 1982)

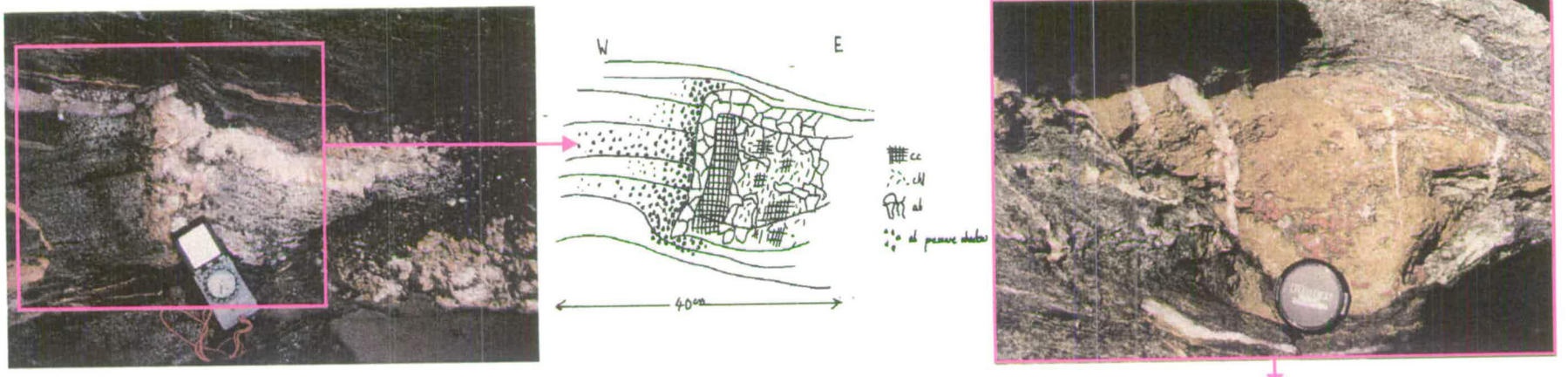

Figure 4.15 Calcite-, albite-, chlorite-segregation with albite pressure shadow, Delfini

Figure 4.16 Epidote-, chlorite-, calcite-, quartz-segregation, cross-cut by albite- chlorite veins, Delfini

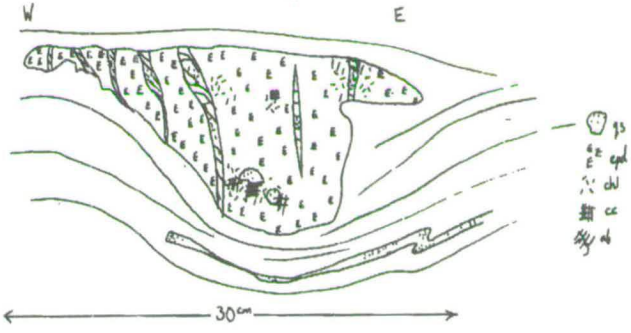

Figure 4.17 Chlorite-, calcite-, quartz-, mica-veins in boudinaged layers, Delfini

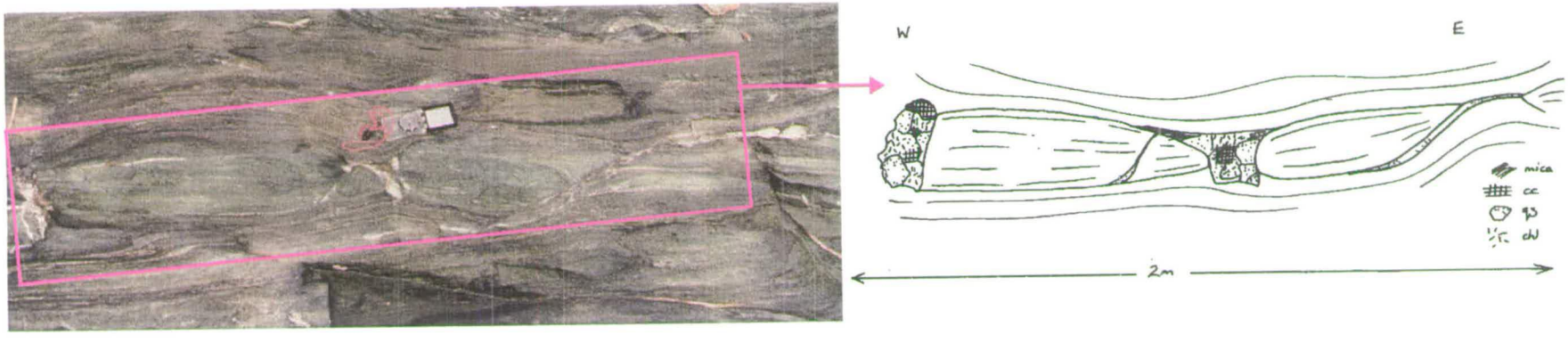

parallel quartz veins which are themselves boudinaged and have greenschist minerals precipitating in their boudin necks.

A calcite-, chlorite-, albite-vein is shown in figure 4.15. It is found in a greenschist extensional shear zone which has boudinaged and pinched-out a 1.5 m thick quartzite horizon. The vein has a pressure shadow of albite and is one of several greenschist segregations in the shear zone. Within 10 m of the shear zone layer parallel epidote segregations are wrapped by the foliation and are cut by albite- and chlorite-veins (figure 4.16).

Delfini Summary

The Delfini section contains veins of blueschist grade through to albite-chlorite veins. All veins are spatially associated with the layer-parallel extension documented in chapter 3. Early layer parallel quartz veins are thought to have formed prior to or during extensional tectonics and are themselves boudinaged. Blueschist veins in boudin necks are cross-cut by later lower pressure veins. Greenschist veins and segregations form in zones of localised high strain, where layers are extremely attenuated. The veining appears to be directly associated with the extensional deformation throughout decompression. In local zones 3-4 m wide, where the schist is completely retrogressed deformation fabrics are defined by greenschist minerals and foliations wrap greenschist segregations. This implies that pervasive deformation on a scale of at least 3-4 metres was concurrent with recrystallisation to greenschist assemblages and fluid infiltration at Delfini.

Summary of central-northern areas

Due to the range in metamorphic assemblages preserved in the central area it is not surprising that the veins represent a range of metamorphic grades. Within the area a range of veins can be identified from early quartz, foliation-parallel, veins and lawsonite-bearing veins, through glaucophane-bearing veins to albite-chlorite veins. The albite-chlorite, greenschist, veins are mainly seen in the schist units at Kini, Oros Syringas and on the Ermoupolis-Kini road section. Higher pressure blueschist veins are

generally found in metabasic lithologies.

The veins particularly at Delfini can be associated with the extensional tectonism described in chapter 3. Early foliation-parallel quartz veins are boudinaged, whilst later veins, associated with fluid infiltration during extensional tectonics, are found in boudin necks or extensional shear zones. Evidence for metasomatism around greenschist grade veins is documented by the formation of albite selvages and pressure shadows.

Serpentinite belt and northern area

The serpentinite belt as a whole contains a range of vein mineral assemblages, from extensional chlorite- and albite-bearing veins to lawsonite-associated quartz veins. The greenschist grade veins generally trend NW-SE, and accommodate NE-SW directed extension. The veins are seen in clusters along lithological contacts between the serpentinite and gneiss, where map-scale boudinage has fractured layers and the contacts between the gneiss and serpentinite are vertical. These vertical tectonic contacts between lithologies are oriented approximately N-S, accommodating E-W extension. The veins sometimes have fibrous growth of minerals perpendicular to the wall rock and have metasomatised the surrounding host rock. Dixon (1969) recognised that these chlorite-albite fracture surfaces without glaucophane rinds were a later, down-pressure extensional phenomenon than the deformed and extended higher pressure metasomatic rocks on other gneiss-serpentinite contact surfaces.

Extensional quartz-glaucophane veins crop out at the northern contact of the serpentinite belt. The quartz-glaucophane veins have precipitated in extensional shear zones (figure 4.18) which continue into the serpentinite below. The glaucophane grows into the vein from the wall rock, whilst the majority of the vein contains quartz.

At the southern side of the serpentinite belt and further north early quartz veins with associated lawsonite precipitation are common. On the south side of Lia Bay a folded quartz vein is seen (figure 4.19) complete with lawsonite halo. The intense schistosity is inferred to be the S2 of Bloor (1998) which is axial planar to the folds. Bloor (1998) showed this foliation to be expressed by high pressure minerals and is

Table 4.4h Vein observations from Oros Syringas

Geographical location	Type of deposit	Mineralogy	Host rock	Structural setting	Metamorphic grade and relative timings of emplacement denoted by numbers	Observation
Oros Syringas	v	qz, ab, chl, cc, oxide	ab, chl, mica, epd greenschist	large pegmatitic vein, parallel foliation	greenschist	CEB
Oros Syringas	v	qz	ab, chl, mica, epd greenschist	qz veins in ductile shearzones	?	CEB
Oros Syringas	v	qz, ab, chl	ab, chl, mica, epd greenschist	large pegmatitic vein, sub-parallel to foliation	greenschist	CEB
Oros Syringas	v	qz +/- cc	dolomite	boudinaged dolomite layer	?	CEB
Oros Syringas	v	qz, chl, ab + ab halo	gl, epd		greenschist	CEB
Oros Syringas	v	qz, epd	ab, chl, mica, epd greenschist	extensional vein	greenschist	CEB

v vein, s segregation, mineral abbreviations (see front of thesis), [1, 2, 3] * refer to associated field sketch or photo, CEB (this study), PB (Bloor, 1998), HB (Barr, 1989), JR (Ridley, 1982)

enveloped in the lawsonites.

Summary of the serpentinite belt and northern area

Like the central-northern areas, the serpentinite belt and north of the island, preserves a range of vein mineral assemblages. Greenschist veins are localised and form sub-vertical planar veins oriented NW-SE to N-S, to accommodate NE-SW to E-W directed extension. Blueschist veins on the edge of the serpentinite belt are also associated with E-W directed extension. The veins have precipitated in shear zones, with glaucophane growing into the vein from the wall rock.

Earlier foliation-parallel quartz veins with associated lawsonite growth are also observed. The veins are folded and have fold axial planes parallel to the regional foliation. The associated lawsonite forms a halo around the vein, increasing in concentration towards the vein. These early quartz veins are not associated with extensional tectonics; their structural association is discussed in detail by Bloor (1998). He concluded that the veins were folded and oriented parallel to the regional foliation as the foliation developed during 'peak' metamorphism.

Discussion of the structural settings of veins and vein mineralogies

Veins are by definition extensional features that open to accommodate the passage of fluid through a rock (Ramsay and Huber, 1983). The alignment of growth fibres in veins and vein orientations can therefore be used to determine the local stress regime during vein opening (e.g. Ramsay, 1980). If vein orientations are found to be consistent over large areas then the local stress regime during vein formation may correspond to the regional stress regime of the area.

Vein orientations of greenschist veins (those containing albite and chlorite, sometimes with other phases) were presented for localities within the structure chapter. Albite-chlorite veins are widespread across the island and easy to measure as they generally form planar features. Figure 4.20 shows the orientations of greenschist veins from localities across the island. There is a general N-S to NW-SE trend in greenschist vein orientation across the island, most obviously in the north.

Table 4.4i Vein observations from the Serpentinite belt

Geographical location	Type of deposit	Mineralogy	Host rock	Structural setting	Metamorphic grade and relative timings of emplacement denoted by numbers	Observation
Serpentinite belt	v	chl, ab	layered metabasite epd-, gl-rich layers (chl-rich vein) gl, gnt (gnts partially pseudomorphed by epd)	extensional fabric in vein	greenschist	CEB
Serpentinite belt	v	chl, ab	epd, chl layer	boudinaged layer	greenschist	CEB
Serpentinite belt	v	ab	epd/zois layer	boudinaged layer	?	CEB
Serpentinite belt[17]*	v	qz, gl	cc, gl, ank, mica, gnt	extensional shears	blueschist	CEB
Serpentinite belt	v	ab	px, gnt	extensional veins in boudinaged layer	?	CEB
Serpentinite belt	v	qz, gl	px, gnt	extensional veins in boudinaged layers	blueschist	CEB
Serpentinite belt	v	chl, ab	px, gnt, gl	extensional vein	greenschist	CEB
Serpentinite belt	v	cc	gl, epd, gnt, zoisite, mica pelitic blueschist	sometimes forming in en-echelon arrays	? 1	CEB
Serpentinite belt	v	qz	gl, epd, gnt, zoisite, mica pelitic blueschist	cross-cut by later cc vein	? 2	CEB
Serpentinite belt	v	ab + chl halo	gl, epd, gnt, zoisite, mica pelitic blueschist		greenschist	CEB
Serpentinite belt	v	ab +chl + chl halo	gl, epd, gnt, zoisite, mica pelitic blueschist		greenschist	CEB
Serpentinite belt	v	ab +chl +oxide +/- chl halo	gl, epd, gnt, zoisite, mica pelitic blueschist		greenschist	CEB
Serpentinite belt	v	ab +/- chl halo	gl, epd, gnt, zoisite, mica pelitic blueschist		greenschist	CEB
Serpentinite	v	qz, ab, chl	gl, epd, gnt gneiss		greenschist	CEB

belt Serpentinite belt	v	ab, chl	gl, epd, gnt gneiss	greenschist	CEB

v vein, s segregation, mineral abbreviations (see front of thesis), [1,2,3] * refer to associated field sketch or photo, CEB (this study), PB (Bloor, 1998), HB (Barr, 1989), JR (Ridley, 1982)

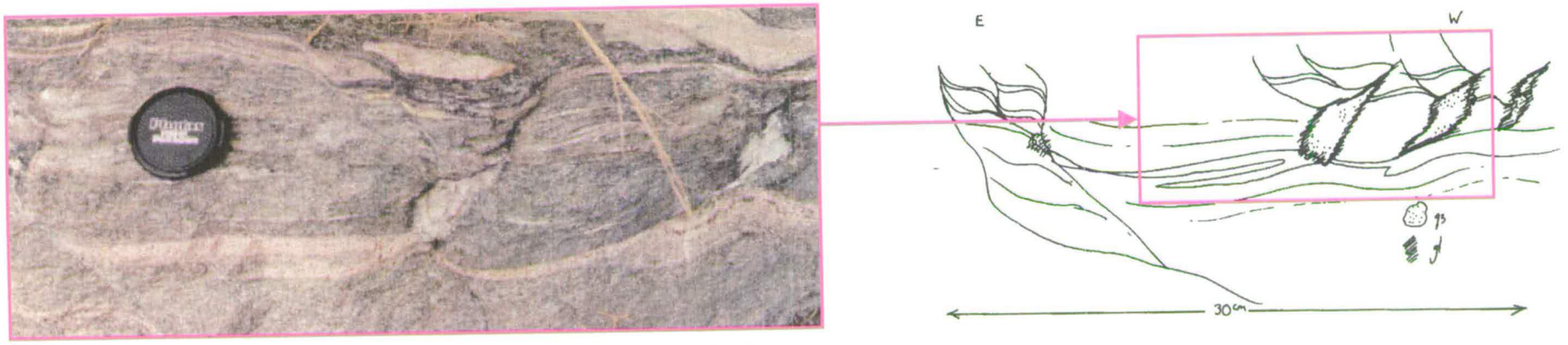

Figure 4.18 Quartz-glaucophane extensional veins in calcite rich metabasite

Figure 4.19 Folded quartz vein with associated lawsonite pseudomorphs, Lia Bay

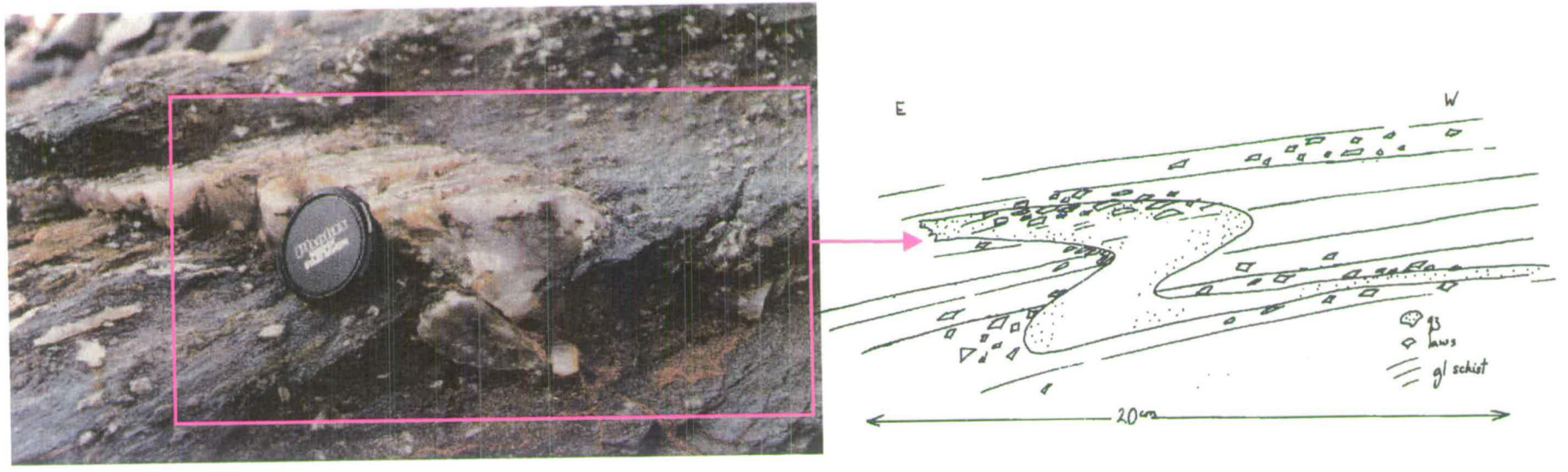

Table 4.4j Vein observations from northern Syros

Geographical location	Type of deposit	Mineralogy	Host rock	Structural setting	Metamorphic grade and relative timings of emplacement denoted by numbers	Observation
Diapori	v	chl, ab +/- ab halo	qz, chl, ab, epd	veins and segregations	greenschist	CEB
Diapori	v	qz	qz, chl, ab, epd	folded veins	blueschist	CEB
Grammata Bay	v	qz + assocaiated laws	px, gl, gnt metabasite	contact between meta-gneiss & basite	lawsonite-blueschist	CEB
Northern grey schist	v	qz	qz + associated laws	folded quartz veins	lawsonite-blueschist	CEB PB
Windy Ridge	v	qz	gl, px, mica, epd, qz, cc schist		?	CEB
Kastri	v	ab, qz	epd, chl, qz, cc metabasite	extensional veins	greenschist	CEB
Kastri	v	qz, cc	?		?	HB
Lia Bay	v	chl +/- ab, qz, cc +/- chlorite haloes	blueschist		greenschist	CEB
Lia Bay	v	cc + Fe stained haloes	blueschist		?	CEB
Lia Bay	v	epd + qz	blueschist	vein is boudinaged	?	CEB
Lia Bay[18]*	v	qz + associated laws	blueschist	vein is folded	lawsonite-blueschist	CEB
Lia Bay	v	epd	px, gl, gnt, qz, mica metabasite		?	CEB
San Mikhali rd section	v	ab, chl, cc, qz +chl , ab haloes	chl, ab, epd schist	feeder veins to larger pegmatite	greenschist	CEB

v vein, s segregation, mineral abbreviations (see front of thesis), [1,2,3] * refer to associated field sketch or photo, CEB (this study), PB (Bloor, 1998), HB (Barr, 1989), JR (Ridley, 1982)

In the south of the island greenschist veining is more pervasive and although shown to be associated with extensional E-W oriented deformation, veins and segregations are more randomly oriented. The greenschist segregations in the south are also often wrapped by a greenschist foliation. In northern Syros the greenschist veins are generally planar and oriented NW-SE to N-S. In the north of Syros, greenschist deformation is observed to be fracture controlled. In southern Syros, greenschist deformation has been identified in the form of fractures and locally as a pervasive fabric forming deformation (e.g. Megas Yialos and Finika). In between the zones of pervasive greenschist deformation, 1-20 m wide, the greenschist facies over-print is apparently static with porphyroblastic albites overprinting earlier fabrics.

Veins with higher grade mineralogies, mainly those confined to the metabasite outcrops at North Ermoupolis, Delfini, and Kini are generally more anastomosing in nature and their orientations were not so obviously consistent. However, blueschist glaucophane-quartz veins have precipitated in extensional shear zones and boudin necks. In the serpentinite belt the shear zones are associated with E-W oriented extensional deformation. At Delfini the boudin necks in which quartz and glaucophane have precipitated are also associated with layer-parallel extensional deformation, on an E-W axis. Field sketches and photographs of the outcrop at Nites and Delfini (figures 4.4, 4.8 and 4.17) show veins that are spatially associated with boudinage accommodating layer parallel east-west extension. The veins infill boudin necks that fractured during boudinage.

Often more than one phase of mineralisation can be identified, either by cross-cutting veins (figures 4.13 and 4.16) or by evidence for multiple fracturing events within boudin necks (figure 4.8). Evidence for different generations of mineralisation within boudin necks from high and lower pressure assemblages suggests that east-west extension occurred at high pressure as well as within the greenschist facies stability field, during progressive exhumation and that fluids were present at different times during exhumation and available to mineralise forming veins. The central issue for the interpretation is this tectonic continuity. The glaucophane-bearing extensional veins could be the deep level expression of unroofing by layer-parallel extension. On the other hand, layer-parallel extension could be a reflection of flattening within the

Figure 4.20
Geological Map of Syros, after Ridley (1982), key is as in figure 4.1.
Equal area projections,lower hemisphere, of poles to greenschist veins are annotated.Note the general NE-SW to E-W clustering of the poles to veins particularly in northern Syros.

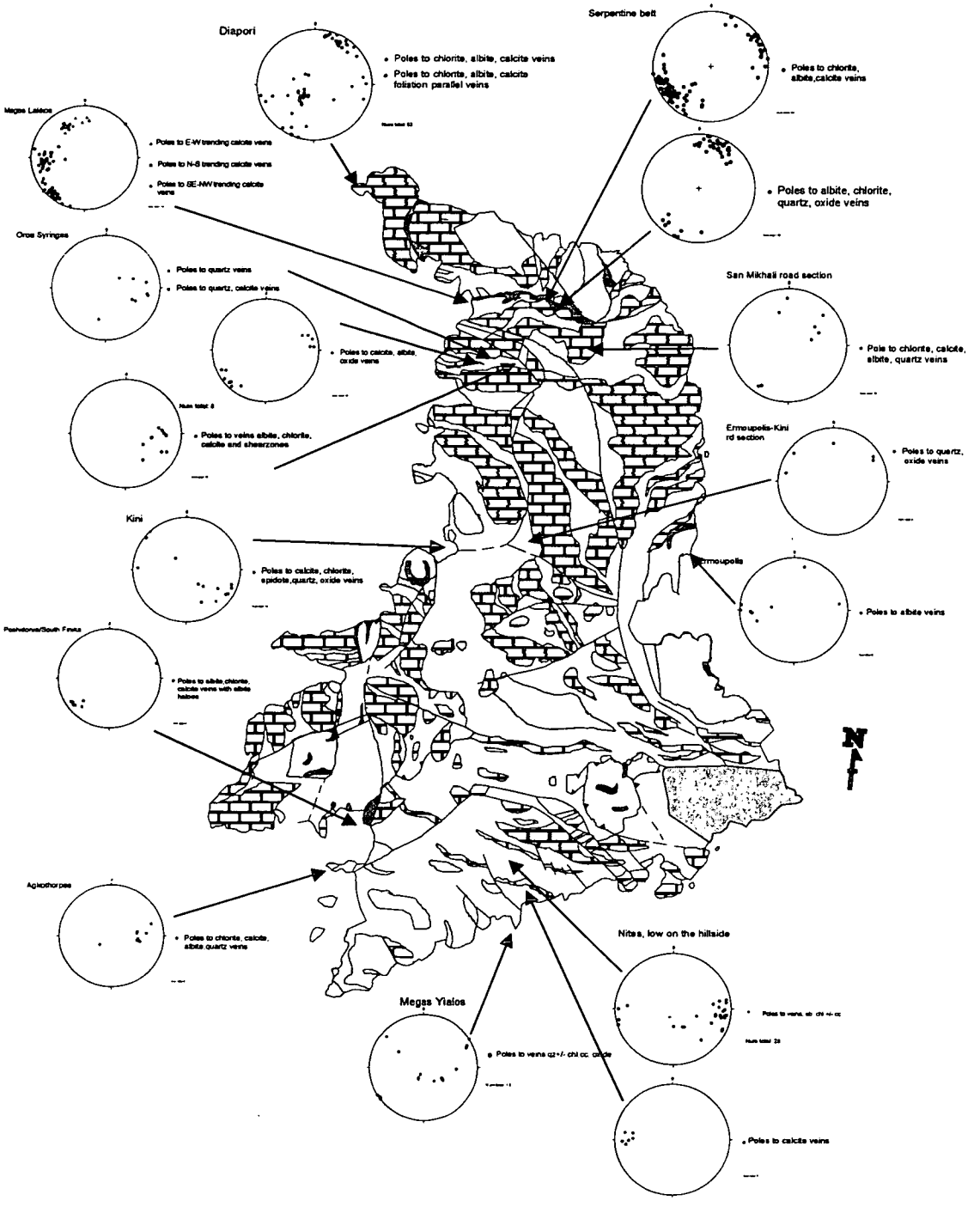

subduction zone, related to burial rather than exhumation. Unfortunately the high-variance assemblages in the high pressure veins rarely allows a distinction to be made between burial-'peak' or early exhumation on PT grounds. The quartz-glaucophane veins and boudin necks that represent high pressure extensional brittle or semi-ductile disruption of earlier high pressure fabrics are here interpreted as being related to the onset of exhumation.

The interpretation, of extension related to exhumation, is supported by the boudinage of the regional foliation, Bloors' S2 fabric, which is related to folding and lawsonite precipitation at peak pressures and temperatures (Bloor, 1998). Evidence for early veins on Syros show subsequent deformation during extensional tectonics. Early quartz veins, in northern Syros with associated lawsonite porphyroblasts in mineral selvages, are folded (e.g. figure 4.19). The veins are now foliation-parallel and have fold axial planes parallel to the regional foliation (Bloor's S2). Quartz veins at Megas Yialos also show layer-parallel boudinage and attenuation of fold limbs. The structural association and geometries of the veins are consistent with modification during E-W oriented extension.

Veins with corresponding mineralogies are seen at many localities across the island, which suggests that veining was wide-spread during the following mineralisation events:

- quartz veins with associated lawsonite
  (Northern Syros-greyschist; N Ermoupolis-metabasite blocks; Grammata Bay, metabasite).

- extensional quartz-, glaucophane-veins
  (N Ermoupolis-metabasite; Delfini-metabasite; Serpentinite belt-metabasite)

- quartz-, glaucophane- ± epidote-veins
  (N Ermoupolis-metabasite; Ermoupolis-Kini road section-metabasite; Kini-metabasite)

- sphene- ± quartz-, epidote-, glaucophane-veins (N Ermoupolis-metabasite; Ermoupolis-Kini road section-metabasite; Kini-metabasite; Delfini-metabasite)

- extensional albite-chlorite veins +/- oxide, calcite, quartz (Megas Yialos-schist; Nites-schist; Posidhonia-schist; Finika-schist; Kikkano-schist; Agathopes-schist; Komito-schist; N Ermoupolis-metabasite; Kini-metabasite; Delfini-metabasite; Oros Syringas-schist; Serpentinite belt-metabasite; Diapori-schist)

Extensional deformation and vein formation are inherently associated on Syros. The veining associated with NE-SW to E-W extension is dominated by the generation of north-south oriented greenschist veins. From the field observations a picture of successive fluid infiltration and veining can be built up for different localities on Syros. By combining field observations of vein mineralogies, cross-cutting relationships and structural associations a story of fracture associated fluid infiltration can be derived for the exhumation history. A summary of the main vein related fluid infiltration events and their relation to the structural evolution are detailed in table 4.11.

Table 4.11 A summary of the main vein associated fluid infiltration events

Mineralogy		Relative timing	Structural association	Geographical location
Quartz +/- lawsonite	1	Lawsonite suggests high P-T, structural association has been inferred to be 'peak' metamorphic (Bloor, 1998)	folded syn-post-formation and in some cases boudinaged on a E-W oriented axis.	northern grey schists N Ermoupolis-metabasite blocks
Quartz-glaucophane	2	Show no evidence for folding	extensional shear zones and boudin necks with an E-W oriented extension direction.	Serpentinite belt-calcite rich metabasite Kini-metabasite blocks Delfini-boudin necks of metabasite
Epidote- quartz	3	Cross-cut gl, qz veins in boudin necks at Delfini	boudin necks, associated with E-W oriented extension.	Delfini-boudin necks of metabasite Nites-boudin necks of metabasite
Albite-chlorite +/- other phases	4	Often seen to be the final infill in boudin necks e.g. Nites, Delfini. The veins cross-cut folding at Diapori	extensional veins and boudin necks	Wide spread across the island
Calcite	5	Cross-cut albite-chlorite veins	none	Wide spread across the island

Dating veins

Sphenes can potentially be dated by U-Pb and as sphenes have precipitated in the blueschist veins it was thought that it may be possible to date the precipitation of the veins. Sphenes precipitated in the blueschist veins were generally large (up to 2 cm x 5 cm). The amount of sphene material available meant that it was very easy to assess whether the sphenes were suitable for dating. The sphene was crushed for X-Ray Fluoresence (XRF) analysis to find out the approximate ratio of U/Pb. The ratio of U/Pb needed to be > 4 to get a resolvable age for the vein (Simon Inger *pers comm.*) as the terrain is relatively young. The U/Pb ratio was less than half that required for a resolvable age and the vein sphene was inferred not to be suitable for dating.

Isotope geothermometry of veins

Samples of quartz, calcite, albite and oxide were collected from greenschist veins from Nites, Oros Syringas, Kini and Delfini. The mineral separates were analysed for their $\delta^{18}O$ compositions, by the method described in chapter 5. The $\delta^{18}O$ compositions of the individual minerals can be used to find the temperature of precipitation of the minerals in the vein by the isotope fractionations between the individual minerals. The fractionations of $\delta^{18}O$ between the different minerals in individual veins were not mutually consistent and some of the veins showed isotopic reversals between minerals. The isotopic reversals mean that the veins are unsuitable for isotope geothermometry. The presence of isotopic reversals suggests that precipitation of the minerals in the vein did not occur during a single infiltration event. Barr (1989) also carried out isotope work on mineral separates from greenschist veins and found isotopic reversals. She also came to the conclusion that multiple infiltration events had occurred in the veins.

Summary

- The variety of vein mineral assemblages, indicates that veining was an important mechanism for fluid infiltration during metamorphism.

- Veins are generally associated with extensional deformation fabrics and are found in zones of localised deformation, including boudin necks and extensional shear zones.

- Isotopic fractionations between minerals in individual veins are not mutually consistent and document isotopic reversals, indicating more than one fluid infiltration event occurred in single veins.

4.5 *Metasomatism and mineral selvages associated with channelled fluid infiltration*

Evidence for metasomatism of vein wall rock was first observed in the field within the serpentinite belt, where alteration haloes of chlorite are clearly seen around veins in blueschist host rock. Alteration haloes of chlorite around veins were also identified at Kikkano (photograph 4.1) and North Ermoupolis. Photograph 4.2 shows a thin section (S'95/26) of a small vein and alteration halo from the blueschist boudins at Kambos, within the serpentinite belt. Alteration haloes and pressure shadows of albite were also recognised in the field at Delfini, the serpentinite belt and Kini. Photograph montage 4.3 shows an alteration halo in thin section from a vein in the northern serpentinite belt that exhibits unusually large albite porphyroblasts in a chlorite, albite, epidote alteration halo.

Metasomatic alteration of vein wall rock has been documented by other workers (e.g. Barnicoat, 1988; Ague, 1997). Bloor (1998) studied metasomatic alteration associated with quartz vein formation and lawsonite growth during peak metamorphism on Syros. He found that the rock was affected chemically and mineralogically by the metasomatism. The work presented here on lower grade greenschist facies vein metasomatism will be compared to that of Bloor (1998) in the discussion, to assess the change in fluid composition and mass transport properties between peak and retrogressive greenschist facies metamorphism.

Photograph 4.1
Chlorite alteration halo around greenschist vein, Kikkano.
The edge of metasomatic alteration to chlorite is outlined.
Note the wavey nature of the alteration front which implies preferential fluid infiltration along more permeable layers in the wall rock.

Photograph 4.2 Field and thin section examples of alteration to chlorite, around a vein at Kambos (S'95/26).

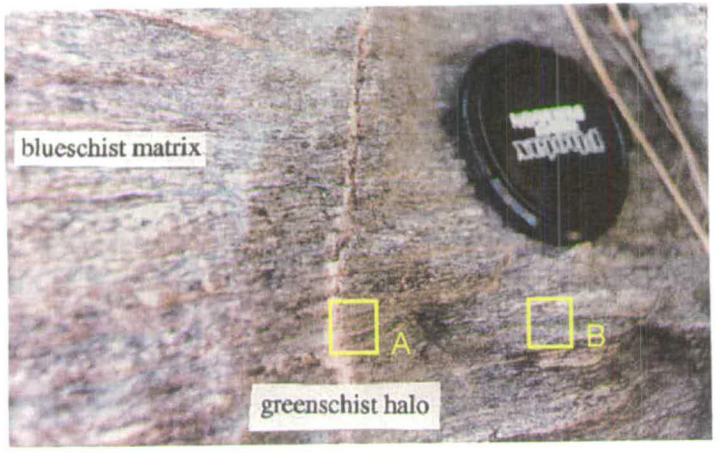

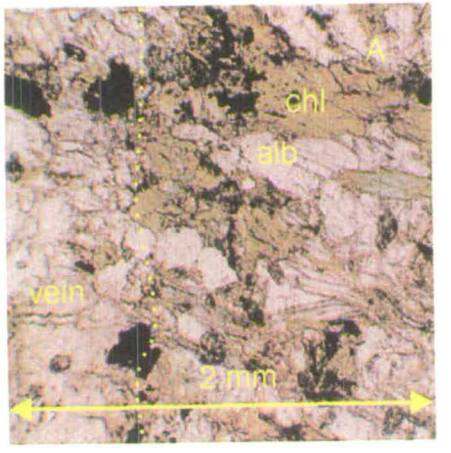

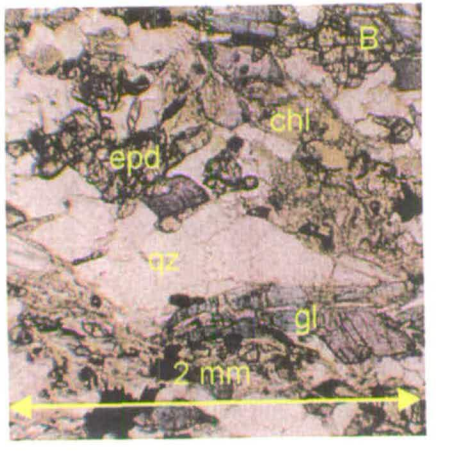

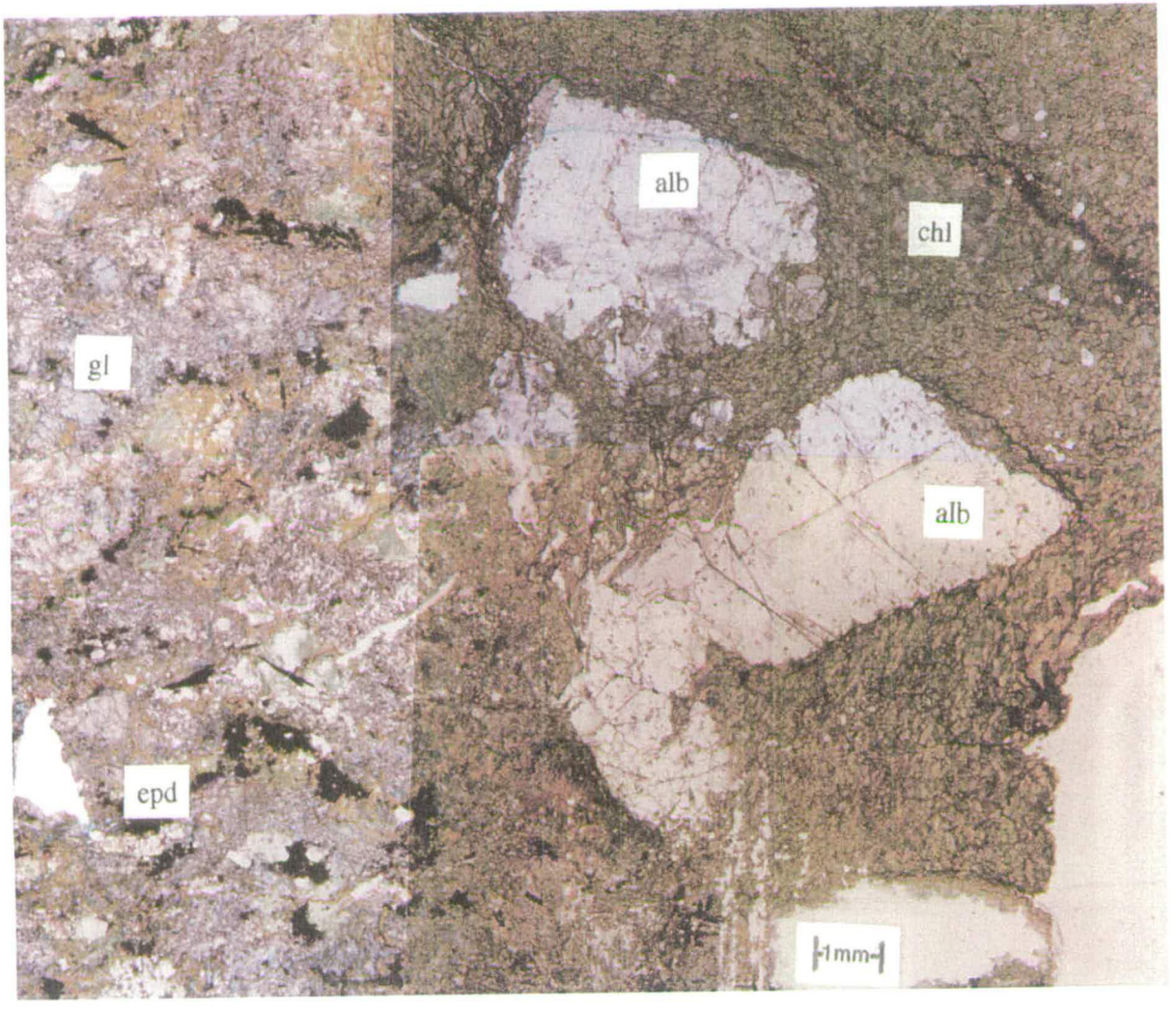

Photograph 4.3
Photo-montage of thin section (S'96/89B) an albite-chlorite vein halo. The vein (not shown) is to the right of the montage. The host rock contains glaucophane and epidote. Glaucophane is reacting to chlorite and albite. The epidote is stable.

Sampling

Samples were collected on two field seasons. The first was a reconnaissance study to assess the potential for detailed sampling of alteration haloes for XRF work. A total of eight samples were collected from four veins, one sample from the alteration halo and one from the adjacent unaltered host rock. The first four samples (S'95/26g and b; S'95/63g and b), from the Kambos goat cave area in the serpentinite belt were from veins in pods of boudinaged blueschist, that lie within a faulted and brecciated marble unit, just below Kambos village. A sketch of the boudins from the southern side of the valley is shown in figure 4.21. Stereonets of vein orientations in the schist boudins are annotated and show NE-SW extension associated with the veining. Samples S'95/26g and b come from the wall rock to a vein in boudin F, whilst samples S'95/63g and b are from boudin G. The haloes around veins in the boudins at Kambos contain chlorite-, albite-, mica- and calcite-, the unaltered rock has a glaucophane-, epidote-, mica- and calcite-assemblage (photograph 4.2).

The second four samples (S'95/116g and b, S'95/117g and b) from North Ermoupolis are from gneiss host rock with an albite-, chlorite-, epidote-, sphene-assemblage in the alteration halo around the vein. Elsewhere, vein haloes in the gneiss thin in zones that are garnet rich and coarser grained and show alteration to epidote and chlorite photograph 4.4. Photograph 4.5 shows the halo sampled for S'95/116. The thin section photograph shows large clots of glaucophane which are mantled by veins in zones of deformation and retrogression. It is only in deformed zones that fluids have infiltrated and caused retrogressive crystallisation. Sample S'95/117 is finer grained (photograph 4.6), the alteration halo around the vein contains albite-, chlorite-, epidote-, green-amphibole and sphene ± rutile. The epidote has partially retrogressed to chlorite-, calcite-, quartz- and mica-, probably by the reaction:

3 glaucophane + 6 epidote + $\rightarrow$ 1 chlorite + 19 quartz +
8 H_2O + 12 CO_2 12 calcite + 6 paragonite

Micro-veins in the halo have precipitated albite in small, mm-wide, shear zones (photograph 4.6). The amount of green amphibole in the halo decreases away from the

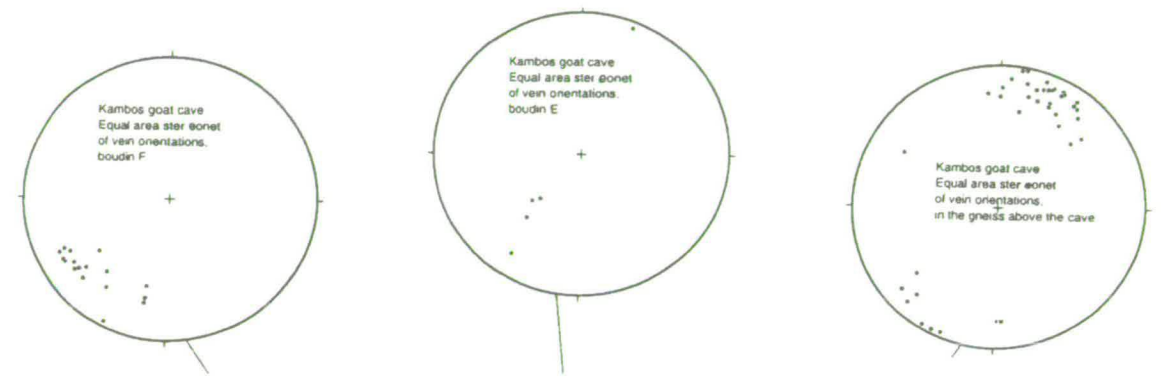

Figure 4.21 Sketch of Kambos goat cave, northern Serpentinite belt and equal area stereonets of poles to greenschist veins

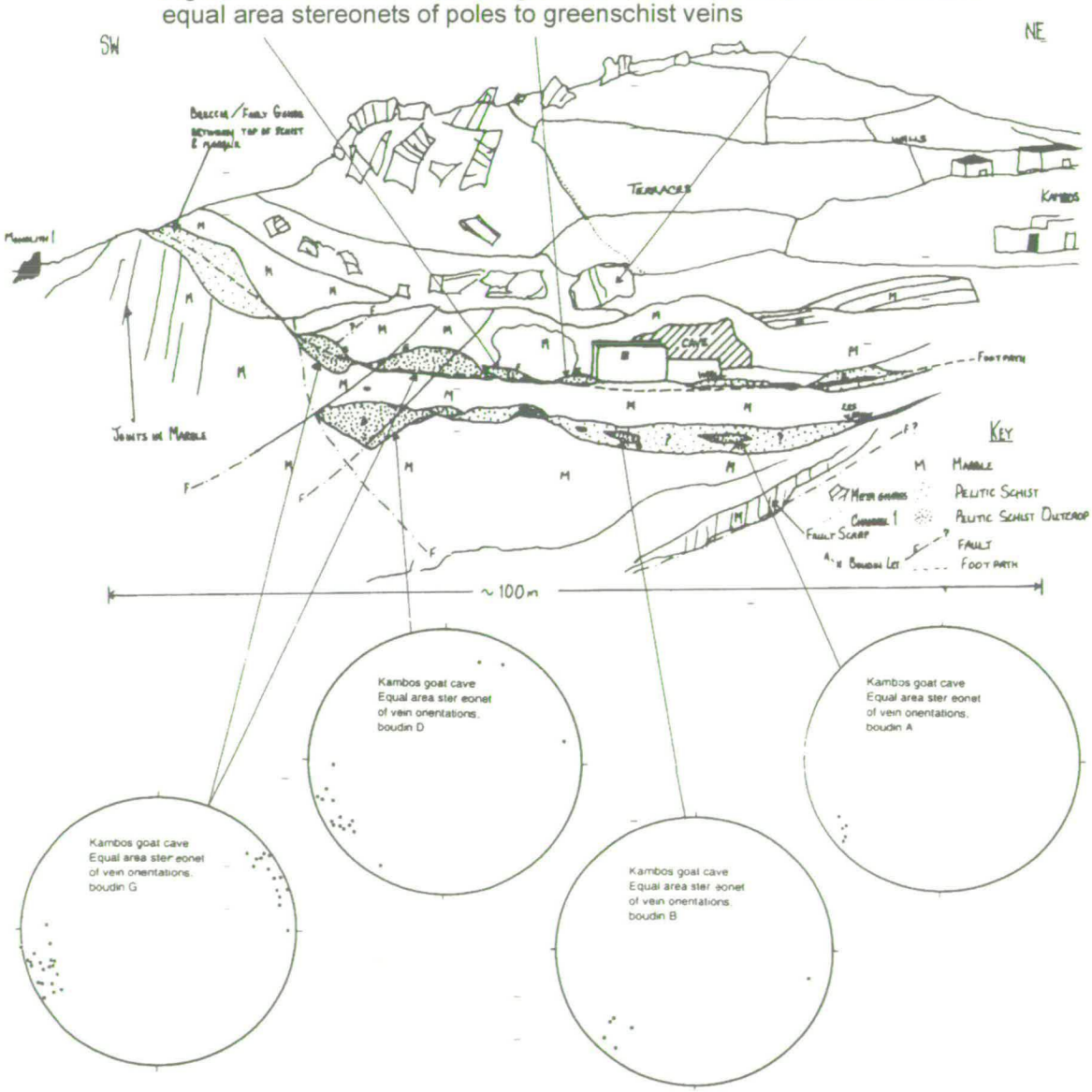

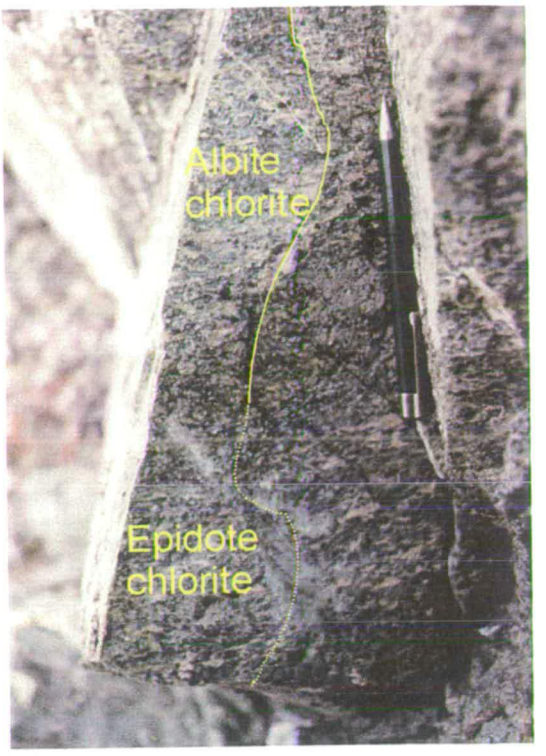

Photograph 4.4
Example of a vein halo, North Ermoupolis, that shows retrogression to an epidote-chlorite assemblage and albite-chlorite

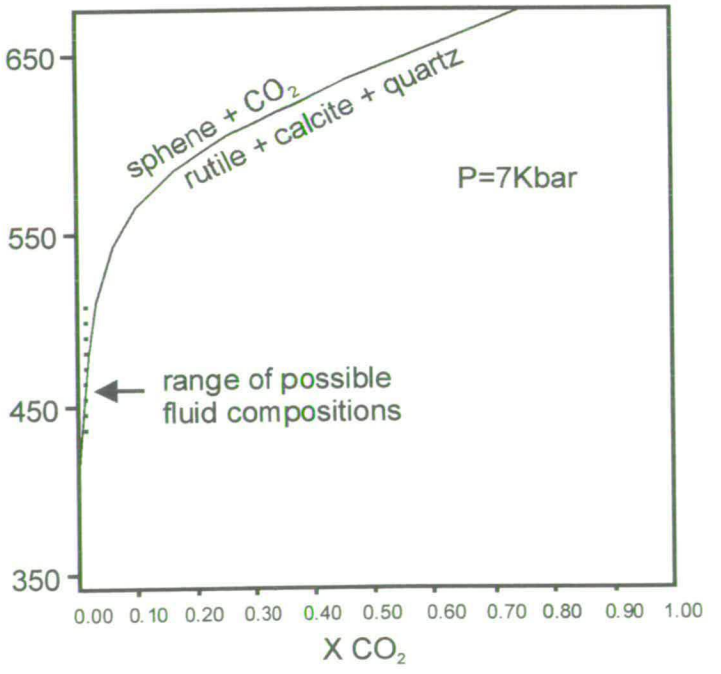

Figure 4.22
Plot of T-XCO2 for a fixed pressure of 7 Kbars, and a sphene activity of 0.948. The plot was calculated using the thermodynamic data set of Holland and Powell (1988). The plot is redrawn from Barr (1989).

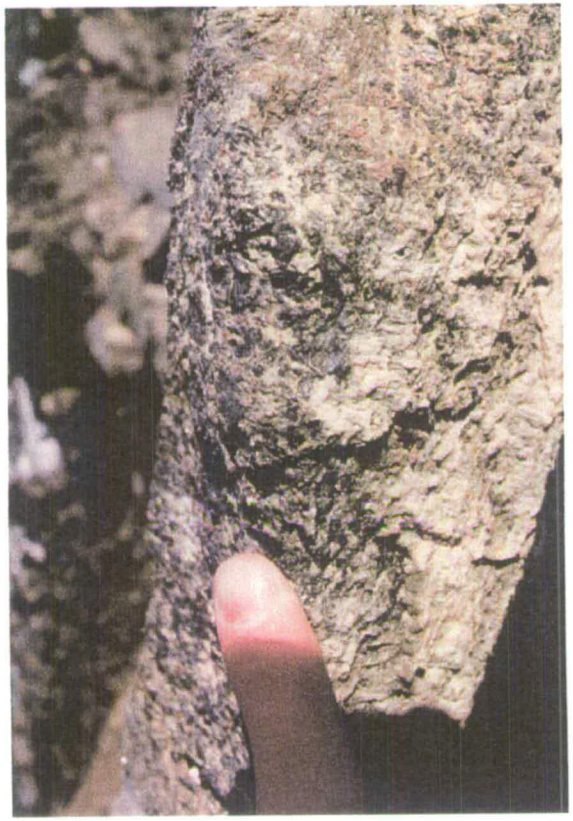

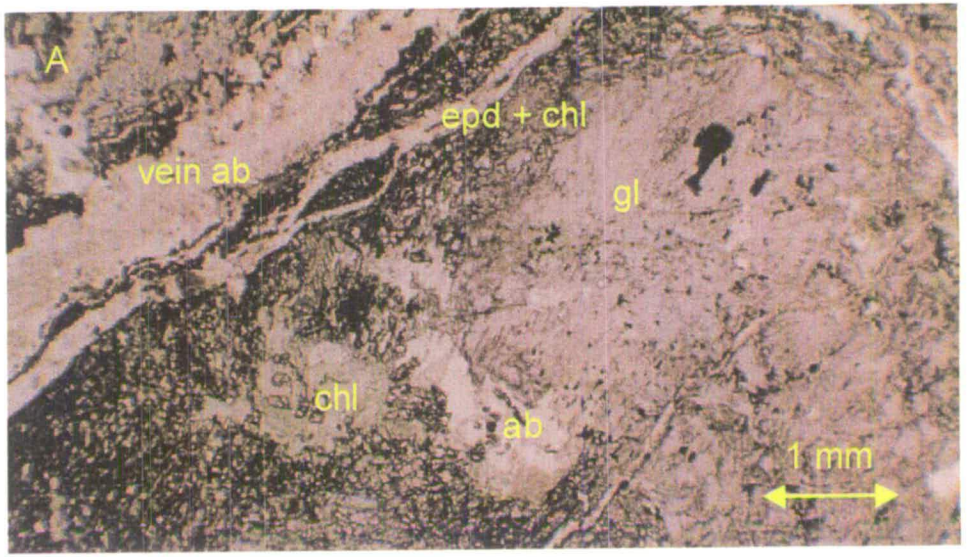

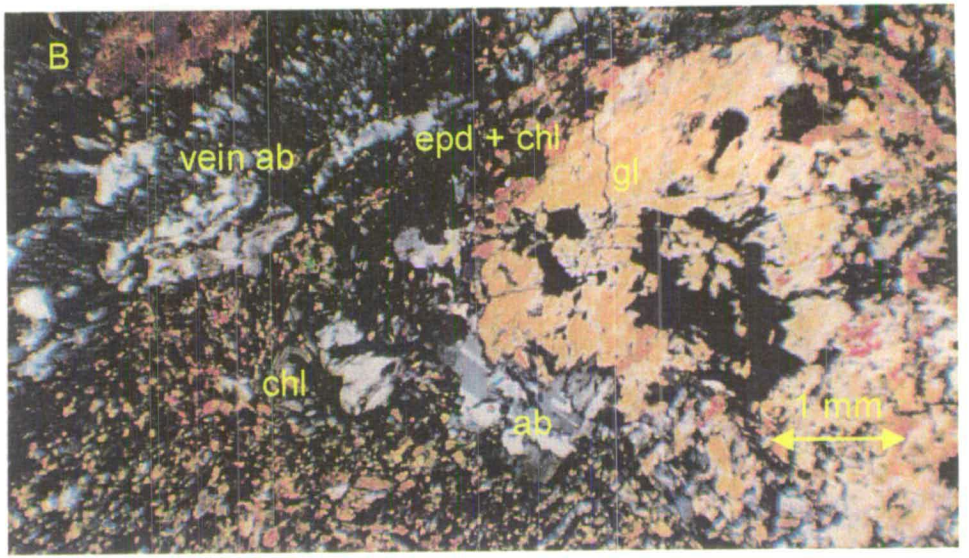

Photographs 4.5
Vein halo, sampled for S'95/116
North Ermoupolis. A) is a PPL thin section
photograph of the deformed albite vein
It shows alteration of epd and gl to ab and
chl. Large 'clots' of gl remain, mantled by a
retrogression zone, B) is the XPL equivalent

Photograph 4.6
Vein halo sampled for S'95/117 North Ermoupolis. Thin section photograph A) shows the assemblage close to a small vein in a shear zone. B) 1.5 cm from a small vein shows alteration of gl to chl at its rim.

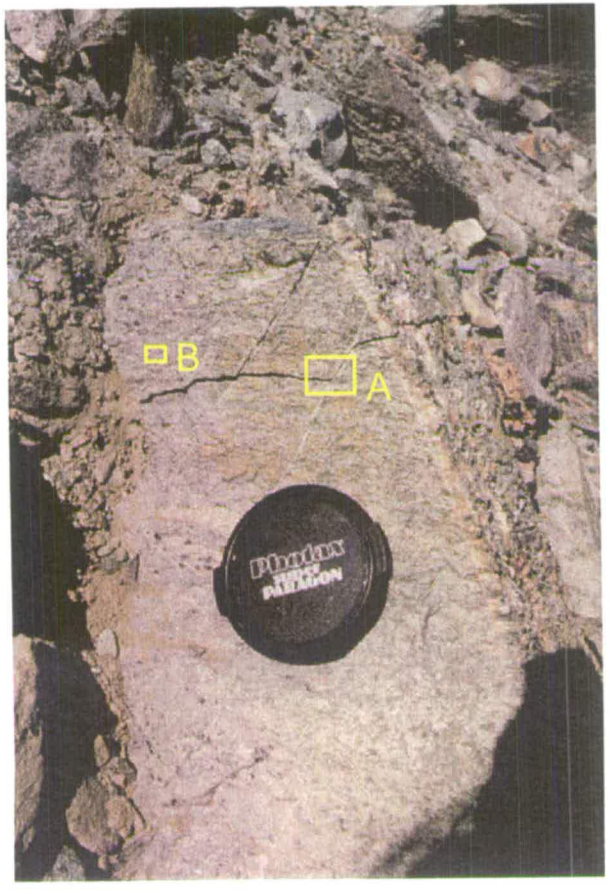

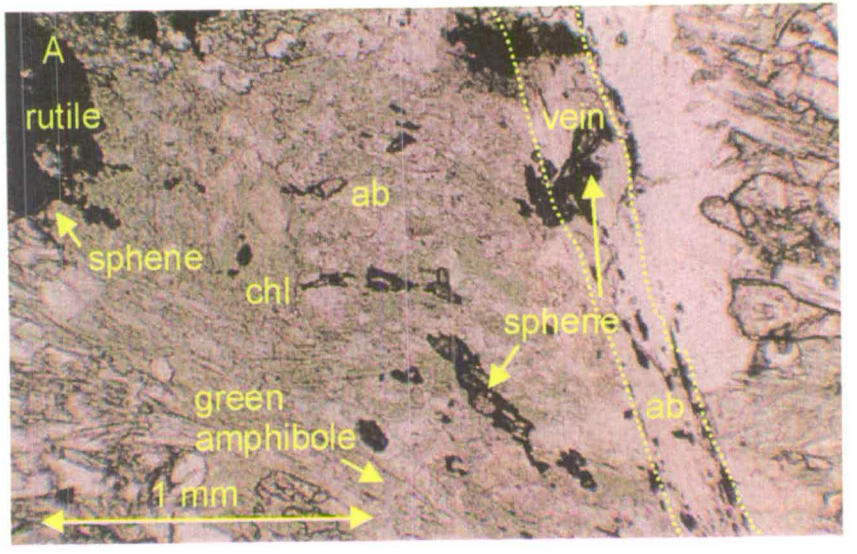

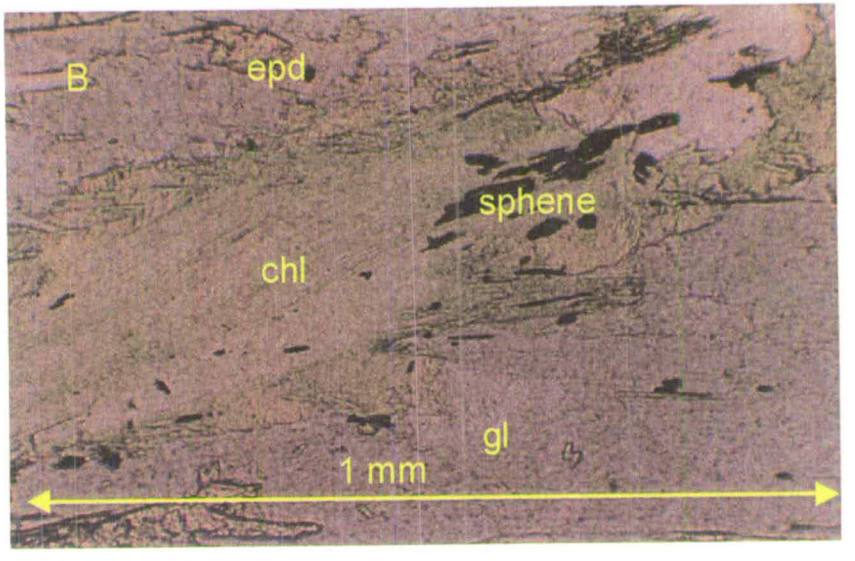

vein. The unaltered host rock assemblage is glaucophane and epidote with rutile ± sphene. The veins predominantly consist of albite with some sphene. Rutile in the alteration halo is mantled by sphene, which implies infiltration of a H_2O-rich fluid. The relative stability of rutile and sphene is controlled by fluid composition (Hunt and Kerrick, 1977) and can be represented by the reaction:

$$\text{rutile} + \text{calcite} + \text{quartz} \rightarrow \text{sphene} + CO_2$$

Figure 4.22 shows the relative stability of rutile and sphene for a T-XCO_2 plot at a pressure of 7 kbar. The plot shows that only very H_2O-rich fluid compositions would support the presence of sphene for the pressures and temperatures associated with retrogressive greenschist facies metamorphism on Syros, as was first noted by Barr (1989).

The second phase of sampling involved sample traverses from veins into wall rock, to document metasomatic alteration in vein wall rock with distance. Sample traverses away from veins at: Delfini (S'97/113 A-E) figure 4.23; Nites (S'97/31 A-E) figure 4.24; Oros Syringas (S'97/71 A-H) figure 4.25; Kini (S'97/80 A-J) figure 4.26 were made through albitised metasomatic haloes. At Delfini (S'97/86A-H) a sample traverse across a shear zone was also completed to assess the extent of fluid infiltration during shearing as the shear zone showed preferential albitisation figure 4.27.

XRF-results

Raw data is given by weight percent oxide for each major element and can be found in appendix A, along with the preparatory method. Samples with totals including loss on ignition, that fell outside the range of 99.5-100.5% were repeated.

For an initial assessment of element mobility within the haloes, the isocon plot method of Grant (1986) has been adopted. The isocon method is based on a mass balance calculation, which was adopted for metasomatic alteration by Gresens (1967). Grant (1986) used a graphical display of mass balance for metasomatic alteration by plotting the composition of unaltered rock against metasomatically altered rock. All immobile elements during metasomatism should have the same mass in both unaltered

Figure 4.23
Photograph and sketch of sample traverse for Delfini S'97/113

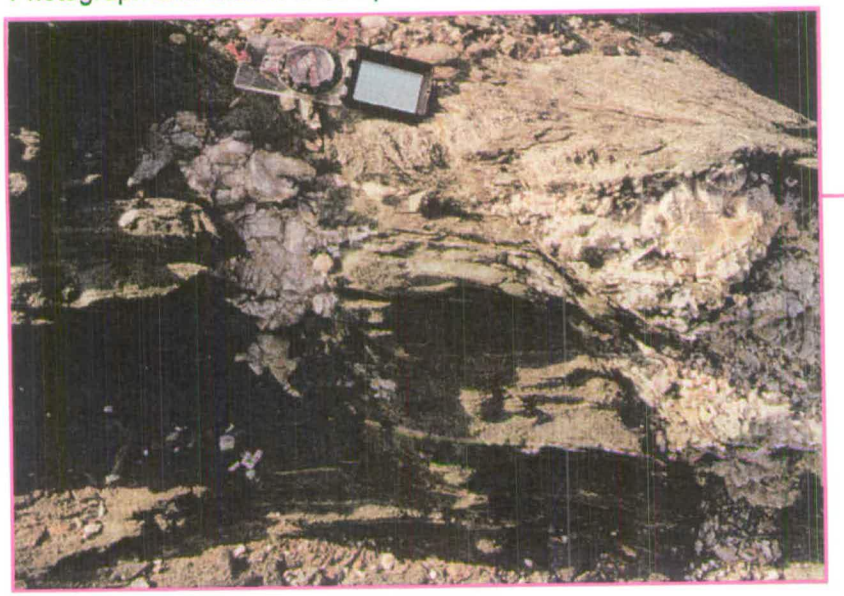

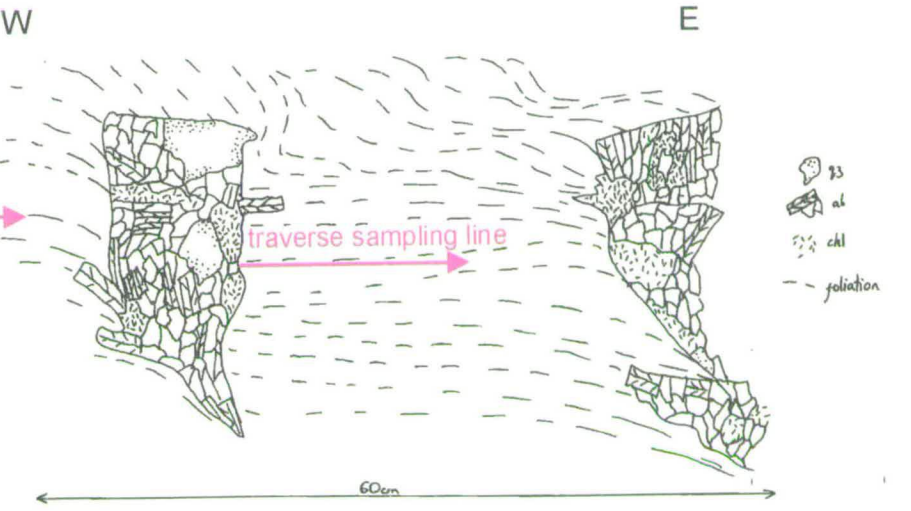

Figure 4.24
Schematic sketch of sample traverse S'97/31, Nites, of an albite halo around a layer parallel segregation

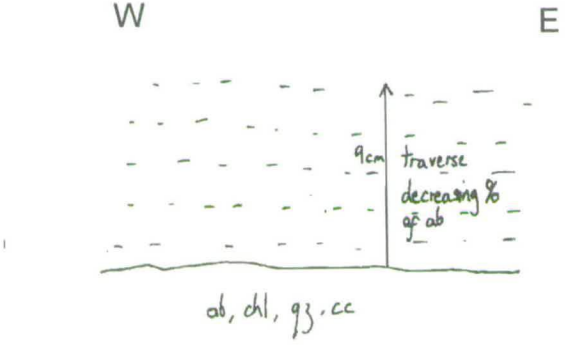

Figure 4.25
Schematic sketch of sample traverse S'97/71, Oros Syringas, of an albite-chlorite halo to a vein

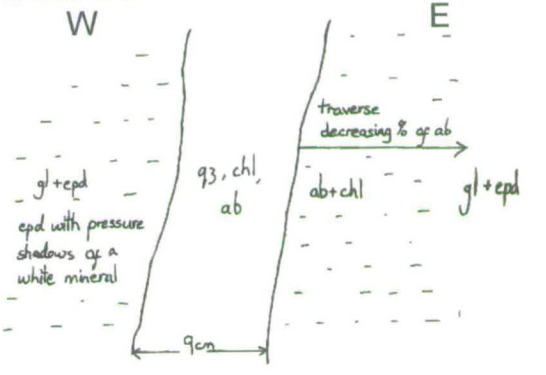

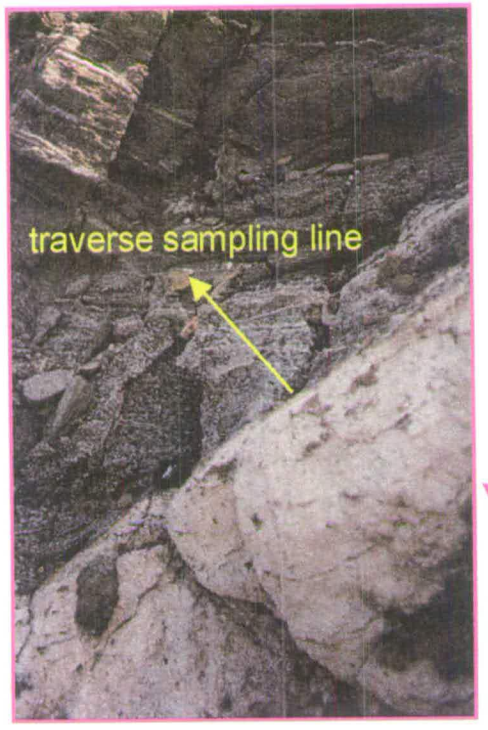

Figure 4.26
Location and photograph of vein and halo (S'97/80) sampled for XRF analysis. See chapter 3, figure 3.13 for an enlarged version of the Kini section.

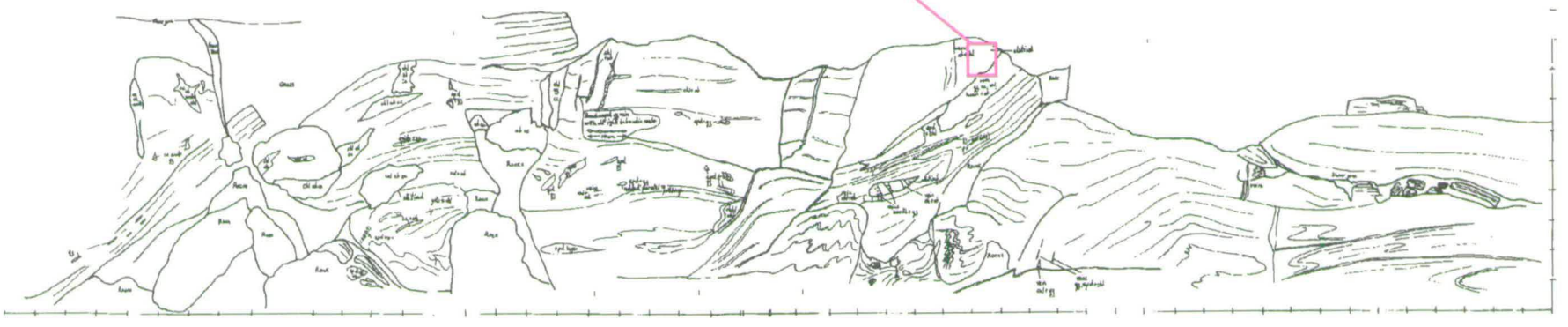

Figure 4.27
Photograph of sample traverse S'97/86. The sample traverse is marked on the photograph and crosses an albitised shear zone.

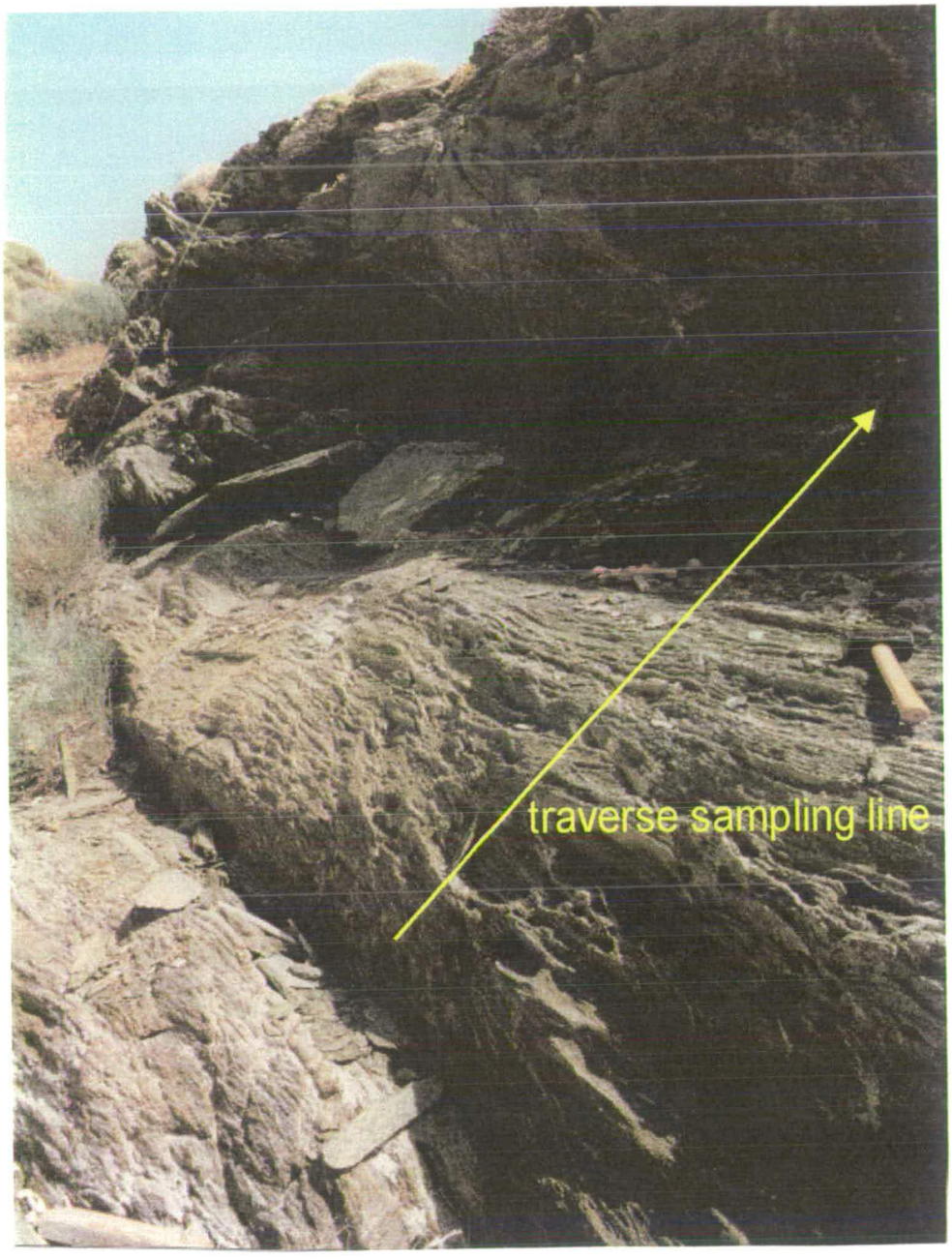

and altered samples. These immobile elements plot on a line that passes through the origin, the isocon. Elements depleted during metasomatism fall below the line (or isocon) and those replenished lie above. If the overall mass of the rock alters during metasomatism then the slope of the isocon will not be 1:1. The change in slope of the line gives the change in mass due to metasomatism.

The number of immobile components identified during metasomatism depends on how well the isocon can be defined. Grant (1986) suggested the use of a scaling factor applied to both unaltered and altered analyses so that no points overlapped on the plot and the isocon was easier to define. Olsen and Grant (1991) suggest that scatter in data points even using the scaling technique to determine the isocon can still be problematic. They proposed the following reasons for scatter in the data:

- the altered rock not being the compositional equivalent of the chosen unaltered rock prior to alteration;
- 'closure problem', the degree to which an element becomes immobile;
- analytical uncertainties;

of which they deem the first as being by far the greatest contributor to scatter in data. They proposed the use of scaling or normalisation of concentration of components in the unaltered rock to a fixed value, with the same scaling factor being applied to the altered rock. If all the components have a fixed compositional value then all immobile elements will overlap, whilst mobile elements will plot away from the main group of points. The isocon can then easily be drawn between the origin and the point of all immobile components. The scaling does not alter the slope of the graph or the ratio of gain or loss of a component to the original amount.

I have adopted the technique of Olsen and Grant (1991) and normalised all major element wt% oxides to 30 wt% and plotted the isocon through the cluster of immobile components. For samples S'97/80, S'97/71, S'97/31, S'97/113 and S'97/86, the samples collected nearest to the vein or shear zone are plotted as altered and the samples collected at the farthest point from the veins or shear zone are plotted as

unaltered rock. All final samples were taken from rock that appeared to be unaltered in hand specimen, with the exception of S'97/113. The isocon plots for all samples are presented in figures 4.28-4.36. The plots show variable depletions and enrichments in oxides. The data are discussed below.

Discussion of isocon plots, with reference to thin section and field observations

Field and thin section observations clearly show metasomatic alteration of vein wall rock. Fluid-induced retrogressive metamorphic reactions create a visible alteration halo around veins. The alteration haloes seem to take two obvious forms in the field. Green alteration haloes which in thin section are observed to consist mainly of chlorite and alteration haloes containing albite porphyroblasts in a chlorite selvage around the vein.

Chlorite haloes

The green chloritic vein haloes sampled in blueschist boudins at Kambos are characterised by increases in volatile content (Loss On Ignition, LOI) within the halo. Sample S'95/26 (figure 4.28) shows depletion of Ca in the vein halo whereas S'95/63 (figure 4.29) documents a slight increase in Na in the vein halo, indicative of small scale mass transport. The retrogression reaction equations:

$$5 \text{ glaucophane} + 3 \text{ paragonite} + 4\ H_2O \rightarrow 13 \text{ albite} + 3 \text{ chlorite} + 1 \text{ quartz}$$

$$3 \text{ glaucophane} + 6 \text{ epidote} + 8\ H_2O + 12\ CO_2 \rightarrow 6 \text{ paragonite} + 1 \text{ chlorite} + 19 \text{ quartz} + 12 \text{ calcite}$$

can be written to describe fluid-induced alteration to retrogressive greenschist assemblages in vein wall rock margins, as well as the breakdown of epidote. The haloes containing chlorite are characterised by an increase in volatile content of the host rock around the vein.

Figure 4.28 S95/26 Kambos Goat Cave area, boudin F. Isocon plot of major elements in vein halo compared to unaltered wall rock. Immobile elements are Si, Al, Fe, Mg, Na, K, Ti, Mn and P.

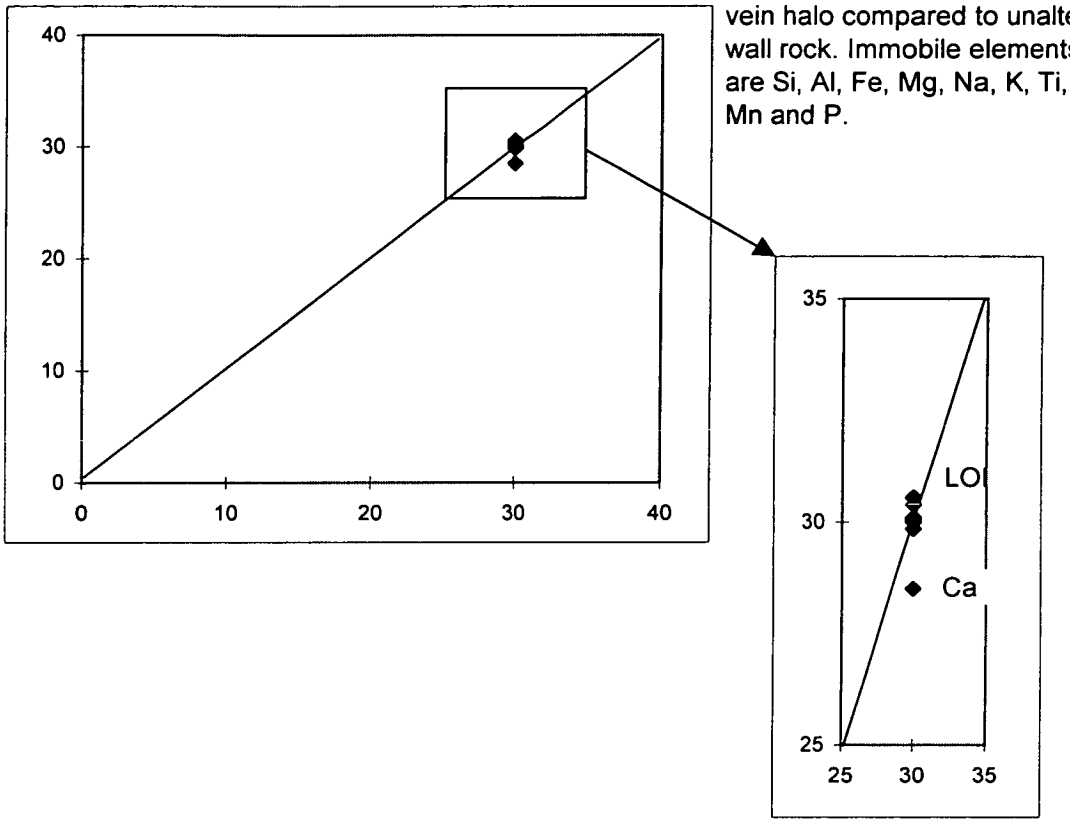

Figure 4.29 S95/63 Kambos Goat Cave area, boudin G. Isocon plots of major elements in vein halo compared to unaltered wall rock. Immobile elements are Si, Al, Fe, Mg, K, Ti, Mn and P.

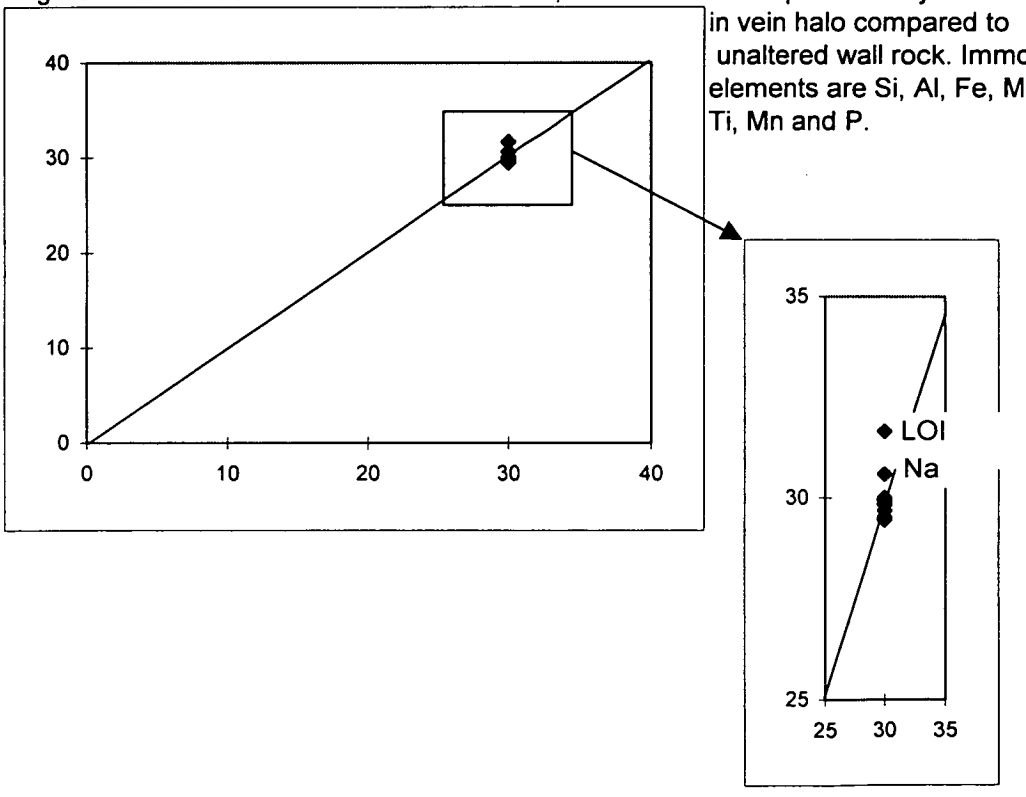

Figure 4.30 S95/116 North Ermoupolis, Isocon plot of major elements in vein halo compared to unaltered wall rock. Immobile elements are Fe, Mg, Na, K, Ti, Mn and P.

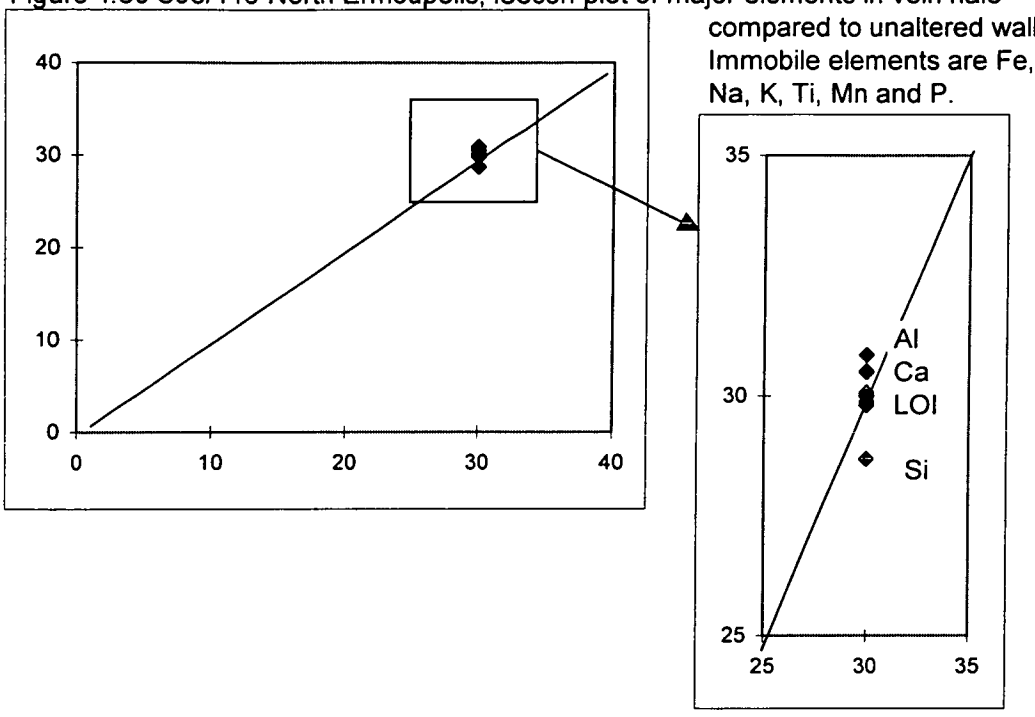

Figure 4.31 S95/117 North Ermoupolis. Isocon plot of major elements in vein halo compared to unaltered wall rock. Immobile elements are Al, Fe, Mg, Na, K, Tl, Mn and P.

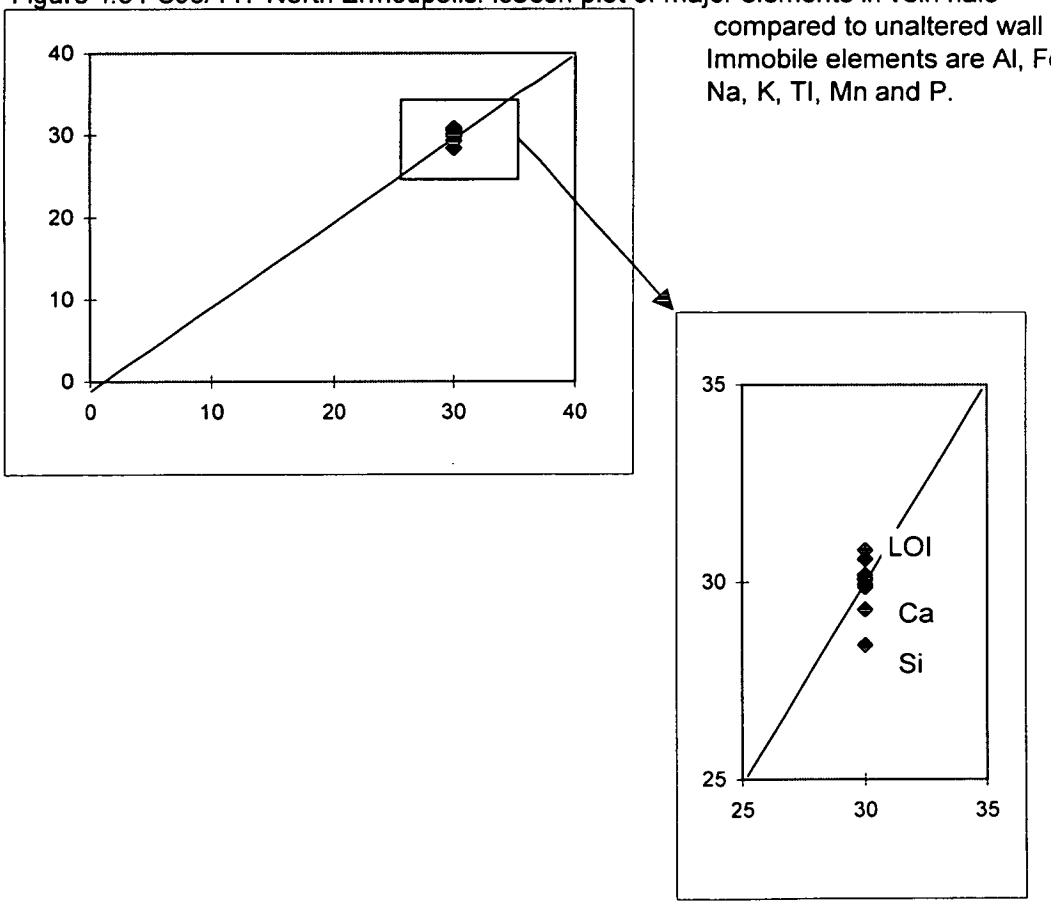

Figure 4.32 S'97/31 Nites. Isocon plot of vein halo compared to unaltered wall rock. Immobile elements are Al, K,Ti, Mn and P.

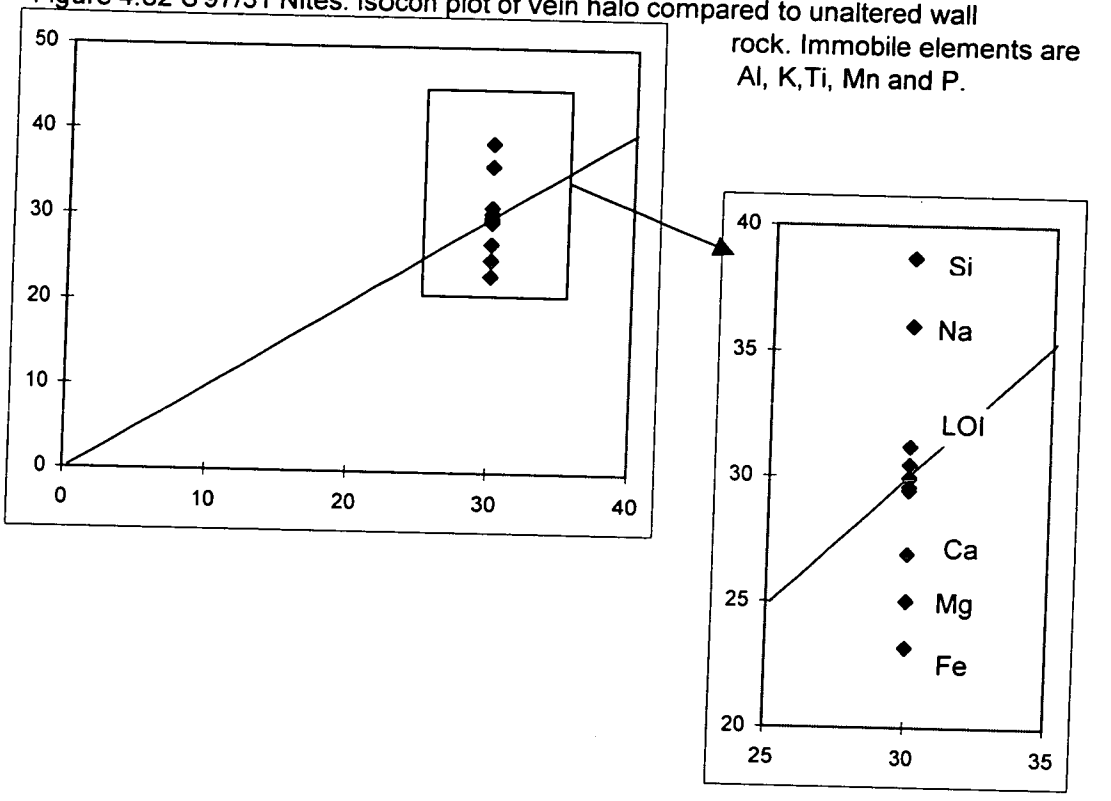

Figure 4.33 S97/113 Delfini. Isocon plot of vein halo compared with unaltered wall rock. Immobile elements are Ca, Na, Ti, Mn and P.

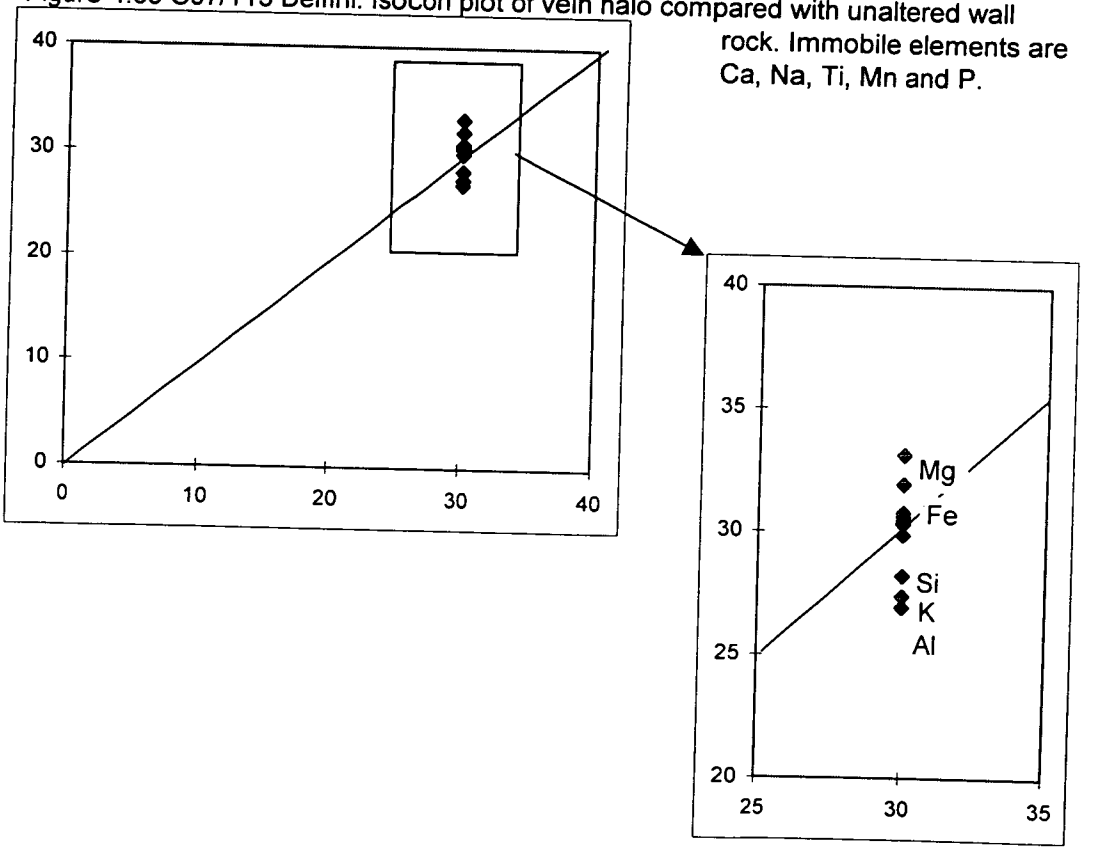

Figure 4.34 S'97/80 Kini. Isocon plot of vein halo compared to unaltered wall rock. Immobile elements are Al, Fe, Ca, K, Ti, Mn and P.

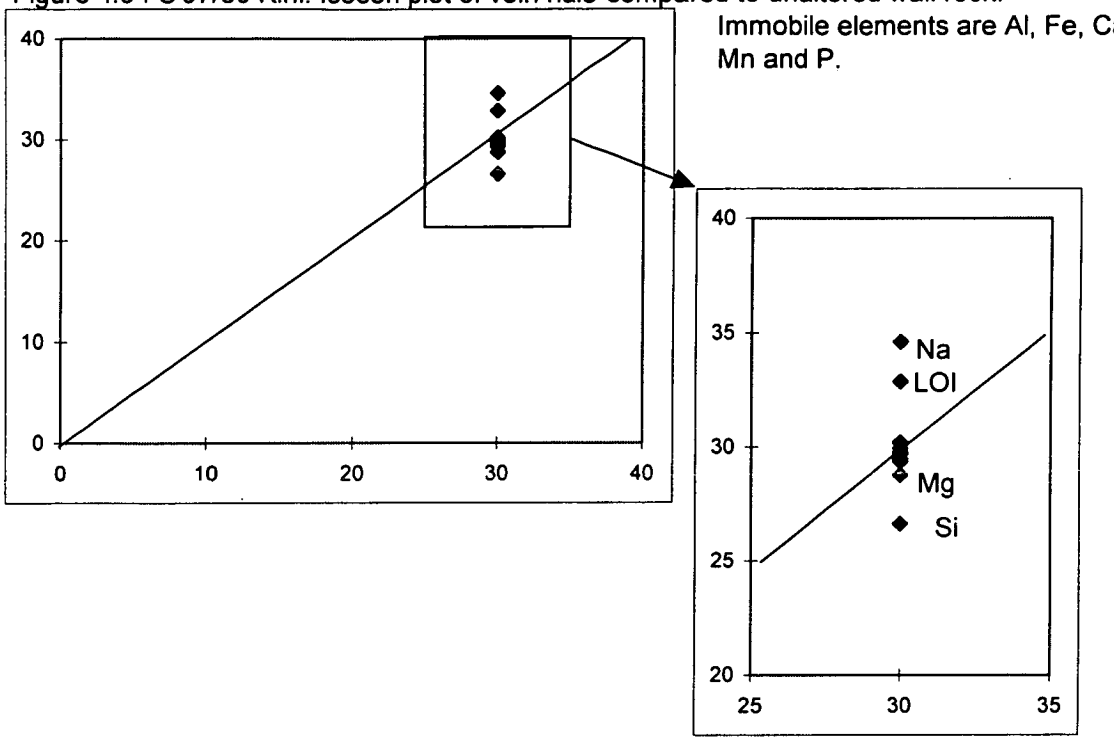

Figure 4.35 S'97/71 Oros Syringas. Isocon plot of vein halo compared to unaltered wall rock. Immobile elements are Al, Fe, Mg, K, Ti, Mn and P.

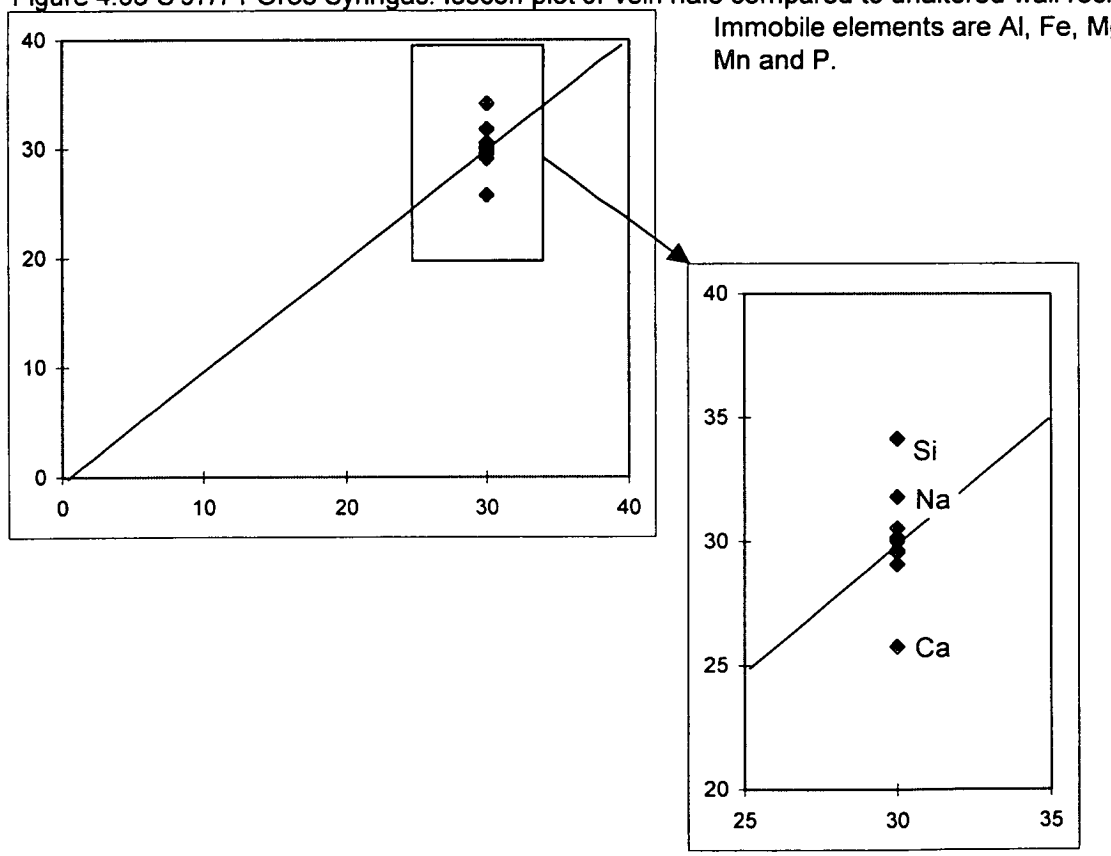

Figure 4.36 S'97/86 Delfini. Isocon plot of vein halo compared to unaltered wall rock. Immobile elements are Al, Fe, Mg, K, Ti, Mn and P.

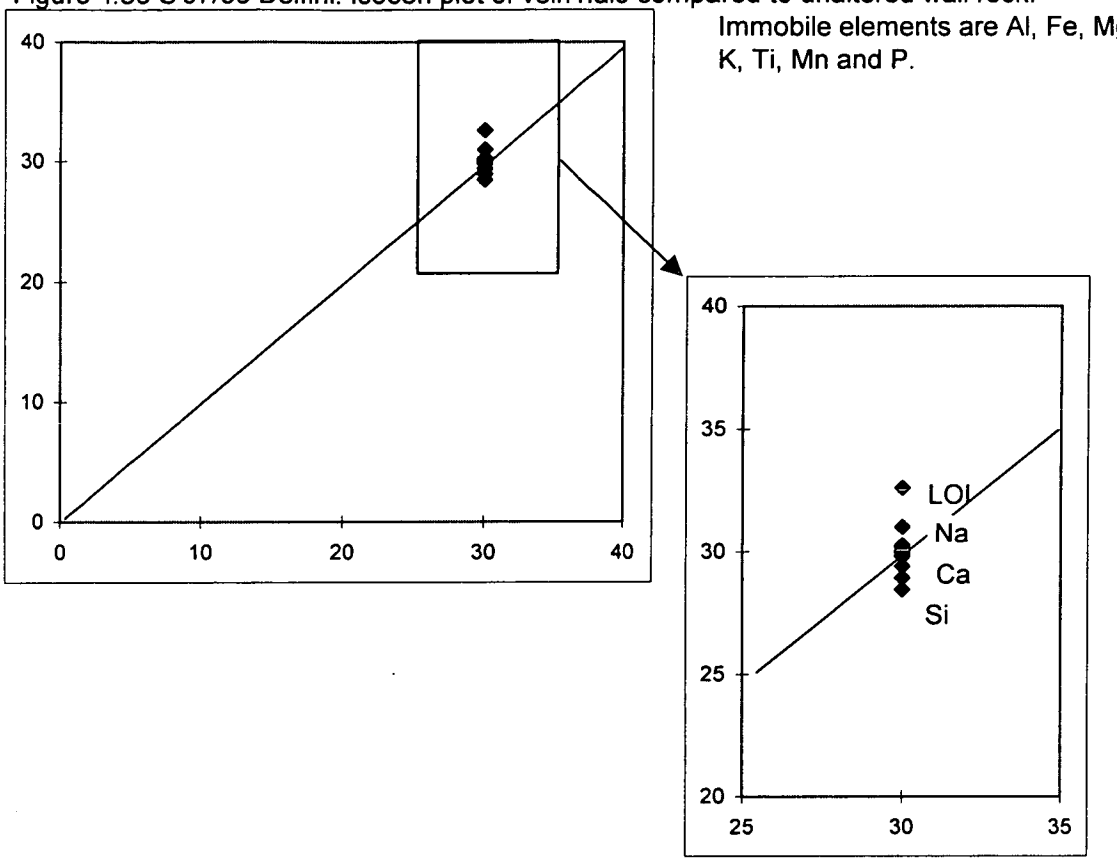

Gneiss haloes

Alteration haloes around veins in the gneiss at North Ermoupolis (figures 4.30 and 4.31) have depletions of silica within their alteration haloes. They show some increase in volatile content in the halo and also mobility of Al, Fe and Ca oxides. Retrogression of vein wall rock may be complicated in these examples by several periods of metasomatism. Early fluid infiltration events may have retrogressed the high pressure assemblages to epidote-bearing assemblages which are observed in some vein haloes, photograph 4.4. Subsequent fluid infiltration, may have then caused overprinting of the assemblage by albite and chlorite. The haloes are more complicated than other examples but consistently document increases in the volatile content of the rock around the vein.

Albite selvages

Alteration haloes which contain albite porphyroblast selvages show consistent enrichment of Na and volatiles in the alteration halo. The one exception is sample S'97/113 (figure 4.33) in which the unaltered host rock sample did not lie outside the albite porphyroblast selvage (figure 4.23) and therefore it is not a true representation of chemical exchange between the vein halo and unaltered host rock. Other mobile oxides include Si, Mg, Ca, K, Al and Fe, which are variably depleted or enriched in individual samples.

The sample from the shear zone (figure 4.36) shows both enrichment in Na and an increase in volatiles in the centre of the shear zone. This is inferred to be related to fluid infiltration associated with retrogression in the shear zone and that the growth of albite porphyroblasts was aided by an influx of sodium.

Summary

The slope of the isocon line in individual plots varies slightly, but there has been limited change in the total mass of rock in any of the alteration haloes. Of the ten elements which were analysed (Si, Al, Fe, Mg, Ca, Na, K, Ti, Mn, P) Ti, Mn and P remained immobile in all cases. The results of the isocon plots are summarised in table 4.12.

Table 4.12. Summary table of mass transport and mass change in alteration haloes of veins and across a shear zone. A + symbolises an increase, - a loss and 0 no change. Starred symbols note a consistent trend in all haloes of that type.

Sample description	LOI	Si	Na	Ca	Fe	Al	Mg	K	Mass
S'95/26 chlorite halo	+*	0	0	-	0	0	0	0	0
S'95/63 chlorite halo	+*	0	+	0	0	0	0	0	+
S'95/116 gneiss halo	+*	-	0	+	0	+	0	0	+
S'95/117 gneiss halo	+*	-	0	-	+	0	0	0	-
S'97/80 albite selvage	+	-	+*	0	0	0	-	0	+
S'97/71 albite selvage	0	+	+*	-	0	0	0	0	+
S'97/31 albite selvage	+	+	+*	-	-	0	-	0	+
S'97/113 (discounted due to choice of unaltered protolith rock)	0	-	0	0	+	-	+	-	+
S'97/86 shear zone with high albite conc	+	-	+*	-	0	0	0	0	+

Discussion of traverses

The results of the isocon plots can be compared with the detailed traverses made across albite selvages around veins and across the shear zone which documented a concentration of albite porphyroblasts. Detailed changes in the chemical components of the rock with distance from the veins (S'97/80, S'97/71, S'97/31, S'97/113) and the shear zone (S'97/86) are presented in figures 4.37-4.41. The sampled traverses were made perpendicular to veins. However, the lack of three-dimensional control on vein geometries below the surface means that some traverses may not have been sampled exactly perpendicular to veins.

Sample S'97/113 from Delfini (figure 4.37) is again discounted as the sample traverse does not extend outside the zone of altered rock. However, the traverse does highlight two trends, increasing volatile and MgO content towards the vein. Na which may have been expected to show an increase towards the vein, as this is an albite rich halo, does not. The lack of Na variability does not necessarily mean that the halo is not enriched in Na merely that the edge of the zone of enrichment may not have been

Figure 4.37 Delfini S'97/113. Plots of wt % oxide against distance from greenschist vein

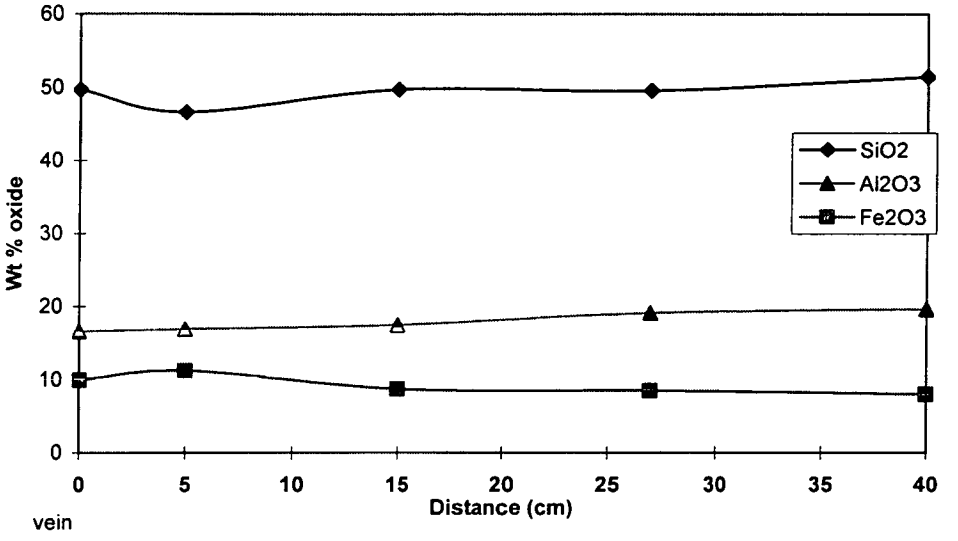

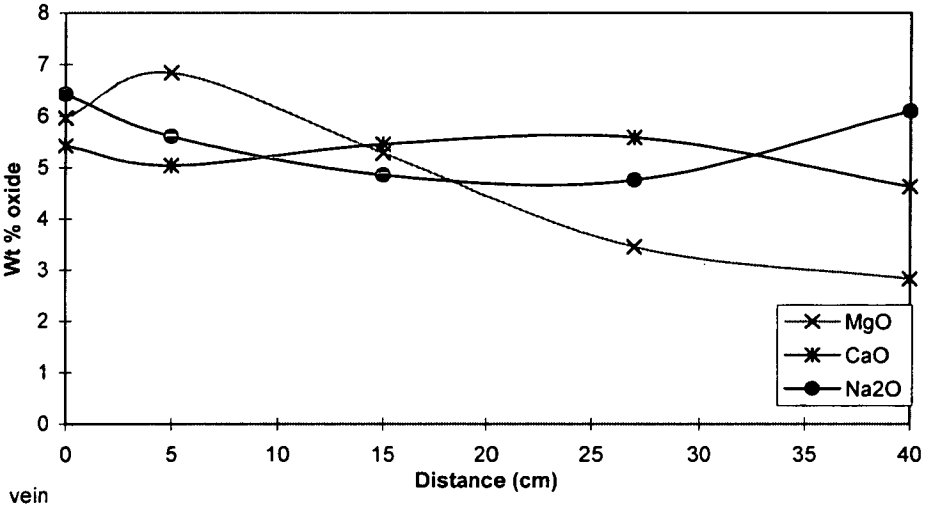

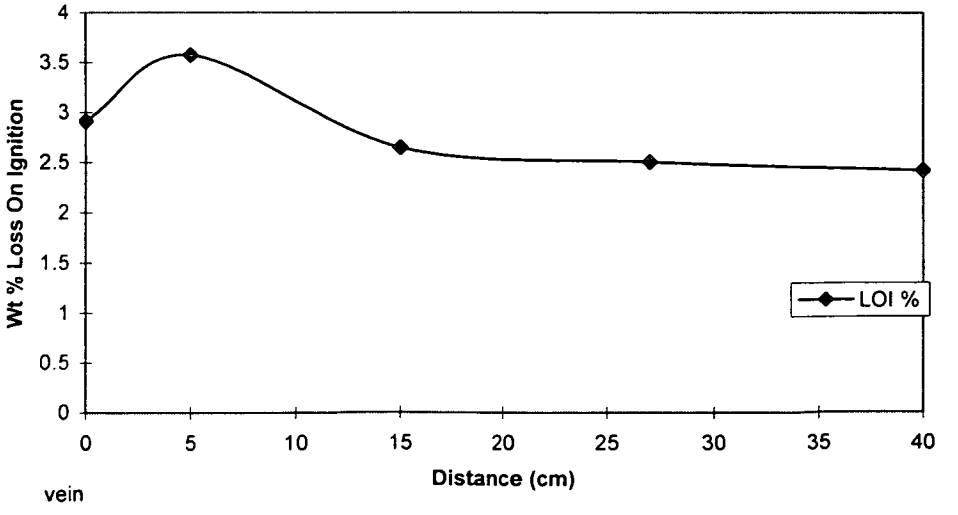

Figure 4.38 Kini S'97/80. Plots of wt % oxide against distance from greenschist vein

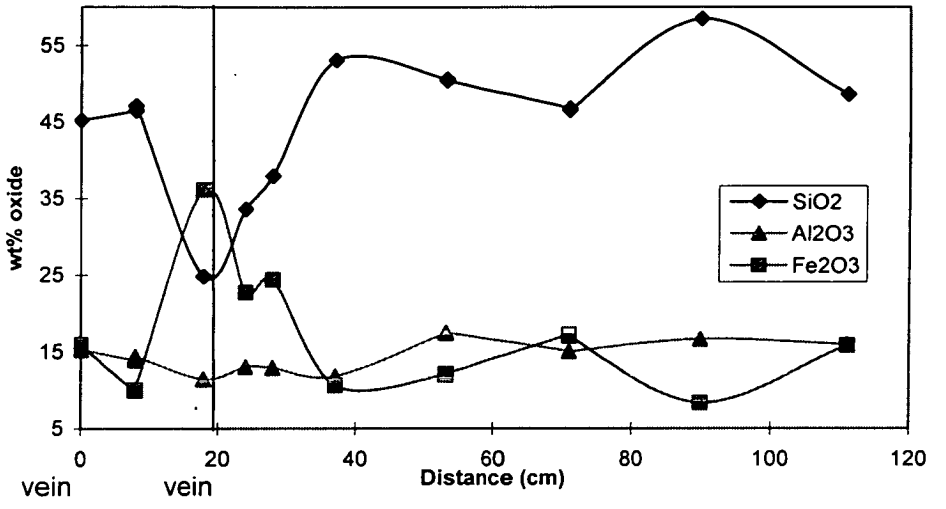

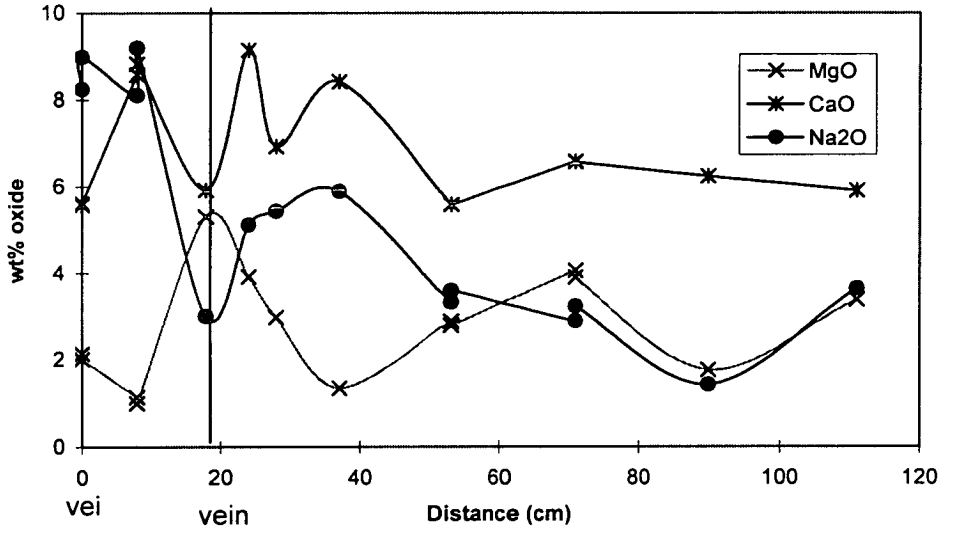

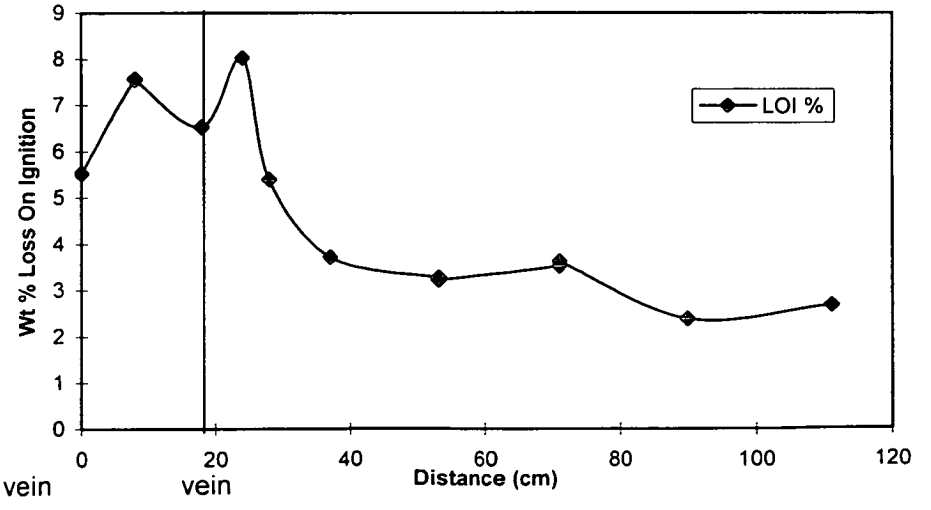

Figure 4.39 Oros Syringas S'97/71. Plots of wt % oxide against distance from greenschist vein

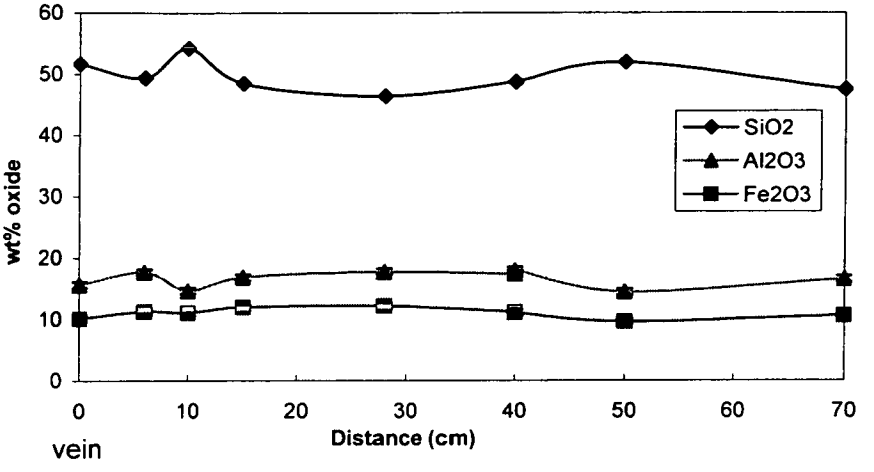

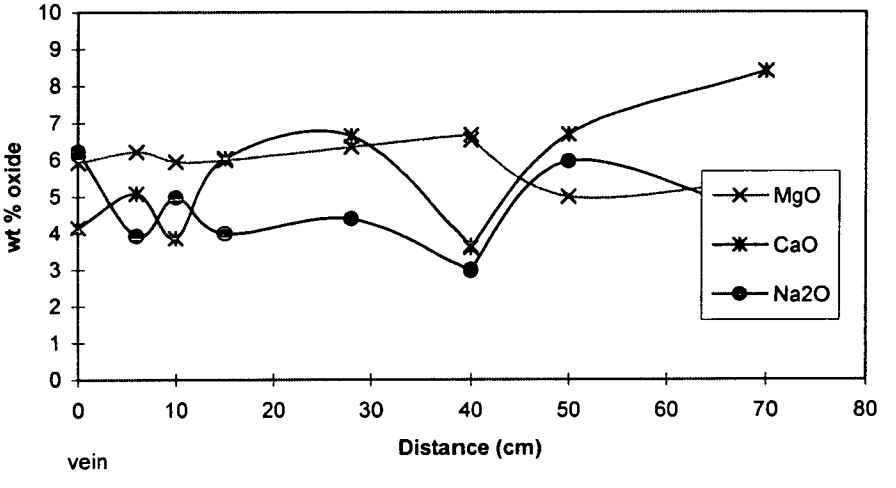

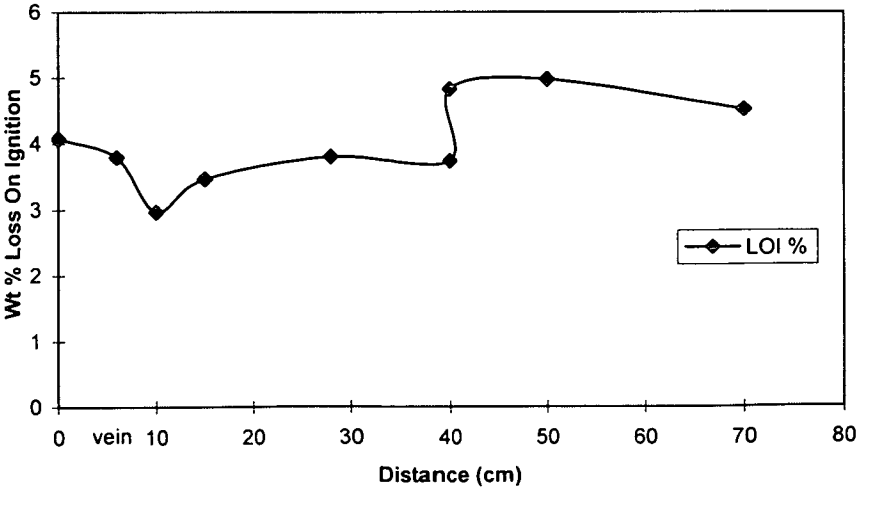

Figure 4.40 Nites S'97/31. Plots of wt% oxide against distance from greenschist vein

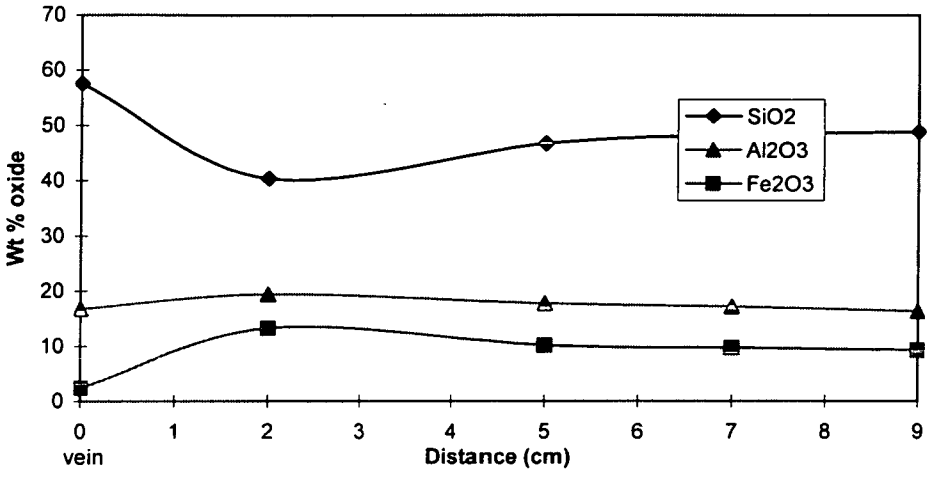

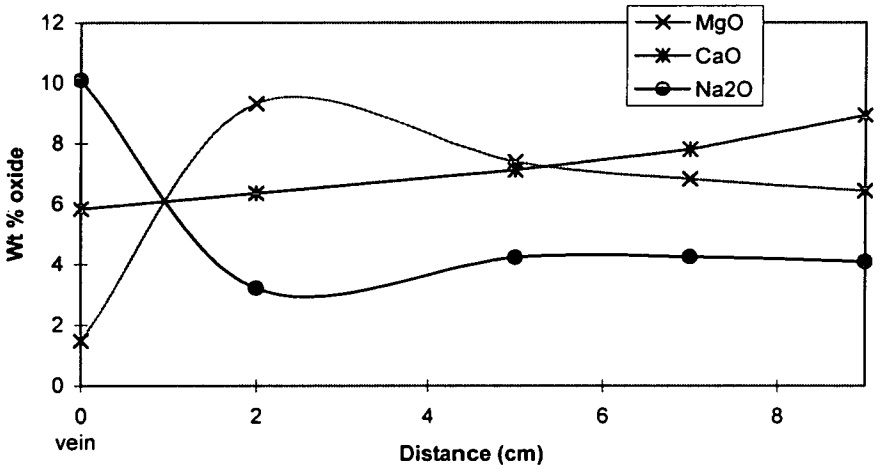

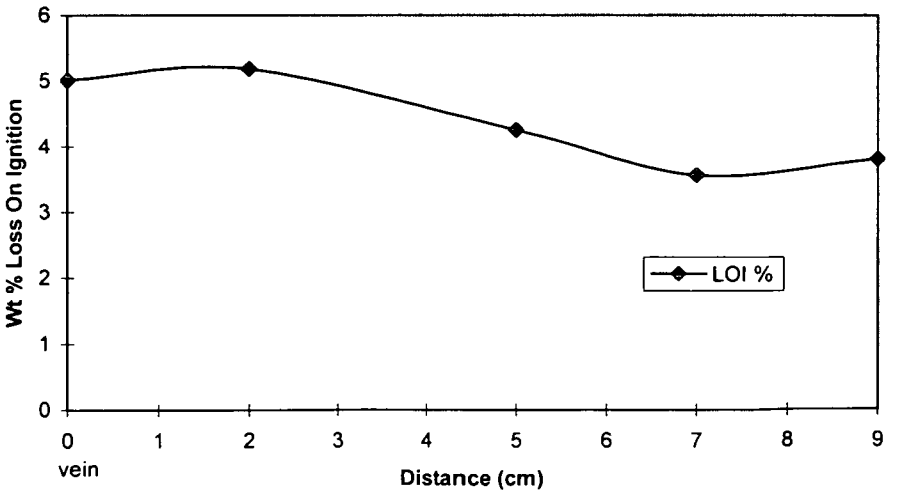

Figure 4.41 Delfini S'97/86. Plots of wt % oxide against distance from intense deformation in a shear zone

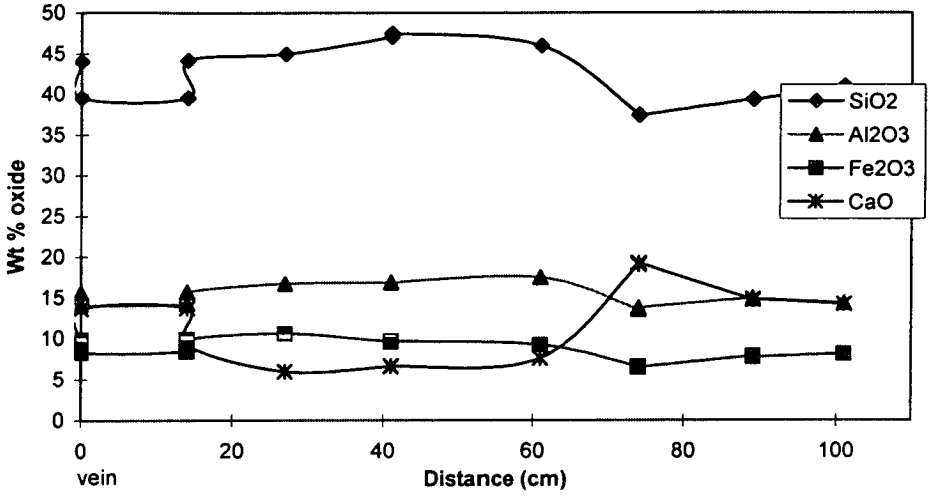

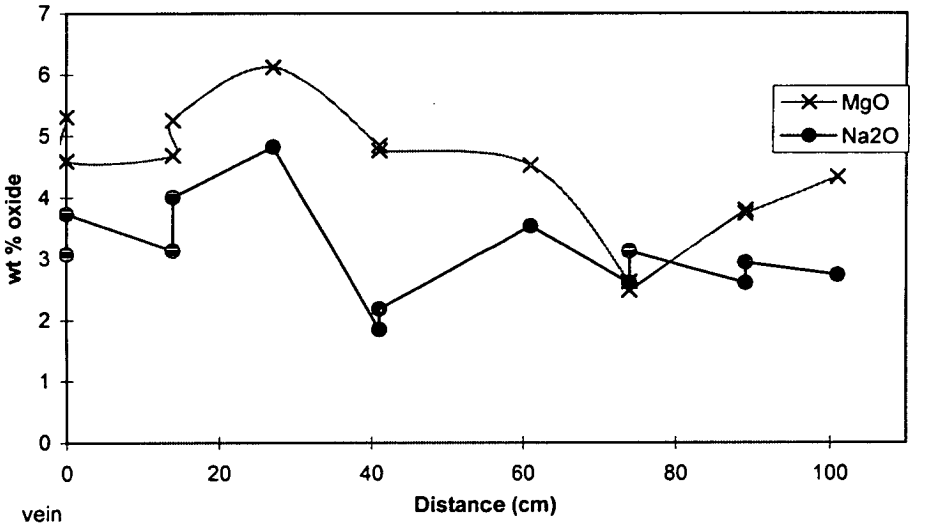

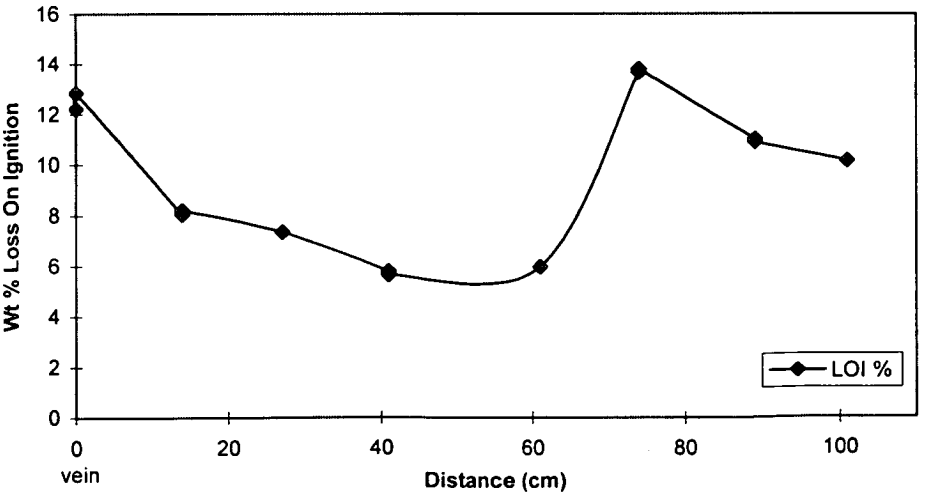

reached.

Figure 4.38, S'97/80 from Kini shows decreases in silica content within a few cms of the vein. A small vein was sampled at a distance of 15 cm from the main vein and this shows a greater depletion of silica around it with a silica alteration halo of approximately 25 cm; this may be an off-shoot from the main vein. An increase in the aluminium content can also be identified within a few cm of the veins. Most notable are the increases of LOI and Na towards the vein. This corresponds well with the metasomatic alteration documented by the isocon plot method and the requirement of a Na-influx to create the albite selvage.

S'97/71, from Oros Syringas (figure 4.39), shows comparatively little exchange and the increase in Na that seemed clear on the isocon plot (figure 4.35) appears not to be a true enrichment of Na around the vein. Instead the traverse shows variability in Na content across the traverse with no systematic trend. This example suggests that interpretation of isocon plots should be treated with care as local variations in the chemical composition of the host rock that cannot be identified in the field or thin section can affect the results. Isocon plots are based solely on two analyses, one of altered and one of unaltered host rock. Their accuracy may be improved if several analyses were made for altered and unaltered host rock so the original chemical heterogeneity of the rock could be assessed.

The sample S'97/31 from Nites (figure 4.40) has both depletion and enrichment of oxides in its alteration halo. The alteration halo is small, but depletion in Fe and Mg is identified within a few cm of the vein and Ca is depleted across the 9 cm traverse. This correlates with calcite mineralisation in the vein. Increase in Na, Si and LOI content are noted within 2 cm of the vein; the increase in Na is inferred to be related to the precipitation of albite porphyroblasts in the vein halo.

Finally a sample traverse starting from the centre of an albitised shear zone was completed (figure 4.41). There are two distinct peaks in the LOI profile, one at the edge of the shear zone where deformation was intense and the other 70 cm into the shear zone where there may have been further intensification of deformation, although it is hard to identify as the outcrop is weathered and the increase of LOI may be related to hydration associated with the weathering. The chemical variation is less systematic, but

the Mg and Na content increase towards the zone of intense deformation at the edge of the shear zone.

Discussion

Metasomatic alteration of vein wall rock, and shear zones has been documented for greenschist grade metamorphism on Syros. Albitisation and retrogressive metamorphism of vein wall rock has also been documented in other regional metamorphic terranes. Notable are the discussions based on the Dalradian schist of Scotland (e.g. Watkins, 1983) and more recently (Ague, 1997), on whether a net influx of Na was required to produce albitisation within the schists. Watkins (1983) analysed zones of albite porphyroblast schist from the central Scottish Dalradian, he found no evidence for influx of Na in zones of albite porhyroblast growth. He proposed that an influx of H_2O-rich fluid had caused a redistribution of Na^+ ions to form the albite schists. In contrast (Ague, 1997) showed Na enrichment around veins in Dalradian schists from NE Scotland to prove that locally infiltration of Na enriched fluids was directly related to albitisation.

Barr (1989) made some bulk chemical analyses on albite-bearing greenschists and unaltered blueschist from Syros. Her results showed no significant difference in Na content between the two lithologies. This study in contrast has shown an increase in volatile content in vein haloes associated with retrogressive reaction to chlorite and that albitisation in mineral selvages is in the majority of examples associated with a net Na-influx. Na has also been enriched in a shear zone that contains a high percentage of albite porphyroblasts. These observations on Syros have documented similar chemical characteristics to those of Ague (1997) for the Dalradian schists, with increases in volatile and Na content in vein alteration haloes.

Greenschist vein haloes that document alteration of glaucophane to chlorite, but show limited growth of albite porphyroblasts in their haloes, have little to no Na influx into the halo. The chemistry of vein haloes implies that to grow albite porphyroblasts on the scale observed in some of the vein haloes on Syros a local influx of Na is required.

Bloor (1998) completed XRF analysis on mineralisation haloes of lawsonite

around early quartz veins observed in the northern greyschists of Syros. He found enrichment in Ca, Al, Si and Mn and depletion in Na and possibly K around veins and related it to the formation of lawsonite by reaction of muscovite:

$$3\ Ca^{2+} + 1\ \text{muscovite} + 1\ H_2O \rightarrow 3\ \text{lawsonite} + 2\ K^+$$

$$3\ Ca^{2+} + 1\ \text{muscovite} + 1\ H_2O \rightarrow 3\ \text{lawsonite} + 2\ Na^+$$

$$1\ Ca^{2+} + 2\ Al^{3+} + 7\ SiO_2 + 2\ H_2O \rightarrow 1\ \text{lawsonite}$$

Bloor discusses the possible sources of fluids to form these early veins and their associated metasomatic alteration haloes. He suggested that the most likely source of fluid deep in subduction zones is from dehydration reactions occurring in the down-going slab. If this is the case then fluid sourced at depth in the subduction zone from dehydration reactions will pass through the material above. It should be possible to build a pattern of mass transport at different stages along the fluid pathway, with each stage influencing the next (figure 4.42). The fluids that infiltrated Syros and promoted lawsonite growth, enriching the rock in Ca, Al, Si, Mn and depleting the rock in Na and K would go on to infiltrate the rocks above. These higher rocks will be at a lower pressure, they can be thought of as analogous to the lower pressure blueschist rocks of Syros documented in this study, metastable under greenschist facies metamorphic conditions. As the fluid infiltrates these metastable blueschist assemblages, they will react to stable greenschist assemblages along fluid pathways, the presence of fluid hydrating the silicates to an equilibrium assemblage. Exchange of chemical species transported in the fluid may take place during this infiltration and reaction.

Figure 4.42 is a schematic sketch of the process. Each "package" of rock will experience all stages of the cycle as it is exhumed. So Syros, our "package", should have passed through every part of the cycle. In an ideal world the rock should document the whole process by superimposition of veining and chemical alteration. Combining the results of this study with those of Bloor (1998), a schematic, and

Figure 4.42
Schematic sketch of fluid-rock interaction during exhumation

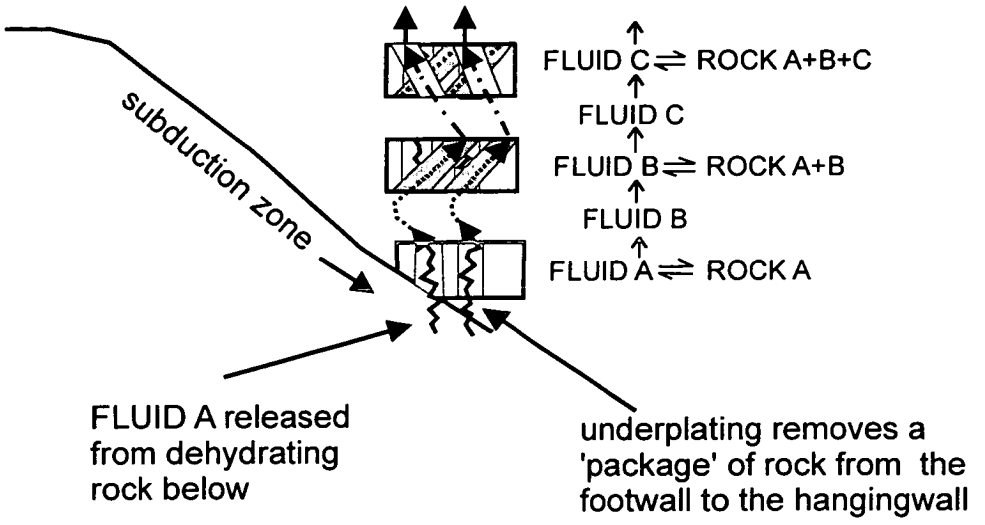

Figure 4.43
Schematic sketch of fluid-rock interaction during exhumation with examples of metasomatic alteration of wall rock and fluid composition from XRF analysis Bloor (1998) and (this study).

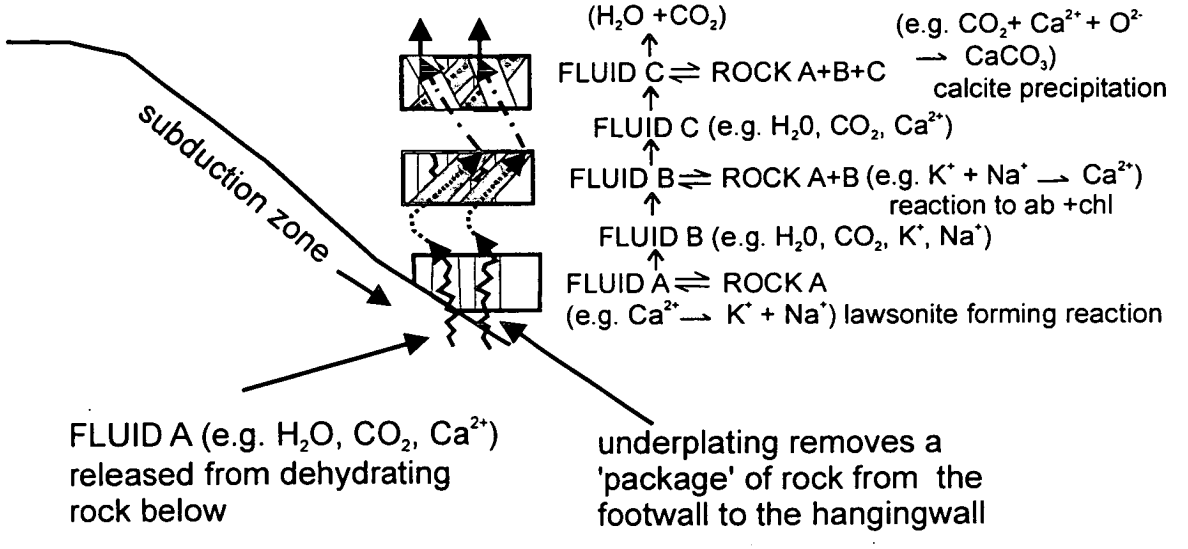

undoubtedly oversimplified, part of the cycle can be established for channelised fluid infiltration in veins (figure 4.43). Such a fluid pathway appears to be the most obvious mechanism for dehydration and rehydration of subducted and exhumed lithologies.

Summary

- Infiltration of fluid and the transport and depletion of elements in vein wall rock has caused localised retrogressive metamorphism to chlorite-bearing assemblages.

- Mass transport has affected the bulk chemical composition of vein wall rock.

- Infiltration of fluid was controlled by deformation enhanced permeability in the form of fractures/veins and by variations in the relative permeability of vein wall rock (fingering of vein haloes around veins), presumably controlled by mineralogy and anisotropy.

- Increases in wt% sodium in vein haloes has lead to the formation of albite porphyroblast selvages around veins.

- Increases in the volatile and Na content in a shear zone, which documents greenschist retrogression and albite porphyroblast growth, suggests retrogression was aided by deformation and fluid infiltration.

4.6 Electron probe analysis of veins and host rock

Following from the XRF work on vein halo metasomatism, three veins were targeted for electron probe analysis of vein mineralogy and alteration of host rock. The three veins targeted were an example of an albite-, chlorite-, Ca-amphibole vein from Kastri (S'95/17), an albite-calcite vein from the Kambos goat cave area (S'95/63) and

an albite-, chlorite-, epidote-vein from the Ermoupolis-Kini road section (S'95/5). A short discussion of the main findings is given below.

Sample S'95/17 is a vein from a greenschist area at Kastri. The vein mineralogy is Ca-amphibole, chlorite and albite. The average compositions of the minerals are shown in table 4.13. Barr (1989) distinguished secondary retrogressive chlorite from primary blueschist chlorite on Syros by chemical composition. The Hey diagram (figure 4.44) shows increasing Fe (total)/ Fe (total) + Mg values for secondary chlorite replacing garnet and glaucophane (Barr, 1989). The composition of chlorite in the vein implies that it is secondary (figure 4.44). The mineralogy of the vein appears to be controlled by the mineralogy of the host rock, with host rock assemblages growing into the vein. Crack-seal events can clearly be identified in the thin section photograph 4.7. The crack-seal events suggest multiple periods of infiltration and fracture to accommodate small increments of extensional strain. Crack-seal textures are seen in many greenschist veins.

For sample S'95/63 from Kambos goat cave, the retrogression in the halo to the vein was targeted, rather than the vein itself. An electron probe traverse was made across a blue amphibole crystal in the halo, the blue amphibole has a dark blue rim. Dark blue rims on amphiboles are fairly common on Syros and are associated with the break down of aegirine augite (Barr, 1989); they are also often found in the haloes to greenschist veins. Brown (1974) and Maruyama et al. (1986) noted that the stability of blue amphibole at the lower pressure end of the blue amphibole stability field is increased by solid solution towards the riebeckitic end member. Grütter (1993) noted dark blue crossitic rims on blue amphiboles on Ios and associated them with post peak decompression.

The grain-scale traverse shows chemical zoning (figure 4.46) of the amphibole, with substitution of Fe^{2+} for Mg^{2+} and Al^{3+} exchange for Fe^{3+}. The graph (figure 4.46) shows an increase in Fe^{2+} towards the rims of the amphibole and a decrease in Fe^{3+}. The zoning in the glaucophane does not show a step like growth and exchange may have been diffusive/metasomatic? The solid solution may have been aided by the influx of volatiles into the halo. XRF data suggest that the fluid was not enriched in Fe (figure 4.30), and the total Fe in the glaucophane has remained approximately constant.

Table 4.13 a Compositions of vein amphiboles, sample S'95/17

Sample	cam	cam	cam	cam	cam	cam	cam	cam	cam	cam	cam
Min	amph	amph	amph	amph	amph	amph	amph	amph	amph	amph	amph
SiO2	53.4	53.3	53.9	54.2	55.9	52.4	52.9	55	51.2	54.7	57.5
TiO2	0.03	0.04	0.06	0.07	0.04	0.04	0.06	0.06	0.07	0.05	0.01
Al2O3	1.74	2.04	3.13	2.06	9.55	2.26	2.21	1.3	1.95	2.57	10.1
Cr2O3	0	0	0	0	0	0	0	0	0	0	0
Fe2O3	2.3	2.93	0.31	1.43	2.36	3	2.25	2.16	2.63	1.1	1.19
FeO	9.9	10.33	13.08	13.9	7.48	14.37	14.81	12.9	14.34	12.22	8.11
MnO	0.32	0.33	0.33	0.39	0.1	0.54	0.47	0.39	0.43	0.33	0.1
MgO	15.4	14.9	12.7	13.3	11.4	12.5	12.3	14.6	12.8	13.6	11.4
CaO	10.5	10.4	9.13	10.1	2.06	10.5	10.4	10.8	9.95	10.3	0.97
Na2O	1.46	1.68	1.96	1.56	6.47	1.47	1.48	1.38	1.76	1.85	6.72
K2O	0.09	0.09	0.1	0.15	0.04	0.16	0.14	0.1	0.13	0.08	0.02
Totals	95.14	96.05	94.71	97.16	95.4	97.24	97.02	98.68	95.26	96.81	96.11
Oxygens	23	23	23	23	23	23	23	23	23	23	23
Si	7.836	7.782	7.963	7.891	7.876	7.72	7.793	7.874	7.707	7.917	7.985
Ti	0.003	0.004	0.007	0.008	0.005	0.004	0.007	0.006	0.008	0.006	0.001
Al	0.301	0.351	0.545	0.354	1.586	0.393	0.384	0.219	0.346	0.439	1.653
Cr	0	0	0	0	0	0	0	0	0	0	0
Fe3	0.254	0.322	0.034	0.157	0.25	0.332	0.249	0.233	0.298	0.119	0.124
Fe2	1.215	1.261	1.617	1.693	0.881	1.771	1.825	1.544	1.805	1.479	0.941
Mn	0.04	0.041	0.041	0.047	0.012	0.068	0.059	0.048	0.055	0.041	0.011
Mg	3.368	3.242	2.796	2.886	2.394	2.744	2.701	3.115	2.871	2.933	2.359
Ca	1.651	1.627	1.445	1.576	0.311	1.657	1.642	1.657	1.605	1.597	0.144
Na	0.416	0.476	0.562	0.44	1.768	0.421	0.423	0.382	0.513	0.521	1.81
K	0.016	0.017	0.019	0.029	0.007	0.029	0.026	0.017	0.025	0.015	0.003
Sum	15.1	15.124	15.031	15.08	15.089	15.139	15.108	15.094	15.232	15.067	15.032

Table 4.13 b Compositions of vein chlorite, sample S'95/17

Sample	chl	chl	chl	chl	chl	chl	chl	chl	chl
Min	chl	chl	chl	chl	chl	chl	chl	chl	chl
SiO2	27.19	30.14	29.29	26.35	29.65	27.3	29.13	27.86	27.33
TiO2	0.03	0.03	0.05	0.02	0.02	0.03	0.02	0.03	0.03
Al2O3	17.9	19.5	18.1	17.2	19.2	17.8	18.7	17.3	17.6
Cr2O3	0	0	0	0	0	0	0	0	0
Fe2O3	0.32	0	0	4.9	0	0	0	2.39	0.44
FeO	22.54	22.34	22.45	17.62	22.74	23.02	22.59	19.64	22.24
MnO	0.45	0.4	0.41	0.4	0.41	0.41	0.41	0.38	0.45
MgO	17.9	19.5	18.3	20.3	18.1	17.6	19.2	18.7	18.2
CaO	0.04	0.04	0.07	0.04	0.02	0.04	0.02	0.05	0.05
Na2O	0.03	0.09	0.03	0.03	0.02	0.02	0.01	0.6	0.02
K2O	0.03	0.04	0.05	0.03	0.01	0.01	0.03	0.04	0.03
Totals	86.43	92.08	88.74	86.88	90.17	86.23	90.12	86.98	86.38
Oxygen	14	14	14	14	14	14	14	14	14
Si	2.874	2.95	2.989	2.751	2.972	2.895	2.928	2.904	2.887
Ti	0.003	0.002	0.004	0.001	0.001	0.002	0.002	0.002	0.002
Al	2.231	2.25	2.178	2.117	2.269	2.225	2.216	2.126	2.192
Cr	0	0	0	0	0	0	0	0	0
Fe3	0.026	0	0	0.385	0	0	0	0.188	0.035
Fe2	1.993	1.829	1.916	1.539	1.906	2.042	1.899	1.712	1.965
Mn	0.04	0.033	0.036	0.035	0.035	0.036	0.035	0.033	0.04
Mg	2.82	2.844	2.783	3.159	2.704	2.782	2.876	2.905	2.866
Ca	0.005	0.004	0.008	0.004	0.002	0.005	0.002	0.006	0.006
Na	0.007	0.017	0.005	0.005	0.004	0.005	0.002	0.12	0.003
K	0.003	0.005	0.006	0.004	0.001	0.001	0.004	0.005	0.003
Sum	10	10	10	10	10	10	10	10	10

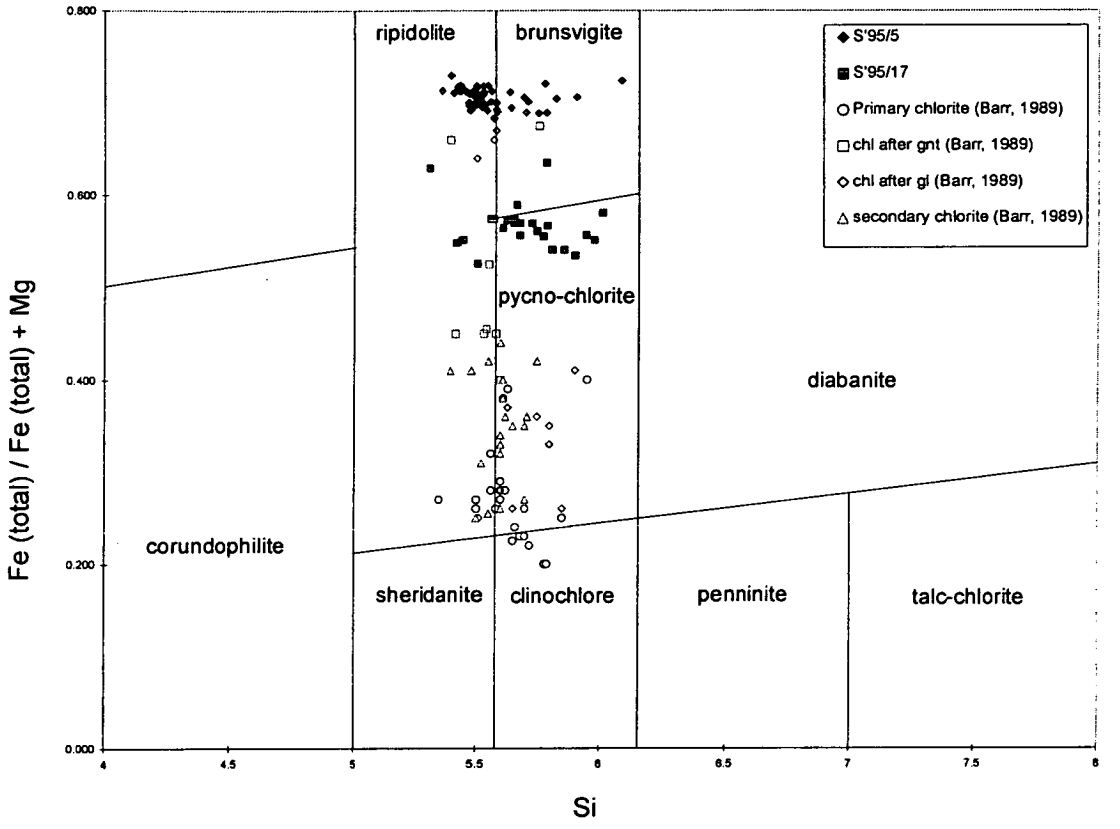

Figure 4.44 Chlorite compositions plotted on a Hey diagram (Hey, 1954). The plot shows data from the study of Barr (1989) of primary and secondary chlorite and chlorite from this study from retrogressive veins.

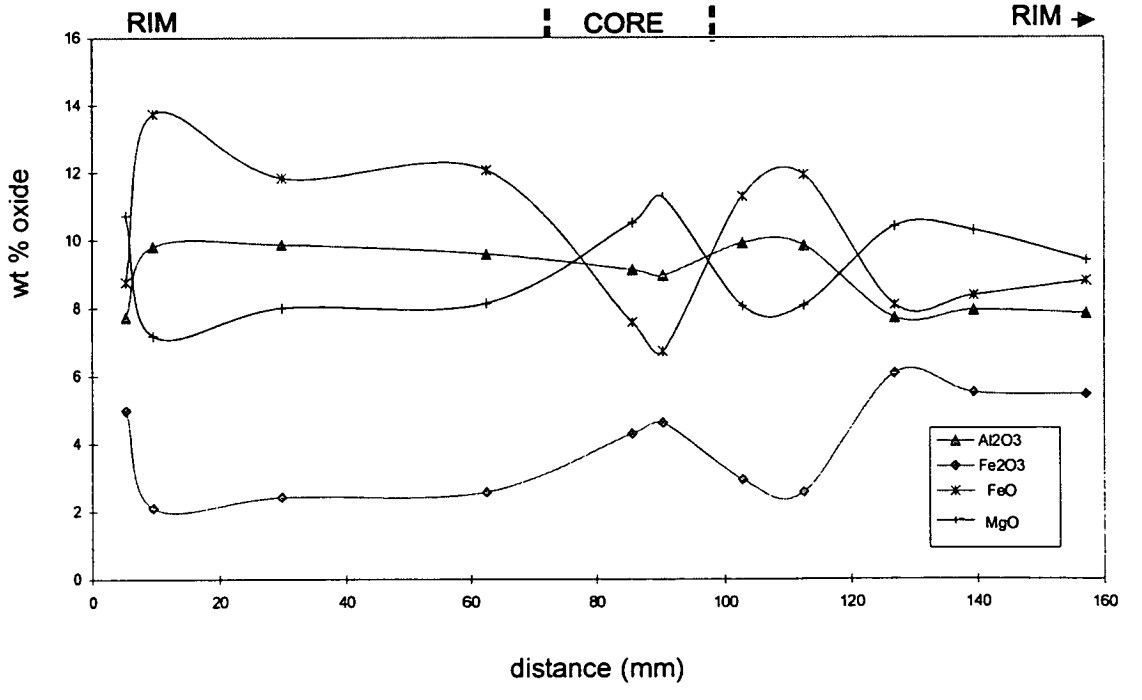

Figure 4.45 Electron probe traverse across amphibole crystal, sample S'95/63.

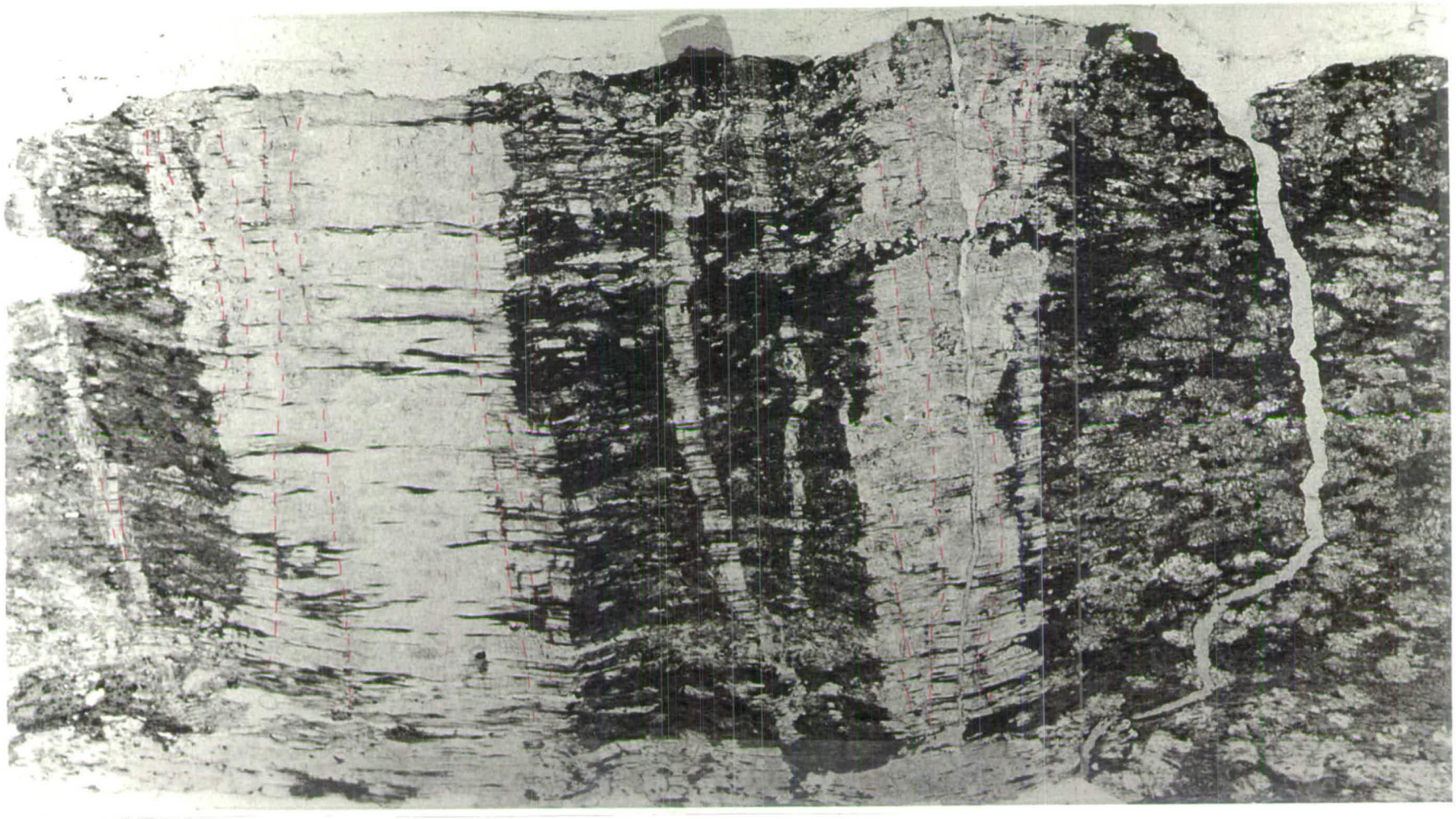

Photograph 4.7
Black and white photograph of albite-, chlorite-, Ca-amphibole veins. The crack-seal events are marked in red. Albite porphyroblasts (pale areas) can be seen on the right handside. Field of view approximately 4 cm wide.

Similar amphibole zoning is identified in blue amphibole growing into an epidote-, albite-, chlorite-vein from the Ermoupolis-Kini road section, sample S'95/5. However, in this sample the total Fe content changes between the original amphibole and the new growth into the vein. The vein from the Ermoupolis-Kini road section (photograph 4.8) contains chlorite-, albite- and epidote, the average compositions of which are shown in Table 4.14. The chlorite in the vein has a secondary chlorite composition, sample S'95/5 (figure 4.44). Thin section observations of the host rock show alteration of glaucophane to chlorite. The glaucophanes are also chemically altered at their rims and where they have grown into the vein.

Traverses of three glaucophanes were made adjacent to the vein across blue amphiboles that appear to have grown into the vein (photograph 4.8). Photographs 4.9-4.11, show the glaucophane crystals and traverses made. The results are plotted in figures 4.46-4.48. The three glaucophanes adjacent to the vein show increases in Fe^{2+} and decreases in Mg^{2+} content where they have grown into the vein. The chemical zoning correlates with observed darkening of the glaucophane crystals viewed in plane polarised light (PPL) (photographs 4.9-4.11). The blue amphibole, S'95/5 (C), (photograph 4.9 and figure 4.46) shows a minor increase in Ca^{2+} content at the edge of the rim, which is coupled with a decrease in Na^{+} and decreases in Fe^{2+} and an increase in Mg^{2+}. The growth of crossitic amphibole into the vein is identified chemically and by the change in glaucophane colour to deep blue in PPL. The blue amphiboles in the surrounding wall rock (photograph 4.12) are also rimmed with dark blue amphibole. However in these example the rim appears to be more diffusive/metasomatic as in sample S'95/63, rather than new growth. These characteristics are seen in other thin sections where the retrogression is not spatially associated with veins (e.g. glaucophanes at Diapori).

The core and rim (growth into the vein) compositions are plotted on a Miyashiro diagram to show the increase in riebeckite content of the new growth into the veins. The Miyashiro plot (figure 4.49) shows Fe-rich crossite growth of amphibole into the vein, whilst the cores contain relatively less Fe. The growth of crossite into a vein which has a greenschist composition of albite-, chlorite- and epidote, suggests that this growth was 'metastable'. The amphibole is never seen to be in direct contact with chlorite, only

Table 4.14 a Compositions of chlorite from the vein, sample S'95/5

Sample	chl	chl	chl	chl	chl	chl	chl	chl	chl	chl	chl	chl	chl	chl	chl	chl	chl	chl	chl	chl
Min	chl	chl	chl	chl	chl	chl	chl	chl	chl	chl	chl	chl	chl	chl	chl	chl	chl	chl	chl	chl
SiO2	24.89	24.92	26.57	24.68	24.74	24.55	24.55	24.53	25.21	25.29	25.05	24.52	26.13	24.45	24.83	25.14	25.08	25.02	25.07	24.27
TiO2	0.03	0.04	0.07	0.04	0.04	0.03	0.04	0.02	0.03	0.03	0.04	0.03	0.06	0.04	0.04	0.04	0.04	0.04	0.04	0.05
Al2O3	17.78	17.59	17.3	17.83	17.73	17.64	17.67	17.76	18.15	17.96	17.67	17.78	17.37	17.72	17.72	17.69	17.69	17.69	17.93	17.7
Cr2O3	0	0	0	0	0	0	0	0	0	0	0	0	0	0	0	0	0	0	0	0
Fe2O3	2.14	2.08	0	2.57	2.45	3.29	3.14	3.14	1.67	2.71	2.29	2.76	0.06	3.65	2.7	2.17	1.54	2.16	2.11	3.88
FeO	28.23	28.58	29.48	28.23	28.14	28.07	27.91	28.19	28.96	27.98	28.43	28.23	30.14	27.15	27.81	28.34	28.5	28.32	28.44	26.88
MnO	0.59	0.58	0.56	0.56	0.59	0.62	0.55	0.53	0.51	0.53	0.55	0.57	0.57	0.56	0.49	0.48	0.49	0.52	0.52	0.57
MgO	12.5	12.35	12.36	12.47	12.54	12.26	12.51	12.34	12.6	13.15	12.42	12.31	11.7	12.51	12.94	12.79	12.64	12.73	12.76	13
CaO	0.03	0.03	0.06	0.01	0.02	0.05	0.02	0.04	0.02	0.04	0.02	0.01	0.07	0.03	0.03	0.03	0.03	0.02	0.01	0.02
Na2O	0.04	0	0.05	0.01	0.01	0.04	0.02	0.02	0.01	0.02	0.03	0.02	0.03	0.16	0	0.02	0.01	0.01	0.01	0.01
K2O	0.02	0.06	0.37	0.02	0.01	0.06	0.04	0.03	0.01	0.07	0.12	0.01	0.37	0.02	0.01	0.03	0	0.01	0.01	0.01
Totals	86.24	86.23	86.82	86.42	86.27	86.61	86.44	86.61	87.15	87.78	86.64	86.23	86.5	86.3	86.57	86.73	86.02	86.52	86.9	86.38
Oxygens	14	14	14	14	14	14	14	14	14	14	14	14	14	14	14	14	14	14	14	14
Si	2.754	2.764	2.912	2.73	2.74	2.718	2.718	2.714	2.759	2.745	2.764	2.722	2.89	2.707	2.735	2.764	2.779	2.759	2.752	2.682
Ti	0.002	0.004	0.006	0.003	0.003	0.003	0.004	0.002	0.002	0.002	0.003	0.003	0.005	0.003	0.003	0.003	0.003	0.003	0.004	0.004
Al	2.32	2.299	2.236	2.325	2.315	2.302	2.306	2.316	2.342	2.298	2.299	2.327	2.265	2.312	2.301	2.294	2.311	2.299	2.32	2.307
Cr	0	0	0	0	0	0	0	0	0	0	0	0	0	0	0	0	0	0	0	0
Fe3	0.178	0.173	0	0.214	0.204	0.274	0.261	0.262	0.137	0.221	0.19	0.23	0.005	0.304	0.224	0.18	0.129	0.18	0.174	0.322
Fe2	2.613	2.651	2.702	2.611	2.606	2.599	2.584	2.609	2.651	2.539	2.623	2.621	2.788	2.514	2.562	2.606	2.641	2.612	2.61	2.485
Mn	0.056	0.055	0.052	0.053	0.056	0.058	0.051	0.05	0.047	0.048	0.052	0.054	0.053	0.053	0.046	0.045	0.046	0.049	0.049	0.054
Mg	2.062	2.041	2.019	2.056	2.07	2.023	2.063	2.034	2.056	2.127	2.042	2.036	1.928	2.064	2.125	2.096	2.087	2.093	2.088	2.141
Ca	0.003	0.003	0.006	0.002	0.002	0.006	0.002	0.004	0.002	0.005	0.003	0.001	0.009	0.004	0.003	0.004	0.004	0.002	0.001	0.002
Na	0.009	0.001	0.011	0.003	0.003	0.009	0.004	0.005	0.002	0.005	0.007	0.005	0.006	0.035	0	0.005	0.002	0.002	0.002	0.001
K	0.003	0.008	0.052	0.002	0.002	0.009	0.006	0.005	0,001	0.009	0.017	0.001	0.052	0.003	0.001	0.004	0	0.001	0.002	0.001
Sum	10	10	10	10	10	10	10	10	10	10	10	10	10	10	10	10	10	10	10	10

Sample	chl	chl	chl	chl	chl	chl	chl	chl	chl	chl	chl
Min	chl	chl	chl	chl	chl	chl	chl	chl	chl	chl	chl
SiO2	24.97	25.15	24.83	25.3	25.48	25.43	25.63	24.85	25.1	24.89	25
TiO2	0.05	0.04	0.05	0.04	0.02	0.03	0.04	0.03	0.03	0.04	0.04
Al2O3	17.86	17.88	17.84	17.8	17.87	17.72	18.24	17.83	17.87	17.72	17.9
Cr2O3	0	0	0	0	0	0	0	0	0	0	0
Fe2O3	2.35	2.47	2.52	1.38	1.47	1.77	1.91	2.65	2.24	2.26	2.17
FeO	27.86	27.35	27.74	28.54	28.21	27.95	28.52	27.87	27.89	28.3	28.52
MnO	0.56	0.56	0.57	0.47	0.46	0.45	0.54	0.51	0.53	0.53	0.55
MgO	12.95	13.46	12.85	12.67	13.09	13.01	13.27	12.86	13.01	12.64	12.62
CaO	0.03	0.01	0.03	0.05	0.05	0.08	0.04	0.03	0.03	0.02	0.04
Na2O	0.01	0	0.04	0.01	0	0.04	0	0.02	0.02	0	0.01
K2O	0.01	0.02	0.01	0.08	0.08	0.12	0.03	0.02	0.03	0.02	0.01
Totals	86.65	86.95	86.47	86.34	86.73	86.6	88.22	86.64	86.75	86.42	86.87
Oxygens	14	14	14	14	14	14	14	14	14	14	14
Si	2.744	2.746	2.737	2.79	2.79	2.79	2.763	2.735	2.754	2.75	2.748
Ti	0.004	0.003	0.004	0.003	0.002	0.003	0.003	0.002	0.002	0.004	0.003
Al	2.314	2.302	2.318	2.314	2.307	2.292	2.318	2.313	2.311	2.308	2.32
Cr	0	0	0	0	0	0	0	0	0	0	0
Fe3	0.194	0.203	0.209	0.114	0.121	0.146	0.155	0.219	0.185	0.188	0.18
Fe2	2.561	2.498	2.557	2.633	2.584	2.565	2.571	2.565	2.559	2.615	2.622
Mn	0.052	0.052	0.053	0.044	0.043	0.042	0.049	0.047	0.049	0.049	0.051
Mg	2.121	2.191	2.11	2.082	2.136	2.128	2.132	2.108	2.127	2.081	2.067
Ca	0.004	0.002	0.003	0.006	0.006	0.01	0.004	0.004	0.004	0.002	0.005
Na	0.003	0	0.008	0.003	0.001	0.008	0.001	0.004	0.004	0	0.001
K	0.002	0.003	0.001	0.012	0.011	0.016	0.004	0.003	0.004	0.003	0.002
Sum	10	10	10	10	10	10	10	10	10	10	10

Table 4.14 b Composition of albite in the vein, sample S'95/5

Sample	ab	ab
Min	fsp	fsp
SiO2	69.99	68.36
TiO2	0.02	0.02
Al2O3	20.82	19.29
Cr2O3	0	0
Fe2O3	0.19	0.04
FeO	0	0
MnO	0.02	0
MgO	0.01	0.02
CaO	0.07	0.04
Na2O	7.43	11.71
K2O	0.02	0.02
Totals	98.58	99.51
Oxygens	8	8
Si	3.037	2.999
Ti	0.001	0.001
Al	1.065	0.997
Cr	0	0
Fe3	0.006	0.001
Fe2	0	0
Mn	0.001	0
Mg	0.001	0.001
Ca	0.003	0.002
Na	0.626	0.996
K	0.001	0.001
Sum	4.74	5.00

Table 4.14 c Compositions of epidote in the vein, sample S'95/5

Sample	ep	ep
Min	ep	ep
SiO2	35.61	35.92
TiO2	0.15	0.09
Al2O3	19.79	20.73
Cr2O3	0	0
Fe2O3	14.22	13.04
FeO	0	0
MnO	0.76	0.53
MgO	0.01	0.03
CaO	21.94	22.39
Na2O	0.01	0
K2O	0	0.01
Totals	93.83	93.91
Oxygens	12.5	12.5
Si	3.04	3.04
Ti	0.01	0.01
Al	1.49	1.55
Cr	0.00	0.00
Fe3	0.91	0.83
Fe2	0.00	0.00
Mn	0.02	0.02
Mg	0.00	0.00
Ca	1.00	1.01
Na	0.00	0.00
K	0.00	0.00
Sum	6.48	6.46

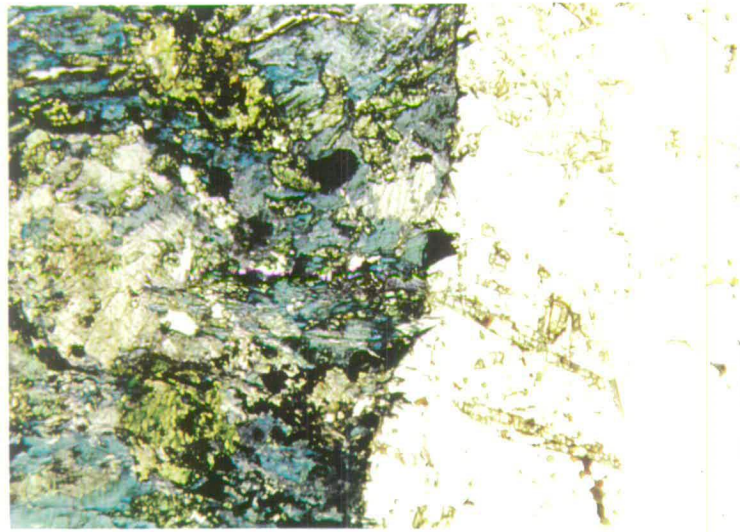

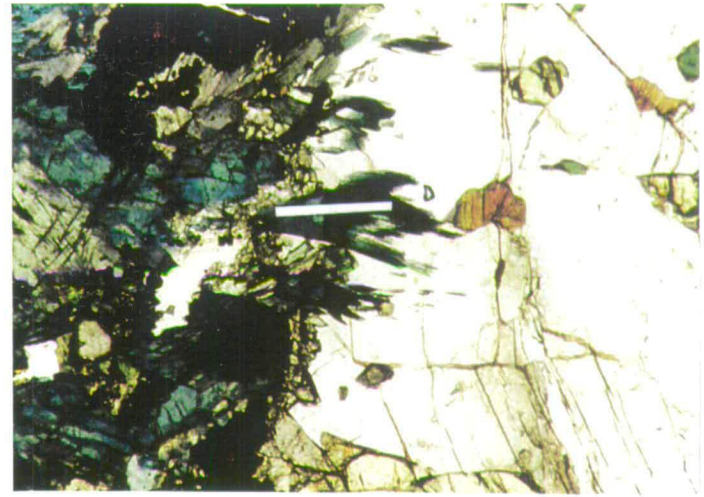
D

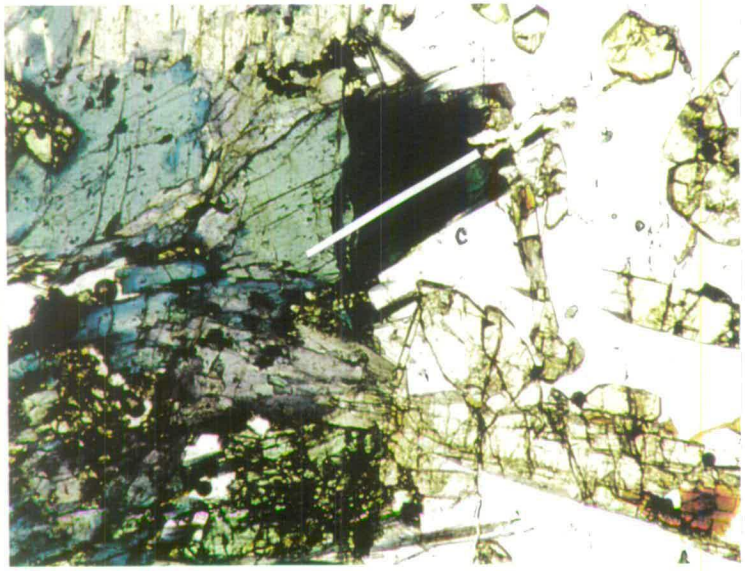
C
A


E'

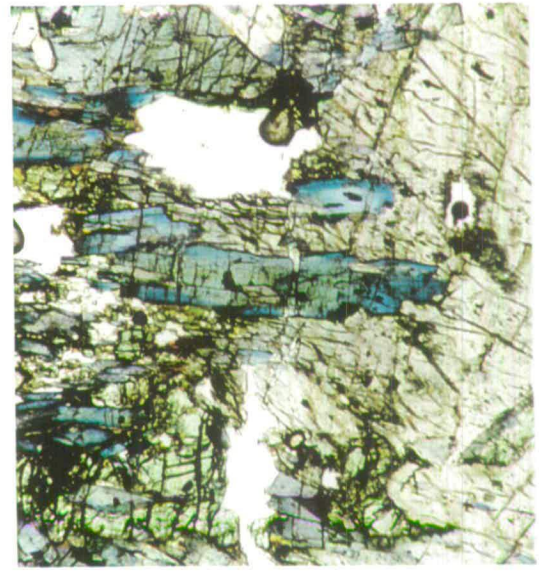

Photograph 4.8
Thin section photograph of vein and wall rock in S'95/5. The vein is on the right handside and contains, albite, chlorite and epidote. Dark blue amphibole can be seen growing into the vein from the wall rock.
Field of view approximately 1 cm wide.

Photograph 4.10
Thin section photograph of vein and wall rock in S'95/5. The blue amphibole (D) growing into the vein, is dark blue. The location of the electron probe traverse shown in figure 4.47 is annotated with a white line; the traverse is 475 μm long.

Photograph 4.9
Thin section photograph of vein and wall rock in S'95/5. The blue amphibole (C) growing in to the vein, shows dark blue growth into the vein. The electron probe traverse figure 4.46 is shown by a white line; the traverse is 1000 μm long.

Photograph 4.11
Thin section photograph of vein and wall rock in S'95/5. The blue amphibole (E) growing into the vein, is dark blue. The location of the electron probe traverse shown in figure 4.48 is annotated with a white line; the traverse is 180 μm long.

Photograph 4.12
Thin section photograph of the vein wall rock in S'95/5. The blue amphiboles are rimmed with dark blue amphibole.

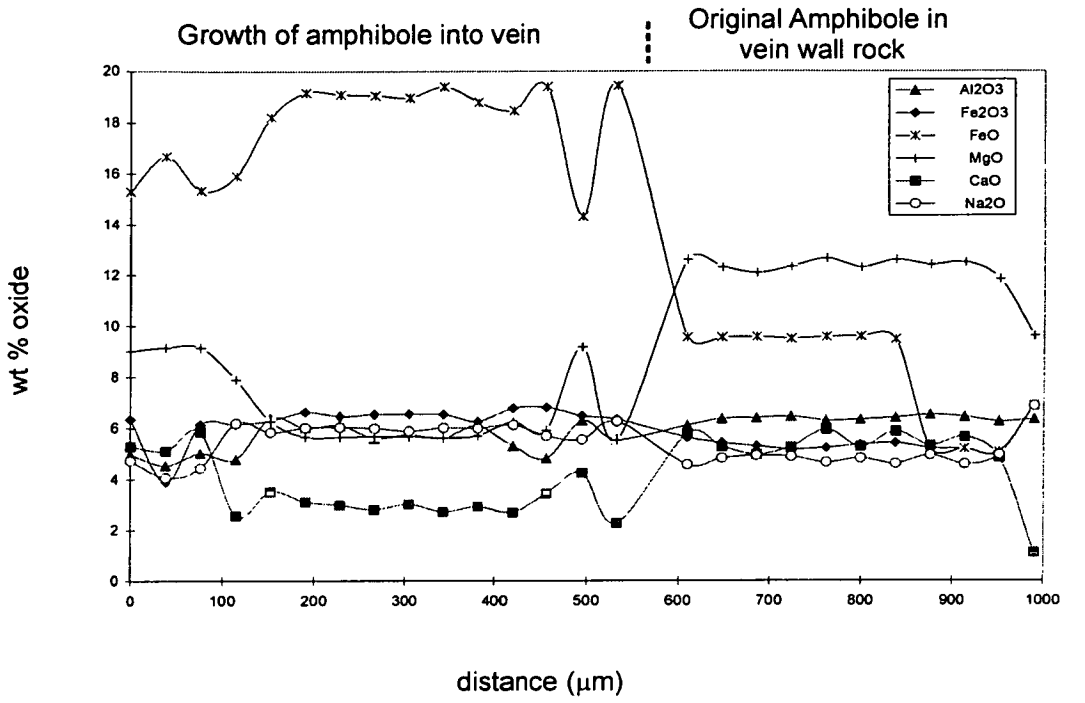

Figure 4.46 Electron probe traverse across amphibole crystal C, sample S'95/5. See photograph 4.9 for location of the traverse.

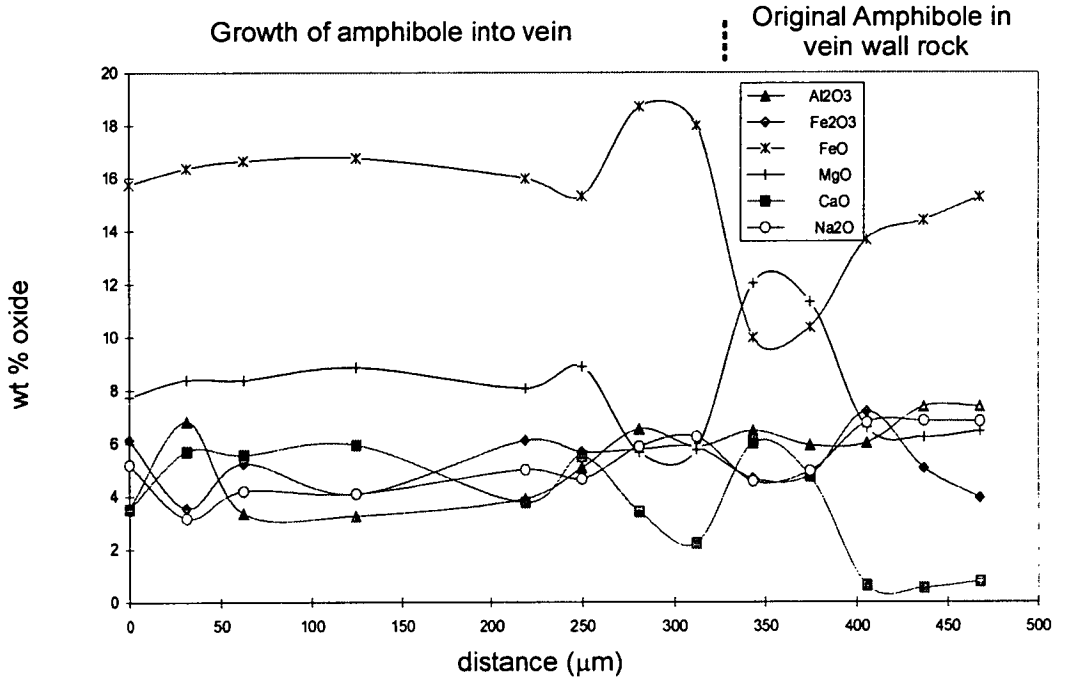

Figure 4.47 Electron probe traverse across amphibole crystal D, sample S'95/5. See photograph 4.10 for location of the traverse.

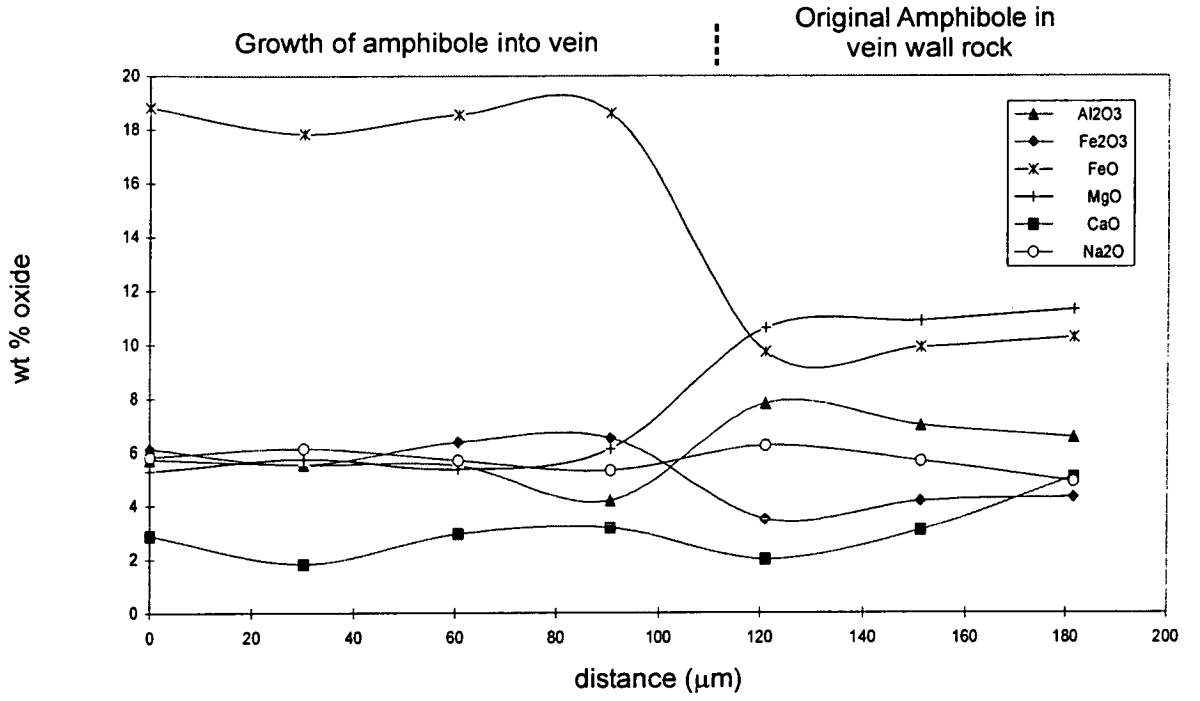

Figure 4.48 Electron probe traverse across amphibole crystal E, sample S'95/5.

See photograph 4.11 for location of the traverse.

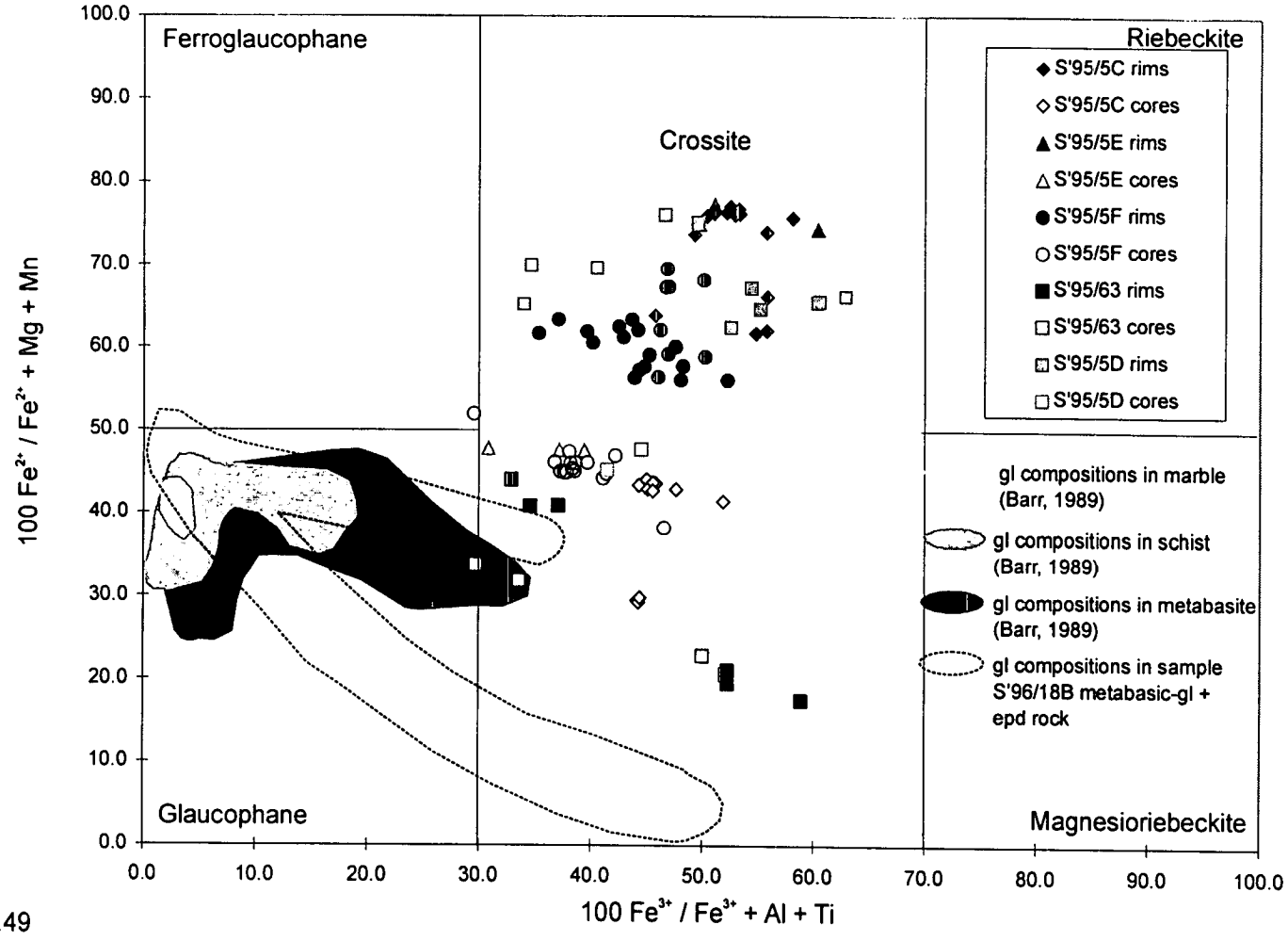

Figure 4.49

Miyashiro plot (Miyashiro, 1957) of sodic amphiboles. The analyses plotted are from the haloes of retrogressive veins. Note the increase in riebeckitic content at the rims of the amphiboles (filled symbols). Sample S'95/5 is from a metabasite and the amphiboles are richer in Fe than those in sample S'95/63 a schist. The shaded areas denote compositions of glaucophane from Barr (1989). The dashed line outlines the compositions of glaucophane in sample S'96/18B a glaucophane-epidote rock.from Kini.

albite in the vein. The increase in total Fe content may be the result of an influx of Fe in the vein, particularly as the composition of chlorite in the vein is Fe-rich (figure 4.44). An Fe-rich fluid could have resulted in the growth of the Fe-enriched amphibole. However, other examples of dark blue amphibole growth on the rims of pre-existing amphiboles, rather than diffusive/metasomatic exchange, that do not grow into veins require the reaction of other phases, such as that below:

$$3\ \text{Paragonite} + 9\ \text{Hematite} + 16\ SiO_2 + 13\ H_2O \rightarrow 3\ \text{Riebeckite} + 2\ \text{Chlorite}.$$

This reaction requires the influx of fluid and the presence of oxidised Fe as hematite.

Maruyama et al. (1986) showed that the changing composition of glaucophane can be used as a geobarometer. The affect of glaucophane composition on the placement of the blueschist-greenschist transition reaction was also highlighted by Evans (1990) (figure 4.50). The PT plots in figure 4.50 show the effect of glaucophane composition on the position of the blueschist-greenschist reaction line and the shape and size of the epidote-blueschist field. The small number of glaucophane analyses made in this study combined with those of Barr (1989), span a range of composition (figure 4.50), which includes five of the six compositions modelled by Evans (1990). Compositions 3 and 6 from Evans (1990) were chosen to represent the original amphibole composition and the new growth of the amphibole into the vein, respectively in sample S'95/5.

The PT plots (figure 4.50) based on these compositions document a 2 kbar difference in the placement of the blueschist-greenschist reaction line. Variation in whole rock composition, would result in the stability of both greenschist and blueschist assemblages in the rock sequence, within this 2 kbar range. The growth of crossite into the albite- and chlorite-bearing vein suggests that this new growth into the vein was metastable.

The glaucophane data of Barr (1989) are also shown on the Miyashiro plot (figure 4.49). Barr's data record amphiboles with a lower Fe content than samples S'95/5 or S'95/63. Metabasite samples show a broader range in composition including more Fe rich compositions. Barr found that core to rim zonations of amphiboles were

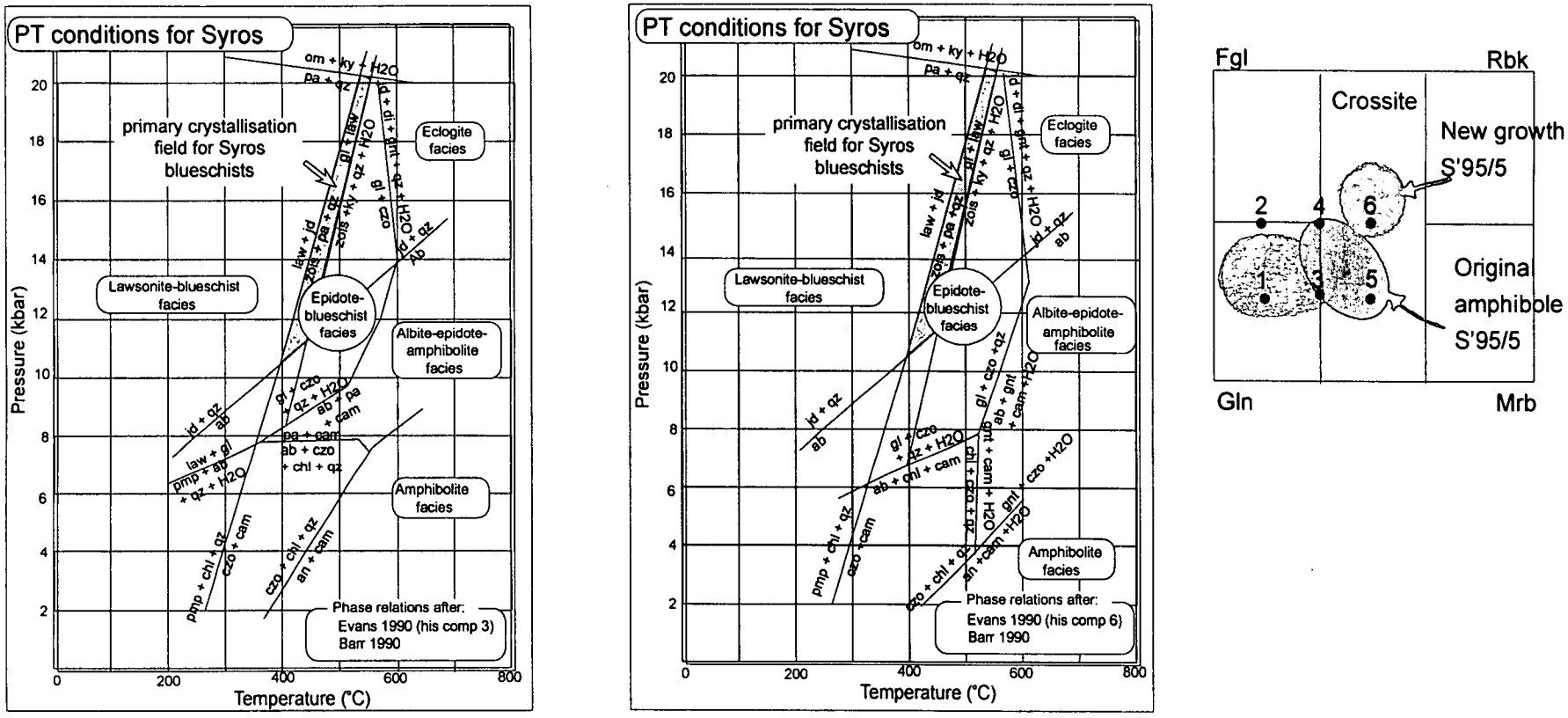

Figure 4.50

The diagram shows 2 PT plots for Syros. The shape and size of the epidote-blueschist field in the 2 plots have been determined using the compositions of Evans (1990), the primary field of crystallisation for Syros blueschist is from Barr (1990). The plots are for the glaucophane compositions 3 and 6 respectively (left-right) as seen in the right hand diagram redrawn from Evans (1990). The area shaded pale grey in this diagram outlines the compositions of glaucophanes analysed by Barr (1990). The darker shaded areas denote original and new growth compositions of glaucophane crystals in sample S'95/5 surrounding a retrogressive vein.

not systematic and did not record down-pressure crystallisation. The data of Barr are more comparable to the amphibole compositions of sample S'96/18B a glaucophane-epidote rock from Kini (figure 4.49). The sample records lower Fe-amphibole contents than samples S'95/5 and S'95/63, overlapping those of Barr (1989). The glaucophanes are generally unzoned and those that are show no systematic trend in composition. The rock is a pristine glaucophane-epidote rock with no evidence for greenschist recrystallisation, or metastable amphibole growth. It is inferred that for new growth of amphibole to increasingly riebeckitic compositions during decompression that an influx of fluid is required.

Summary

- Secondary chlorite was present in the veins analysed, associating them with fluid infiltration during retrogression and exhumation.

- Crack-seal events in greenschist veins, suggest multiple fractures and periods of infiltration.

- Growth of increasingly riebeckitic glaucophane appears to be associated with fluid infiltration during down-pressure recrystallisation. Growth of crossite into an albite-chlorite bearing vein suggests that amphibole growth was locally metastable during the blueschist-greenschist transition.

4.7 Discussion

This chapter aimed to identify evidence for fluid infiltration of the terrain, to document whether fluid infiltration was channelled or pervasive and to determine what controlled the style and type of fluid infiltration. The final aim was to document the affect of fluid infiltration on the recrystallisation of metamorphic assemblages.

The study has documented channelled fluid infiltration in the form of veins. The

relative timing of the precipitation of minerals in the veins has been related to the metamorphic and structural evolution of the terrain by mineral assemblage and the relationship of the veins to the host rock structure. The formation of the veins, resulting in channelled fluid infiltration, has been controlled by extensional deformation. The extensional deformation has been accommodated by fractures within which minerals have precipitated. In many examples minerals have precipitated in the necks of boudins after rupture.

Veins were identified from the 'peak' metamorphic quartz-lawsonite veins of Bloor (1998) through to sub-greenschist calcite veins. A greenschist veining 'event' was noted, and identified by planar sub-vertical veins trending N-S to NW-SE. In thin section these greenschist veins often show multiple fractures, documenting the accumulation of small increments of extensional strain between periods of sealing. The veins accommodated E-W to NE-SW directed extension. Higher pressure veins were also documented, notably glaucophane-quartz veins, often found in extensional shear zones. The growth of crossite into an albite-chlorite-bearing vein suggests that there was a continuum of extension and fracture associated fluid infiltration from 'peak' meatmorphism through the blueschist-greenschist transition and into the greenschist facies.

I have linked channelled fluid infiltration to localised recrystallisation of metamorphic assemblages by observations of greenschist haloes around veins cross-cutting blueschist. Bulk geochemistry documented an increase in the volatile content of the rock in the haloes and associated hydration of silicates to chlorite-bearing assemblages. Around some greenschist veins albite selvages were also identified, and bulk geochemistry of the halo and host rock material in general documented a Na-influx into the halo to precipitate albite.

Pervasive fluid infiltration during the blueschist-greenschist transition is thought to have occurred in the south of the island, as the majority of the rock is retrogressed to greenschist facies assemblages. The reactions, like those in the haloes to greenschist veins cutting blueschist, are inferred to have been the result of hydration. The control on the pervasiveness of the fluid infiltration is unknown. High fluid pressures in the south of the island may have resulted in more pervasive fluid

infiltration as compared to the north. There is also evidence for localised zones, up to 20 m wide of pervasive greenschist deformation in southern Syros. These zones of pervasive deformation may have allowed fluid to infiltrate the schist.

The results of this study correlate well with those of other workers in terms of metasomatism in vein haloes and the observation of both channelled and pervasive fluid infiltration in regional metamorphic terrains. Barnicoat (1988) documents metasomatism around albite veins in the Alps and Ague (1997) has show that albite porphyroblast growth is locally associated with Na-influx around veins in the Scottish Dalradian. Metasomatism associated with lawsonite precipitation around veins was documented on Syros by Bloor (1998). Pervasive fluid infiltration resulting in retrogression of blueschist to greenschist facies assemblages is commonly documented in the Cyclades. On the neighbouring island of Sifnos (Schliestedt and Matthews, 1987) propose that high pressure assemblages are preserved in the north of the island due to impermeable marble bands separating fluid infiltration and greenschist retrogression in the south from the northern blueschists. Lithological controls on fluid infiltration and the relative impermeability of marble are addressed in chapters 5 and 6.

4.8 Summary

The main points of the chapter are summarised below.

- Both channelled and pervasive fluid infiltration has been documented.
- Veining resulting from fracture controlled extension occurred from 'peak' metamorphism through to sub-greenschist facies.
- Channelling of fluid resulted in local retrogression of blueschist assemblages, during the blueschist-greenschist transition.
- Retrogressive mineral assemblages are locally controlled by

metasomatism, notably in the case of the influx of Na to precipitate albite porphyroblasts.

- The composition of the infiltrating fluid during greenschist retrogression was H_2O-rich, as documented by Barr (1989).

- Multiple infiltration events are documented in greenschist veins by crack-seal textures and isotopic ($\delta^{18}O$) reversals between coexisting minerals.

Chapter 5 Bulk stable isotope profiles, across schist-marble contacts

5.1 Introduction

Fluid infiltration has been shown to play a major role in controlling retrogression of metamorphic assemblages (e.g. Schliestedt & Matthews, 1987; Bröcker, 1990; Barrientos and Selverstone, 1993; and this study (chapter 4)). Therefore, rock permeability will determine whether high pressure metamorphic assemblages are preserved. In the previous chapter (chapter 4) deformation has been proposed as a key mechanism for enhancing permeability in schist and metabasite units. On a larger scale, in a layered meta-sedimentary sequence such as Syros, the variation in permeability between different lithologies may also be a primary control on fluid infiltration and hence retrogressive metamorphism within the sequence.

The meta-sedimentary sequence on Syros is dominated by a series of alternating schist and marble bands (figure 5.1). Fluid infiltration upwards through the meta-sedimentary pile will be controlled by the relative permeabilities of the schist and marble, their fabrics and their geometrical arrangement. The structure of Syros on a broad scale is simple, generally consisting of a layered sequence dipping northward at approximately 30°. This layered geometry means that variations in permeability between different lithologies (e.g. marble and schist) will have a simple effect on fluid pathways through the terrain.

Experimental determination of marble permeability shows that under static conditions and for limited fluid compositions under the conditions of interest (P >2 kbar, T > 300°C) fluid infiltration cannot occur by pervasive grain edge flow in non-deforming texturally equilibrated marbles (Holness and Graham, 1995). The presence of marbles, in the layered meta-sedimentary sequence of Syros, may therefore restrict fluid infiltration upwards through the pile and retrogression of high pressure metamorphic assemblages. However, stable isotope studies of natural marbles show that they are variably permeable under metamorphic conditions. Holness and Graham (1995) stress the importance of deformation mechanisms in enhancing marble permeability in metamorphic environments. This is corroborated by studies of deformed marble (e.g. McCaig et al. 1995) which suggest that permeability is increased during deformation enabling fluid infiltration. Recent ion

Figure 5.1
Map of Syros (after, Ridley 1982a). Isotope localities and small scale location maps annotated

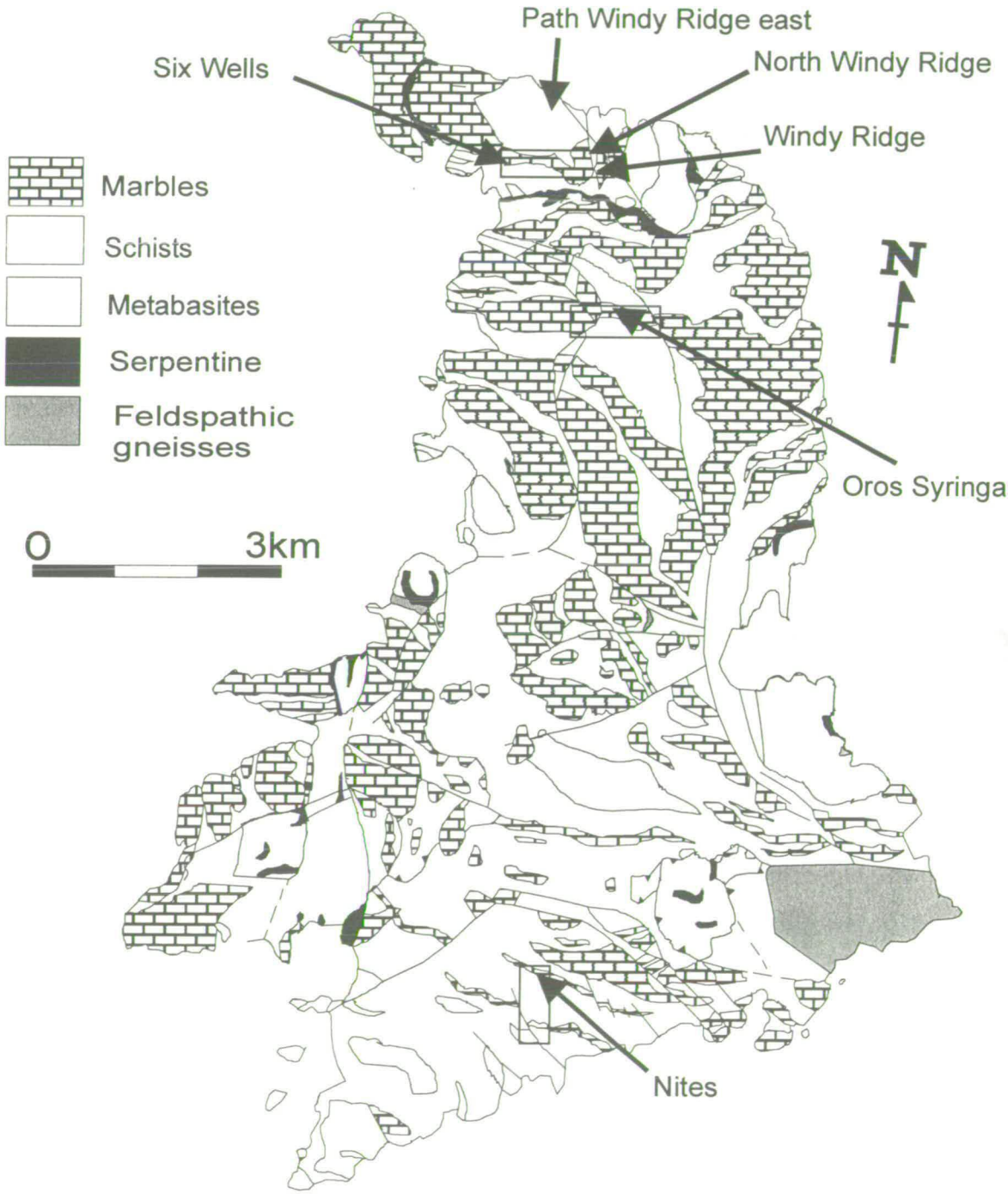

microprobe studies on marble have also concluded that deformation was the mechanism by which fluid infiltration and isotopic alteration occurred (e.g. Lewis et al. 1998, Graham et al. 1998).

The propagation of fronts from lithological boundaries identified by geochemical tracers and/or reactions has been widely documented and used in the literature to describe fluid infiltration and calculate time integrated fluid fluxes (e.g. Rye et al., 1976; Matthews & Schliestedt, 1984; Bickle and McKenzie, 1987; Schliestedt & Matthews, 1987; Baker et al., 1989; Ganor et al., 1989; Bickle & Baker, 1990b; Baker & Matthews, 1995; Ganor et al., 1996). The technique, which requires that the two adjacent lithologies have known, but different isotope compositions prior to exchange, may be used across schist-marble contacts (e.g. Schliestedt & Matthews, 1987; Baker et al., 1989; Bickle & Baker, 1990a). $\delta^{18}O$ and $\delta^{13}C$ profiles across schist-marble contacts were measured, in order to determine if Syros marble bands had remained impermeable under natural conditions, and if not to quantify fluid infiltration into the marble bands. Isotope exchange, either by diffusion or advection-diffusion across the lithological contact can be determined from the profiles. Figure 5.2 shows a schematic geochemical front formed across a lithological contact. Geochemical fronts can be assessed qualitatively from their shape to give an indication of whether fluid has infiltrated a relatively impermeable lithology, or as in more recent studies modelled by chromatographic theory to determine integrated fluid fluxes and the mechanisms of infiltration (e.g. Ganor et al., 1989; Bickle and Baker, 1990a; and Bickle and Baker, 1990b).

5.2 Aims

The stable isotope study of schist-marble contacts across Syros, addresses three main questions.

- Are the variations in isotope composition, documented at lithological contacts, inherited original sedimentary heterogeneities in isotope

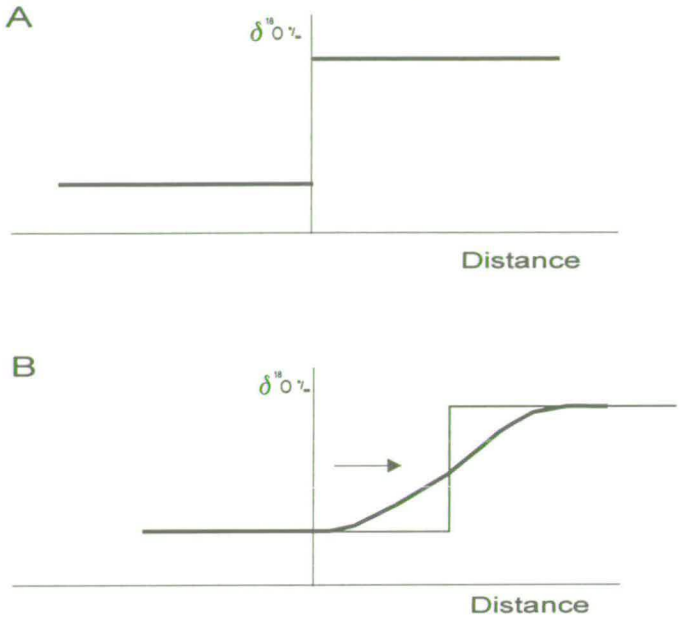

Figure 5.2
A) Schematic change in $\delta^{18}O$ composition across a lithological contact (vertical line).
B) Advective transport of the step in $\delta^{18}O$ composition into the right hand lithology. The step has been broadened by diffusion or kinetic controlled exchange.

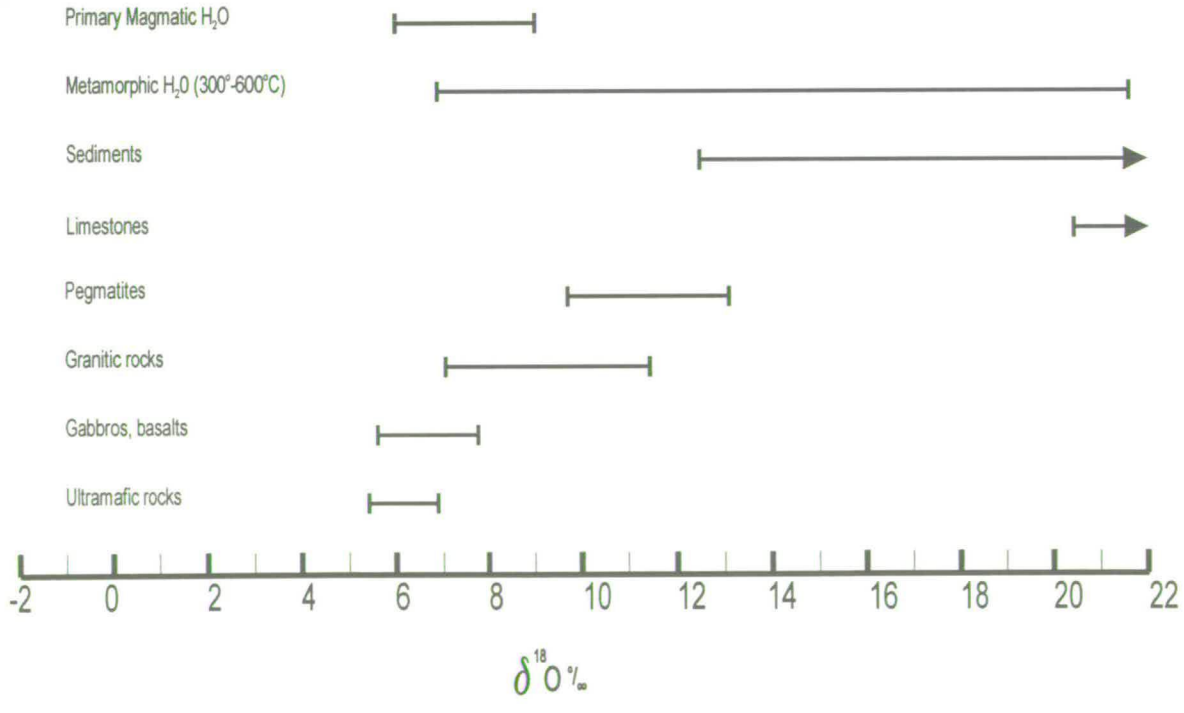

Figure 5.3
Ranges in $\delta^{18}O$ isotope compositions for rocks and H_2O, diagram modified from Faure (1986) and Sheppard (1986).

composition, or are they the result of isotope exchange between the two lithologies, aided by fluid infiltration?

- Is there a greater degree of fluid infiltration into marble in contact with hydrated greenschist assemblages compared to marble in contact with blueschist assemblages?

- Is there evidence that fluid associated with greenschist retrogression infiltrated from south to north, upwards through the sedimentary pile, thus preserving unretrogressed blueschist assemblages in the north?

Marble bands generally preserve a distinct sedimentary isotope signature (figure 5.3) a testament to their relative impermeability as compared to other meta-sediments. The isotopic compositions of marine carbonates are well documented (Keith and Weber, 1964) so the initial, pre-metamorphic, isotopic composition of a pure marble is well constrained. However, marbles containing silicates may have different initial isotope signatures (e.g. Ganor et al., 1996). Therefore, in an impure marble isotopic exchange with an exotic fluid may be hard to distinguish from sedimentary isotopic heterogeneities in the marble $\delta^{18}O$ composition. Banded impure marbles containing varying amounts of quartz, glaucophane, mica, epidote, sodic-pyroxene and garnet are common on Syros particularly in the north. The variations in the isotope composition of these impure marbles on Syros, must be interpreted with care, since the effect of the silicate content of the marble must be accounted for.

The sampled localities were chosen to record differences in isotope profiles across greenschist-marble contacts and blueschist-marble contacts, in order to determine whether fluid infiltration and isotopic alteration of marble bands was directly linked to infiltration of a greenschist retrogressive fluid. The study also aimed to document evidence for fluid infiltration upwards south to north through the meta-sedimentary sequence, which was progressively limited by the presence of relatively impermeable marble bands. This is the reason proposed for the

preservation of high pressure assemblages in the north of Sifnos (Matthews and Schliestedt, 1984) and Syros (Barr, 1989).

5.3 Previous stable isotope work on Syros

Stable isotope analyses of marble and schist units were completed by Barr (1989). Barr sampled calcite from Syros marbles, and silicates in schist units to obtain $\delta^{18}O$ and, for calcite, $\delta^{13}C$ compositions. Silicates from schist layers recorded oxygen isotope equilibration within single layers from both blueschist and greenschist horizons. This agrees with later work by Bloor (1998) who analysed silicates in greyschist units in the north of the island and noted little variation in $\delta^{18}O$ composition. They both concluded that locally the schists were in isotopic equilibrium.

Barr (1989) also compared the $\delta^{18}O$ and $\delta^{13}C$ compositions of impure and pure marbles from southern and northern Syros (figure 5.4), and reported depletions in both $\delta^{18}O$ and $\delta^{13}C$ for impure marble relative to pure marble in the north of the island. Barr (1989) ascribed the depletions in $\delta^{18}O$ and $\delta^{13}C$ to: (1) isotope exchange with depleted silicates and (2) loss of isotopically enriched CO_2, due to decarbonation reactions. Figure 5.4b for the south of the island shows depletion in the $\delta^{18}O$ and $\delta^{13}C$ composition of pure marbles in the south as compared to the north (figure 5.4a). The depletion may be related to fluid infiltration during pervasive retrogression to greenschist assemblages, which are seen in the south.

Barr also constructed several isotope profiles across schist-marble contacts, to assess the extent of fluid infiltration into marble from schist units. The profile samples were collected at a sample spacing of 1 to 20 m. Barr concluded for the schist-marble traverses that:

'in general the marble bands on Syros have not been sampled in sufficient detail, particularly next to the contact zone, to define the exact form of the isotopic variation across them.'

Figure 5.4
Graphs of $\delta^{18}O$ vs $\delta^{13}C$ for Syros marbles (Barr, 1989).

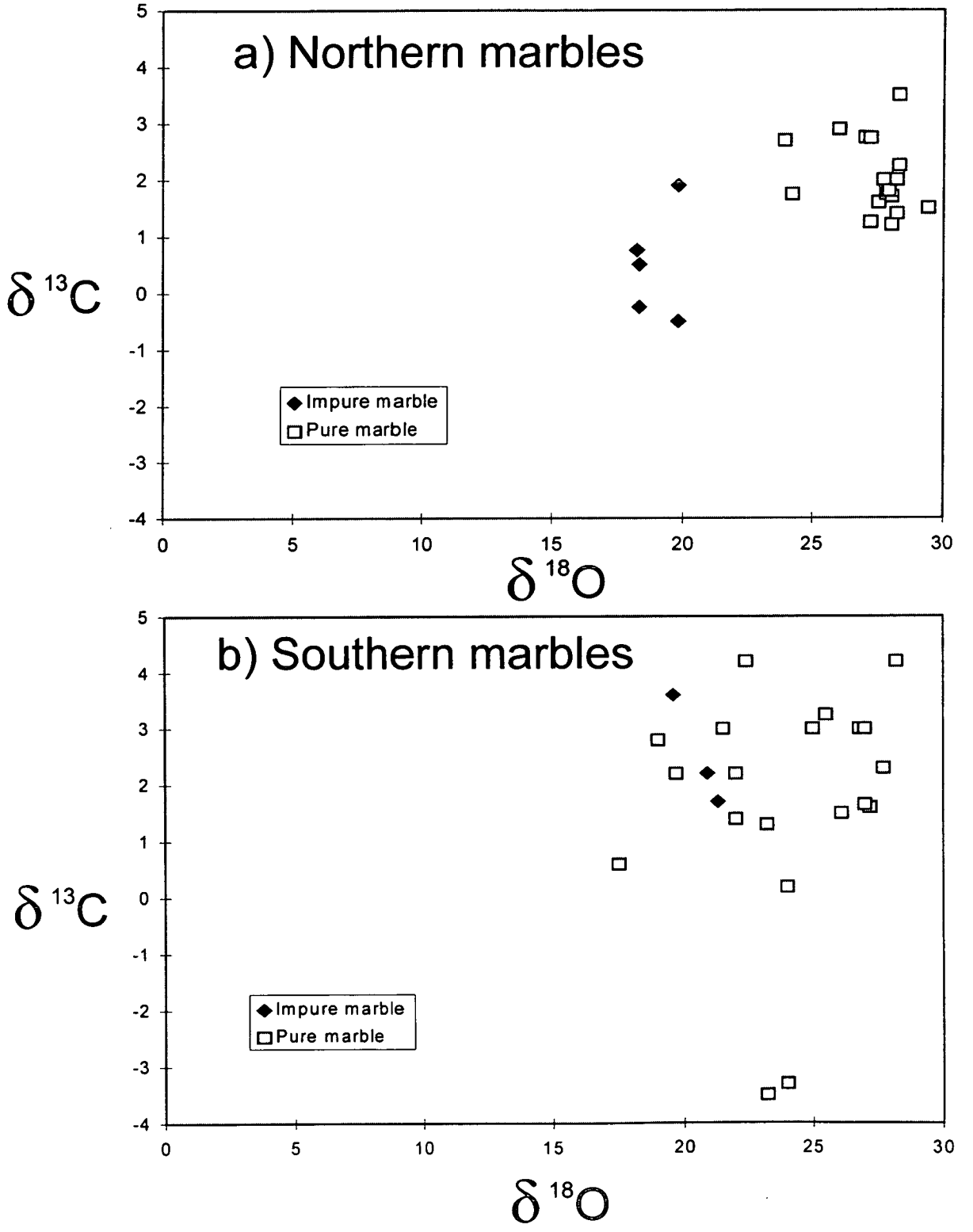

This statement is justified, if compared to the results of other workers, such as Baker et al., (1989) who describe marble band boundary layers, less than 2 m wide, of isotope alteration, on Naxos.

The work presented here builds on that of Barr (1989) and Holness (unpublished), who collected preliminary data during reconnaissance for the present study. The data of Holness are presented for individual localities, together with data from the present study. Re-sampling and analysis of Holness's data points and samples are indicated where relevant. For this study I have collected marble samples at a spacing of 5-20 cm, allowing the shape of isotope exchange profiles to be documented sufficiently accurately to draw firm conclusions regarding fluid behaviour.

5.4 Locality descriptions

Figure 5.1 shows the locations of small-scale maps (outlined by black boxes) that were made during collection of samples for isotope analysis. The maps were drafted to document the locations of the profiled schist-marble contacts. The localities are described from south to north across the island, noted in ***bold***, and information that is pertinent to the study aims is noted in *italics.*

i) Nites

The Nites massif forms the prominent set of hills in ***southern Syros***. The massif consists of variably retrogressed metabasites and pelites interbedded with calcitic marble bands. Five isotope traverses across marble bands were collected on this hillside; all are described and presented in chapter 6. One profile is included here to present isotope data from the south of the island.

Patches of metabasite, glaucophane-epidote schist, as well as a retrogressed chlorite-epidote equivalent, crop out on the Nites hillside. The isotope profile presented comes from low on the hillside where the schist is *fully retrogressed to greenschist facies*. It is one of two traverses made across a *quartz-calcite interbedded unit*, approximately 2 m thick. The layer is discontinuous (see figure 5.5) and

heterogeneously deformed. The profile presented here (locality D) crosses an undeformed section at outcrop scale.

The schist below is calcareous and consists of quartz, calcite, chlorite, albite and white mica. It is strongly deformed with crenulations defined by chlorite and mica, with porphyroblastic albite. Veins and segregations of quartz, calcite, chlorite ± oxide cut the schist with no preferred orientation.

ii) Oros Syringas

The Syringas hillside, ***in mid-north Syros***, is composed of a series of thick marble bands, separated by thin and thick layers of schist and cut by normal faults. Ridley (1982a) interpreted this sequence to be a thrust stack, duplicating the original sedimentary sequence either pre or syn-M1. Textural evidence of tectonic contacts has not been found within the succession (Ridley, 1982a and this study).

Three localities were chosen on the south facing slopes of Oros Syringas (figure 5.6). Working from the base of the sequence upwards, the first locality, *locality I*, is a 2 m wide *marble band* within a schist unit near the base of the hill. The second locality, *locality II*, is a thin *marble band containing weathered schistose laminations*, which gives the marble band an orange staining. The final traverse, *locality III*, crosses the thin schist layer within the uppermost *marble unit.* The *schist at the structurally lowest locality, locality I,* is almost completely *retrogressed to greenschist facies assemblages*; veins and coarse grained segregations of albite, chlorite, quartz, and oxide veins are abundant. This is in contrast with the *upper-most locality, locality III,* where the *schist retains abundant glaucophane* and is only sporadically retrogressed. The first and third localities were originally sampled using a rock drill by Holness in 1993 and 1994 (unpublished data). Further sampling for both isotope and thin section work has been made at these localities during the present study.

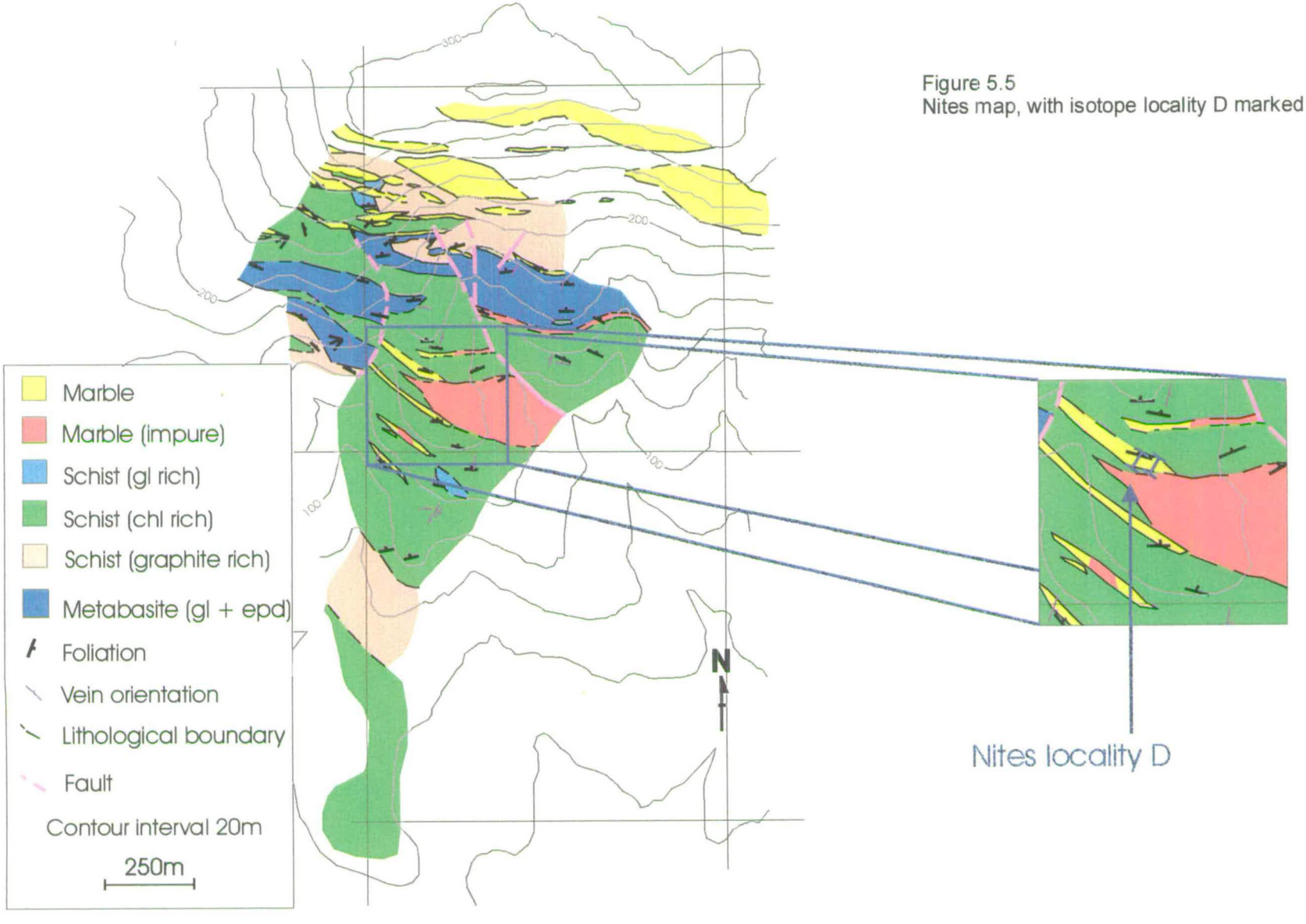

Figure 5.5
Nites map, with isotope locality D marked

Figure 5.6
Map of Oros Syringas, with isotope traverse localities marked

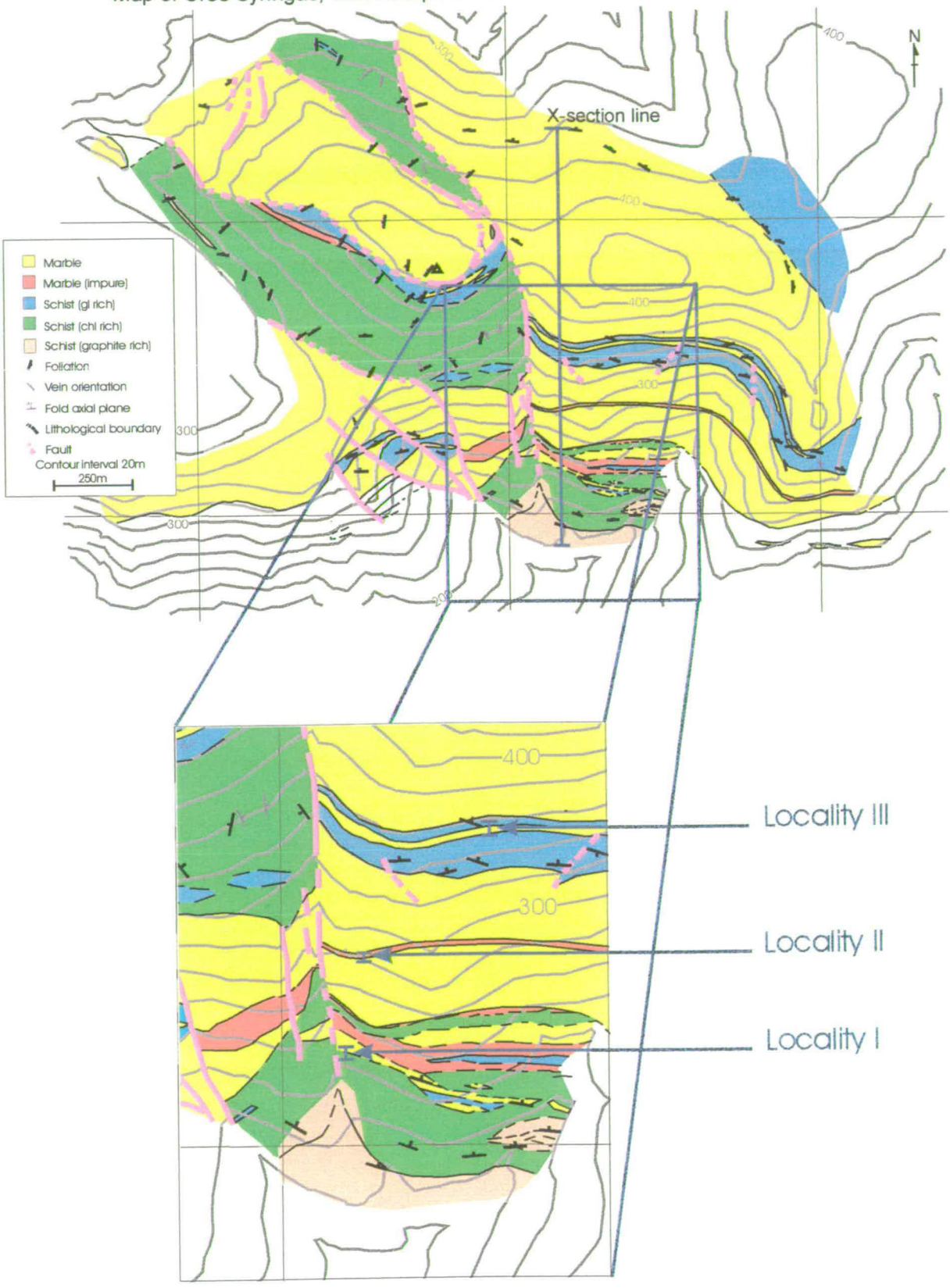

iii) Windy Ridge

Windy Ridge profiles A and B, in ***northern Syros***, are separated by a fault and lie within a complex region of folded and faulted marble and schist units (figure 5.7). The localities of iv) North Windy Ridge and v) Six Wells are also marked on this figure. The *schist* below the marble at *locality A contains glaucophane, graphite, epidote, white mica, calcite and quartz.* At *locality B the* schist is poorly exposed, weathered, and has a grey sheen, probably from *graphite* present within the schist. The *contact of the schist and marble at locality A is transitional* and marble sampled at the furthest point from the contact contains some silicate impurities. The *contact at locality B is sharp* but the marble still contains *layers of silicate impurities*. At both localities quartz segregations in the schist were sampled for oxygen isotope analysis.

iv) North Windy Ridge

The marble band traversed at North Windy Ridge is distinctly banded with *pure and impure marble layers*. Large glaucophane and epidote crystals can be seen in hand specimen within impure marble horizons. The schist below is weathered and the outcrop poor. The *schist* appears to have retained its high pressure assemblage; *glaucophane, white mica and epidote* are clearly seen in hand specimen. Calcite segregations in the schist were collected for stable isotope analysis.

v) Six Wells

The marble band sampled for *Six Wells (locality C)* crops out in the walled area of a small house clearly labelled ΓZM, 1896. The *marble band* exposed here is banded and consists of cm scale bands of *creamy calcite, interbedded with layers containing up to 40% silicates* (hand specimen observations), mainly glaucophane and epidote. The *schist* above and below the band also retains high pressure minerals including *glaucophane, epidote, white mica, quartz and calcite.*

In the base of the steep sided valley to the south are six wells bearing the same signature as the house. As the path nears the valley floor the contact between a thick *marble band and graphitic schist* which crop out in the bottom of the valley is

Figure 5.7
Map of Windy Ridge and Six Wells area, with isotope traverse localities marked

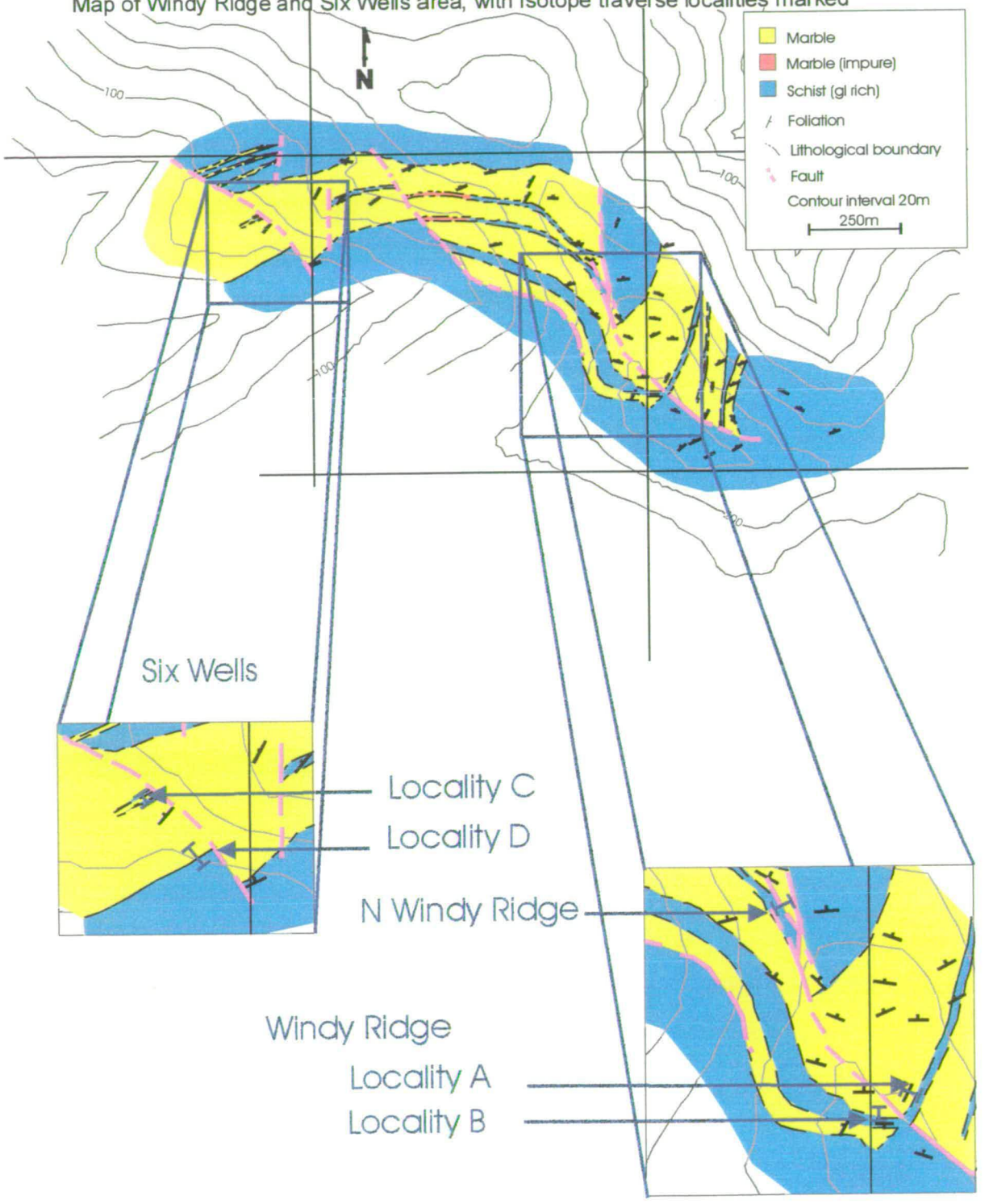

crossed. The contact was sampled on the path and forms the stable isotope traverse of *Six Wells (locality D)*. Calcite and quartz segregations were collected from the schist.

vi) Path Windy Ridge East

This locality was not mapped on a small-scale, so its geological context is not as well constrained as the other localities. The locality and its location with respect to the other localities on Syros is shown in figure 5.1. Two thin *marble bands*, 1.5 m thick are interbedded with *graphitic schist, containing graphite, mica, glaucophane, and garnet*. The schist has a distinct silvery sheen, like that seen at Windy Ridge locality B. One sample of calcite and two quartz segregations were collected from the schist and a sample traverse of the lower marble band.

5.5 Techniques

Marble samples were collected at a spacing of less than 5 cm near the contact and at 10-20 cm intervals at distances greater than 20 cm from the contact. Distance measurements were made perpendicular to the marble fabric, which lies parallel to lithological contacts across the island, with minimal along-strike movement.

Obtaining a representative isotope composition for the schist is crucial if it is to be used as the basis for determining the extent of isotope equilibration between schist and marble. Most studies (e.g. Baker, 1990) have used quartz and calcite segregations sampled from schists to represent a schist matrix calcite isotope composition. However, there are problems involved in using segregations to obtain schist isotope compositions. Fluids forming segregations within the schist may not have equilibrated isotopically with the surrounding schist. The schist may also undergo later isotopic exchange with infiltrating fluid whilst early veins and segregations remain isotopically distinct. In this study I have used a combination of veins and segregations as well as calcite drilled from the schist matrix, to compare relative $\delta^{18}O$ values and thus assess the extent of isotopic equilibration between matrix calcite and segregations.

5.6 Results

The results are presented in the conventional δ notation in per mil (‰) relative to the PDB standard for carbon and SMOW standard for oxygen. The precision of values is ± 0.2 ‰ for oxygen and carbon isotopes of carbonate. The silicate $\delta^{18}O$ values have a precision of ± 0.5 ‰. Graphs of distance versus $\delta^{18}O$ and distance versus $\delta^{13}C$ for each profile are shown in figures 5.8 through to 5.17. In each graph the structurally lowest lithology is on the left, moving upwards towards the right across the profile. Logs indicate the nature of the marble and or schist sampled across the traverse. Quartz data from the schist have not been modified for quartz-calcite fractionation. The stable isotope techniques and data are presented in appendix B.

Calcite marble away from contacts with adjacent schist have values of $\delta^{18}O$ in the range 23 to 29 ‰. This is within the range of expected marine limestone composition (Keith and Weber, 1964). The $\delta^{18}O$ of calcite and quartz from schist lie in the range 17 to 22 ‰, with the exception of a carbonate rich band at Windy Ridge A (figure 5.12) and calcareous schist at Six Wells locality C (figure 5.15). The $\delta^{13}C$ values tend to mimic the $\delta^{18}O$ profiles, although there is generally more scatter in the carbon isotope data. The results are discussed under the subheadings of the three aims of the study.

Are the variations in isotope composition, documented at lithological contacts, inherited original sedimentary heterogeneities in isotope composition, or are they the result of isotope exchange between the two lithologies aided by fluid infiltration?

Barr (1989) documented depletions in $\delta^{18}O$ and $\delta^{13}C$ in impure marbles relative to pure marbles in northern Syros (figure 5.4). She interpreted the depletions as being the result of a combination of two processes: 1)isotope exchange with ^{18}O

Figure 5.8 Nites, locality D, undeformed
Variations in $\delta^{18}O$ and $\delta^{13}C$ with distance across a schist-marble contact. The lithological log, centre of page describes the sampled traverse. Legends are given with individual graphs.

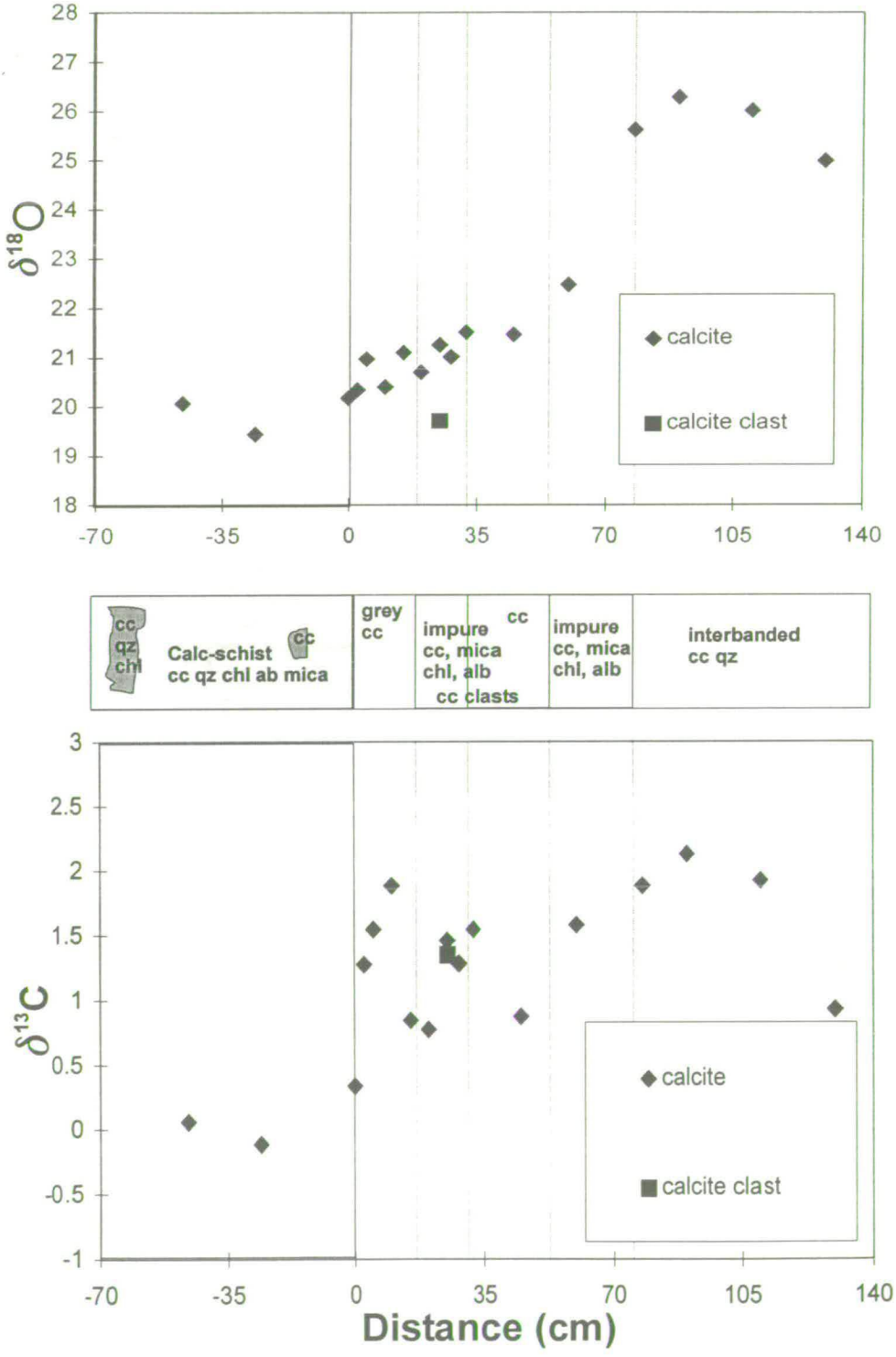

Figure 5.9 Oros Syringas, locality I

Variations in $\delta^{18}O$ and $\delta^{13}C$ across a schist-marble contact. The lithological log, centre of page describes the sampled traverse. Legends are given with individual graphs.

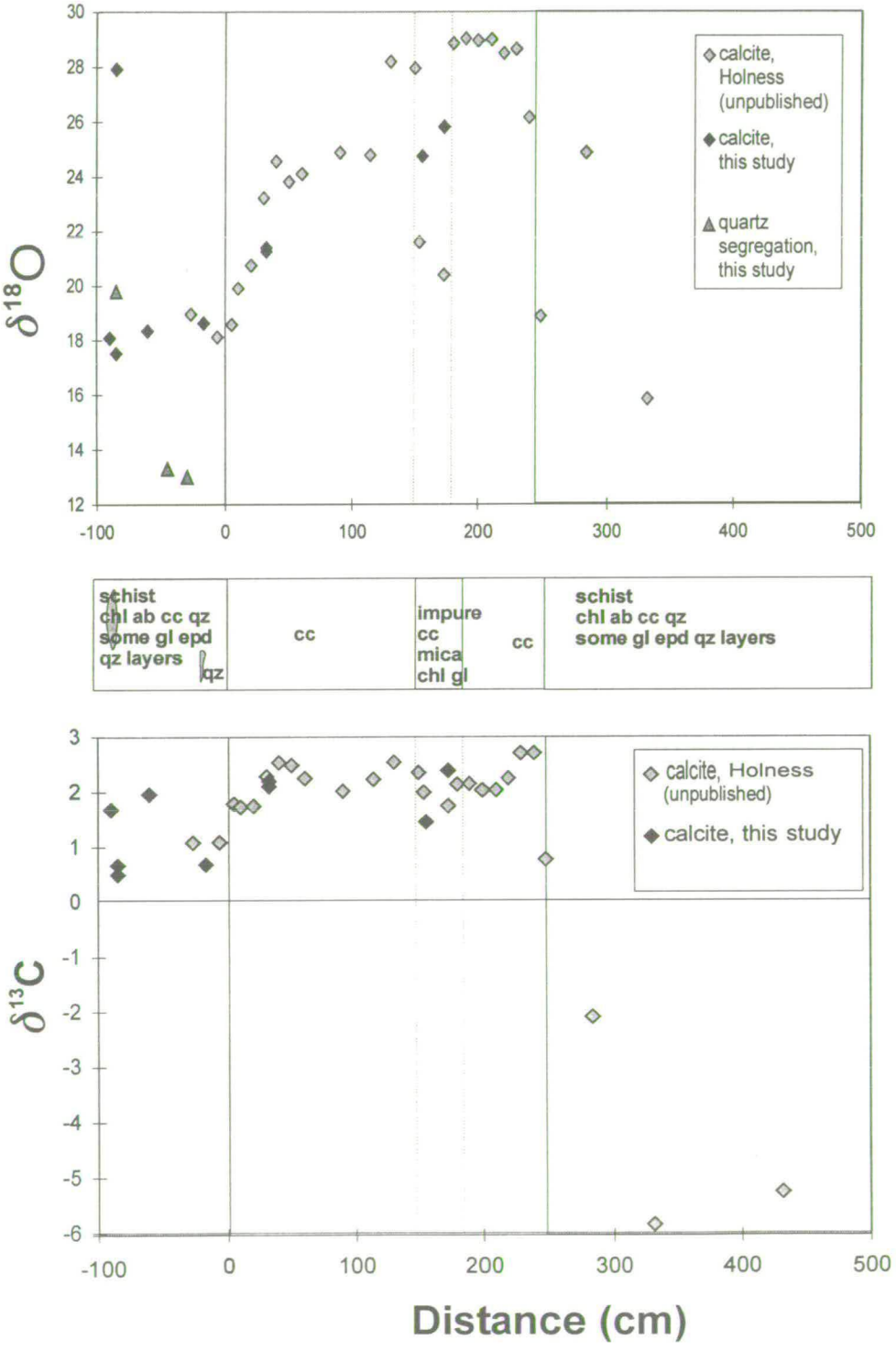

Figure 5.10 Oros Syringas, locality II
Variations in $\delta^{18}O$ and $\delta^{13}C$ across an impure marble/calc-schist -marble contact.
The lithological log, centre of page describes the sampled traverse. Legends are given with individual graphs.

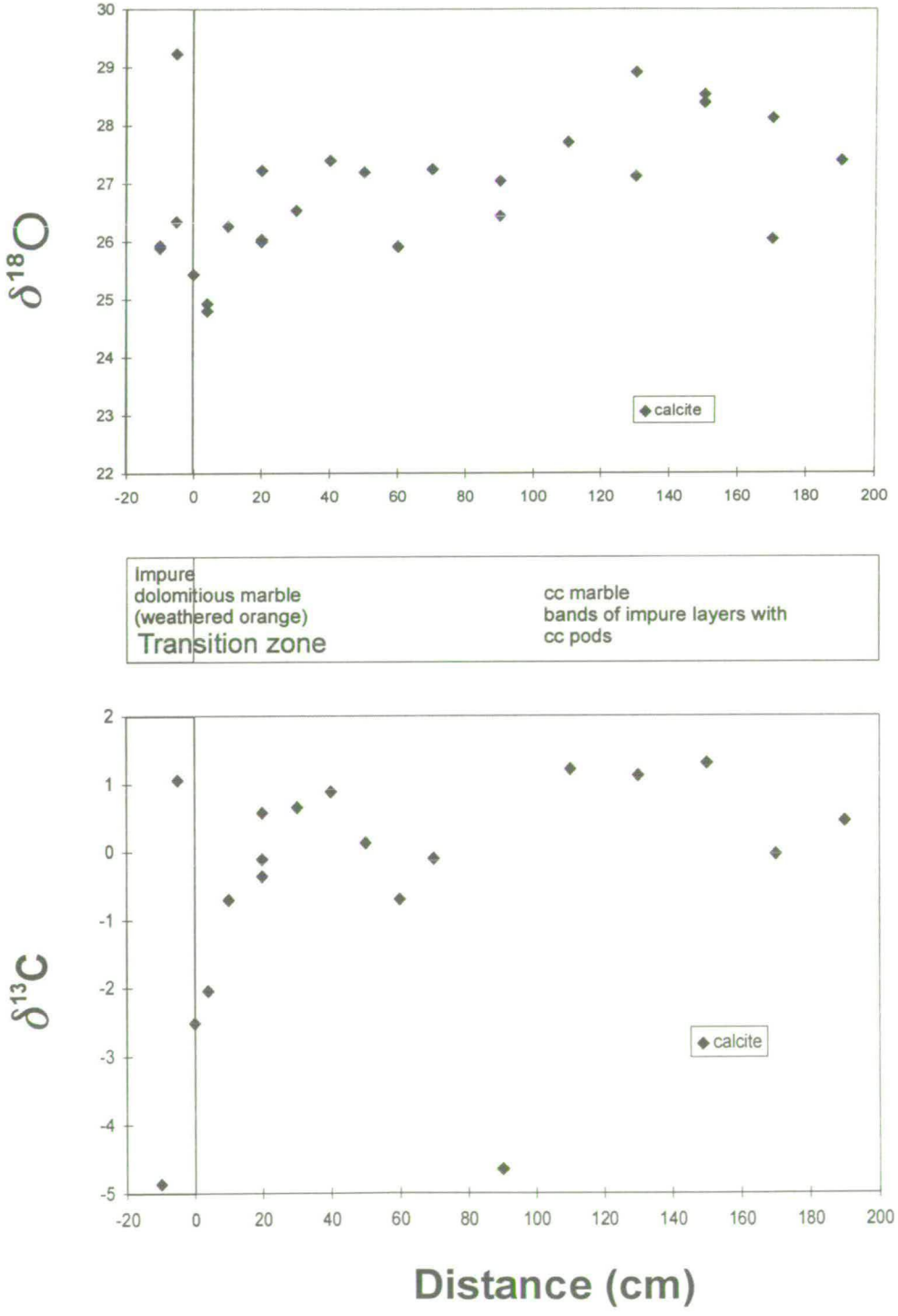

Figure 5.11 Oros Syringas, locality III

Variations in $\delta^{18}O$ and $\delta^{13}C$ across a blueschist-marble contact. The lithological log, centre of page describes the sampled traverse. Legends are given with individual graphs.

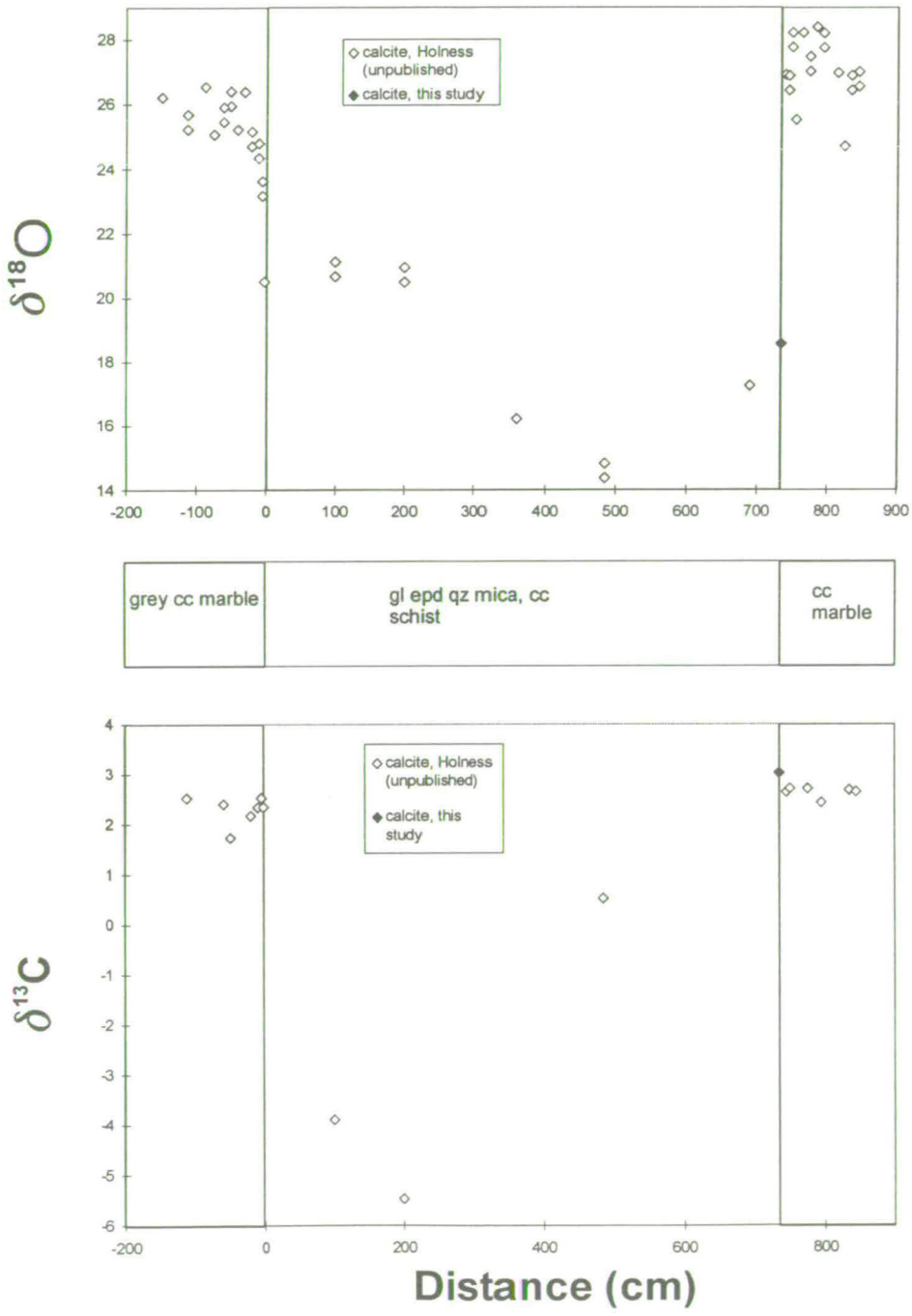

Figure 5.12 Windy Ridge, locality A

Variations in $\delta^{18}O$ and $\delta^{13}C$ across a calc-schist-banded impure marble transition zone. The lithological log, centre of page describes the sampled traverse. Legends are given with individual graphs. A sample of calcite precipitate (ppn) on the surface of the marble is annotated.

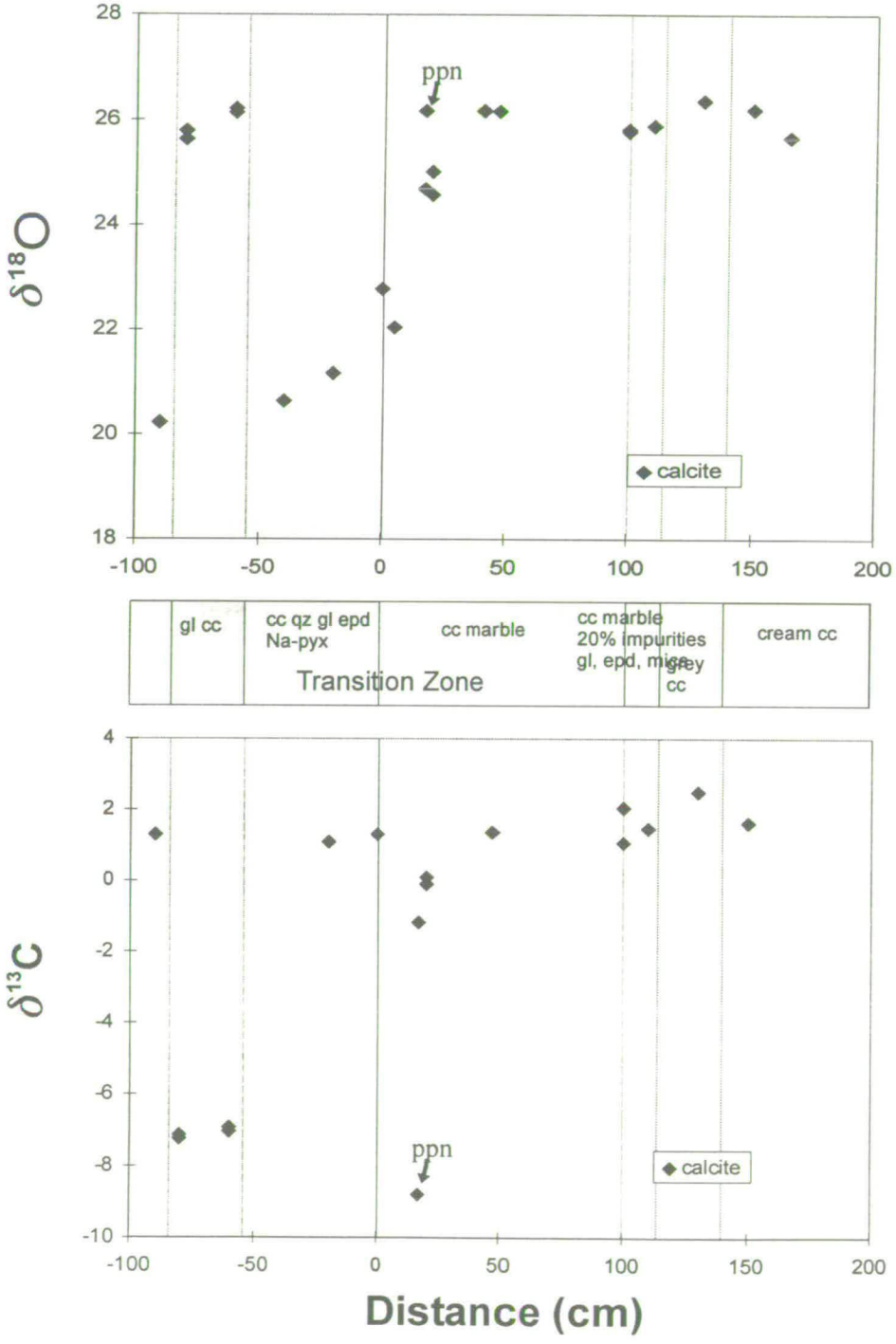

Figure 5.13 Windy Ridge, locality B
Variations in $\delta^{18}O$ and $\delta^{13}C$ across a graphtic-schist-marble contact. The lithological log, centre of page describes the sampled traverse. Legends are given with individual graphs.

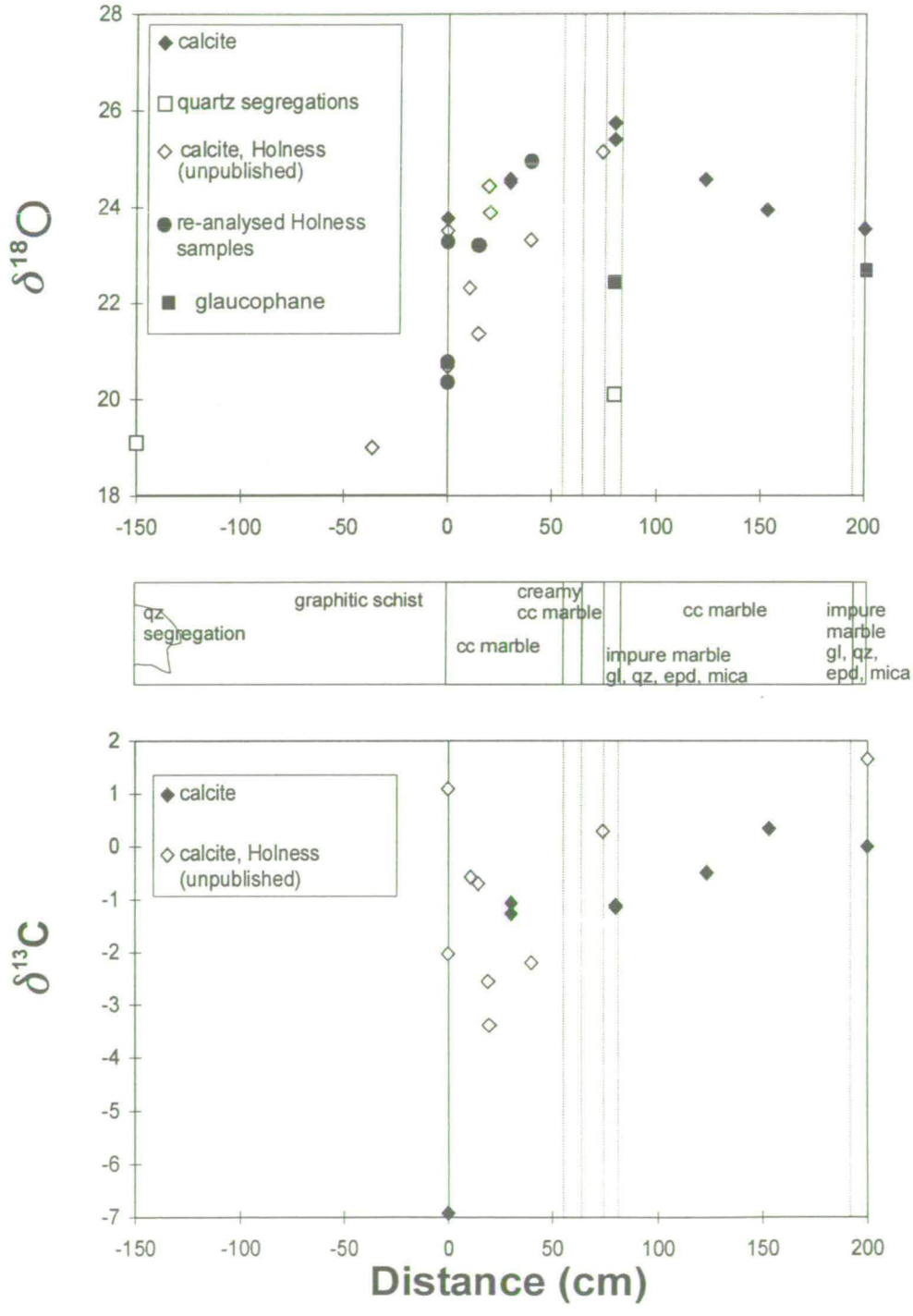

Figure 5.14 North Windy Ridge
Variations in $\delta^{18}O$ and $\delta^{13}C$ across blueschist-marble contact. The lithological log, centre of page describes the sampled traverse. Legends are given with individual graphs.

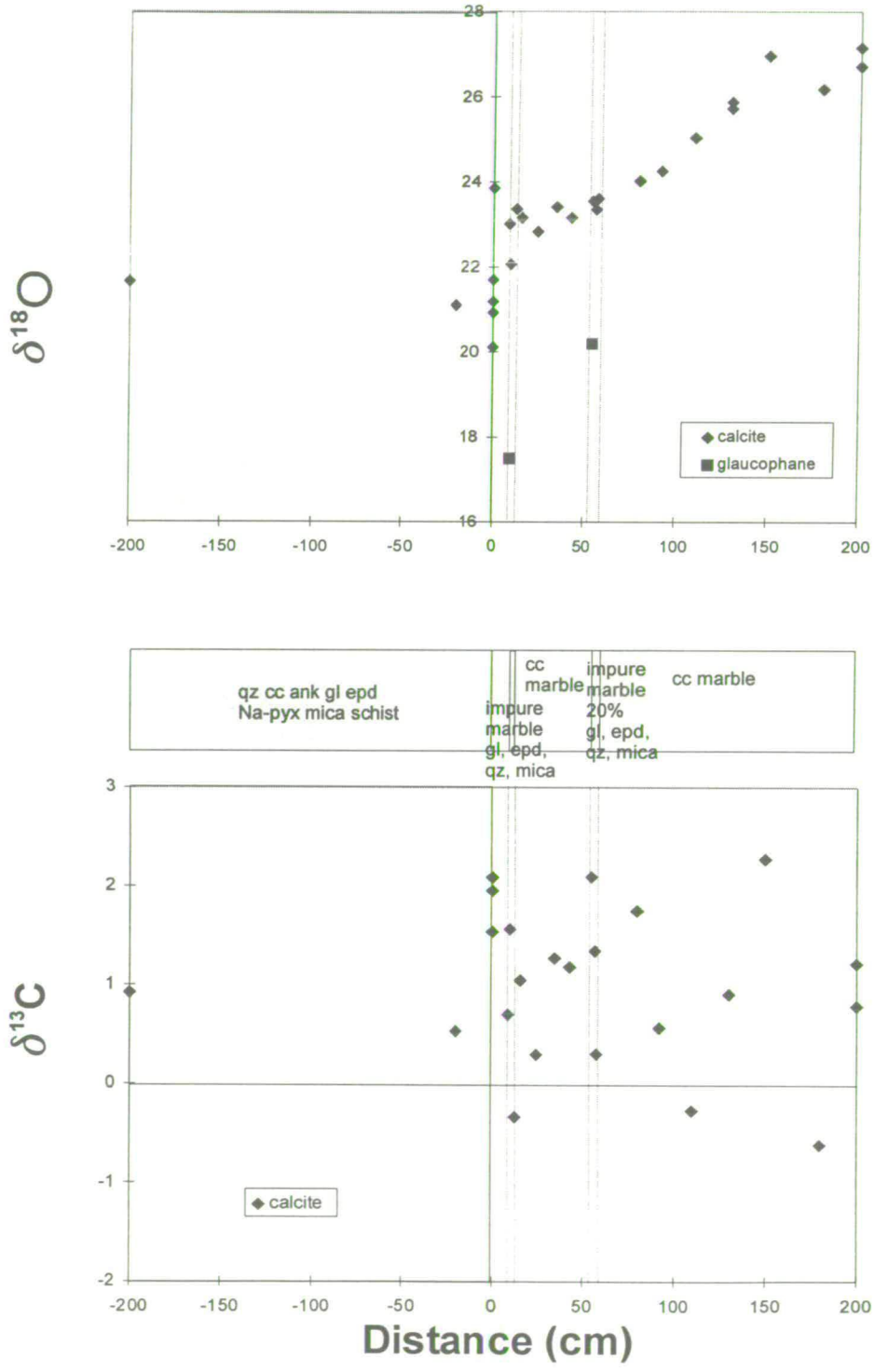

Figure 5.15 Six Wells, locality C

Variations in $\delta^{18}O$ and $\delta^{13}C$ across calc-blueschist-marble contact. The lithological log, centre of page describes the sampled traverse. Legends are given with individual graphs.

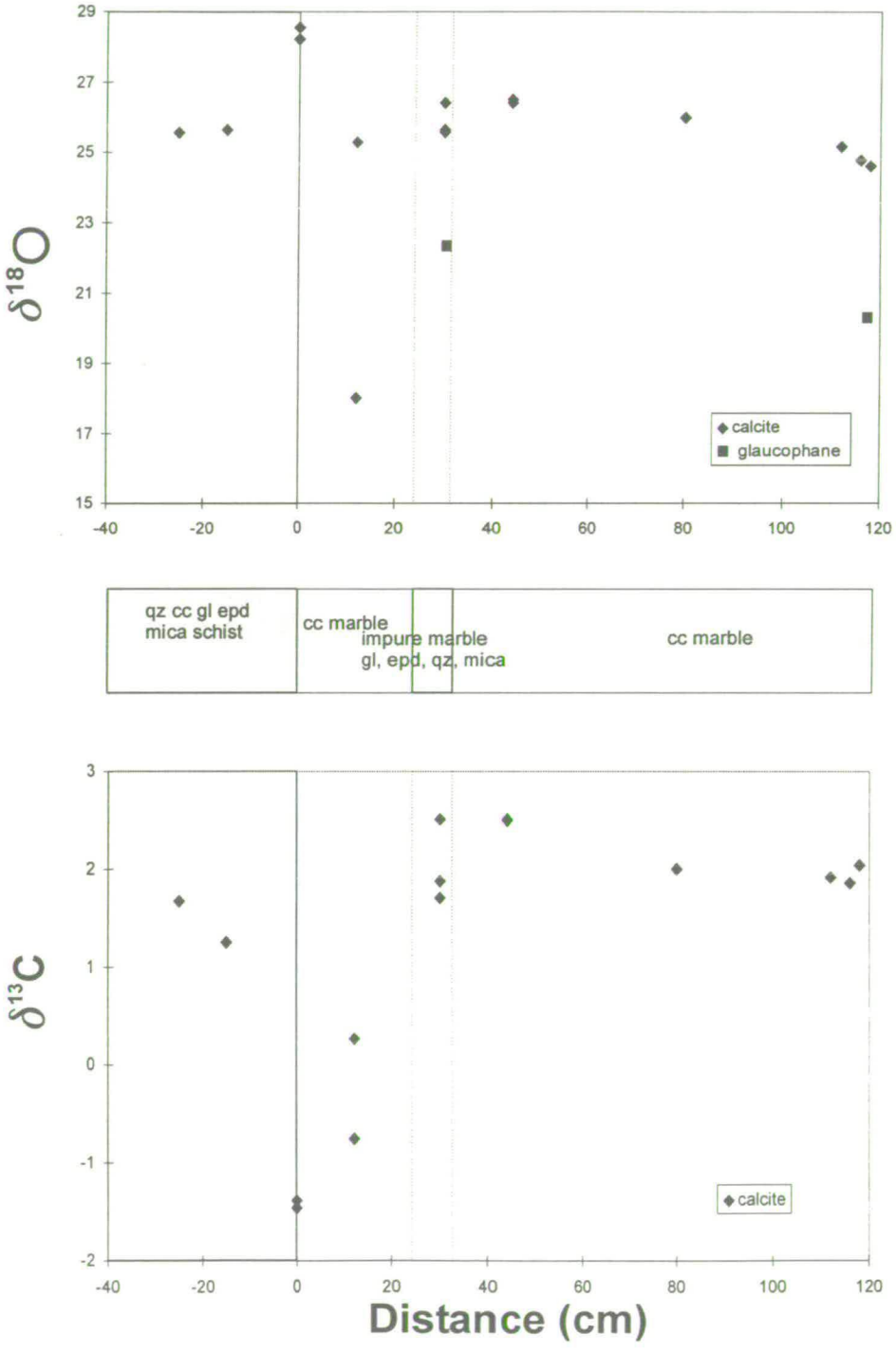

Figure 5.16 Six Wells, locality D
Variations in $\delta^{18}O$ and $\delta^{13}C$ across graphitic schist-marble contact. The lithological log, centre of page describes the sampled traverse. Legends are given with individual graphs.

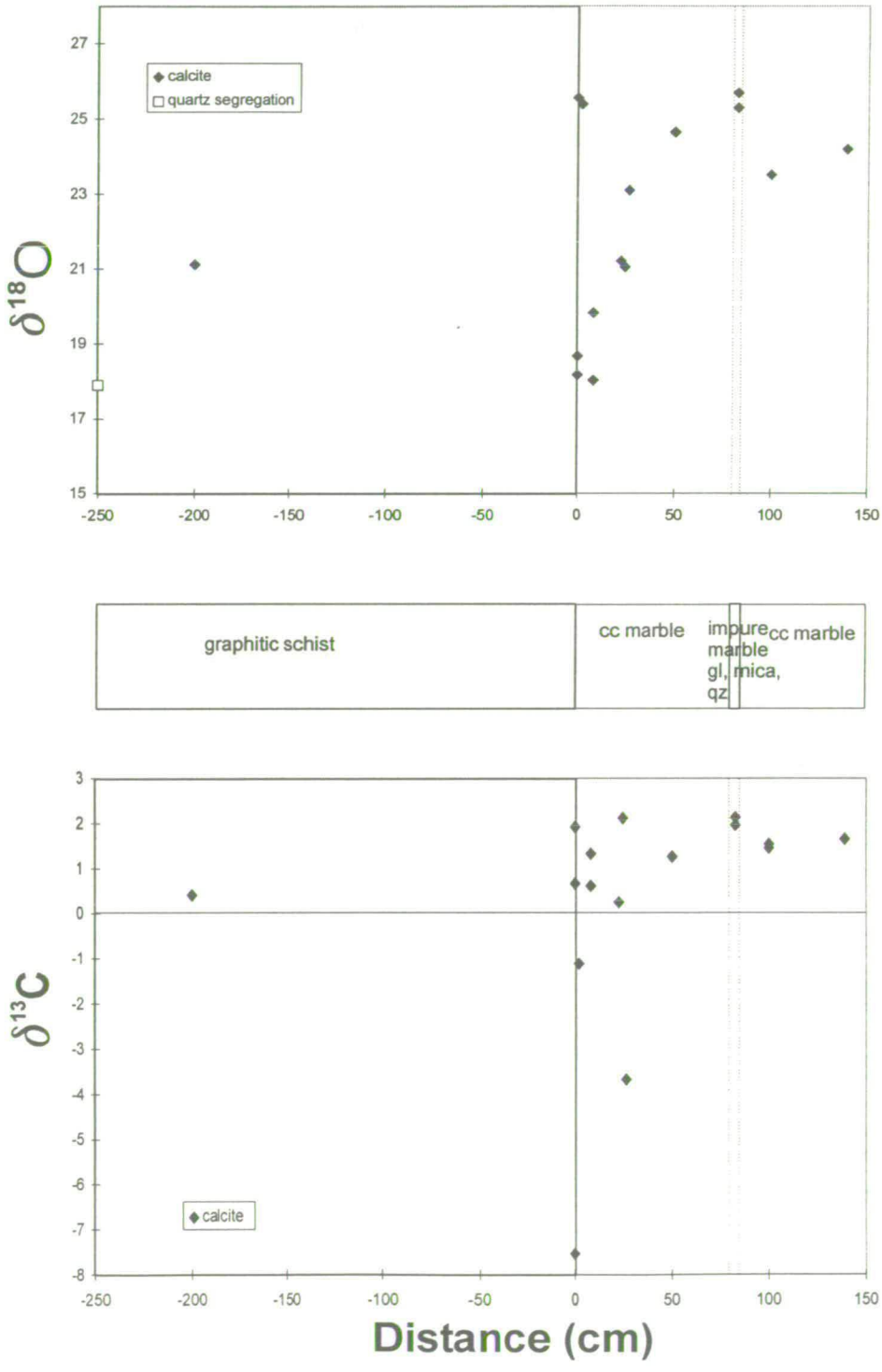

Figure 5.17 Path Windy Ridge east

Variations in $\delta^{18}O$ and $\delta^{13}C$ across garnet, graphite schist-marble contact. The lithological log, centre of page describes the sampled traverse. Legends are given with individual graphs.

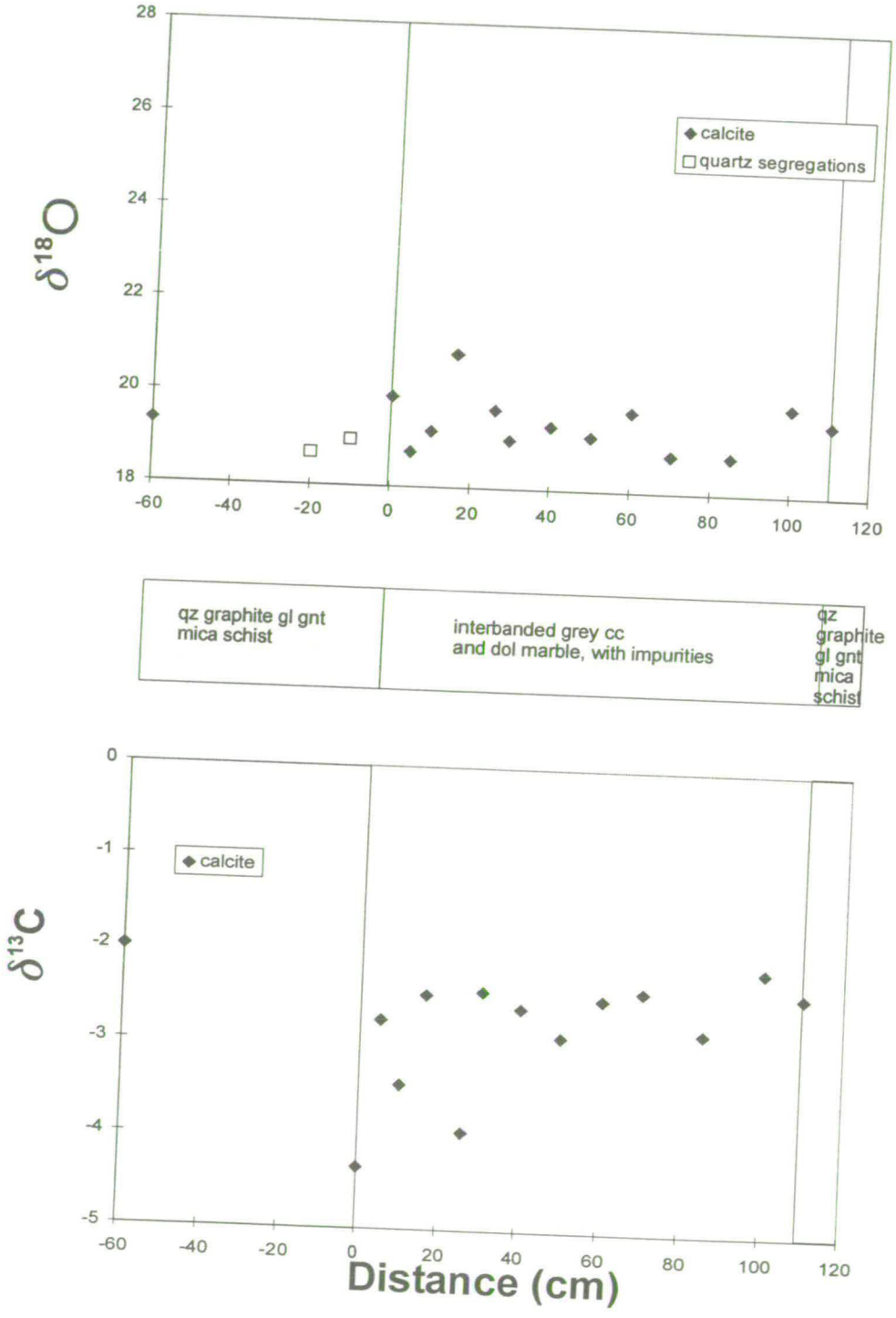

depleted silicates and 2) loss of isotopically enriched CO_2 via decarbonation reactions.

In marbles containing detrital silicate, oxygen isotope exchange between the carbonate and silicate can result in relative depletion of the carbonate and $\delta^{18}O$ enrichment of silicate. The depletion is dependent on the amount and type of silicate and whether the carbonate and silicate have equilibrated. Equilibration of oxygen isotopes between carbonate and silicate will not affect the carbon isotope composition. Decarbonation reactions however, produce CO_2 enriched in both ^{18}O and ^{13}C which leaves the marble depleted in both isotopes. Marble bands may also be depleted in either oxygen and carbon isotopes if they have exchanged with an isotopically light infiltrating fluid. I have attempted to discern these effects, for impure marble bands on Syros.

The marbles in northern Syros are generally banded, consisting of pure and impure layers. It is not clear whether Barr's samples were collected from pure and impure layers or from individual units. Barr (1989) also does not specify whether the marble was collected away from contacts with adjacent schist. Data from this study are added to that of Barr for northern Syros (figure 5.18). The isotope data presented for this study are from samples collected away from lithological contacts. Data plotted as impure marble are from silicate rich layers, and pure marbles are from pure layers in banded marble. The overall spread of data from the present study correlates well with that of Barr's. However, there is no systematic depletion of marble $\delta^{18}O$ or $\delta^{13}C$ in silicate rich layers. Unfilled symbols denote data collected from marble bands adjacent to graphite rich schist. These samples are depleted in $\delta^{13}C$ relative to other carbonate, due to exchange with fluid in equilibrium with the graphitic schist, or production of carbonate from graphite by oxidation. For these reasons I have focused on the $\delta^{18}O$ profiles.

In the profiles there is some evidence for depletion of both $\delta^{18}O$ and $\delta^{13}C$ in silicate rich horizons in marble bands. Figure 5.9 of the Oros Syringas I profile shows quite marked depletion of $\delta^{18}O$ in calcite in a silicate-rich horizon at 150-180 cm. The layer is also slightly depleted in $\delta^{13}C$. The depletions may be related to

Figure 5.18
Graph of impure and pure marble, from this study and Barr (1989) for northern marbles.

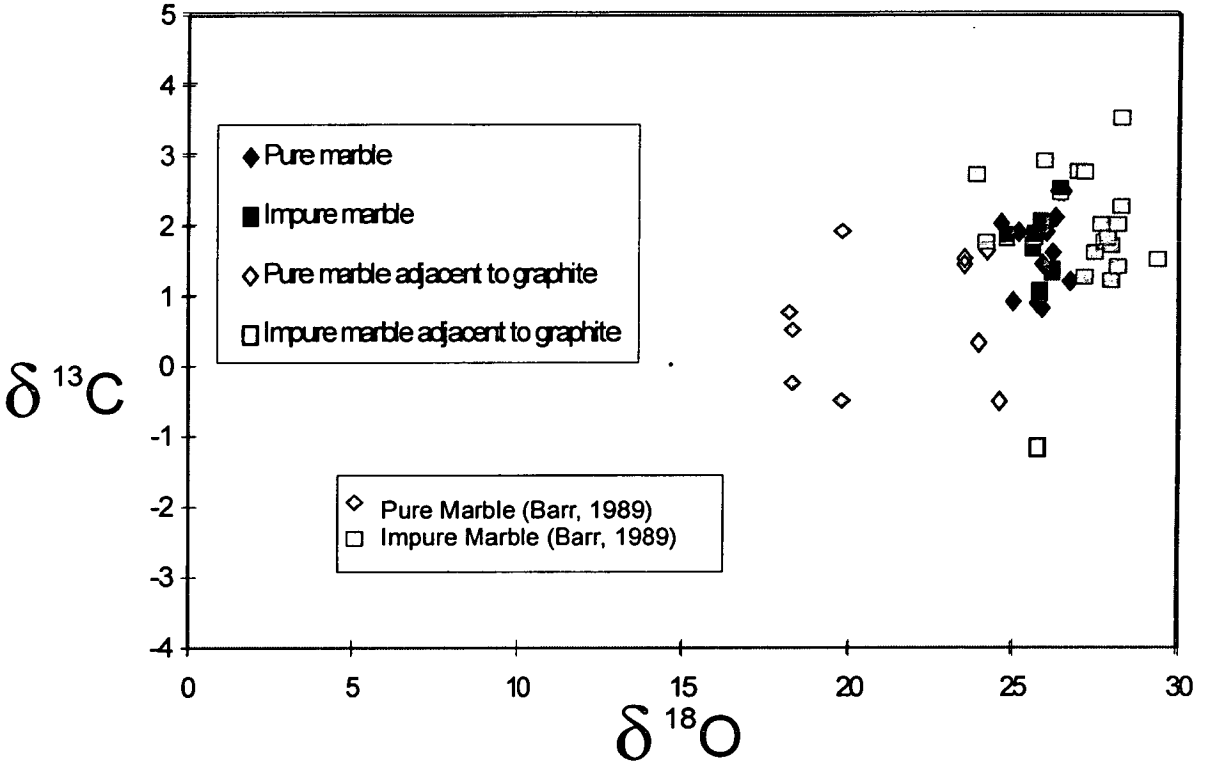

preferential channelling of fluid in the silicate-rich layer, or calcite equilibration with the silicate. Localisation of fluid flow in silicate-rich layers may occur for two reasons. Firstly, deformation may localise in impure layers due to competence contrasts between silicate and carbonate. Secondly, fabric anisotropy in impure layers due to alignment of mica, chlorite and glaucophane may have increased layer parallel fluid flow in silicate-rich layers.

Figure 5.12 of the profile at Windy Ridge A crosses a transition zone from carbonate-rich schist into marble containing silicate-rich horizons. The transition zone is documented isotopically by variation in $\delta^{18}O$, which is systematic across a metre-wide band. The change spans the lithological transition and could be related to a decrease in the silicate percentage or fluid infiltration. This locality also documents variation in the schist $\delta^{18}O$ and $\delta^{13}C$ composition. Enrichment of $\delta^{18}O$ and depletion in $\delta^{13}C$ in a thin marble band containing glaucophane is seen between -60 and -80 cm.

To assess the relative contributions of sedimentary heterogeneities in isotope composition and influx of an isotopically exotic fluid, at these and other localities, on carbonate ^{18}O depletion, the following techniques were used:

- comparative analyses of the $\delta^{18}O$ composition of coexisting silicate and carbonate in impure marble and
- correlation of the modal percent silicate in impure layers with $\delta^{18}O$ composition.

Analyses of coexisting silicate and carbonate were used to determine whether silicate and carbonate in impure layers were in isotopic equilibrium. There are several reasons why coexisting phases may not be in equilibrium. Equilibrium may never be reached between two coexisting phases due to: 1) slow diffusion rates; 2) one of the phases closes to exchange as a consequence of cooling, whilst the other phase continues to exchange. An alternative to these two scenarios is partial exchange with an infiltrating fluid.

The results of the analyses of coexisting silicate and calcite in impure marble horizons are plotted on a δ–δ plot (figure 5.19). Temperature lines have been calculated for qz-cc fractionation from Faure (1986), Sharp and Kirschner (1994) and for cc-gl from Javoy et al. (1970) using data from Taylor and Coleman (1986).

The qz-cc data points do not show constant fractionation (figure 5.19). The qz-cc data point in the bottom right on the graph is from a quartz segregation in the Windy Ridge B marble band (figure 5.13). The quartz and calcite are not in isotopic equilibrium, at any reasonable temperature, approximately 450 ± 50 °C (Dixon, 1969) for the terrain. It is inferred that as the quartz is from a segregation, the two phases formed at different times and have not since fully equilibrated. The other qz-cc data point is from the interbedded marble-quartzite layer, Nites (figure 5.8). The quartz and calcite may be in equilibrium, although the temperature is poorly constrained by variations in cc-qz fractionation data at low temperatures.

The calcite-glaucophane data form a more consistent data set as all the glaucophane analyses are from glaucophane crystals surrounded by calcite matrix in impure marble layers. The glaucophane was separated from the calcite by dissolving the carbonate in HCl acid before washing and picking. Four of the data points lie within error of a 650 °C temperature line (figure 5.19). The lower two of these cc-gl pairs are from the North Windy Ridge profile (figure 5.14). Constant and systematic fractionation of both calcite and glaucophane occur across the profile, indicating that both the glaucophane and the carbonate exchanged with the infiltrating low $\delta^{18}O$ fluid. The other two points on the 650 °C isotherm are from the profile Six Wells locality C (figure 5.15), at which there appears to be no fluid infiltration into the marble and there is a constant fractionation between calcite and glaucophane. The temperature of 650 ± 50 °C for the fractionation is poorly constrained, due to the very limited availability of equilibrium glaucophane fractionation data.

The final two data points are from Windy Ridge locality B (figure 5.13). In this example there is not a constant fractionation between the glaucophane and calcite. The cc-gl pair from 200 cm on the bulk traverse has an unreasonably high fractionation temperature for the terrain, which implies that cc-gl equilibrium has not

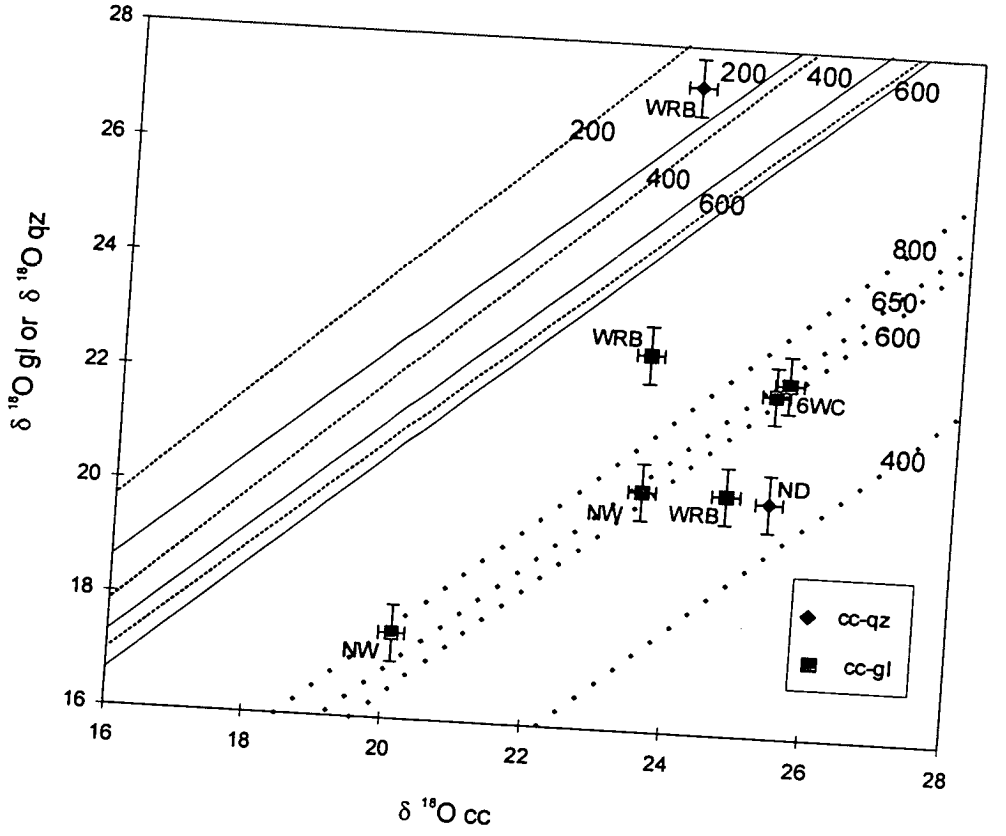

Figure 5.19

δ–δ plot for cc-gl and cc-qz. The plot is marked with temperature lines, fractionations were calculated using the fractionation equation for Δqz-cc from Faure (1986) ——, Sharp and Kirschner (1994) ..... , and Δcc-gl from Fourcade et al., (1970) calculated from data in Taylor and Coleman (1968) ▪ ▪ ▪. Letters stand for sample locations: NW - North Windy Ridge, WRB - Windy Ridge B, 6WC - Six wells C, ND - Nites D.

been attained. The inconsistency across the profile suggests that this may be related to channelled fluid infiltration or the calcite or glaucophane in the impure layers may have exchanged with other silicates present, which include quartz, epidote, mica and chlorite, whilst the other was closed to exchange.

To see what effect the presence of silicate had on the calcite $\delta^{18}O$ composition in impure marble, the modal percent of silicate was calculated and compared with the $\delta^{18}O$ composition. Samples from Windy Ridge A (figure 5.12) and B (figure 5.13) were used. Windy Ridge A was chosen as the boundary of the marble with the calc-schist below is a transition zone and it is was unclear whether the isotope profile obtained was the result of the decrease in percentage silicate in the marble or fluid infiltration. Samples from Windy Ridge B were used to see if depletion in $\delta^{18}O$ in individual impure layers was the result of the composition.

The samples were polished and coated in carbon, to minimise charging, in preparation for scanning electron microscope (SEM) analysis. Back-scatter electron microscope (BSEM) images were collected of impure marble samples. Ten images, 2.9 x 1.9 mm, were collected from each sample. The images were analysed using the image analysis package Scion Image. Density slices, highlighting silicate phases, were taken of the images (figure 5.20). Scion Image calculated the area of silicate and carbonate in each image. The percentage of silicate in individual images was used to calculate an average percentage from the 10 images collected from each sample. An error was calculated to one standard deviation for the silicate percentage of each sample.

The graph (figure 5.21) shows the silicate percentage and calcite $\delta^{18}O$ composition of the samples studied. A negative trend would be expected if there was a correlation between silicate content and $\delta^{18}O$ depletion. There is no correlation between the modal percent silicate in a sample and the $\delta^{18}O$ composition of the samples analysed. For example the sample at the contact, 0 cm, from the Windy Ridge A profile has the lowest modal percent silicate (17.8 %) and the lowest $\delta^{18}O$ composition (22.8 ‰). Even carbonate from impure marble samples with a modal

Figure 5.20
a) Back scatter electron microprobe image of sample S'97/171. Silicates in the impure marble are dark grey, carbonate is pale grey. b) Density slice of the same image, highlighting in red silicate phases, with the image analysis package Scion Image.

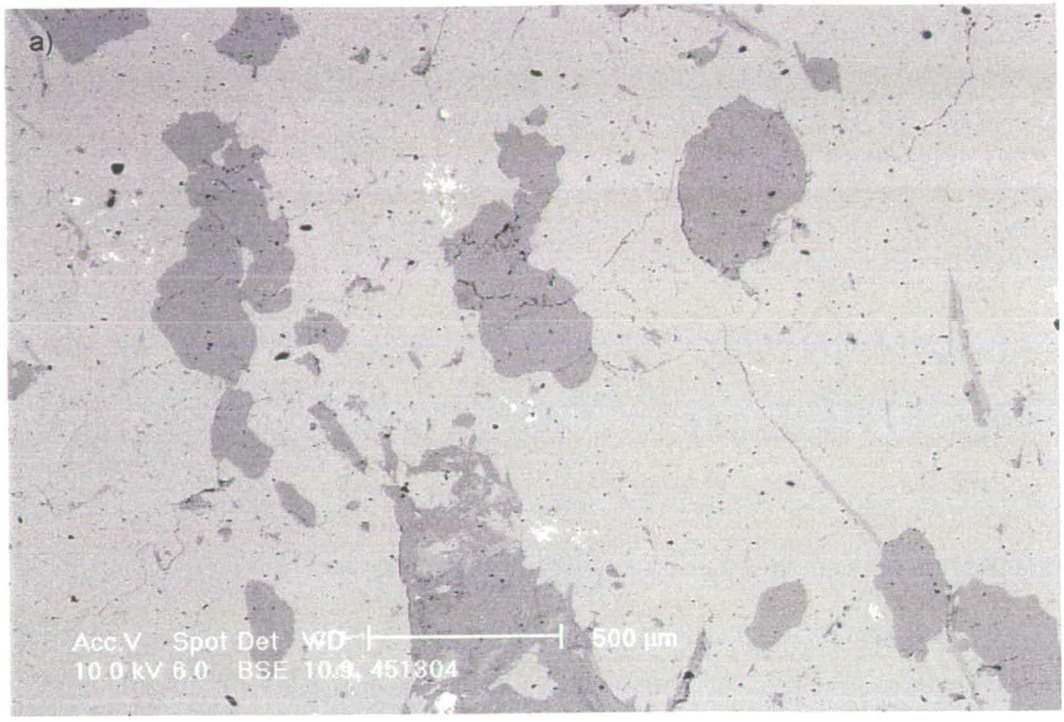

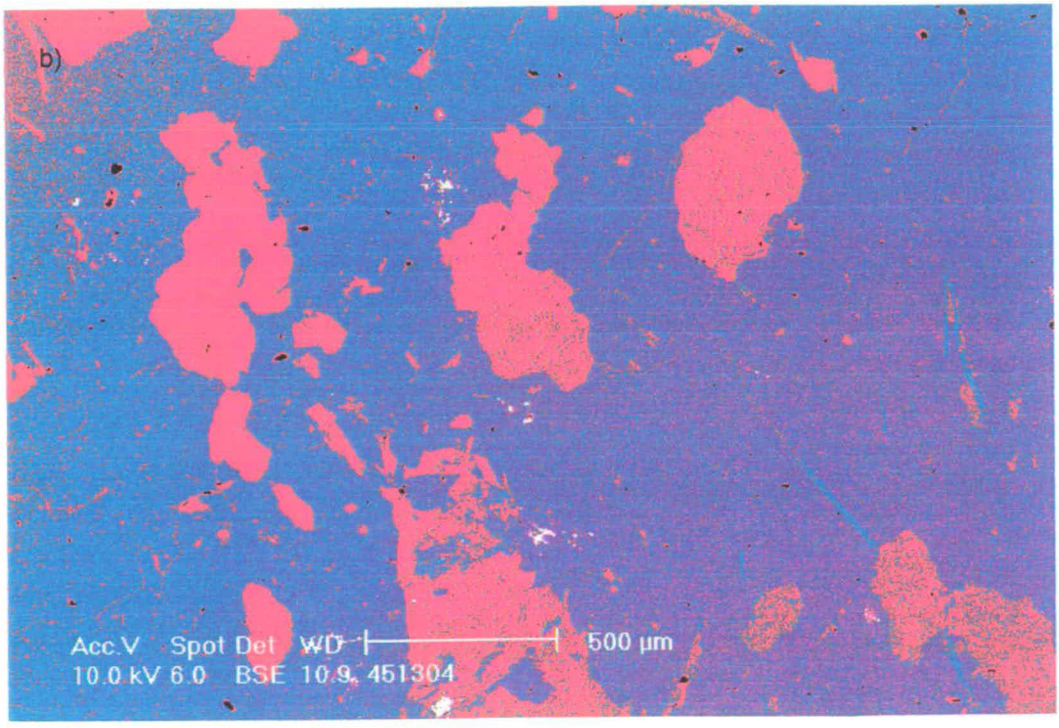

Figure 5.21

a) percentage silicate material versus the $\delta^{18}O$ composition of calcite, b) distance versus the $\delta^{18}O$ composition of calcite, for impure marble horizons

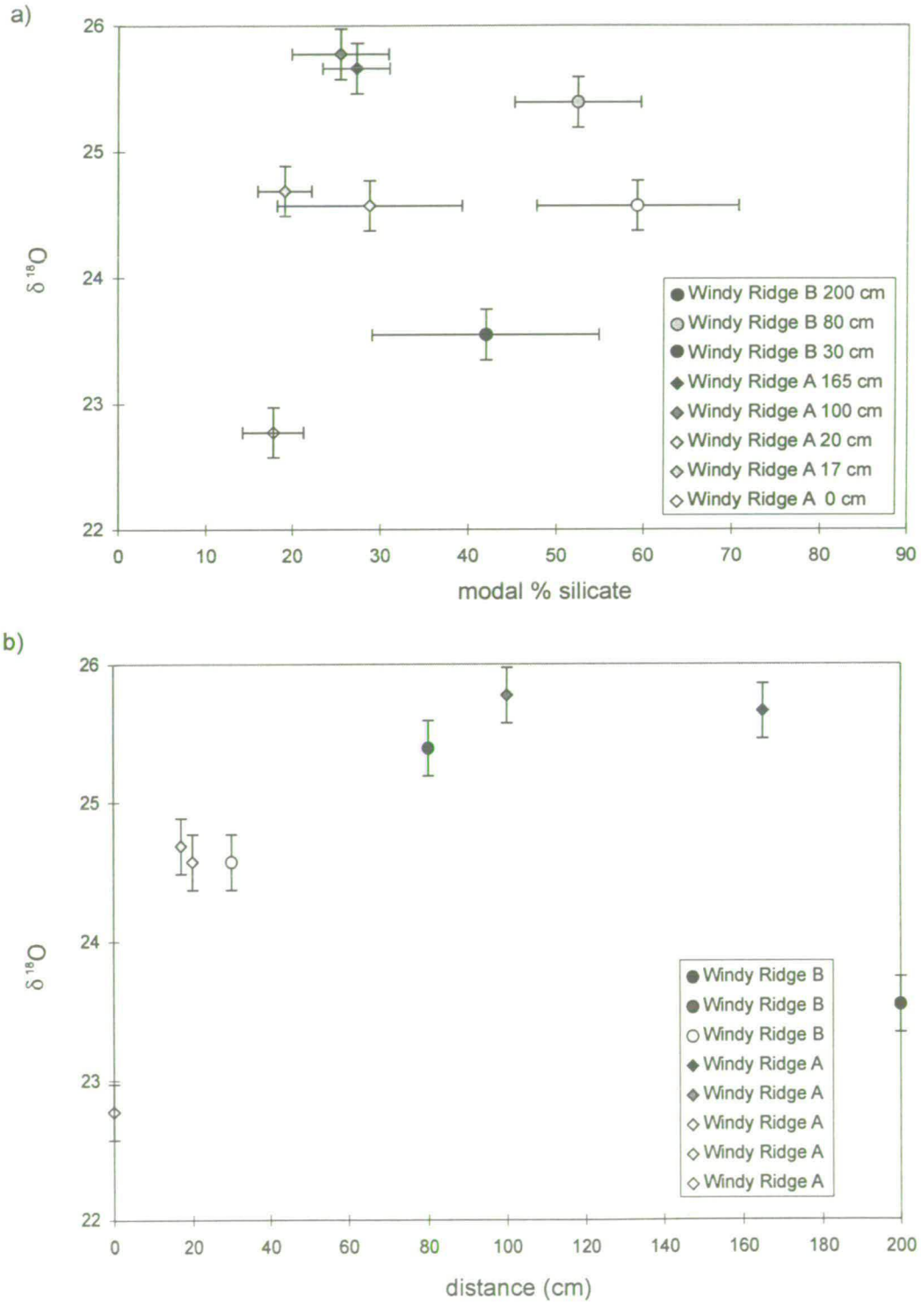

silicate content >50 % lie within the expected range of marine limestone composition.

For comparison the $\delta^{18}O$ compositions of the samples are plotted against distance from the adjacent schist (figure 5.21b). Samples within 50 cm of the contact are relatively depleted in $\delta^{18}O$ by comparison to calcite further from the contact. Samples at distances >50 cm from the contact are apparently undepleted, forming an upper $\delta^{18}O$ limit of 25.5-26 ‰. I have therefore inferred that the $\delta^{18}O$ profiles have formed as a result of infiltration of a low $\delta^{18}O$ fluid. Original sedimentary heterogeneities in isotope composition may have been present, but these have been overprinted by isotope exchange with the infiltrating fluid.

The exception to this pattern is the isotope composition at 200 cm on the Windy Ridge B profile (figure 5.13). This sample contains a high modal percent silicate of 42.0 %. The fractionation of $\delta^{18}O$ between calcite and glaucophane for this sample (figure 5.19) gives a high fractionation temperature, which is inconsistent with predicted maximum temperatures from mineral equilibria for peak metamorphism on Syros. An alternative explanation is that an isotopically light fluid has infiltrated this silicate rich layer, exchanging with the carbonate and not the silicate.

Discussion

The evidence documented by the different techniques shows that depletion of marble $\delta^{18}O$ compositions is not related to original sedimentary heterogeneities. Fractionations between glaucophane and calcite pairs at North Windy Ridge (figure 5.14) suggest that exchange of $\delta^{18}O$ between both minerals and an infiltrating fluid phase occurred and resulted in systematic fractionation of oxygen isotopes between calcite and glaucophane. A constant fractionation was also recorded at Six Wells locality C (figure 5.15), but there was no systematic depletion in $\delta^{18}O$ across the profile associated with fluid infiltration.

Modal percent silicate analyses from Windy Ridge A and B suggest that the composition of the calcite marble is unrelated to documented $\delta^{18}O$ depletions. Impure marble bands containing up to 50 modal percent silicate have carbonate $\delta^{18}O$

compositions within the range of those expected for marine limestones. At Windy Ridge A the modal percent silicate does not correspond to changes in $\delta^{18}O$ composition across the transitional boundary from calc-schist to marble. At Windy Ridge locality B the modal percent silicate in individual impure layers was also found to be unrelated to $\delta^{18}O$ composition.

Summary

- Sedimentary heterogeneities in $\delta^{18}O$ composition are not the cause of isotope depletion in marble band boundary layers.

Is there a greater degree of fluid infiltration into marble in contact with hydrated greenschist assemblages as compared to marble in contact with blueschist assemblages?

This question addresses whether the fluid infiltration event associated with isotopic depletion in marble band boundary layers is linked to retrogression. If the same fluid infiltration event is responsible both for hydration of high pressure assemblages and isotopic depletion, then marble bands adjacent to fully retrogressed greenschist should show a greater degree of isotopic depletion than marble adjacent to blueschist. To support the isotope study I have documented hydration reaction textures in marble horizons containing silicates.

Thin sections of silicate-bearing marble were examined for evidence of hydration reaction of the silicate phases. Samples were examined from Oros Syringas I (figure 5.9), Windy Ridge A (figure 5.12), Windy Ridge B (figure 5.13), North Windy Ridge (figure 5.14) and Six Wells locality C (figure 5.15). The following reactions were identified, in some of the impure marble samples, from textures preserved.

3 glaucophane + 6 epidote $\rightarrow$ 1 chlorite + 12 calcite +
+ 8 H_2O + 12 CO_2 19 quartz + 6 paragonite

5 glaucophane + 3 paragonite → 13 albite + 3 chlorite
+ 4 H_2O + 1 quartz

The table below (table 5.1) lists the thin sections examined from each locality. The mineralogy of the impure layer is recorded together with any reaction textures that were observed. The petrographic analysis of silicates in impure marbles documents evidence for fluid infiltration in the form of hydration reaction textures at three of the five localities. Glaucophane and epidote are locally partially retrogressed to chlorite, calcite, albite and quartz. On the scale of both a thin section and of a profile retrogression of silicate is variable. Marble sampled closest to the schist does not always document retrogressive reaction textures, whereas samples further from the contact do (e.g. Windy Ridge A, table 5.1). This suggests that fluid infiltration was channellised rather than pervasive and reactions localised rather than forming a pervasive front as documented elsewhere (e.g. Graham et al., 1983 and Skelton et al. 1997).

The lack of a reaction identified in sample S'95/68 from North Windy Ridge suggests that the fluid infiltration event, documented by depletion in $\delta^{18}O$ of both glaucophane and calcite across the profile (figure 5.14), occurred whilst glaucophane was able to exchange oxygen isotopes with a fluid phase and remain stable. I have therefore inferred that fluid infiltration of marble bands was not purely associated with greenschist retrogressive fluid infiltration. To determine the degree of fluid infiltration into marble bands adjacent to blueschists and greenschists, isotope profiles were assessed both qualitatively and quantitatively. For quantitative assessment the profiles were modelled by chromatographic theory, which is described below.

Table 5.1 Reactions identified in thin section of silicates in impure marble horizons. + reaction texture identified in the sample, - reaction texture not identified, O secondary minerals but no obvious reaction texture.

Sample	Mineral assemblage	Reaction gl + epd + H_2O + CO_2→chl + cc + qz + pg	Reaction gl + H_2O→ ab + chl
S97/55 Oros Syringas I	cc, gl, chl, qz, epd, mica	+	-
S97/155 (0 cm) Windy Ridge A	cc, dol, gl, epd, qz, mica, px (mantled by epd)	-	-
S97/157 (17 cm) Windy Ridge A	cc, gl, epd, qz, mica, chl, ab	+	+
S97/158 (20 cm) Windy Ridge A	cc, gl, epd, qz, mica, chl	O chl present but no reaction texture	O chl present but no reaction texture
S97/163 (100 cm) Windy Ridge A	cc, epd, qz, mica, gl	-	-
S97/167 (165 cm) Windy Ridge A	cc, mica, qz, chl	O chl present but no reaction texture	O chl present but no reaction texture
S96/53 Windy Ridge A	cc, gl, epd, qz, mica, chl, ab	+	+
S97/171 (30 cm) Windy Ridge B	cc, qz, mica	NA no epd to react	NA no gl to react
S97/172 (80 cm) Windy Ridge B	cc, gl, mica, qz, epd	-	-
S97/175 (200 cm) Windy Ridge B	cc, px, gl, epd	-	-
S96/58 North Windy Ridge	cc, gl, epd, chl, mica, qz	O chl present but no reaction texture	O chl present but no reaction texture
S96/88 Six Wells loc C	cc, epd, chl, mica, qz, gl, oxide	+ only very localised	-
S95/15M Six Wells loc C	cc, gl, epd, qz, mica, chl	+	-

Modelling

Flux of fluid through layers of rock can be modelled using an advection-diffusion-reaction equation (e.g. Hoffman, 1972 and Bickle and McKenzie, 1987). The method uses an identifiable heterogeneity (i.e. a chemical, petrological or isotopic difference between two layers), and then identifies the advective displacement, and diffusive/kinetic modification, of the heterogeneity. The transport characteristics are inferred by fitting simplified models to the profiles recorded by the advection- diffusion and kinetic exchange of the heterogeneity between the layers. The controls on the transport of the tracer can be described by chromatographic theory which is described below. Chromatographic theory was used, in attempt to quantify the time integrated fluid fluxes of infiltration of Syros marble bands. The stable isotope profiles were modelled using the computer program, based on chromatographic theory written by Alasdair Skelton (see Skelton et al. 1997 and Graham et al. 1997).

Theory

Chromatographic theory is based on solutions to a one-dimensional differential equation which describes transport through a porous medium by advection and diffusion:

$$\phi \frac{\partial C_f}{\partial_t} = -\varpi\phi \frac{\partial^2 C_f}{\partial z^2} - \frac{\partial C_s}{\partial_t} \frac{(1-\phi)\rho_s}{\rho_f}$$

(advection) (diffusion) (kinetic)

(A glossary of terms for the equations is given in table 5.2.)

Table 5.2 Glossary of terms for modelling equations (after Graham et al, 1997)

Symbol	Definition	Units
C_f	Concentration of chemical component in fluid	Various
C_s	Concentration of chemical component in solid	Various
D	Diffusion coefficient	m^2s^{-1}
t	Time	s
z	Distance	m
ϕ	Porosity	None
ρ_s	Density of solid	gm^{-2}
ρ_f	Density of fluid	gm^{-2}
ω	Fluid velocity	ms^{-1}
K_v	Fluid/solid partition coefficient	None
Pe	Peclet number	None
h	Length	m
N_D	Damköhler number	None
κ	Exchange rate	s^{-1}
$C_{s,2}$	Concentration of chemical component in the solid down stream of front	Various

The equation describes the change in concentration of a geochemical tracer with time (left-hand side of equation) in terms of advection, diffusion and kinetic exchange (first, second and third terms respectively on the right-hand side). The solutions to the equation depend on the initial starting parameters chosen and the boundary conditions (Bickle and Baker, 1990a). The model assumes an initial step function (figure 5.22) of concentration across the lithological contact. One of two conditions has then been modelled: 1) uniform flow in which fronts migrate down stream (figure 5.22A). For uniform flow the relative permeabilities between layer must be small and the major component of flow is across layers (figure 5.22A); and 2) 'pinned boundary' flow, in which the permeability of one of the lithologies greatly exceeds that of the other. The fluid is channelled in the permeable lithology parallel to layering with only a minor component of the cross-layer flow entering the less permeable lithology (figure 5.22B). The composition of the permeable layer will be buffered by the composition of the fluid. In metamorphic terrains where marbles are interbedded with schist units it is generally assumed that for a pinned boundary

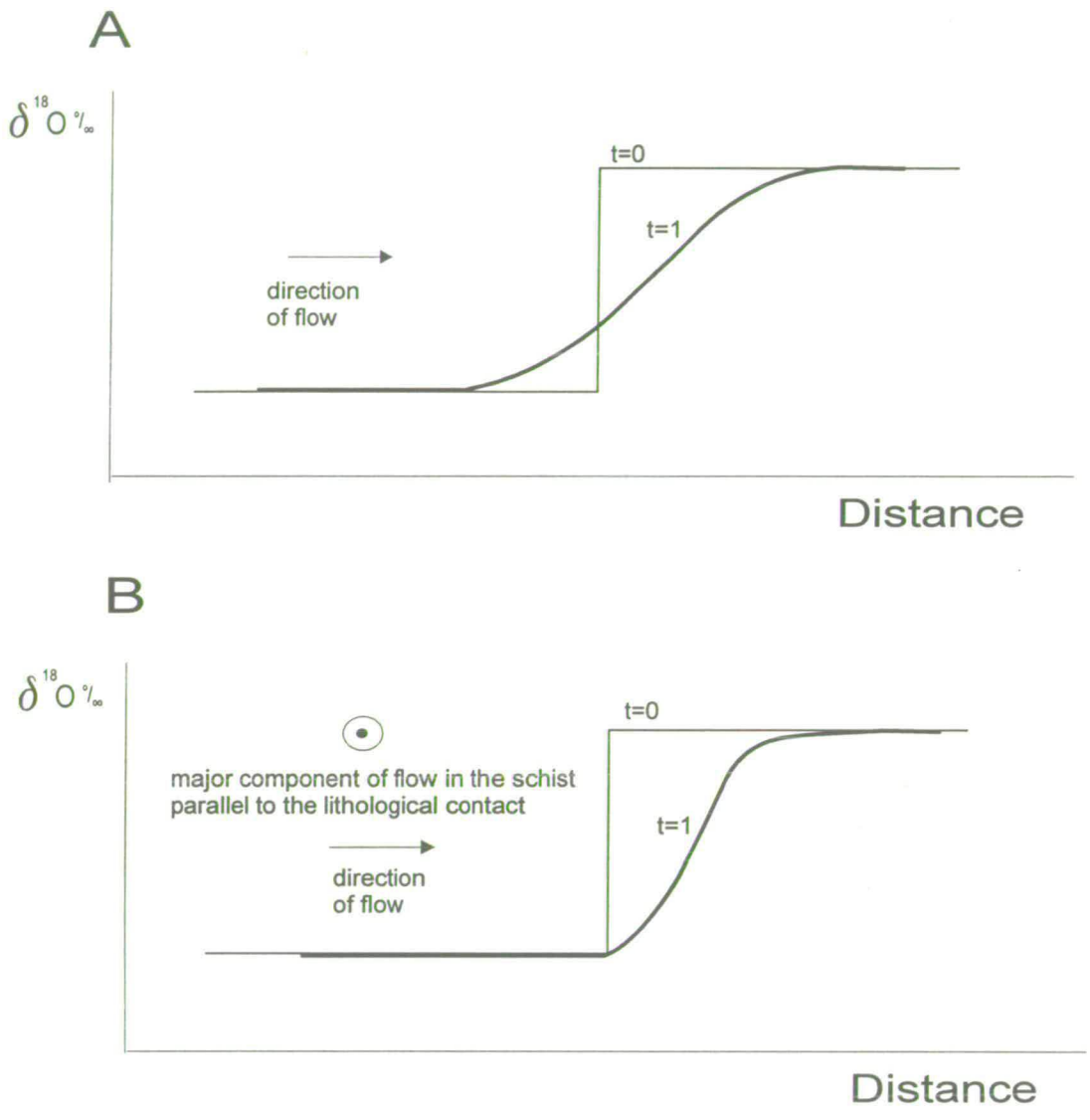

Figure 5.22
A) Schematic diagram of uniform flow (t=1), from an initial step function (t=0).
B) Schematic diagram of pinned boundary flow (t=1) in which the major flow direction is parallel to the lithological contact within the schist. After Bickle and Baker (1990a).

solution the marble will be the relatively impermeable lithology (e.g. Bickle and Baker, 1990a). Pinned boundary flow is also thought to be the most likely model, given that experimental data implies that marbles are relatively impermeable (Holness and Graham, 1995).

In both models the initial step profile is transported by advection while the shape of the profile is modified by diffusion and kinetic controls on the geochemical exchange. To solve the equation some simplifying assumptions have to be made. The equation can be simplified if fluid-solid exchange is assumed to be more rapid than the advective transport of the chemical component equilibrium is attained at a grain scale. This assumption simplifies the equation to:

$$\frac{1}{K_v}\frac{\partial C_f}{\partial_t} = -\varpi\phi\frac{\partial C_f}{\partial_z} + D\phi\frac{\partial^2 C_f}{\partial z^2}$$

where K_v is the fluid/solid partition coefficient. This equation can be solved by dimensionless transformations and depends on the dimensionless constant the Peclet number (Pe):

$$Pe = \frac{\varpi\phi h}{D\phi}$$

dimensionless- time, -distance and the boundary conditions. The Peclet number describes the ratio of advection to diffusion. High Peclet numbers are indicative of an advection dominated system, whilst low Peclet numbers are indicative of diffusion. By knowing K_v it is possible to calculate the time integrated fluid flux ($\omega\phi t$) and the diffusion distance ($2\sqrt{d\phi t}$) (Bickle and Baker, 1990a).

The alternative simplification to grain-scale equilibrium, is to limit fluid-solid exchange kinetically, in the absence of diffusion. The equation may be solved by any specified kinetic fluid-solid exchange, although available information does not justify complex exchange models (Graham et al. 1997). The equation is therefore solved by

a simple kinetic exchange law, expressed as a linear function of fluid-solid compositions by:

$$\frac{\partial C_s}{\partial_t} = \kappa(C_s - C_{s,2})$$

where κ is an exchange rate (dimensions of t^{-1}) and the term in brackets is a measure of the disequilibrium between fluid and solid. The equation can be used in more general situations than simply linear kinetics as diffusion controlled exchange in many cases can be approximated to linear functions (Bickle, 1992). The equation can again be transformed by dimensionless parameters and depends on the dimensionless constant the Damköhler Number (N_D):

$$N_D = \frac{\kappa h}{\varpi \phi}$$

as well as dimensionless -time and -distance and the boundary conditions. The Damköhler Number is determined by the ratio of the rate of kinetic exchange to the flux of fluid.

Goodness of fit - the χ^2 value

The model fits a best fit line to the raw isotope data, to see how well each model fits the data. The program calculates diffusion and advection distances, a time integrated fluid flux and a χ^2 value. The χ^2 value gives the goodness of the fit of the model to the data. The analytical uncertainties in the calcite $\delta^{18}O$ data of ± 0.2 ‰ are incorporated into the model. The χ^2 value is a function of the number of degrees of freedom. The degrees of freedom are determined by the number of data points modelled minus the number of parameters fitted for. The number of parameters fitted for varies depending on the type of model the data are fitted to. For a diffusion only model, three parameters may be fitted: C0 (composition of the schist), C1 (composition of the marble) and Dt (diffusion with time). In most of the profile it is possible to constrain C0 and C1 from the plateau in $\delta^{18}O$ composition on either side

of the front. For the two advective-diffusion models the original compositions of the schist (C0) and the marble (C1) must be fixed. The uniform flow model fits for the parameters Z, the distance of advection of the front, and D, diffusion of the front. The pinned boundary model fits for Z and the Peclet number. Fitting for one less parameter gives an extra degree of freedom and could improve the fit of the data, making it statistically valid.

For each profile modelled all parameters were initially fitted for, to see if the data could be modelled to a statistically valid solution. If the data modelled did not provide a statistically valid fit then in the case of the diffusion model C0 and C1 parameters were fixed and the data re-modelled. For each profile and model the parameters fitted for are indicated. Outliers, $\delta^{18}O$ compositions which do not fall in the general trend, have been occasionally omitted from the models. The validity of omitting data points from the models is discussed in the text associated with each modelled data set.

The χ^2 distribution can be converted to a P value, which is the probability that the χ^2 distribution should exceed a specified value by chance. The P values range from 0-1 and were read from a data table in Fisher (1954) for the appropriate number of degrees of freedom. If P is between 0.1 and 0.9 the model is in good agreement with the data. If it is below 0.02 the model fails to account for the trends in the data. Conventionally, models with P values > 0.05 are taken as statistically meaningful and this convention has been adopted here. In the program used, the χ^2 distribution can be correlated with 68%, 95% and 99% confidence levels. The χ^2 distribution was in all cases calculated to a 95% confidence level, as in the previous studies of Bickle and Baker (1990a) and Graham et al. (1998).

Model Assumptions and Limitations

There are three main assumptions on which chromatographic theory is based:

1) porosity and permeability are constant,

2) local fluid rock equilibrium is attained at a grain-scale,

3) a fluid filled network already exists in the rock.

The three assumption rely on knowledge of how fronts form across geochemical gradients in rocks. Until recently few studies had addressed the mechanisms of front formation and the assumptions have never been validated. The recent work of Lewis et al. (1998) and Graham et al. (1998) challenge the first two assumptions. They show grain-scale $\delta^{18}O$ heterogeneities and relate them to the deformation enhanced permeability creation. Their work demonstrates that permeably in the two marbles studied was created dynamically and transiently and that grain scale equilibrium was not attained. Other studies have also drawn the conclusion that deformation plays a critical role in creating and destroying permeability in metamorphic rocks, resulting in transient permeability networks. (e.g. McCaig et al. 1995). Permeable networks created by deformation will change both temporally and spatially, as they are part of a dynamic system. The controls on deformation on the creation of dynamic permeability and local isotopic disequilibrium are addressed in chapter 6.

Cartwright (1997) showed that if fluids infiltrate 'dry' rocks then chromatographic theory is an unrealistic model for infiltration. He suggests that the model should only be used when geochemical tracers such as isotopes are reset behind a mineral reaction front. Front theory based on chromatographic models has been used both on reactive (Skelton et al. 1997) and unreactive lithologies (Bickle and Baker 1990a). Impure marble bands on Syros do show very localised hydration reactions, but whether these are related to isotope front formation is unknown.

Previous studies have shown that during burial, associated with regional metamorphism, an interconnected grain boundary network of fluid becomes unstable (e.g. Holness and Graham, 1995). The rocks become compacted and fluid is expelled from the rock (Walther and Orville, 1982). These observations imply that most rocks prior to metamorphic infiltration will not support a fluid filled network.

Chromatographic theory also has two main limitations:

1) fluid-flow is only considered in one-dimension and

2) fluid fluxes, Pe and N_D are time integrated.

The models only ever consider fluid-flow in one-dimension unless three one-dimensional fluid-flow vectors are resolved (e.g. Skelton et al, 1995), limiting the

amount of information that can be obtained, particularly in relation to values calculated for fluid fluxes, Peclet and Damköhler numbers which are only for one directional component of the flow.

The input data to the model are the result of time integrated geochemical exchange, therefore the output data in terms of fluid fluxes, Peclet and Damköhler numbers are also time integrated. The chromatographic model cannot discern the effects of several fluid infiltration events.

The Oros Syringas case study

Two profiles from the Oros Syringas hillside were chosen for a preliminary case study. The profiles were chosen as the hillside consists of a simple sequence of interlayered marble and pelite (figure 5.6). The schist at the base of the hillside is retrogressed almost pervasively to an albite- and chlorite-bearing greenschist assemblage. The isotope profile (figure 5.9) into the marble structurally above the greenschist shows a broad trend in $\delta^{18}O$ composition from approximately 18 ‰ at the contact to 29 ‰ 2 m into the marble. The marble band contains an impure horizon between 150-180 cm on the bulk profile (figure 5.9). The horizon is isotopically depleted relative to the surrounding marble. Silicates within the impure layer show evidence for hydration and are partially replaced by chlorite (table 5.1). This layer is thought to have focused infiltrating fluid, causing the observed depletion in $\delta^{18}O$ relative to adjacent layers. **The marble in contact with the greenschist shows a broad band of depleted $\delta^{18}O$ over 2 m. Further evidence for fluid infiltration of the marble band can be identified in the form of retrogressed silicate phases.**

Near the top of the Syringas hillside the schist is unretrogressed and contains pristine blueschist assemblages. The isotope profile into the marble above the blueschist (figure 5.11) shows little depletion in $\delta^{18}O$. At the contact the $\delta^{18}O$ composition of the marble is depleted to approximately 18.5 ‰. At distances greater than 5 cm from the contact $\delta^{18}O$ compositions of approximately 25- 28 ‰ are recorded. **The marble above the blueschist shows isotopic depletion of ^{18}O only at the contact.**

Qualitatively the $\delta^{18}O$ profiles indicate fluid infiltration into the lower marble band adjacent to the underlying greenschist, with preferential fluid flow in a silicate-rich horizon resulting in isotope depletion and hydration of silicate phases. In comparison the isotope profile into the marble above the blueschist suggests no fluid infiltration in the marble. An initial interpretation of the profiles would suggest that fluid associated with retrogression was the cause of isotope modification of marble band boundary layers.

The two profiles were modelled as described above. Firstly the Oros Syringas I profile was modelled for uniform flow (table 5.3). All the data points of calcite $\delta^{18}O$ were initially modelled. The data have a very poor fit to the model and with a P value of < 0.01. Data points were then removed from the model. These omitted points included those from the impure layer and ones that appeared by eye not to follow the trend in $\delta^{18}O$ composition. The data were then modelled again, this time giving a much better fit, but not one that was statistically valid. The modelled profile is shown in figure 5.23. Very few of the data points lie within analytical error of the modelled fit; the data points omitted are annotated. Omission of the data points was not particularly valid. There was no analytical reason to omit these points and the heterogeneities are thought to be true variations in $\delta^{18}O$ composition. The fact that the model does not fit the profile even with the heterogeneities removed suggests that the fluid did not infiltrate the marble in a manner that is representative of uniform flow.

Table 5.3 Modelling results for Oros Syringas I - uniform flow

Oros Syringas I - Uniform Flow								
Fitted parameters Z & D								
C0	C1	Z	D	χ^2	time integrated fluid flux	no.data points	n	P
18	28.9	29.349 ± 647.798	1.817 ± 18776.1	9680.013	49.893 ± 11101.257	31	29	<0.01
18	28.9	38.380 ± 01.216	77.664 ± 3.704	358.784	65.247 ± 2.066	24	22	<0.01

The same data were also modelled for pinned boundary flow and the results are tabulated in table 5.4. A P <0.01 was obtained for both data sets, implying that the data cannot be fitted to a pinned boundary chromatographic model and that both uniform flow and pinned boundary advection-diffusion models are inappropriate for the profile.

Table 5.4 Modelling results for Oros Syringas I - pinned boundary flow

Oros Syringas I - Pinned boundary flow								
Fitted parameters Z & Pe								
C0	C1	Z	Pe	χ^2	time integrated fluid flux	no.data points	n	P
18	28.9	36.466 ± 0.902	2.015 ± 0.49	7367.165	61.992 ± 1.533	31	29	<0.01
18	28.9	58.136 ± 1.522	3.014 ± 0.213	982.758	98.831 ± 2.581	24	22	<0.01

The profile from the schist into the top marble at Oros Syringas III (figure 5.11) was also modelled. The profile has been modelled for diffusive exchange at the contact, as well as for the advective-diffusion models uniform and pinned boundary flow. The results are tabulated in tables 5.5, 5.6 and 5.7 respectively.

Table 5.5 Modelling results for Oros Syringas III - diffusion

Oros Syringas III-Diffusion						
Fitted parameters Dt, C0 & C1						
C0	C1	Dt	χ^2	no.data points	n	P
16.92 ± 308.79	27.819 ± 0.179	4.214 ± 165.238	233.421	11	8	<0.01

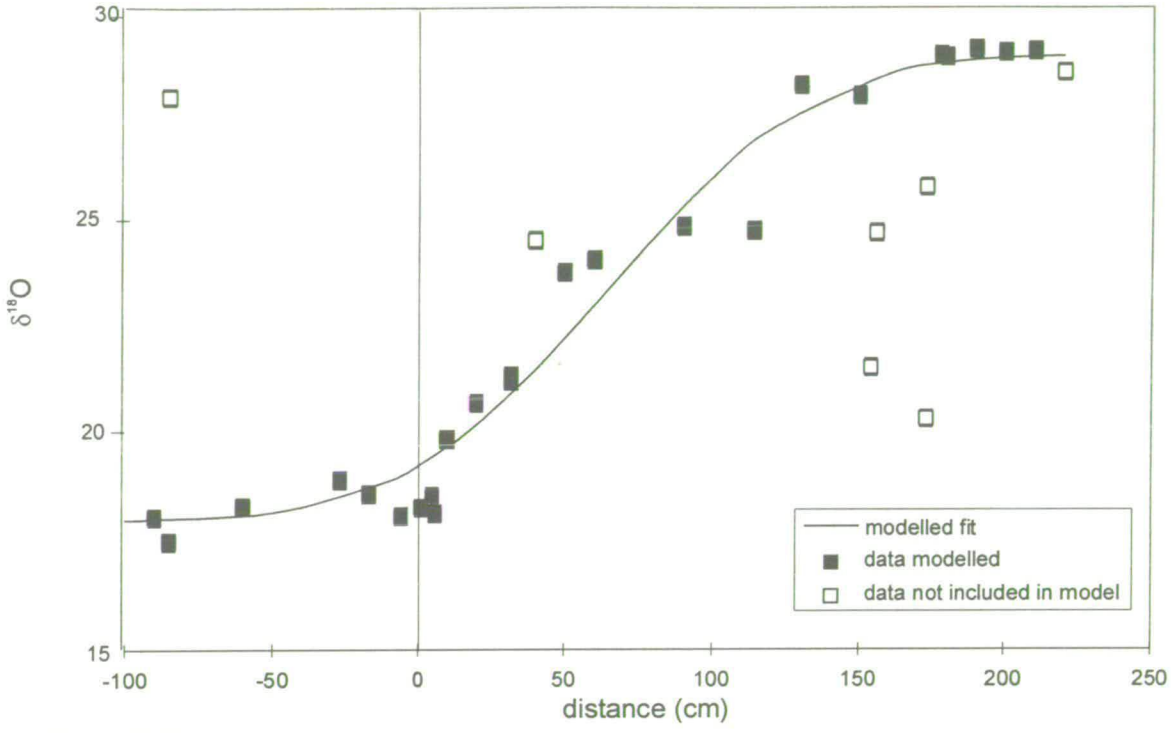

Figure 5.23
Uniform flow chromatographic model for Oros Syringas profile I. The fit of the data to the model is statistically invalid.

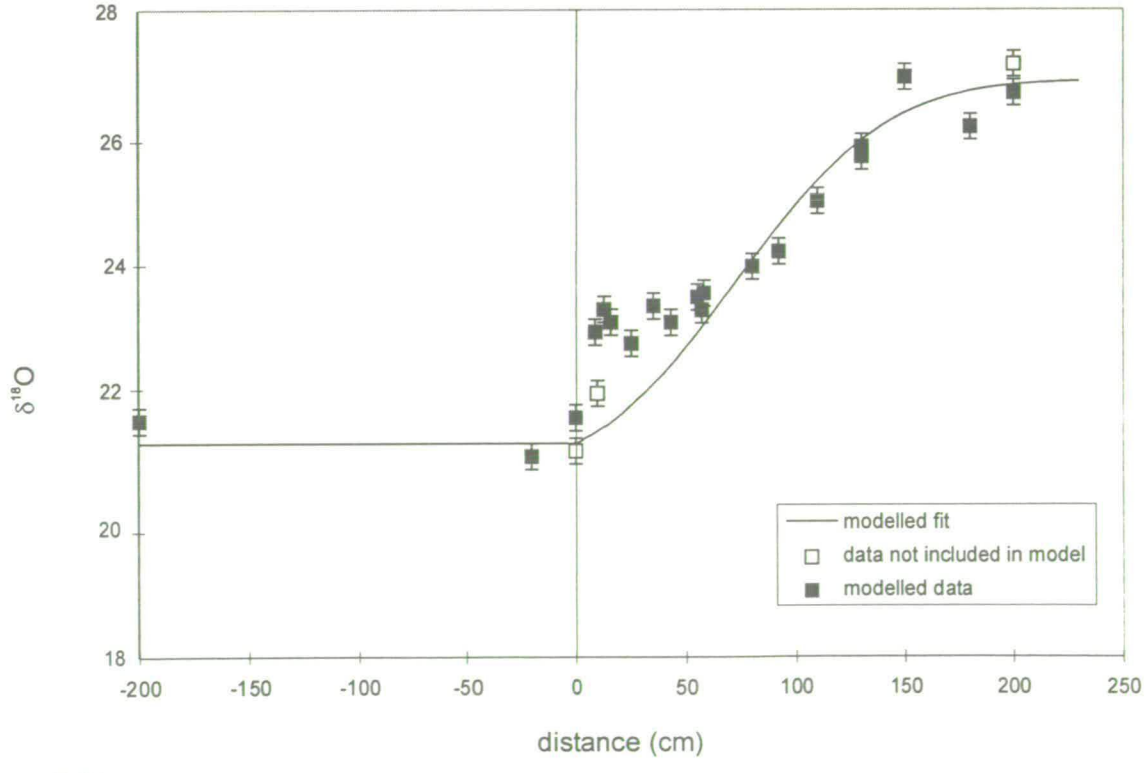

Figure 5.24
Pinned boundary flow chromatographic model for North Windy Ridge. The fit of the data to the model is statistically invalid.

Table 5.6 Modelling results for Oros Syringas III - uniform flow

Oros Syringas III - Uniform Flow								
Fitted parameters Z & D								
C0	C1	Z	D	χ^2	time integrated fluid flux	no.data points	n	P
16	28.3	1.19 ± 0.140	3.533 ± 0.354	150.79	2.023 ± 0.237	11	9	<0.01
16	28.2	1.161± 0.141	3.470 ± 0.356	137.959	1.974 ± 0.24	11	9	<0.01

Table 5.7 Modelling results for Oros Syringas III - pinned boundary flow

Oros Syringas I - Pinned boundary flow								
Fitted parameters Z & Pe								
C0	C1	Z	Pe	χ^2	time integrated fluid flux	no.data points	n	P
16	28.2	*	*	*	*	11	9	*

*-no solution

Again the chromatographic models did not produce a statistically valid fit to the data at Oros Syringas III. The uniform flow model was improved by varying the fixed C1 composition by 0.1 ‰, but all the fits remain far from statistical validity. The invalid fits suggest that diffusion, uniform flow and pinned boundary flow based on chromatographic theory do not describe the data.

Oros Syringas Discussion

Qualitative analysis of isotope profiles across schist-marble contacts on the Oros Syringas hillside suggest that fluid infiltration associated with retrogression was related to isotopic alteration of the marble bands. The lower isotope profile (figure 5.9) documents a 2 m wide $\delta^{18}O$ front in the marble boundary layer. Fluid infiltration of the lower profile Oros Syringas I (figure 5.9) during retrogressive greenschist facies metamorphism is recorded by hydration of silicates in an impure marble horizon (table 5.1). The heterogeneities in isotope composition in this front imply that fluid infiltration was localised. The mechanisms by which fluid infiltrated the

marble band are therefore inferred to have played a key role in the degree and spatial variability of isotopic alteration. This is reflected by the fact that the profile does not fit a chromatographic model for fluid infiltration.

The upper profile Oros Syringas III (figure 5.11) shows no isotopic alteration, apart from at the contact. It was thought that a diffusive model or minor amount of advection (i.e. < 10 cm) may fit the data. However, none of the models gave a statistically valid fit to the profile.

Other profiles

The simple pattern of isotopic alteration in marble bands above greenschist and not above blueschist documented on the Oros Syringas hillside is not seen across the whole of Syros. At Path Windy Ridge east, where the marble lies above a graphitic garnet-bearing schist, there appears to have been isotopic alteration across the width of the marble band (figure 5.17). Isotope profiles are also seen above blueschist at Six Wells locality D, North Windy Ridge, Windy Ridge A and B (figures 5.16, 5.14, 5.12 and 5.13 respectively), although in impure marble horizons at Windy Ridge A local retrogression of silicate phases is identified (table 5.1).

North Windy Ridge

At North Windy Ridge the glaucophane in impure marble horizons is not retrogressed and shows systematic exchange across the $\delta^{18}O$ profile (figure 5.14). This profile was targeted for modelling to see if the fluid infiltration and isotopic alteration could be modelled by a chromatographic advection-diffusion model. The profile was modelled for both uniform (table 5.8) and pinned boundary flow (table 5.9). Initially all the data points were modelled, then points were omitted from the contact, 10 cm and 200 cm, as these data points did not fit the observed trend in $\delta^{18}O$ composition. Omitting these points did not improve the fit for uniform flow, but improved it slightly for pinned boundary flow. However, all fits are statistically invalid. A pinned boundary flow model for the profile is shown in figure 5.24.

Table 5.8 Modelling results for North Windy Ridge - uniform flow

North Windy Ridge - Uniform Flow								
Fitted parameters Z & D								
C0	C1	Z	D	χ^2	time integrated fluid flux	no.data points	n	P
21.3	26.9	0.894 ± 8258.6	1.091 ± 10085.2	4116.831	1.519 ± 14039.668	23	21	<0.01
21.3	26.9	*	*	*	*	20	18	<0.01

*-no solution

Table 5.9 Modelling results for North Windy Ridge - pinned boundary flow

North Windy Ridge - Pinned boundary flow								
Fitted parameters Z & Pe								
C0	C1	Z	Pe	χ^2	time integrated fluid flux	no.data points	n	P
21.3	26.9	59.061 ± 2.385	1.204 ± 0.159	330.480	100.404 ± 4.055	23	21	<0.01
21.3	26.9	59.390 ± 2.409	1.137 ± 0.166	318.967	100.962 ± 4.095	20	18	<0.01

The modelled fits for the North Windy Ridge profile again suggest that the chromatographic models applied, uniform- and pinned boundary-flow are not applicable to front formation associated with fluid infiltration in the marble band.

Windy Ridge A

The profile at Windy Ridge A (figure 5.12) was also modelled. **This profile crosses a transition zone from calc-schist into impure marble.** The change in $\delta^{18}O$ composition has been shown not to be related to silicate composition (figure 5.21). The $\delta^{18}O$ profile was modelled to see if it could be fitted by a diffusional model (table 5.12) or by an advective-diffusion model, uniform flow (table 5.13) or pinned boundary flow (table 5.14).

Table 5.12 Modelling results for Windy Ridge A - diffusion

Windy Ridge A - Diffusion						
Fitted parameters Dt, C0 & C1						
C0	C1	Dt	χ^2	no.data points	n	P
20.945 ± 0.665	26.021 ± 0.157	136.875 ± 45.873	101.333	13	10	<0.01
Fitted parameter Dt						
20	26	104 ± 20.373	255.629	13	12	<0.01

The data were inputted twice into the diffusion model. The first time all the data were modelled and all three parameters were fitted for. The second time the concentrations of $\delta^{18}O$ in the schist and the marble were fixed and only the Dt parameter was fitted for. Although this improved the modelled fit the diffusion model was shown not to be suitable for the data and P values of < 0.01 were again obtained.

Table 5.13 Modelling results for Windy Ridge A - uniform flow

Windy Ridge A - Uniform Flow								
Fitted parameters Z & D								
C0	C1	Z	D	χ^2	time integrated fluid flux	no.data points	n	P
20	26	2.69 ± 1.136	30.433 ± 4.66	57.532	4.575 ± 1.932	13	11	<0.01
20.6	26	4.986 ± 1.019	23.411 ± 4.358	41.344	8.476 ± 1.732	13	11	<0.01
20.8	26	5.604 ± 0.996	81.655 ± 4.202	39.293	9.528 ± 1.694	13	11	<0.01

The uniform flow model seems to fit the data best although it did not produce a statistically valid fit. The model was refined until the lowest χ^2 value was achieved by changing the fixed $\delta^{18}O$ composition of the schist from 20 to 20.8 ‰.

Table 5.14 Modelling results for Windy Ridge A - pinned boundary flow

Windy Ridge A - Pinned boundary flow								
Fitted parameters Z & Pe								
C0	C1	Z	Pe	χ^2	time integrated fluid flux	no.data points	n	P
20.6	26	16.378 ± 1038.883	395.90 ± 52133.7	238.786	27.843 ± 1766.101	13	11	<0.01
20.8	26	16.018 ± 5.483	57.35 ± 42.116	191.078	27.230 ± 9.321	13	11	<0.01

The data were also modelled twice for pinned boundary flow changing the $\delta^{18}O$ composition of the schist. Neither fit was statistically valid.

Nites locality D

The isotope profile of Nites locality D (figure 5.8) crosses the contact between a retrogressed calc-schist and an inter-banded quartzite-marble. This profile was modelled as an example of an isotope front above retrogressed greenschist. Isotopic depletion occurs within 80-90 cm of the contact. The variation in the $\delta^{18}O$ composition of the marble varies from 19 to 20 ‰ at the contact to approximately 25 to 26 ‰ at distances greater than 90 cm. **The profile shows isotopic depletion over the first 90 cm in the marble band**.

The profile was modelled for both uniform (table 5.10) and pinned boundary flow (table 5.11). As before all points were initially modelled and as in the other profiles the fits were not statistically valid. Two points were then omitted, although this still did not produce a statistically valid fit.

Table 5.10 Modelling results for Nites locality D - uniform flow

Nites D - Uniform Flow								
Fitted parameters Z & D								
C0	C1	Z	D	χ^2	time integrated fluid flux	no.data points	n	P
20	26	32.584 ± 1.371	37.028 ± 3.736	184.836	55.393 ± 2.331	20	18	<0.01
20	26	31.723 ± 1.421	40.554 ± 4.025	128.512	53.929 ± 2.416	18	16	<0.01

Table 5.11 Modelling results for Nites locality D - pinned boundary flow

Nites D - Pinned boundary flow								
Fitted parameters Z & Pe								
C0	C1	Z	Pe	χ^2	time integrated fluid flux	no.data points	n	P
20	26	50.669 ± 1.742	15.051 ± 3.795	260.824	86.138 ± 2.961	18	16	<0.01

Discussion

The modelling of all isotopic profiles indicates that they have not formed by pinned boundary or uniform flow described by chromatographic theory. None of the modelled profiles gave a statistically valid fit to the chosen models. The number of parameters fitted for were minimised where possible and outliers from the $\delta^{18}O$ trend were removed. The validity of removing the outliers was not strong and their removal did not statistically improve the fits. From the poor fits to the model, the observed heterogeneities in $\delta^{18}O$ composition of the profiles and the localisation of hydration reaction of silicates in impure marble layers it is though that the profiles formed as a result of heterogeneous rather than chromatographic flow. The heterogeneity of the flow could be the result of several processes: 1) the isotope fronts have formed as a result of several fluid infiltration events, 2) fluid infiltration was localised as permeability in the marble was dynamically created by deformation, 3) fluid infiltration was channelled by fabric anisotropy in impure marble horizons.

In a metamorphic environment, rocks will undergoing compaction, deformation and reactions, of which many will be devolatilisation reactions. These processes will result in the production of fluids and dynamically created permeability in metamorphic rocks. The transient nature of both processes suggests that evidence for fluid infiltration preserved in metamorphic rocks by geochemical tracers will be the result of several fluid infiltration events accommodated by dynamically created permeability. Once fluid has infiltrated a lithology it will flow along pathways with the greatest permeability, which will be controlled by fabric anisotropies, and deformation (Graham et al. 1997).

The isotope profiles have documented fluid infiltration of marble bands adjacent to both blueschist and greenschist schist horizons. I have shown at North Windy Ridge, that glaucophane was stable and exchanged isotopically with the infiltrating fluid which produced the $\delta^{18}O$ profile. In other profiles hydration reactions alter glaucophane and epidote in impure marble layers to chlorite, calcite, quartz and albite. It is inferred from this that fluid infiltration of marble bands occurred both prior to and during greenschist facies retrogression. Many of the $\delta^{18}O$ profiles may record a composite $\delta^{18}O$ signature from these, and other fluid infiltration events.

To answer some of the questions that have been posed by the stable isotope study I have completed a micro-scale stable isotope study on selected marble bands in chapter 6. The micro-scale study addresses: whether a dynamic permeability was created by localised deformation resulting in spatially heterogeneous stable isotope alteration, and whether more than one fluid infiltration event can be identified in any of the marble bands.

Summary

- Isotopic alteration and fluid infiltration have been shown to have occurred both prior to and during greenschist facies retrogression.
- Statistically the stable isotope profiles do not fit to chromatographic fluid infiltration models.

- The poor fit to chromatographic flow, the heterogeneity in $\delta^{18}O$ across the profiles and localised hydration reaction of silicates suggests that fluid infiltration of marble bands was locally controlled rather than pervasive.

Is there evidence that fluid associated with greenschist retrogression infiltrated from south-north, upwards through the sedimentary pile, preserving unretrogressed blueschist assemblages in the north?

The schist in the south of Syros is generally retrogressed, whereas the schist in the north preserves unretrogressed pristine blueschist assemblages (Ridley, 1982a and Barr, 1989). Barr (1989) noted this biased distribution of retrogressive assemblages and suggested that the marble bands had acted as impermeable barriers to structurally upward fluid infiltration. The hypothesis is based on the requirement of hydration for retrogressive recrystallisation, as demonstrated in chapter 4, and it also relies on the premise that marble bands are relatively impermeable compared to schist units. This hypothesis has also been used to explain the preservation of blueschist assemblages above marble bands on Sifnos (Matthews and Schliestedt, 1984).

Evidence for upward, south-north, directed retrogressive fluid infiltration.

Rye et al (1976), in their study of isotope profiles across marble bands on Naxos, describe asymmetry of isotope profiles across marble bands. They suggest that the observed asymmetry is caused by advection of fluid through the marble in a single direction, with the maximum isotopic alteration at the contact with the schist, where the fluid infiltrates the marble and minor alteration at the opposing contact, as the fluid leaves the marble.

The lowest $\delta^{18}O$ profile (figure 5.9) on the Oros Syringas hillside (figures 5.6) is thought to be the result of fluid infiltration associated with greenschist facies recrystallisation. The marble contains glaucophane reacting to chlorite in an impure horizon and marble bands higher up the sequence, on the same hillside, adjacent to

blueschists show little or no isotopic alteration (figure 5.11). At the base of the marble band, the structurally lowest contact, the marble is isotopically depleted over 2 m. At the top contact the marble is isotopically depleted over 10 cm. This asymmetry of the profile is indicative of fluid infiltration upwards through the meta-sedimentary sequence, south to north. However, if the fluid pathways are controlled by dynamically created permeability then asymmetry in $\delta^{18}O$ profile may be related to deformation partitioning rather than, 'upward' flow.

Evidence for marble bands as barriers to upward fluid flow.

The Oros Syringas hillside (figure 5.6) provides a simple case study. The Oros Syringas area is where the majority of the large marble bands span the island and it also provides an example (on a small scale) of retrogressed greenschist assemblages separated from structurally higher blueschist assemblages by a series of marble bands. As described earlier the lower profile of the marble band above the greenschist shows isotopic depletion and textural evidence for hydration of silicates (figure 5.9). The profile across the upper marble, above the blueschist, shows no isotopic alteration (figure 5.11).

A cartoon of fluid infiltration through the metasedimentary sequence on the Oros Syringas hillside is shown in figure 5.25. The cartoon assumes that each successive marble band allows progressively less fluid into the schist layer above. There are several problems with the model.

- It does not provide an explanation for all the spatial occurrences of retrogressed schist, across the island.
- It assumes that the marble horizons continue to infinity.
- It does not take into account the reasons why some marble bands are at least partially permeable.

The occurrence of retrogressed assemblages north of the main marble bands suggests that fluid was infiltrating northern schists and indeed marble bands during the greenschist-blueschist transition. The areas of retrogression in the north are more

Figure 5.25
Schematic cross-section of the Oros Syringas hillside, with 2x vertical exageration, cross section line marked on figure 5.6
Widths of isotopic alteration of marble bands are marked at 2 localities. A schematic idealisation of fluid infiltration associated with retrogressive greenschist facies metamorphism is annotated on the cross section.

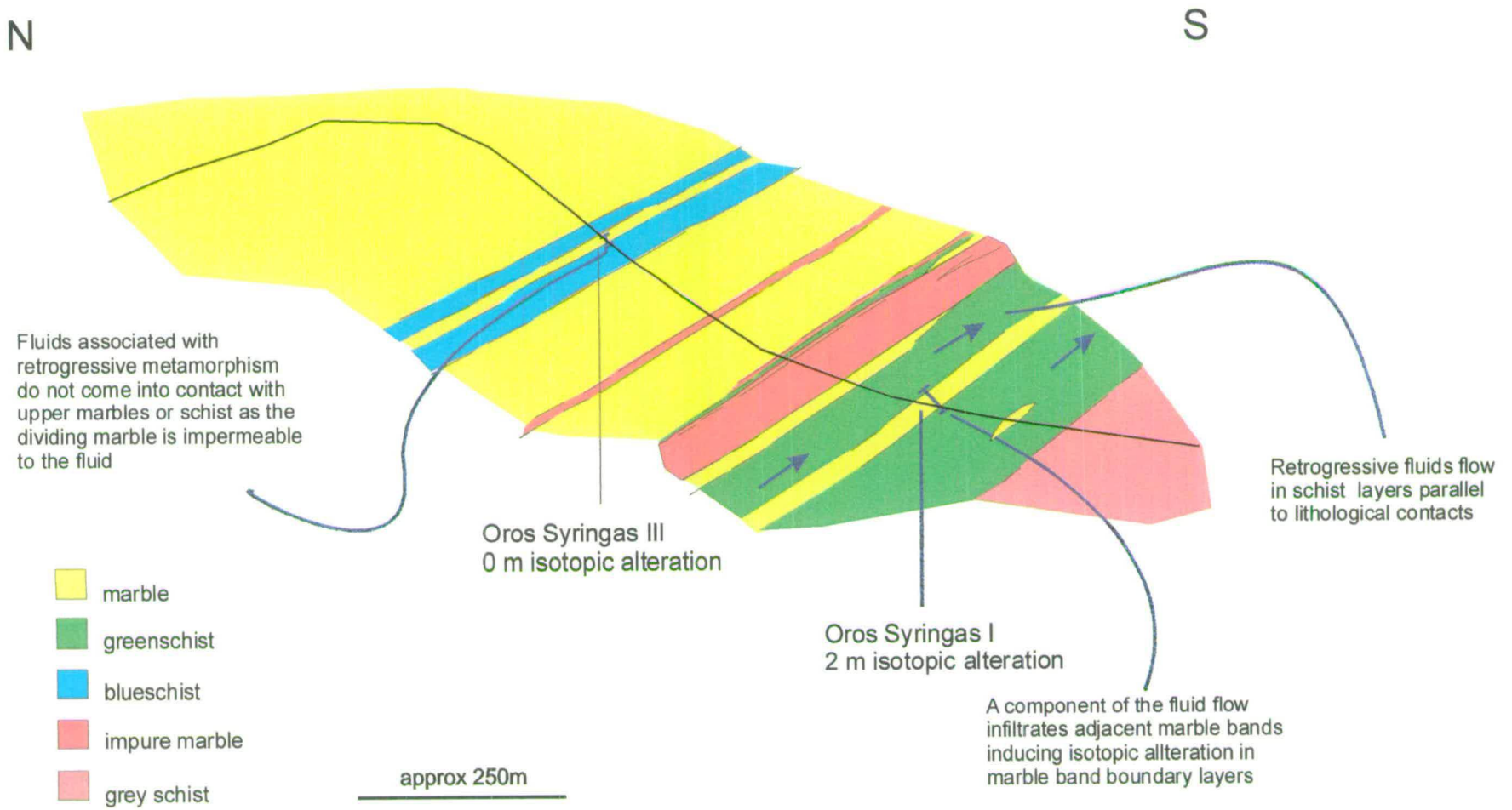

localised suggesting that fluid infiltration was less pervasive during the blueschist-greenschist transition than in the south. Localisation of fluid infiltration could be the result of two processes: 1) the formation of high permeability pathways in which fluid was channelled; 2) a decreasing fluid flux. The presence of so many marble bands is indeed likely to have channelled fluid infiltration into the more permeable schist layers. However, fluid infiltration may be more localised in the north due to partitioning of deformation forming localised zones of high permeability. Indeed, greenschist retrogression of schist in the north has been found mainly in haloes around veins, linking retrogression to fracture controlled fluid infiltration.

Discussion

Evidence for structurally upward, south-north, fluid infiltration during retrogressive metamorphism is documented by an asymmetric isotope profile across a marble band. The asymmetry in the profile may also be related to fluid infiltration controlled by deformation partitioning, although buoyancy of fluid will in general result in upward flow where possible. Whether marble bands are acting as barriers to fluid flow is however less clear. Observations of greenschist mineral assemblages being dominant in the south as compared to the north are not disputed. However, localised zones of greenschist retrogression are seen north of the main marble bands. Marble bands in the northern areas also document isotopic alteration of marble band boundary layers and localised retrogressive hydration of silicate phases in impure layers. The marble bands have not remained totally impermeable during fluid infiltration as all show some degree of isotopic alteration in their boundary layer. It seems more likely that deformation has controlled the relative permeability of marble bands affecting retrogressive fluid infiltration across the island in both the schist and marble. The partitioning of this deformation may also control the asymmetry of the profiles. The control of deformation on marble permeability will be addressed in chapter 6.

If the structural observations of chapter 3 are compared with the pattern of retrogression across Syros, it is clear that strain partitioning played a key role in fluid infiltration during the blueschist-greenschist transition and hence metamorphic

recrystallisation. In the northern areas, particularly in the serpentinite belt, where deformation was localised, extensional fabrics are defined by high pressure minerals including glaucophane and sodic-pyroxene. In this area localised retrogression of blueschist assemblages is limited to metasomatic reaction haloes around veins. Fluid infiltration associated with retrogression is dominated by fracture flow.

Structures documented in the south of the island are dominated by extensional fabrics, which are often defined by greenschist minerals. At Megas Yialos, Finika and Delfini I have documented deformation that was concurrent with greenschist recrystallisation. Fracture controlled fluid infiltration is also seen in the south. It appears that the more homogeneous nature of the deformation in the south of the island during the blueschist-greenschist transition may have resulted in more pervasive infiltration of fluid in schist layers than in the north. It is thought that this strain partitioning was the main control on greenschist recrystallisation, leading to the observed retrogression in the south as compared to the north.

5.7 Discussion

Marble bands on Syros have isotopic heterogeneities that could be linked either to exchange with isotopically light silicates or infiltration of an isotopically light fluid. The results from this study have been interpreted to show that the heterogeneities in isotope composition in marble bands are associated with fluid infiltration rather than original sedimentary heterogeneities in marble composition.

The isotope profiles have documented evidence for fluid infiltration and isotopic alteration of marble bands in contact with both blueschist and greenschist metamorphic assemblages. I have shown that fluid infiltration of marble bands occurred both when glaucophane was stable and during greenschist retrogression. This has been inferred to represent infiltration of fluid into marble bands both prior to and during greenschist facies retrogression. The spatial variability of hydration reactions of silicates in impure marble layers suggests that fluids infiltrating marble bands were channelled rather than pervasive during the blueschist- greenschist transition.

The spatial arrangement of hydrated silicate phases is not consistent with pervasive chromatographic flow into the marble bands. This conclusion is supported by the statistically invalid fits of the $\delta^{18}O$ data to chosen chromatographic models, implying that the assumptions on which the models are based are invalid, at least for Syros marble bands. The validity of some of the chromatographic theory assumptions are further tested in chapter 6.

An isotope profile records asymmetrical depletion in $\delta^{18}O$ across a marble band. This has been interpreted to represent, structurally upward flow of fluid, but the asymmetry may also be the result of localised fluid infiltration in a zone of partitioned deformation. The $\delta^{18}O$ front is thought to be the result of fluid infiltration during retrogressive greenschist facies metamorphism. The locations of marble bands documenting isotope alteration of boundary layers and greenschist retrogression of schist across the island, suggests that marble bands did not act as impermeable barriers to upward fluid flow or controlled greenschist facies recrystallisation. Fluid was however, probably channelled along relatively permeable horizons such as schist layers and in zones of dynamically created permeability.

5.8 Summary

- Isotopic variations in calcite marble $\delta^{18}O$ are not artefacts of original sedimentary heterogeneities in isotope composition.
- Fluid infiltration of marble bands occurred both prior to and during the blueschist-greenschist transition.
- The asymmetry of an isotope profile thought to have formed during infiltration of a greenschist retrogressive fluid implies upward, south-north, directed fluid infiltration of the marble band.
- The presence of marble bands in the meta-sedimentary succession were not the reason for the preservation of blueschist assemblages in the north of the island.

Chapter 6 Mechanisms for fluid infiltration of marble: a macro and micro stable isotope study

6.1 Introduction

In chapter 5 stable isotope analyses of carbonates in marble bands were inferred to document evidence for fluid infiltration. The heterogeneity of $\delta^{18}O$ composition in the stable isotope profiles, the spatial variability of hydrated silicate phases in impure marble horizons and the statistically invalid fit of the profiles to chromatographic models all attest to channelled fluid infiltration of marble bands on Syros. The mechanisms by which the fluids infiltrated the marble bands were not addressed. This chapter aims to determine the mechanisms by which fluid infiltrated three boudinaged marble bands, to assess the impact of deformation in enhancing marble permeabilities and creating heterogeneities in, and homogenising, stable isotope compositions.

Grain edge flow will not occur in a texturally equilibrated marble at P>2 kbar and T> 300 °C for limited fluid compositions (Holness and Graham, 1995). The creation of dynamic permeability will therefore be crucial to fluid infiltration of marble bands above these pressures and temperatures, including the PT range in which Syros marble bands are thought to have been infiltrated. Dynamic permeability can be created by fluid-enhanced processes, reaction-enhanced processes and deformation. Fluid-enhanced processes are those in which the fluid plays a critical role in enabling fluid migration through the rock mass, either as a result of increased fluid pressure or fluid reactivity or both. Fluid-enhanced processes include hydro-fracture, pressure solution and fluid driven reactions (chemical disequilibrium between fluid and rock). Reaction-enhanced permeability is created by reactions which involve a reduction in the rock volume to create a secondary porosity (e.g. Yardley and Lloyd, 1989). Rumble et al. (1982) suggest that shifts in isotopic composition of metamorphosed marble are caused by transient increases in porosity and permeability induced by volume decrease during decarbonation reactions.

Dynamic permeability formation during deformation, is thought to be the main mechanism by which fluids infiltrated marble bands on Syros. Field examples of deformed marble bands have been targeted for stable isotope studies on a cm- to μm-scale to determine the spatial variability in isotopic alteration associated with fluid infiltration. Textural observations have been used to correlate deformation textures with

isotopic alteration, and thus to link deformation to fluid infiltration. The main aims of the chapter are outlined below. The aims are followed by a review of the effects of deformation on permeability enhancement. A textural and stable isotope study is then presented of the three marble bands, which have all been deformed by layer parallel extension.

6.2 Aims

The aims of the chapter are:

- to determine the deformation mechanisms by which dynamic permeability was created in three marble bands from Syros to allow fluid infiltration and isotopic alteration, and
- to document the affects of the deformation on permeability creation, isotopic alteration and homogenisation on a cm- to μm-scale by a stable isotope study.

6.3 Review of dynamic permeability creation by deformation

Brittle deformation

The mechanisms by which the upper crust deforms involve brittle deformation, either fracture or cataclasis (e.g. Groshong, 1988). Both mechanisms may be aided by high fluid pressures, but can occur in dry rocks. Fractures are closed either by sealing, growth of minerals across the void (Ramsay, 1980) or healing, when the dilation associated with fracture cannot be sustained and the crack closes and heals by diffusional exchange (e.g. Smith and Evans, 1984). The dilation and permeability created by fracture are therefore generally transient effects, but if fluid pressure is great enough fractures may remain open for extended periods. Fractures accommodate extensional strain by dilation of the rock. Knipe and White (1979) and Ramsay (1980)

show how fracture followed by crack sealing are often repetitive processes accommodating significant extension, by small increments, within the upper crust. Permeability in some areas of the upper crust will be dominated by interconnected fracture networks. The overall permeability will be determined by the duration and extent of dilation of fractures as well as their interconnection at any time (Knipe and McCaig, 1994).

Cataclasis involves brittle fracture, due to stress concentrations at grain contacts. The grain size of a cataclasite in comparison to its host rock is reduced by fracture, fragmentation, separation and rotation. Grain scale micro-fractures are generally extensional (Aydin, 1978), resulting in dilation of the rock. The dilation will result in a transient increase in both porosity and permeability. Between periods of cataclasis, the resulting fault gouge may be relatively impermeable, effectively sealing the cataclastic zone (Knipe, 1993). Cataclasites are found in thin fault zones < a few mm in width and, the gouge or cataclasite will often have a lighter colour than the host rock (Groshong, 1988).

Brecciation also occurs in fault zones and can be vein or fault derived (Groshong, 1988). In vein breccias the host rock fragments are surrounded by veins. Vein fills have been shown to be locally derived from pressure solution or to be the result of fracture by high pressure fluids (Rye and Bradbury, 1988). Fragments in fault derived breccias are often bounded by shear zones or injected cataclasite (Groshong, 1988). Many studies have documented an association between pressure solution, fracture/veining, cataclasis and brecciation (e.g. Rutter, 1983; Hadizadeh, 1994 and Losh, 1997). These studies often document a cycle of pressure solution and fracture events, with periods of sealing and cementation.

Ductile deformation

The transition from brittle to ductile deformation with depth occurs over a range of pressures and temperatures due to differences in physical and chemical rock properties. Knipe (1989 and 1990) and Lloyd and Knipe (1992) have shown that there is a considerable range in pressure and temperature over which both ductile and brittle-fracture processes are involved in deformation. Ductile deformation occurs by a range of

processes which generally operate concurrently and result in dynamic recrystallisation of the rock.

The combination of dislocation glide and climb is generally termed dislocation creep. Dislocation creep is dominant in the mid to lower crust and is not generally associated with permeability enhancement, as voids present prior to dislocation creep will tend to close (Knipe and McCaig, 1994). Knipe and McCaig (1994) however point out that: 1) the closure of fluid filled voids may lead to fracture propagation as a result of increased confining pressure; 2) dislocation creep may also create voids due to strain incompatibilities between grains. Other workers have also suggested that stress concentrations during ductile deformation may enable transient periods of brittle deformation, resulting in quasi-plastic deformation. Fisher and Paterson (1989) completed high temperature (564 °C) and pressure (300 MPa) experiments on sandstone and marble to assess permeability during deformation. They concluded that transient dilation occurred as a result of strain incompatibilities caused by orientation differences of grains. The two mechanisms described lead to the transient migration of fluids trapped in pores or fractures, which will link depending on individual characteristics. The permeability of the rock during the deformation and transient dilation is dependent on the linkage of trapped fluids within the rock.

Dynamic recrystallisation enables a rock to minimise its energy state during deformation by replacement of old grains, with a high percentage of dislocation densities, by new grains. The new grains are formed either by sub-grain rotation or grain boundary migration. Dynamic recrystallisation often results in grain size reduction. Rutter and Brodie (1995) propose that dynamic recrystallisation in ductile shear zones may transiently increase the permeability of a rock during this grain size reduction.

Superplasticity is the stable flow of fine grained material, which occurs at low stresses and moderate to high temperatures (Barber, 1990). The critical parameter in its development appears to be a fine grain size, and is sometimes termed grain-size sensitive flow. The mechanisms by which the material flows are disputed, but it is generally thought that at least 50% of the strain must be accounted for by grain boundary sliding (GBS) (Barber, 1990). This process of GBS accompanied by crystal

plastic deformation, may cause transient increases in permeability by the dilation of grain boundaries during super-plastic flow (Walker et al. 1990).

Summary

Both brittle and ductile deformation can enhance rock permeability to allow fluid infiltration. Fracture controlled brittle deformation will result in channelled fluid infiltration in fractures and along fault zones during dilation associated with cataclasis and brecciation. The dilation associated with the deformation is transient and therefore enhancement of permeability is also transient. Processes act to seal, heal and cement fractures and cataclastic zones, when the dilation can no longer be sustained.

Ductile deformation will result in more pervasive fluid infiltration over time by the integrated effect of fluid infiltration along migrating and recrystallising grain boundaries and small scale micro-fractures. Dynamic recrystallisation and associated grain boundary migration will homogenise geochemical variations associated with fluid infiltration. Fluid flow associated with ductile deformation will also be transient, with only a small percentage of the grain boundaries linked at any time, so that the rock can maintain its strength (Knipe and McCaig, 1994).

6.4 Techniques

Ion microprobe- stable isotope analysis

The ion microprobe has been used to make in-situ, μm-scale, $\delta^{18}O$ analyses, so that heterogeneities in oxygen isotope composition may be related to grain-scale textures in the marbles. Previously micro-scale fluid channelling has been ackowledged by fluid inclusion studies and trace element chemistry (e.g. McCaig and Knipe, 1990; Knipe and McCaig, 1994). These studies have linked micro-fracturing, grain edge flow and pressure solution to micro-scale fluid infiltration. Most work has been based on brittle deformation structures (as they are more readily preserved) and on variations in trace element geochemistry due to technical problems in in-situ stable isotope analysis on a micro-scale. However, recent work has focused on grain scale isotope studies to

determine the mechanisms of fluid infiltration of marble bands under metamorphic conditions, aided by advancement in micro-analysis techniques, notably the use of the ion microprobe.

The first microscopic isotope analysis of marble (Wada, 1988 and Arita & Wada, 1990) used approximately 1 mm^2 x 25 μm slivers of marble from a contact aureole to show grain scale isotopic zoning at the rims of calcite grains. The zoning was attributed to fluid infiltration along grain boundaries and volume diffusion of oxygen into calcite grains. Later studies (Satish-Kumar et al. 1998, Lewis et al. 1998, Graham et al. 1998), the latter two using ion microprobe techniques, show similar results, with low $\delta^{18}O$ compositions along grain boundaries, cleavage planes, and micro-fractures implying fluid-flow along these discontinuities. The present study has used these newly established techniques to: 1) compare permeability enhancement created by brittle and ductile deformation; 2) record the isotopic and geochemical alteration associated with fluid infiltration in these zones of dynamically created permeability and 3) determine the effects of brittle and ductile deformation on homogenisation of isotopic and geochemical variations in the host rock associated with fluid infiltration. The ion-probe methods and results are described and tabulated in appendix C.

Optical microscopy and staining-textures

In order to link the micro-scale stable isotope analyses to deformation textures in the marble, hand specimens were slabbed and sectioned for optical microscopy. Textures observed in the calcite were documented. At one locality the thin sections were also stained with alizarin red and potassium ferricyanide, to identify dolomite and ankerite within the calcite marble (appendix D).

Cathodoluminescence-textures and chemistry

Polished thin sections were observed under cathodoluminescence (CL) to identify variations in the calcite trace element geochemistry. CL of carbonate is used to highlight chemical zonation and is commonly used in carbonate sedimentology (e.g. Tucker, 1992), to show grain overgrowth textures and growth zoning. Latterly it has also been used in metamorphic fluid flow studies to highlight chemical alteration of calcite

(e.g. Yardley & Lloyd, 1989; Lewis et al. 1998; Graham et al. 1998). In these studies brightly luminescent calcite has been used as an indicator for palaeo-fluid pathways, where infiltrating fluid is assumed to have caused chemical alteration. The CL set-up and the activators of luminescence are described in appendix E.

Electron probe-trace element chemistry

To quantify the changes in trace element chemistry of the calcite marble indicated by CL observations, electron probe traverses of the calcite were completed across areas where a range in luminescence was identified. A 10 kV accelerating voltage and a beam current of 15 nA were used in raster mode due to the instability of calcite under the electron beam. The elements Mg, Fe, Ca, Mn, Si and Sr were analysed with the Cameca, Camebax electron microprobe at Edinburgh University. Detection limits and errors were calculated using the method described in appendix F. Average detection limits and errors were calculated to be; Sr> 0.05 +/-0.03 wt %, Mn> 0.05 +/-0.03 wt %, Mg> 0.07 +/-0.03 wt % and Fe>0.05 +/-0.03 wt %.

Summary

A textural study of each thin section was completed first and the results of the textural studies used to target areas for macro- and micro-scale stable isotope study. The combination of techniques has been used to link textures to chemical and isotopic alteration in the marble samples. The results and interpretations of the combined textural, isotopic and chemical studies of samples from the three deformed marble bands form the remainder of this chapter.

6.5 Nites massif - brittle and semi-brittle deformation and boudinage

The Nites massif consists of variably retrogressed metabasites and pelites interbedded with boudinaged calcitic marble bands. Two boudinaged marble bands on the Nites hillside were targeted to assess the control of brittle and semi-brittle

deformation, associated with boudinage, on permeability enhancement, fluid infiltration and isotopic alteration of the marble.

Nites boudin I

The location of boudin I is shown in figure 6.1. The marble boudin is 23 m long x 5 m thick in its centre. The neck of the boudin is 1.1 m thick and brecciation occurs in the neck region over a 1.5 m wide band (photograph 6.1). Angular clasts in the breccia range in size from 1-10 cm and lie in an orange stained matrix (photograph 6.2). The unit consists of interbanded calcite and dolomite; the dolomite acts competently relative to the surrounding calcite and is seen in this and other units on the hillside to be macroscopically boudinaged within the marble band. As well as the 1.5 m wide brecciation zone in the boudin neck, the whole boudin is fractured. These fractures are orientated NW-SE (figure 6.2). The more intense brecciation in the boudin neck appears to have developed from these fractures. The surrounding schist is comparatively poorly exposed and near the boudin is a rusty-silver colour. On the hillside below patches of metabasic glaucophane-epidote schist can be seen, as well as a retrogressed chlorite-albite-epidote compositional equivalent.

Detailed structural observations

In thin section laterally discontinuous layers of dolomite crystals, identified by staining, form fine grained aggregates (photographs 6.8 and 6.9). The brecciation in the neck is concentrated in these dolomitic horizons which parallel layering (photographs 6.3 and 6.4). Small vertical linkage zones of brittle deformation cross the calcite, linking the deformation in dolomite layers. The calcite in the breccia clasts remains undeformed and consists of aligned crystals, which lie approximately perpendicular to the fabric and layering (photograph 6.3), and are thought to be calcite pseudomorphs after aragonite (Barr, 1989). Layer-parallel pressure solution seams are identified by dark insolubles parallel to layering in the boudin neck. Small cracks and veins are also observed within

Figure 6.1
Nites map, with isotope localities marked

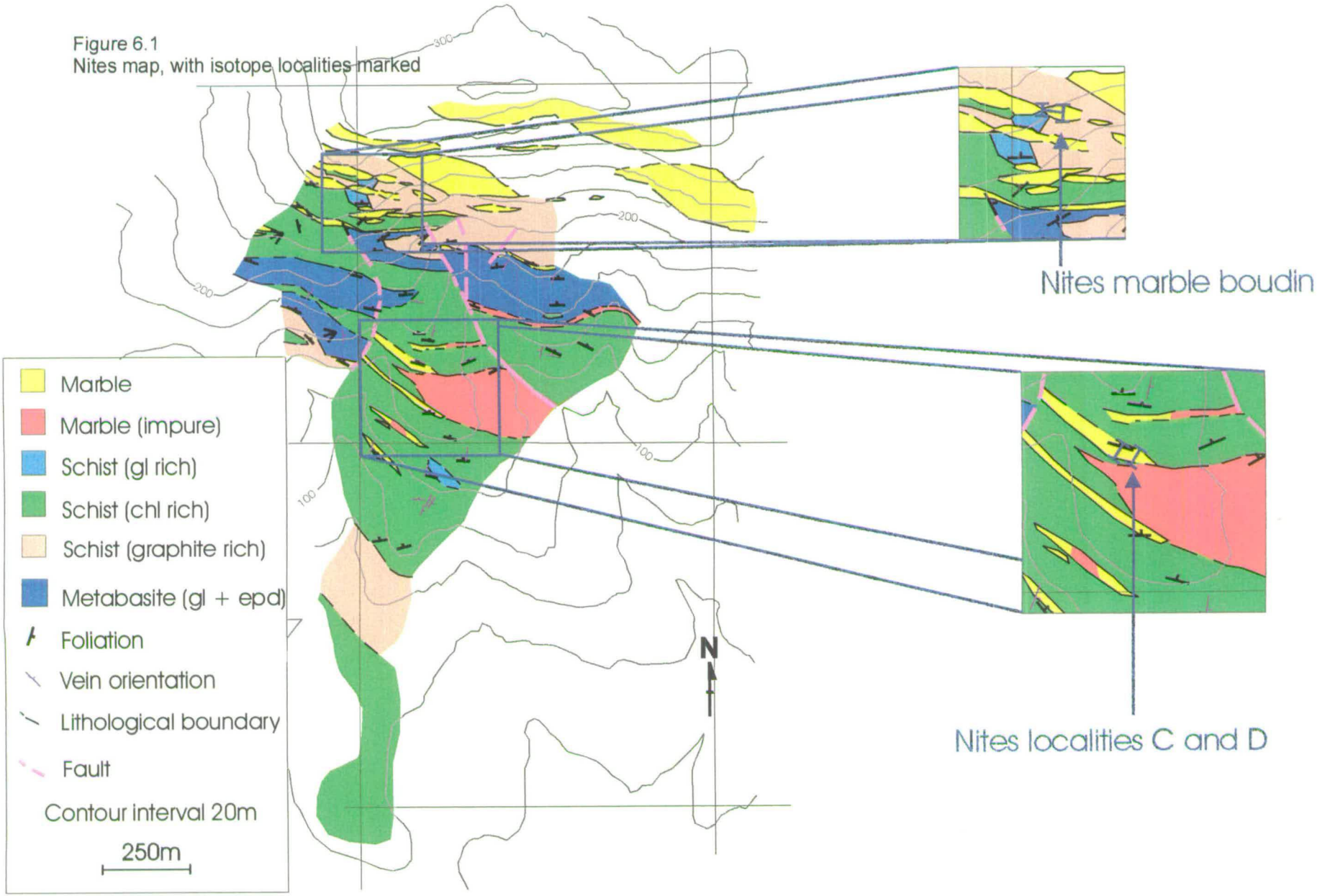

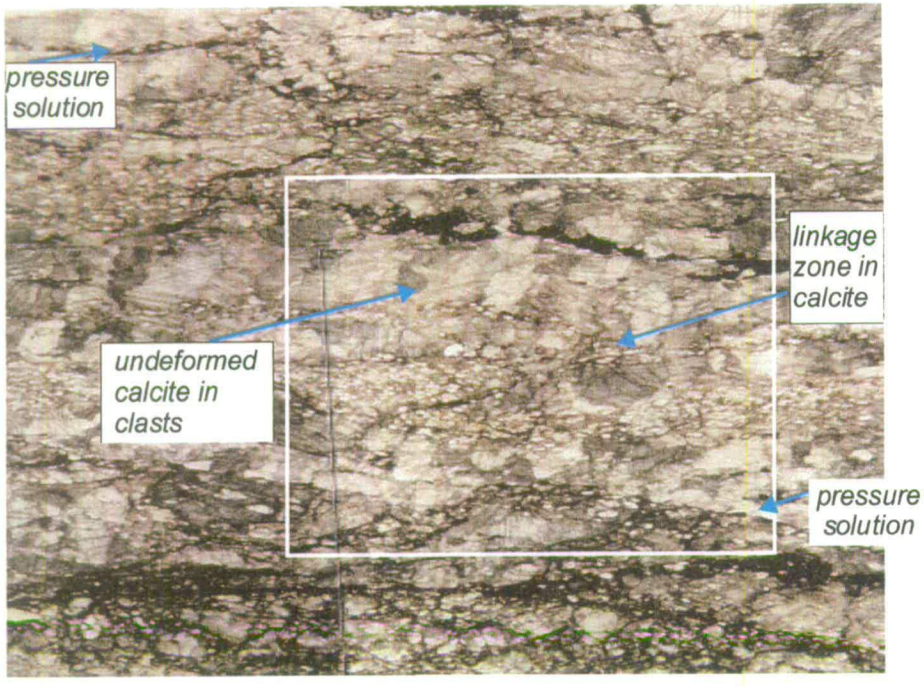
pressure solution
linkage zone in calcite
undeformed calcite in clasts
pressure solution

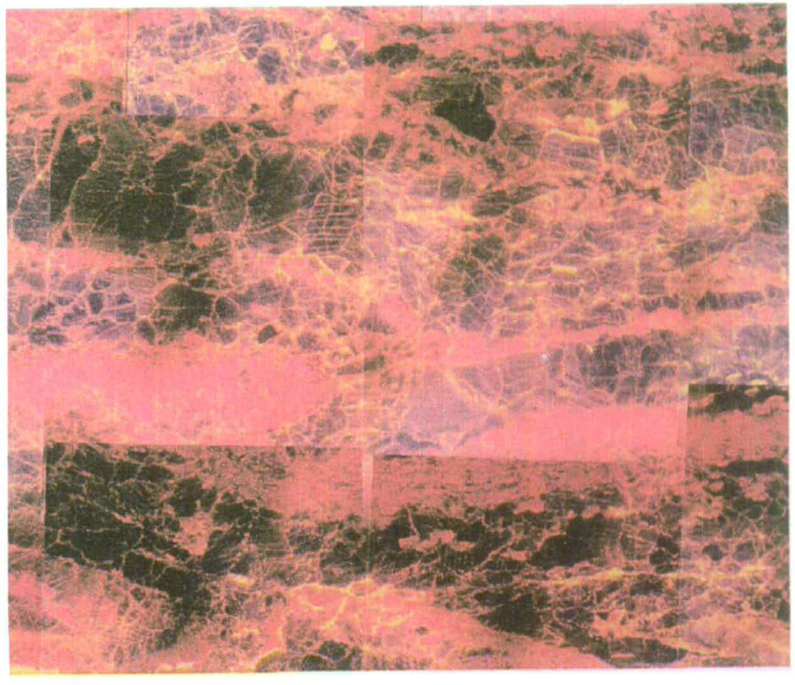

Photograph 6.1

Boudinaged marble band, Nites. Field of view approximately 10m.

Photograph 6.2

Brecciation in the boudin neck, Nites. The stripey appearance of the marble is caused by interbanding of dolomite and calcite.

Photograph 6.3

Thin section photomicrograph of breccia in the boudin neck, Nites, sample S'96/187. Note pressure solution seams outlined by dark insolubles. Calcite in breccia clasts is undeformed. Thin zones of localised deformation link deformed dolomite layers. The white box outlines the approximate field of view for the CL photograph 6.4. Field of view is approximately 1mm wide.

Photograph 6.4

CL photograph of breccia in the boudin neck. Fine grained dolomite luminesces red. Calcite is predominantly black, but yellow where altered by fluid infiltration.

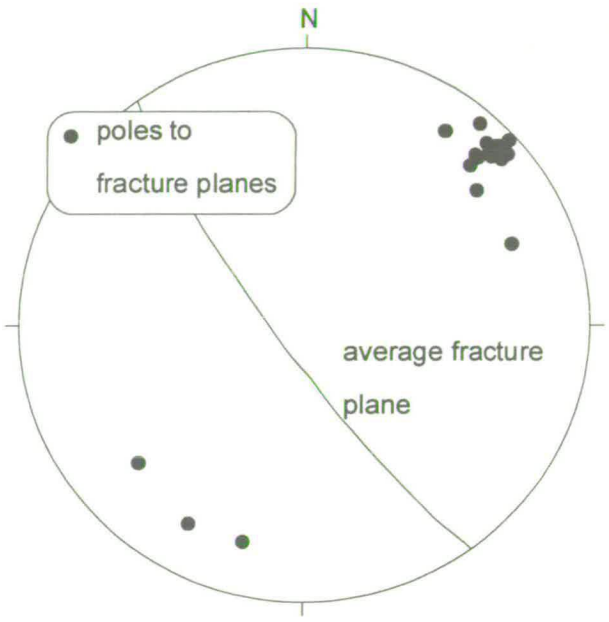

Figure 6.2

Equal area stereonet of fractures in marble boudin, Nites

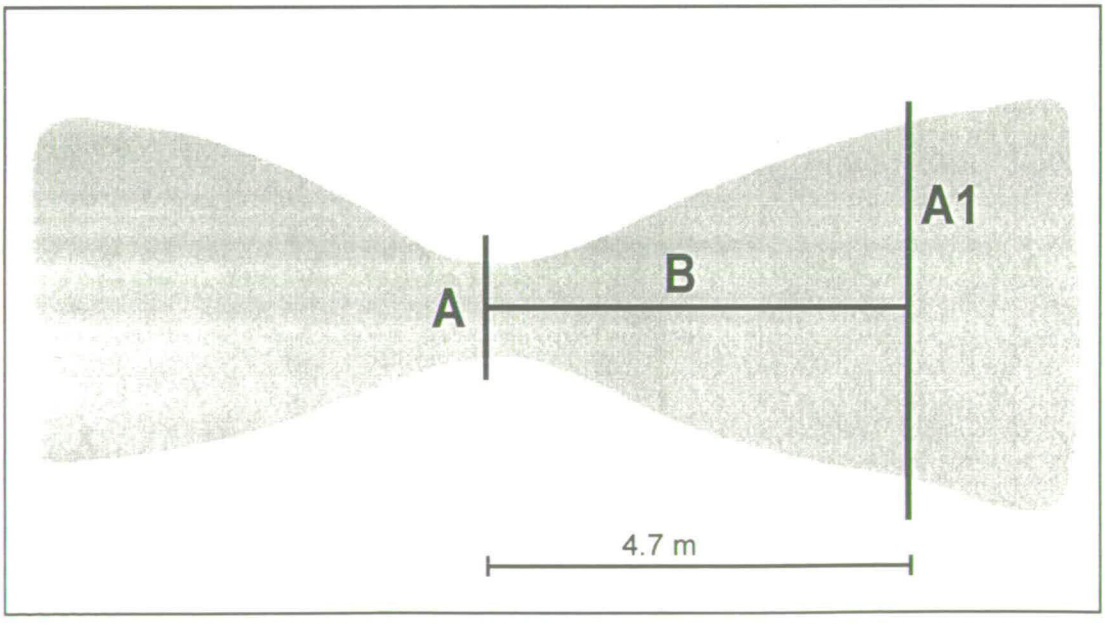

Figure 6.3
Schematic sketch of marble boudin, Nites. Stable isotope profiles A, A1, and B marked.

the boudin neck at the basal contact of the marble (photographs 6.6 and 6.7). The veins open perpendicular to the direction of extensional boudinage. The combination of pressure solution seams and veins suggests redistribution of calcite within the neck to accommodate thinning and extension (Mullenaux and Gray, 1984; De Paor et al. 1991).

Bulk stable isotope traverses

Three bulk stable isotope traverses were made across the marble boudin, the locations of which are shown in figure 6.3. The results of the bulk stable isotope traverses are shown in figures 6.4, 6.5 and 6.6. The profile across the boudin neck (profile A, figure 6.4) appears to show no systematic trend in $\delta^{18}O$, with variations from 20 to 25 ‰. The majority of the $\delta^{13}C$ values fluctuate between 0 and 2 ‰, although three negative $\delta^{13}C$ values are concentrated within 20 cm of the base of the marble band. The profile 4.7 m to the east of the marble band (profile A1, figure 6.5) documents a $\delta^{18}O$ value of 23 ‰ at the contact with the schist and 26.5 ‰ at a distance of 2 m into the marble band. The $\delta^{18}O$ compositions between the contact and 2 m show large variations, notably depletions in $\delta^{18}O$ to values between 21 and 22 ‰ at distances of 75-80 cm and 120-135 cm. Decreases in the carbon $\delta^{13}C$ composition are also seen at these distances. Figure 6.6 (profile B) shows the traverse away from the centre of the boudin neck parallel to layering. There is a scatter in $\delta^{18}O$ value between 20 to 26 ‰ over the first 2 m before remaining at approximately 26.5 ‰ from 2 to 4.7 m.

Isotopic alteration from an assumed unaltered marble isotope $\delta^{18}O$ signature of 26.5 ‰ to lower $\delta^{18}O$ values in the boudin neck of the marble band at the contact of the marble with the surrounding schist, and in zones within the marble are documented by the profiles. A 2.3 m wide band from the centre of the boudin neck shows a range of depleted $\delta^{18}O$ values (profile B, figure 6.6.), the heterogeneity in which is similar to that documented in the boudin neck profile A (figure 6.4). The heterogeneity in isotope composition implies that fluid infiltration in the neck area did not occur by pervasive grain edge flow. Instead, the bulk sampling is thought to record a mixed isotope signature, from areas of isotopically altered and unaltered calcite.

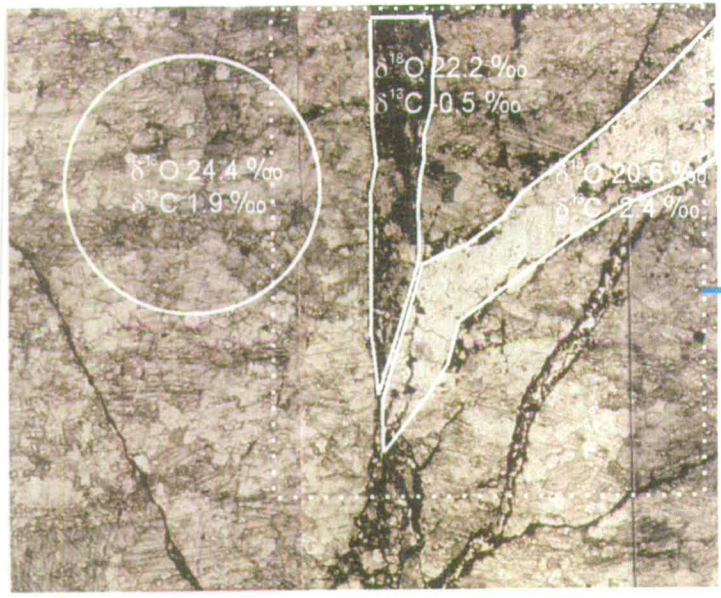
δ18O 22.2 ‰
δ13C 0.5 ‰
δ18O 24.4 ‰
δ13C 1.9 ‰
δ18O 20.6 ‰
δ13C 2.4 ‰

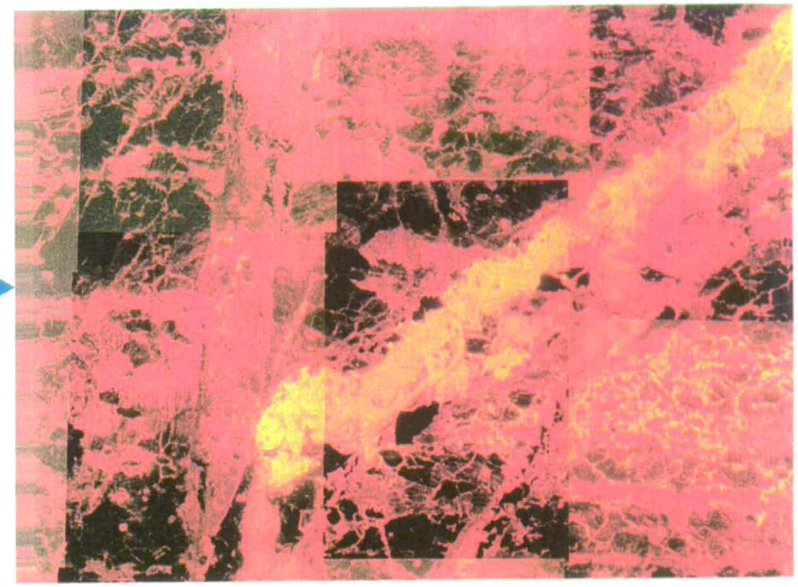

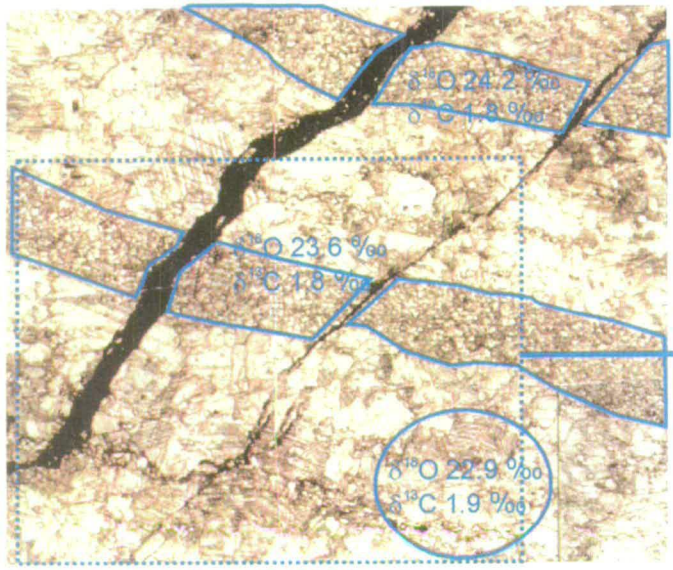
δ18O 24.2 ‰
δ13C 1.8 ‰
δ18O 23.6 ‰
δ13C 1.8 ‰
δ18O 22.9 ‰
δ13C 1.9 ‰

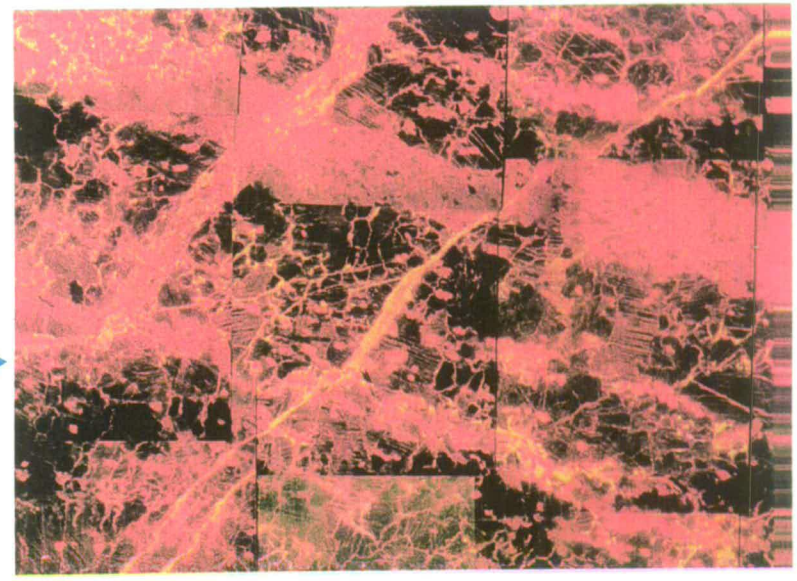

Photograph 6.6

Photomicrograph of calcite veins in the boudin neck, sample, S'96/176. Areas targeted for macroscale stable isotope study are highlighted and annotated with their isotopic compositions. The white box outlines the area of the CL photograph 6.5.h.
Field of view approximately 1.5 cm.

Photograph 6.7

CL photograph of sample, S'96/176. Zoned yellow luminescent calcite can be identified in the vein (right). Dolomite luminesces red and calcite black-yellow.

Photograph 6.8

Photomicrograph of calcite and dolomite layers, sample, S'96/201. Calcite and dolomite layers targeted for macroscale isotope study are highlighted and their isotopic compositions annotated. The box defines the area of the Cl photograph 6.9.
Field of view is approximately 1.5 cm wide.

Photograph 6.9

CL photograph of sample, S'96/201. Dolomite layers luminesces red.
Field of view approximately 1 cm wide.

Figure 6.4
Profile A. Variations in $\delta^{18}O$ and $\delta^{13}C$ across a boudin neck. The log in the centre of the page describes the sampled traverse.

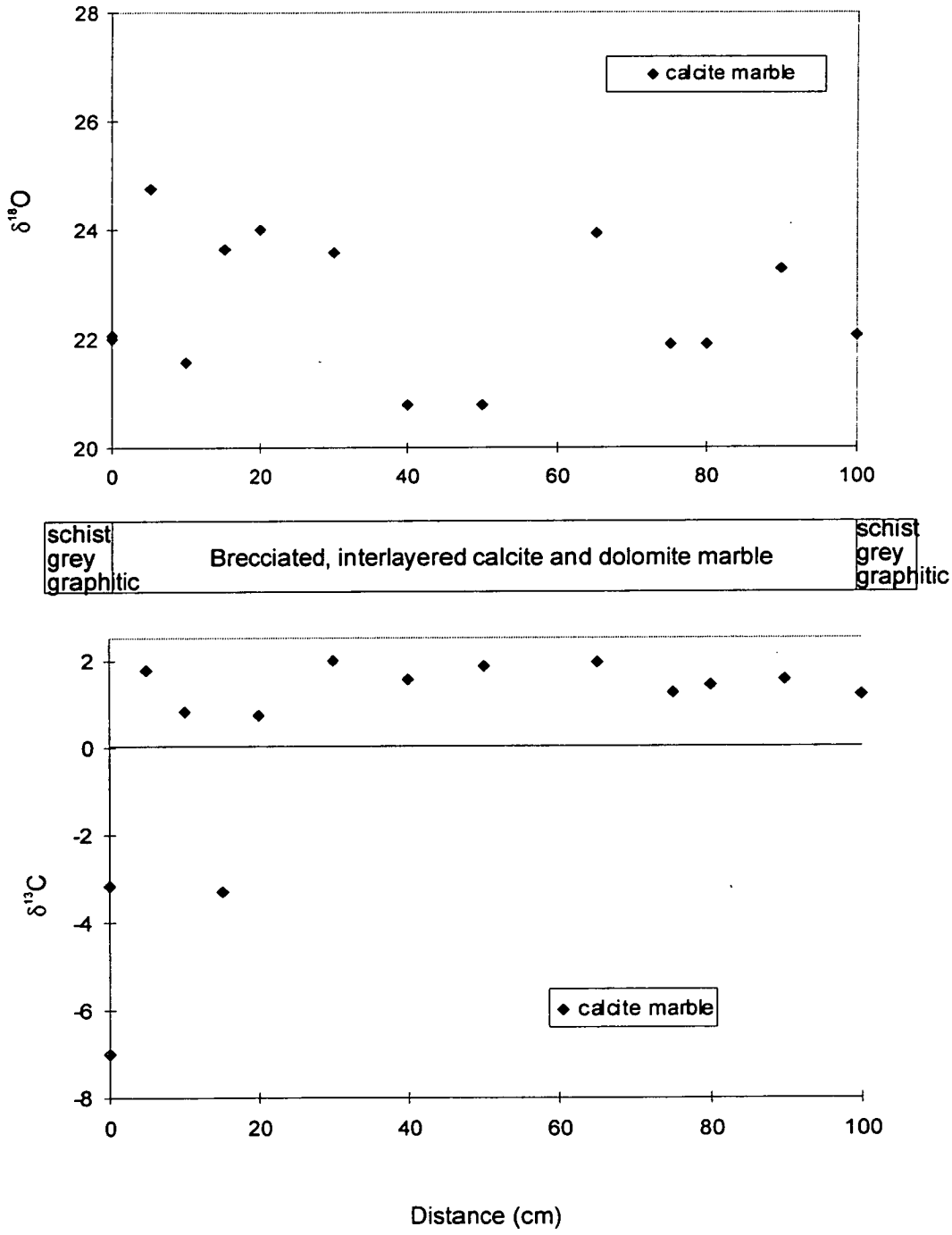

Figure 6.5
Profile A1. Variations in $\delta^{18}O$ and $\delta^{13}C$ from the basal contact of the marble band, 4.7m to the east of the boudin neck. The log in the centre of the page describes the sampled traverse.

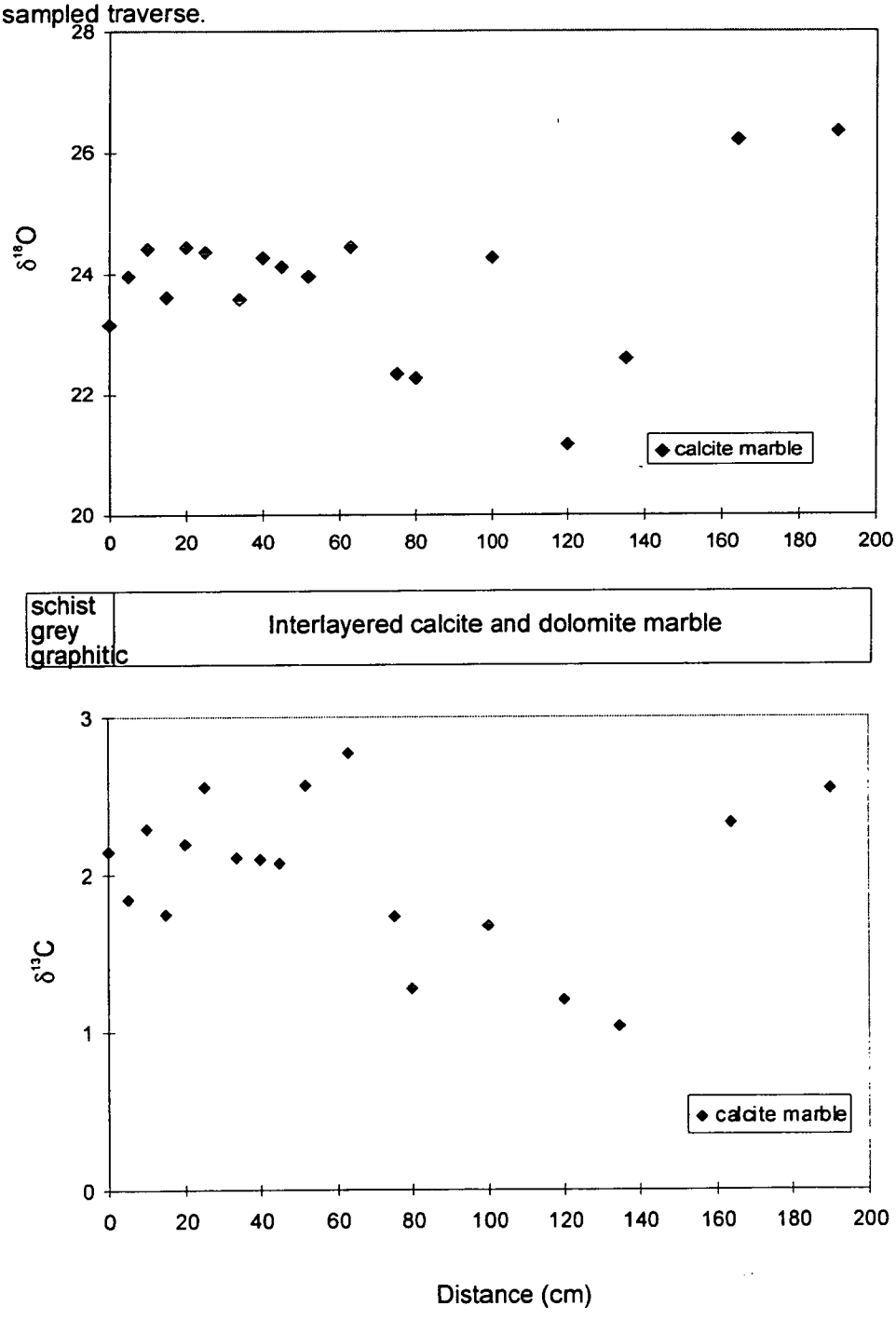

Figure 6.6
Profile B. Variations in $\delta^{18}O$ and $\delta^{13}C$ from the centre of the boudin neck to 4.7m to the east, parallel to strike. The log in the centre of the page describes the sampled traverse.

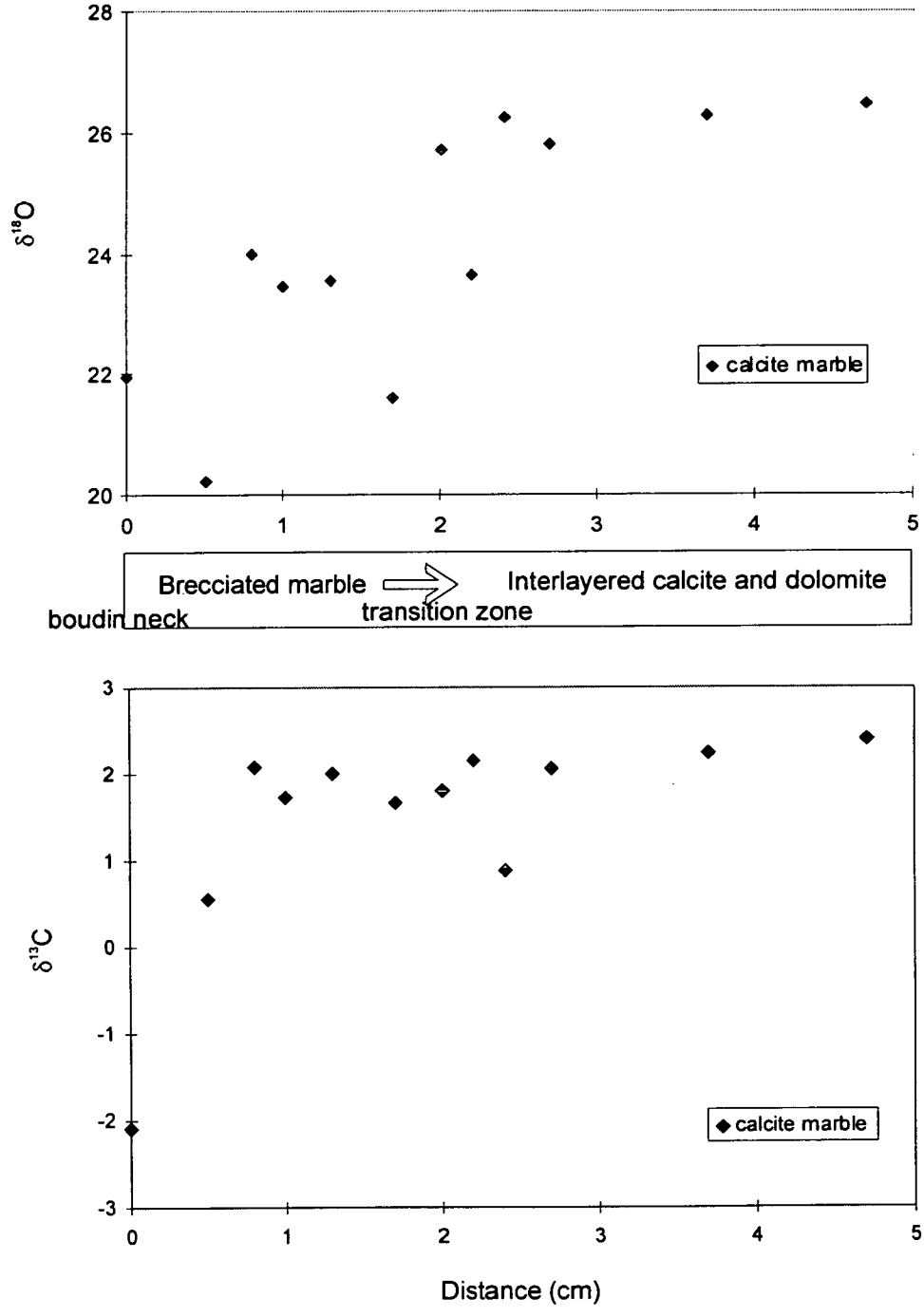

The evidence for fluid channelling from the bulk data leads to a hypothesis in which infiltrating fluid has been channelled in the breccia matrix. The bulk sampling is thought to have been on too coarse a scale to distinguish isotopically depleted breccia matrix from breccia clast material, but too fine to record a homogeneous mixed isotope composition. To test this hypothesis samples of breccia and clast material from the boudin neck were separated and analysed. Slabbed sections of rock from the boudin neck were sampled using a hand held dental drill to target breccia matrix, breccia clasts and macro-veins of calcite. The macro-scale sampling was combined with thin section observations of deformation textures in the breccia and CL studies.

Macroscopic (mm scale) stable isotope sampling and correlation with deformation and CL textures

Figure 6.7 shows a plot of $\delta^{13}C$ versus $\delta^{18}O$ for breccia matrix, breccia clasts, macro-veins and adjacent dolomite and calcite layers from the boudin neck. The data fall into two discrete groups defined by low $\delta^{18}O$ (20 to 21.5 ‰) and low $\delta^{13}C$ (-0.5 to 0.5 ‰) compositions and a second group with high $\delta^{18}O$ (22.5 to 24.5 ‰) and high $\delta^{13}C$ (1 to 2 ‰) compositions. Breccia matrix and calcite macro-veins are depleted in both $\delta^{18}O$ and $\delta^{13}C$, whereas breccia clasts and calcite adjacent to veins have relatively undepleted $\delta^{18}O$ and $\delta^{13}C$ signatures. None of the clasts record the assumed completely unaltered signature of 26.5 ‰, either because of inaccurate sampling with the drill or simply that clasts were altered on a smaller scale.

CL photomicrographs, 6.4, 6.7 and 6.9 from samples collected within the boudin neck highlight chemical alteration of the marble. Photograph 6.4 is of breccia within the boudin neck. Dolomite luminesces red and is distinct from the orange-black calcite. Orange luminescence highlights chemically altered calcite whilst unaltered calcite is black. Photomicrographs 6.6 and 6.8 are annotated with the $\delta^{18}O$ and $\delta^{13}C$ values of areas targeted by the macro-sampling. The areas of isotope depletion correlate with areas of bright orange luminescence indicative of trace element variations in calcite chemistry.

Figure 6.7

Graph of $\delta^{18}O$ versus $\delta^{13}C$ for breccia clasts, matrix, veins and wall rock in the boudin neck

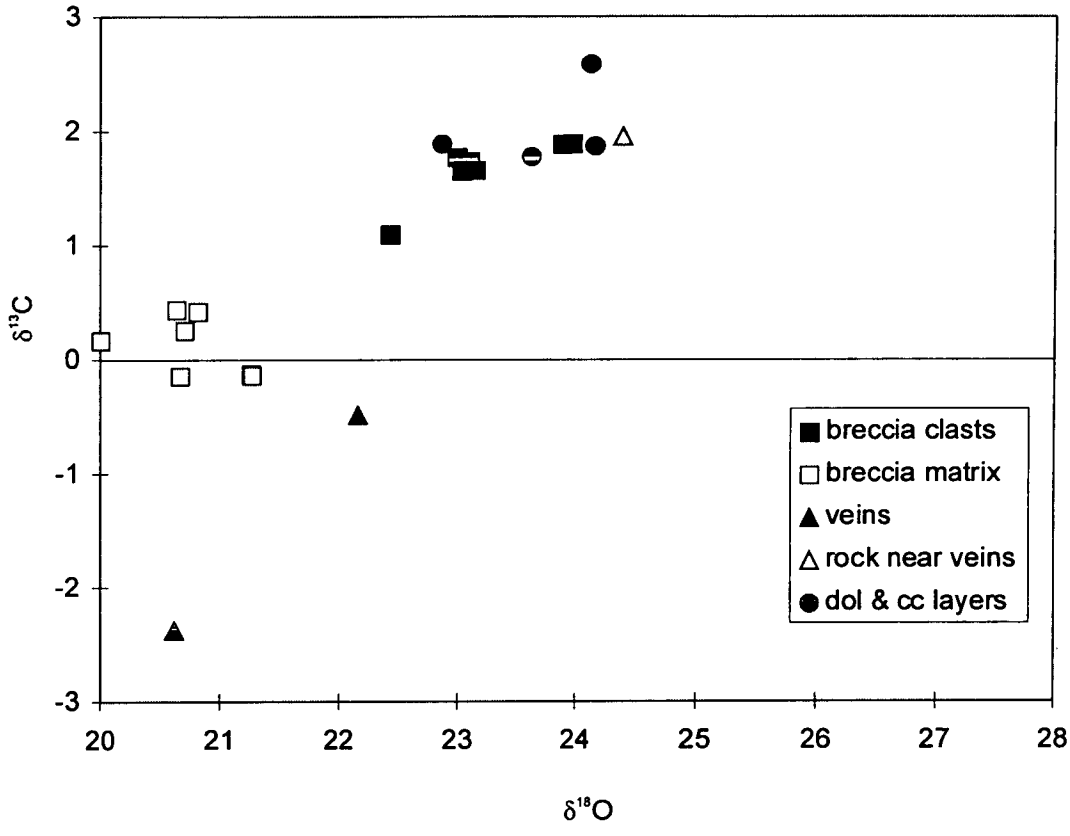

The combined structural and macroscopic isotope study shows that the infiltrating fluids were depleted in $\delta^{18}O$ and channelled in vein and fracture networks as well as within the cataclastically deformed breccia matrix. This has resulted in localised chemical and isotopic alteration within brittle deformation zones in the boudin neck. Pressure solution and veining are common mechanisms by which material is redistributed to accommodate layer extension and boudinage (e.g. Mullenaux and Gray, 1984). In this case the fracture and veining is associated with external fluid infiltration and the brecciation may have been aided by hydrofracture.

Summary

- Deformation associated with NE-SW to E-W layer parallel extension of the boudin is accommodated in the boudin neck by pressure solution, veining and brittle fracture, resulting in brecciation.
- cm-mm scale sampling shows isotopic depletions in $\delta^{18}O$ and $\delta^{13}C$ in breccia matrix and macro-veins in comparison to breccia clasts. The isotopic depletions are associated with fluid infiltration in zones of deformation accommodating layer-parallel boudinage.
- CL studies highlight chemical variation of the calcite in the breccia matrix and macro-veins by bright luminescence.

Nites boudin II

The second locality on the Nites hillside is a 2 m thick marble-quartzite layer, which is discontinuous (figure 6.1) and heterogeneously deformed (photographs 6.10 and 6.11). At the eastern side it is thinned by normal faults and shear zones (photographs 6.11, 6.12 and 6.13). The faults and shear zones accommodate E-W oriented layer parallel extension (figure 6.8). The same deformation event can be identified in the schist above and below the marble-quartzite layer (figure 6.8 and photograph 6.14). The deformation is concentrated in a 5 m wide band and dies out along strike to the west. To the east the marble band is 'pinched out' by the deformation.

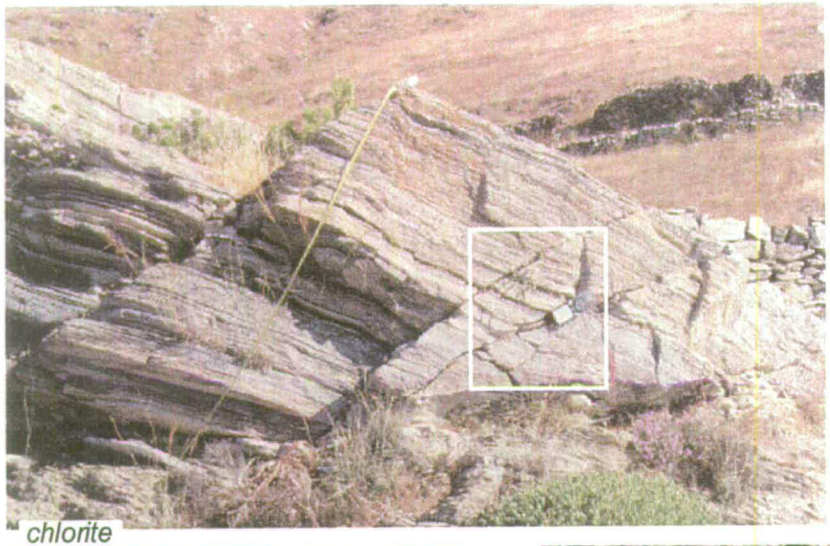

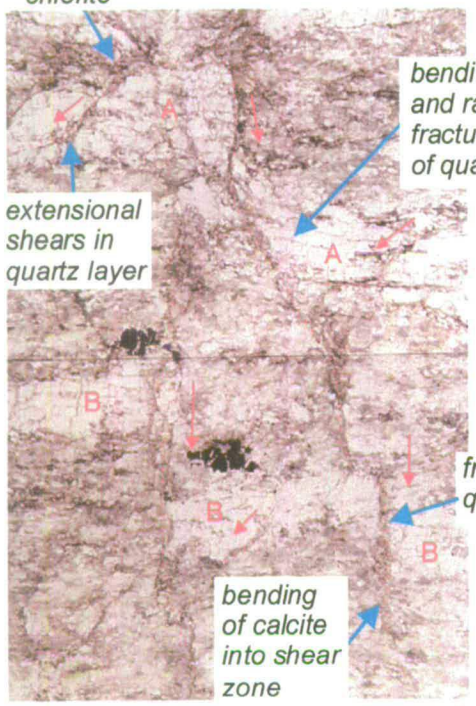
chlorite
bending and radial fracture of quartz
extensional shears in quartz layer
A
A
B
B
B
fractured quartz
bending of calcite into shear zone

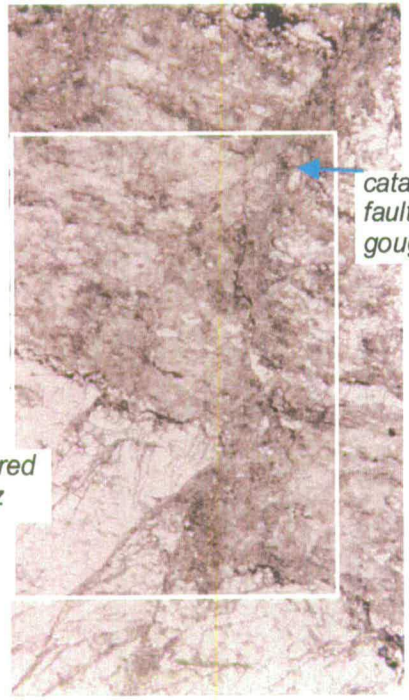
cataclastic fault gouge

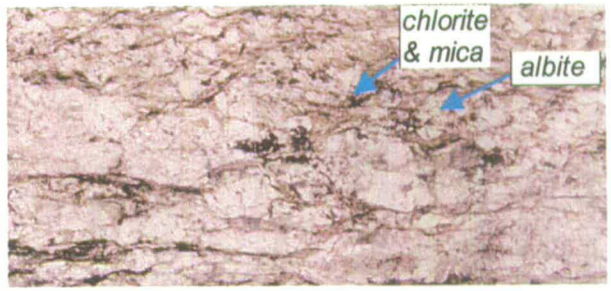
chlorite & mica
albite

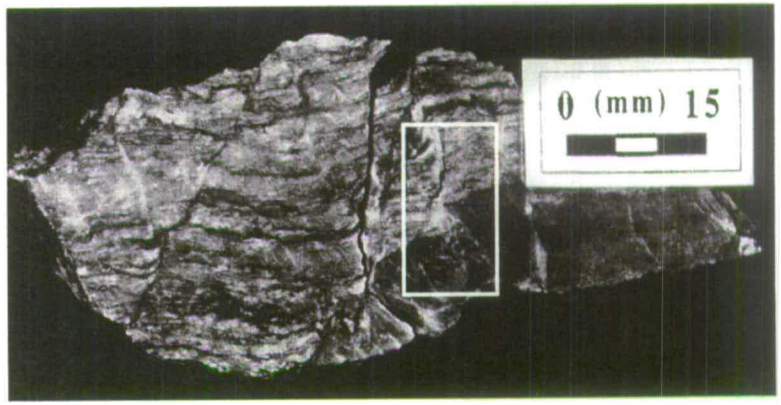
0 (mm) 15

Photograph 6.10

Deformed interlayered marble-quartzite band, locality C, Nites. The white box defines the area of the close up photograph 6.11. Tape measure is approximately 2.5 m long.

Photograph 6.11

Close up of deformation in the marble-quartzite. Layers are offset by annotated shear zones and fractures. Tape measure is approximately 70 cm long.

Photograph 6.12

Photomicrograph of sample, S'97/102, 30cm on the bulk traverse. Quartz layers (low relief) are off set by shear zones and fractures. Individual quartz layers are annotated. Field of view approximately 2.5 cm x 1.5 cm.

Photograph 6.13

Photomicrograph of sample, S'97/101, 27cm on the bulk traverse. Quartz layers have low relief. The boxed area defines the area of the CL photograph 6.16. Field of view approximately 7 mm x 13 mm.

Photograph 6.14

Photomicrograph of calc-schist below the marble-quartzite band, sample, S'97/37. Shear zones are outlined by chlorite and mica, early fabrics outlined by epidote are included in albite porphyroblasts. Field of view approximately 7 mm wide.

Photograph 6.15

Slabbed and polished hand specimen drilled for macroscale isotope sampling. Box defines the area shown in the photograph 6.13 (reverse view)

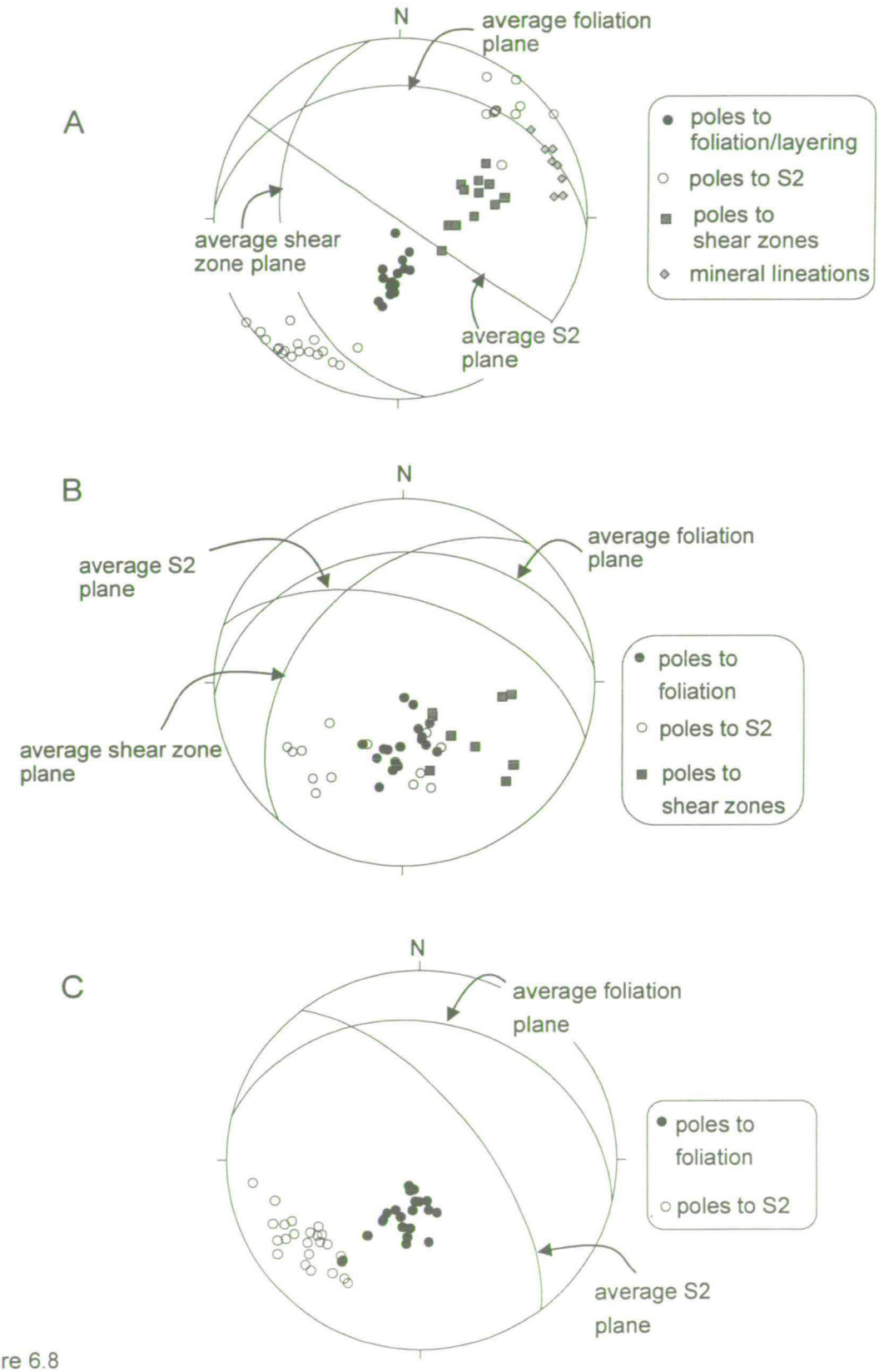

Figure 6.8

Stereonets of fabrics in: A) deformed marble band (Nites, locality C); B) calc-schist below marble band (Nites localities C and D); C) fabric in schist above the marble band.

The calcite marble and quartzite layers are interbedded with impure silicate rich layers containing mica and chlorite in a calcite marble matrix. There are also layers of calcite clasts in a calcite matrix. Shear zones defined by deformed calcite have in places fractured to form fault zones containing a distinctive white carbonate that can clearly be seen in hand specimen (photograph 6.15). Deformation is complicated by competence contrasts between layers in the banded unit and is thought to have had an important effect on deformation and potentially therefore, fluid infiltration of the marble band.

The schist below the marble is calcareous and consists of quartz, calcite, chlorite, epidote, albite and mica (photograph 6.14). It is also deformed and crenulations are defined by chlorite and mica. The albite is porphyroblastic and includes earlier deformation textures defined by epidote crystals. Veins and segregations of quartz, calcite, chlorite +/- oxide cut the schist, with no preferred orientation.

Detailed structural observations

In thin section the deformation and faulting are clearly identified by off-set layers and shear zones (photograph 6.12). Quartz layers generally deform by brittle failure, although there is some evidence for plastic deformation of quartz bands with bending of quartz crystals into shear zones. These bent quartz crystals have radial fractures concentrated along their outside edges (photograph 6.12). Fractures in the quartz crystals are filled with calcite. The calcite in comparison generally exhibits more ductile deformation textures with bending of calcite crystals into shear zones (photograph 6.12). However, in the larger shear zones the calcite forms a cataclastic fault gouge (photograph 6.13). The calcite fault gouge is identified in hand specimen by its distinctive white colour (photograph 6.15). Single deformation zones are variably manifest in different layers and may behave as shear zones within calcite layers, linking into brittle fracture zones in adjacent quartz layers (photograph 6.12). Healed micro-fractures are present in both calcite and quartz, identified by trails of fluid inclusions. The unit is also thinned by extensional micro-faulting along multiple slip surfaces within quartz layers (photograph 6.12). Similar extensional structures are described by Platt and Vissers (1980). Layer parallel zones of dirty-looking chlorite and mica form fine crenulated layers within the marble-quartzite (photograph 6.12).

Less than 10 m to the west the unit appears to be completely undeformed in hand specimen, with no evidence for faulting or shear zone formation. In thin section the marble and quartzite layers are undeformed with equant grains, 200-1000 μm in diameter.

Bulk stable isotope profiles

Two bulk stable isotope traverses were made across the interbedded quartzite-marble unit. One profile crosses the deformed section at the eastern end (locality C, photograph 6.10); the second, 10 m to the west, crosses the undeformed section (locality D). At locality C samples were carefully collected to avoid sampling calcite from shear zones and fractures. The results of the bulk stable isotope traverses for localities C and D are shown in figures 6.9 and 6.10, respectively. The graphs are very similar, with $\delta^{18}O$ isotopic compositions of 19 to 20 ‰ at the contact, changing to 25 to 26 ‰ 1 m into the marble. The bulk stable isotope profiles suggest fluid infiltration and isotopic alteration of the marble-quartzite band.

Macroscopic (mm-scale) stable isotope study

The deformation zones avoided whilst sampling for the bulk profile at locality C were then targeted as part of a mm-scale stable isotope study. The $\delta^{18}O$ compositions of calcite in shear zones and along faults was compared with those of adjacent undeformed calcite. The calcite was drilled, with a hand held dental drill, from slabbed hand specimens (e.g. photograph 6.15). The results of the macroscopic study at locality C are superimposed on the bulk stable isotope profile in figure 6.11. Data from the mm-scale study straddle the trend in the isotope composition of the bulk profile.

The data are sub-divided and calcite drilled from veins and shear zones has a lower $\delta^{18}O$ composition, and in some cases a lower $\delta^{13}C$ composition, with respect to the bulk value at the corresponding distance (figure 6.11). Localised isotope depletion

Figure 6.9
Graphs of $\delta^{18}O$ and $\delta^{13}C$ versus distance for a traverse across a marble-schist contact at Nites, locality C (deformed).

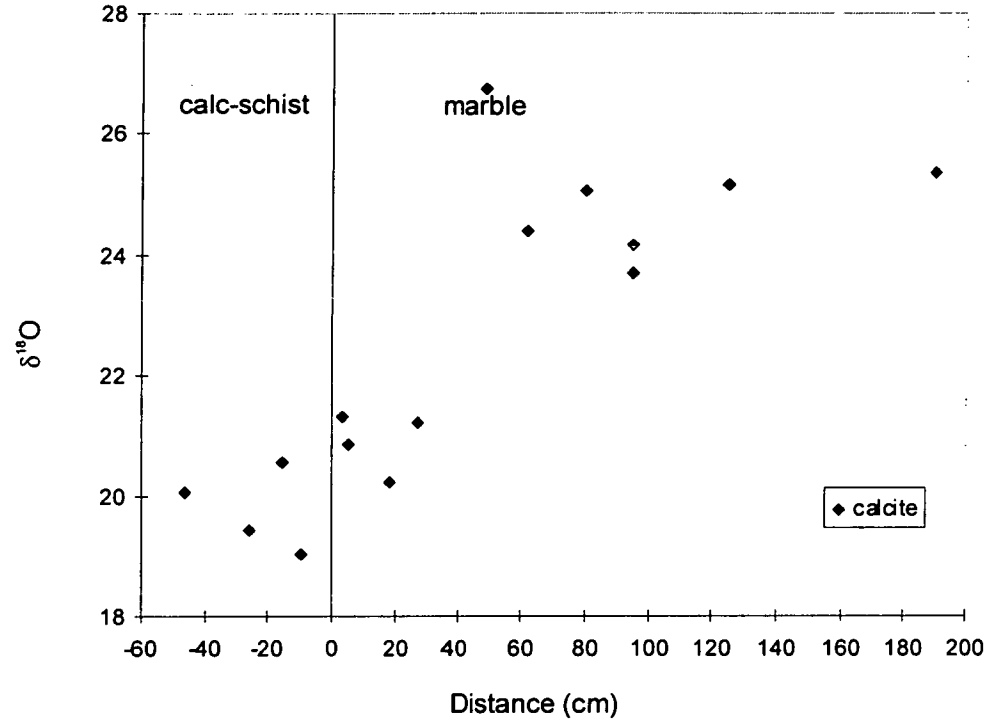

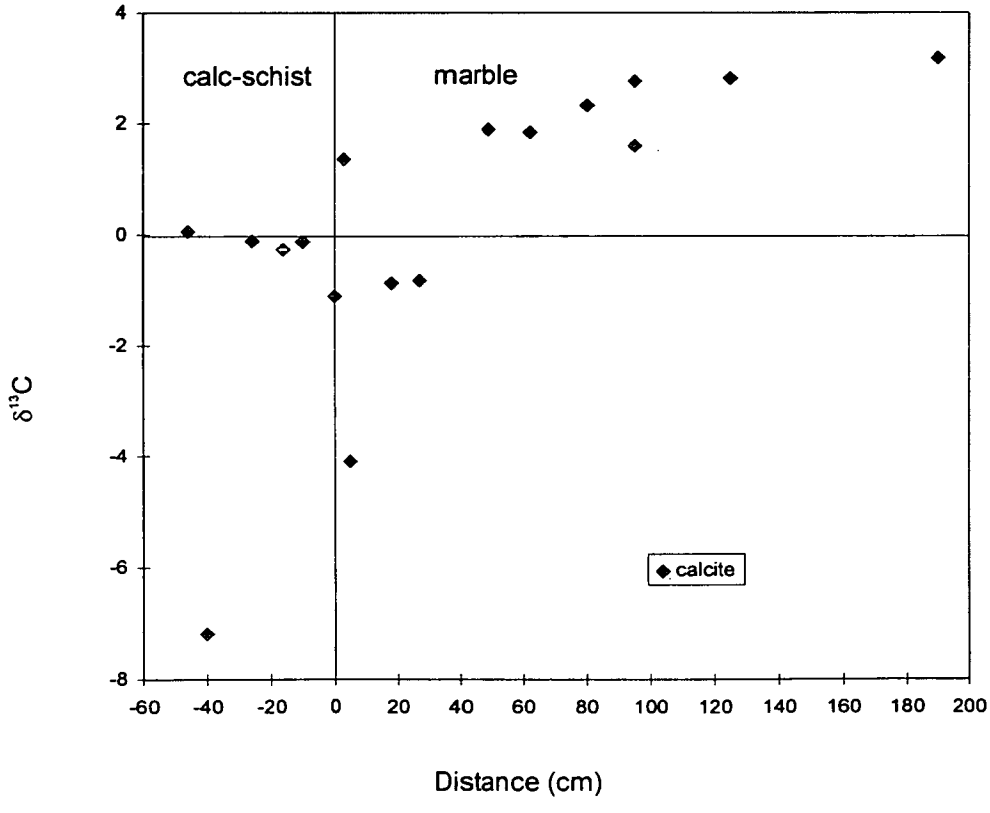

Figure 6.10
Graphs of $\delta^{18}O$ and $\delta^{13}C$ versus distance for a traverse across a marble-schist contact at Nites, locality D (undeformed).

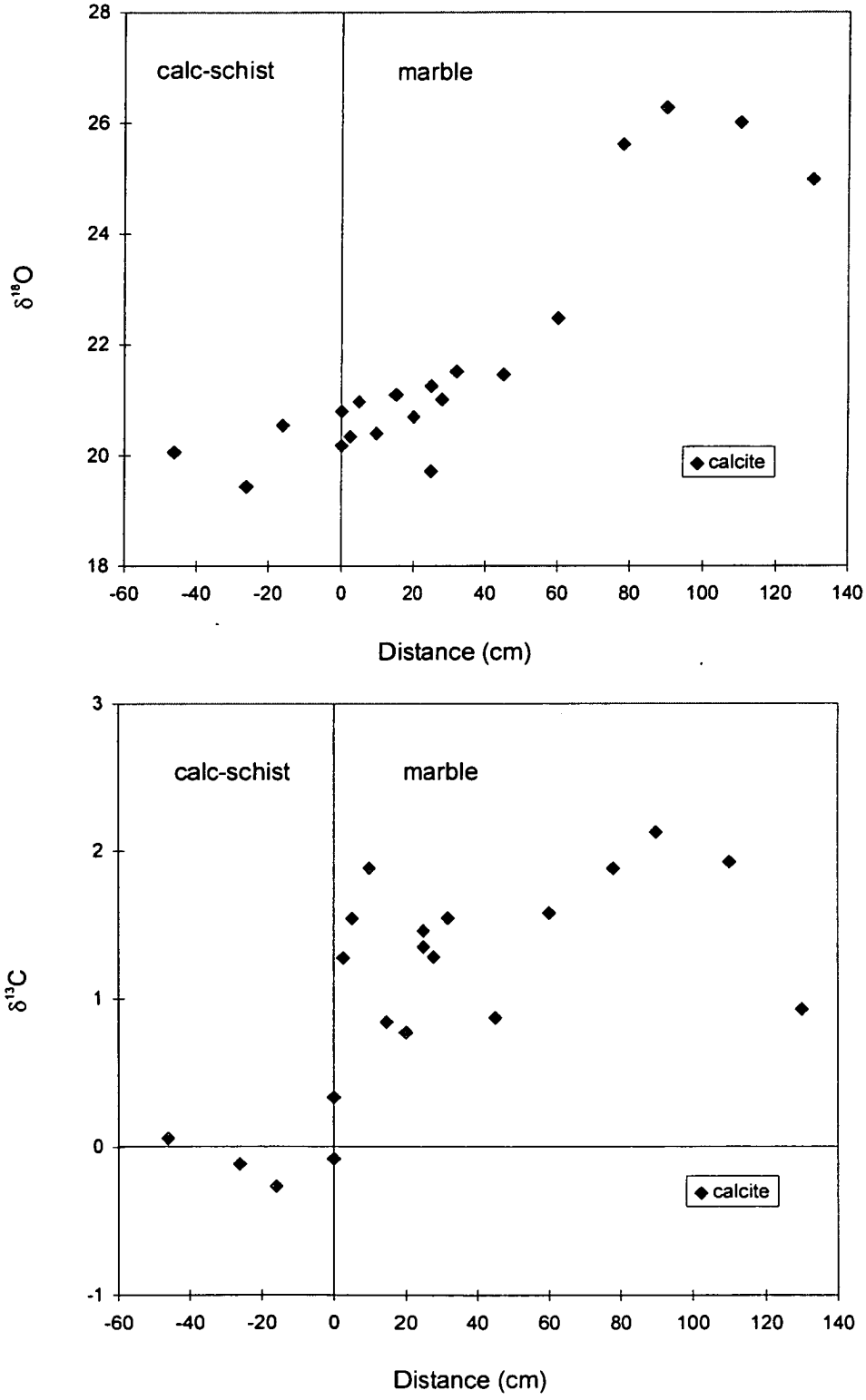

Figure 6.11
Graphs of $\delta^{18}O$ and $\delta^{13}C$ versus distance for a traverse across a marble-schist contact at Nites locality C (deformed). To the bulk data (diamonds) macro data has been added for various distances on the traverse from zones of deformation, veining and associated wall rock.

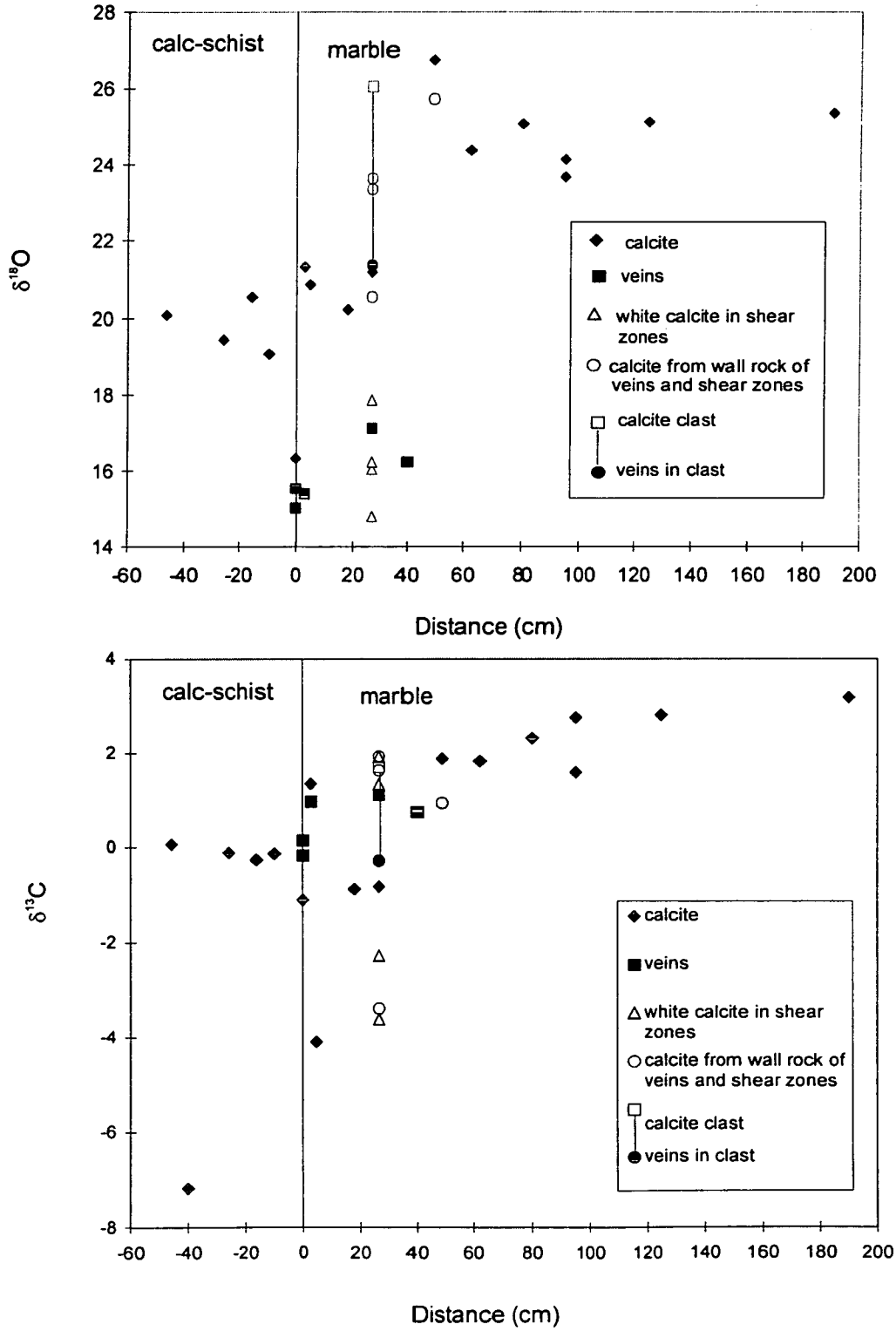

has occurred within the fracture and fault zones. The depletions in $\delta^{18}O$ are inferred to be the result of channelling of a low $\delta^{18}O$ fluid in these deformation zones.

The $\delta^{18}O$ and $\delta^{13}C$ values of calcite marble in zones of deformation are lower than those obtained from calcite in the matrix of the calc-schist below, implying that the fluid infiltrating the marble was not in grain scale equilibrium with the adjacent schist. Fluid is inferred to have been channelled in: 1) greenschist veins and segregations, 2) high permeability zones in the schist, or 3) along the lithological contact between the schist and marble. Material collected for stable isotope analysis from the schist, included calcite and quartz from greenschist segregations, as well as calcite drilled from the schist matrix. The variations in the schist isotope composition in both segregations and schist matrix are shown in figure 6.12. The range in isotope composition in the schist suggests fluid channelling and/or partial isotopic equilibration of calcite in the schist.

Mineral separates from chlorite-, calcite- and quartz, and some quartz-oxide segregations and veins, were also collected for stable isotope analysis. The fractionations between the minerals are not consistent and single veins often show an isotopic reversal between coexisting quartz and calcite, implying that calcite and quartz did not precipitate from the same fluid. In figure 6.13 a $\delta^{18}Occ$-$\delta^{18}Oqz$ plot shows examples of $\delta^{18}O$ compositions of coexisting quartz and calcite in veins below the marble quartzite. The ^{18}O fractionations between the two phases are inconsistent with equilibrium at the temperatures of metamorphism for Syros.

The mm-scale stable isotope study has documented isotopic heterogeneities on a cm and sub-cm scale in calcite from the marble band and the calc-schist. In the marble, areas of local isotopic depletion are spatially associated with shear zones and fractures. In the calc-schist the spatial variation in the $\delta^{18}O$ composition is unconstrained.

Comparison of CL with the macroscopic stable isotope study

The marble was examined under CL to see if there was a correlation between isotopically altered deformation zones and chemical variation in the calcite. Photograph 6.16, shows a thin section of calcite marble under CL from a distance of 27 cm from the schist-marble contact. The brightly luminescent shear zone on the slabbed hand

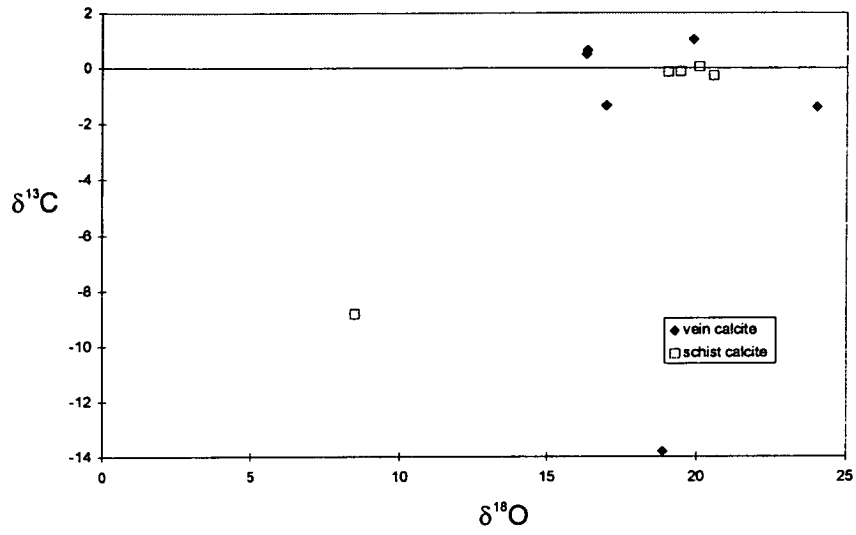

Figure 6.12
Plot of $\delta^{18}O$ versus $\delta^{13}C$ for calcite from schist and veins on the Nites hillside

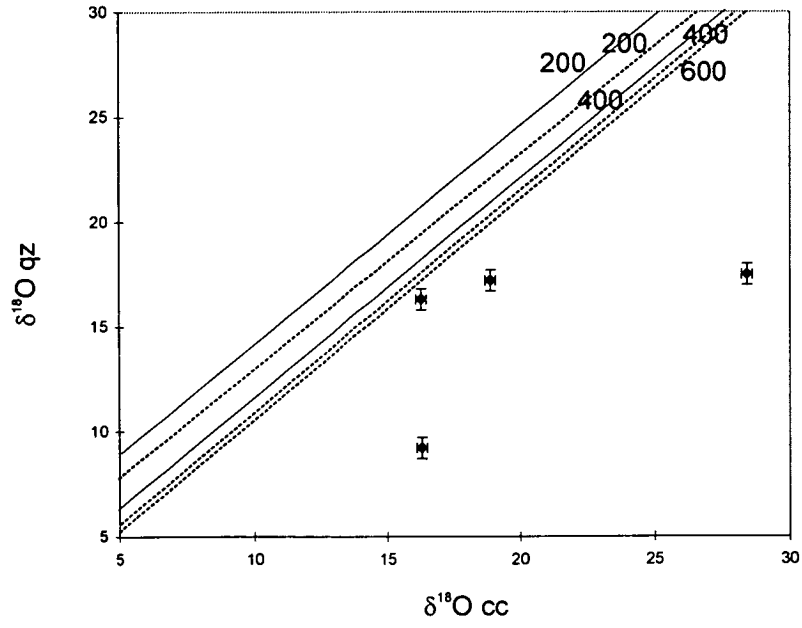

Figure 6.13
Plot of $\delta^{18}O$ cc against $\delta^{18}O$ qz coexisting in veins below the marble-quartzite band, Nites localities C and D. Fractionation temperature lines have been calculated from Faure (1986) (dashed lines) and Sharp and Kirschner (1994) (solid lines).

specimen is shown in photograph 6.15 and the thin section in photograph 6.13. White calcite in the shear zone is brightly luminescent under CL compared to undeformed zones. Calcite infill of fractures in quartz layers also luminesces brightly. The CL also highlights micro-fractures within the calcite. Calcite crystals cut by micro-fractures outlined by trails of fluid inclusions in thin section, show bands of bright luminescence under CL (photograph 6.16). These luminescent bands are thought to be zones of chemically altered calcite associated with fluid infiltration during micro-fracturing events.

CL observations of marble from locality D were compared with CL observations of locality C. Observations of thin sections from locality D in CL show grain boundary luminescence and zonation of calcite crystals. Bright luminescence is also seen along cleavage planes in calcite and around crystals of mica. The calcite at locality C, away from the shear zones and fractures, looks similar to that at locality D under CL.

The CL observations suggest a link between chemical and isotopic alteration of calcite and deformation zones. The CL studies highlight cm, mm and μm zones of calcite alteration, which I have correlated with isotopic depletion on a cm to mm scale. I therefore propose that isotopic alteration of the marble also occurred on a μm-scale. To test this hypothesis and to see if microscale fluid channelling could be linked to micro-scale fractures and deformation and CL textures at locality C, an ion microprobe study was undertaken.

Microscopic (μm-scale) stable isotope study

The apparent link between deformation textures and chemical variation highlighted by CL warranted micro-scale $\delta^{18}O$ analysis by ion microprobe. The ion microprobe was used to identify isotopic heterogeneity on a micro-scale and to correlate these isotopic depletions with micro-textural information. For locality C thin sections from 2 cm, 27 cm, 30 cm and 100 cm from the bulk stable isotope profile were chosen for micro sampling. For locality D thin sections were targeted for the micro study at -16 cm (in the calc-schist), 0 cm, 32 cm and 78 cm. The samples were chosen for their

Photograph 6.16
CL photomicrographs of sample S'97/101. The white boxed areas are shown as enlargements in the subsequent plates. Field of view of main photograph approximately 5 mm wide. Field of view of enlargement approximately 2.5 mm wide.

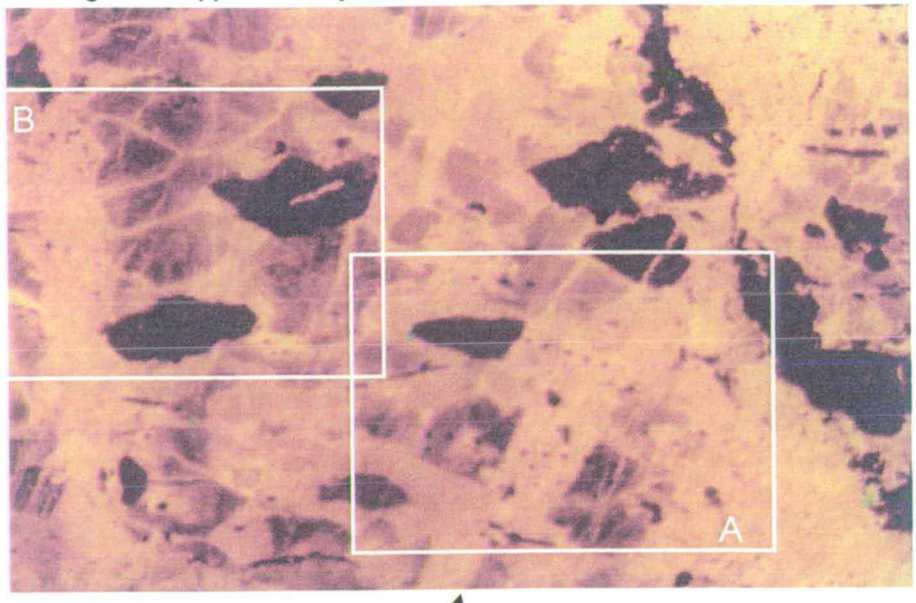

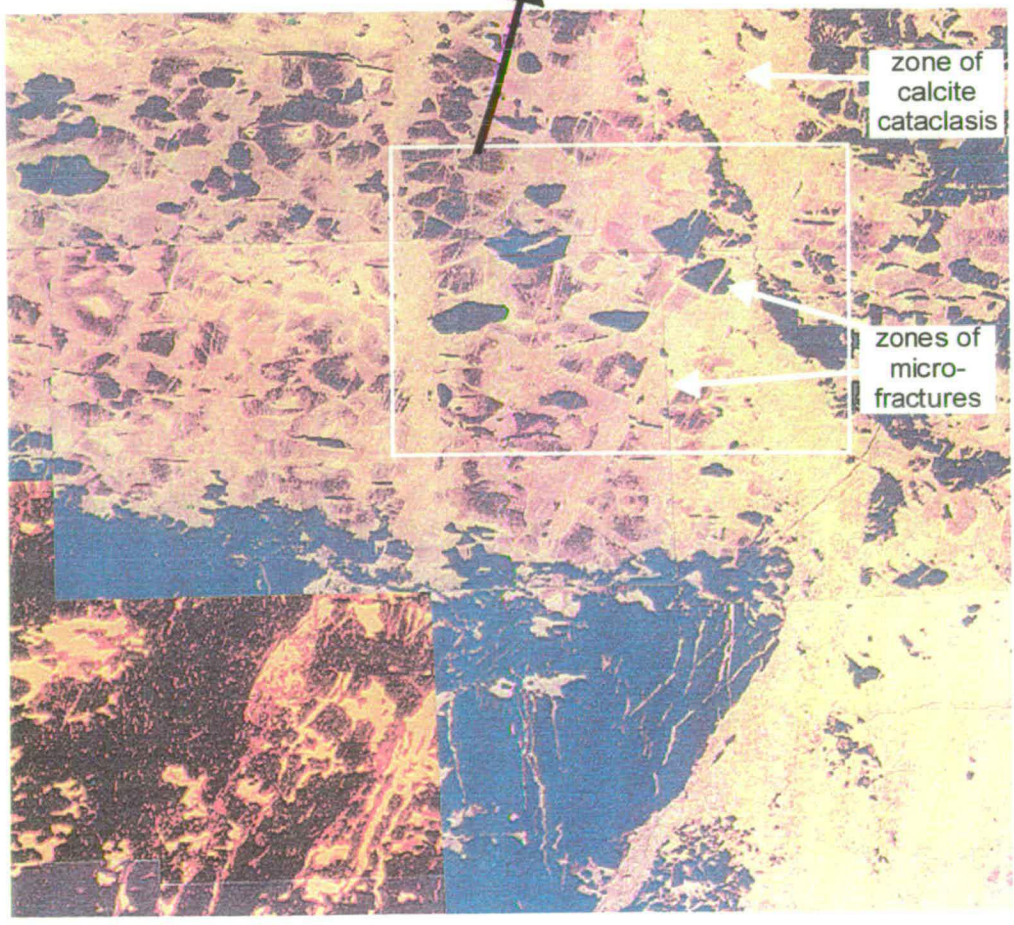

micro-structural diversity and to link with the bulk stable isotope and macro-sampling results.

Locality C

The bulk stable isotope traverse of locality C is shown in figure 6.14, with the results of the macro and microscale sampling superimposed. The first 3 samples targeted S'97/97 (2 cm), S'97/101 (27 cm), S'97/102 (30 cm) span a broad range in $\delta^{18}O$ from approximately 10 to 35 ‰. The range brackets the values obtained by bulk sampling at the corresponding distances on the main profile. The micro data for each sample fall into two discrete groups: 1) a group with high $\delta^{18}O$ values, the same as or greater than those obtained in the bulk traverse; and 2) a group with $\delta^{18}O$ values lower than the bulk value. The sample at 100 cm documents $\delta^{18}O$ compositions above those documented in the bulk study.

The range in $\delta^{18}O$ values obtained in the μm-study is much greater than for the mm-scale sampling, but the data fall into similar groupings. The macro-sampling highlights zones of low $\delta^{18}O$ which spatially correlate with shear zones and veins (figure 6.11). The micro-scale data are presented in the form of graphs and annotations on CL and PPL photographs to document the spatial correlation of textural features with isotopic heterogeneities. Ion probe traverse lines are marked on PPL photographs and labelled X-Y, where X is the start of the traverse. Examples of the results are discussed and illustrated below, where they have been grouped by deformation mechanism. The full data set is presented in appendix C.

Micro-fracture

In sample S'97/101 from 27 cm on the bulk traverse, zones of micro-fracturing outlined by trails of fluid inclusions cut through calcite crystals. The trails of fluid inclusions link into a zone of calcite cataclasite, and the cataclastic zone off-sets cm-scale quartz and calcite layers. The micro-fractures and cataclasite zone are best seen in CL where they stand out due to their bright luminescence (photograph 6.16). Examples

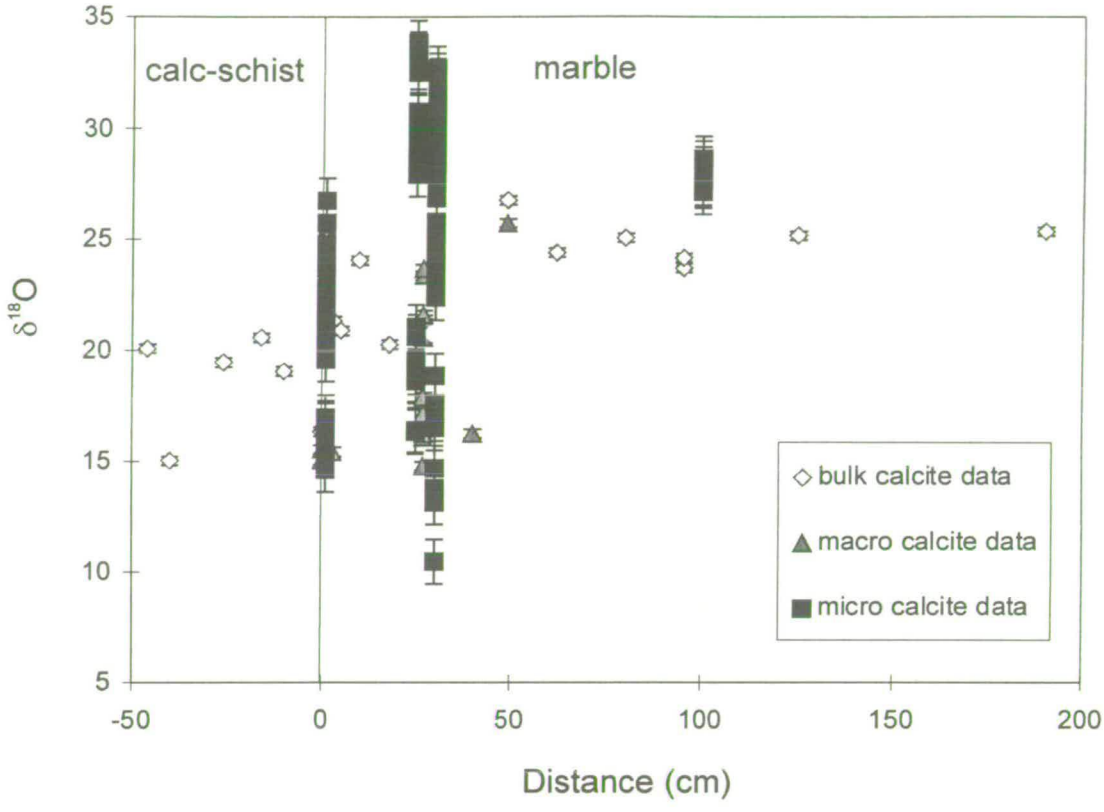

Figure 6.14
Bulk data (cm^3) and macro data (mm^3) from the stable isotope traverse at locality C Nites, with the results of the microscale study superimposed.

of two traverses across zones of micro-fracturing are presented and discussed, from areas A and B in photograph 6.16.

Photographs 6.17 and 6.18 are enlarged CL and PPL photographs respectively, of area A in photograph 6.16. The CL photograph (photograph 6.17) is annotated with the ion probe pits and their respective $\delta^{18}O$ compositions. Black areas in CL are quartz, brown/orange or yellow material is calcite. The lower photograph (photograph 6.18) is a PPL photograph of the same area, in which the poor polish on the calcite gives a very high relief. The location of the lower of the two ion probe traverses is marked on this photograph, and this traverse is shown as a graph in figure 6.15. A corresponding electron probe traverse has been made just below the ion probe points which is also shown graphically in figure 6.15. The electron probe traverse can be identified in the CL photograph 6.17 as a series of small squares formed by the rastering electron gun.

The ion probe traverse show depletion in the $\delta^{18}O$ composition of the calcite across the zone of micro-fractures, which is the brightly luminescent area in the centre of the traverse (photograph 6.17). The $\delta^{18}O$ compositions of the micro-fractured zone are lower than the bulk $\delta^{18}O$ signature at 27 cm on the bulk profile, whilst the calcite away from the micro-fractures has a higher $\delta^{18}O$. The corresponding electron probe traverse shows enrichment in Mg, Mn and Fe in the micro-fractured area. The data suggest that micro-fracturing was associated with infiltration of a relatively low $\delta^{18}O$ fluid, that depleted the surrounding calcite in ^{18}O and enriched it in Mg, Fe and Mn.

A second traverse was made in sample S'97/101 into a band of micro-fracturing in the calcite. The traverse is shown in photographs 6.19 (CL) and 6.20 (PPL). The CL photograph is annotated with ion probe pits and $\delta^{18}O$ compositions. The lower of the two traverses, which crosses a quartz crystal, is briefly discussed here. The $\delta^{18}O$ compositions of the quartz fall in the range 29.1 to 29.7 ‰, apart from locations where micro-fractures cut the grain. The micro-fractures lower the $\delta^{18}O$ composition to 27.0 % and 27.5 ‰.

The traverse into the micro-fractured zone in the calcite is marked on the PPL photograph 6.20. The $\delta^{18}O$ compositions are plotted as a graph in figure 6.16. A

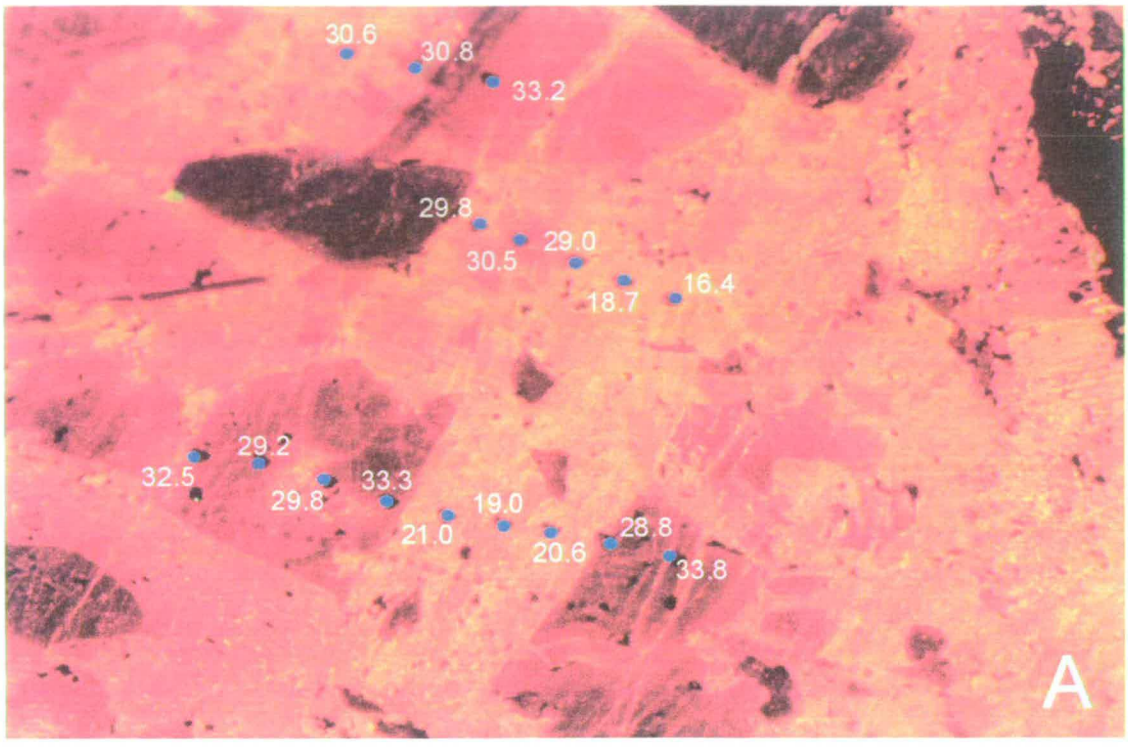

Photograph 6.17
CL photomicrograph of sample S'97/101, the ion probe pits are marked by blue dots, their $\delta^{18}O$ compositions are annotated. The lower profile crosses a single calcite grain that is cut by a band of fluid inclusions. Field of view approximately 1 mm wide.

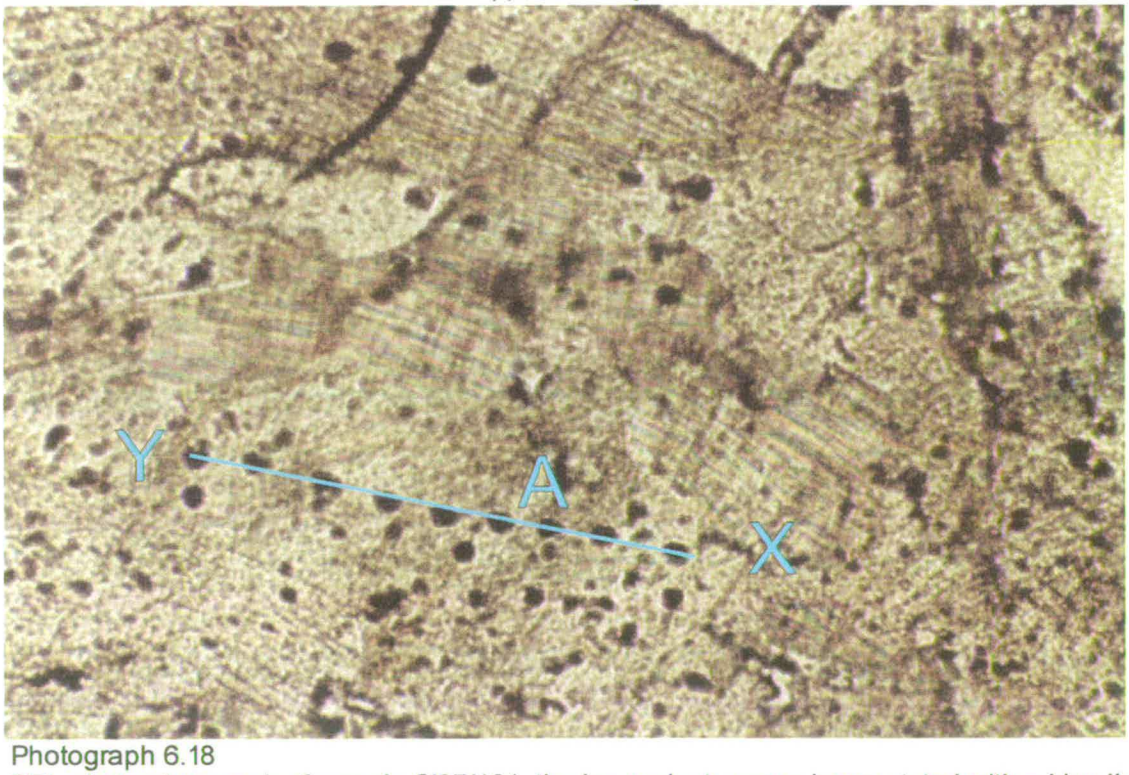

Photograph 6.18
PPL photomicrograph of sample S'97/101, the ion probe traverse is annotated with a blue line. The high relief is due to a poor calcite polish. Field of view approximately 1 mm wide.

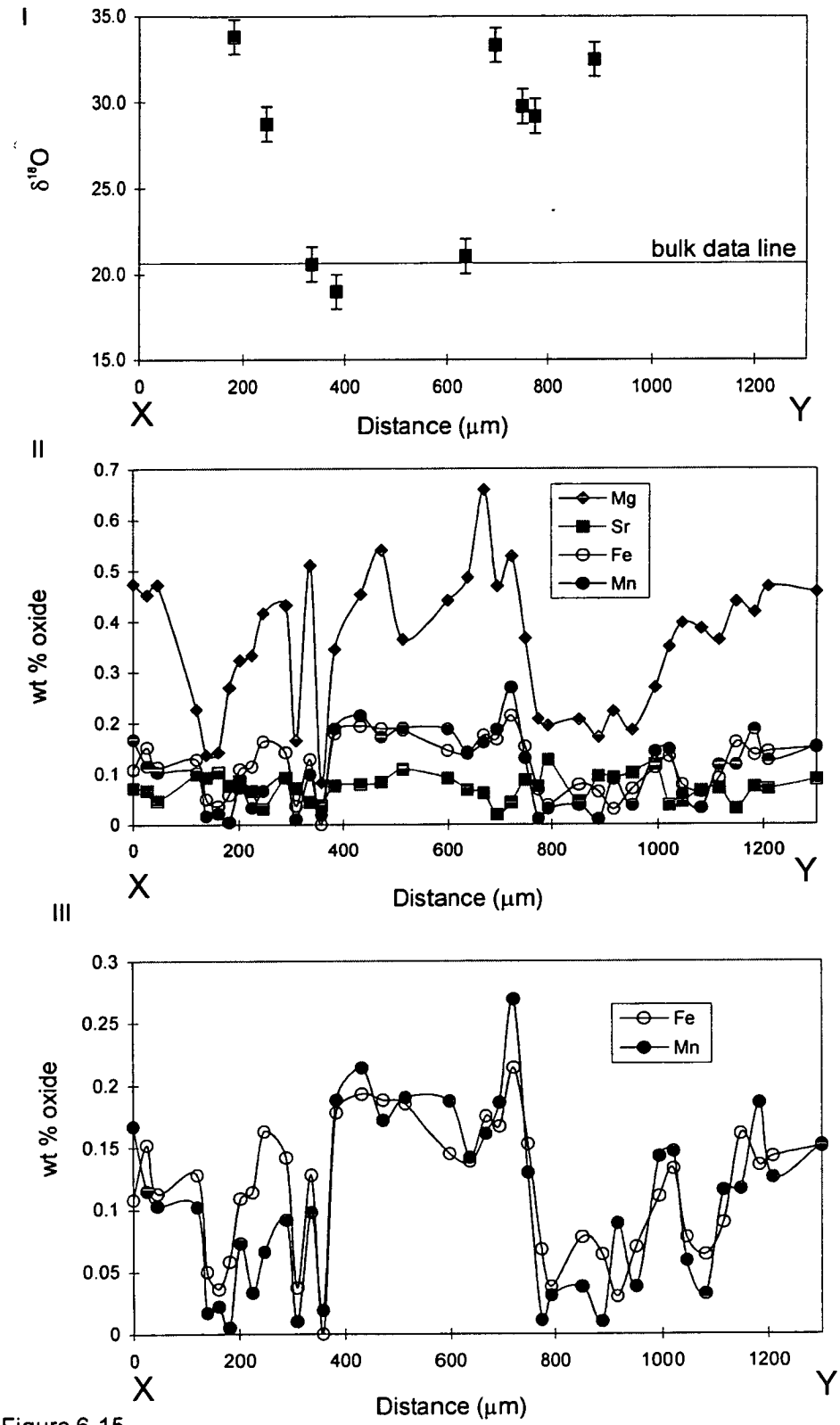

Figure 6.15

Graph of I) $\delta^{18}O$ versus distance for profile A S'97/101, and II) wt % oxides versus distance across the same microfractured calcite, see photograph 6.17. Graph III) is an enlarged version of the wt % oxide plot to show the trends in Fe and Mn.

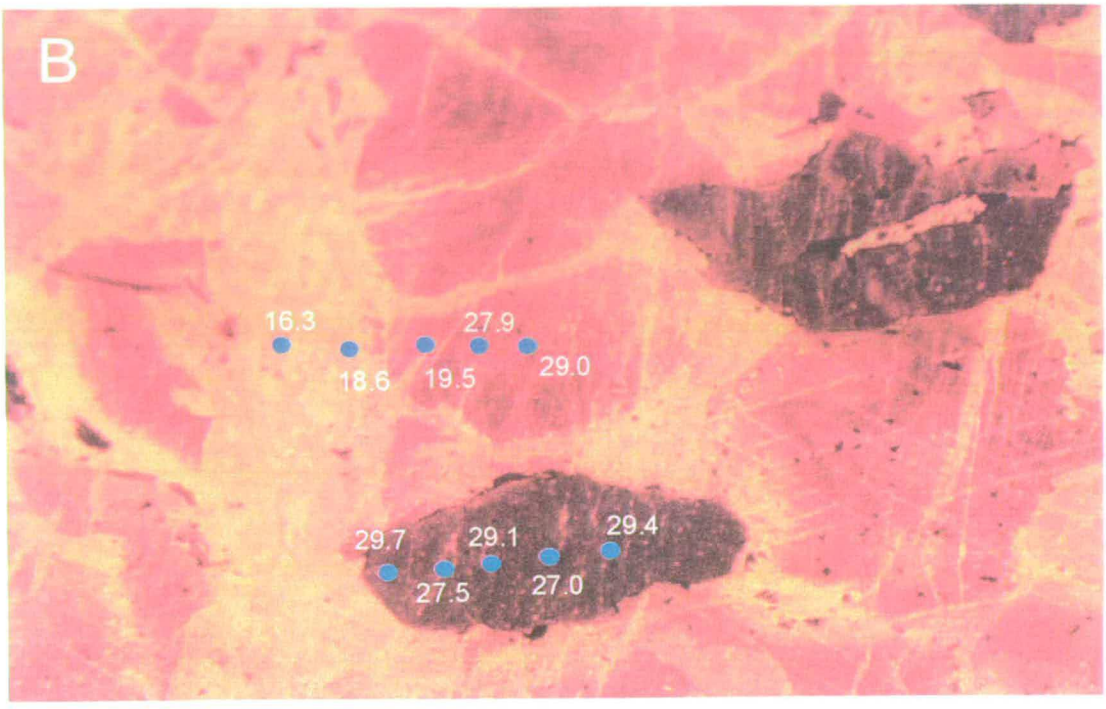

Photograph 6.19
CL photograph of sample S'97/101, enlargement of area B in photograph 6.16. Ion probe pits are marked by blues dots and $\delta^{18}O$ compositions are annotated. Brightly luminescent areas outline micro-fractures in the calcite. Field of view is approximately 1.2 mm wide.

Photograph 6.20
PPL photograph of sample S'97/101, enlargement of area B in photograph 6.15. The ion probe traverse is marked by a blue line. The high relief is due to poor polish of the calcite. Field of view is approximately 1.2 mm wide.

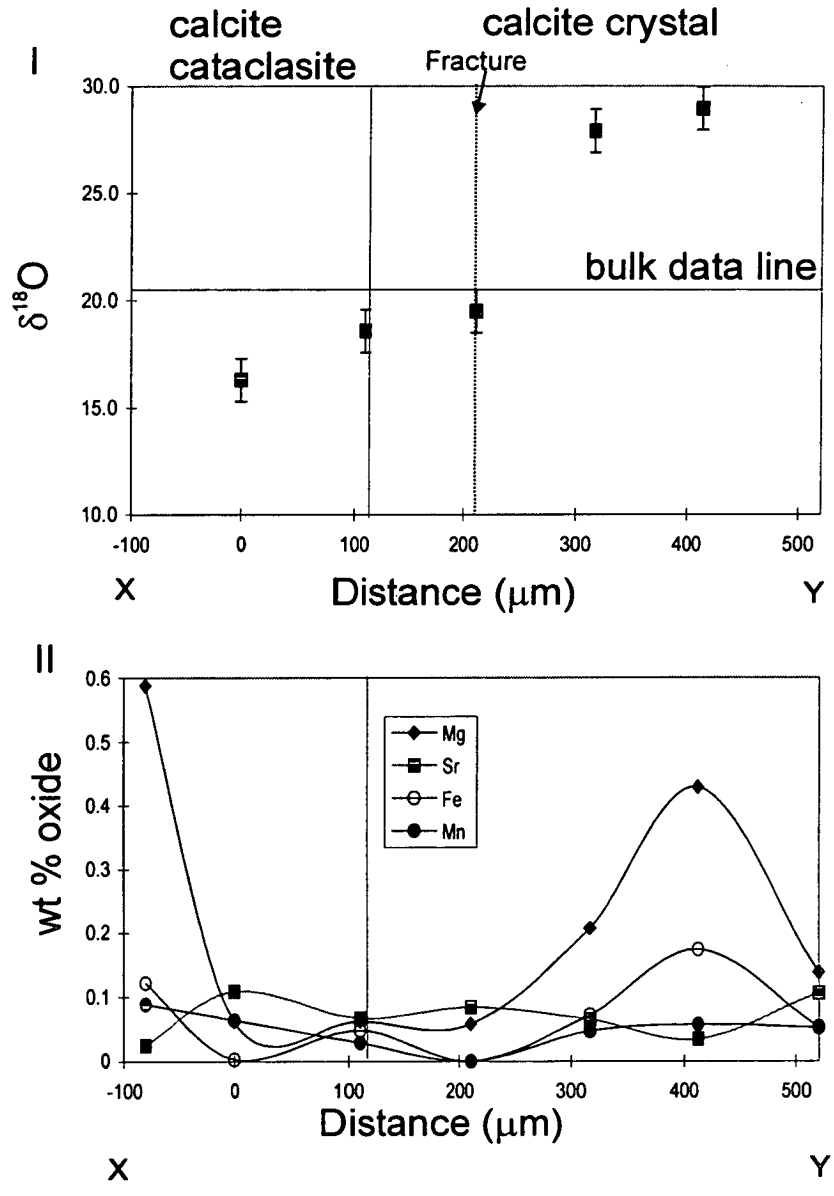

Figure 6.16
I) Graph of d^{18}O versus distance across a calcite crystal, profile B S'97/101, photographs 6.19 and 6.20 II) wt % oxide versus distance for profile B.

corresponding electron probe traverse was also made (figure 6.16). As in the previous example the $\delta^{18}O$ composition of the calcite outside the micro-fracture zone lies above that recorded by the bulk stable isotope traverse. The $\delta^{18}O$ composition decreases as the micro-fracture zone is approached, falling to a level below that of the bulk analysis. The electron probe traverse however, shows depletions rather than enrichment in calcite trace elements (Mg, Mn and Fe) in the fractured area (figure 6.16).

Micro-fracture summary

The ion probe traverses made across micro-fracture zones in sample S'97/101 are inferred to show that micro-fracturing channelled fluid of a relatively low $\delta^{18}O$ composition into the marble, resulting in localised, μm-scale, isotopic and chemical exchange between the fluid and calcite. This local exchange has produced the observed microscale heterogeneities in $\delta^{18}O$ composition of the calcite. The bulk stable isotope analyses are inferred to record a mixed signature from unaltered calcite grains and zones of micro-fracturing, which could not be identified when sampling with the drill at a cm-mm scale.

Local exchange of trace elements between the calcite and the infiltrating fluid phase is thought to have produced the variation in luminescence of the calcite in CL. Brightly luminescent zones are spatially associated with trails of fluid inclusions outlining micro-fractures. These zones have been shown to be both enriched and depleted in Mg, Mn and Fe relative to calcite away from fracture zones.

Cataclasis

Sample S'97/102, 30 cm on the bulk traverse, was targeted for microscale stable isotope analysis in zones of calcite cataclasis (photograph 6.21, 6.22 and 6.23). The main traverse crosses a zone of calcite cataclasis between an off-set quartz layer and a calcite crystal. In CL (photograph 6.21) the zone of cataclasis is brightly luminescent, the quartz is black and cut by fractures infilled with luminescent calcite, elsewhere the calcite is orange-brown. The traverse is marked on the PPL photograph 6.22. An

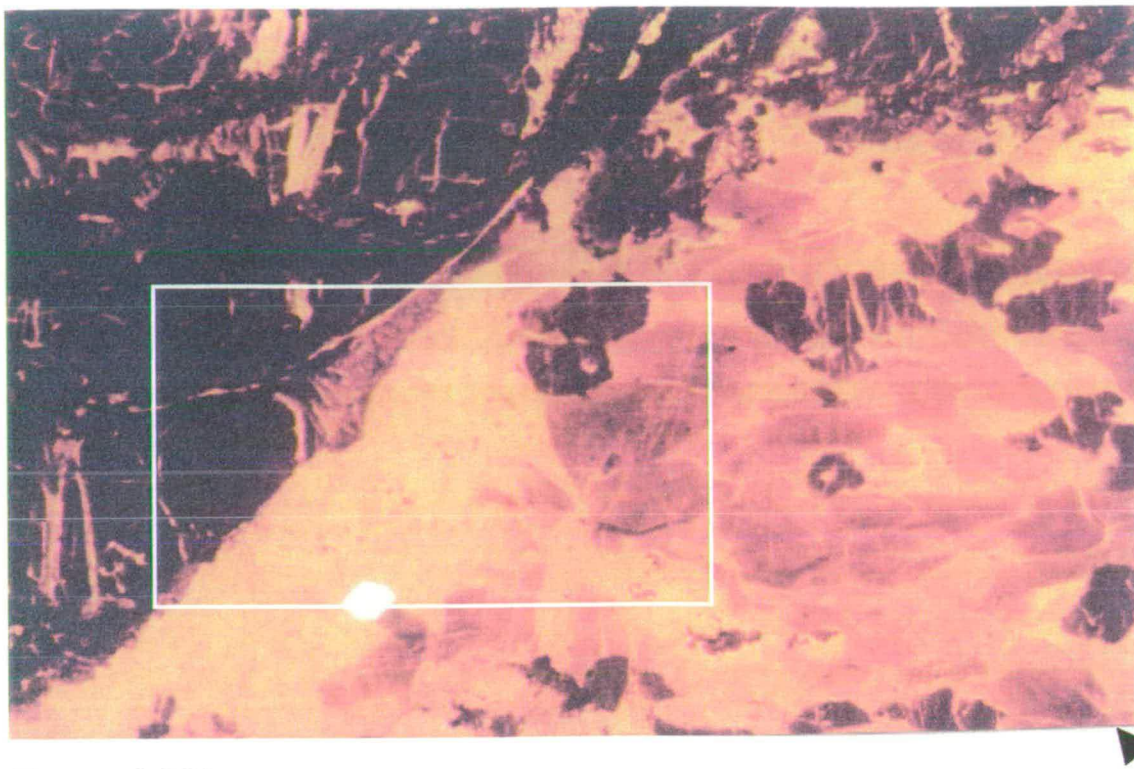

Photograph 6.21
CL photograph of sample S'97/102. Calcite cataclasite, calcite grain boundaries and micro-fractures are brightly luminescent, elsewhere the calcite is brown/orange. Quartz is black. The white boxed area is enlarged in photograph 6.23. Field of view approximately 2.5 mm wide.

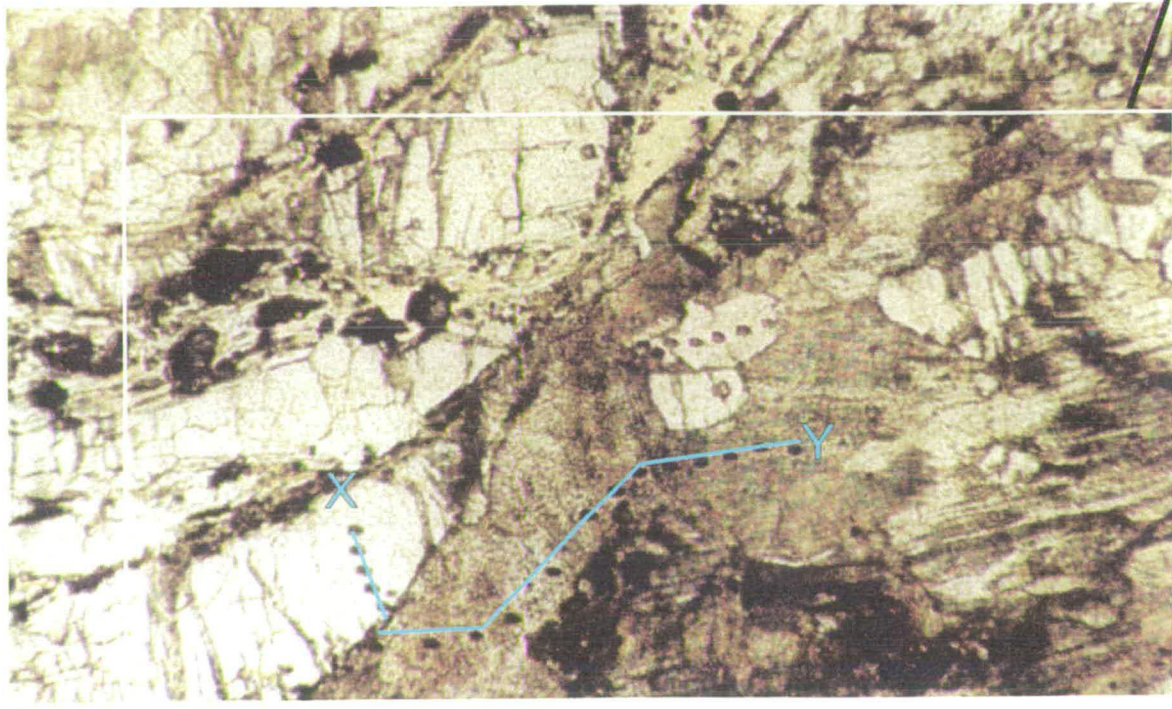

Photograph 6.22
PPL photograph of sample S'97/102. Quartz is pale with a low relief, calcite has a high relief due to a poor polish. The ion probe traverse is marked by the pale blue line. Field of view approximately 2.5 mm wide.

enlarged CL photograph of the area is shown in photograph 6.23. The $\delta^{18}O$ compositions and ion probe pits are annotated on this photograph.

The $\delta^{18}O$ compositions across the traverse are plotted in figure 6.17. The calcite in the cataclasite zone has a low $\delta^{18}O$ composition, up to 10 ‰ less than the $\delta^{18}O$ composition determined by bulk stable isotope analysis. The calcite on the right side of the traverse documents some depletion in $\delta^{18}O$ adjacent to the zone of cataclasis, but has a $\delta^{18}O$ signature higher than that of the bulk traverse. The quartz adjacent to the cataclasite zone appears to be have a relatively undepleted $\delta^{18}O$ signature.

The zone of cataclasis is inferred to have acted as a high permeability channel allowing infiltration of a fluid relatively depleted in $\delta^{18}O$ into the marble. Minimal isotope exchange is inferred to have taken place between the fluid in the cataclasite and the bounding quartz. In comparison, the calcite on the right side of the cataclastic zone documents some modification in isotope composition adjacent to the zone.

The calcite section of the ion probe traverse is repeated in figure 6.18 so that it can be directly compared with an electron probe traverse across the same area (figure 6.18). The zone of calcite cataclasis is enriched in Mg, Fe and Mn trace elements with respect to adjacent calcite. Infiltrating fluid is inferred to have enriched the calcite in trace elements whilst depleting it in $\delta^{18}O$.

Cataclasis summary

The zone of calcite cataclasis in sample S'97/102 has been shown to be depleted in $\delta^{18}O$ and enriched in Fe, Mn and Mg. It is inferred that the zone of cataclasis was a high permeability pathway in which, low $\delta^{18}O$ infiltrating fluid was channelled during deformation. During infiltration the fluid exchanged chemically and isotopically with the calcite. Differences in isotope composition within the cataclasite are caused by controls on the isotope exchange during infiltration. These controls include: the length of time over which fluids infiltrated, the tortuosity of fluid pathways and the surface area of the calcite fragments in contact with the fluid. It is also likely that within the

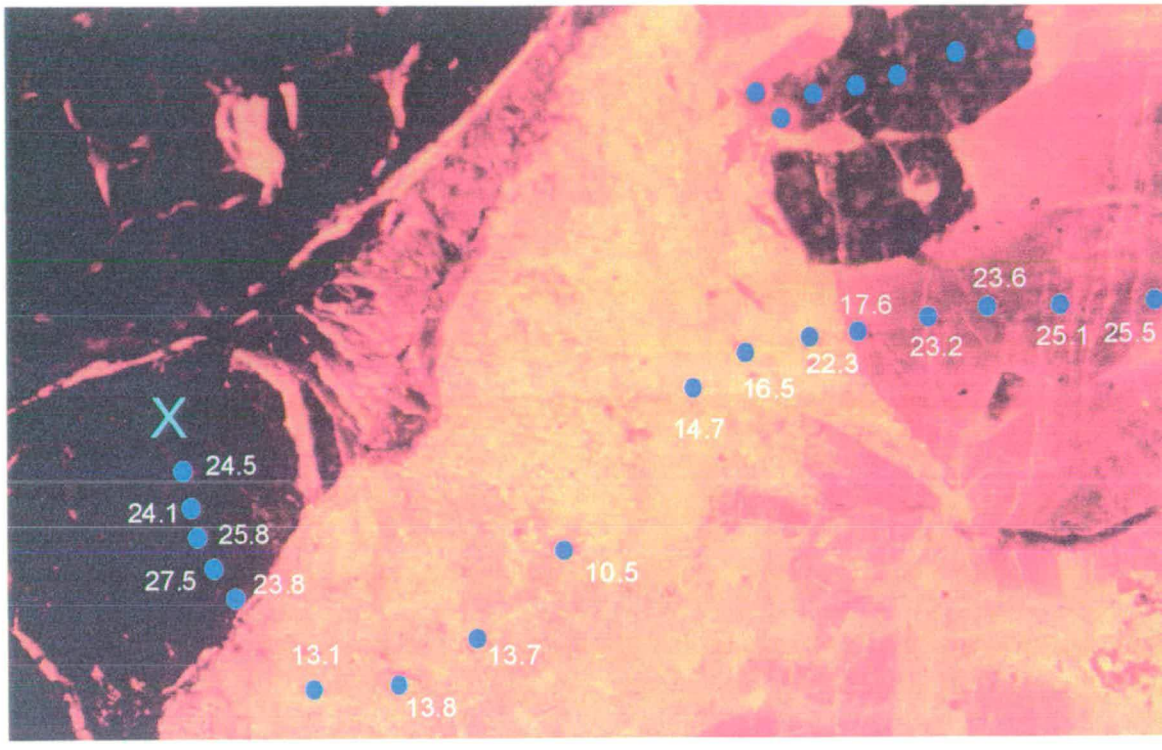

Photograph 6.23
CL photomicrograph of sample S'97/102, enlarged from photograph 6.21. Ion probe pits are marked by blue dots and annotated with their $\delta^{18}O$ compositions. The traverse (X-Y) is plotted in the graph below. Field of view approximately 1.3 mm wide.

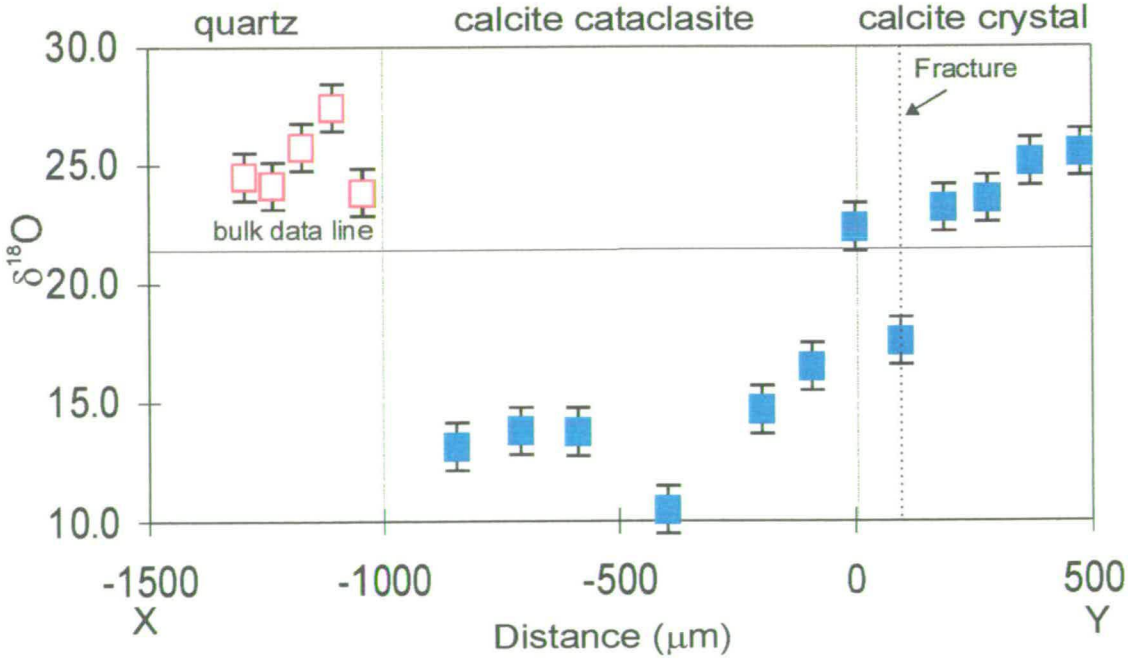

Figure 6.17
Distance between ion probe pits against $\delta^{18}O$ across a carbonate cataclasite, S'97/102. The traverse is marked on the photograph above. Open squares are quartz $\delta^{18}O$ data, filled squares are calcite $\delta^{18}O$ data.

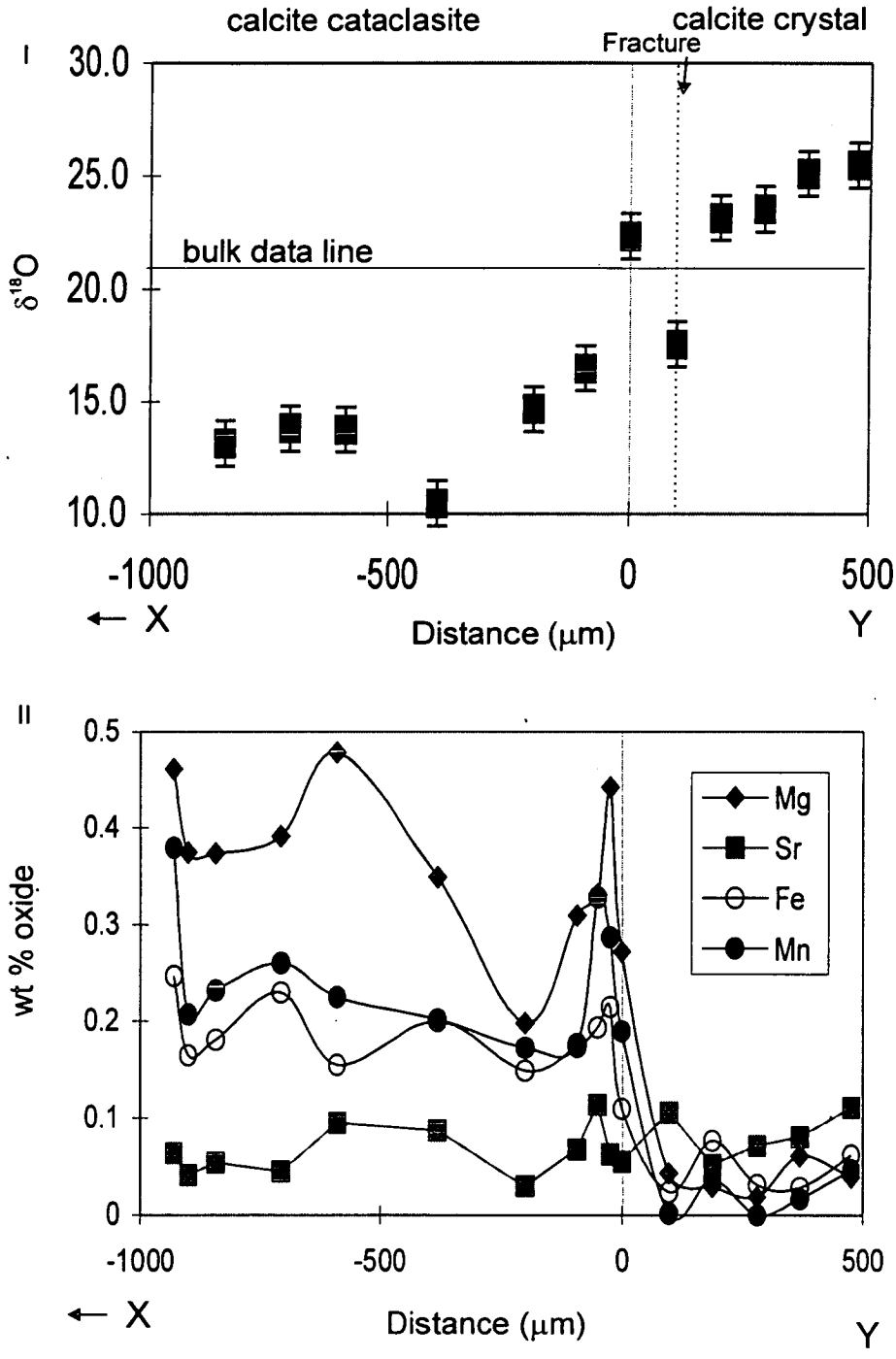

Figure 6.18
Graph I) Shows $\delta^{18}O$ against distance for the calcite part of the profile in, S'97/102, see photograph 6.23. II) wt % oxide against distance for the same profile. Note that the calcite cataclasite depleted in $\delta^{18}O$ is enriched in Mg, Fe and Mn.

cataclasite there were higher permeability zones in which fluid would have been preferentially channelled.

Veins

Sample S'97/97, 2 cm from the contact with the schist, shows a range of structures in thin section including a calcite vein. The vein was targeted for ion probe analysis to: 1) compare the $\delta^{18}O$ composition of the vein with the bulk $\delta^{18}O$ composition; and 2) identify isotope zoning in a single zoned crystal within the vein. The calcite crystals in the vein are zoned in CL (photograph 6.24). A micro-sampling stable isotope and electron probe traverse was made across the marked crystal (figure 6.19). Ion probe pits and $\delta^{18}O$ composition are annotated, on the CL photograph (6.24), and are plotted in figure 6.19. The results of the electron probe traverse are also shown in figure 6.19.

The $\delta^{18}O$ values are all within error of each other, with a $\delta^{18}O$ composition of approximately 16 ‰, except one which falls on a grain boundary. The analysis made on the grain boundary may have a high value due to edge effects, similar to those reported by Valley and Graham (1991) for magnetite $\delta^{18}O$ compositions, in which crystal edges gave unusually high $\delta^{18}O$ values. All the compositions, bar the one on the grain boundary, are approximately 4 ‰ lower than the bulk average for 2 cm. The slight fluctuations in $\delta^{18}O$ correspond to zone boundaries in the calcite crystal highlighted in CL photograph 6.24. However, the variations in the trace element chemistry of the calcite have a far stronger correlation to the observed zoning in CL. The zones visible in CL correspond to increases and decreases in Mn, Mg and Fe as the zone boundaries are crossed (figure 6.19).

Vein summary

The vein is depleted in $\delta^{18}O$ relative to the bulk stable isotope composition at 2 cm, suggesting that the infiltrating fluid was relatively depleted in $\delta^{18}O$ in comparison to the calcite in the marble matrix. Despite the zoning visible in CL, which is interpreted to

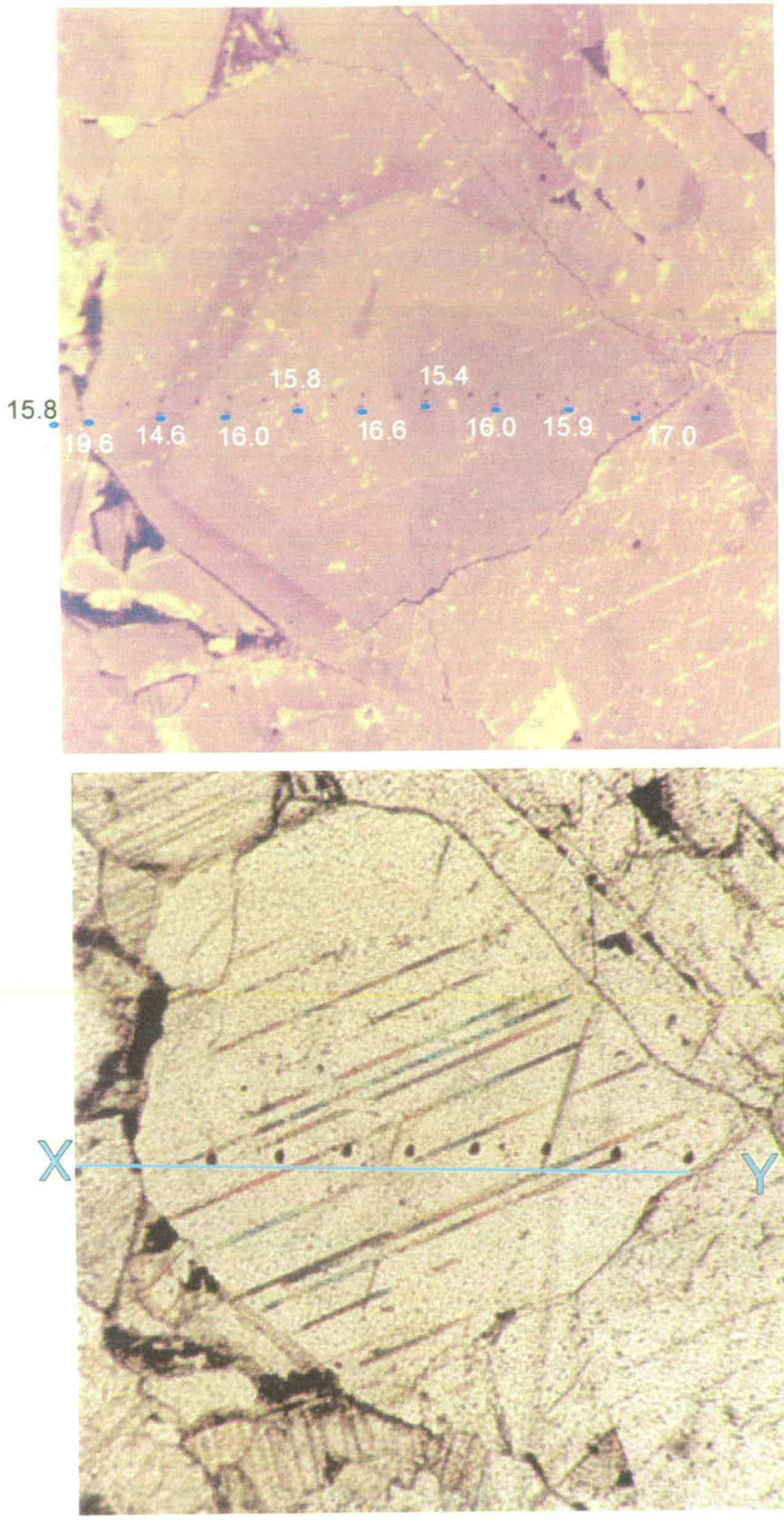

Photograph 6.24
CL (top) and PPL (bottom) photographs of calcite in a vein from sample S'97/97 . The calcite in the vein is euhedral and under CL exhibits zoning. Ion probe pits and $\delta^{18}O$ compositions are annotated. The field of view is approximately 1.5 mm wide.

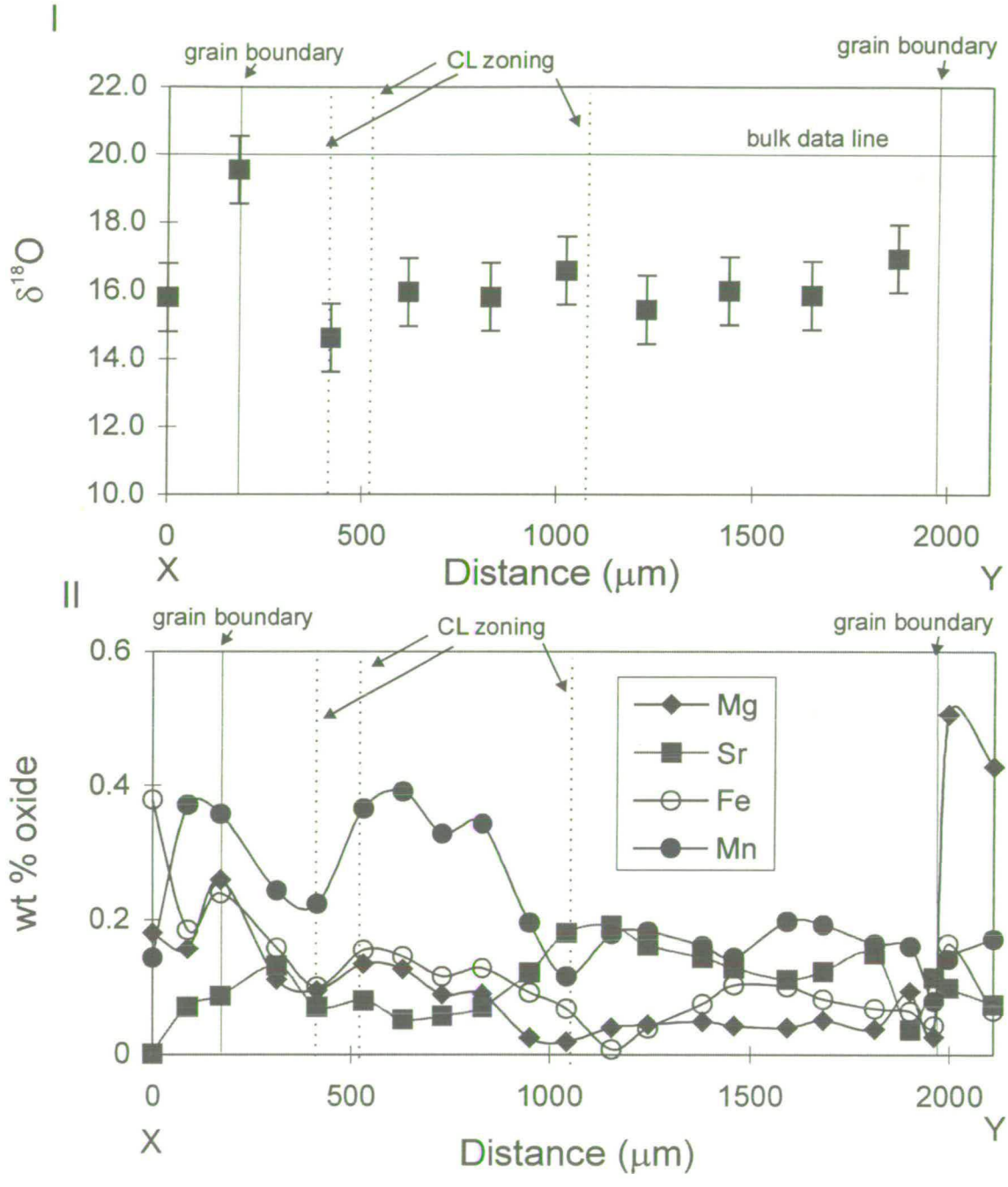

Figure 6.19

Graph of I) $\delta^{18}O$ against distance for the ion probe profile across the vein in sample S'97/97 photograph 6.24 II) wt % oxides against distance across the same calcite crystal. The variation in Mg, Mn, Sr and Fe trace elements in the calcite correlates to the observed zoning of the calcite crystal in CL, photograph 6.24.

be growth zoning of the calcite in the vein, the $\delta^{18}O$ composition of the calcite crystal is homogeneous. This homogeneity in isotope composition suggests the source of the fluid was not buffered by isotopic exchange during infiltration. In contrast the electron probe traverse shows variations in the calcite trace element chemistry which correspond with zoning visible in CL. The chemical zoning implies that either the fluid from which the calcite precipitated was chemically buffered or the fluid rock equilibrium changed during calcite crystal growth.

Locality D

Figure 6.20 shows the results of the microscale study superimposed on the bulk $\delta^{18}O$ data for locality D. Locality D lies approximately 10m to the west of locality C and crosses the marble-quartzite horizon where deformation cannot be identified in the field (figure 6.1). The range in $\delta^{18}O$ for individual thin sections targeted for microscale analysis is < 10 ‰. Of the four thin sections targeted, two bracket the stable isotope value indicated by the bulk sampling traverse and the other two have $\delta^{18}O$ ranges that lie above the bulk $\delta^{18}O$ values at the corresponding distances. The range in $\delta^{18}O$ values obtained in the ion probe study are thought to represent heterogeneities in isotope composition resulting from fluid channelling in discrete micro-scale zones. However, the samples from locality D show relatively few micro-structural features in CL with comparison to those from locality C. The CL studies of samples from locality D show bright luminescence along grain boundaries and cleavage planes and the calcite crystals are often zoned. Calcite away from deformation zones in locality C shows very similar features. Samples from locality D have been used as a proxy for the calcite at locality C prior to fracturing and cataclasis. Isotopic heterogenities were expected within the marble samples, as the bulk stable isotope profile showed exchange of $\delta^{18}O$ within the marble band boundary layer at locality D (figure 6.10). A similar profile was documented by bulk sampling at locality C (figure 6.9). The deformation zones were avoided whilst sampling for bulk analysis at locality C. The CL observations suggest that fluid infiltration was mainly by grain edge flow. To test this hypothesis, in-situ ion probe analyses for $\delta^{18}O$ were used to pin-point grain boundaries, cores and cleavage

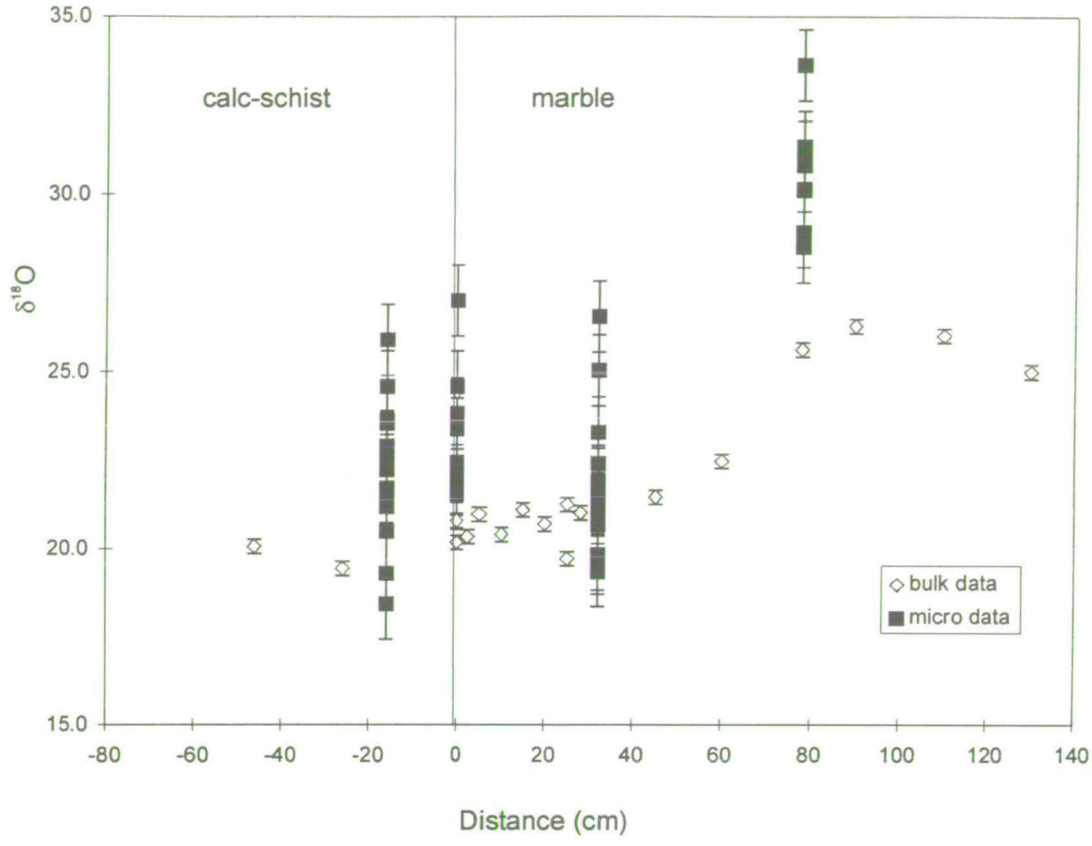

Figure 6.20
Bulk data (cm^3) from the stable isotope traverse at locality D Nites, with the results of the microscale study superimposed.

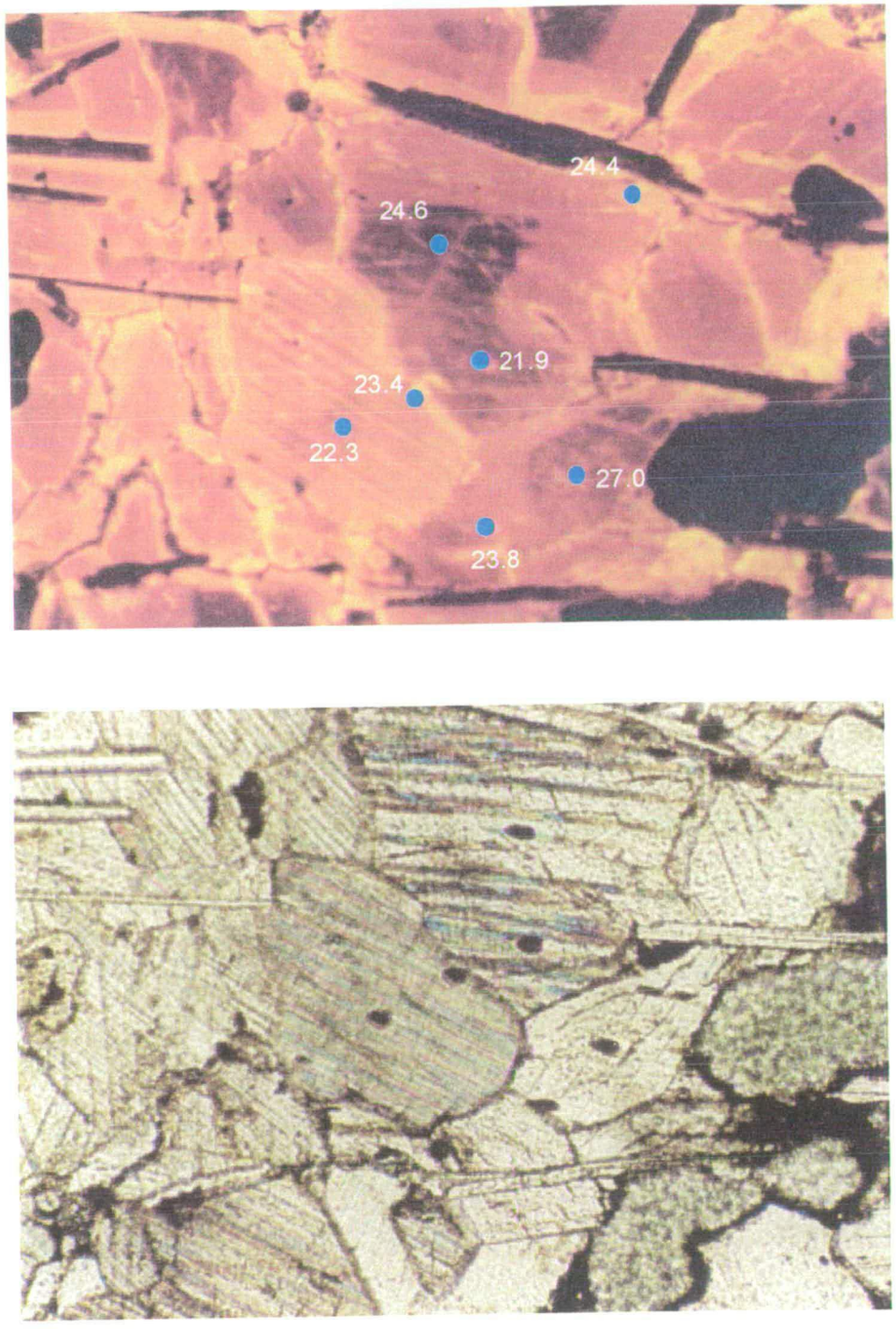

Photograph 6.25
CL (top) and PPL (bottom)photographs of sample S'97/39. $\delta^{18}O$ compositions and ion probe pits are annotated. The field of view in each photograph is approximately 0.5 mm wide.

planes. Examples of the results from three of the thin sections targeted are discussed below.

Grain edge flow

Sample S'97/39 is from the contact of the marble and schist. One of the areas targeted in this thin section is shown in the CL and PPL photographs 6.25. The $\delta^{18}O$ compositions are annotated on the CL photograph. The $\delta^{18}O$ compositions range from 21.9 to 27.0 ‰. This variation in $\delta^{18}O$ composition does not correlate systematically with textures identified in the calcite. The brightly luminescent areas in CL do not correlate with isotopic enrichment or depletion and there is no evidence for grain edge flow.

A similar study was made in sample S'97/47 from 32 cm on the bulk traverse. CL and PPL photographs are shown in photograph 6.26. The $\delta^{18}O$ compositions are annotated on the CL photograph and plotted against distance in figure 6.20. In this example the variations in $\delta^{18}O$ do bear some correlation to the textures in the rock. The $\delta^{18}O$ compositions range from 19.4 to 25.0 ‰, the lowest $\delta^{18}O$ (19.4 ‰) is found on a brightly luminescent micro-fracture, whilst the highest $\delta^{18}O$ (25.0 ‰) is found in the centre of a zoned calcite grain. Other grain boundaries and brightly luminescent areas also give low $\delta^{18}O$ compositions.

Grain edge flow summary

The results of the ion probe studies of samples from locality D suggest that early grain scale isotopic and chemical heterogeneities in composition prior to fracture have been partially retained. The isotopic heterogeneities in sample S'97/39 did not correlate either with CL textures or physical structures such as grain boundaries and cleavage planes. The CL and physical textures of the calcite in sample S'97/47 are very similar to those in sample S'97/39, but in this example the isotopic heterogeneities did correlate with marble textures. The reasons for the observed heterogeneities in calcite $\delta^{18}O$ and their variability in terms of spatial correlation to physical textures are thought to be the

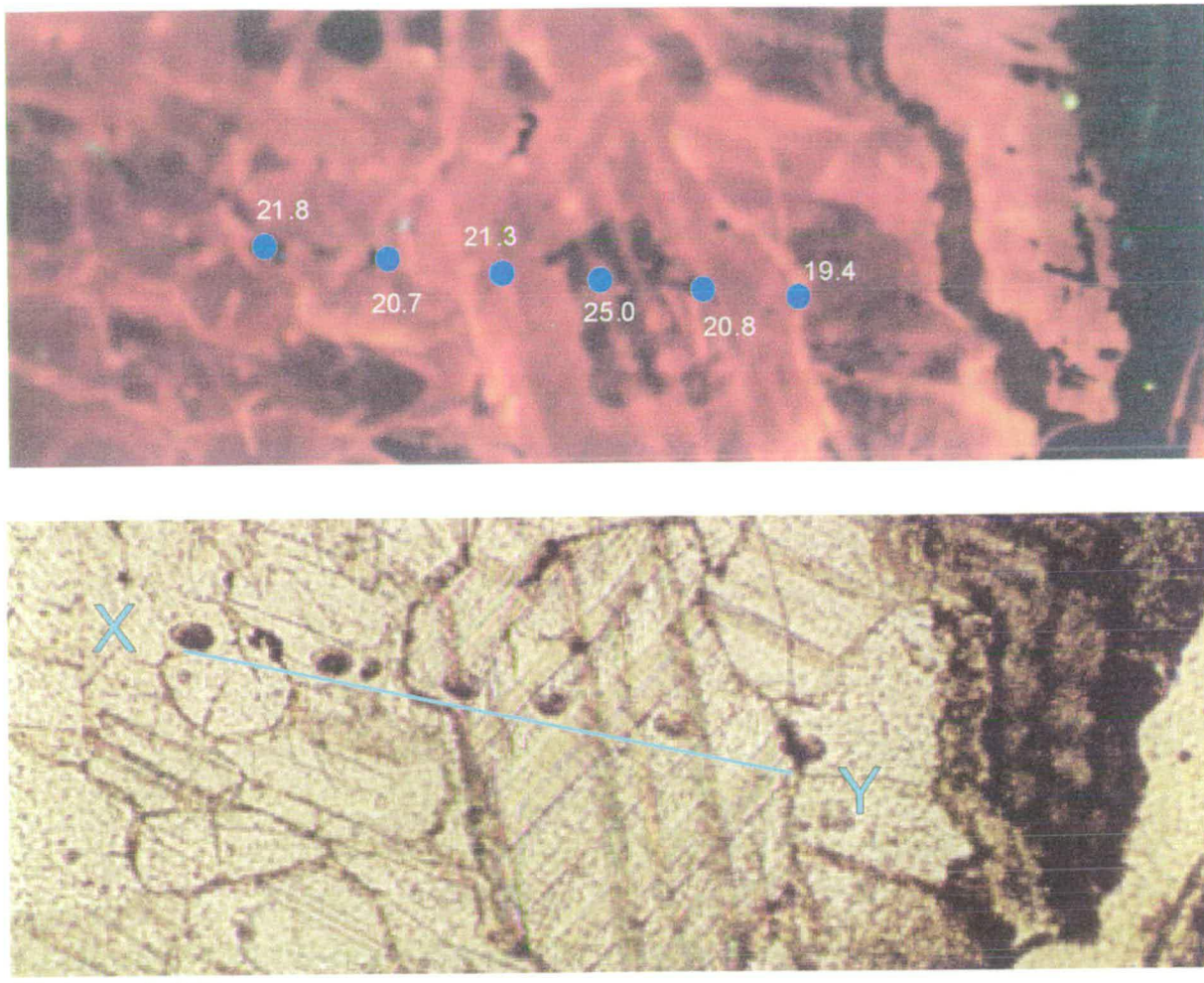

Photograph 6.26
CL (top) and PPL (bottom) photographs of sample S'97/47. Ion probe pits and $\delta^{18}O$ compositions are annotated.

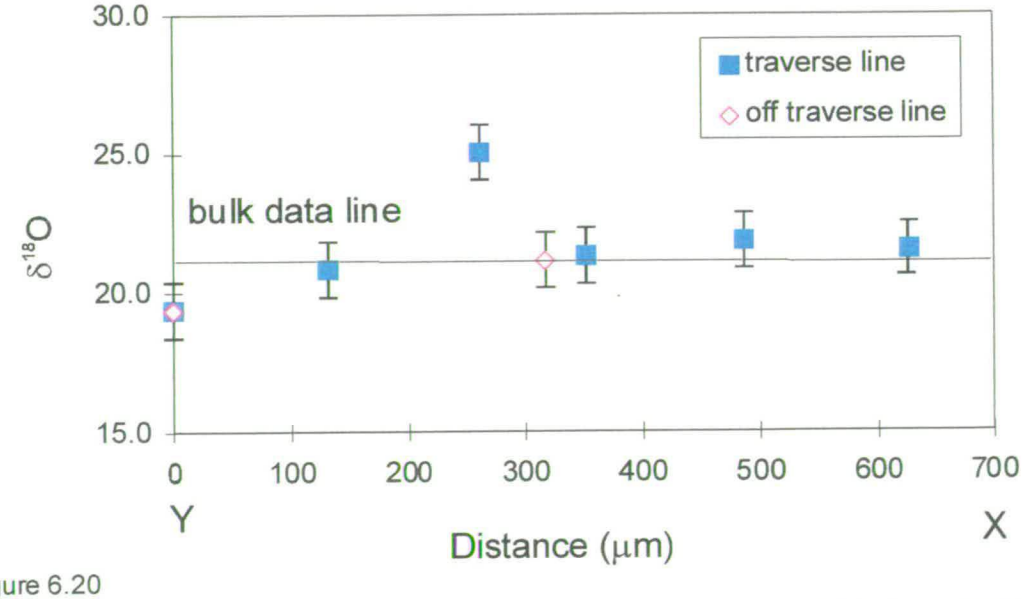

Figure 6.20
Graph of the ion probe traverse (X-Y) marked on the PPL photograph 6.26 above S'97/47. Note that the graph is reversed with respect to the photograph.

result of partial recrystallisation. McCaig and Knipe (1990) suggest that dynamic recrystallisation and grain boundary migration may provide an effective means of homogenising zoned grains. Partial recrystallisation may result in the preservation of heterogeneities in $\delta^{18}O$ composition which may not correlate with the final grain boundary distribution. Knipe and McCaig (1994) present an example of a deformed calcite vein from the Pyrennes which shows truncation of zoning patterns within the dynamically recrystallised calcite. They attribute the zoning patterns to either preferential growth on grain boundaries undergoing extension or pervasive infiltration during dynamic recrystallisation and grain boundary migration.

The heterogeneities in isotope composition at locality D appear to be unrelated to fluid infiltration during the micro-fracturing and cataclasis documented at locality C. The isotopic heterogeneities at locality C occur in discrete fracture-zones and have not been modified by subsequent deformation or diffusional exchange. The isotopic alteration and heterogeneities recorded in locality D samples record an earlier infiltration event of a low $\delta^{18}O$ fluid phase. The heterogeneities on a μm-scale are less pronounced than those documented in fracture zones at locality C, probably as a result of both diffusional exchange between grain boundaries and cores and also grain boundary migration and recrystallisation of the calcite. It is this early fluid infiltration event which caused the observed depletions in $\delta^{18}O$ in the marble band boundary layer, identified by bulk sampling.

Isotopic homogeneity in the schist

To determine the extent of isotopic heterogeneity within the schist, a sample was taken from the schist below locality D for in-situ ion probe analysis. Sample S'97/37 is from the schist at a distance of -16 cm from the schist-marble contact. A micro-scale stable isotope traverse was made across a zoned calcite grain which, in CL, has bright rims and dark cores (photograph 6.27). The $\delta^{18}O$ compositions across the grain are annotated on the CL photograph, and the traverse line is marked on the PPL photograph. The $\delta^{18}O$ composition is plotted against distance in figure 6.21. The brightly luminescent rim of the grain gives a $\delta^{18}O$ composition of 18.4 ‰, whilst the

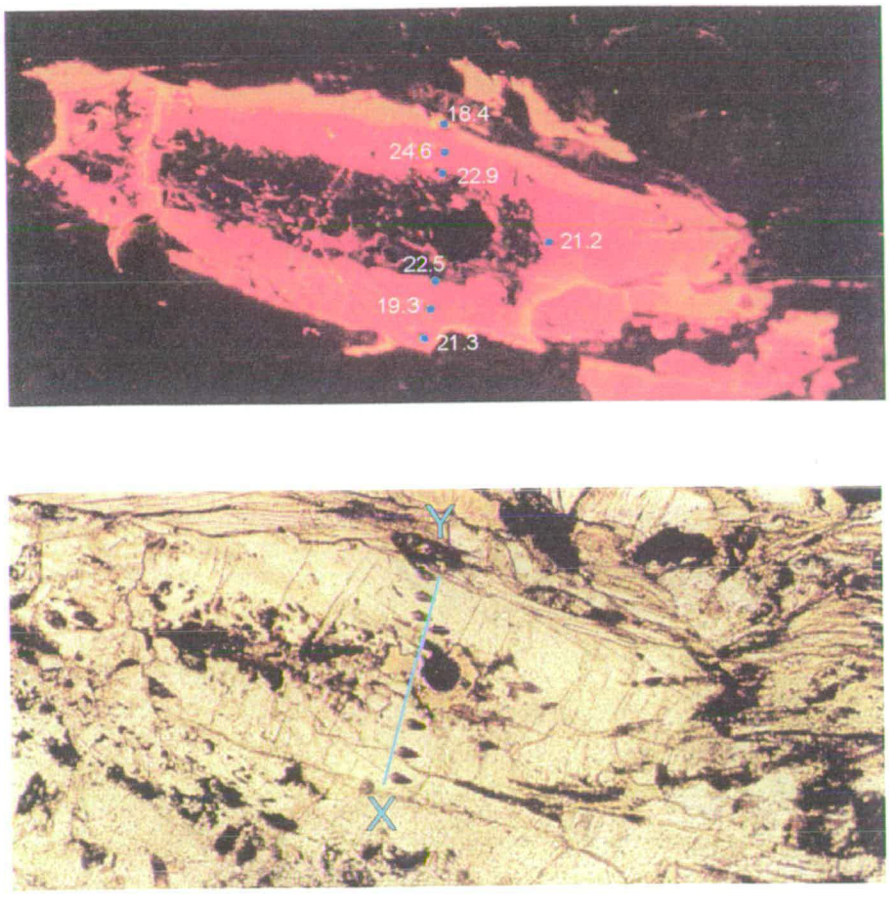

Photograh 6.27
CL (top)and PPL (bottom) photographs of calcite in sample S'97/37. The calcite shows zoning in CL from core to rim. Ion probe pits and $\delta^{18}O$ compositions are annotated. Field of view in each photograph is approximately 1.5 mm wide.

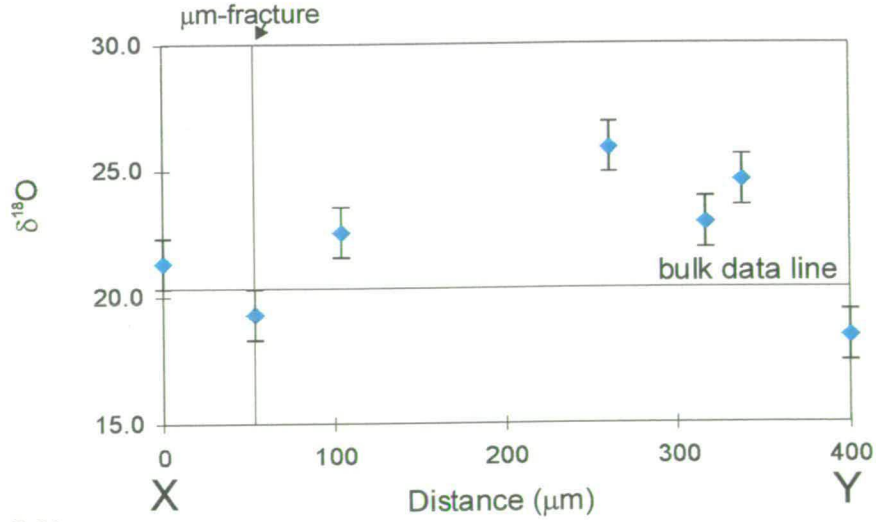

Figure 6.21
Graph of the $\delta^{18}O$ isotope profile X-Y marked on the PPL photograph 6.27 above.

composition of the centre of the grain varies from 21.2 to 24.6 ‰. The range in $\delta^{18}O$ composition recorded in the single grain shows that the isotopic composition of the calcite in the schist is heterogeneous at the grain scale.

Discussion

Evidence for fluid channelling on a cm-μm scale was identified in the inter-banded marble-quartzite at Nites. Two fluid infiltration events have been identified, which have resulted in the depletion of the calcite $\delta^{18}O$ composition, although the early event identified may itself be the result of several superimposed events. The early infiltration was identified by two bulk stable isotope profiles 10 m apart. The bulk profiles documented isotopic alteration in the first metre of the marble band above the calc-schist. Under CL the marble showed bright luminesence along grain boundaries and it was thought that fluid had infiltrated by grain edge flow to produce the isotope fronts and the grain boundary luminescence. A μm-scale ion microprobe stable isotope study showed that the marble was isotopically heterogeneous on a grain scale and that this grain scale heterogeneity did not correspond systematically to textural or CL features in the calcite. I propose that diffusional exchange and partial dynamic recrystallisation have produced the present spatial, μm-scale, distribution in isotope composition.

How fluids infiltrated the marble-quartzite band to produce the isotope front is unknown. The m-scale profile at locality D was modelled by chromatographic theory in chapter 5 and was found not to produce a statistically valid fit to the model (see, tables 5.10 and 5.11). It is not particularly surprising that the model does not fit the data, as the marble band is heterogeneous in nature with quartzite horizons and impure layers containing aligned mica and chlorite crystals. Although the two bulk profiles, which are 10 m apart, show very similar patterns in $\delta^{18}O$ alteration on a bulk scale (figures 6.9 and 6.10) there are heterogeneities along strike. The infiltrating fluid was probably channelled in zones of high permeability created dynamically during ductile deformation. Fluid pathways within the band would then be affected by fabric anisotropies, deformation and permeability contrasts between the layers.

The later fluid infiltration event was channelled in discrete zones at locality C, resulting in localised, μm-scale, zones of isotopic and chemical alteration. A low $\delta^{18}O$ infiltrating fluid was channelled in veins, cataclastic fault zones and micro-fractures. The fluid chemically and isotopically altered the rock on a very local scale. The amount of isotopic depletion of the calcite is related to the composition of the fluid, the length or tortuosity of the fluid pathway, the surface area of rock it is in contact with and the timescale of flow at a particular temperature. The lowest $\delta^{18}O$ composition recorded was from the calcite cataclasite, in which $\delta^{18}O$ compositions vary from 10.5-16.5 ‰. Micro-fractured calcite at the same distance from the contact with the schist recorded $\delta^{18}O$ compositions of 16.3 to 21.0 ‰, whilst the $\delta^{18}O$ composition of the vein at the contact records a $\delta^{18}O$ composition of 14.6 to 16.6 ‰. The zone of cataclasis is inferred to be most depleted as it would have had the largest surface area of calcite in contact with the fluid and possibly also the largest transient increase in permeability. This large dynamic increase in permeability would have 'short circuited' other fluid pathways. In comparison micro-fractures would have transported much smaller volumes of fluid. The fractures, veins and cataclastic fault zones accommodate E-W oriented layer parallel extension of the unit. The source of this late, channelised fluid is unknown. The adajacent calc-schist is itself not in isotopic equilibrium at a grain scale.

Quartz adjacent to zones of calcite cataclasis and calcite cut by micro-fractures did not equilibrate on a grain scale with the low $\delta^{18}O$ fluid. Hydrous diffusion rates in quartz (Sharp and Kirschner, 1994; Zheng and Fu, 1998) are slower than in calcite by an order of magnitude (figure 6.22b) (Farver, 1990; Valley and Graham, 1991; Zheng and Fu, 1998). Approximate calcite diffusion rates are also shown (figure 6.22a). For wet diffusion in calcite at 450 °C, the estimated peak metamorphic temperature for Syros (Dixon, 1969), it will take approximately 316 years for oxygen to diffuse 10 μm. For dry calcite the diffusion is much slower, 1×10^{10} years for 10 μm. The longer diffusion rates in dry calcite suggest that isotopic heterogeneities will be preserved for longer if fluid is expelled after infiltration. For diffusion distances of 50 μm and more, discernible by ion probe $\delta^{18}O$ analyses, diffusion times are > 10,000 years in wet calcite at 450 °C. These

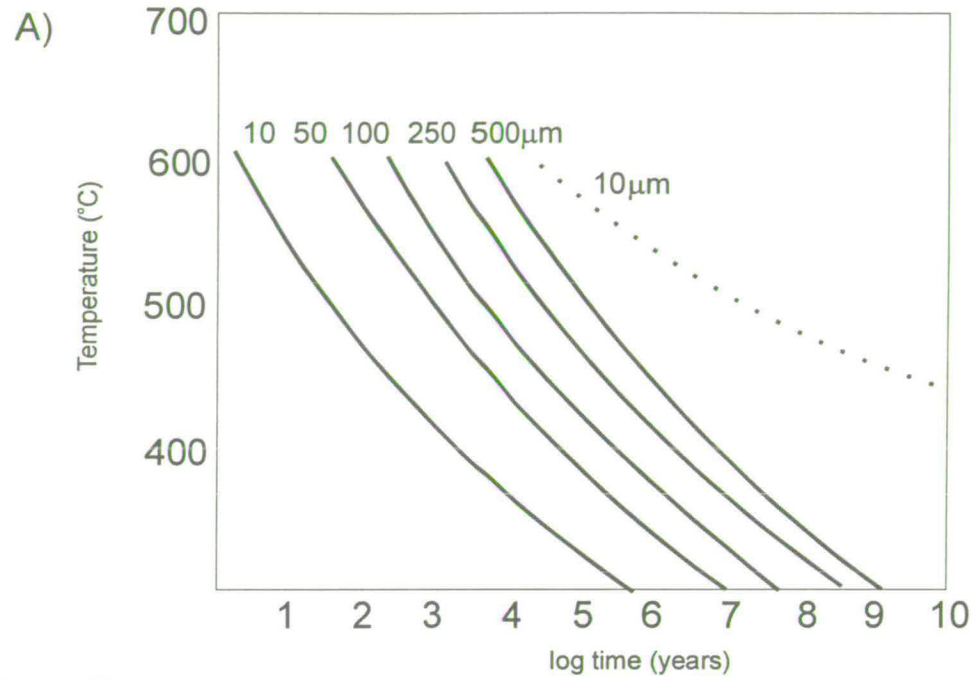

Figure 6.22a
Graph of oxygen diffusion distances in calcite at temperatures from 300-600 °C, after Graham et al.(1998) and Valley and Graham (1991). Diffusion distances calculated from Farver (1994) for wet calcite (solid lines) , Anderson (1969) for dry calcite (dotted line).

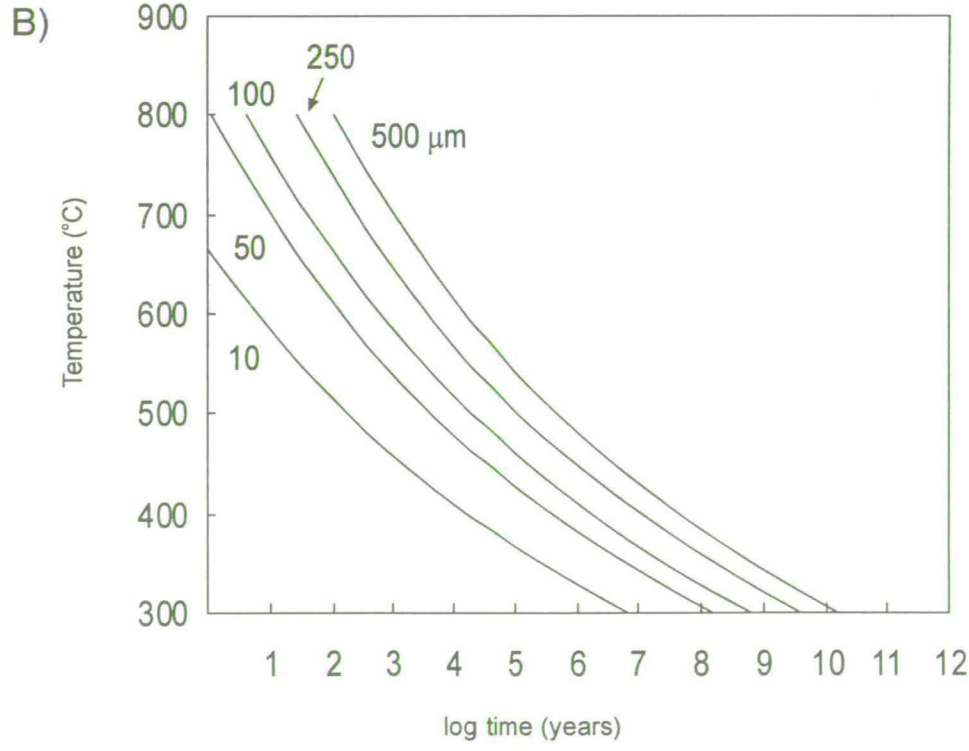

Figure 6.22b
Graph of hydrous oxygen diffusion distances in quartz at temperatures from 500-850 °C. Diffusion distances calculated from Elphick and Graham (1992a and 1992b).

figures explain the lack of quartz and calcite $\delta^{18}O$ alteration adjacent to micro-fractures and catclastic zones. The fact that zones of cataclasis often cement after dilation (Knipe, 1993) and micro-fractures heal (Smith and Evans, 1984) implies that fluid would only have been present in these zones for short time scales. The transient nature of micro-fracturing means that diffusion rates would need to have been high (i.e. high temperatures) for diffusion into the surrounding calcite, during fluid presence. Dry diffusion is thought not to have occurred due to the very long time-scales required at 450 °C and below. Texturally there is no evidence for deformation or dynamic recrystallisation since that associated with the fluid infiltration, so isotopic heterogeneities have remained.

Summary

- Early isotopic heterogeneities were identified in the marble band that has no systematic relationship to textures in the calcite or CL.
- Partial homogenisation of isotope heterogeneities may have occurred as a result of grain boundary migration and dynamic recrystallisation.
- The early heterogeneities are overprinted by $\delta^{18}O$ depletion which is spatially associated with deformation textures, CL and heterogeneity in calcite Mn, Fe and Mg composition.
- Permeability enhancement by cataclasis, micro-fracture and veining has resulted in localised isotopic depletion and chemical alteration.
- Quartz and calcite grains adjacent to deformation zones in which fluid was channelled show little to no depletion in $\delta^{18}O$.
- Calcite in the matrix of the adjacent schist was not in isotopic equilibrium and the isotopic composition of veins and segregations suggest fluid channelling on a range of scales in the schist.

6.6 Serpentinite belt - ductile boudinage

To contrast with the results of the southern study at Nites a marble band was chosen from the serpentinite belt in the north of the island (figure 6.23), which was deformed by ductile extension. The boudin is surrounded by serpentinite ultramafic, and is approximately 22 m x 2.8 m. The marble contains layers of impurities which are folded and boudinaged. The impure layers consist mainly of sodic-pyroxene, with some garnet, chlorite and epidote. The marble boudin was chosen to compare with those from Nites as it has deformed by ductile deformation, rather than localised brittle failure as seen in the Nites examples. The aim was to document the effects of the different types of deformation on marble permeability and hence isotopic alteration of the calcite marble, and to relate the preservation of isotopic heterogeneities in the marble to deformation.

Serpentinite belt marble boudin

Structural observations

The calcite generally forms elongate crystals which are aligned sub-perpendicular to the regional foliation and lithological contacts. These elongate calcite crystals are observed elsewhere on the island and have been interpreted as calcite pseudomorphs after aragonite (Barr, 1989). The calcite adjacent to silicate phases does not form these elongate crystal forms and has a smaller and more equant habit.

Bulk stable isotope profile

A bulk stable isotope traverse was made across the centre of the marble boudin, the results of which are shown in figure 6.24. The bulk stable isotope data form a symmetrical bell-shaped profile indicative of fluid infiltration from both sides of the marble band. The $\delta^{18}O$ composition of the marble band has been lowered across the width of the boudin. Values of $\delta^{18}O$ of <13.5 ‰ in the centre of the marble band are

Figure 6.23
Map of western serpentine belt from Kambos-Lia Bay, after Dixon (1969) and this study. The marble band targeted for isotope study is annotated.

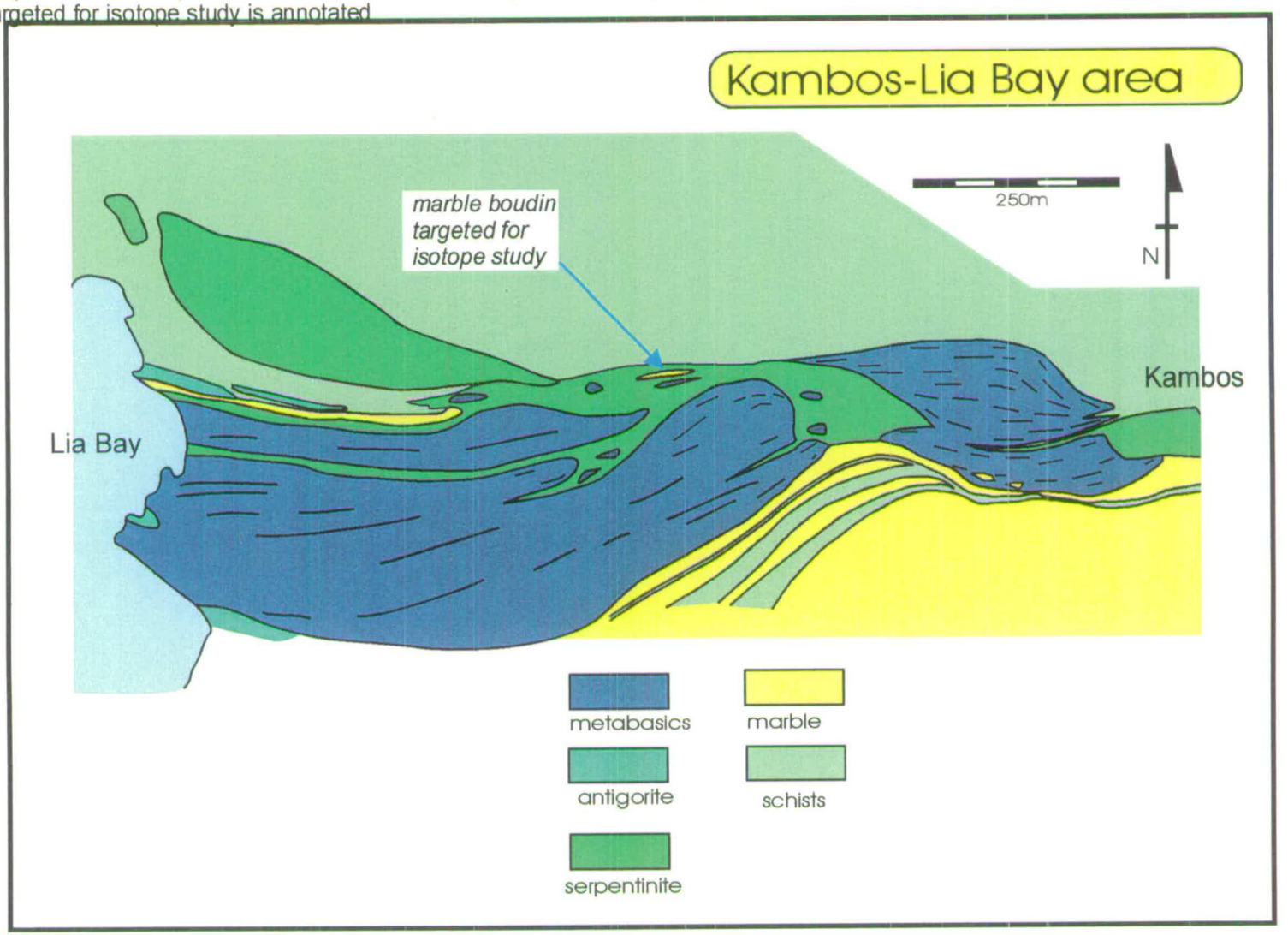

Figure 6.24
$\delta^{18}O$ and $\delta^{13}C$ profiles across a boudinaged marble band in ultramafic. The log in the centre of the page describes the sampled traverse.

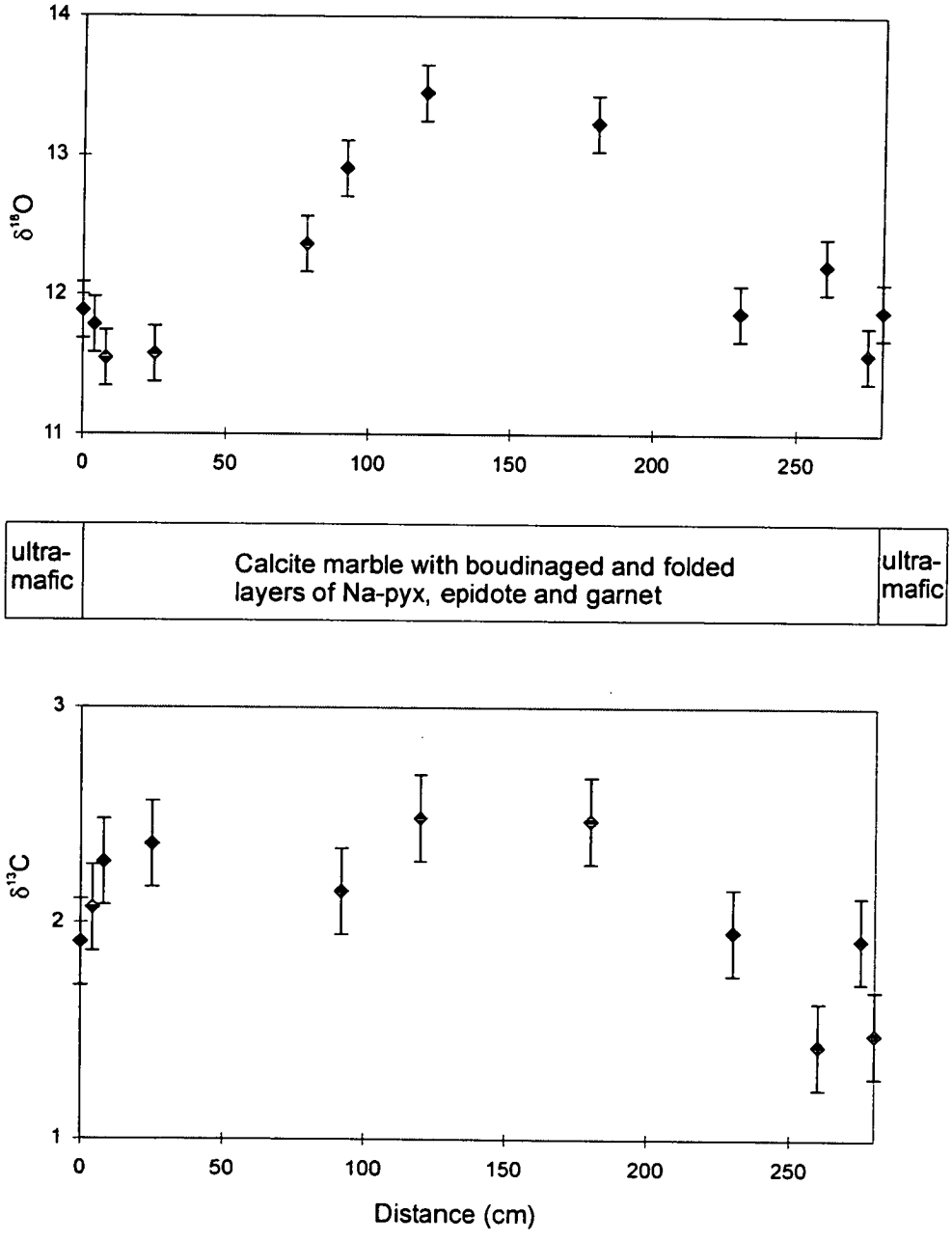

strongly depleted in ^{18}O with respect to unaltered marble away from marble band boundary layers on Syros which have $\delta^{18}O$ compositions of >25 ‰.

Microscopic (μm-scale) study

Two thin sections were targeted for ion microprobe analysis of calcite $\delta^{18}O$, from near both contacts with the ultramafic at 6 cm and 275 cm on the bulk traverse. The results are superimposed on the bulk data in figure 6.25. The variation in $\delta^{18}O$ recorded by the micro-sampling is greater at 6 cm than at 275 cm. In both cases the results bracket the $\delta^{18}O$ value obtained by the bulk analyses. An example from each of the thin sections is documented and discussed in terms of CL and physical textures of the calcite marble in each thin section.

The example from sample S'95/29, 6 cm on the bulk traverse, forms a small traverse away from a garnet. CL and PPL photographs of the sample and traverse are shown in photograph 6.28 and figure 6.25. The high relief phase in PPL is the garnet. The location of the traverse is also marked. The CL photograph shows bright luminescence of calcite along grain boundaries and in fractures across the garnet. The ion probe pits and $\delta^{18}O$ compositions are annotated. The luminescence of the calcite or structures such as grain boundaries appears to bear no relation to the $\delta^{18}O$ composition.

In sample S'95/70 from 275 cm, a long traverse was made across the centre of the thin section (photograph 6.29). The calcite in the centre of the thin section away from zones of sodic-pyroxene is generally prismatic and forms aligned elongate crystals which can be partially seen in photograph 6.29. It was these structures that Barr (1989) believed to be pseudomorphs after aragonite. The slide was very dark under CL and luminesced in thin zones along grain boundaries and near sodic-pyroxene impurities (photograph 6.29). The calcite grains show domains of 'subtle' orange luminescence within a single crystal that do not appear to be the result of grain rim-core zoning. The ion probe pits and $\delta^{18}O$ compositions are annotated on the CL photograph. The results of the ion probe traverse and an electron probe traverse along the same traverse line are shown in figure 6.26. The stable isotope analyses are almost homogeneous,

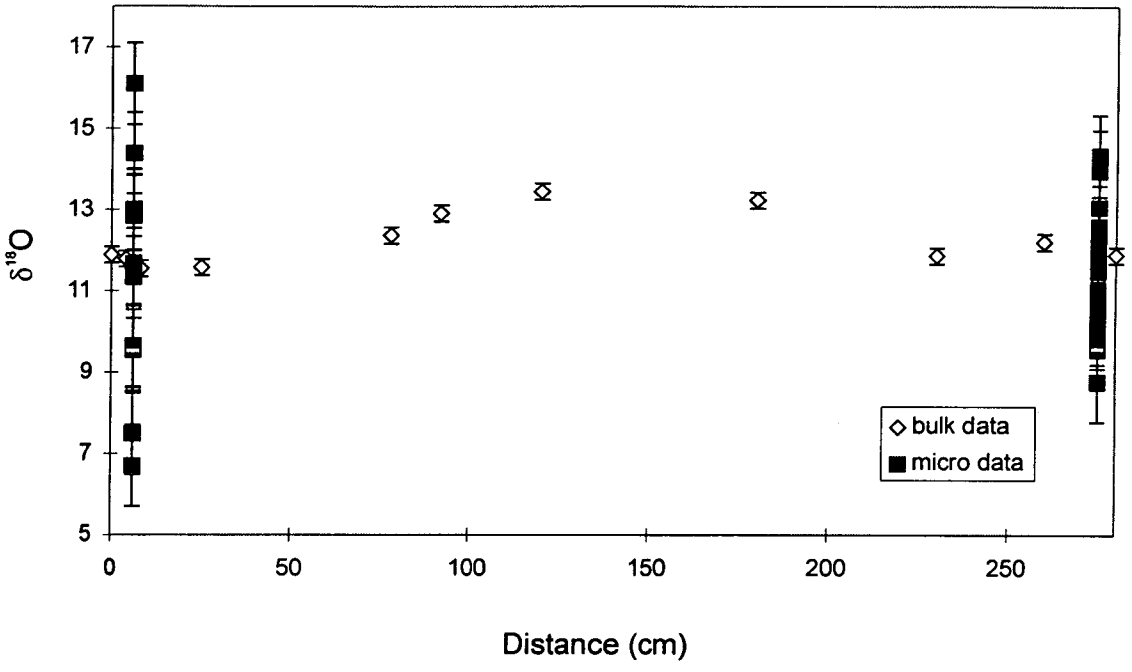

Figure 6.26
Bulk data (cm^3) from the stable isotope traverse across a marble boudin in the north. The results of the microscale study are superimposed.

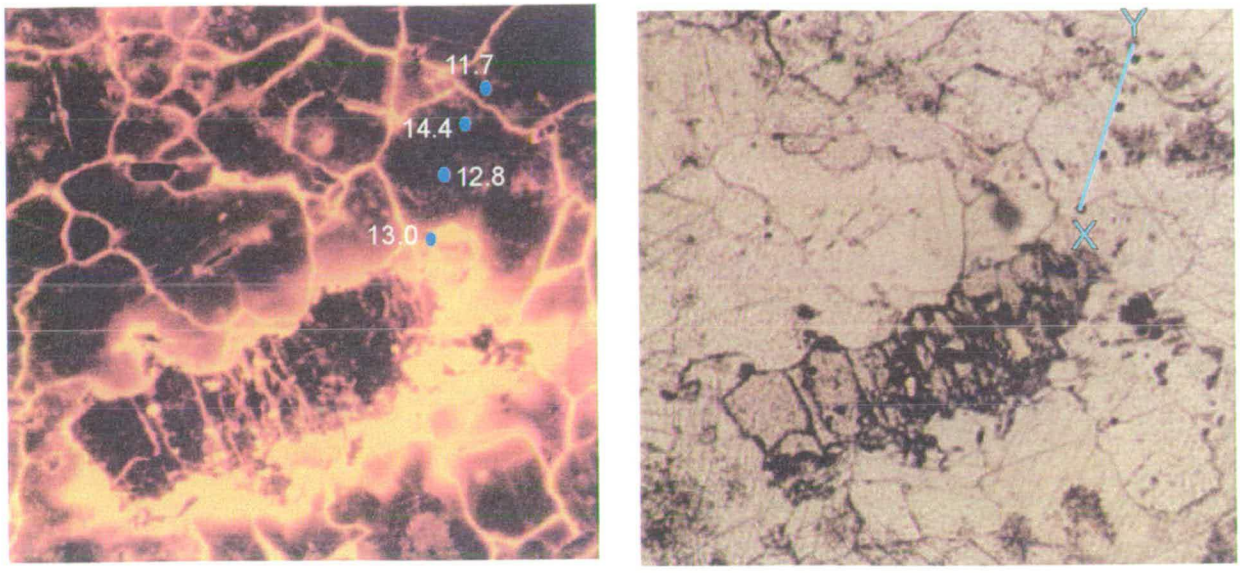

Photograph 6.28
CL (top) and PPL (bottom) photographs of sample S'95/29. The high relief phase in PPL is garnet. The CL photograph is annotated with ion probe pits and $\delta^{18}O$ compositions. Field of view in each photograph is approximately 1.5 mm wide.

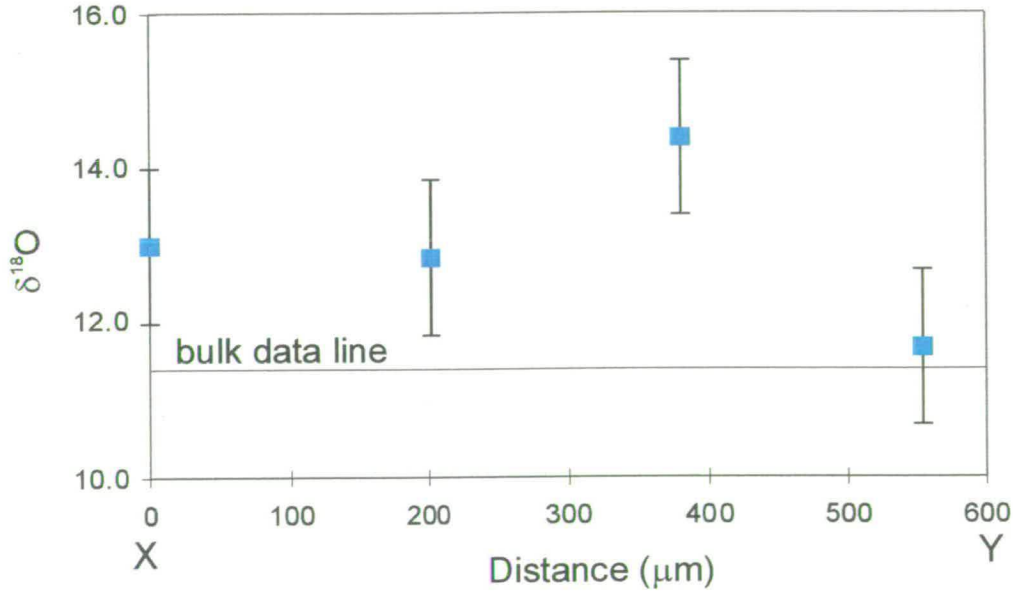

Figure 6.26
$\delta^{18}O$ against distance for the profile shown in the photograph 6.28 above , S'95/29.

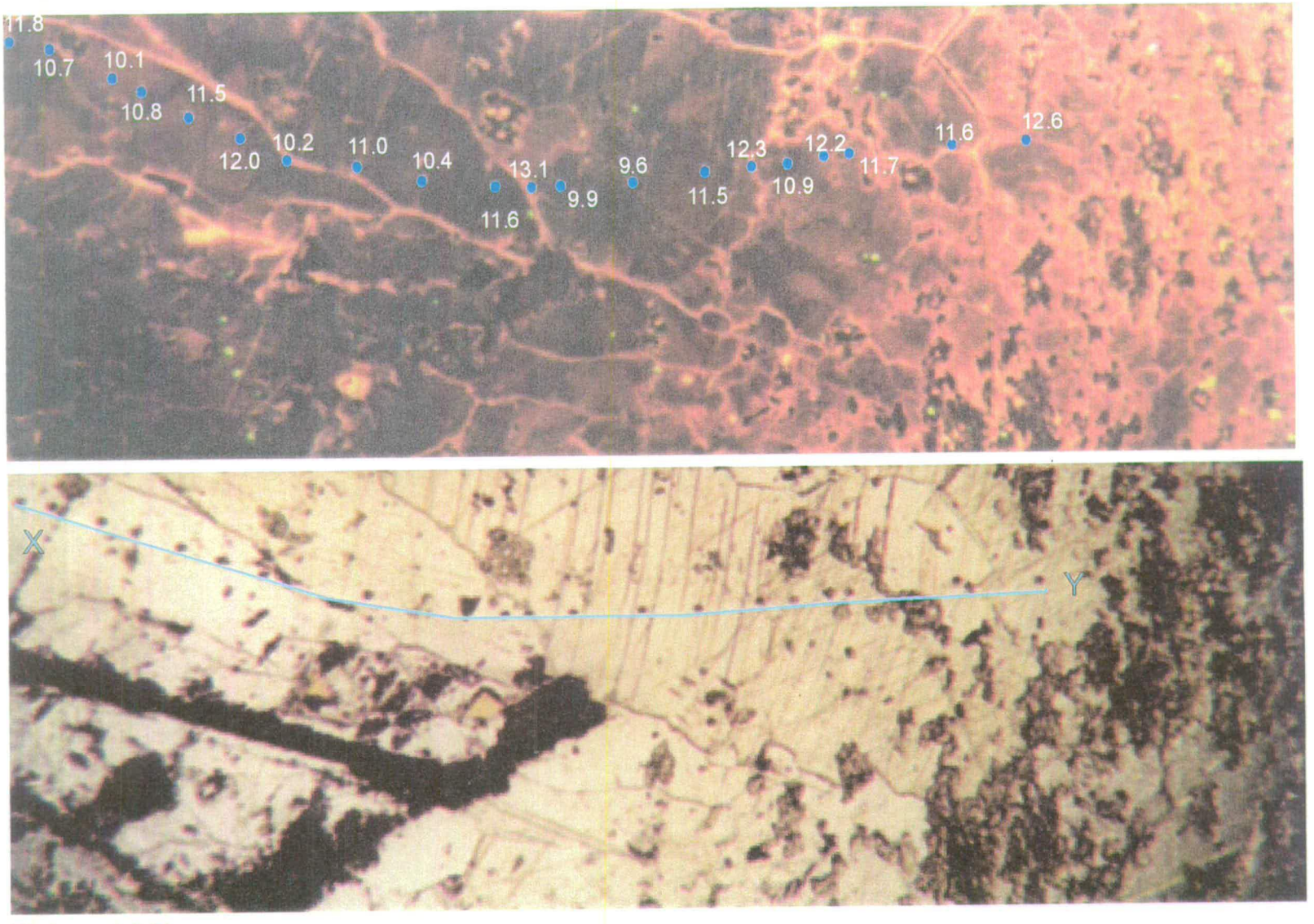

Photograph 6.29
CL (top) and PPL (bottom) photographs of sample S'95/70. High relief phase in PPL is sodic-pyroxene. The calcite is brightly luminescent around sodic-pyroxene and in thin zones along calcite grain boundaries. Ion probe pits and $\delta^{18}O$ compositions are annotated.

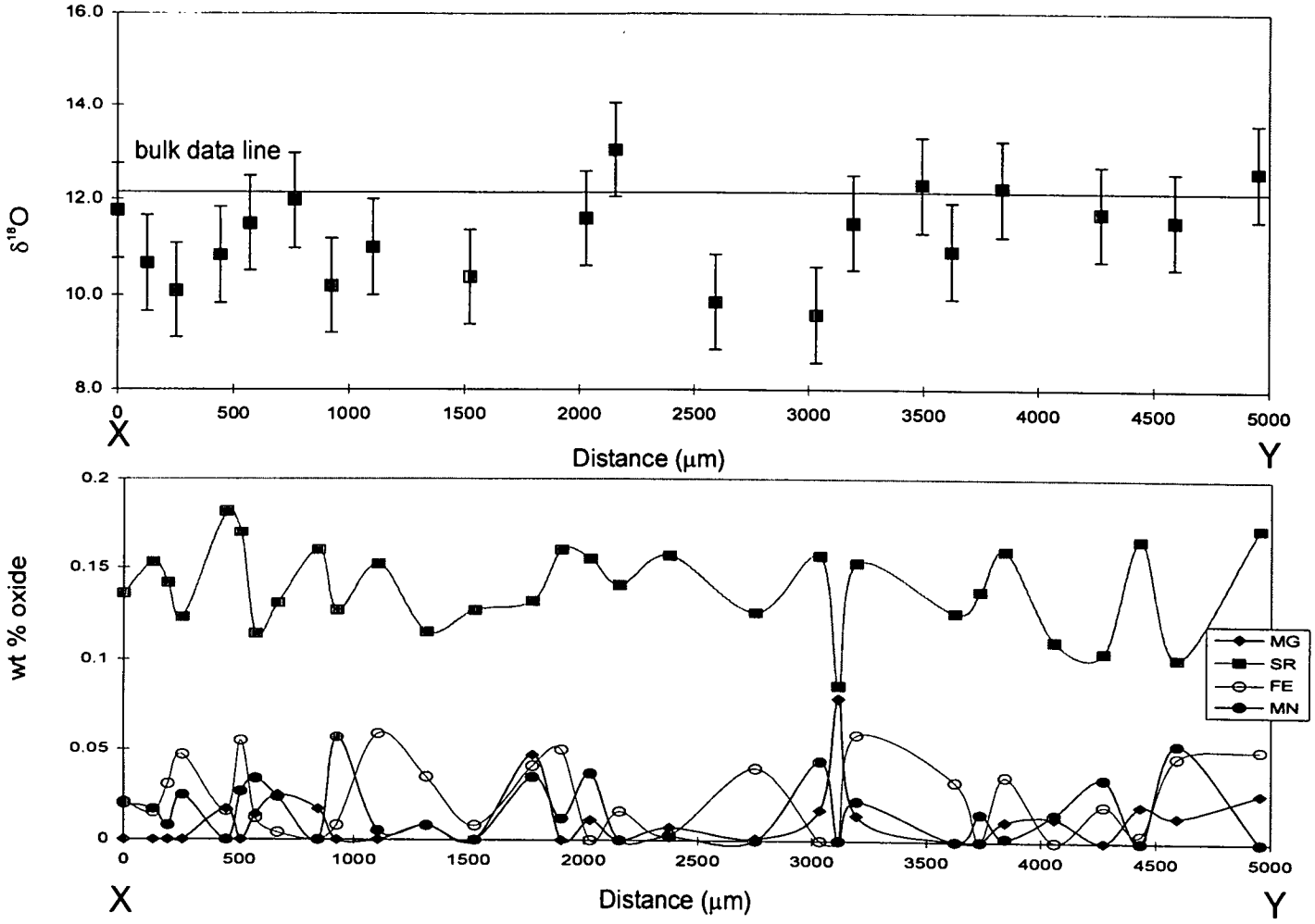

Figure 6.27
$\delta^{18}O$ and wt% oxide plots for profile A S'95/70. photograph 6.29

approximately within analytical error of each other and the $\delta^{18}O$ composition of the bulk sample at this distance. The trace element profile shows minimal variation and almost all the trace element analyses are below the detection limit of approximately 0.05 wt %, apart from Sr.

Discussion

The bulk stable isotope profile attests to depletion of ^{18}O in the boudinaged marble band, as the $\delta^{18}O$ compositions recorded are much lower than those expected for undepleted marble on Syros. The presence of unretrogressed sodic-pyroxene and garnet, which recrystallised as a result of extensional deformation, suggests that the marble was boudinaged at high pressures and temperatures by ductile deformation. The calcite (aragonite at the time) is likely to have continually recrystallised during the deformation, but is inferred not to have recrystallised since passing through the aragonite-calcite transition, as calcite crystal have an aragonite crystallographic form as though pseudomorphing after it.

I interpret the micro-sampling at this locality as recording the homogenising effect of recrystallisation on stable isotopes and potentially trace elements within the calcite marble. It is hypothesised that deformation associated with ductile boudinage of the marble allowed infiltration of a low $\delta^{18}O$ fluid. Ductile deformation has been proposed as the method by which fluid has infiltrated calc-mylonites in the Pyrennees (McCaig et al. 1995) and has been shown to create transient dynamic permeability networks (see section 6.3). Fluid must have infiltrated at temperatures and pressures above the lower stability limit of sodic-pyroxene and garnet. The calcite texture indicates recrystallisation since boudinage, as away from areas of sodic-pyroxene and garnet the calcite has the habit of aragonite as though pseudomorphing. The deformation is therefore thought to have taken place above the transition of aragonite-calcite at a pressure 9-10 kbar at 450 °C. These PT conditions lie within the sodic-pyroxene stability field and within the range of temperatures associated with Syros metamorphism (figure 6.28). Continual recrystallisation of the calcite as the result of deformation at high pressures would lead to homogenisation of the calcite $\delta^{18}O$ signature by grain

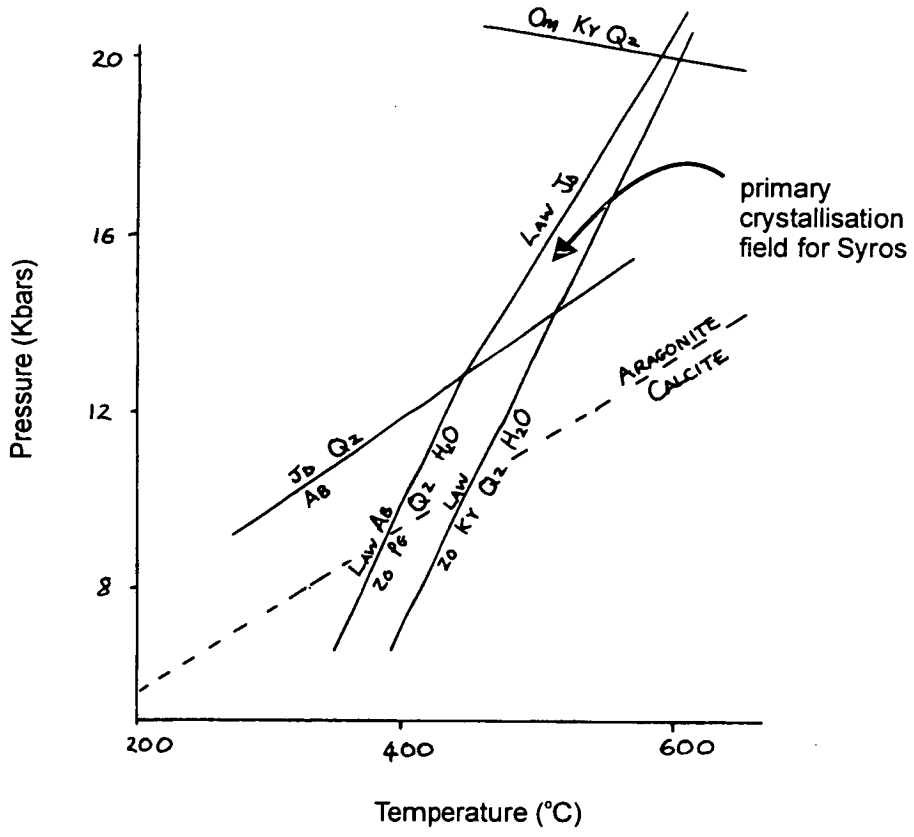

Figure 6.28
Pressure temperature plot, showing the primary crystallisation field for Syros after, Barr (1990) and the aragonite-calcite transition after Yardley (1989). Abbreviations are: JD-jadeite, QZ-quartz, LAW-lawsonite, AB-albite, ZO-zoisite, PG-paragonite, OM-omphacite, KY-kyanite.

boundary migration and dynamic recrystallisation. If fluid infiltration was associated with dynamic recrystallisation and grain boundary migration, the continual renewal of the grain boundary structure would mean that grain edge flow maintained fluid contact with 'new' calcite. At any single instance only a limited network of grain boundaries would be connected to form a permeable network (Knipe and McCaig, 1994). The time integrated effect of the dynamic permeability creation results in pervasive fluid infiltration and isotopic homogenisation through time. Areas adjacent to silicate phases such as garnet and sodic-pyroxene may well preserve more heterogeneity in $\delta^{18}O$, as a result of grain boundary pinning and limited re-crystallisation due to the presence of the silicate phases. Domains of 'ghost' luminescence observed within single calcite crystals in S'95/70 could document the relics of earlier crystals which were isotopically heterogeneous as a result of deformation-enhanced fluid infiltration of the marble band. Any evidence for the mechanisms of fluid infiltration have been destroyed during recrystallisation and geochemical homogenisation of the calcite.

The bright luminescence around silicate impurities in both samples appears to be unrelated to the isotopic signature and is thought to be caused by chemical variation in the calcite from the adjacent silicates. The small wt % of trace elements in the calcite means that the variation cannot be quantified.

Recrystallisation as a mechanism for homogenisation of mineral chemistry is noted by McCaig and Knipe (1990), Knipe and McCaig (1994), and is discussed by McCaig (1988) in relation to overprinting of transient brittle microstructures by plastic creep, as a way of producing observed quasi-plastic microstructures. This study has documented depletion and homogenisation of $\delta^{18}O$ in calcite marble as a result of fluid infiltration during deformation and recrystallisation of the calcite during and after deformation.

Summary

- The symmetrical 'bell' shape of the bulk profile implies fluid infiltrated the marble boudin from both sides.
- Areas of bright luminescence in CL do not correlate with zones of isotope depletion.

- Areas of the marble where calcite textures imply recrystallisation after aragonite are almost isotopically and chemically homogeneous.
- It is proposed that fluid infiltration and homogeneous isotopic alteration occurred as a result of ductile deformation, including dynamic recrystallisation and grain boundary migration.

6.7 Conclusions and discussion

All three marble bands chosen for study had been deformed during east-west oriented layer parallel extension. Deformation of the marble bands to accommodate the extension was manifested differently in each of the chosen examples. The deformation mechanisms operating during the deformation were presumed to be dependent on rheological properties controlled by composition, the pressure and temperature conditions of deformation and the strain rate.

The two examples from the Nites hillside preserved textures that documented components of both ductile and brittle deformation. In *Nites boudin I*, extension had been accommodated by ductile deformation and boudinage of the whole marble band, with brittle failure in the boudin neck. The extension in the neck was accommodated by pressure solution, veining, fracture and brecciation. The deformation is thought to have been aided by competence contrasts between the dolomite and calcite marble.

The stable isotope studies documented isotopic heterogeneity in the boudin neck. Depletions in the $\delta^{18}O$ composition are spatially linked to zones of fracture, brecciation and veining. Permeability is inferred to have been dynamically enhanced in these zones during deformation to allow infiltration of a low $\delta^{18}O$ fluid. The fluid pathways were identified texturally and isotopically by CL studies and macro-scale sampling for $\delta^{18}O$ analysis of breccia clasts, matrix and veins. The fluid was channelled in high permeability pathways in the breccia matrix, causing localised isotopic alteration.

In the sheared and fractured marble-quartzite horizon lower on the same hillside, *Nites boudin II*, ductile and cataclastic shear zones off-set layers. Micro-fracturing and small veins were also identified, in thin section and CL. At locality D, 10 m from the

deformation zone, an early isotopic heterogeneity was observed in the calcite, which formed the bulk stable isotope profiles at both locality C and D. The variations in $\delta^{18}O$ on a grain scale were not systematically related to CL and physical textures, such as grain boundaries, in the calcite. The spatial variation in $\delta^{18}O$ is thought to be caused by partial homogenisation of grain scale isotopic heterogeneities by diffusion, recrystallisation and grain boundary migration.

The 'background' $\delta^{18}O$ alteration is overprinted at locality C by a later fluid infiltration event. The later fluid infiltration event was channellised in discrete fluid pathways, resulting in localised isotopic depletion, and geochemical alteration of the calcite marble. The chemical and isotopic alteration are spatially correlated to zones of cataclasis, micro-fracture and veining. The localisation of fluid infiltration in zones of dynamically created permeability has resulted in localised, μm-scale, $\delta^{18}O$ isotopic heterogeneities of >10 ‰. Slow diffusion rates at low temperatures, resulting from water loss, and absence of later deformation or recrystallisation have preserved these μm-scale hetrogeneities in the calcite.

In contrast the *Serpentinite belt marble boudin* from the northern serpentinite belt was deformed by ductile deformation and has not retained its textural deformation characteristics. The nature of ductile deformation is such that the calcite is likely to have been continually recrystallising during ductile boudinage. However, the present calcite texture in the marble band suggests static recrystallisation after aragonite.

The bulk stable isotope profile across the boudin documents symmetrical depletion in $\delta^{18}O$ of the calcite from both sides of the marble band. This depletion in $\delta^{18}O$ is inferred to be related to fluid infiltration. A μm-scale stable isotope study was completed to assess the extent of isotopic homogeneity in the marble as a result of fluid infiltration during ductile deformation. The μm -scale stable isotope study documented both homogeneity and heterogeneity in isotope composition on a microscale. Areas that showed calcite recrystallisation textures after aragonite were isotopically and chemically homogeneous. Calcite close to silicate impurities of sodic-pyroxene and garnet documented more heterogeneous $\delta^{18}O$ signatures. These heterogeneities in $\delta^{18}O$ compositions at the grain-scale are thought to be preserved due to silicate pinning of

calcite grain boundaries, allowing minimal recrystallisation and therefore restricting isotopic homogenisation.

The general homogeneity of the $\delta^{18}O$ composition is thought to represent the homogenising effects of recrystallisation during and after fluid infiltration. Dynamic recrystallisation during the fluid infiltration would result in 'pervasive' infiltration of the marble band over time, as the grain boundary network will be constantly changing. Post infiltration recrystallisation and grain boundary migration will also lead to homogenisation of chemical and isotopic heterogeneities (Knipe and McCaig, 1994).

The study has shown that fluids infiltrated marble bands on Syros as a result of both brittle and ductile deformation. Extension was accommodated in the brittle regime by pressure solution, veining, brecciation, fracture and cataclasis. Fluid was channelled along micro-fractures and veins and in zones of brecciation and cataclasis. This has resulted in isotopic heterogeneity in the marble bands on the scale of cm to μm.

In the ductile regime the extension was accommodated by ductile boudinage, but deformation textures or evidence for the mechanisms of fluid infiltration are no longer preserved. Fluid infiltration during ductile deformation is reported to occur by transient micro-cracking and quasi plastic flow (McCaig, 1988 and McCaig and Knipe, 1990). Dislocation creep may induce fracture by confining fluids present in voids or by creating transient dilatancy to accommodate strain (Knipe and McCaig, 1994).

An important factor for fluid infiltration during ductile deformation is its dynamic nature. This means that the fluid pathways are transient and constantly changing as the rock deforms plastically and recrystallises. The time integrated effect of fluid infiltration will therefore result in pervasive alteration and isotopic and chemical homogenisation. This isotopic and chemical homogenisation by recrystallisation remains a problem in understanding rock properties and the creation of permeability during ductile deformation.

6.8 Summary

The main summary points of this chapter are:

- Fluid infiltration of marble bands occurred as a result of deformation associated with layer parallel extension.

- Permeability was enhanced by cataclasis, brecciation, micro-fracturing and veins. These brittle deformation mechanisms resulted in localised isotopic alteration on the scale of cm to μm.

- Evidence for permeability enhancement and fluid infiltration during ductile deformation is established by bulk stable isotope profiles. The homogeneity in microscale sampling of these marble boudins attests to the homogenising affects of recrystallisation and fluid infiltration during dynamic recrystallisation.

Chapter 7 Synthesis

The thesis set out to characterise deformation, fluid infiltration and recrystallisation during exhumation of a metamorphic terrain. Its aim was to determine the interactions of these three processes and their combined affects on the structural and metamorphic evolution of the terrain. This synthesis chapter discusses the findings of the present study in the context of the current debates on the exhumation of metamorphic terrains, and the controls on fluid infiltration, deformation partitioning and metamorphic reactions. It does so in the form of answers to a number of key questions in which the relevant results of this study are presented and discussed in relation to current understanding.

How are HP-LT terrains exhumed?

The main structural interpretation of this study is based on field evidence of extensional structures, accommodating layer-parallel extension of the terrain. Many units are boudinaged on scales of tens of metres to cms. The boudinage is generally symmetrical indicative of coaxial deformation. To link the observed extensional structures to exhumation of the terrain, a down-pressure continuum of structures and a constant orientation of the extension direction was identified. Most of the extensional structures were observed in the HP 'blueschist' grade assemblages, with only localised zones of greenschist facies ductile deformation, up to 20 m wide, being identifiable. The interpretation of when these high pressure extensional structures formed is crucial. Are they related to pro-grade burial and subduction or are they related to deformation in the hanging wall of a subduction zone, when the extension will contribute to unroofing and exhumation? How much unroofing is actually occurring while the observed extension is being imposed on the terrain depends on whether, similar extension is occurring in the overlying material.

A considerable amount of exhumation may have taken place within the blueschist facies stability field, so fabrics related to exhumation should, if present, overprint earlier subduction related fabrics. Distinguishing between subduction related fabrics and exhumation fabrics in blueschist facies assemblages is not easy due to the complexities involved in both processes and on Syros by the lack of clear

evidence of prograde up-pressure changes. On Syros, the arguments for post 'peak' boudinage are based on the relationship of the boudinage to other structures, evidence for a single extension direction from HP to LP and on evidence for a continuum of extensional structures from ductile blueschist to greenschist and finally brittle extension.

The main regional foliation on Syros is the S2 of Bloor (1998). Bloor described this regional foliation as forming during folding to create an axial planar fabric. He was able to relate the timing of lawsonite growth, to a deformation chronology both by the folding of veins associated with lawsonite growth and the inclusion of micro-fabrics in lawsonites. Bloor (1998) suggested that the folding and foliation formed at 'peak' metamorphic conditions, as the minerals (garnet-glaucophane-lawsonite-muscovite-paragonite-quartz-chlorite) forming the S1 were still actively crystallising and re-forming through the folding and the S2 development. Later boudinage of the foliation and boudinage of early quartz veins were identified by Bloor (1998). This study also documents boudinage of an earlier foliation, correlated with the S2 of Bloor (1998).

The consistent trend in the extension axis for both blueschist and greenschist deformation fabrics and brittle faults, is inferred to represent a continuum of extensional deformation from high pressure boudinage through to low pressure. Further evidence was found for a continuum of deformation by the micro-boudinage of glaucophane crystals which had calcic-amphibole growing into fractures, which is inferred to represent extensional deformation associated with the transition from HP to LP, prior to complete greenschist facies retrogression. An albite-chlorite bearing vein was also shown to have growth of crossitic blue amphibole into the vein, suggesting extension in the form of veins at the blueschist-greenschist transition.

Extensional deformation dominates current models and structural observations of fabrics related to the exhumation of the metamorphic rocks in the Cyclades (e.g. Lister et al. 1984; Urai, 1990; Buick, 1991; Gautier et al. 1993; Jolivet et al. 1994, 1996 and 1998). The models are generally based on simple-, rather than, pure-shear models of extensional deformation. However, conflicting opinions of extensional shear criteria on Naxos (e.g. Lister et al. 1984; Urai, 1990; Buick, 1991),

suggest a range of extensional deformation structures. The key to the debate of coaxial versus non-coaxial strain appears to centre around the scale of the study area. Unless strain is partitioned homogeneously through the crust, terrains that are deforming by broadly coaxial deformation will be separated from each other by areas of non-coaxial deformation, for strain compatibility reasons. Given the heterogeneities in crustal composition and hence rheology it seems likely that all terrains will, on some scale, record areas of non-coaxial deformation. The structures identified on Syros were interpreted as being representative of broadly coaxial deformation, as many structures were symmetrical and only localised areas of asymmetry were observed.

Whether a broadly coaxial extensional deformation model is applicable to other exhumed HP-LT metamorphic terrains is debatable. It seems that most models of exhumation are determined by broader tectonic processes, i.e. whether the region is undergoing compression (e.g. Wheeler, 1991 and Hacker et al. 1995) or extension (e.g. Avé Lallement and Guth, 1990 and Schermer, 1990).

What controls retrogressive recrystallisation?

On Syros it is clear that fluid infiltration was the major control on greenschist facies recrystallisation, and was identified in many areas as being spatially related to veining. Hydration reactions were required to react HP blueschist assemblages to greenschist facies assemblages. Bulk geochemistry of greenschist vein haloes as compared to blueschist host rock, show an increase in the volatile content of the greenschist facies retrogression halo in comparison to the blueschist host rock. These observations of fluid controlled retrogressive greenschist facies recrystallisation, support the conclusions of other workers (e.g. Bröcker, 1990 and Barrientos and Selverstone, 1993).

Barrientos and Selverstone (1993) describe features from the blueschist terrain of Ile de Groix that are very similar to those seen on Syros, including greenschist haloes around veins. They attribute preservation of blueschist assemblages to channelled fluid infiltration, rather than fast exhumation rates. Bröcker (1990) asked whether greenschist facies retrogression on Tinos island, in the

Cyclades, was controlled by composition or fluid infiltration. In his paper he notes that high pressure assemblages are preserved adjacent to lower pressure assemblages and suggests that this spatial distribution is due to fluid channelling causing localised retrogression in more permeable horizons. He shows that the bulk chemistry of the, HP and LP, assemblages in adjacent layers has not controlled the spatial distribution of retrogression.

On Syros the mineral assemblage is in places controlled by metasomatic exchange as well as hydration. In this study an influx of Na was associated with a high percentage of albite porphyroblast growth in vein haloes. A Na influx from veins into vein wall rock, to account for albite porphyroblast growth has also been proposed by Ague (1997) in the Scottish Dalradian and Barnicoat (1988) in the Alps. The study of Bloor (1998) showed similar metasomatism, involving an influx of Ca, to grow lawsonite pseudomorphs in selvages to quartz veins in the grey schists of Syros. Similar lawsonite distributions were described by Pognante (1989) for the Alpine Sesia zone. Perhaps the most comprehensive published study of metasomatism associated with veining is that for the metamorphic terrain of Santa Catalina Island, California (Bebout and Barton, 1993). They record a wide range in vein mineral assemblage in the blueschist terrain and demonstrate metasomatic exchange of Si, Al, Na and K and trace elements.

This study and those briefly discussed above suggest that fluid infiltration is a major control on greenschist facies retrogressive recrystallisation. Infiltration of exotic fluids will also control the final composition and mineral assemblage by metasomatic exchange. The controls on the localisation of fluid infiltration in metamorphic terrains, will therefore control the spatial distribution and extent of retrogressive recrystallisation. Localisation of fluid infiltration occurs as a result of permeability contrasts, which will be controlled by deformation partitioning, lithological contrasts and fabric anisotropies.

The chicken and egg of metamorphic fluid flow: what came first deformation or fluid infiltration ± reaction?

In schist and metabasite units on Syros the mechanisms of fluid infiltration are less well constrained than those for fluid infiltration into marble bands. Clearly fluid infiltration in schist units was in part controlled by fracture, indicating that deformation enabled fluid infiltration and localised reaction. However, in some areas of Syros, particularly in the South, retrogressive reaction to greenschist assemblages is more pervasive and is not in many cases associated with an identifiable deformation event that is synchronous with the recrystallisation or with a specific set of veins. There are areas of localised greenschist facies deformation, but whether these zones of deformation were initiated prior to, synchronous with, or post fluid infiltration is unknown. Recrystallisation was taking place in these zones of localised deformation, but whether deformation and fluid infiltration were enhanced by reaction is also unknown.

The relative timing of deformation, fluid infiltration and reaction in the Syros marble bands is easier to constrain. Texturally equilibrated calcite marbles at the pressures and temperatures associated with metamorphic fluid infiltration on Syros are impermeable (Holness and Graham, 1995). The experimental data of Holness and Graham (1995) are backed up by the fact that marble bands on Syros do not fit simple fluid infiltration models based on chromatographic theory, suggesting that fluid infiltration did not occur by pervasive grain edge flow. If texturally equilibrated calcite marble is impermeable to fluid infiltration then infiltration will only occur if permeability is created dynamically (i.e. by deformation), thus implying that deformation must occur prior to, or synchronous with fluid infiltration of the Syros marbles.

The macro- and micro-scale study of oxygen isotope heterogeneities in Syros marble bands supports the conclusion that deformation is the key to fluid infiltration of marble bands. The heterogeneities in $\delta^{18}O$ composition were spatially associated with zones of partitioned deformation. Other recent micro-scale work on calcite marble from metamorphic terrains drew the same conclusions (Lewis et al. 1998 and Graham et al. 1998). Lewis et al. (1998) show with an example from a marble band

on Naxos in the Cyclades that grain-scale heterogeneities in $\delta^{18}O$ composition are related to both fracture networks and grain edge flow. They show by bulk stable isotope analysis of the same marble band, that the heterogeneities on a grain scale are homogenised by the bulk sampling (Lewis et al. 1998). Graham et al. (1998) relate grain-scale variations in the oxygen isotope composition of the Wada marble (Wada 1988) from the Hida metamorphic belt, Japan, to small scale deformation features such as calcite cleavage planes.

Reaction of silicate phases, by hydration, in impure marble layers on Syros is inferred to have occurred as a consequence of deformation and associated fluid infiltration. However, reaction fronts in impure marbles may create a transient permeability allowing fluid to infiltrate. Rumble et al. (1982) suggest that shifts in isotopic composition of metamorphosed marble are caused by transient increases in porosity and permeability induced by volume decrease during decarbonation reactions. Yardley and Lloyd (1989) showed that reactions in a banded dolomite-tremolite marble from Connemara, Ireland, had resulted in the creation of a secondary porosity and metamorphic permeability. Such reactions may allow fluid infiltration into marble bands if the reaction front propagates into the marble.

In the case of pure calcite marble bands under metamorphic conditions, it seems that deformation must occur prior to fluid infiltration, due simply to the impermeable nature of marble bands under metamorphic conditions. However, in impure marbles that are reactive, fluid may infiltrate by a reaction front creating a secondary permeability in the marble. For more heterogeneous and reactive lithologies the relationships between fluid infiltration, deformation and reaction are less well constrained and individual sample characteristics are thought to dominate.

Can bulk stable isotope profiles be used to determine the extent of fluid infiltration in metamorphic terrains and the mechanisms for fluid infiltration in relatively impermeable marble horizons?

The results of this study show that simple chromatographic models do not fit the isotope fronts formed in marble band boundary layers on Syros. This together with a detailed micro-scale oxygen isotope study suggests that deformation was the

key factor in controlling fluid infiltration into the marble bands. With these observations in mind it is clear that the partitioning of deformation within an individual marble band will control the extent, spatially and temporally, of fluid infiltration and isotopic alteration.

The scale of the partitioning of deformation and localised fluid infiltration is crucial to identification by bulk stable isotope analysis. Deformation partitioning on a metre-scale may be identified by collection of several bulk stable isotope profiles along strike. Even if the deformation zones were identified isotopically the exact mechanisms for fluid infiltration would still be unknown unless the data were combined with a textural study. If deformation is partitioned on a smaller scale, grain-scale, as suggested by the studies of Lewis et al. (1998) and Graham et al. (1998), heterogeneities in $\delta^{18}O$ composition and hence the mechanisms for fluid infiltration will not be recorded by bulk stable isotope sampling. The extent and scale of the partitioning of the deformation is clearly critical in controlling fluid infiltration. In this study partitioning of deformation was identified on a μm-scale, but also bands of μm-scale deformation were found concentrated in zones several metres wide. The actual deformation mechanisms which control fluid infiltration occur on a μm-scale and therefore will not be determined by bulk sampling.

In the example of Lewis et al. (1998) the grain-scale heterogeneities in the $\delta^{18}O$ composition were homogenised by bulk sampling resulting in a bulk stable isotope profile that could be fitted to a chromatographic flow model. The degree to which deformation is partitioned and fluid localised in calcite marble bands clearly controls the extent of isotopic alteration. If the grain-scale deformation mechanism and hence heterogeneities in $\delta^{18}O$ composition are on a small enough scale, then their overall effect may simulate that of pervasive grain edge flow if sampled for bulk stable isotope analysis.

Heterogeneities in $\delta^{18}O$ composition may also be homogenised by diffusion and deformation. This study, and the studies of Lewis et al. (1998) and Graham et al. (1998), have shown that the rate of diffusion of oxygen in calcite has not been high enough to homogenise the observed, μm-scale, $\delta^{18}O$ heterogeneities. In this study deformation has however homogenised stable isotope compositions, presumably by

grain boundary migration and recrystallisation. In examples where deformation has resulted in homogenisation of the $\delta^{18}O$ composition chromatographic models may be of use. However, care must be taken as the direction of fluid transport will be controlled by the anisotropy of the partitioned deformation.

In summary, bulk stable isotope profiles will probably never identify the mechanisms for metamorphic fluid infiltration of marble bands. They may however be used in a broad sense to establish whether fluid infiltration has occurred.

This study has shown that fluid infiltration, deformation and recrystallisation are intrinsically linked. Fluid appears to have been present at all stages in the exhumation process. Fluid infiltration, notably in marble bands, is controlled by deformation partitioning. The deformation partitioning within the metamorphic terrain, will be controlled by the regional tectonic setting and lithological and rheological heterogeneities within the metamorphic pile. A summary of the fluid infiltration and related deformation events is shown in figure 7.1.

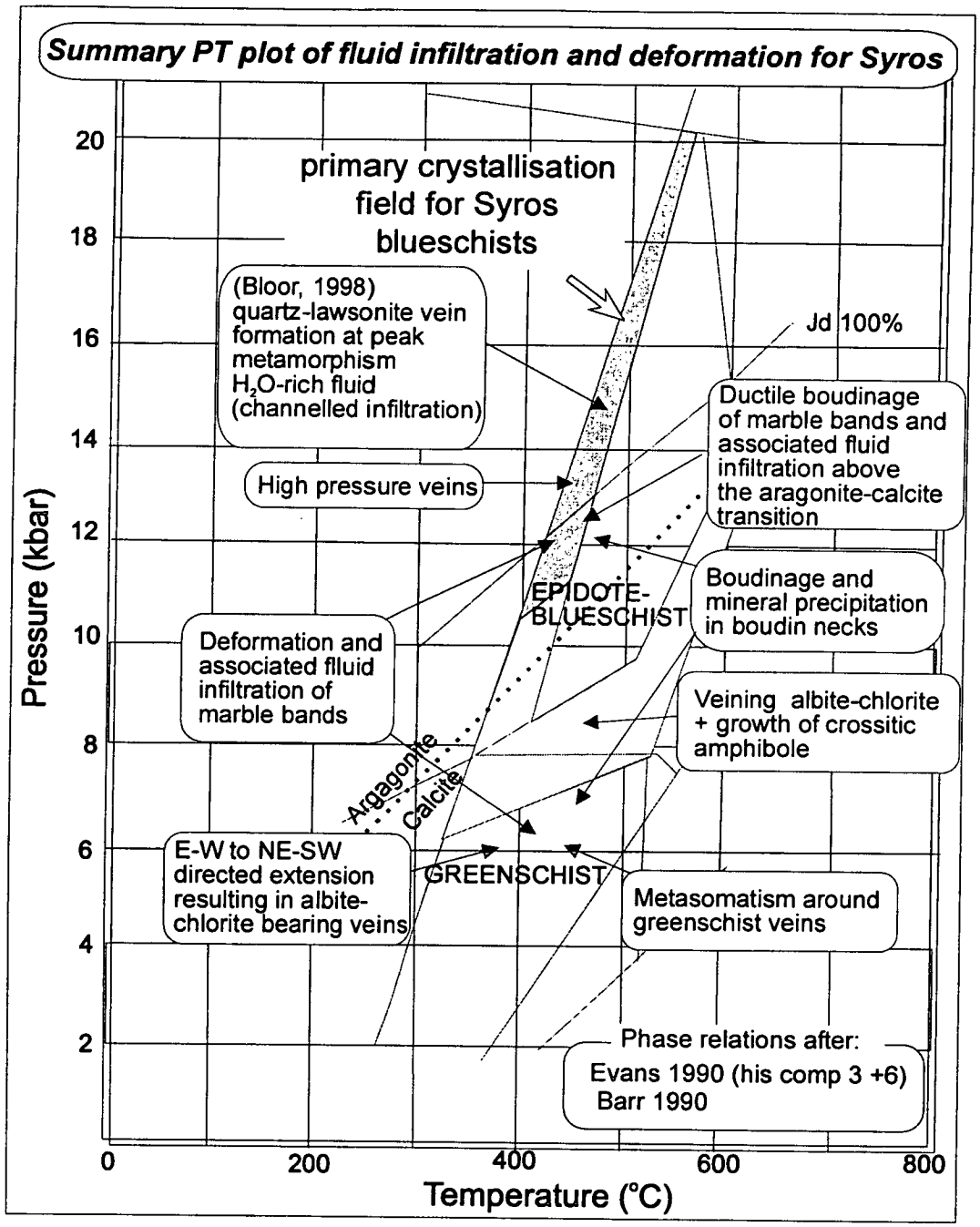

Figure 7.1

PT plot for Syros, combining the field of primary crystallisation for Syros blueschist (Barr, 1990), shaded area, with the epidote-blueschist facies stability field of Evans (1990). The white area shows blueschist-greenschist transition zone, which varies with amphibole composition. The white area is defined by combining the plots for amphibole compositions 3 and 6 (Evans, 1990). These compositions lie in the range of those recorded from the rims and cores of partially retrogressed glaucophane in metabasite on Syros, $Fe^{3+}/Fe^{3+} + Al + Ti$ in the range 0.3-0.5 and $Fe^{2+}/Fe^{2+} + Mg + Mn$ in the range 0.25-5.0. Aragonite-calcite transition after Yardley (1989). Annotated on the PT plot are fluid infiltration and associated deformation events described by this study, and the lawsonite associated veining event identified by Bloor (1998). For reactions see earlier figures (e.g. Figure 3.2).

Chapter 8 Conclusions and further work

The results and conclusions discussed in the previous chapter are summarised below:

- E-W oriented layer parallel coaxial extension is documented in peak mineral assemblages, through to greenschist assemblages and is parallel to brittle faults documented by Ridley (1984b). This extensional deformation is inferred to have accommodated the exhumation of the terrain.

- Hydration of blueschist assemblages was required for greenschist crystallisation.

- Influx of Na resulted in zones of concentrated albite porphyroblast growth in the schist.

- Greenschist recrystallisation is locally spatially associated with deformation. Fracture flow in the north during greenschist retrogression limits greenschist crystallisation to haloes around veins. Both fractures and ductile fabrics are documented in southern Syros associated with greenschist recrystallisation. However, ductile deformation associated with greenschist crystallisation is only very localised and in the majority of examples albite porphyroblasts grew after ductile deformation.

- Fluids infiltrated marble bands prior to and during the blueschist-greenschist transition.

- Geochemical front formation in marble bands could not be modelled by simple uniform- and pinned boundary-flow based on chromatographic theory, implying that the assumptions on which

chromatographic theory are based are invalid for the fluid infiltration associated with front formation in Syros marbles. The main assumptions include a constant porosity and permeability, local fluid rock equilibrium at a grain-scale, and an existing fluid filled network in the rock.

- Dynamic permeability was created in marble bands by deformation associated with E-W oriented layer parallel extension in both the brittle and ductile regimes.

Finally, some ideas for further work are suggested, which would improve our understanding of fluid infiltration, deformation and exhumation in this and other HP-LT metamorphic terrains.

In the present study many different types of veins were identified by their mineral compositions. Some of these veins were dominated by mineral assemblages including albite and chlorite and were thus termed greenschist veins. Isotope analysis of minerals within these veins were shown to be isotopically distinct (i.e. they do not show systematic fractionation from a single source). A detailed isotopic and geochemical study of the greenschist and higher grade veins could be undertaken to identify the number and chemical variability of fluid infiltration events in fractures.

The timing and rates of exhumation paths in the Cyclades and in many metamorphic terrains are poorly constrained. Recent work concentrating on the dating of deformation textures in alpine shear zones suggests that exhumation of alpine metamorphic terrains has occurred much faster than previously thought (e.g. Inger et al. 1996; Freeman et al. 1998a). An integrated structural and geochronological study of extensional fabrics on Syros and in the Cyclades would improve the constraints on the timing and rates of exhumation, by dating deformation fabrics of micas in mica- and carbonate-bearing rock; see Freeman et al. (1998b) for the method.

Finally the development of new models for geochemical front formation to take into account the creation of dynamically created and transient permeabilities in

metamorphic environments may increase our understanding of fluid infiltration and fluid fluxes in metamorphic environments.

Appendix A X-Ray Fluorescence

Preparation and analysis

The samples were prepared for major element XRF analysis by removal of weathered areas with a diamond tipped rotary saw. Individual samples were crushed and ground in a tungsten carbide tema mill for up to 4 minutes, until the samples were a fine homogenous powder. Samples were dried at 110 °C overnight before preparation. Dried powder samples were weighed to 1.0 g ± 0.05g and placed in a pre-weighed platinum crucible. The weighed samples were then ignited at 1100 °C for 20 minutes, cooled in a desiccator and re-weighed. Five times the original sample weight of flux (spectroflux 105) was then added to the ignited sample, plus 0.03g in anticipation of volatiles lost from the sample. The flux and powdered sample were then mixed and placed in the furnace for a further 20 minutes at 1100 °C. Samples were swirled on removal from the furnace, to mix, covered and left on a cooling block for 10 minutes. The samples were then re-weighed and flux was added until the target weight was reached, ± 0.0003g. The samples were finally fused over a bunsen flame, mixed and annealed on a 220 °C hot plate into glass rounds. The samples were analysed for major elements using the XRF instrument in the Department of Geology and Geophysics, Edinburgh University.

XRF-results

1995-1996

Kambos goat cave

S95/26	SiO2	Al2O3	Fe2O3	MgO	CaO	Na2O	K2O	TiO2	MnO	P2O5	LOI (%)	Total
vein halo	50.3	13.2	7.3	3.96	10.03	3.14	1.742	0.82	0.137	0.159	9.54	100.301
host rock	50.3	12.81	7.2	3.4	11.53	3.12	1.897	0.78	0.141	0.147	9	100.327

S95/63	SiO2	Al2O3	Fe2O3	MgO	CaO	Na2O	K2O	TiO2	MnO	P2O5	LOI (%)	Total
vein halo	55.7	14.23	8.39	4.97	5.71	4.43	0.709	0.87	0.115	0.133	5.11	100.364
host rock	55.8	14.4	8.86	5.04	6.25	3.84	1.016	0.87	0.114	0.12	3.46	99.813

North Ermoupolis

S95/116	SiO2	Al2O3	Fe2O3	MgO	CaO	Na2O	K2O	TiO2	MnO	P2O5	LOI (%)	Total
vein halo	51	15.77	8.5	7.7	9.48	3.69	0.039	1.5	0.149	0.058	2.46	100.31
host rock	52.3	14.92	8.43	7.9	8.97	3.82	0.014	1.53	0.142	0.064	1.97	100.038

S95/117	SiO2	Al2O3	Fe2O3	MgO	CaO	Na2O	K2O	TiO2	MnO	P2O5	LOI (%)	Total
vein halo	49.4	16.47	8.51	8.77	7.99	4.17	0.04	1.01	0.18	0.11	3.23	99.828
host rock	50.9	16.42	7.93	8.82	8.68	4.07	0.174	0.82	0.131	0.028	2.42	100.436

1997-1998

Kini	pg 64 ntbk3											
S'97/80	(cm)	SiO2	Al2O3	Fe2O3	MgO	CaO	Na2O	K2O	TiO2	MnO	P2O5	LOI %	Total
A	0	45.22	15.3	16	2.13	5.57	8.24	0.16	2.311	0.24	0.47	5.54	101.177
A98	0	45.2	15.33	15.9	2.01	5.61	8.98	0.08	2.314	0.239	0.459	5.52	101.646
C	8	46.47	13.94	9.92	1.13	8.57	8.1	0.07	1.907	0.282	0.463	7.57	98.426
C98	8	47.09	14.39	10.13	0.99	8.82	9.19	0.07	1.96	0.28	0.458	7.55	100.93
B	18	24.79	11.42	36.15	5.3	5.91	3	0.14	5.218	0.371	0.993	6.52	99.808
D	24	33.59	13.02	22.71	3.91	9.14	5.11	0.14	3.324	0.407	0.916	8.02	100.282
E	28	37.92	12.9	24.39	2.97	6.92	5.43	0.08	3.347	0.319	0.584	5.39	100.247
F	37	53.06	11.82	10.6	1.34	8.41	5.88	0.11	1.657	0.261	0.676	3.71	97.526
G	53	50.54	17.4	12	2.88	5.58	3.32	2.19	1.734	0.268	0.408	3.27	99.585
G98	53	50.37	17.84	12.12	2.79	5.57	3.59	2.2	1.732	0.263	0.402	3.22	100.093
H	71	46.74	15.07	17.25	4.05	6.57	2.89	0.45	2.453	0.287	0.555	3.52	99.832
H98	71	46.48	15.01	17.04	3.9	6.56	3.23	0.44	2.441	0.282	0.536	3.62	99.543
I	90	58.44	16.68	8.35	1.76	6.23	1.42	3.03	0.874	0.123	0.256	2.38	99.54
J	111	48.61	15.96	15.81	3.38	5.9	3.64	0.71	2.153	0.307	0.706	2.67	99.841

Oros Syringas pg 48-49 ntbk3

S'97/71	(cm)	SiO2	Al2O3	Fe2O3	MgO	CaO	Na2O	K2O	TiO2	MnO	P2O5	LOI %	Total
A	0	51.61	15.62	10.14	5.92	4.14	6.22	0.54	1.262	0.182	0.248	4.07	99.951
B	6	49.37	17.63	11.28	6.21	5.07	3.92	1.4	1.278	0.183	0.116	3.79	100.251
C	10	54.19	14.63	11.05	5.94	3.86	4.97	1.01	1.439	0.161	0.146	2.96	100.359
D	15	48.49	16.78	11.94	5.99	6.04	3.99	1.17	1.437	0.201	0.143	3.46	99.637
E	28	46.4	17.71	12.18	6.34	6.65	4.39	0.63	1.287	0.194	0.157	3.8	99.742
F	40	48.71	17.4	11.14	6.67	3.65	2.96	2.84	1.45	0.136	0.191	3.73	98.88
F98	40	48.67	17.97	11.04	6.53	3.6	3	2.82	1.463	0.137	0.185	4.82	100.239
G	50	51.91	14.44	9.59	4.99	6.68	5.95	0.19	1.065	0.16	0.23	4.97	100.178
H	70	47.49	16.55	10.61	5.4	8.39	4.43	0.89	1.116	0.194	0.174	4.51	99.753

Delfini pg 66 ntbk3

S'97/86	(cm)	SiO2	Al2O3	Fe2O3	MgO	CaO	Na2O	K2O	TiO2	MnO	P2O5	LOI %	Total
A	0	43.99	15.61	9.83	5.31	9.15	3.07	2.63	0.904	0.124	0.63	12.21	103.461
A98	0	39.48	14.15	8.28	4.59	13.61	3.73	2.09	0.768	0.163	0.52	12.83	100.206
B	14	39.53	14.24	8.39	4.68	13.68	3.13	2.08	0.772	0.166	0.546	8.03	95.246
B98	14	44.15	15.67	9.87	5.25	9.16	4	2.64	0.903	0.126	0.614	8.18	100.566
C	27	44.95	16.7	10.55	6.12	5.93	4.82	1.77	0.89	0.11	0.593	7.33	99.767
D	41	47.07	16.83	9.58	4.84	6.55	1.84	4.61	0.911	0.106	0.566	5.79	98.692
D98	41	47.49	16.88	9.65	4.76	6.58	2.18	4.63	0.918	0.115	0.554	5.65	99.405
E	61	45.98	17.5	9.2	4.52	7.57	3.53	3.13	0.865	0.141	0.804	5.96	99.199
F	74	37.47	13.57	6.54	2.62	19.06	2.6	2.05	0.728	0.129	0.572	13.67	99.004
F98	74	37.38	13.76	6.47	2.48	19.25	3.12	2.06	0.732	0.136	0.556	13.8	99.741
G	89	39.38	14.97	7.85	3.79	14.76	2.6	3.11	0.884	0.136	0.622	11.03	99.135
G98	89	39.29	14.92	7.71	3.73	14.81	2.93	3.13	0.893	0.131	0.602	10.92	99.067
H	101	41.03	14.39	8.1	4.33	14.23	2.73	3.16	0.812	0.115	0.667	10.18	99.748

Nites

S'97/31	(cm)	SiO2	Al2O3	Fe2O3	MgO	CaO	Na2O	K2O	TiO2	MnO	P2O5	LOI %	Total
A	0	57.52	16.76	2.4	1.47	5.83	10.09	0.06	0.624	0.058	0.112	5.01	99.932
B	2	40.39	19.36	13.24	9.31	6.34	3.21	0.21	1.855	0.15	0.176	5.18	99.425
C	5	46.69	17.72	10.13	7.39	7.11	4.23	0.51	1.357	0.129	0.157	4.25	99.676
D	7	48.28	17.18	9.66	6.82	7.8	4.25	0.45	1.309	0.125	0.118	3.56	99.549
E	9	48.82	16.28	9.23	6.43	8.92	4.09	0.47	1.176	0.125	0.146	3.81	99.498

Delfini

S'97/113	(cm)	SiO2	Al2O3	Fe2O3	MgO	CaO	Na2O	K2O	TiO2	MnO	P2O5	LOI	Total
A	0	49.66	16.58	9.95	5.96	5.42	6.42	0.34	1.186	0.133	1.198	2.91	99.752
B	5	46.63	16.9	11.22	6.83	5.04	5.6	0.84	1.42	0.142	1.208	3.57	99.403
C	15	49.71	17.48	8.72	5.28	5.45	4.85	3.2	1.007	0.097	1.05	2.65	99.493
D	27	49.55	19.13	8.5	3.45	5.58	4.75	3.5	1.053	0.136	0.737	2.5	98.889
E	40	51.42	19.63	8	2.82	4.62	6.09	2.92	0.818	0.194	0.56	2.42	99.48

Appendix B Bulk stable isotope analysis

Sample preparation and analysis

Pieces of marble approximately 2 cm x 1 cm were cut from field samples. All weathered areas were removed by a diamond tipped rotary saw before crushing. The crushed samples were ground in a tungsten carbide tema mill for approximately 30 seconds. Powdered calcite marble samples (15-40 mg) were reacted with degassed phosphoric acid at 25 °C for 3 hours, dolomite at 100 °C for 12 hours and ankerite at 100 °C for 24 hours. Carbon dioxide gas released was extracted via a slush condenser trap (acetone and dry ice) and a liquid nitrogen freeze bath, before collection and analysis on the Sira 10 mass spectrometer at the Scottish Universities Research and Reactor Centre (SURRC). A few samples extracted in February 1998 were analysed on the Sira II or Optima mass spectrometer at SURRC.

The isotope composition of schist was obtained by sampling quartz and/or calcite segregations in the schist and in some cases calcite drilled from calc-schist using a hand-held dental drill. All calcite samples were prepared and extracted as described above.

Quartz segregations from the schist were prepared in the same manner as the calcitic marble. Weathered areas were removed by a diamond tipped saw and samples were crushed and then ground in a tungsten carbide tema mill, for up to 2 minutes. Extraction of oxygen from silicate samples was carried out using the laser ablation technique developed by Sharp (1990, 1992). Powdered quartz samples (1-2 mg) were ablated by a 10 W, CO_2 laser for several minutes with a trichloroethylene reagent present, until no material remained. Excess reagent was frozen down in liquid nitrogen baths and the gas purified. Released oxygen gas was reacted with a degassed hot carbon rod and converted to carbon dioxide, for analysis on the PRISM III mass spectrometer at SURRC.

Nites locality D

S'97	Location	dist (cm)	δ18O cc	δ13C cc	δ18O qz	δ18O ox	orientation	description	samp
33	Nites	-66	8.494	-8.836	?			-66cm cc+qz+chl from seg	
34Q	Nites	-64			20.6			-64cm qz/haem	
35	Nites	-46	20.06	0.058				-46cm impure marble	wr
36	Nites	-26	19.435	-0.116				-26cm imp marble	wr
37	Nites	-16	20.54	-0.266				-16cm cc seg	seg
38	Nites	0	20.789	-0.079				0cm impure marble	
39	Nites	0	20.172	0.335				0cm marble crud	wr
40	Nites	2.5	20.334	1.273				0-5cm beige/grey cc	wr
41	Nites	5	20.965	1.541				5cm	wr
42	Nites	10	20.394	1.881				10cm	wr
43	Nites	15	21.089	0.843				15cm impure layer	wr
44	Nites	20	20.691	0.772				20cm imp	wr
45	Nites	25	19.712	1.348				25cm cc	wr
45	Nites	25	21.244	1.456				25cm cc clast	clast
46	Nites	28	21.005	1.279				28cm	wr
47	Nites	32	21.507	1.542				30-34cm cc	wr
48	Nites	45	21.455	0.87				45cm cc slightly imp	wr
49	Nites	60	22.465	1.577				60cm cc "	wr
50	Nites	78	25.614	1.879				78cm cc with qz layers	wr
51	Nites	90	26.278	2.125				90cm	wr
52	Nites	110	26.009	1.922				110cm interb' cc+-qz	wr
53	Nites	130	24.986	0.927			078/26N	130cm	wr

Nites Locality C (deformed)

S'97	Location	dist (cm)	δ18O cc	δ13C cc	δ18O qz	δ18O ox	orientation	description	samp
89Q	Nites	-95			20.2			Nites II -95cm qz	
90	Nites							-60cm cc	
91	Nites							-80cm cc	
92	Nites	-40	15.01	-7.185				-40cm cc	?
93Q	Nites	-20			20.8			-20cm qz	
94	Nites	-10	19.036	-0.131				-10cm cc (dirty)	?
95	(see below 98)								
96	Nites	0	16.316	-1.109				0-2cm cc (schist)	drilled
97	Nites							0-2cm cc (marble)	
98D	Nites	3	21.31	1.351			056/22	2-4cm cc	wr white cc
95	Nites	5	20.855	-4.094				5cm cc	wr
99	Nites	10	24.028	-1.41				10cm cc	wr!!!!
99Q	Nites				27.3				
100	Nites	18	20.227	-0.878				18cm cc	wr
101G	Nites	27	21.204	-0.827			066/52N	grey cc no veins	
102	Nites						041/18E	cc	
103	Nites	49	26.749	1.882			052/24E	whole rock cc sample	
104	Nites (see below)						052/24E	40cm base of sz	
105	Nites	62	24.389	1.831				wr cc	
106	Nites	80	25.057	2.315				wr	
107B	Nites	95	23.695	2.754			305/44E	pure cc layer in impure stuff	
107D	Nites	95	24.148	1.592				impure cc layer	
108	Nites	125	25.146	2.808			284/41NE	cc-imp layer	
109	Nites	190	25.343	3.176				fractured marble-impure	

Nites locality C, sampling with dental drill

S'97	Location	dist (cm)	δ18O cc	δ13C cc	δ18O qz	δ18O ox	orientation	description
97A	Nites	0	15.513	-0.17				vein
97B	Nites	0	15.038	0.151				vein
97C	Nites	0	24.027	-8.381				spurious!
98B	Nites	3	15.411	0.969				white cc in sz/vein
101A	Nites	27	17.87	1.087				white cc in sz
101B	Nites	27	14.765	1.341				white cc in sz
101C	Nites	27	16.046	-3.613				white cc in sz
101D	Nites	27	23.35	1.931				white/grey cc in sz
101F	Nites	27	20.547	-3.39				brown cc
101H	Nites	27	17.126	1.114				grey cc with veins
102A	Nites	27	26.048	1.708				grey cc clast
102B	Nites	27	21.363	-0.283				white cc veins through clast
102D	Nites	27	16.217	-2.276				white cc in sz
102F	Nites	27	23.651	1.633				white/grey cc in sz
102H	Nites	27	21.577	1.178				sz
104C	Nites	40	16.222	0.749				pale cc vein
103A	Nites	49	25.719	0.943				cc from small shear

Nites sampling of veins

S'97	Location	dist (cm)	δ18O cc	δ13C cc	δ18O qz	δ18O ox	orientation	description
65A	Nites		28.315	1.144				grey cc (wall rock)
65B	Nites							white cc +qz (vein)
65C	Nites							orange cc
65Q	Nites				22.0			
67C	Nites		16.952	-1.357				qz+cc
67Q	Nites				18.4			

Nites, western end-profile through boudin neck

S'96	Location	dist (cm)	δ 18O	δ 13C	Comments
174	Nites	0	22	-6.987	SCHIST
175	Nites	0	22.055	-3.171	MARBLE
176	Nites	5	24.764	1.776	
177	Nites	10	21.579	0.817	
178	Nites	15	23.639	-3.3	
179	Nites	20	24.004	0.742	
180	Nites	30	23.588	2	
181	Nites	40	20.801	1.537	
182	Nites	50	20.787	1.842	
183	Nites	65	23.926	1.919	
184	Nites	75	21.916	1.24	
185	Nites	80	21.902	1.413	
186	Nites	90	23.27	1.567	
187	Nites	100	22.08	1.188	Upper contact

Nites, western end- traverse outwards from boudin neck

S'96	Location	dist (m)	δ 18O	δ 13C	Comments
188	Nites	0	21.958	-2.094	
189	Nites	0.5	20.233	0.556	
190	Nites	0.8	23.983	2.076	
191	Nites	1	23.439	1.728	
192	Nites	1.3	23.544	2.003	
193	Nites	1.7	21.615	1.665	
194	Nites	2	25.697	1.805	
195	Nites	2.2	23.63	2.152	
196	Nites	2.4	26.252	0.879	
197	Nites	2.7	25.808	2.056	
198	Nites	3.7	26.28	2.235	
199	Nites	4.7	26.448	2.398	

Nites, western end- profile at 4.7m from boudin neck

S'96	location	dist (cm)	δ 18O	δ 13C	Comments
	Nites	-10000			QZ
201	Nites	0	23.156	2.145	MARBLE
202	Nites	5	23.959	1.841	
203	Nites	10	24.412	2.285	
204	Nites	15	23.61	1.751	
205	Nites	20	24.436	2.195	
206	Nites	25	24.354	2.558	
207	Nites	34	23.575	2.111	
208	Nites	40	24.263	2.095	
209	Nites	45	24.114	2.067	
210	Nites	52	23.954	2.572	
211	Nites	63	24.435	2.771	
212	Nites	75	22.337	1.739	
213	Nites	80	22.264	1.277	
214	Nites	100	24.263	1.676	
215	Nites	120	21.163	1.203	
216	Nites	135	22.59	1.033	
217	Nites	164	26.206	2.324	
218	Nites	190	26.342	2.546	

Nites boudin neck sampling with dental drill 1996/97

S'96	dist (cm)	δ18 O	δ13 C	description
187A	100	23.975	1.884	breccia
187B	100	23.883	1.881	breccia
187F	100	22.987	1.765	breccia
187H	100	23.028	1.647	breccia
187J	100	23.152	1.657	breccia
187L	100	22.429	1.092	breccia
187N	100	23.102	1.73	breccia
187D	100	20.706	0.254	matrix
187E	100	20.637	0.435	matrix
187G	100	20.818	0.417	matrix
187I	100	21.259	-0.129	matrix
187K	100	20.006	0.165	matrix
187M	100	20.668	-0.146	matrix
187O	100	21.266	-0.138	matrix
201A	0	24.159	1.868	dolomitic
201C	0	23.619	1.774	dolomitic
201B	0	24.123	2.587	cc
201D	0	22.861	1.886	cc
176A	5	20.617	-2.374	vein
176B	5	22.163	-0.485	vein
176C	5	24.382	1.947	rock!

Oros Syringas I (M'91 & 93) S'97

samp	dist (cm)	δ18O (1)	δ18O (2)	δ18O (3)	δ13C	orientation	Comments	
S1.20	-300	17.719			0.329			
S1.17	-190	17.943			3.086			
S1.18	-190	18.264						
S1.19	-115	18.957						
97/58	-90	18.082			1.683	098/67	veins schist into marble	
97/57	-85	17.518			0.669		qz/chl/ab segs	
97/57F	-85	27.913			0.496			
57Q	-85		19.8Q					
	-70			8.0?			weird under laser, from qz/gl layer	
S1.16	-73	17.696			1.71		SCHIST	
97/62C	-60	18.337		13.3	1.958		qz	
	-45			23.7			qz	
97/61C	-30			13			qz	
S1.29	-27	18.952			1.085			
97/60	-17	18.625			0.684			
S1.28	-6	18.111			1.088		SCHIST	
S1.1	1	18.307			0.879		MARBLE	
S1.30	5	18.578			1.787		MARBLE	
S1.2	6	18.171			1.735			
S1.31	10	19.906			1.729			
S1.3	13		19.603		1.808		18 O (1)	contaminated
S1.32	20	20.754			1.748			
S1.4	24	23.937			2.317			
S1.33	30	23.227			2.286			
97/54	32	21.263			2.099	279/40N		
97/54 I	32	21.394			2.198			
S1.34	40	24.56			2.53			

Oros Syringas I (M'91 & 93) S'97 (continued)

samp	dist (cm)	δ18O (1)	δ18O (2)	δ18O (3)	δ13C	orientation	Comments
S1.35	50	23.81			2.486		
S1.36	60	24.099			2.25		
S1.6	77	26.12			2.657		
S1.37	90	24.881			2.02		
S1.24	114	24.784			2.231		
S1.23	130	28.19			2.54		
S1.7	132	30.077			3.352		
S1.21	150	27.945			2.347		
S1.27	154	21.597			1.994		
97/55	156	24.739			1.457	097/59N	
S1.25	173	20.39			1.748		
97/56	173	25.806			2.386		
S1.8	178	28.891	28.854		2.245		
S1.44	180	28.854			2.134		
S1.43	190	29.034			2.149		
S1.42	200	28.958			2.03		
S1.9	208	20.785			2.355		
S1.41	210	28.992			2.034		
S1.40	220	28.495			2.251		
	221						MARBLE/SCHIST contact
S1.11	224	20.5					Qz segregation in schist
S1.39	230	28.637			2.703		
S1.38	240	26.16			2.702		
S1.22	249	18.871			0.774		TOP OF MARBLE
S1.12	251						Ultra low, inconsistent value
S1.45	284	24.871			-2.091		SCHIST
S1.46	332	15.838			-5.846		
S1.47	432	21.424			-5.253		

unused data Oros Syringas from just above locality I

samp	dist (cm)	δ18O (1)	δ18O (2)	δ18O (3)	δ13C	Comments
S1.13	776	20.669				Vein in boudin neck
S1.14	776	20.388			2.29	Edge of neck
S1.15	776	25.715			2.816	1m away

Oros Syringas locality II 1995

S'95	dist (cm)	δ18 O (1)	δ18 O (2)	δ13 C	Comments
54	-10	25.927	25.885	-4.866	
53	-5	29.227	26.338	1.058	SCHIST
37	0	25.429		-2.518	MARBLE
38	4	24.922	24.797	-2.043	
39	10	26.259		-0.703	Schist is cruddy Fe stained &
40	20	27.223		0.576	shows no obvious
41	30	26.53		0.655	greenschisting.
42	40	27.389		0.887	Marble is also pretty schisty.
43	50	27.19		0.132	
44	60	25.903	25.912	-0.69	
45	70	27.24		-0.094	
47	90	26.435	27.041	-4.651	
48	110	27.708		1.215	
49	130	28.906	27.123	1.123	
50	150	28.53	28.388	1.302	
51	170	26.04	28.121	-0.031	
52	190	27.393		0.454	

Oros Syringas III (M'91)

samp	dist (m)	δ18O (1)	δ18O (2)	δ18O (3)	δ13C	Comments
S2.3	-2.4	27.068			2.668	
S2.2	-1.2					Where are these samples/results?
S2.1	-0.1	25.076			3.163	MARBLE
S2.9	2.5	14.765				SCHIST Qz seg layer parallel
S2.10	3.5	15.252			-3.826	Qz seg layer parallel
S2.11	8.5	10.316			-0.266	Qz seg layer parallel
S2.12	15.5	10.906				Qz seg layer parallel
	40					SCHIST/MARBLE contact
S2.13	40.25	22.623			2.682	
S2.14	40.5	19.709			2.822	Continuous qz layer in calcite
S2.15	42	26.125			1.763	
S2.16	44.6	26.122			2.734	
S2.17	47.1	25.798			2.952	
S2.18	47.7	25.729			3.115	
S2.19	48.05	25.201			2.729	
S2.20	48.5	25.629			2.639	
S2.21	48.65	20.289	19.639	17.893	3.052	MARBLE
S2.22	52	15.979				SCHIST Qz seg layer parallel
S2.23	52.5	16.31				Qz seg layer parallel
S2.24	56	17.562			2.989	MARBLE schist/marble contact
S2.25	56.04	26.688			3.065	
S2.26	56.1	27.343			2.966	
S2.27	56.45	28.421			2.968	
S2.28	56.75	27.307			2.56	
S2.29	57.5	26.172			3.154	
S2.30	58.25	26.705			2.802	
S2.31	59.47	27.516			2.476	
S2.32	61	27.239			2.672	
S2.33	63	28.03			1.996	
S2.36	66.5	26.122			0.949	

Oros Syringas III (M'93)

samp	dist (cm)	δ18O (1)	δ18O (2)	δ18O (3)	δ13C	Comments
S2.51	-148		26.207			
S2.50	-112	25.22	25.675		2.517	
S2.49	-87		26.539			
S2.48	-74		25.068			
S2.45	-60	25.45	25.906		2.399	
S2.44	-50	25.939	26.395		1.731	
S2.43	-40		25.214			
S2.42	-30		26.383			
S2.41	-20	24.698	25.154		2.173	
S2.40	-10	24.337	24.792		2.337	
S2.39	-5	23.165	23.62		2.525	
S2.38	-2	20.502	20.502		2.341	MARBLE
S2.46	100	20.67	21.124		-3.896	SCHIST
S2.47	200	20.497	20.951		-5.47	
S2.54	360		16.219			
S2.52	485	14.372	14.823		0.529	
S2.53	690		17.252			TOP OF SCHIST 735 cm
S2.55	740		26.904			MARBLE
S2.56	745	26.416	26.872		2.632	
S2.57	750	27.755	28.212		2.708	
S2.58	755		25.51			
S2.59	765		28.212			
S2.60	775	27.008	27.465		2.703	
S2.61	785		28.387			
S2.62	795	27.739	28.195		2.428	
S2.63	815		26.966			
S2.64	825		24.688			
S2.65	835	26.422	26.878		2.675	
203	735	18.561	3.017			267/52S contact marble/schist

Windy Ridge A

S'97	Location	dist (cm)	δ18O cc	δ13C cc	δ18O qz	d18O ox	orientation	description	samp
150	WRA	-90	20.224	1.293				-90cm qz in qz/cc schist	
151	WRA	-80	25.788	-7.139				-80cm gl/cc layer	
151R	WRA	-80	25.624	-7.232					
152	WRA	-60	26.209	-7.043			182/00	-60cm gl/cc layer-grey	
152R	WRA	-60	26.134	-6.936				?	
153	WRA	-40	20.632				062/30	-40cm cc,gl, Na pyx	wr
154	WRA	-20	21.17	1.087				-20cm	
155	WRA	0	22.774	1.301			008/16N	0cm approx contact	
156	WRA	5	22.041					5-8cm	wr
157A	WRA	17	26.164	-8.802				precipitation	
157B	WRA	17	24.686	-1.174					
158	WRA	20	25.009	0.093			130/60	17-24cm	
158R	WRA	20	24.57	-0.098					
159	WRA	41	26.165					40-42cm	wr
160	WRA	47	26.159	1.366	gl 22.6		031/46	45-50cm gl rich imp	wr
161	WRA	70						70cm	
162	WRA	90						90cm	
163	WRA	100					043/48	100cm grey cc impure	
163A	WRA	100	25.814	2.052				20% gl + bits	
163B	WRA	100	25.775	1.064				50% gl+bits	
164	WRA	110	25.881	1.463			043/48	110cm	
165	WRA	130	26.359	2.501				130cm grey cc	
166	WRA	150	26.188	1.624				150cm creamy cc	
167	WRA	165	25.661				030/23	165cm	wr

Windy Ridge B M'94/95 S'97

samp	Location	dist (cm)	δ18O cc	δ18O (2)	δ18O (3)	δ13C cc	δ18O qz	orientation/descriptiom
94/75N	WRB	-200					20.3	
169Q	WRB	-150					19.1	-150cm qz
169QR	WRB	-159					19.3	
94/74N	WRB	-36					19	
168Q	WRB	-30					19.2	-30cm qz
170	WRB	0	23.768			-6.928		227/00
94/67N	WRB	0	23.503	20.353	23.283	1.091		
95/17N	WRB	0	20.677	20.775		-2.03		
95/18N	WRB	11	22.318			-0.576		
94/69N	WRB	15	21.357	23.203		-0.704		Schist below the marble band
94/70N	WRB	19.5	24.431			-2.556		appears to be partially
95/19N	WRB	20	23.879			-3.384		retrogressed
171	WRB	30	24.51			-1.269		307/22W
171 R	WRB	30	24.57			-1.071		
94/71N	WRB	40	23.318	24.95		-2.203		Chl replaces gnt. The rock is
94/72N	WRB	74	25.14			0.29		chl rich but still contains gl
172	WRB	80	25.392			-1.115		230/38NW grey impure cc
172R	WRB	80	25.734			-1.151	20.1	
172gl	WRB						22 gl	
173	WRB	123	24.563			-0.497		
174	WRB	153	23.94			0.337		
175	WRB	200	23.546					230/43
175gl	WRB						22.6 gl	
94/73N	WRB	200	23.54			1.65		

N Windy Ridge

96/97	Location	dist (cm)	δ 18O	δ 13C	δ18O gl	orientation	Comments
	NWR	-400					QZ
55	NWR	-200	21.649	0.92			SCHIST
176	NWR	-20	21.096	0.529			cc in schist
57	NWR	0	21.18	2.086			MARBLE
177	NWR	0	23.85	1.952		091/30E	
57	NWR	0	21.694	2.306			
178	NWR	0	20.108	1.534			0cm impure
57	NWR	0	20.925	1.528			
58	NWR	9	23.008	0.698			
58	NWR	10	22.065	1.561		342/22	10cm gl + epd
58	NWR	10			17.5		
59	NWR	13	23.358	-0.337			
60	NWR	16	23.16	1.044			
61	NWR	25	22.833	0.295			
62	NWR	35	23.409	1.269			
63	NWR	43	23.157	1.179			
179	NWR	55	23.547	2.09		343/30	55cm pure (almost)
179	NWR	55			20.2		
64	NWR	57	23.347	1.341			55cm impure gl + other (20%)
64	NWR	58	23.607	0.298			
65	NWR	80	24.019	1.747			
66	NWR	92	24.252	0.564			
67	NWR	110	25.034	-0.271			
68	NWR	130	25.718	0.902		090/40	
68	NWR	130	25.871	0.828			
180	NWR	150	26.952	2.272			
69	NWR	180	26.18	-0.615			
70	NWR	200	26.705	1.214		296/00	
181	NWR	200	27.15	0.786			

Path Windy Ridge east

96/97	location	Dist (cm)	δ 18O	d18O qz	δ 13C	orientation	Comments
184	PWR	-60	19.351		-1.998	017/36W	
183	PWR	-20		18.7	SCHIST		qz
71	PWR	-10		19.0	QZ		qz
72	PWR	0	19.93		-4.342		
73	PWR	5	18.756		-2.749		
74	PWR	10	19.205		-3.444		
75	PWR	16	20.867		-2.473		
76	PWR	26	19.696		-3.944		
77	PWR	30	19.052		-2.426		
78	PWR	40	19.364		-2.601		
79	PWR	50	19.164		-2.901		
80	PWR	60	19.72		-2.491		
81	PWR	70	18.807		-2.399		
82	PWR	85	18.797		-2.829		
83	PWR	100	19.883		-2.147		
84	PWR	110	19.531		-2.412		Upper contact

6 wells locality C

S'97	Location	dist (cm)	δ18O cc	δ13C cc	δ18O qz	δ18O ox	orientation	description	samp
185	6WC	0	28.552	-1.388			029/78	0cm	
185	6WC	0	28.224	-1.464					
186	6WC	12	18.005	-0.76				12cm	
186	6WC	12	25.28	0.266					
187	6WC	30	25.568	1.705			025/44	30cm-impure gl layer	
187R	6WC	30	26.402	2.509					
187R	6WC	30	25.639	1.875					
187 gl	6WC				22.2				
188	6WC	44	26.499	2.493			023/41	44cm- almost pure cc	
188R	6WC	44	26.402	2.509					
189	6WC	80	25.986	1.996				80cm	
190A	6WC	112	25.16	1.915			089/44	pure cream cc	
190B	6WC	116	24.769	1.857				grey +gl +bits	
190gl	6WC				20.2				
190C	6WC	118	24.613	2.039				pure cream cc	
191	6WC	-15	25.634	1.253				-15cm cc in schist	
192	6WC	-25	25.548	1.673				-25cm cc in schist	

6 wells locality D

S'97	Location	dist (cm)	δ18O cc	δ13C cc	δ18O qz	δ18O ox	orientation	description	samp
193	6WD	-200	21.105	0.411				-200cm cc in schist	
194Q	6WD	-250			17.9			-250cm qz in schist	
195	6WD	0	25.55	-7.538				0cm crud from contact	
196A	6WD	0	18.159	1.915			035/58	0cm cream cc	
196AR	6WD	0	18.665	0.664					
196B	6WD	2	25.392	-1.115				grey cc	
197	6WD	8	19.814	1.325				8cm	
197R	6WD	8	18.012	0.61					
198A	6WD	22	21.205	0.25				25cm impure layer gl	
198B	6WD	24	21.048	2.115				25cm rel pure altho' amph	
198C	6WD	26	23.091	-3.676			007/50	25cm weathered layer (ppn)	
199	6WD	50	24.637	1.261				50cm	
200	6WD	83	25.68	2.131				80-85cm gl rich	
200R	6WD	83	25.288	1.965					
201	6WD	100	23.502	1.457				100cm	
201R	6WD	100	23.501	1.541					
202	6WD	139	24.181	1.652				139cm	

Marble band, monolith 2 ('95)

S'95	Location	Dist (cm)	δ18O (1)	δ13C	Comments
27 a	m2bou	0	11.886	1.909	MARBLE
27b	m2bou	4	11.784	2.068	The profile is taken across the centre of
28	m2bou	8	11.545	2.282	a broken marble boudin surrounded by
30	m2bou	25	11.576	2.365	ultramafic. (Boudin approx 3m x 20m)
31	m2bou	78	12.362		Pelitic layers within the marble are also
32	m2bou	92	12.908	2.146	highly deformed and distinctively green
66	m2bou	120	13.45	2.486	
67	m2bou	180	13.231	2.473	
68	m2bou	230	11.868	1.957	
69	m2bou	260	12.207	1.432	
70	m2bou	275	11.569	1.921	
71	m2bou	280	11.882	1.486	

Appendix C Ion microprobe $\delta^{18}O$ analysis

Sample preparation & method

A Cameca ims-4f ion microprobe (Slodzian, 1980), with Charles Evans and Associates computer controlled system, was used for in situ microscopic analysis of $\delta^{18}O$ for calcite and some quartz specimens. Polished 1 inch rounds were coated in gold to minimise charging and analysed with a defocused 20 μm primary beam of $^{133}Cs^{+}$ ions. The surface charge of the sample was neutralised with a normal-incidence electron flood gun. Secondary $^{18}O^{-}$ and $^{16}O^{-}$ ions were collected and counted on an ETP electron multiplier, using an energy off-set of 350 ± 25 eV. Counting times of 600 s for $^{18}O^{-}$ and 120 s for $^{16}O^{-}$ were used to give to a theoretical precision of ± 1 ‰. An intial burn in time of 3 minutes was used to burn through the gold coat and to stabilise the secondary ion current prior to each analysis.

Ion microprobe analyses were made over a period over two weeks in December 1998. At the start of each day a set of standard analyses were made, a further two or three standard analyses were made for every 6-8 unknowns. The standard analyses were used to calibrate the daily drift in the instrument. The drift was approximately linear and can be corrected for by least squares regression, as in previous studies (e.g. Valley and Graham, 1991). Calcite analyses were standardised against the University of Wisconsin calcite (UWC) standard, $\delta^{18}O$ = 23.28 ‰ +/- 0.06 ‰ (Valley, pers comm.). Quartz analyses were standardised against Bogola quartz (BOG), $\delta^{18}O$ = 12.3 ‰ +/-0.3 ‰ (Elsenheimer and Valley, 1993).

The results are tabulated for individual samples. The standard data for each day are also presented with regression graphs of the daily drift.

Results

S'95/29

sample/analysis	Date	hrs	min	no.	corr standard	δ18O	18O/16O ratio	error 1σ
B:S9529-1.DAT	6/12/98	11	18	10	0.0018925818	16.1	0.00187926	0.000002230
B:S9529-2.DAT	6/12/98	11	37	11	0.0018925432	12.9	0.00187324	0.000002073
B:S9529-3.DAT	6/12/98	11	57	12	0.0018925047	11.3	0.00187038	0.000001898
B:S9529-4.DAT	6/12/98	12	16	13	0.0018924662	9.5	0.00186702	0.000002170
B:S9529-5.DAT	6/12/98	12	40	14	0.0018924277	13.0	0.00187336	0.000001681
B:S9529-6.DAT	6/12/98	12	58	15	0.0018923892	12.8	0.00187304	0.000002082
B:S9529-7.DAT	6/12/98	13	17	16	0.0018923507	14.4	0.00187586	0.000001941
B:S9529-8.DAT	6/12/98	13	36	17	0.0018923122	11.7	0.00187081	0.000001802
B:S9529-9.DAT	6/12/98	14	51	20	0.0018921966	13.0	0.00187316	0.000001806
B:S9529-10.DAT	6/12/98	15	11	21	0.0018921581	10.8	0.00186909	0.000001690
B:S9529-9B.DAT	15/12/98	22	42	40	0.0018807388	6.7	0.00185024	0.000001917
B:S9529-10B.DAT	15/12/98	23	2	41	0.0018806690	9.6	0.00185558	0.000001538
B:S9529-11.DAT	15/12/98	23	21	42	0.0018805992	9.6	0.00185546	0.000001717
B:9529-12.DAT	15/12/98	23	40	43	0.0018805294	7.5	0.00185149	0.000001995
B:S9529-13.DAT	15/12/98	23	59	44	0.0018804597	7.5	0.00185140	0.000001853
B:S9529-14.DAT	16/12/98	0	18	45	0.0018803899	11.5	0.00185878	0.000001876

S'95/70

sample/analysis	Date	hrs	min	no.	corr standard	δ18O	18O/16O ratio	error 1σ
B:S9570-1.DAT	4/12/98	21	8	31	0.0018892030	14.3	0.00187264	0.000002055
B:S9570-2.DAT	4/12/98	21	29	32	0.0018891545	8.8	0.00186235	0.000001530
B:S9570-3.DAT	4/12/98	21	49	33	0.0018891060	14.0	0.00187186	0.000001782
B:S9570-4.DAT	4/12/98	22	18	34	0.0018890575	11.6	0.00186748	0.000001758
B:S9570-5.DAT	4/12/98	22	37	35	0.0018890090	13.1	0.00187010	0.000001748
B:S9570-6.DAT	4/12/98	22	56	36	0.0018889605	9.9	0.00186414	0.000001604
B:S9570-7.DAT	4/12/98	23	16	37	0.0018889121	9.6	0.00186360	0.000001670
B:S9570-8.DAT	4/12/98	23	34	38	0.0018888636	11.5	0.00186712	0.000001774
B:S9570-9.DAT	4/12/98	23	54	39	0.0018888151	12.3	0.00186854	0.000001637
B:S9570-10.DAT	5/12/98	11	3	9	0.0018879145	10.9	0.00186509	0.000001611
B:S9570-11.DAT	5/12/98	11	35	10	0.0018879268	11.8	0.00186665	0.000001818
B:S9570-12.DAT	5/12/98	11	55	11	0.0018879391	10.7	0.00186463	0.000001509
B:S9570-13.DAT	5/12/98	12	14	12	0.0018879514	10.1	0.00186359	0.000001825
B:S9570-14.DAT	5/12/98	12	34	13	0.0018879637	10.8	0.00186497	0.000001822
B:S9570-15.DAT	5/12/98	12	53	14	0.0018879760	11.5	0.00186622	0.000001773
B:S9570-16.DAT	5/12/98	13	12	15	0.0018879883	12.0	0.00186712	0.000001825
B:S9570-17.DAT	5/12/98	14	21	18	0.0018880252	10.2	0.00186385	0.000001824
B:S9570-18.DAT	5/12/98	14	40	19	0.0018880375	11.0	0.00186535	0.000001676
B:S9570-19.DAT	5/12/98	15	0	20	0.0018880498	10.4	0.00186421	0.000002056
B:S9570-20.DAT	5/12/98	15	19	21	0.0018880621	12.2	0.00186766	0.000001851
B:S9570-21.DAT	5/12/98	15	39	22	0.0018880744	11.7	0.00186671	0.000001710
B:S9570-22.DAT	5/12/98	15	58	23	0.0018880867	11.6	0.00186644	0.000001925
B:S9570-23.DAT	5/12/98	16	19	24	0.0018880990	12.6	0.00186835	0.000001602

S'96/53

sample/analysis	Date	hrs	min	no.	corr standard	δ18O	18O/16O ratio	error 1σ
B:S9653-1.DAT	6/12/98	15	46	22	0.0018921196	29.6	0.00190386	0.000001962
B:S9653-2.DAT	6/12/98	16	7	23	0.0018920811	24.9	0.00189513	0.000001795
B:S9653-3.DAT	6/12/98	16	27	24	0.0018920426	23.8	0.00189304	0.000001935
B:S9652-4.DAT	6/12/98	17	0	25	0.0018920041	24.6	0.00189446	0.000002057
B:S9653-5.DAT	6/12/98	17	19	26	0.0018919656	25.3	0.00189567	0.000001889
B:S9653-6.DAT	6/12/98	17	39	27	0.0018919271	23.4	0.00189219	0.000001806
B:S9653-7.DAT	15/12/98	18	25	29	0.0018815063	23.5	0.00188190	0.000001870
B:9653-8.DAT	15/12/98	18	45	30	0.0018814365	24.3	0.00188319	0.000001743
B:9653-9.DAT	15/12/98	19	4	31	0.0018813667	25.5	0.00188540	0.000001823
B:S9653-10.DAT	15/12/98	19	24	32	0.0018812970	23.8	0.00188224	0.000001695
B:S9653-11.DAT	15/12/98	19	48	33	0.0018812272	28.6	0.00189101	0.000001833
B:S9653-12.DAT	15/12/98	20	11	34	0.0018811574	28.3	0.00189026	0.000001666
B:S9653-13.DAT	15/12/98	20	31	35	0.0018810876	24.3	0.00188299	0.000001976
B:S9653-14.DAT	15/12/98	21	1	36	0.0018810179	24.7	0.00188361	0.000001582
B:S9653-15.DAT	15/12/98	21	20	37	0.0018809481	21.2	0.00187700	0.000001719

S'97/155

sample/analysis	Date	hrs	min	no.	corr standard	δ18O	18O/16O ratio	error 1σ
B:97155-1.DAT	5/12/98	17	32	27	0.0018881359	24.3	0.00189007	0.000001574
B:97155-2.DAT	5/12/98	17	50	28	0.0018881482	23.9	0.00188933	0.000002044
B:97155-3.DAT	5/12/98	18	10	29	0.0018881605	24.9	0.00189118	0.000001734
B:97155-4.DAT	5/12/98	18	29	30	0.0018881729	23.4	0.00188836	0.000001656
B:97155-5.DAT	5/12/98	18	49	31	0.0018881852	24.9	0.00189118	0.000002091
B:97155-6.DAT	5/12/98	19	8	32	0.0018881975	22.4	0.00188653	0.000001954
B:97155-7.DAT	5/12/98	19	27	33	0.0018882098	23.7	0.00188895	0.000001867
B:97155-8.DAT	5/12/98	19	46	34	0.0018882221	22.5	0.00188671	0.000001770
B:97155-9.DAT	5/12/98	21	19	38	0.0018882713	24.8	0.00189104	0.000001919
B:97155-10.DAT	5/12/98	21	38	39	0.0018882836	27.2	0.00189554	0.000001768
B:97155-11.DAT	5/12/98	21	57	40	0.0018882959	25.9	0.00189303	0.000002014
B:97155-12.DAT	5/12/98	22	16	41	0.0018883082	25.0	0.00189136	0.000001708
B:97155-13.DAT	5/12/98	22	35	42	0.0018883205	27.7	0.00189653	0.000001929
B:97155-14.DAT	5/12/98	23	3	43	0.0018883328	21.7	0.00188535	0.000001772
B:97155-15.DAT	5/12/98	23	23	44	0.0018883451	37.4	0.00191442	0.000001756
B:97155-16.DAT	5/12/98	23	49	45	0.0018883574	22.7	0.00188728	0.000001648
B:97155-17.DAT	6/12/98	0	10	46	0.0018883697	29.5	0.00189975	0.000005668

S'97/171

sample/analysis	Date	hrs	min	no.	corr standard	δ18O	18O/16O ratio	error 1σ
B:97171-1.DAT	6/12/98	22	26	40	0.0018914264	27.7	0.00189948	0.000001573
B:97171-2.DAT	6/12/98	22	44	41	0.0018913879	29.7	0.00190325	0.000001898
B:97171-3.DAT	6/12/98	23	2	42	0.0018913494	26.3	0.00189686	0.000002130
B:97171-4.DAT	6/12/98	23	22	43	0.0018913109	30.7	0.00190490	0.000001930
B:97171-5.DAT	6/12/98	23	40	44	0.0018912724	25.8	0.00189587	0.000001918
B:97171-6.DAT	6/12/98	23	58	45	0.0018912339	29.5	0.00190274	0.000002006
B:97171-7.DAT	7/12/98	11	0	9	0.0018902786	29.4	0.00190150	0.000001997
B:97171-8.DAT	7/12/98	11	18	10	0.0018900233	28.8	0.00190011	0.000001916
B:97171-9.DAT	7/12/98	11	37	11	0.0018897680	29.1	0.00190051	0.000001681
B:97171-10.DAT	7/12/98	11	56	12	0.0018895127	32.1	0.00190572	0.000001751
B:97171-11.DAT	7/12/98	12	15	13	0.0018892574	31.0	0.00190346	0.000001926

S'96/58

sample/analysis	Date	hrs	min	no.	corr standard	δ18O	18O/16O ratio	error 1σ
B:S9658-1.DAT	16/12/98	11	43	11	0.0018759737	22.8	0.00187511	0.000001765
B:S9658-2.DAT	16/12/98	12	3	12	0.0018758686	21.3	0.00187229	0.000001872
B:S9658-3.DAT	16/12/98	12	21	13	0.0018757636	21.5	0.00187255	0.000001926
B:S9658-4.DAT	16/12/98	12	39	14	0.0018756586	25.3	0.00187934	0.000001676
B:S9658-5.DAT	16/12/98	12	58	15	0.0018755535	25.0	0.00187872	0.000002030
B:S9658-6.DAT	16/12/98	13	16	16	0.0018754485	21.2	0.00187158	0.000001638
B:S9658-7.DAT	16/12/98	14	28	19	0.0018751334	25.6	0.00187931	0.000001924
B:S9658-8.DAT	16/12/98	14	48	20	0.0018750284	23.3	0.00187500	0.000001875
B:S9658-9.DAT	16/12/98	15	7	21	0.0018749234	25.0	0.00187811	0.000001807
B:S9658-10.DAT	16/12/98	15	27	22	0.0018748183	22.3	0.00187293	0.000001816
B:S9658-11.DAT	16/12/98	15	46	23	0.0018747133	24.3	0.00187653	0.000001797
B:S9658-12.DAT	16/12/98	16	5	24	0.0018746083	23.0	0.00187412	0.000001560
B:S9658-13.DAT	16/12/98	17	33	27	0.0018742932	24.2	0.00187601	0.000001803
B:S9658-14.DAT	16/12/98	17	51	28	0.0018741882	22.8	0.00187328	0.000001707
B:S9658-15.DAT	16/12/98	18	9	29	0.0018740831	23.6	0.00187456	0.000001812
B:S9658-16.DAT	16/12/98	18	28	30	0.0018739781	27.4	0.00188153	0.000001987
B:S9658-17.DAT	16/12/98	18	46	31	0.0018738731	26.5	0.00187967	0.000001938
B:S9658-18.DAT	16/12/98	19	4	32	0.0018737680	28.1	0.00188247	0.000001550
B:S9658-19.DAT	16/12/98	19	23	33	0.0018736630	27.1	0.00188060	0.000001861
B:S9658-20.DAT	16/12/98	19	41	34	0.0018735580	27.2	0.00188068	0.000002061

S'97/37

sample/analysis	Date	hrs	min	no.	corr standard	δ18O	18O/16O ratio	error 1σ
B:9737-1.DAT	14/12/98	17	6	20	0.0018811493	21.3	0.00187750	0.000001671
B:9737-2.DAT	14/12/98	17	25	21	0.0018810340	19.3	0.00187367	0.000001866
B:9737-3.DAT	14/12/98	17	43	22	0.0018809187	22.5	0.00187952	0.000001722
B:9737-4.DAT	14/12/98	18	3	23	0.0018808033	25.9	0.00188555	0.000001839
B:9737-5.DAT	14/12/98	18	25	24	0.0018806880	22.9	0.00187995	0.000001604
B:9737-6.DAT	14/12/98	18	43	25	0.0018805727	24.6	0.00188291	0.000001509
B:9737-7.DAT	14/12/98	19	1	26	0.0018804573	18.4	0.00187150	0.000001585
B:9737-8.DAT	14/12/98	19	20	27	0.0018803420	21.2	0.00187645	0.000001721
B:9737-9.DAT	14/12/98	20	28	30	0.0018799960	23.5	0.00188042	0.000001803
B:9737-10.DAT	14/12/98	20	46	31	0.0018798807	21.7	0.00187687	0.000001670
B:9737-11.DAT	14/12/98	21	6	32	0.0018797654	23.6	0.00188036	0.000001860
B:9737-12.DAT	14/12/98	21	24	33	0.0018796500	22.8	0.00187881	0.000001867
B:9737-13.DAT	14/12/98	21	42	34	0.0018795347	22.2	0.00187755	0.000001773
B:9737-14.DAT	14/12/98	22	1	35	0.0018794194	21.4	0.00187589	0.000001956
B:9737-15.DAT	14/12/98	22	19	36	0.0018793040	20.5	0.00187415	0.000001943
B:9737-16.DAT	14/12/98	22	38	37	0.0018791887	21.7	0.00187626	0.000001880

S'97/39

sample/analysis	Date	hrs	min	no.	corr standard	δ18O	18O/16O ratio	error 1σ
B:9739-1.DAT	15/12/98	0	27	42	0.0018786121	24.4	0.00188071	0.000001686
B:9739-2.DAT	15/12/98	0	46	43	0.0018784967	24.6	0.00188082	0.000001660
B:9739-3.DAT	15/12/98	1	5	44	0.0018783814	23.8	0.00187932	0.000002113
B:9739-4.DAT	15/12/98	1	24	45	0.0018782661	27.0	0.00188505	0.000001986
B:9739-5.DAT	15/12/98	12	9	11	0.0018827622	22.3	0.00188096	0.000002125
B:9739-6.DAT	15/12/98	12	28	12	0.0018826925	23.4	0.00188283	0.000001717
B:9739-7.DAT	15/12/98	12	46	13	0.0018826227	21.9	0.00188011	0.000001835
B:9739-8.DAT	15/12/98	13	5	14	0.0018825529	22.3	0.00188072	0.000001728
B:9739-9.DAT	15/12/98	13	30	15	0.0018824831	21.5	0.00187924	0.000001788
B:9739-10.DAT	15/12/98	13	52	16	0.0018824134	22.4	0.00188082	0.000001968

S'97/50

sample/analysis	Date	hrs	min	no.	corr standard	δ18O	18O/16O ratio	error 1σ
B:S9750-1.DAT	6/12/98	19	11	31	0.0018917730	30.8	0.00190570	0.000001710
B:S9750-2.DAT	6/12/98	19	30	32	0.0018917345	33.6	0.00191084	0.000001923
B:S9750-3.DAT	6/12/98	19	49	33	0.0018916960	28.5	0.00190133	0.000001817
B:S9750-4.DAT	6/12/98	20	7	34	0.0018916575	28.9	0.00190208	0.000002150
B:S9750-5.DAT	6/12/98	20	25	35	0.0018916190	31.3	0.00190649	0.000002287
B:S9750-6.DAT	6/12/98	20	44	36	0.0018915805	30.1	0.00190418	0.000001894
B:S9750-7.DAT	6/12/98	21	5	37	0.0018915420	31.1	0.00190590	0.000001628

S'97/47

sample/analysis	Date	hrs	min	no.	corr standard	δ18O	18O/16O ratio	error 1σ
B:S9747-1.DAT	4/12/98	11	40	8	0.0018903183	19.4	0.00188303	0.000001715
B:S9747-2.DAT	4/12/98	12	0	9	0.0018902698	21.1	0.00188628	0.000001588
B:S9747-3.DAT	4/12/98	12	23	10	0.0018902213	19.4	0.00188296	0.000001912
B:S9747-4.DAT	4/12/98	12	44	11	0.0018901728	20.8	0.00188559	0.000001787
B:S9747-5.DAT	4/12/98	13	4	12	0.0018901243	25.0	0.00189332	0.000001777
B:S9747-6.DAT	4/12/98	13	23	13	0.0018900758	21.3	0.00188637	0.000001895
B:S9747-7.DAT	4/12/98	14	47	16	0.0018899304	20.7	0.00188507	0.000001831
B:S9747-8.DAT	4/12/98	15	6	17	0.0018898819	21.8	0.00188717	0.000001707
B:S9747-9.DAT	4/12/98	15	32	18	0.0018898334	21.9	0.00188728	0.000001785
B:S9747-10.DAT	4/12/98	15	59	19	0.0018897849	-20.3	0.00180925	0.000001485
B:S9747-11.DAT	4/12/98	16	30	20	0.0018897364	19.7	0.00188310	0.000001677
B:S9747-12.DAT	4/12/98	16	50	21	0.0018896879	23.3	0.00188966	0.000001770
B:S9747-13.DAT	4/12/98	18	13	24	0.0018895424	22.4	0.00188788	0.000001742
B:S9747-14.DAT	4/12/98	18	40	25	0.0018894939	19.8	0.00188308	0.000001711
B:S9747-15.DAT	4/12/98	19	0	26	0.0018894455	26.6	0.00189545	0.000001708
B:S9747-16.DAT	4/12/98	19	20	27	0.0018893970	21.4	0.00188592	0.000001708

S'97/97B

sample/analysis	Date	hrs	min	no.	corr standard	δ18O	18O/16O ratio	error 1σ
B:9797B-1.DAT	7/12/98	13	46	17	0.0018882362	19.6	0.00188134	0.000002340
B:9797B-2.DAT	7/12/98	14	5	18	0.0018879810	14.6	0.00187194	0.000001830
B:9797B-3.DAT	7/12/98	14	23	19	0.0018877257	16.0	0.00187417	0.000001823
B:9797B-4.DAT	7/12/98	15	12	21	0.0018872151	15.8	0.00187341	0.000001959
B:9797B-5.DAT	7/12/98	15	31	22	0.0018869598	16.6	0.00187459	0.000001999
B:9797B-6.DAT	7/12/98	15	49	23	0.0018867045	15.4	0.00187221	0.000001893
B:9797B-7.DAT	7/12/98	16	7	24	0.0018864492	16.0	0.00187299	0.000001857
B:9797B-8.DAT	7/12/98	16	26	25	0.0018861939	15.9	0.00187249	0.000002011
B:9797B-9.DAT	7/12/98	16	44	26	0.0018859386	17.0	0.00187424	0.000001906
B:97978-10.DAT	7/12/98	17	5	27	0.0018856834	15.8	0.00187186	0.000002125
B:9797B-11.DAT	7/12/98	18	32	31	0.0018846622	22.1	0.00188242	0.000001913
B:9797B-12.DAT	7/12/98	18	51	32	0.0018844069	24.9	0.00188731	0.000001650
B:9797B-13.DAT	7/12/98	19	9	33	0.0018841516	25.7	0.00188864	0.000002055
B:9797B-14.DAT	7/12/98	19	27	34	0.0018838963	20.3	0.00187829	0.000001735
B:9797B-15.DAT	7/12/98	19	46	35	0.0018836410	24.2	0.00188524	0.000001771
B:9797B-16.DAT	7/12/98	20	5	36	0.0018833858	24.8	0.00188609	0.000001758
B:9797B-17.DAT	7/12/98	20	24	37	0.0018831305	21.7	0.00188026	0.000001900
B:9797B-18.DAT	7/12/98	20	42	38	0.0018828752	24.7	0.00188553	0.000001952
B:9797B-19.DAT	7/12/98	21	49	41	0.0018821093	16.7	0.00186997	0.000002005
B:9797B-20.DAT	7/12/98	22	7	42	0.0018818540	23.7	0.00188256	0.000001817
B:9797B-22.DAT	7/12/98	22	25	43	0.0018815987	22.8	0.00188071	0.000001898
B:9797B-21.DAT	7/12/98	22	45	44	0.0018813434	21.2	0.00187743	0.000001980
B:9797B-23.DAT	7/12/98	23	3	45	0.0018810882	20.3	0.00187564	0.000001813
B:9797B-24.DAT	7/12/98	23	21	46	0.0018808329	23.7	0.00188161	0.000001743
B:9797B-25.DAT	7/12/98	23	41	47	0.0018805776	24.3	0.00188236	0.000001835
B:9797B-27.DAT	8/12/98	0	2	48	0.0018803223	26.7	0.00188664	0.000001581
B:9797B-26.DAT	8/12/98	0	20	49	0.0018800670	21.1	0.00187607	0.000001511

S'97/101

sample/analysis	Date	hrs	min	no.	corr standard	δ18O	18O/16O ratio	error 1σ
B:97101-1.DAT	8/12/98	22	4	41	0.0018816605	32.5	0.00189856	0.000001769
B:97101-2.DAT	8/12/98	22	22	42	0.0018816148	29.2	0.00189245	0.000001888
B:97101-3.DAT	8/12/98	22	41	43	0.0018815691	29.8	0.00189345	0.000001675
B:97101-4.DAT	8/12/98	22	59	44	0.0018815234	33.3	0.00189995	0.000001799
B:97101-5.DAT	8/12/98	23	18	45	0.0018814777	21.0	0.00187732	0.000001839
B:97101-6.DAT	8/12/98	23	36	46	0.0018814319	19.0	0.00187349	0.000001638
B:97101-7.DAT	8/12/98	23	54	47	0.0018813862	20.6	0.00187640	0.000001894
B:97101-8.DAT	9/12/98	0	13	48	0.0018813405	28.8	0.00189138	0.000002045
B:97101-9.DAT	9/12/98	0	32	49	0.0018812948	33.8	0.00190065	0.000002108
B:97101-10.DAT	14/12/98	12	51	8	0.0018825333	29.8	0.00189443	0.000001731
B:97101-11.DAT	14/12/98	13	10	9	0.0018824180	30.5	0.00189568	0.000001980
B:97101-12.DAT	14/12/98	13	29	10	0.0018823026	29.0	0.00189280	0.000001663
B:97101-13.DAT	14/12/98	13	47	11	0.0018821873	18.7	0.00187366	0.000001624
B:97101-14.DAT	14/12/98	14	6	12	0.0018820720	16.4	0.00186936	0.000001792
B:97101-15.DAT	14/12/98	15	13	15	0.0018817260	30.6	0.00189512	0.000001872
B:97101-16.DAT	14/12/98	15	32	16	0.0018816106	30.8	0.00189531	0.000001826
B:97101-17.DAT	14/12/98	15	50	17	0.0018814953	33.2	0.00189975	0.000001864
B:97101-25.DAT	18/12/98	3	12	14	0.0018816914	18.6	0.00187303	0.000001880
B:97101-26.DAT	18/12/98	3	31	15	0.0018817439	19.5	0.00187478	0.000001741
B:97101-27.DAT	18/12/98	3	50	16	0.0018817964	27.9	0.00189028	0.000001842
B:97101-28.DAT	18/12/98	4	9	17	0.0018818489	29.0	0.00189227	0.000001941

B:97101-29.DAT	18/12/98	4	28	18	0.0018819014	16.3	0.00186904	0.000001536

S'97/101 qz

sample/analysis	Date	hrs	min	no.	corr standard	δ18O	18O/16O ratio	error 1σ
B:97101-18.DAT	17/12/98	17	58	30	0.0018786422	29.7	0.00191087	0.000001688
B:97101-19.DAT	17/12/98	18	16	31	0.0018785265	27.5	0.00190669	0.000001971
B:97101-20.DAT	17/12/98	18	34	32	0.0018784109	29.1	0.00190959	0.000001771
B:97101-21.DAT	17/12/98	18	53	33	0.0018782952	27.0	0.00190551	0.000001672
B:97101-22.DAT	17/12/98	19	11	34	0.0018781795	29.4	0.00190997	0.000001833
B:97101-23.DAT	17/12/98	19	30	35	0.0018780638	30.8	0.00191233	0.000001813
B:97101-24.DAT	17/12/98	19	49	36	0.0018779482	21.1	0.00189427	0.000001615

S'97/102

sample/analysis	Date	hrs	min	no.	corr standard	δ18O	18O/16O ratio	error 1σ
B:97102-1.DAT	8/12/98	10	59	8	0.0018831688	26.9	0.00188973	0.000001800
B:97102-2.DAT	8/12/98	11	18	9	0.0018831231	31.0	0.00189735	0.000001612
B:97102-3.DAT	8/12/98	11	37	10	0.0018830774	30.7	0.00189678	0.000001721
B:97102-4.DAT	8/12/98	11	57	11	0.0018830317	30.4	0.00189608	0.000001988
B:97102-5.DAT	8/12/98	12	15	12	0.0018829860	30.6	0.00189643	0.000001874
B:97102-6.DAT	8/12/98	12	34	13	0.0018829403	30.6	0.00189642	0.000001751
B:97102-7.DAT	8/12/98	12	53	14	0.0018828946	31.9	0.00189874	0.000001707
B:97102-8.DAT	8/12/98	13	11	15	0.0018828488	32.3	0.00189948	0.000001614
B:97102-9.DAT	8/12/98	13	30	16	0.0018828031	32.0	0.00189875	0.000001982
B:97102-10.DAT	8/12/98	14	58	20	0.0018826203	32.7	0.00189985	0.000001905
B:97102-11.DAT	8/12/98	15	17	21	0.0018825746	31.2	0.00189716	0.000001602
B:97102-12.DAT	8/12/98	15	37	22	0.0018825289	31.9	0.00189843	0.000001721
B:97102-13.DAT	8/12/98	15	56	23	0.0018824832	30.2	0.00189521	0.000001752
B:97102-14.DAT	8/12/98	16	15	24	0.0018824375	30.2	0.00189521	0.000001768
B:97102-15.DAT	8/12/98	16	33	25	0.0018823918	31.5	0.00189743	0.000001895
B:97102-16.DAT	8/12/98	16	52	26	0.0018823461	30.2	0.00189499	0.000001976
B:97102-17.DAT	8/12/98	18	16	30	0.0018821633	30.5	0.00189537	0.000001959
B:97102-18.DAT	8/12/98	18	35	31	0.0018821175	31.3	0.00189688	0.000001802
B:97102-19.DAT	8/12/98	18	54	32	0.0018820718	30.9	0.00189596	0.000002249
B:97102-20.DAT	8/12/98	19	12	33	0.0018820261	29.5	0.00189350	0.000001855
B:97102-21.DAT	8/12/98	19	37	34	0.0018819804	28.7	0.00189190	0.000001710
B:97102-22.DAT	8/12/98	19	56	35	0.0018819347	30.6	0.00189541	0.000002043
B:97102-23.DAT	8/12/98	20	17	36	0.0018818890	32.1	0.00189811	0.000001890
B:97102-24.DAT	8/12/98	20	35	37	0.0018818433	29.6	0.00189351	0.000001964
B:97102-25.DAT	15/12/98	15	19	20	0.0018821343	28.2	0.00189109	0.000001889
B:97102-26.DAT	15/12/98	15	42	21	0.0018820645	30.3	0.00189499	0.000001464
B:97102-27.DAT	15/12/98	16	0	22	0.0018819947	18.8	0.00187378	0.000001875
B:97102-28.DAT	15/12/98	16	19	23	0.0018819249	16.9	0.00187011	0.000001781
B:97102-29.DAT	15/12/98	16	38	24	0.0018818552	17.6	0.00187131	0.000001903
B:97102-30.DAT	15/12/98	16	59	25	0.0018817854	20.7	0.00187708	0.000001795
B:97102-31.DAT	15/12/98	17	20	26	0.0018817156	23.0	0.00188113	0.000002078
B:97102-32.DAT	17/12/98	1	32	50	0.0018718775	17.6	0.00186137	0.000001578
B:97102-33.DAT	17/12/98	1	50	51	0.0018717725	23.2	0.00187152	0.000001736
B:97102-34.DAT	17/12/98	2	9	52	0.0018716674	23.6	0.00187213	0.000001687
B:97102-35.DAT	17/12/98	2	27	53	0.0018715624	25.1	0.00187488	0.000001812
B:97102-50.DAT	17/12/98	23	44	4	0.0018811664	22.3	0.00187942	0.000002010
B:97102-51.DAT	18/12/98	0	2	5	0.0018812189	16.5	0.00186868	0.000001876
B:97102-52.DAT	18/12/98	0	21	6	0.0018812714	14.7	0.00186541	0.000001624
B:97102-53.DAT	18/12/98	0	46	7	0.0018813239	10.5	0.00185772	0.000002012

B:97102-54.DAT	18/12/98	1	5	8	0.0018813764	13.7	0.00186381	0.000001838
B:97102-55.DAT	18/12/98	1	25	9	0.0018814289	13.8	0.00186395	0.000001951
B:97102-56.DAT	18/12/98	1	44	10	0.0018814814	13.1	0.00186279	0.000001719
B:97102-57.DAT	18/12/98	2	4	11	0.0018815339	25.5	0.00188557	0.000002041

S'97/102 qz

sample/analysis	Date	hrs	min	no.	corr standard	δ18O	18O/16O ratio	error 1σ
B:97102-36.DAT	17/12/98	11	44	11	0.0018808399	22.0	0.00189895	0.000001860
B:97102-37.DAT	17/12/98	12	3	12	0.0018807242	25.4	0.00190515	0.000001761
B:97102-38.DAT	17/12/98	12	21	13	0.0018806086	21.8	0.00189832	0.000001577
B:97102-39.DAT	17/12/98	12	40	14	0.0018804929	27.4	0.00190860	0.000001751
B:97102-40.DAT	17/12/98	12	58	15	0.0018803772	25.1	0.00190408	0.000001727
B:97102-41.DAT	17/12/98	13	18	16	0.0018802616	25.1	0.00190411	0.000001918
B:97102-42.DAT	17/12/98	13	36	17	0.0018801459	26.7	0.00190698	0.000001887
B:97102-43.DAT	17/12/98	15	0	21	0.0018796832	1.6	0.00185982	0.000001633
B:97102-44.DAT	17/12/98	15	19	22	0.0018795676	23.8	0.00190100	0.000001937
B:97102-45.DAT	17/12/98	15	37	23	0.0018794519	27.5	0.00190760	0.000002010
B:97102-46.DAT	17/12/98	15	56	24	0.0018793362	25.8	0.00190436	0.000001953
B:97102-47.DAT	17/12/98	16	14	25	0.0018792205	24.1	0.00190121	0.000001520
B:97102-48.DAT	17/12/98	16	33	26	0.0018791049	24.5	0.00190180	0.000001932
B:97102-49.DAT	17/12/98	16	55	27	0.0018789892	29.1	0.00191013	0.000001978

S'97/104

sample/analysis	Date	hrs	min	no.	corr standard	δ18O	18O/16O ratio	error 1σ
B:97104-1.DAT	16/12/98	20	52	37	0.0018732429	27.5	0.00188097	0.000001876
B:97104-2.DAT	16/12/98	21	10	38	0.0018731379	27.5	0.00188080	0.000001730
B:97104-3.DAT	16/12/98	21	29	39	0.0018730328	28.0	0.00188155	0.000001767
B:97104-4.DAT	16/12/98	21	47	40	0.0018729278	27.1	0.00187991	0.000001671
B:97104-5.DAT	16/12/98	22	6	41	0.0018728228	27.4	0.00188040	0.000001760
B:97104-6.DAT	16/12/98	22	24	42	0.0018727177	28.4	0.00188208	0.000001882
B:97104-7.DAT	16/12/98	22	47	43	0.0018726127	27.8	0.00188081	0.000002026
B:97104-8.DAT	16/12/98	23	6	44	0.0018725077	28.6	0.00188222	0.000002009
B:97104-9.DAT	16/12/98	23	24	45	0.0018724027	27.4	0.00187989	0.000002109
B:97104-10.DAT	16/12/98	23	43	46	0.0018722976	28.1	0.00188117	0.000001671

File	Date	Hrs	Min	No.	corr standard	Delta	18/16 Ratio	Error	AVG	STD
Standards						12.3		1σ		DEV
4/11/98										
B:UWC16-1.DAT	3/12/98	14	47	10	0.001894433	23.8	1.8953E-03	1.8E-06		
B:UWC16-2.DAT	3/12/98	15	7	11	0.001893633	23.4	1.8937E-03	1.7E-06		
B:UWC16-3.DAT	3/12/98	15	27	12	0.001892833	24.0	1.8941E-03	1.7E-06		
B:UWC16-4.DAT	3/12/98	15	47	13	0.001892033	18.9	1.8839E-03	1.6E-06		
B:UWC16-5.DAT	3/12/98	16	6	14	0.001891232	25.8	1.8959E-03	1.8E-06		
B:UWC16-6.DAT	3/12/98	16	25	15	0.001890432	24.0	1.8918E-03	2.0E-06		
B:UWC16-7.DAT	3/12/98	16	45	16	0.001889632	24.9	1.8927E-03	1.7E-06		
B:UWC16-8.DAT	3/12/98	17	4	17	0.001888832	21.6	1.8857E-03	1.8E-06	23.3	2.16
4/12/1998										
B:UWC16-9.DAT	4/12/98	9	15	2	0.001890609	23.1	1.8902E-03	1.9E-06		
B:UWC16-10.DAT	4/12/98	9	35	3	0.001890561	22.0	1.8882E-03	1.8E-06		
B:UXC16-11.DAT	4/12/98	9	53	4	0.001890512	22.5	1.8891E-03	1.7E-06		
B:UWC16-12.DAT	4/12/98	10	11	5	0.001890464	22.7	1.8893E-03	2.0E-06		
B:UWC16-13.DAT	4/12/98	10	33	6	0.001890415	23.7	1.8911E-03	2.0E-06		
B:UWC16-14.DAT	4/12/98	10	52	7	0.001890367	24.9	1.8933E-03	1.8E-06		
B:UWC16-15.DAT	4/12/98	13	55	14	0.001890027	24.2	1.8918E-03	1.9E-06		
B:UWC16-16.DAT	4/12/98	14	14	15	0.001889979	22.7	1.8890E-03	2.0E-06		
B:UWC16-17.DAT	4/12/98	17	20	22	0.001889639	24.6	1.8921E-03	1.5E-06		
B:UWC16-18.DAT	4/12/98	17	39	23	0.001889591	24.1	1.8911E-03	1.9E-06		
B:UWC16-19.DAT	4/12/98	19	58	28	0.001889348	20.3	1.8838E-03	1.6E-06		
B:UWC16-20.DAT	4/12/98	20	17	29	0.0018893	24.5	1.8915E-03	1.9E-06		
B:UWC16-21.DAT	4/12/98	20	36	30	0.001889251	24.2	1.8909E-03	2.0E-06		
B:UWC16-22.DAT	5/12/98	0	20	40	0.001888767	26.2	1.8941E-03	1.8E-06		
B:UWC16-23.DAT	5/12/98	0	39	41	0.001888718	22.7	1.8877E-03	2.0E-06		
B:UWC16-24.DAT	5/12/98	0	58	42	0.00188867	21.3	1.8850E-03	1.6E-06		
B:UWC16-25.DAT	5/12/98	1	18	43	0.001888621	22.4	1.8869E-03	2.0E-06	23.3	1.45

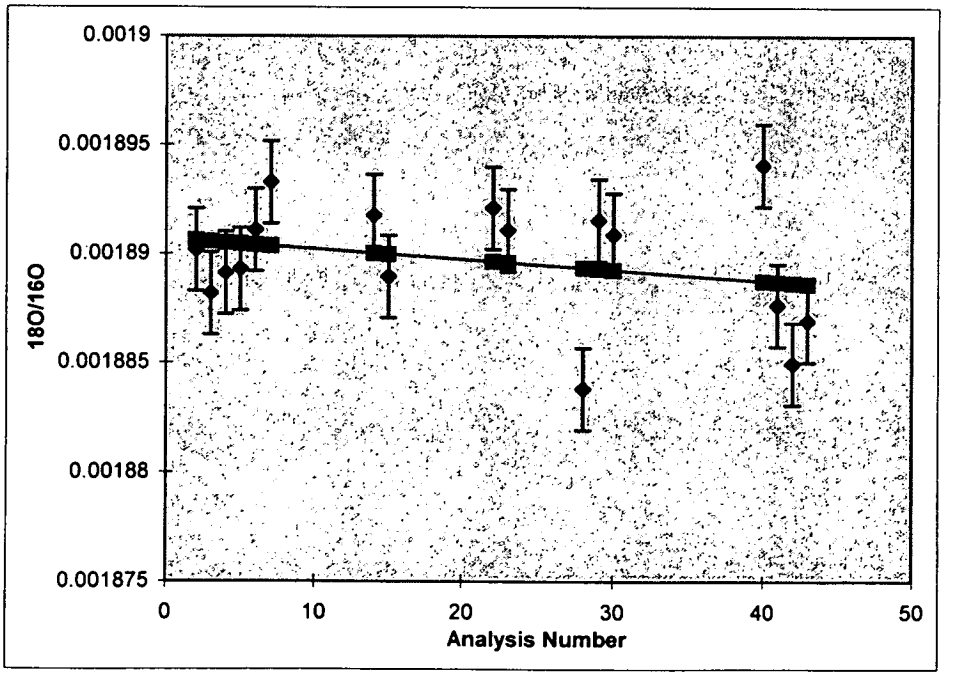

File	Date	Hrs	Min	No.	corr standard	Delta	18/16 Ratio	Error	AVG	STD
Standards						12.3		1σ		DEV
6/12/1998										
B:UWC16-26.DAT	*5/12/98*	*8*	*36*	*2*	*0.001887828*	***18.3***	*1.8786E-03*	*1.7E-06*		
B:UWC16-27.DAT	5/12/98	8	54	3	0.001887841	**24.6**	1.8903E-03	1.6E-06		
B:UWC16-28.DAT	5/12/98	9	13	4	0.001887853	**22.4**	1.8861E-03	1.6E-06		
B:UWC16-29.DAT	5/12/98	9	31	5	0.001887865	**26.3**	1.8935E-03	2.0E-06		
B:UWC16-30.DAT	5/12/98	9	49	6	0.001887878	**25.2**	1.8914E-03	1.5E-06		
B:UWC16-31.DAT	5/12/98	10	7	7	0.00188789	**21.4**	1.8843E-03	1.6E-06		
B:UWC16-32.DAT	5/12/98	10	26	8	0.001887902	**20.9**	1.8834E-03	1.5E-06		
B:UWC16-33.DAT	5/12/98	13	36	16	0.001888001	**22.7**	1.8869E-03	1.7E-06		
B:UWC16-34.DAT	5/12/98	13	55	17	0.001888013	**22.9**	1.8872E-03	2.1E-06		
B:UWC16-35.DAT	5/12/98	16	43	25	0.001888111	**22.3**	1.8863E-03	1.5E-06		
B:UWC16-36.DAT	5/12/98	17	2	26	0.001888124	**22.7**	1.8870E-03	1.7E-06		
B:UWC16-37.DAT	5/12/98	20	12	35	0.001888234	**22.2**	1.8861E-03	1.7E-06		
B:UWC16-38.DAT	5/12/98	20	30	36	0.001888247	**26.6**	1.8943E-03	1.5E-06		
B:UWC16-39.DAT	5/12/98	20	51	37	0.001888259	**22.7**	1.8871E-03	1.8E-06		
B:UWC16-40.DAT	6/12/98	0	34	47	0.001888382	**21.6**	1.8852E-03	2.0E-06		
B:UWC16-41.DAT	6/12/98	0	52	48	0.001888394	**23.6**	1.8890E-03	1.4E-06		
B:UWC16-42.DAT	6/12/98	1	12	49	0.001888407	**24.7**	1.8911E-03	2.0E-06	**23.0**	**2.07**

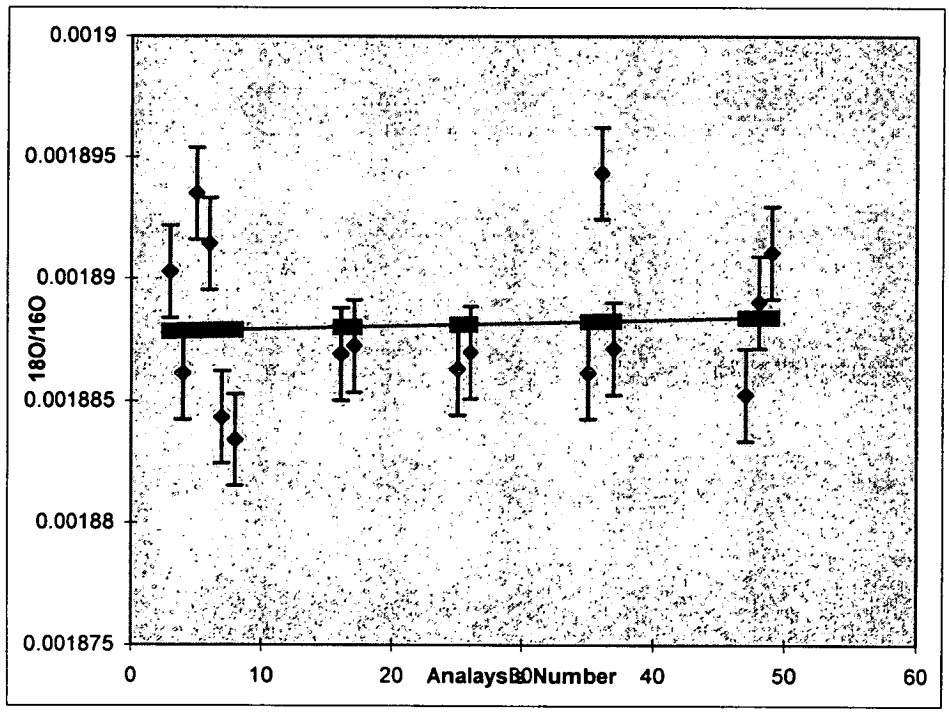

File	Date	Hrs	Min	No.	corr standard	Delta	18/16 Ratio	Error	AVG	STD
Standards						12.3		1σ		DEV
6/12/1998										
B:UWC16-43.DAT	6/12/98	8	40	2	0.00189289	24.3	1.8947E-03	1.7E-06		
B:UWC16-44.DAT	6/12/98	8	59	3	0.001892851	23.1	1.8925E-03	2.0E-06		
B:UWC16-45.DAT	6/12/98	9	17	4	0.001892813	23.0	1.8923E-03	1.7E-06		
B:UWC16-46.DAT	6/12/98	9	35	5	0.001892774	25.0	1.8960E-03	1.7E-06		
B:UWC16-47.DAT	6/12/98	9	53	6	0.001892736	22.3	1.8909E-03	1.7E-06		
B:UWC16-48.DAT	6/12/98	10	12	7	0.001892697	24.7	1.8953E-03	1.7E-06		
B:UWC16-49.DAT	6/12/98	10	31	8	0.001892659	23.6	1.8932E-03	1.7E-06		
B:UWC16-50.DAT	6/12/98	10	50	9	0.00189262	21.6	1.8895E-03	1.9E-06		
B:UWC16-51.DAT	6/12/98	13	59	18	0.001892274	21.9	1.8897E-03	2.1E-06		
B:UWC16-52.DAT	6/12/98	14	18	19	0.001892235	22.4	1.8906E-03	2.1E-06		
B:UWC16-53.DAT	6/12/98	18	2	28	0.001891889	22.9	1.8911E-03	1.7E-06		
B:UWC16-54.DAT	6/12/98	18	20	29	0.00189185	23.4	1.8921E-03	1.9E-06		
B:UWC16-55.DAT	6/12/98	18	41	30	0.001891812	22.6	1.8906E-03	2.0E-06		
B:UWC16-56.DAT	6/12/98	21	37	38	0.001891503	24.7	1.8941E-03	2.0E-06		
B:UWC16-57.DAT	6/12/98	21	55	39	0.001891465	24.7	1.8941E-03	1.8E-06		
B:UWC16-58.DAT	7/12/98	0	21	46	0.001891195	22.9	1.8904E-03	1.7E-06		
B:UWC16-59.DAT	7/12/98	0	39	47	0.001891157	22.9	1.8904E-03	1.7E-06	23.3	1.06

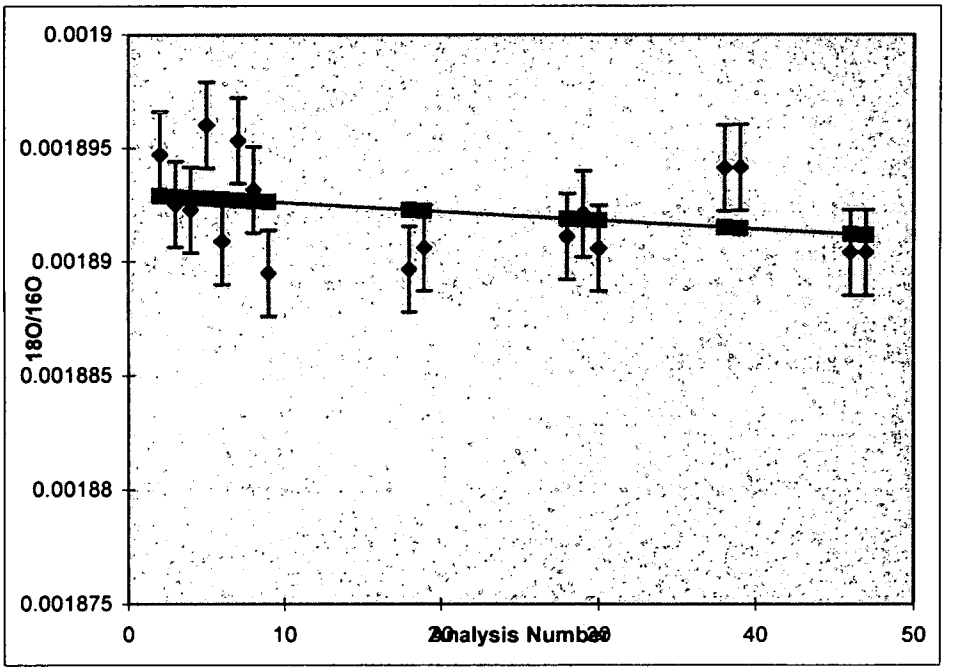

File	Date	Hrs	Min	No.	corr standard	Delta	18/16 Ratio	Error	AVG	STD
Standards						12.3		1σ		DEV
7/12/1998										
B:UWC16-60.DAT	7/12/98	8	40	2	0.001892066	24.8	1.89E-03	2.06E-06		
B:UWC16-61.DAT	7/12/98	8	58	3	0.00189181	25.5	1.90E-03	1.41E-06		
B:UWC16-63.DAT	7/12/98	9	16	4	0.001891555	22.2	1.89E-03	1.78E-06		
B:UWC16-65.DAT	7/12/98	9	54	6	0.001891044	22.2	1.89E-03	1.91E-06		
B:UWC16-66.DAT	7/12/98	10	13	7	0.001890789	22.3	1.89E-03	1.74E-06		
B:UWC16-67.DAT	7/12/98	10	32	8	0.001890534	22.4	1.89E-03	1.85E-06		
B:UWC16-68.DAT	7/12/98	12	37	14	0.001889002	23.6	1.89E-03	1.74E-06		
B:UWC16-69.DAT	7/12/98	12	56	15	0.001888747	24.4	1.89E-03	1.98E-06		
B:UWC16-70.DAT	7/12/98	13	14	16	0.001888492	22.4	1.89E-03	1.94E-06		
B:UWC16-71.DAT	7/12/98	14	49	20	0.00188747	23.2	1.89E-03	1.58E-06		
B:UWC16-72.DAT	7/12/98	17	30	28	0.001885428	22.8	1.88E-03	1.54E-06		
B:UWC16-73.DAT	7/12/98	17	49	29	0.001885173	24.3	1.89E-03	1.65E-06		
B:UWC16-74.DAT	7/12/98	18	8	30	0.001884917	23.3	1.88E-03	1.60E-06		
B:UWC16-75.DAT	7/12/98	21	6	39	0.00188262	22.3	1.88E-03	2.04E-06		
B:UWC16-76.DAT	7/12/98	21	25	40	0.001882365	22.6	1.88E-03	1.92E-06		
B:UWC16-77.DAT	8/12/98	0	44	50	0.001879812	24.4	1.88E-03	1.86E-06		
B:UWC16-78.DAT	8/12/98	1	2	51	0.001879556	23.5	1.88E-03	1.54E-06	23.3	1.03

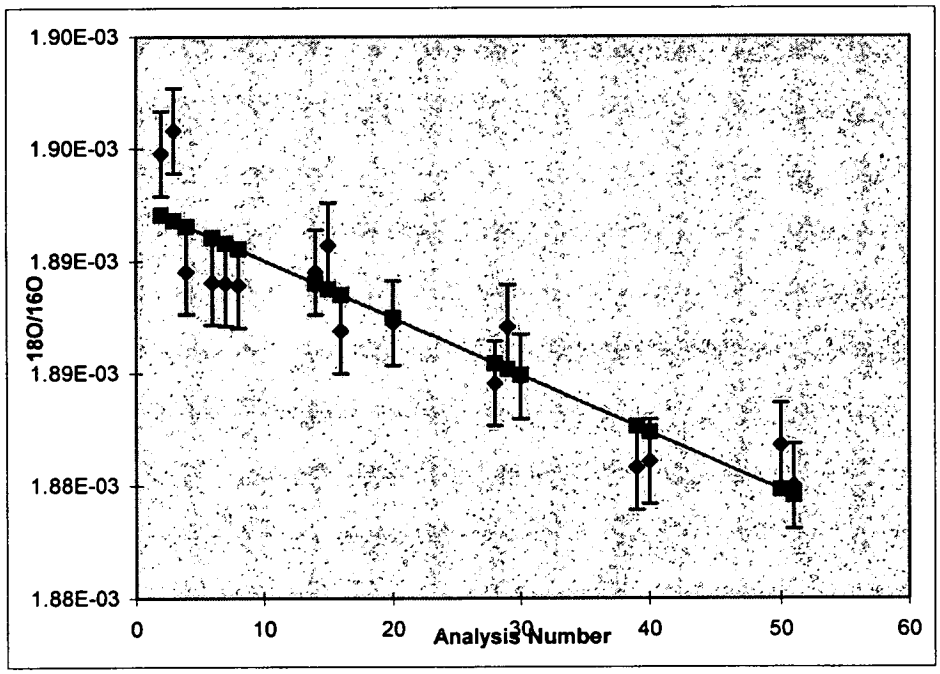

File	Date	Hrs	Min	No.	corr standard	Delta	18/16 Ratio	Error	AVG	STD
Standards						12.3		1σ		DEV
8/12/1998										
B:UWC16-80.DAT	8/12/98	8	47	2	0.001883443	23.8	1.88E-03	1.96E-06		
B:UWC16-81.DAT	8/12/98	9	6	3	0.001883397	22.8	1.88E-03	1.73E-06		
B:UWC16-82.DAT	8/12/98	9	23	4	0.001883352	23.0	1.88E-03	1.87E-06		
B:UWC16-83.DAT	8/12/98	9	41	5	0.001883306	23.7	1.88E-03	1.71E-06		
B:UWC16-84.DAT	8/12/98	9	59	6	0.00188326	22.8	1.88E-03	1.76E-06		
B:UWC16-85.DAT	8/12/98	10	18	7	0.001883214	23.3	1.88E-03	2.16E-06		
B:UWC16-86.DAT	8/12/98	13	54	17	0.001882757	24.6	1.89E-03	1.59E-06		
B:UWC16-87.DAT	8/12/98	14	12	18	0.001882712	22.9	1.88E-03	2.01E-06		
B:UWC16-88.DAT	8/12/98	14	31	19	0.001882666	23.7	1.88E-03	1.94E-06		
B:UWC16-89.DAT	8/12/98	17	14	27	0.0018823	22.2	1.88E-03	1.60E-06		
B:UWC16-90.DAT	8/12/98	17	33	28	0.001882255	23.8	1.88E-03	2.05E-06		
B:UWC16-91.DAT	8/12/98	17	52	29	0.001882209	23.8	1.88E-03	1.96E-06		
B:UWC16-92.DAT	8/12/98	20	58	38	0.001881798	23.6	1.88E-03	1.89E-06		
B:UWC16-93.DAT	8/12/98	21	16	39	0.001881752	21.8	1.88E-03	2.01E-06		
B:UWC16-94.DAT	8/12/98	21	35	40	0.001881706	22.3	1.88E-03	1.84E-06		
B:UWC16-95.DAT	9/12/98	0	55	50	0.001881249	24.3	1.88E-03	2.17E-06		
B:UWC16-96.DAT	9/12/98	1	14	51	0.001881203	23.7	1.88E-03	1.60E-06	23.3	0.76

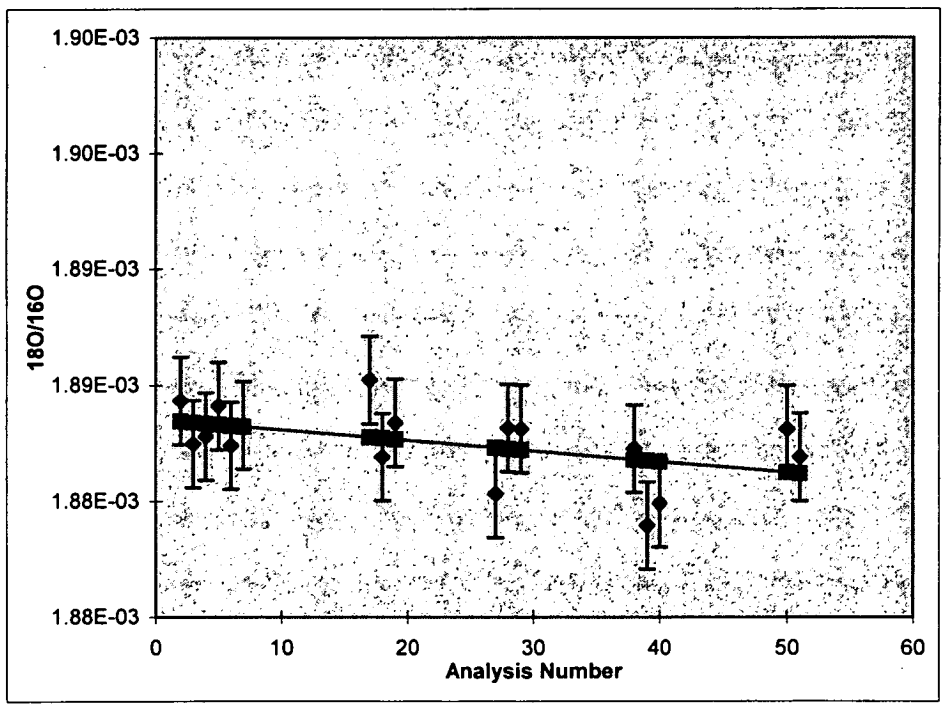

File	Date	Hrs	Min	No.	corr standard	Delta	18/16 Ratio	Error	AVG	STD
Standards						12.3		1σ		DEV
14/12/98										
B:UWC16-97.DAT	14/12/98	10	48	2	0.001883225	22.5	1.88E-03	2.32E-06		
B:UWC16-98.DAT	14/12/98	11	8	3	0.00188311	23.3	1.88E-03	1.99E-06		
B:UWC16-99.DAT	14/12/98	11	27	4	0.001882995	24.4	1.89E-03	1.61E-06		
B:UWC16-10.DAT	14/12/98	11	46	5	0.001882879	21.9	1.88E-03	1.85E-06		
B:UWC16-11.DAT	14/12/98	12	4	6	0.001882764	23.1	1.88E-03	1.81E-06		
B:UWC16-12.DAT	14/12/98	12	24	7	0.001882649	24.0	1.88E-03	1.73E-06		
B:UWC16-13.DAT	14/12/98	14	29	13	0.001881957	23.3	1.88E-03	1.67E-06		
B:UWC16-14.DAT	14/12/98	14	48	14	0.001881841	23.5	1.88E-03	1.68E-06		
B:UWC16-15.DAT	14/12/98	16	14	18	0.00188138	23.7	1.88E-03	1.71E-06		
B:UWC16-16.DAT	14/12/98	16	33	19	0.001881265	23.8	1.88E-03	1.70E-06		
B:UWC16-17.DAT	14/12/98	19	44	28	0.001880227	23.6	1.88E-03	2.05E-06		
B:UWC16-18.DAT	14/12/98	20	2	29	0.001880111	23.7	1.88E-03	1.69E-06		
B:UWC1-19.DAT	14/12/98	23	0	38	0.001879073	24.7	1.88E-03	1.92E-06		
B:UWC16-20.DAT	14/12/98	23	18	39	0.001878958	21.0	1.87E-03	1.80E-06		
B:UWC16-21.DAT	14/12/98	23	37	40	0.001878843	22.5	1.88E-03	2.14E-06		
B:UWC16-22.DAT	14/12/98	23	55	41	0.001878727	21.9	1.88E-03	1.65E-06		
B:UWC16-23.DAT	15/12/98	1	46	46	0.001878151	24.5	1.88E-03	1.75E-06		
B:UWC16-24.DAT	15/12/98	2	6	47	0.001878035	23.9	1.88E-03	2.05E-06	23.3	0.99

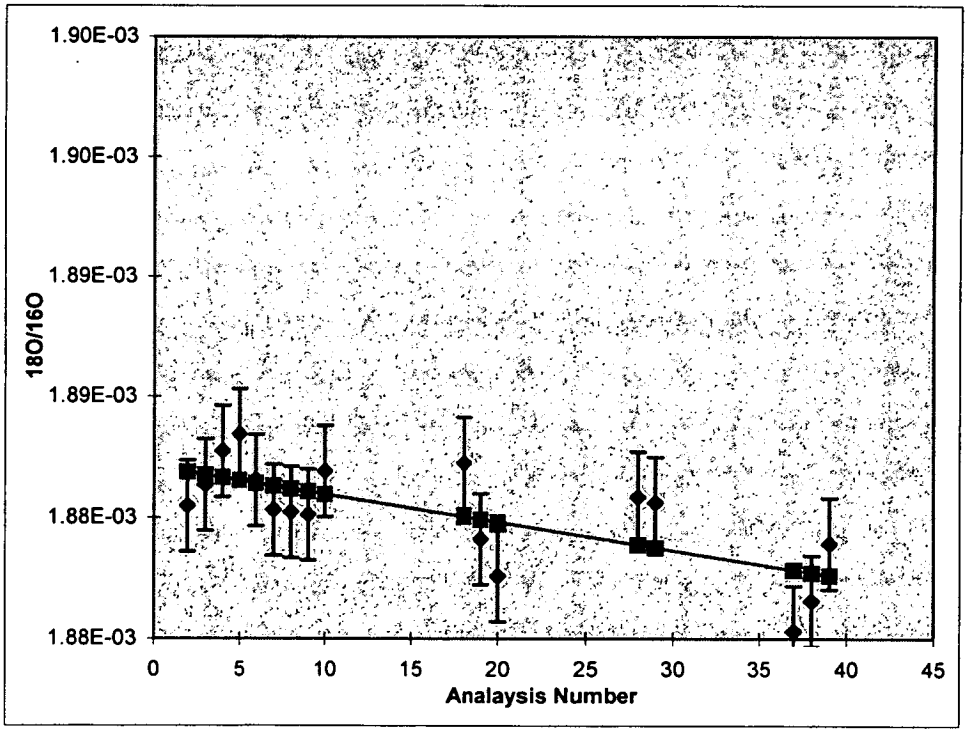

File	Date	Hrs	Min	No.	corr standard	Delta	18/16 Ratio	Error	AVG	STD
Standards						12.3		1σ		DEV
15/12/1998										
B:UWC16-25.DAT	15/12/98	8	33	1	0.00188346	23.8	1.88E-03	2.01E-06		
B:UWC16-27.DAT	15/12/98	9	11	3	0.00188332	23.2	1.88E-03	1.93E-06		
B:UWC16-28.DAT	15/12/98	9	31	4	0.001883251	22.5	1.88E-03	1.82E-06		
B:UWC16-30.DAT	15/12/98	10	22	6	0.001883111	23.0	1.88E-03	1.67E-06		
B:UWC16-31.DAT	15/12/98	10	39	7	0.001883041	21.9	1.88E-03	1.96E-06		
B:UWC16-32.DAT	15/12/98	10	57	8	0.001882972	22.7	1.88E-03	1.76E-06		
B:UWC16-33.DAT	15/12/98	11	16	9	0.001882902	24.8	1.89E-03	1.94E-06		
B:UWC16-34.DAT	15/12/98	11	35	10	0.001882832	23.2	1.88E-03	1.60E-06		
B:UWC16-35.DAT	15/12/98	14	14	17	0.001882344	24.8	1.89E-03	1.57E-06		
B:UWC16-36.DAT	15/12/98	14	34	18	0.001882274	23.4	1.88E-03	1.78E-06		
B:UWC16-37.DAT	15/12/98	14	52	19	0.001882204	23.9	1.88E-03	1.88E-06		
B:UWC16-38.DAT	15/12/98	17	41	27	0.001881646	23.4	1.88E-03	1.65E-06		
B:UWC16-39.DAT	15/12/98	18	0	28	0.001881576	23.2	1.88E-03	1.66E-06		
B:UWC16-40.DAT	15/12/98	21	44	38	0.001880878	22.9	1.88E-03	1.78E-06		
B:UWC16-41.DAT	15/12/98	22	3	39	0.001880809	23.4	1.88E-03	1.80E-06		
B:UWC16-42.DAT	16/12/98	0	43	46	0.00188032	23.6	1.88E-03	1.75E-06		
B:UWC16-43.DAT	16/12/98	1	2	47	0.00188025	22.4	1.88E-03	1.79E-06		
B:UWC16-44.DAT	16/12/98	1	20	48	0.001880181	23.4	1.88E-03	1.73E-06	23.3	0.74

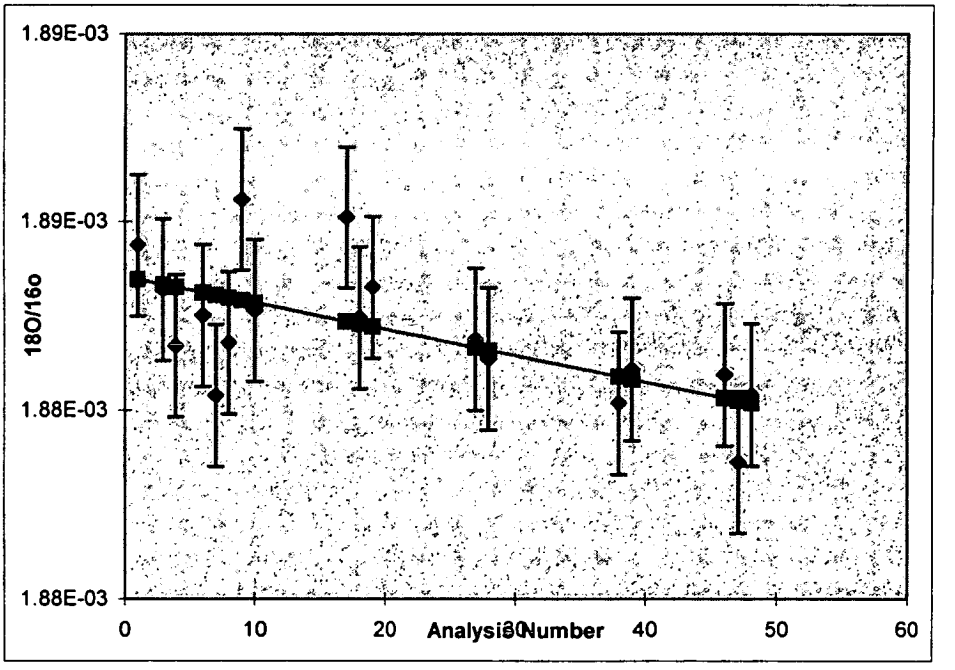

File	Date	Hrs	Min	No.	corr standard	Delta	18/16 Ratio	Error	AVG	STD
Standards						12.3		1σ		DEV
16/12/1998										
B:UWC16-45.DAT	16/12/98	8	11	1	0.001877024	22.3	1.88E-03	1.79E-06		
B:UWC16-46.DAT	16/12/98	8	30	2	0.001876919	23.8	1.88E-03	1.47E-06		
B:UWC16-47.DAT	16/12/98	8	48	3	0.001876814	25.2	1.88E-03	1.88E-06		
B:UWC16-48.DAT	16/12/98	9	6	4	0.001876709	23.6	1.88E-03	1.70E-06		
B:UWC17-1.DAT	16/12/98	9	24	5	0.001876604	23.2	1.88E-03	1.86E-06		
B:UWC17-2.DAT	16/12/98	9	42	6	0.001876499	21.2	1.87E-03	1.97E-06		
B:UWC17-3.DAT	16/12/98	10	0	7	0.001876394	23.9	1.88E-03	1.60E-06		
B:UWC17-4.DAT	16/12/98	10	19	8	0.001876289	23.0	1.88E-03	1.94E-06		
B:UWC17-5.DAT	16/12/98	10	37	9	0.001876184	24.7	1.88E-03	2.09E-06		
B:UWC17-6.DAT	16/12/98	10	56	10	0.001876079	22.7	1.87E-03	1.86E-06		
B:UWC17-7.DAT	16/12/98	13	40	17	0.001875343	23.8	1.88E-03	1.90E-06		
B:UWC17-18.DAT	16/12/98	13	58	18	0.001875238	22.0	1.87E-03	1.67E-06		
B:UWC17-19.DAT	16/12/98	16	29	25	0.001874503	23.9	1.88E-03	1.83E-06		
B:UWC17-20.DAT	16/12/98	16	48	26	0.001874398	23.2	1.87E-03	1.88E-06		
B:UWC17-21.DAT	16/12/98	20	6	35	0.001873453	23.2	1.87E-03	1.83E-06		
B:UWC17-22.DAT	16/12/98	20	24	36	0.001873348	22.6	1.87E-03	1.74E-06		
B:UWC17-23.DAT	17/12/98	0	8	47	0.001872193	22.4	1.87E-03	2.05E-06		
B:UWC17-24.DAT	17/12/98	0	26	48	0.001872088	23.9	1.87E-03	2.17E-06		
B:UWC17-25.DAT	17/12/98	0	45	49	0.001871983	23.9	1.87E-03	1.75E-06		
B:UWC17-26.DAT	17/12/98	2	51	54	0.001871457	23.6	1.87E-03	1.62E-06		
B:UWC17-27.DAT	17/12/98	3	10	55	0.001871352	23.4	1.87E-03	1.59E-06	23.3	0.91

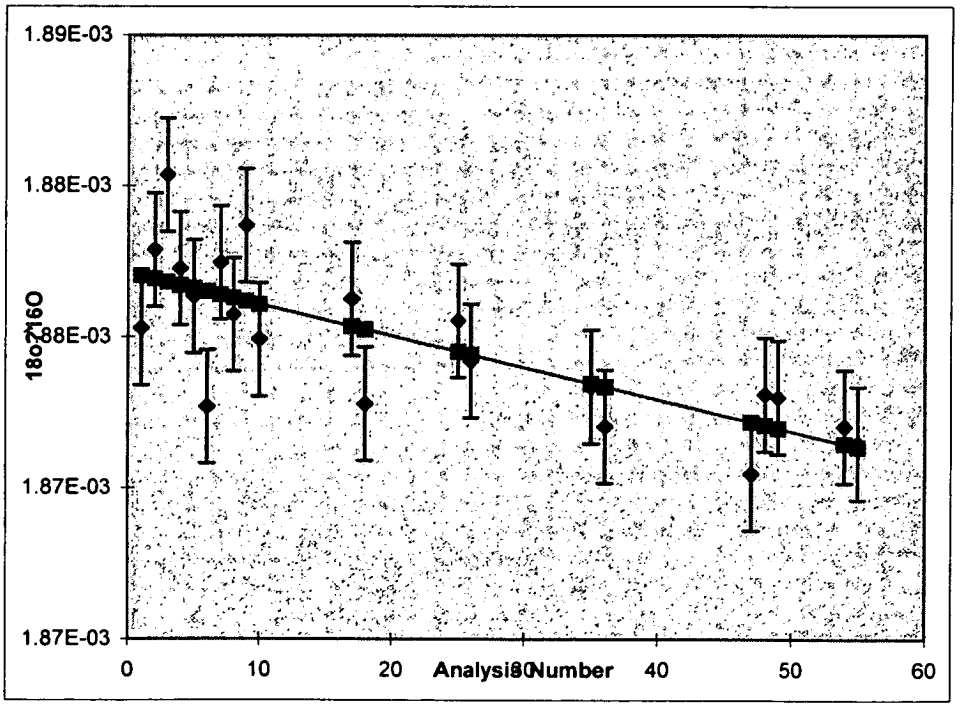

File	Date	Hrs	Min	No.	corr standard	Delta	18/16 Ratio	Error	AVG	STD
Standards						12.3		1σ		DEV.
17/2/1998										
B:UWC17-28.DAT	17/12/98	21	15	1	0.001881009	23.3	1.88E-03	2.10E-06		
B:UWC17-29.DAT	17/12/98	21	33	2	0.001881061	23.5	1.88E-03	1.90E-06		
B:UWC17-30.DAT	17/12/98	21	52	3	0.001881114	23.7	1.88E-03	1.95E-06		
B:UWC17-31.DAT	18/12/98	2	28	12	0.001881586	22.5	1.88E-03	1.90E-06		
B:UWC17-32.DAT	18/12/98	2	47	13	0.001881639	22.7	1.88E-03	1.98E-06		
B:UWC17-33.DAT	18/12/98	4	50	19	0.001881954	24.1	1.88E-03	2.21E-06		
B:UWC17-34.DAT	18/12/98	5	12	20	0.001882006	23.3	1.88E-03	2.07E-06	23.3	0.55

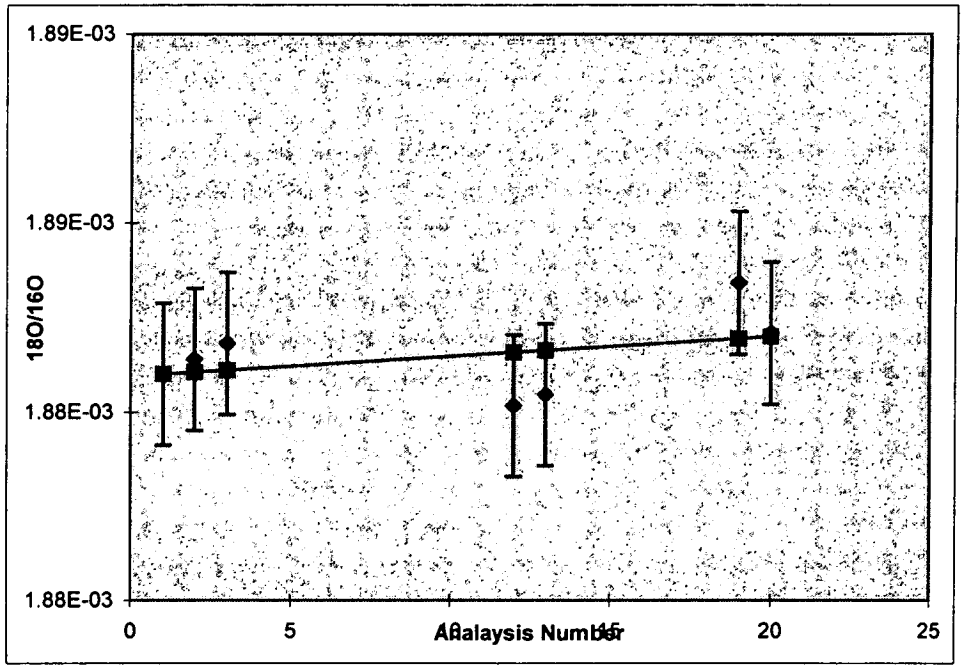

File	Date	Hrs	Min	No.	corr standard	Delta	18/16 Ratio	Error	AVG	STD
Standards						12.3		1σ		DEV
17/12/1998 (qz)										
B:BOG12-2.DAT	17/12/98	8	53	2	0.001881881	11.5	1.88E-03	1.70E-06		
B:BOG12-3.DAT	17/12/98	9	11	3	0.001881765	12.1	1.88E-03	1.85E-06		
B:BOG12-4.DAT	17/12/98	9	30	4	0.00188165	12.9	1.88E-03	1.99E-06		
B:BOG12-5.DAT	17/12/98	9	48	5	0.001881534	13.3	1.88E-03	1.55E-06		
B:BOG12-6.DAT	17/12/98	10	6	6	0.001881418	12.4	1.88E-03	1.63E-06		
B:BOG12-7.DAT	17/12/98	10	24	7	0.001881303	11.8	1.88E-03	1.59E-06		
B:BOG12-8.DAT	17/12/98	10	42	8	0.001881187	11.8	1.88E-03	1.98E-06		
B:BOG12-9.DAT	17/12/98	11	0	9	0.001881071	11.8	1.88E-03	1.84E-06		
B:BOG12-10.DAT	17/12/98	11	19	10	0.001880956	12.8	1.88E-03	1.67E-06		
B:BOG12-11.DAT	17/12/98	13	59	18	0.00188003	13.5	1.88E-03	1.77E-06		
B:BOG12-12.DAT	17/12/98	14	17	19	0.001879915	11.9	1.88E-03	2.15E-06		
B:BOG12-13.DAT	17/12/98	14	36	20	0.001879799	11.1	1.88E-03	1.92E-06		
B:BOG12-14.DAT	17/12/98	17	16	28	0.001878874	13.4	1.88E-03	2.12E-06		
B:BOG12-15.DAT	17/12/98	17	34	29	0.001878758	13.3	1.88E-03	1.63E-06		
B:BOG12-16.DAT	17/12/98	20	13	37	0.001877833	10.9	1.88E-03	1.77E-06		
B:BOG12-17.DAT	17/12/98	20	32	38	0.001877717	11.7	1.88E-03	2.08E-06		
B:BOG12-19.DAT	17/12/98	20	51	39	0.001877601	13.0	1.88E-03	1.97E-06	12.3	0.83

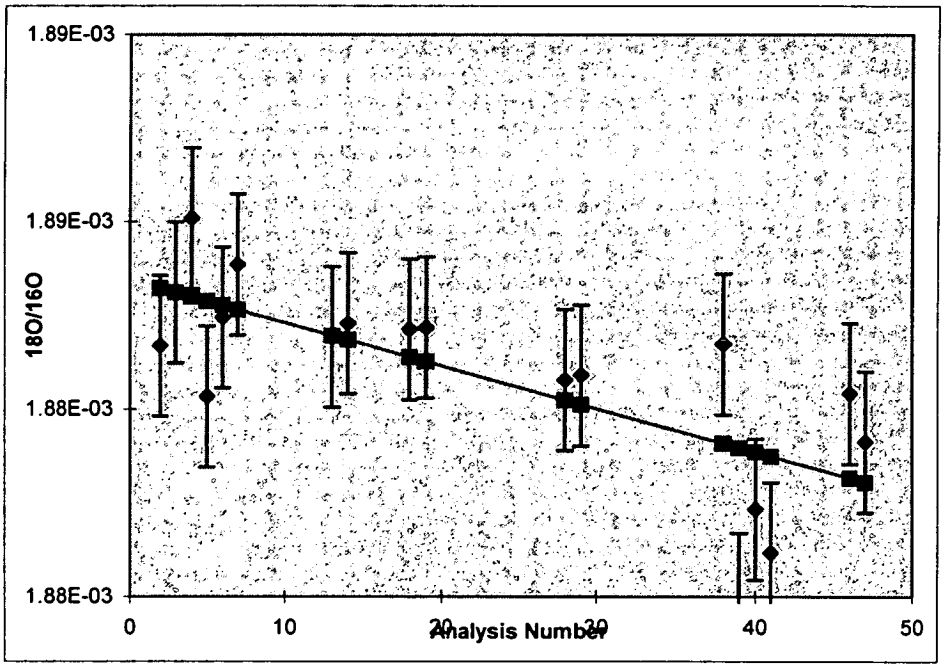

Appendix D Carbonate staining

Method

Thin sections from the boudianged marble band at Nites were stained with alizarin red and potassium ferricyanide. Staining was used to identify dolomite and ankerite within the calcite marble. Thin sections were stained and etched with 2 mg of stain and 2% hydrochloric acid for 75 seconds. The thin sections were washed and studied under an optical microscope. Table D1 describes the results of staining for different carbonate minerals. For further information see Dickson (1966).

Table D1 Reaction of common carbonates with stain, after Dickson (1966).

CARBONATE	ALIZARIN-RED	K-FERRICYANIDE	COMBINED RESULT
Rhodochrosite $MnCO_3$		Very pale brown	Very pale brown
Magnesite $MgCO_3$			
.Siderite $FeCO_3$			
Fe Dol		Pale-deep turquoise	Pale-deep turquoise
$Ca(Mg,Fe)(CO_3)_2$			
Dol $CaMg(CO_3)_2$			
Fe Calc$(Ca,Fe)CO_3$	Pink-pale pink	Pale-deep turquoise	Mauve-purple-royal blue
Calcite $CaCO_3$	Pink-pale pink		Pink-pale pink
Aragonite $CaCO_3$	Pale pink		Pale pink
Witherite $BaCO_3$	Red		Red
Cerussite $PbCO_3$	Mauve		Mauve

Appendix E Cathodoluminescence

Current usage

CL of carbonate is used to highlight chemical zonation and is commonly used in carbonate sedimentology (e.g. Tucker, 1992), to show grain overgrowth textures and growth zoning. Latterly it has also been used in metamorphic and fluid flow studies to highlight chemical alteration of calcite (e.g. Yardley & Lloyd, 1989; Lewis et al. 1998; Graham et al. 1998). In these studies brightly luminescent calcite has been used as an indicator for palaeo-fluid pathways, where infiltrating fluid is assumed to have caused chemical alteration. In this study polished thin sections were observed under cathodoluminesence (CL) to identify variations in the calcite trace element geochemistry.

Reasons for Luminescence

Luminescence is controlled by 'key' elements which act as activators or quenches. Carbonates are activated by the presence of Mn^{2+} but often also contain the quencher Fe^{2+}, the relative amounts of Mn^{2+} and Fe^{2+} in carbonate therefore play an important role in the luminescence characteristics of the sample. Luminescence is caused by excitation of electrons to higher energy levels. Electrons remain temporarily at the higher energy state before returning to the lower level and in doing so emit photons. The wavelength of the photon is determined by the energy difference between the two levels. The use of CL for analysis of geological materials is discussed in detail by Marshall (1988).

CL-setup & method

The set-up used in this study was a desk top petrographic microscope with a camera for photomicrographs and CL conversion. A cold cathode electron gun mounted on the side of the specimen chamber, which is pumped to vacuum, is used when in CL mode to bombard the sample with electrons. The electron bombardment excites electrons within the calcite to higher energy levels. To understand CL emission spectra the energy levels in the mineral under study must be known. In this

study CL was used qualitatively and an understanding of relative energy levels was not required. Relative luminescence within a single calcite thin section was used as an indication of chemical alteration. Due to changes in cathode gun voltage, current, the vacuum in the specimen chamber, as well as differences in photomicrograph exposure times and photograph development, relative luminescence of samples and photomicrographs of samples were not compared quantitatively.

Polished marble thin sections were placed in the specimen chamber which is sealed and pumped to a vacuum of approximately 10^{-1} mbar. The desk top set up has the advantage that the sample can be viewed with transmitted light or CL interchangeably. For the best results in CL mode the transmitted light must be switched off and the room darkened. The cathode gun was run at approximately 1173 μA and between 12-20 KeV.

Appendix F Electron probe detection limits

Electron probe set-up

The variations in trace element chemistry of calcite marble indicated by CL, were analysed with the Cameca, Camebax electron microprobe Edinburgh University, at the Department of Geology and Geophysics. Electron probe traverses of the calcite were completed across areas where a range in luminescence was identified. A 10 KV accelerating voltage and a beam current of 15 nA were used in raster mode due to the instability of calcite under the electron beam. Marble samples were polished and coated in carbon to minimise surface charging. The elements Mg, Fe, Ca, Mn, Si and Sr were analysed with the detection limits and errors were calculated using the method described below.

Calculations of detection limits

Average detection limits and errors were calculated from the counting statistics of an analysis. The average error is calculated by the following equation:

$$\%\ error = \frac{100}{\sqrt{T}\,\frac{((\sqrt{Rp}) - (\sqrt{Rb}))}{}}$$

where T is the count time on the peak, Rp is the counts per second on the peak and Rb is the counts per second on the back ground. The detection limits were also calculated to a 3σ confidence level:

$$detection\ limit = \frac{3}{m}\sqrt{\frac{Rb}{Tb}}$$

where m = counts /second / % element in material, Rb is the background count rate (counts / second), Tb the count time on the background. The factor m is calculated from the count rates obtained from the standard of each element; the counts per second are determined from the peak counts minus the background counts.

The count rates on the standard are used due to the poor precision on the unknown. The detection limits are given in table F1:

Table F1 Detection limits of elements

Element	Detection limit	error
Sr	> 0.05	+/-0.03 wt %
Mn	> 0.05	+/-0.03 wt %
Mg	> 0.07	+/-0.03 wt %
Fe	>0.05	+/-0.03 wt %

References

Ague J.J., 1997. Crustal mass transfer and index mineral growth in Barrow's garnet zone, northeast Scotland. *Geology.* **25,** 73-76.

Altherr R., Schliestedt M., Okrusch M., Seidel E., Kreuzer H., Harre W., Lenz H., Wendt I. and Wagner G.A., 1979. Geochronology of high-pressure rocks on Sifnos (Cyclades, Greece). *Contributions to Mineralogy and Petrology.* **70,** 245-255.

Anderson T.F., 1969. Self-diffusion of carbon and oxygen in calcite by isotope exchange with carbon dioxide. *Journal of Geophysical Research.* **76,** 3918-3932.

Arita Y., and Wada H., 1990. Stable isotopic evidence for migration of metamorphic fluids along grain boundaries of marbles. *Geochemical Journal,* **24,** 173-186.

Avé Lallemant H.G. and Guth L.R., 1990. Role of extensional tectonics in exhumation of eclogites and blueschists in an oblique subduction setting: Northeastern Venezuela. *Geology,* **18,** 950-953.

Avigad D., 1990. *The geodynamic evolution of the Cycladic blueshist belt (Aegean Sea, Greece) - a contribution to the study of continental collision.* Hebrew University of Jerusalem. Unpublished PhD thesis.

Aydin A., 1978. Small faults formed as deformation bands in sandstone. *Pure and Applied Geophysics.* **116,** 913-930.

Baker J.M., 1990. *Petrological and isotopic constraints on metamorphism and metamorphic fluid flow on Naxos, Greece.* Unpubl. Ph.D. thesis, University of Cambridge.

Baker J.M., Bickle M.J., Buick I.S., Holland T.J.B. and Matthews A., 1989. Isotopic and petrological evidence for the infiltration of water-rich fluids during the Miocene M2 metamorphism on Naxos, Greece. *Geochim. Comochimica Acta.* **53,** 2037-2050.

Baker J., and Matthews A., 1995. The stable isotopic evolution of a metamorphic complex, Naxos, Greece. *Contributions to Mineralogy and Petrology*. **120**, 391- 403.

Barber D.J., 1990. Regimes of plastic deformation-processes and microstructures: an overview. In: Deformation Processes in Minerals, Ceramics and Rocks. Barber D.J., and Meredith P.G. (eds). Unwin-Hyman, London, 138-171.

Barnicoat A.C., 1988. The mechansims of veining and retrograde alteration of alpine eclogites. *Journal of Metamorphic Geology*. **6,** 545-558.

Barr H. M., 1989. *Fluid-rock interactions during blueschist and greenschist metamorphism in the Aegean area of Greece*. Unpubl. Ph.D. thesis, Edinburgh University.

Barr H.M., 1990. Preliminary fluid inclusion studies in a high-grade blueschist terrain, Syros, Greece. *Mineralogical Magazine*. **54**, 159-168.

Barrientos X and Selverstone J., 1993. Infiltration vs. thermal overprinting of epidote blueschists, Ile de Groix, France. *Geology* **21**, 69-72.

Bebout G.E., and Barton M.D., 1993. Metasomatism during subduction:products and possible paths in the Catalina Schist, California. *Chemical Geology*, **108**, 61-92.

Bickle M.J., 1992. Transport Mechanisms by fluid-flow in metamorphic rocks - oxygen and strontium decoupling in the trois-seigneurs massif - a consequence of kinetic dispersion. *American Journal of Science,* **292,** 289-316.

Bickle M.J., and McKenzie D.P., 1987.The transport of heat and matter by fluids during metamorphism. *Contributions to Mineralogy and Petrology*. **95**, 384-392.

Bickle M.J., and Baker J.M., 1990a. Advective-diffusive transport of isotopic fronts: an example from Naxos, Greece. *Earth and Planetary Science Letters*. **97**, 78-93.

Bickle M.J., and Baker J.M., 1990b. Migration of reaction and isotopic fronts in infiltration zones: Assessments of fluid flux in metamorphic terrains. *Earth and Planetary Science Letters*. **98**, 1-13.

Bloor P.M., 1998. *Genesis and distribution of Ca-Al silicates in Aegean blueschists and implications for fluid flow in subduction zones*. Unpublished Ph.D. thesis, Edinbugh University.

Bröcker M., 1990. Blueschist-to-greenschist transition in metabasites from Tinos island, Cyclades, Greece: compositional control or fluid infiltration? *Lithos* **25**, 25-39.

Brown E.H., 1974. Comparison of the mineralogy and phase relations of blueschists from the North Cascades, Washington and greenschists from Otago, New Zealand. *Bulletin of the Geological Society of America*. **85,** 333-344.

Buick I.S., 1991. Mylonite fabric development on Naxos, Greece. *Journal of Structural Geology*, **13**, 643-655.

Cartwright I., 1997. Permeability generation and resetting of tracers during metamorphic fluid flow: implications for advection-dispersion models. *Contributions to Mineralogy and Petrology*, **129,** 198-208.

De Paor D.G., Simpson C., Bailey C.M., McCaffery K., Beam E., Gower R.J.W, and Aziz G., 1991. The role of solution in the formation of boudinage and traverse veins in carbonate rocks at Rheems, Pennsylvania. *Geological Society of America Bulletin*, **103**, 1552-1563.

Dickson J.D.D., 1966. Carbonate identification and genesis as revealed by staining. *Journal of Sedimentary Petrology.* 36, 499-505.

Dixon J. E., 1969. *The metamorphic rocks of Syros, Greece*. Unpubl. Ph.D. thesis, University of Cambridge.

Dixon J.E. and Ridley J., 1987. Excursion guide to field trip on Syros. In: H.C. Helgeson (ed) *Chemical Transport in Metasomatic Processes*, 489-518.

Dürr S., Altherr R., Keller J., Okrush M. and Seidel E., 1978. The median Aegean crystalline belt: stratigraphy, structure, metamorphism and magamatism. In Closs, H., Roeder, D. and Schmidt, K. (eds) *Alps, Appennines, Hellenides*. Stuttgart: Schweizerbart, 453-477.

Elsenheimer D. and Valley J.W., 1993. Submillimeter scale zoning of $\delta^{18}O$ in quartz and feldspar, Isle of Skye, Scotland. *Geochimica Cosmochimica Acta.* **57,** 3669-3676.

Elphick S.C., and Graham C.M., 1992a. Measurements of oxygen diffusivity in minerals under high pressure, high aH^+ conditions: applications to α-quartz. *EOS*, **73,** 373.

Elphick S.C., and Graham C.M., 1992b. The effect of pressure on the diffusion of oxygen in α-quartz. *Terra Abstracts*, **7,** 16.

Evans B.W., 1990. Phase-relations of epidote-blueschists. *Lithos.* **25,** 3-23.

Farver J.R., 1990. Oxygen self-diffusion in calcite: dependence on temperature and water fugacity. *EOS Trans AM Geophysical Union.* **71,** 1655.

Farver J.R., 1994. Oxygen self-diffusion on calcite - dependence on temperature and water fugacity. *Earth and Planetary Science Letters,* **121,** 575-587.

Faure G,. 1986. Principles of isotope geology. John Wiley, New York.

Fisher R.A., 1954. Statistical Methods for Research Workers, twelfth edition. Oliver and Boyd, London.

Fisher G.J. and Paterson M.S., 1989. Dilatancy during rock deformation at high temperatures and pressures. *Journal of Geophysical Research*, **94**, 17607-17617.

Freeman S.R., Butler R.W.H., Cliff R.A., Inger S, and Branicoat A.C., 1998a. Deformation migration in an orogen-scale shear zone array: an example from the Basal Briançonnais Thrust, internal Franco-Italian Alps. *Geological Magazine*, **135**, 349-367.

Freeman S.R., Butler R.W.H., Cliff R.A., and Rex D.C., 1998b. Direct dating of mylonite evolution; a multi-disciplinary geochronological study from the Moine Thrust Zone, NW Scotland. *Journal of the Geological Society*, **155**, 745-758.

Ganor J., Matthews A., and Paldor N., 1989. Constraints on effective diffusivity during oxygen isotope exchange at a marble-schist contact, Sifnos (Cyclades), Greece. *Earth and Planetary Science Letters*. **94**, 208-216.

Ganor J., Matthews A., Schliestedt M., and Garfunkel Z., 1996.Oxygen isotopic heterogeneities of metamorphic rocks: an original tectonostratigraphic signature, or an imprint of exotic fluids? A case study of Sifnos and Tinos islands (Greece). *European Journal of Mineralogy*. **8**, 719-732.

Gautier P., Brun J-P., and Jolivet L. 1993. Structure and kinematics of upper Cenozoic extensional detachment on Naxos and Paros (Cycaldes Islands, Greece). *Tectonics*, **12**, 1180-1194.

Graham C.M., Greig K.M., Sheppard S.M.F., and Turi B., 1983. Genesis and mobility of the H_2O-CO_2 fluid phase during regional greenschist and epidote amphibolite facies metamorphism: a petrological and stable isotope study in the Scottish Dalradian. *Journal of the Geological Society of London*, **140**, 577-579.

Graham C.M., Skelton A.D.L., Bickle M.J., and Cole C., 1997. Lithological, structural and deformation controls on fluid flow during regional metamorphism. In: Holness M.B., ed. Deformation-enhanced Fluid Transport in the Earth's crust and Mantle. The Mineralogical Society Series. **8**, 196-222.

Graham C.M., Valley J.W., Eiler J.M., and Hideki W., 1998. Timescales and mechanisms of fluid infiltration in a marble: an ion microprobe study. *Contributions to Mineralogy and Petrology*, **132**, 371-389.

Grant J.A., 1986. The isocon diagram - A simple solution to the Gresens equation for metasomatic alteration. *Economic Geology*. **81,** 1976-1982.

Gresens R.L., 1967. Composition-volume relationships of metasomatism. *Chemical Geology*. **2,** 47-55.

Groshong R.H., 1988. Low-temperature deformation mechanisms and their interpretation. *Geological Society of America Bulletin*, **100**, 1329-1360.

Grütter H.S., 1993. Structural and metamorphic studies on Ios, Cyclades, Greece. University of Cambridge, *unpublished PhD thesis*.

Hacker B.R., Ratschbacher L., Webb L., and Shuwen D., 1995. What bought them up? Exhumation of the Dabie Shan ultrahigh-pressure rocks. *Geology*, **23**, 743-746.

Hadizadeh J., 1994. Interaction of Catclasis and Pressure Solution in a Low-temperature Carbonate Shear Zone. *Pageoph,* **143,** 255-280.

Hatzfeld D., Pedotti G., Hatzidimitrou P and Makropoulos K., 1990. The strain pattern in the western Hellenic arc deduced from a microearthquake survey. *Geophysical Journal International.* **101**, 181-202.

Hofmann A.W., 1972. Chromatographic theory of infiltration metasomatism and its applications to feldspars. *American Journal of Science,* **272**, 69-90.

Holness M.B., and Graham C.M., 1995. P-T-X effects on equilibrium carbonate H2O-CO2-NaCl dihedral angles: constraints on carbonate permeability and the role of deformation during fluid infiltration. *Contributions to Mineralogy and Petrology*, **119**, 301-313.

Hunt J.A., and Kerrick D.M., 1977. The stability of sphene; experimental redetermination and geological implications. *Geochemica et Cosmochimica Acta.* **41,** 279-288.

Inger S., Ramsbotham W., Cliff R.A., and Rex D.C., 1996. Metamorphic evolution of the Sesia-Lanzo Zone, Western Alps: time constraints from multisystem geochronology. *Contributions to Mineralogy and Petrology*, **126**, 152-168.

Jackson J., 1994. Active tectonics of the Aegean region. *Annual Review of Earth and Planetary Science Letters.*, **22**, 239-271.

Javoy M., Fourcade S., and Allegre C.J., 1970. Graphical method for examination of $^{18}O/^{16}O$ fractionations in silicate rocks. *Earth and Planetary Science Letters.* **10,** 12-16.

Jolivet L., Daniel, M., Truffert, C., and Goffé B, 1994. Exhumation of deep crustal metamorphic rocks and crustal extension in back-arc regions. *Lithos*, **33**, 3-30.

Jolivet L., Goffé B., Moiné P., Truffert-Luxey, C., Patriat, M., and Bonneau M., 1996. Miocene detachment in Crete and exhumation P-T-t paths of high pressure metamorphic rocks. *Tectonics*, **15**, 1129-1153.

Jolivet L., Faccena C., Goffé B., Mattei M., Rosetti F., Burnet C., Storti F., Funiciello R., Cadet J., d'Agostino N., and Parra T., 1998. Midcrustal shear zones in postorogenic extension: Example from the northern Tyrrhenian Sea. *Journal of Geophysical Research*, **103**, 12123-12160.

Keith M.L., and Weber J.N., 1964. Carbon and oxygen isotopic composition of selected limestones and fossils. *Geochimica et Cosmochimica Acta*. **28**, 1787-1816.

Knipe R.J., 1989. Deformation mechanisms - recognition from natural tectonites. *Journal of Structural Geology*, **11**, 127-146.

Knipe R.J., 1990. Microstructural analysis and tectonic evolution in thrust systems:examples from the assynt region of the Moine Thrust Zone, NW Scotland. In: Barber, D.J. and Meredith, P.G. (eds) Deformation Processes in Minerals, Ceramics and Rocks. The Mineralogical Society Series, **1**, 228-259.

Knipe R.J., 1993. The influence of fault processes on fluid flow and diagenesis. In: Horbury, E.D., and Robinson, A.G. (eds) Diagenesis and Basin development. American Association of Petroleum Geologists Studies in Geology, 36, 135-154.

Knipe R.J., and White, S.H., 1979. Deformation in low grade shear zones in the O.R.S. from S.W. Wales. *Journal of Structural Geology*, **1**, 53-66.

Knipe R.J., and McCaig A.M., 1994. Microstructural and microchemical consequences of fluid flow in deforming rocks. Geological Society Special Publication, 78, 99-111.

Kornprobst J., Kienast J.-R. and Violminot J.-C., 1979. The high-pressure assemblages at Milos, Greece. A contribution to the petrological study of the basement of the Cyclades archipelago. *Conributions to Mineralogy and Petrology*. **69**, 49-63.

Lewis S., Holness M., and Graham C., 1998. Ion microprobe study of marble from Naxos, Greece: Grain-scqale fluid pathways and stable isotope equilibration during metamorphism. *Geology.* **26**, 935-938.

Liou J.G., and Maruyama S., 1987. Parageneses and compositions of amphibole from Franciscan jadeite-glaucophane type facies series metabasites at Cazadero, California. *Journal of Metamorphic Geology.* **5,** 371-395.

Liou J.G., Maruyama S. and Cho S., 1987. Very low-grade metamorphism of volcanic and volcaniclastic rocks: mineral assemblages and mineral facies. In: Frey, M. (ed) *Low temperature metamorphism.* London:Blackie, 59-113.

Lister G.S., and Banga G., and Feenstra A., 1984. Metamorphic corre complexes of Cordillerean type in the Cyclades, Aegean Sea, Greece. *Geology.* **12**, 221-225.

Lloyd G.E., and Knipe R.J., 1992. Deformation mechanisms accommodaating faulting of quartzite under upper crustal conditions. *Journal of Structural Geology.* **14,** 127-144.

Losh S., 1997. Stable isotope and modeling studies of fluid-rock interaction associated with the Snake Range and Mormon peak detachment faults, Nevada. *Geological Society of America Bulletin.* **109,** 300-323.

Marshall D.J., 1988. Cathodoluminesence of geologic materials. Unwin Hyman, London.

Maruyama S., Cho M. and Liou J.G., 1986. Experimental investigations of blueschist-greenschist transition equilibria: pressure dependence of Al_2O_3 contents in sodic amphiboles-a new geobarometer. *Geological Society of America Memoirs*, **164**, 1-16.

Matthews A., and Schliestedt M., 1984. Evolution of the blueschist and greenschist facies rocks of Sifnos, Cyclades, Greece: a stable isotope study of subduction related metamorphism. *Contributions to Mineralogy and* Petrology. **88**, 150-163.

McCaig A.M., 1984. Fluid-rock interaction in some shear zones from the Pyrennes. *Journal of Metamorphic Geology*, **2**, 129-141.

McCaig A.M., 1988. Deep fluid circulation in fault zones. *Geology*, **16**, 867-877.

McCaig A.M., 1989. Geology-fluid-flow through fault zones. *Nature*. **340,** 600.

McCaig A.M., and Knipe R.J., 1990. Mass-transport mechanisms in deforming rocks: Recognition using microstructural and microchemical criteria. *Geology*, **18**, 824-827.

McCaig A.M., Wayne D.M., Marshall J.D., 1995. Isotopic and fluid inclusion studies of fluid movement along the Gavernie Thrust, central Pyrenees: reation fronts in carbonate mylonites. *American Journal of Science*. **295**, 309-343.

Mullenaux A.C., and Gray D.R., 1984. Interaction of bed-parallel stylolites and extension veins in boudinage. *Journal of Structural Geology*, **6**, 63-71.

Nitsch K., 1972. Das P-T-X_{CO2} stabilitätsfeld von lawsonit. *Contributions to Mineralogy and Petrology*. **34,** 116-134.

Nitsch K., 1974. Neve Erkentnisse zur Stabilität von Lawsonit. *Fortschr Mineral*. **51,** 34-35.

Okrusch M. and Bröcker M., 1990. Eclogites associated with high-grade blueschists in the Cyclades archipelago, Greece: a review. *European Journal of Mineralogy*. **2**, 451-478.

Oliver N.H.S., 1996. Review and classification of structural controls on fluid flow during regional metamorphism. *Journal of Metamorphic Geology*, **14**, 477-492.

Olsen S.N., and Grant J.A., 1991. Isocon analysis of migmatisation in the front range, Colorado, USA. *Journal of Metamorphic Geology*. **9,** 151-164.

Peacock S.M., 1990. Fluid processes in subduction zones. *Science*, **248**, 329-337.

Platt J.P., and Vissers R.L.M., 1980. Extensional structures in anisotropic rocks. *Journal of Structural Geology*, **2**, 397-410.

Pognante U., 1989. Lawsonite, blueschist and eclogite formation in the southern Sesia zone (western Alps, Italy). *European Journal of Mineralogy*. **1**, 89-104.

Ramsay J.G., 1980. The crack-seal mechanism of rock deformation. *Nature,* **284,** 135-139.

Ramsay J.G., and Huber M.I., 1983. The Techniques of Modern Structural Geology, volume 1, strain analysis. Academic Press, London.

Ridley J.R., 1982a. *Tectonic style, strain history, and fabric development in a blueschist terrain, Syros, Greece.* Unpublished. Ph.D., University of Edinburgh.

Ridley J.R., 1982b. Arcuate lineation trends in a deep level, ductile thrust belt, Syros, Greece. *Tectonophysics* **88**, 347-360.

Ridley J, 1984a. The significance of deformation associated with blueschist facies metamorphism on the Aegean island of Syros. In: Dixon, J.E., and Robertson, A.H.F., (eds.) *The geological evolution of the eastern mediterranean.* Spec. Publ. Geol. Soc. Lond., **17**, 545-551.

Ridley J., 1984b. Listric normal faulting and the reconstruction of the synmetamorphic structural pile of the Cyclades. In: Dixon, J.E., and Robertson, A.H.F., (eds.) *The geological evolution of the eastern mediterranean.* Spec. Publ. Geol. Soc. Lond., **17**, 755-761.

Ridley J., 1986. Parallel stretching lineations and fold axes oblique to a shear displacement direction-a model and observations. *Journal of Structural Geology.* **8**, 647-653.

Ridley J. and Dixon J.E., 1984. Reaction pathways during the progressive deformation of a blueschist metabasite: the role of chemical disequilibrium and restricted range equilibrium. *Journal of Metamorphic Geology.* **2**, 115-128.

Robertson A.H.F. and Dixon J.E., 1984. Introduction: aspects of the geological evolution of the eastern mediterranean. In: Dixon, J.E. and Robertson, A.H.F., (eds) *The geological evolution of the eastern mediterranean.* Spec. Publ. Geol. Soc. Lond., **17**, 755-761.

Rumble D., Ferry J.M., Hoerring T.C., Boucot A.J., 1982. Fluid flow during metamorphism at the Beaver Brook fossil locality, New Hampshire. *American Journal of Science*, **282**, 886-919.

Rutter E.H., 1983. Pressure solution in Nature, Theory and Experiment. *Journal of the Geological Society*, **140**, 725-740.

Rutter E.H., and Brodie K.H., 1995. Mechanistic inteactions between deformation and metamorphism. *Geological Journal*, **30**, 227-240.

Rye R.O., Schuiling R.D., Rye D.M., Jansen J.B.H., 1976. Carbon, hydrogen, and oxygen isotope studies of the regional metamorphic complex at Naxos, Greece. *Geochimica et Cosmochima Acta.* **40**, 1031-1049.

Rye D.M., and Bradbury H.J., 1988. Fluid flow in the crust: An example from a Pyrenean thrust ramp. *American Journal of Science,* **288,** 197-235.

Satish-Kumar M., Yoshida M., Wada H., Niitsuma N., and Santosh M., 1998. Fluid flow along microfractures in calcite from a marble from East Antarctica: Evidence from gigantic (21‰) oxygen isotopic zonation. *Geology.* **26**, 251-254.

Schermer E.R., 1990. Mechanisms of blueschist creation and preservation in an A-type subduction zone, Mount Olympus region, Greece. *Geology,* **18**, 1130-1133.

Schliestedt M., and Matthews A., 1987. Transformation of blueschist to greenschist facies rocks as a consequence of fluid infiltration, Sifnos (Cyclades), Greece. *Contributions to Mineralogy and Petrology.* **97**, 237-250.

Schliestedt M., Altherr R. and Matthews A., 1987. Evolution of the Cycladic crystalline complex: petrology, isotope geochemistry and geochronology. In: Helgeson, H.C. and Schuiling, R.D. (eds.) *Chemical transport in metasonamtic processes*. Reidel Publishing Company, 389-428.

Schuiling R.D., and Vink B.W., 1967. Stability relations of some titanium minerals (sphene, pervoskite, rutile, anastase). *Geochimica et Cosmochimica Acta.* **31,** 2399-2411.

Sharp Z., 1990. A laser based microanalytical method for in situ determinations of oxygen isotope ratios of silicates and oxides. *Geochimica et Cosmochima Acta.* **54**, 1353-1357.

Sharp Z., 1992. In situ laser microprobe techniques for stable isotope analysis. *Chemical Geology.* **101**, 3-19.

Sharp Z.D., and Kirschner D.L., 1994. Quartz-calcite isotope thermometry: A calibration based on natural isotopic variations. *Geochimica et Cosmochimica Acta.* **58**, 4491-4501.

Sheppard S.M.F., 1986. Characterization and isotopic variations in natural waters. In: Valley J.W., Taylor H.P. (JR), O'Neil J.R., (eds). Stable isotopes in high temperature geological processes. *Reviews in Mineralogy.* **16**, 165-184.

Skelton A.D.L., Graham C.M., and Bickle M.J., 1995. Lithological and structural controls on regional 3-D fluid flow patterns during greenschist facies metamorphism of the Dalradian of tyhe SW Scottish Highlands. *Journal of Petrology*, **36**, 563-586.

Skelton A.D.L., Bickle M.J., Graham C.M., 1997 Fluid-flux and reaction rate from advective-diffusive carbonation of mafic sill margins in the Dalradian, southwest Scottish Highlands. *Earth and Planetary Science Letters*, **146,** 527-539.

Slodzian G., 1980. Microanalyzes using secondary ion emission. In: Advances in Electronics and Electron Physics, 1-44. Academic press.

Smith D.L., and Evans B., 1984. Diffusional crack healing in quartz. *Journal of Geophysical Research.* **89,** 4125-4136.

Taylor H. P., JR. and Coleman R.G., 1968. O^{18}/ O^{16} Ratios of coexisting Minerals in Glaucophane-Bearing Metamorphic. *Geological Society of America Bulletin.* **79**, 1727-1756.

Taymaz T., Jackson, J and McKenzie, D., 1991. Active tectonics of the north and central Aegean sea. *Geophysical Journal International.* **106**, 433-490.

Tucker M.E., 1992. Sedimentary Petrology an introduction to the origin of sedimentary rocks. Second Edition. Blackwell Scientific Publications, Oxford.

Urai J.L., Schuiling R.D., and Jansen J.B.H., 1990. Alpine deformation on Naxos (Greece). In: *Deformation mechanisms, Rheology and Tectonics*. Knipe R.J., and Rutter E.H., (eds). Geological Society Special Publication, **54**, 509-522.

Valley J.W., and Graham C.M., 1991. Ion microprobe analysis of oxygen isotope ratios in granulite facies magetites: diffusive exchange as a guide to cooling history. *Contributions to Mineralogy and Petrology*. **109,** 38-52.

Van der Maar P.A., 1981. Metamotrphism on Ios and the geological history of the southern Cyclades,Greece. *Geologica Ultrajectina* **28**,1-142.

Wada H,. 1988. Microscale isotopic zoning in calcite and graphite crystals in marble. *Nature*. **331**, 61-63.

Walker A.N., Rutter E.H., and Brodie K.H., 1990. Experimental study of grain size sensitive flow of synthetic, hot-pressed calcite rocks. In: Knipe R.J., and Rutter E.H. (eds) Deformation Mechanisms, Rheology and Tectonics. Geological Society Special Publication, 54, 259-282.

Walther J.V., and Orville P.M., 1982. Volatile Production and Transport in Regional Metamorphism. *Contributions to Mineralogy and Petrology*. **79,** 252-257.

Watkins K.P., Petrogenesis of Dalradian albite porphyroblast schists. *Journal of the Geological Society.***140,** 601-618.

Wheeler J., 1991. Structural evolution of a subducted continental sliver: the northern Dora Maira massif, Italian Alps. *Journal of the Geological Society, London*, **148**, 1101-1113.

Wijibans J.R. Schliestedt M. and York D., 1990. Single grain argon lasert probe dating of phengites from the blueschist to greenschist transition on Sifnos (Cyclades, Greece). *Contributions to Mineralogy and Petrology*. **104**, 582-593.

Yardley B.W.D., 1989. An Introduction to Metamorphic Petrology. Longman Earth Science Series, New York.

Yardley B.W.D., and Lloyd G.E., 1989. An application of cathodoluminescence microscopy to the study of textures and reactions in high-grade marbles from Connemara, Ireland. *Geological Magazine*, **126**, 333-337.

Zheng Y.F., and Fu B., 1998. Estimation of oxygen diffusivity from anion porosity in minerals. *Geochemical Journal*. **32,** 71-89.